

# **Novel Miniaturised and Highly Versatile Biomechatronic Platforms for the Characterisation of Melanoma Cancer Cells**

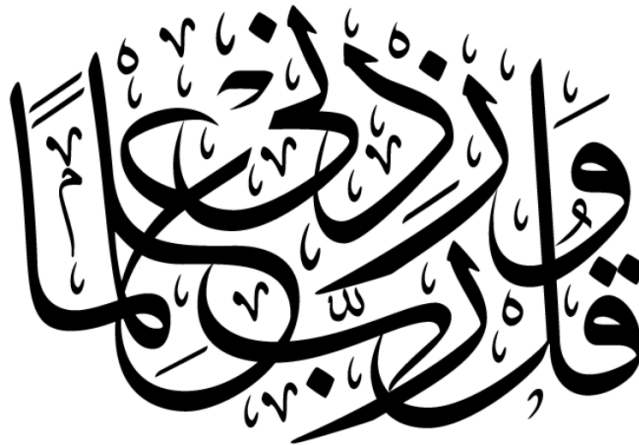
*Author*

**Jassim A. Alqabandi  
CID: 00665978**

**A thesis submitted for  
the degree of Doctor of Philosophy**

**Department of Mechanical Engineering  
Mechatronics in Medicine Laboratory  
Imperial College London**

**May 2014**



**“O my Lord! Advance me in Knowledge”  
[Quran, surah Ta-Ha; 20:114]**

## **Statement of own work**

**I declare that the work presented within this thesis is my own work except where otherwise acknowledged and appropriately referenced.**

**Jassim A. Alqabandi**

**‘The copyright of this thesis rests with the author and is made available under a Creative Commons Attribution Non-Commercial No Derivatives licence. Researchers are free to copy, distribute or transmit the thesis on the condition that they attribute it, that they do not use it for commercial purposes and that they do not alter, transform or build upon it. For any reuse or redistribution, researchers must make clear to others the licence terms of this work’**

This work is dedicated to my Mum, Aunt Salwa, the spirits of my Sister Amal and Grandmother Fatemah, whose suffers and battles against cancer have greatly motivated me and made me more persistent to complete this multidisciplinary work with passion in seeking knowledge and overcoming all study obstacles. This is to a very special person to me, Rawan Elabd

This work is also dedicated to those who think way above the ordinary, not embarrassed to express themselves out despite people's discouragements, and to those who believe in themselves and that science various disciplines do overlap and converge.



# Abstract

There has been an increasing demand to acquire highly sensitive devices that are able to detect and characterize cancer at a single cell level. Despite the moderate progress in this field, the majority of approaches failed to reach cell characterization with optimal sensitivity and specificity. Accordingly, in this study highly sensitive, miniaturized-biomechatronic platforms have been modeled, designed, optimized, microfabricated, and characterized, which can be used to detect and differentiate various stages of melanoma cancer cells. The melanoma cell has been chosen as a legitimate cancer model, where electrophysiological and analytical expression of cell-membrane potential have been derived, and cellular contractile force has been obtained through a correlation with micromechanical deflections of a miniaturized cantilever beam. The main objectives of this study are in fourfold: (1) to quantify cell-membrane potential, (2) correlate cellular biophysics to respective contractile force of a cell in association with various stages of the melanoma disease, (3) examine the morphology of each stage of melanoma, and (4) arrive at a relation that would interrelate stage of the disease, cellular contractile force, and cellular electrophysiology based on conducted *in vitro* experimental findings. Various well-characterized melanoma cancer cell lines, with varying degrees of genetic complexities have been utilized.

In this study, two-miniaturized-versatile-biomechatronic platforms have been developed to extract the electrophysiology of cells, and cellular mechanics (mechanobiology). The former platform consists of a microfluidic module, and stimulating and recording array of electrodes patterned on a glass substrate, forming multi-electrode arrays (MEAs), whereas the latter system consists of a microcantilever-based biosensor with an embedded Wheatstone bridge,

and a microfluidic module. Furthermore, in support of this work main objectives, dedicated microelectronics together with customized software have been attained to functionalize, and empower the two-biomechatronic platforms. The bio-mechatronic system performance has been tested throughout a sufficient number of *in vitro* experiments.

# Acknowledgements

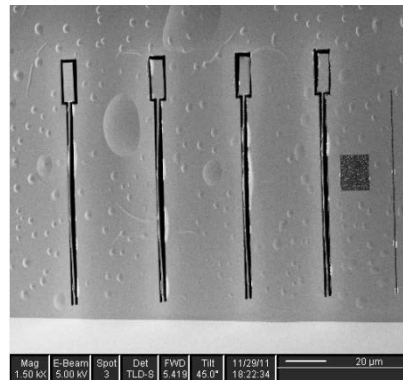
It goes without saying that I'm entirely in debt to my beloved family, especially my mother and aunt Salwa, for their valuable support and inspiration. Furthermore, I'm highly appreciative to Prof. Ejaz Huq, Rutherford Appleton Laboratory (UK), and Prof. Philip Prewett, Birmingham University, for the interactive discussion in terms of microfabrication, and allowing me to fabricate alpha prototypes of my designed cantilevers at their premises (Figure I).

I'm very much grateful for the kind review, and valuable comments received from Prof. Ali Nayfeh, and Dr. Khaled Hazza in terms of nonlinear dynamics aspect of my research. I am indebted to all great scholars who have been in full support of my research especially those at Harvard Medical School, Dana-Farber Cancer Institute, Massachusetts General Hospital (MGH), and my former professors at Massachusetts Institute of Technology (MIT), among them Prof. Kamal Youcef-Toumi, for being solid reviewers of my research and work.

I have been fortunate enough to transmit the motivations of my research to great scholars in respective fields of engineering as well as medical, whose interests overlapped with my research objectives, who have thankfully believed in me! This is manifested first by the widely welcoming open arm that I have received by the kind hospitality of Prof. Ivo W. Rangelow, who has accepted me, together with his lovely team, in his state-of-the-art nano/microfabrication lab at Ilmenau University in Germany, to implement my design, and perform my microfabrication. Similarly, I could never trade the friendship that I have established with Nikolay Nikolov and Stancho Staneve, when I have started working in implementing my microelectronics design. Also, I would like to express my utmost and sincere

appreciation to Dr. Rhiannon David from London Imperial College, Surgery and Cancer department, for her kind support. I would like to thank Rhiannon for her patience, especially when I was going through cell culturing with her. I am also so grateful to Dr. Ussama M. Abdel Mutaal (Dana-Farber Cancer Institute, Harvard Medical School) for his kind review of the bio-aspect of my Ph.D. research. My appreciation goes to Prof. John Dear for being my assessor for the past wonderful years at Imperial College.

Finally, my countless gratitude goes to my advisors Dr. Ferdinando Rodriguez Y Baena, and Dr. Daniel S. Balint for their outstanding patience, kind support of my research, and believing in me to produce the proposed biomechatronic platforms, and my highest appreciation goes to Ms. Nora Al-Seleti, College of Medicine, English Dept. at Kuwait University, for editing and reviewing this work.



**Fig. I** Scanning Electron Microscope (SEM) image of a focused ion beam (FIB) processed Beam-Plate structure of an alpha prototype of the microfabricated-cantilever beam coupled to a plate utilized to initially investigate pull-in phenomena: A proof-of-concept experiment was conducted by inducing a static potential by a voltage generator (Agilent E3611A).

# Contents

Abstract	5
Acknowledgements	7
List of Figures	12
List of Tables	20
List of Uploaded Movies	21
List of Publications	24
<b>1 Introduction</b>	27
1.1 Research Motivations	27
1.2 Cancer Biology Overview	29
1.3 Significance of Melanoma Model	33
1.4 Cancer Detection: Limitations of Conventional Approaches	35
1.5 Research Aims	37
1.6 Research Structure	38
1.7 Conclusion	42
<b>2 Lab-on-a-Chip (LoC)</b>	46
2.1 System Overview	46
2.2 Integrated Microfluidic ( $\mu$ F) System	48
2.2.1 Design Synthesis	48
2.2.1.a System Perfusion	49
2.2.1.b Mimicking <i>In Vivo</i> Environment	51
2.2.1.c Thermal Stability and pH Neutralization	56
2.2.1.d Elimination of Air Pockets	57
2.2.1.e Sufficient Supply of Oxygen	58
2.2.2 Anticipated Objectives of the $\mu$ F System	59
2.2.3 System Level Design ( $\mu$ F Flow)	61
2.2.3.a $\mu$ F Model	62
2.2.3.b CFD: $\mu$ F System Characterization	63
2.3 Integrated Multi Electrode Arrays (iMEAs)	65
2.3.1 Electric Field Cell Manipulation	66
2.3.2 Capturing the Electrophysiology of Cells	68
2.3.3 MEA Configuration	69
2.3.4 System Level Design and Characterization: MEA	69
2.4 Conclusion	72
<b>Chapter 3: Electrophysiology of Cells</b>	77
3.1 Introduction: Electrochemical vs. SAW/Optical Approach	77
3.2 Cell-Membrane Potential: The Electrochemical Approach	79
3.3 Relevant Literature on Cancer Electrophysiology	82
3.4 Mathematical Modeling of a Biological Cell: Analytical Approach	89
3.4.1 Overview	89
3.4.2 Mathematical Model	92
3.5 Empirical Solution	117
3.6 Discussion of Results	126
3.7 Conclusion and Future Outlook	132
<b>Chapter 4: A Miniaturized Biomechatronic Electrophysiology Based Platform</b>	137
4.1 Related Work	137
4.1.1 Dermatological Conventional Prognosis Approach: Pattern Recognition and CAD System for Melanoma Detection	138

4.1.2 Non-Conventional Dermatological Approaches in Detecting Melanoma.....	140
4.2 Research Specific Approach.....	143
4.3 Construction of the Biomechatronic Electrophysiology Based Platform.....	144
4.3.1 Microfabrication of the Mechanical Structure.....	144
4.3.2 Microelectronics Architecture.....	147
4.3.3 The Electrochemical Bio-Mechatronic Platform Operating Software.....	152
4.4 The Biological Model: The Rationale Behind the Selection of the Melanoma Cell Lines.....	155
4.5 Materials and Methods.....	159
4.5.1 Cell Culturing Protocol and Growth Inhibition.....	159
4.5.2 Cell Viability Check, Serial Dilution, and System Sterilization.....	161
4.5.3 <i>In Vitro</i> Experiments.....	163
4.6 Results and Discussion.....	165
4.7 Conclusion.....	168
<b>Chapter 5: Experimental Setup of a Label-Free Microcantilever-Based-Biomass Sensor: Investigating the Effect of Pull-In Phenomena on Sensitivity</b>	172
5.1 Introduction: Versatility Applications of Cantilever-Based Sensors.....	172
5.2 Merits of Cantilever-Based Sensors in Cancer Research.....	174
5.3 Physical Phenomena (Theoretical Background).....	177
5.4 Pull-In Phenomena.....	179
5.5 Analytical Representation of the DC Pull-In Phenomenon.....	181
5.5.1 System Kinematics and Kinetics.....	183
5.5.2 Static Mode Analysis.....	186
5.6 Microfabrication of the Biomass Sensor Mechanical Structure.....	188
5.7 Microelectronic Architecture.....	194
5.8 The $\mu$ -Cantilever Based Bio-Mechatronic Platform Operating Software.....	197
5.9 <i>In Vitro</i> Experiments: Materials and Methods.....	200
5.10 Results and Discussion.....	204
5.11 Conclusions and Future Prospective.....	210
<b>Chapter 6: <i>In Vitro</i> Real-Time Characterization of Melanoma Contractile Force via a Self-Probing Cantilever-Based Biomechatronic Platform</b>	214
6.1 Introduction.....	214
6.2 Different Approaches in Quantifying the Contractile Force of Cells.....	218
6.3 Cantilever-Based N/MEMS platform.....	221
6.4 Mathematical Modeling.....	222
6.5 Materials and Methods.....	227
6.6 Results and Discussions.....	229
6.7 Conclusion and Future Trends.....	238
<b>Chapter 7: Overall Summary, Conclusions, and Future Work</b>	242
<b>References</b>	246
<b>Appendices</b>	270
<b>Appendix A: Glossary</b>	270
<b>Appendix B: Nomenclature</b>	275
<b>Appendix C: Numerical Algorithms</b>	279
C.1 Chapter 3: Cell-Membrane Potential.....	280
C.1.1 Maple Algorithm.....	281
C.1.2 Matlab M File.....	283
C.2 Chapter 5: Pull-In Phenomena.....	285
C.3 Chapter 6: Cellular Contractile Force.....	346
<b>Appendix D: Microelectronic Hardware Architecture</b>	351

D.1 Chapter 4: Electrochemical Biomechatronic Platform.....	351
D.2 Chapter 5: Mechanobiology Biomechatronic Platform.....	354
<b>Appendix E: Customized Controlling Software Manuals</b>	356
E.1 Chapter 4: Electrochemical Biomechatronic Platform.....	356
E.2 Chapter 5: Mechanobiology Biomechatronic Platform.....	362
<b>Appendix F: Pull-In Phenomena (Detailed Derivations)</b>	371
F.1 Model Formulation.....	372
F.2 Analytical Representation: A Quantitative Approach.....	374
F.3 Static Mode Analysis: Pull-In Phenomenon.....	382
F.4 Sensitivity analysis.....	386
F.5 Optimization of the Controlling Parameters.....	389
<b>Appendix G: Reprint Permission</b>	393

# List of Figures

Fig.	Title	Page No.
<b>Fig. I</b>	Scanning Electron Microscope (SEM) image of a focused ion beam (FIB) processed Beam-Plate structure of an alpha prototype of the microfabricated-cantilever beam coupled to a plate utilized to initially investigate pull-in phenomena: A proof-of-concept experiment was conducted by inducing a static potential by a voltage generator (Agilent E3611A).	8
<b>Fig. 1.1</b>	(A) 3-D image of a B16-F10 mouse melanoma cancer cell, (B) Cross-sectional analysis of the B16-F10 cell obtained by an Atomic Force Microscope (AFM).	30
<b>Fig. 1.2</b>	Retinal melanoma formation (Courtesy of Prof. Bertil Damato, Liverpool Ocular Oncology Service).	33
<b>Fig. 1.3</b>	Overlapped research field components in forming a miniaturized bio-mechatronic platform.	38
<b>Fig. 1.4</b>	Structure of the Ph.D. research in investigating cellular biophysics and mechanobiology.	41
<b>Fig. 2.1</b>	A micrograph of 1-mm-diameter-culturing reservoir with perfusion channels prior to adherent to a glass substrate. High aspect ratio design. (a) SEM picture of a single unit of the arrayed device before bonding. Multiple perfusion channels surround the main culture chamber. The microchamber is 40 $\mu\text{m}$ in height with a diameter of 1 mm. Each culture unit has four fluidic access paths. (b) SEM image of perfusion channel dimensions. Each perfusion channel had a width and height of 2 $\mu\text{m}$ – Reproduced with text caption from [55] with permission from the Royal Society of Chemistry.	49
<b>Fig. 2.2</b>	A 3D matrix of central gel cage for cell culturing illustrating <i>in vivo</i> tissue engineering. (a) $\mu\text{F}$ domain consisting of two parallel channels and a central gel cage. (b) Scaffold loading protocol. (c) Microinjection station in sterile laminar flow cell culture hood. (d) Micrograph of assembled $\mu\text{F}$ domain – Reproduced with summarized text caption from [61], with permission of Prof. Roger Kamm, Biological/Mechanical Engineering Dept., Massachusetts Institute of Technology (MIT), and with permission from the Royal Society of Chemistry.	54
<b>Fig. 2.3</b>	Requirements of cell viability by supplying sufficient oxygen rate and nutrition, elimination of air pockets, providing neutralized acidity and thermal	60



	stability environment, removal of wastes and insoluble cell debris, and carbon dioxide from the flow system.	
<b>Fig. 2.4</b>	(A) Pressure at walls and velocity field in the microchannel at $t = 4$ sec, (B) Velocity profile distribution at the neck exit of the culturing reservoir and into the channel, (C) Built-up pressure at sharp edges, (D) Gaussian Poiseuille velocity profile within the microchannel, and (E) Pressure at minimum and velocity distribution at the exit reservoir.	64
<b>Fig. 2.5</b>	(a) Empirical analyses of a stimulated working electrode and recording reference electrode, (b) potential gradient distribution within the electrical field between working and reference electrode, and (c) enlargement of the small dotted circled section showing a uniform current distribution between the two electrodes within a $\mu\text{F}$ channel.	72
<b>Fig. 2.6</b>	(A) A top view of the LoC module with two-sterling British ponds as a scaling factor (B) An image showing connecting pins of culturing and outlet reservoir, and gold plated upper and lower MEAs patterned on two glass substrates (upper and lower) which are crossing the microfluidic channels.	74
<b>Fig. 3.1</b>	Non-conventional methods in studying the characteristics of cells: (A) SAW based sensor, (B) Optical Fluorescent Sensor, (C) Patch Clamp Method, and (D) N/MEMS technology consisting of a microfluidic and multi-electrode-array domain.	82
<b>Fig. 3.2</b>	S-Shaped curve (Phase I-III) together with logarithmic decline curve illustrating the different phases of cell growth versus time. A microscopic image of A375 melanoma cell is taken during the exponentially growing line in Phase II, where other images are just illustrative (non-real) of the different status of cell growth: initial cell growth (Phase I), steady state growth attributable to lack of nutrients (Phase III), and cellular death due to diminishing of cell viability requirements (Phase IV).	87
<b>Fig. 3.3</b>	(A) A biological cell with its 3 distinctive regions: cell membrane, extracellular, and intracellular region (B) Exploded view of the cell membrane, where cellular arrays of phospholipid bilayer are shown in (C). In (D), an electric circuit representation of a series of parallel RC circuits experienced within a cell membrane, where cell-membrane resistance is denoted as $R_m (\Omega)$ , cell-membrane capacitance is denoted as $C_m (F)$ , $R_i$ is the longitudinal internal resistance ( $\Omega$ ), $R_o$ is the longitudinal resistance of current flow ( $\Omega$ ), $R_e$ is the resistance of physiological medium ( $\Omega$ ), $R_w$ is the Warburg resistance ( $\Omega$ ), $C_w$ is the Warburg capacitance ( $F$ ), and $I_{in}$ is the effective current injection from an electrode ( $A$ ). (E) A microscopic image of a population of liver cells showing cell membrane, cytoplasm, and nucleus, which is a very kind courtesy of Dr. John Patrick, Consultant and head of Histopathology, Amiri Hospital Clinical Laboratories.	94

<b>Fig. 3.4</b>	Differential Element of a resistor.	100
<b>Fig. 3.5</b>	Case I. All essential parameters equal to unity, (A-C) cell-membrane potential ( $V_m$ ) with respect to spatial (X) and time (T) profiles.	120
<b>Fig. 3.6</b>	Case II. ( $\kappa = 0.25$ , $v = 2\sqrt{2}$ , $\mu$ is fixed), (A-C) cell-membrane potential ( $V_m$ ) with respect to spatial (X) and time (T) profiles.	121
<b>Fig. 3.7</b>	Case II. ( $\kappa = 0.5$ , $v = 2$ , $\mu$ is fixed), (A-C) cell-membrane potential ( $V_m$ ) with respect to spatial (X) and time (T) profiles.	122
<b>Fig. 3.8</b>	Case II. ( $\kappa = 2$ , $v = \sqrt{6}$ , $\mu$ is fixed), (A-C) cell-membrane potential ( $V_m$ ) with respect to spatial (X) and time (T) profiles.	123
<b>Fig. 3.9</b>	Case III. ( $\mu = 3$ , $v = \sqrt{3}$ , $\kappa$ is fixed), (A-C) cell-membrane potential ( $V_m$ ) with respect to spatial (X) and time (T) profiles.	124
<b>Fig. 3.10</b>	Case III. ( $\mu = 6$ , $v = \sqrt{6}$ , $\kappa$ is fixed), (A-C) cell-membrane potential ( $V_m$ ) with respect to spatial (X) and time (T) profiles.	125
<b>Fig. 3.11</b>	Case III. ( $\mu = 9$ , $v = 3$ , $\kappa$ is fixed), (A-C) cell-membrane potential ( $V_m$ ) with respect to spatial (X) and time (T) profiles.	126
<b>Fig. 3.12</b>	Numerical result of cell-membrane potential ( $V_m$ ) vs. temporal profile (T) based on non-ideal/arbitrary selected parameters ( $\mu = 9$ , $v = 3$ , $\kappa$ is fixed) due to lack of experimental findings of intracellular and extracellular resistive values to illustrate the different phases of cellular potentials: polarization, depolarization, repolarization, and hyperpolarization.	129
<b>Fig. 4.1</b>	3D illustrations and assembling of the proposed $\mu$ -structure consisting of two upper and lower glass substrates and a microfluidic domain. An array of gold electrodes are patterned on the glass substrates. The upper glass substrate is drilled at two locations in line of the two inlet and outlet reservoir. The connecting pin adaptors are adhered to the upper glass by UV adhesion method. The 3 domains ( $\mu$ F system and lower and upper MEA glass substrates) are thermally adhered on a hot plate.	145
<b>Fig. 4.2</b>	Microelectronic hardware architecture of the electrophysiology-based biomechatronic platform connected to a 12-channel ADC module through NI	149

	card, and multifunction voltage/current generator. The system is connected to a PC to collect and analyse experimental data.	
<b>Fig. 4.3</b>	(A) Assembled flexible cable to upper and lower multi-electrode arrays. (B) Soldering of bottom gold electrodes patterned on glass substrate to flexible electrode pads. (C) Transition-printed-circuit board (PCB) showing passive components: input connector pin out, pins and cables. (D) Soldering of upper gold electrodes patterned on glass substrate to flexible cable pads.	150
<b>Fig. 4.4</b>	Schematic diagram illustrating the working principle of the electrophysiology biomechatronic platform of one channel of an ADC. Position 1 and 2 respectively shows measuring and charging regime of the microelectronic characteristics of the platform. A cross sectional view of the $\mu F$ system with a biological cell entrapped between upper and lower electrodes is illustrated.	152
<b>Fig. 4.5</b>	Electrochemical biomechatronic platform operating software control panel.	153
<b>Fig. 4.6</b>	Serially diluted media showing viable and non-viable LM3 intermediate stage melanoma of a second lung metastasis.	162
<b>Fig. 4.7</b>	Experimental setup (A) Anti-vibration table and NI data acquisition card, (B) Miniaturized biomechatronic platform, multifunction voltage generator, 12-channel-ADC module, and power supply module, (C) Cellular water bath to maintain a temperature of 37°C for cultured cells (D) VHX-2000ES Keyence Digital Microscope.	164
<b>Fig. 5.1</b>	Three configurations of the $\mu$ cantilever system: $NA1$ is the non-deformed configuration, $NA2$ defines a new static configuration after inducing a DC potential and development of electrostatic force is reached, and $NA3$ illustrates a third equilibrium configuration after loading a cell.	181
<b>Fig. 5.2</b>	(A) Cross sectional view of cantilever beam-plate structure (not drawn to scale), and (B) Perspective view of the cantilever and patterned gold electrode on a glass substrate showing all controlling parameters.	184
<b>Fig. 5.3</b>	3D drawings of the proposed miniaturized mechanical structure consisting of (A) The mechanical assembly of the patterned gold electrode on a glass substrate, microcantilever, microscopic glass slides, and the diced glass steps. (B) Assembly of the polycarbonate (PC) microfluidic domain with the mechanically assembled components in (A).	190
<b>Fig. 5.4</b>	A microscopic image of the miniaturized mechanical component of the biomechatronic platform featuring the microcantilever (root, and rigid body),	194

	patterned gold electrode, Piezoresistive Wheatstone bridge, and bimorph excitation for future extension of this research study.	
<b>Fig. 5.5</b>	Microelectronic hardware architecture of the microcantilever-based biomechatronic platform connected to a DC-Microbalance-ADC module, and High Voltage (HV) Amplifier. The system is connected to a PC to collect, and analyse experimental data, through NI card.	195
<b>Fig. 5.6</b>	Microelectronic setup in probing deflection(s) of a microcantilever due to an induced DC potential to the stationary gold electrode patterned on a glass substrate via HV Amplifier module. The exploded view illustrates the Piezoresistive Wheatstone bridge (sensor scheme), where $V_{br}$ is the manually selected voltage bridge. The DC-Microbalance-ADC module consists of an input differential filter, fixed-gain preamplifier, ADC with integrated programmable gain amplifier (PGA), bridge supply module, and offset compensation block.	197
<b>Fig. 5.7</b>	DC-Microbalance-ADC module 2-channel configurations, showing two platforms (active, and reference) with HV amplifier feeding port, microdevice, transition PCB module, and 2 connecting copper arms.	199
<b>Fig. 5.8</b>	Registered report of an <i>in vitro</i> trial experiment utilizing the cantilever-based biomass sensor.	200
<b>Fig. 5.9</b>	(A) Experimental setup consisting of an anti-vibration table, NI data acquisition card, ADC-Multiplexer-DC, HV Amplifier, power supply, and Multi-function multi-meter. (B) Cellular water bath to maintain a temperature of 37°C for cultured cells, and (C) VHX-2000ES Keyence Digital Microscope.	202
<b>Fig. 5.10</b>	Experimental results of static transverse deflections of the microcantilever beam corresponding to various induced DC potentials prior to cantilever breakage at 15 V.	205
<b>Fig. 5.11</b>	A comparison between experimental and analytical model results of tip deflection (m) with respect to induced DC potential (V).	206
<b>Fig. 5.12</b>	The sensitivity in $\frac{m}{V}$ (negative slope) of the <i>in vitro</i> experimental findings of the cantilever's tip with respect to the induced DC potential (V).	208
<b>Fig. 6.1</b>	(A) Illustration of cell's cytoskeleton, (B) Four stages of cellular motility.	216

<b>Fig. 6.2</b>	Various approaches in extracting cellular contractile force (A) Shear flow analysis method, (B) Substrate focal adhesion complex approach, (C) AFM approach, (D) MTC approach, (E) Laser trap approach, (F) Micropipette approach, (G) Micropillar approach, (H) 3D-ECM-invasion assay method, and (I) Piezoresistive cantilever-based approach.	221
<b>Fig. 6.3</b>	Schematic illustration of a deflected beam due to exerted contractile force (compressive surface stresses) of a biological cell experiencing motility.	223
<b>Fig. 6.4</b>	SEM images of (A) M4A4, (B) SK-MEL-1, (C) CL16, and (D) NM2C5, as well as depth composition, and 3D pattern generated microscopic images of (E) LM3, (F) A375, (G) MDA-MB-231, (H) CL16, (I) NM2C5, (J) MCF7, (K) WM115, (L) SK-MEL-1, (M) G361, and (N) M4A4.	232
<b>Fig. 6.5</b>	(A) Non-metastatic NM2C5 smooth rounded morphology, and (B) Elongated late invasive malignant melanoma, A375.	235
<b>Fig. D.1</b>	Microelectronic Hardware Architecture of the 12-Channel-ADC module ( <i>Jassim Alqabandi, Imperial College London, All Rights Reserved</i> ).	353
<b>Fig. D.2</b>	Microelectronic Hardware Architecture of the DC-Microbalance-ADC module ( <i>Jassim Alqabandi, Imperial College London, All Rights Reserved</i> ).	353
<b>Fig. E.1.1</b>	Electrochemical biomechatronic platform operating software control panel.	357
<b>Fig. E.1.2</b>	(A) Charging and discharging the pair of electrodes (B) The serial number of NI data acquisition card.	358
<b>Fig. E.1.3</b>	(A) Reference internal assigned voltage for ADC performance (B) Voltage range to assigned experiments (C) Selection of Channel (D) Displaying of values extracted from each channel (pair of electrodes) in mV.	360
<b>Fig. E.1.4</b>	(A) Selection of channels of which the readings shall be obtained, (B) The timer period to collect samples and save them.	361
<b>Fig. E.2.1</b>	A screen image of the customized software to operate the $\mu$ cantilever-based bio-mechatronic platform.	363
<b>Fig. E.2.2</b>	(A) Bridge voltage supply and (B) input range initiation under control panel tab.	364

<b>Fig. E.2.3</b>	(A) executing/terminating the program to obtain readings from the NI data acquisition card, and clearing and updating obtained graph (B) Fine and coarse tuning of the offset, and (C) Display of the graph.	365
<b>Fig. E.2.4</b>	(A) Software recognition of the serial number of the NI USB card, (B) Message indicating the purpose of this segment of the software upon moving the mouse cursor, (C) Setting values for injecting a DC voltage to a stationary electrode to generate electrostatic forces, (D) Setting the injected potential to be in the pulse mode, (E) Display message familiarizing user of the command upon moving the mouse cursor, and (F) New display upon ticking the pulse box that allows setting period and width in milli second.	366
<b>Fig. E.2.5</b>	Upper left menu of the Control Panel tab.	366
<b>Fig. E.2.6</b>	Experiment tab to collect data.	367
<b>Fig. E.2.7</b>	(A) Upper left menu of the Experiment tab (B) Assigned controlling parameters, (C) Adding text notes during experiments.	367
<b>Fig. E.2.8</b>	(A) Selecting recording type mode, (B) Recording in N-sample mode.	368
<b>Fig. E.2.9</b>	Display window of the experimental results.	368
<b>Fig. E.2.10</b>	Data Reports tab.	369
<b>Fig. E.2.11</b>	Upper left menu of the Data Report screen.	369
<b>Fig. E.2.12</b>	Retrieved database and reports on saved experiment.	370
<b>Fig. F.1</b>	MEMS System: Paddle (plate), Root (cantilever), Anchor (insulating material), and Stimulating Stationary Electrode.	372
<b>Fig. F.2</b>	Analytical model of the MEMS structure (A) Design parameters of the microcantilever, (B) Representation of a transversely deformed beam due to a DC electrostatic actuation. $S$ is a body fixed coordinate, and $\theta_c$ is the transverse rotational angle about NA.	374
<b>Fig. F.3</b>	A small angle approximation of the time varying gap.	375

<b>Fig. F.4</b>	(A) Normalized transverse deflection with respect to induced DC potential $V_{DC}$ in Volt, (B) Derivative of normalized transverse deflection with respect to induced static potential in Volt.	386
<b>Fig. F.5</b>	Sensitivity (m/Volt) vs. DC induced dc potential (Volt).	388
<b>Fig. F.6</b>	(A) 3D variations of beam length (250-750 $\mu\text{m}$ ), uniform thickness as per a defined relation of $b = (0.002-0.010) \times L$ (where thickness is denoted as $b$ in this figure), and static pull-in voltage (Volt). (B) 2D representations of varying beam's length, uniform thickness, and static pull-in voltage while fixing a gap distance at 10 $\mu\text{m}$ . The material is Polyimide 2562 conductive polymer.	391
<b>Fig. F.7</b>	(A) 3D variations of beam length (250-750 $\mu\text{m}$ ), gap distance (4-30 $\mu\text{m}$ ), and static pull-in voltage (0-23 Volt). (B) 2D representations of varying beam's length, gap distance, and static pull-in voltage, whereas uniform thickness is fixed as per the defined relation in Table 1 ( $h = 0.006 \times L$ ). The material is Polyimide 2562 conductive polymer.	392

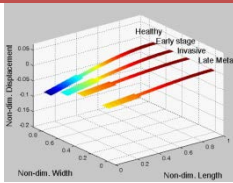
# List of Tables

Table.	Title	Page No.
<b>Table 3.1</b>	Controlling parameters of the electrical circuitry resembling a biological cell.	96
<b>Table 3.2</b>	Ohm's representations at the external node characteristics of a biological cell.	97
<b>Table 3.3</b>	Ohm's representations at the internal node characteristics.	98
<b>Table 3.4</b>	Numerical solution of arbitrarily selected parameters: three different scenarios.	119
<b>Table 4.1</b>	Three groups of cell line models' properties and sources.	158
<b>Table 4.2</b>	Resultant extracted electrophysiology potential of melanoma and breast cancer cell lines in mV (healthy, early stage metastasis, intermediate, late, and highly invasive metastasis).	167
<b>Table 5.1</b>	Controlling parameters of the miniaturized-cantilever-based-biomass sensor.	184
<b>Table. 6.1</b>	Characterization of different stages of cancer metastasis based on their morphology.	234
<b>Table 6.2</b>	Contractile force and cell-membrane potential of different stages of cancer.	237
<b>Table F.1</b>	Microcantilever design parameters.	385
<b>Table F.2</b>	Controlling parameters of the microbeam-microplate structure made of PI-2562 Polyimide.	389



# List of Uploaded Movies

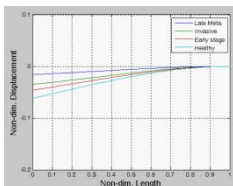
No	Sneak Preview	Description	Link
1		Cell is the building block of life.	<a href="http://www.youtube.com/watch?v=wDHpyNOPTTU&amp;feature=youtu.be">http://www.youtube.com/watch?v=wDHpyNOPTTU&amp;feature=youtu.be</a>
2		Cancer cell growth factors.	<a href="http://www.youtube.com/watch?v=LBH_0OSRgU4&amp;feature=youtu.be">http://www.youtube.com/watch?v=LBH_0OSRgU4&amp;feature=youtu.be</a>
3		Cell Lysis	<a href="http://www.youtube.com/watch?v=rPtCP7rR9y8&amp;feature=youtu.be">http://www.youtube.com/watch?v=rPtCP7rR9y8&amp;feature=youtu.be</a>
5		Endothelial Cells – Source: Cell Applications, Inc.	<a href="http://www.youtube.com/watch?v=0PU4FWwZaIg&amp;feature=youtu.be">http://www.youtube.com/watch?v=0PU4FWwZaIg&amp;feature=youtu.be</a>
6		Motilities of fibroblast to wounded area to perform restoration	<a href="http://www.youtube.com/watch?v=_GtVWyt3lys&amp;list=UU62EfCHc7cZBsYSUW-JY3Dw">http://www.youtube.com/watch?v=_GtVWyt3lys&amp;list=UU62EfCHc7cZBsYSUW-JY3Dw</a>
7		Different phases of cellular potentials	<a href="http://www.youtube.com/watch?v=FjOVYHQ1upM&amp;list=TLRsuMhW1tJSpl6OvqKnGQQWW9sKbiDPEX">http://www.youtube.com/watch?v=FjOVYHQ1upM&amp;list=TLRsuMhW1tJSpl6OvqKnGQQWW9sKbiDPEX</a>
8		Electrophysiology of cells (importance of Cellular signaling)	<a href="http://youtu.be/rRVQZydmqH0">http://youtu.be/rRVQZydmqH0</a>
9			



3D simulation of Artificial nose mechanism consisting of an array of cantilevers responding distinctively to the various stages of cancer: Healthy, early stage, invasive, and late metastasis.

<http://www.youtube.com/watch?v=656uKaAKGDA&feature=youtu.be>

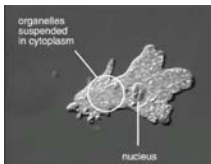
10



2D simulation of Artificial nose mechanism consisting of an array of cantilevers responding distinctively to the various stages of cancer: Healthy, early stage, invasive, and late metastasis.

<http://www.youtube.com/watch?v=iZtUr6p1ioY&feature=youtu.be>

11



Crawling motility

<http://www.youtube.com/watch?v=kQKXvOufeGg&feature=youtu.be>

12



Flagella motility

[http://youtu.be/eqD8aX\\_Yfps](http://youtu.be/eqD8aX_Yfps)

13



Vorticella motility


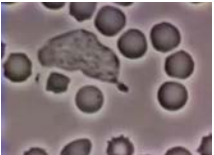
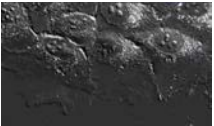
<http://youtu.be/hDfBpQHnsio>

14



Gliding motility

<http://youtu.be/x0RNjE65Ygw>

<p>15</p>		<p>Animated cell crawling motility</p> <p><a href="http://youtu.be/vNlasSiQIM0">http://youtu.be/vNlasSiQIM0</a></p>
<p>16</p>		<p>Neutrophil chasing bacteria</p> <p><a href="http://youtu.be/LYP8MUK3lqk">http://youtu.be/LYP8MUK3lqk</a></p>
<p>17</p>		<p>Cells crawling in a group</p> <p><a href="http://youtu.be/WzLQ0_mKaiU">http://youtu.be/WzLQ0_mKaiU</a></p>

## List of Publications

Peer Reviewed Literature	Status
Alqabandi, J. A., Design syntheses and analyses of a lab on a chip (LoC) module based on biological cell requirements in nature. Design and Nature 2014: 7th International Conference on Comparing Design in Nature with Science and Engineering. WIT. 2014.	Submitted/Accepted

# Chapter 1

---

---

## Introduction

---

---



*"The knowledge of all  
things is possible"*

## Chapter 1: Introduction

### 1.1 Research Motivations

In combating cancer, early detection is central to the prevention of cancer metastasis, not only giving patients a better prognosis but also allowing more cost-effective and minimally invasive treatments to be applied. The need for greater advances in cancer therapy is personally important to me, as I have experienced firsthand the sorrow associated with this disease through the battles endured by both my mother and aunt, as well as the battle my sister lost to colon cancer here in London in the summer of 2009, and the loss of my grandmother due to the advancement of breast cancer in December of 2010. These experiences have deeply motivated me to pursue research focused in cellular medicine, and its applications to the early detection and treatment of cancer.

My efforts to advance cellular medicine are evident in my previous work at Massachusetts Institute of Technology (MIT), Mechatronics Research laboratory. This work was focused on the extraction of electrochemical parameters from cancer cell lines at the single cell level using a novel microfabricated device [1]. This published work is an example of my interdisciplinary approach towards cancer research by incorporating cellular biology, biophysics, and Micro-Electro-Mechanical-System (MEMS) technology to examine, and characterize the electrophysiology of the B16-F10<sup>1</sup> melanoma cell line. In that published research, I developed analytical models with numerical simulations in the design of a microfabricated device to accommodate, and preserve the integrity of a single viable cell throughout an *in vitro* experimental process. Additionally, this method, within that published work, allows images of

---

<sup>1</sup> B16-F10 is a metastatic mouse-melanoma-cell model

---

the single cell to be captured using an Atomic Force Microscope (AFM). The findings of my published work [1] would aid in the design of optimal methods to extract the electrochemical signals of not only cancerous cells, but also cells such as those infected by viruses or intracellular parasites.

Driven by a vast motivation to contribute into allocating a novel approach in enhancing the cancer biomedical research field, on my own initiative, I have contacted prestigious medical institutes such as Harvard Dana-Farber Cancer Institute, Imperial College (Faculty of Medicine: Department of Surgery and Cancer), and Massachusetts General Hospital (MGH) Cancer Center, where I have successfully transmitted my motivations, and my proposed approach to the respective scholars in the field, who are in full support of my argument in further investigating the correlation between cell-membrane potential, and its contractile mechanical properties at different stages and grades of cancer, and to further characterize the physiology of cancer cells in a novel manner through bio-mechatronic means.

Cancer is a very complex and a ubiquitous life threatening disease that requires multi-disciplinary efforts to well-characterize it. Therefore, this has further motivated me to pursue a myriad of different research disciplines within engineering and biomedical sciences, focusing on cellular medicine. Exposure to the multidisciplinary group of faculty members in engineering, medical practitioners, and researchers from London Imperial College, MIT, and Harvard affiliated teaching hospitals has certainly provided an optimal environment for growth as a researcher, which acts as my third motivation factor in further invoking this subject. Moreover, the initial hands-on experience obtained through bio-laboratories, microfabrication, and experimental testing processes have enabled me to validate my analytical and empirical findings, and have made my research focus compatible with my goals of advancing cellular medicine by bridging the gap between experimental biology and engineering field.



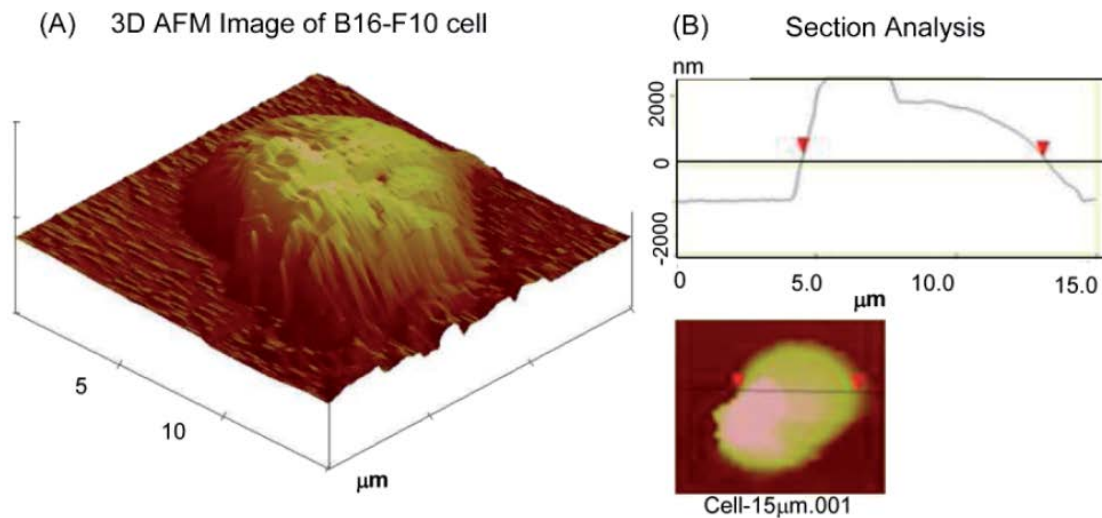
## 1.2 Cancer Biology Overview

Prior to invoking the design synthesis, analysis, microfabrication, and testing of the proposed miniaturized-versatile bio-mechatronic platforms, it is essentially important to first understand the formation of cancer, which is summarized in multi-stages. First, cancer is initiated in a single cell by a disruption of gene expression due to a number of factors associated with the environment and eating habit [2]; cancer is attributable to a damage or loss to critical gene targets. This is followed by a disarrangement or growth of genes [2], where gene mutation or dysregulation leads to the transformations of a **proto-oncogene** (normal gene) into an **oncogene** (mutated gene), which promotes the malignant phenotype. Then, the damage or loss of **Tumor Suppressor Genes (TSGs)** or anti-oncogenes, which are genes encoding proteins required for regulation of normal cell growth and differentiation, contributes in preserving the status of tumorigenesis, while it prevents a cancerous cell from invoking **apoptosis** process (programmed cell death) [2-4]. The damage of TSG is generally in both alleles, where one exception is **p53**, a protein responsible for the apoptosis process of cells, in which a single allele damage is sufficient [2, 4]; p53 performance would be drastically abridged in cancer cells [2, 4]. The deletion or inactivation of TSp53 promotes the neoplastic phenotype, and dysregulation of apoptosis eventually contributes to cancer development. Cancer then invokes cell proliferation mechanism (**mitosis**) [2-4].

It is worth stating that healthy cells can differ from cancerous cells in terms of a number of chromosomes, in which the former exhibits 46 chromosomes (diploid cells), while the latter exhibits irregular structure, and irregular number of chromosomes (aneuploid): a state where a cell either exhibits an excess or loss of the normal number of chromosomes [5]. Also, cancer

cells experience a reduction in the number of gap junctions that are responsible for cell-cell communication among nearby cells [6].

From the mechanical aspect of cells, a biological cell exhibits a mass on the order of 3-4 ng [7], with a volume on the order of 1 pL [8]. The cell typical diameter is on the range of 8-10  $\mu\text{m}$  such as that illustrated in Figure 1.1 [1, 9] – in order for the general reader to appreciate the size of a biological cell, and for a better visualization, consider the diameter of a human hair as a scaling factor tool, which is on the order of 80  $\mu\text{m}$  [10].



**Fig. 1.1** (A) 3-D image of a B16-F10 mouse melanoma cancer cell, (B) Cross-sectional analysis of the B16-F10 cell obtained by an Atomic Force Microscope (AFM).

A distinction between **malignant** and **benign** cancer has been described in [2, 11]: the former goes solely into mitosis stage, attacking neighboring cells and tissues through blood vessels, and incursion of lymph nodes (invasive), whereas the latter doesn't leave the site of its formation. It is of a great interest in this study to analyze the metastasis aspect of cancer cell in which the cells proliferate and migrate into other distanced tissues and organs through

lymphatic vessels (**lymphatic**), blood vessels (**hematogenous**), and **serosal** surfaces (**transcoelomic**) [12]. The proliferation of **carcinomas** (epithelial malignancy) initiates through the lymphatic path, then through blood vessels, whereas bone and soft tissue tumors (**sarcomas**) preferably proliferate initially through blood vessels [12].

Cancer proliferation mechanism heavily depends on the participation of blood vessels that provides oxygen, nutrients, and removal of wastes and carbon dioxide [13]. This shall stimulate the metastasis process, enabling malignant cells to invade other tissues and organs via blood circulatory system. Cells in general are allocated in a very salty, rich-medium of nutrients with other molecules, vitamins, and growth factors, e.g., platelet-derived growth factor (PDGF) [14], MAP kinase coupled growth factors [8], or epidermal growth factor (EGF) [15]. For example, Deoxyribonucleic (DNA) synthesis (replication) is a sign of cell growth [16]. Remarkably, some cancer cells have the mechanism to produce their own growth factor, and some undergo rapid division without the presence of growth factor due to a malfunction of their receptors [16]. For cancer cells to proliferate, some must adhere to a surface performing **extracellular matrix** (ECM) protein mesh communication with neighboring cells (anchorage-dependent), whilst others need to be free from adhesion (anchorage-independent) [17].

On a genetic level, the deactivated performance of Tumor Suppressor Genes (TSGs), normal genes, or presence/activation of oncogenes (abnormal genes), lead to cancer formation [18, 19]. A specific protein can act as a **biomarker** (a biological marker) for the presence of cancer; however, due to the complexity of cancer oncogenes' formation and heterogeneity, detection is quite difficult using a sole biomarker with sufficient sensitivity and specificity [19]. The uncontrolled proliferation process is attributable to irregularities of cell signaling, triggering the growth factor protein of other cells to initiate the rapid-division process, and then attacking neighboring cells, tissues, and invading other organs [1, 2, 20].

This research is a multidisciplinary work, and thus to avoid any confusions with various technical terminologies illustrated herewith, all words in bold are listed in glossary section in Appendix A. This should simplify the concept for both engineers as well as biologists, and hopefully it shall contribute in bridging the gap between the two fields. Also within the body of this research, a number of footnotes shall direct the general reader to various movie presentations for better visualization of various biological phenomena covered within this research, on more emphasis on biological cells, as well as some engineering concepts.

A biological cell is the building block of life that comes in different forms; each cell type performs a specific task; each type experiences a distinctive motility. One of the objectives of this research is deeply analyzing a biological phenomenon (e.g. cellular motility contractile force, cell electrochemical characteristics, etc.), and then transforming such phenomenon into an engineering application: turning biological problems/phenomena into engineering applications/opportunities. The referenced movie presentation in the following footnote illustrates the importance of cells, and gets the readers' attention towards cells' various forms, tasks, signaling, and motilities<sup>2</sup>. Hopefully, through the animated movie presentation within the footnote, a biologist would appreciate the various mechanisms and applications of cells; interestingly enough, from an eye of an engineer, looking at the video images of nasal hair, the motility of nose hair could be correlated to cantilever response as in the artificial nose application within Mechatronics field, which is extensively used in chemical compound gas sensor.

---

<sup>2</sup> <http://www.youtube.com/watch?v=wDHpyNOPTTU&feature=youtu.be>

### 1.3 Significance of Melanoma Model

This work adopts melanoma, a skin cancer, as a legitimate model in the proposed analysis of designing and characterizing versatile bio-mechatronic devices. Melanoma is initiated from melanocytes (pigment-melanin-skin cell); thus, it's gaining the name "melanoma." Melanoma cells are actively generating melanin that to dark coloring and asymmetric pattern resulted on the skin; they can be generated in any part of the human body. As per [21], the frequent occurrence of melanoma is considered relatively high as opposed to other types of cancer occurrences particularly in countries that experience sustained bright sunlight. A unique characteristic of melanoma is that it highly advocates mitosis as it forms on a skin tissue as well as in other internal organs, if injected intravenously. Accordingly, cutaneous melanoma is the one that is generated on the skin surface, whereas ocular malignant melanoma is an example of metastatic cancer [22]. Figure 1.2 illustrates ocular melanoma.



**Fig. 1.2** Retinal melanoma formation (Courtesy of Prof. Bertil Damato, Liverpool Ocular Oncology Service).

In line of melanoma unique characteristic in advocating mitosis, Wilhelm *et al.* [23] have shed light on the pivotal role that malignant melanoma cells play in brain metastases at a very high frequency as opposed to other metastatic cells of other cancer diseases. This manifests the importance of melanoma cells' motility (migration) to other organs via, e.g., capillaries, in forming other metastatic colonies.

As aforementioned in subsection 1.2, the main routes of cells are through main networks of blood vessels: **arteries** (blood stream from heart towards other parts of the mammalian body), **veins** (backward blood stream from body towards heart), and **minuscule** (comparable to the size of a cell) interconnecting capillaries between veins and arteries. This justifies the fact that tumor cells are highly stimulated in the presence of rich blood vessels, e.g., as in a retina (Figure 1.2). This is performed in a process denoted as tumor **angiogenesis** (a formation of new blood vessels) [24-26], which is associated with metastatic cancer. The cancer cells encourage the formation of new blood vessels into the tumor; this occurs by the cancer cells stimulating blood vessel cell proliferation through release of endothelial cell growth stimulating chemicals and proteins.

Malignant melanoma in general is categorized as a deadly disease, especially if it is discovered at an advanced stage. As per the American Cancer Society (ACS) 2013 [27]: Cancer Facts and Figures, the estimated number of new melanoma cancer cases and deaths for both genders is respectively 82,770 and 12,650 within the United States of America – not considering basal and squamous cell-skin cancers. The ACS's 2013 probability (%) analyses of invasive melanoma on Caucasian Americans from 2007-2009 for the first three age clusters of male (M) and female (F) are: birth to 39 (M 0.15, F 0.25), 40-59 (M 0.63, F 0.55), and 60-69 (M 0.77, F 0.4). Caucasians have the highest frequency of developing the disease. Melanoma exhibits four stages based on its thickness and cancer progression status within other tissues, organs, and lymph nodes [21]: Stage 0 (*in situ* melanoma), Stage I (thickness

---

dependency without skin pattern breakage), Stage II (thickness variations with/without skin pattern breakage), Stage III (invading lymph system), and Stage IV (invading other organs and tissues). The majority of skin cancer resulted from exposure to various forms of radiation; mortality is attributed to melanoma (highly invasive) as opposed to squamous and basal cell carcinomas [21].

A unique feature of melanoma is its ability of being self-immune from natural killer<sup>3</sup> (NK) cells, in which the cancerous cell develops a self-defense system against immune response, as well as chemotherapy through molecules denoted as **antigens**, e.g., melanoma tumor specific/associated antigens [28, 29]. In line of this unique feature, an example of the type of research work that is found to be most interesting is that by Tobias Schatton and colleagues [29], which proposed a novel therapeutic approach by targeting ABCB5<sup>+</sup>, a melanoma chemoresistance mediator, and a newly defined marker of malignant-melanoma-initiating cells (MMIC); this ABC transporter arbitrate chemoresistance within human malignant melanoma, by transporting ions (charges) of cell membrane, and hence determines cell-membrane potential of the cancer cell [29]. This shows the importance of electrophysiology of cells that will be presented in Chapter 3. However, thoroughly addressing this specific topic of ABC transporter is beyond the scope of this research.

## **1.4 Cancer Detection: Limitations of Conventional Approaches**

Early detection of cancer at a cellular level could potentially have a great impact in combating the disease since it could prevent cancer metastasis [30-32]. Unfortunately, conventional methods used in cancer diagnosis are costly, hospital based, and suffer from important limitations, which depend on the type of cancer that is being targeted. Imaging-based

approaches such as Position Emission Tomography (PET), Computed Tomography (CT), Magnetic Resonance Imaging (MRI), X-Rays, bone scintigraphy, and ultrasound scans generally suffer from low to moderate sensitivity in detection of certain kinds of cancers, which means early diagnosis is often not possible. For example, PET scans are not satisfactorily reliable for early detection of **gastric carcinoma** [33], **hepatocellular carcinoma** (HCC) [34], or **endometrial cancer** (lymph node metastasis) [35]. Similarly, CT scans are not sufficiently sensitive to identify lymph-node-invasive metastases [36], and neither is MRI to detect lymph-node staging [37]. Furthermore, X-ray scans fail to reliably detect breast cancer [38]; similarly, bone scans are not adequate to detect the formation of micrometastatic prostate cancer cells within bone marrow [39]; moreover, ultrasounds have poor sensitivity as well as specificity for prostate cancer detection [40].

An alternative to non-invasive imaging based methods involve the cytological analysis of biopsied tissue samples. However, these are invasive in nature, time consuming, and may suffer from poor sensitivity for low-grade/stage tumors, which would require second-stage clinical analyses [41].

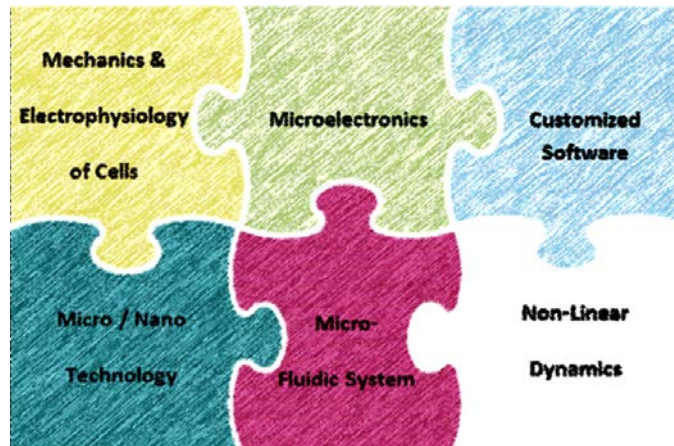
On the implementation perspective, some of these approaches cannot be applied to all patients. For example, the use of techniques involving high levels of radiation, as in, e.g., bone scan [42] can be controversial on children [43]. MRI is arguably not to be utilized, unless it's optimally performed, for cancer patients, who have implanted defibrillator [44], and those with ear implant (cochlear) [45], upon which these implanted devices contribute into artifact (distortion) on the developed image of a suspicious lesion, and shouldn't be performed on.



## 1.5 Research Aims

The aims of this research study are summarized in fivefold: 1. Design and construct novel miniaturized bio-mechatronic platforms, where the electrophysiology of well-established melanoma cells are being quantified; 2. Model, design, and characterize a novel, cantilever-based, miniaturized bio-mechatronic platform that probes the contractile force of cancer cells, which is mainly responsible for cell's motility; 3. investigate a correlation between cell-membrane potential, and cellular contractile force, which would lead to a better understanding of the disease electrophysiology and mechanobiology characteristics: interpreting the behavior of cancer disease and enhancing its prognosis; 4. investigate analytical model of cell-membrane potential for better comprehensiveness, prior to conducting *in vitro* bio-experiments; finally, 5. develop a novel approach of cancer diagnostics by determining the heterogeneity, and stage of cancerous cells through the utilization of microtechnology, cellular mechanics, electrophysiology of cells, and microelectronics.

The pre-stated five objectives shall induce the sixth aim of this Ph.D. research in terms of proposing highly versatile, and fully automated miniaturized biomechatronic systems on the essence of various fields presented in Figure 1.3. It is worth mentioning that a full capture of the definition of Biomechatronic field should encompass economic analyses as well, but it is beyond the scope of this Ph.D. dissertation.



**Fig. 1.3** Overlapped research field components in forming a miniaturized bio-mechatronic platform.

## 1.6 Ph.D. Research Structure

In this research, relevant literature and research methodology are deliberately addressed at each chapter. Furthermore, there shall be a smooth transition from one chapter to the other, where a summary and conclusion section is devoted at the end of each chapter. The future outlook is provided towards the end of this Ph.D. dissertation.

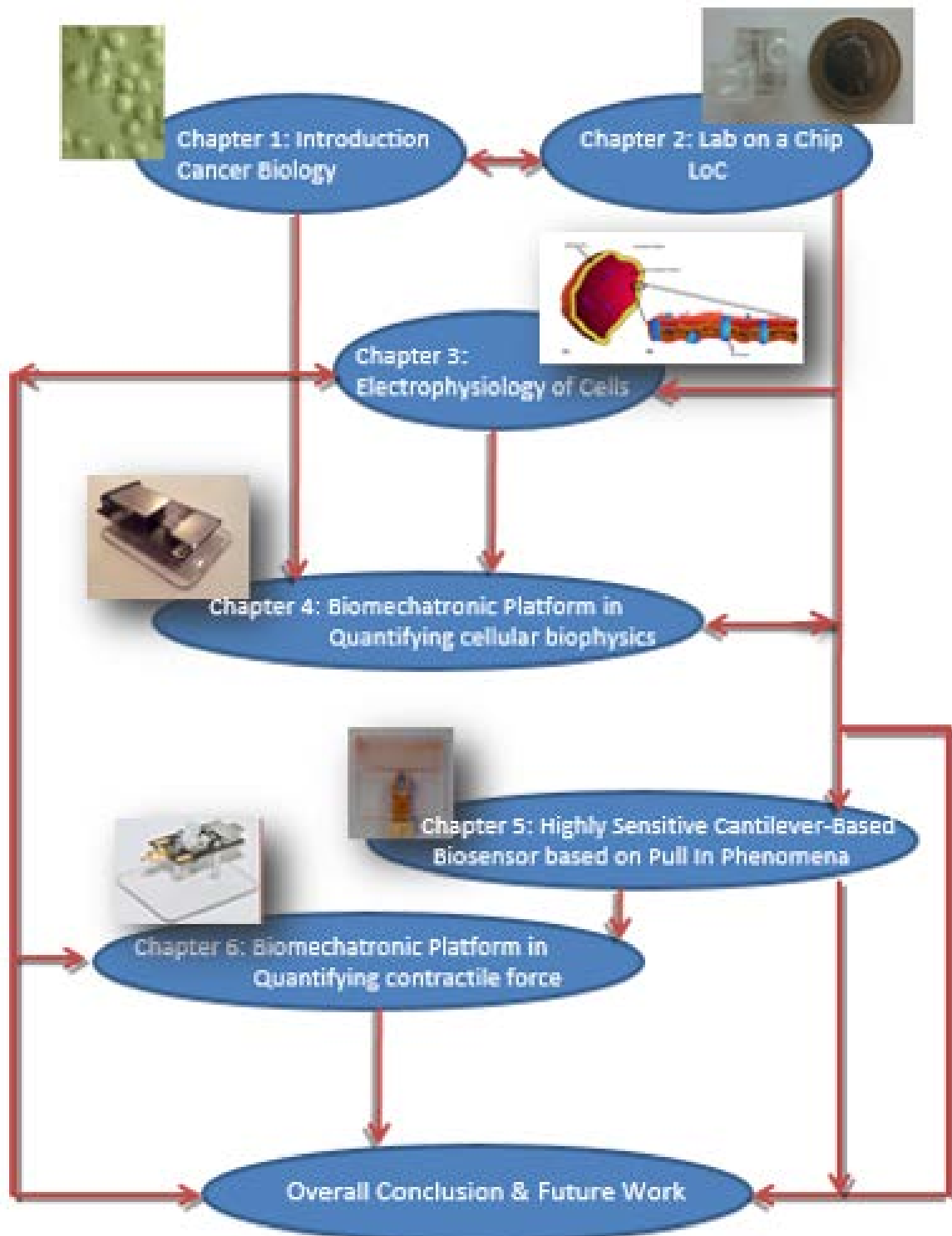
Chapter 2 highlights the importance of the exponentially growing field of Lab-on-a-Chip (LoC). On the basis of cancer cell requirements in maintaining viability addressed in the first chapter, modeling and fluid visualization through computational fluid dynamic (CFD) tool, as well as finite element analysis (FEA) approach shall be addressed in designing an integrated LoC, consisting of a microfluidic module (culturing chamber, channels, etc.), and multi-electrode arrays. Furthermore, Chapter 2 provides literature review, materials and methods required in order to achieve a versatile, and fully-automated miniaturized biomechatronic platform that is able to nurture and harvest biological cells, manipulate and trap cells via electrophoresis mechanism, and analyze the electrophysiology of cells, and cell-cell communication that could be of additional future research aspects of this Ph.D. thesis.

Chapter 1 has addressed the basic foundation for the succeeding chapters. It has been pre-stated that cancer cell initiation due to a disruption of gene expression is attributable to the electrophysiology of cells as per [1, 2, 20]. Therefore, Chapter 3 shall address the subject of electrophysiology of cells by highlighting the structure of a biological cell, and its analogical electric circuit representation, where Fourier and Laplace Transform, and their respective Inverse Transforms are implemented. Also, literature reviews on the electrophysiology aspects of cancer cells are discussed. This chapter reports the limitations of nonconventional methods implemented to characterize biological cells such as Surface Acoustic Wave (SAW), and optical fluorescence approach. An empirical analysis is discussed at the end of this chapter to simulate the stimulation of a cell, and monitor its response on the basis of cell-membrane potential. This in-depth analysis shall assist in understanding the mechanism, and skeleton of cell electrophysiology prior to microfabrication of a biosensor.

Chapter 4 shall present the biomechatronic platform, and its components and microelectronics architecture, dedicated controlling software, and microfabricated mechanical structure. A number of *in vitro* experiments are performed in this chapter on eight melanoma cell lines of different genetic complexities: SK-MEL-1 (malignant metastatic melanoma), A375 (late invasive malignant melanoma), G-361 (malignant melanoma), WM-115 (melanoma), NM2C5 (weakly/virtually non-metastatic melanoma), M4A4 (early stage metastatic), M4A4 LM3-2 GFP (intermediate stage second lung metastasis), and M4A4 LM3-4 CL16 GFP (highly metastatic third generation lung metastasis). Well-documented cell models, breast cancer adenocarcinoma human (*homo sapiens* MDA-MB-231), and early stage breast cancer (MCF7) have been used as calibration-cell models for the microfabricated biomechatronic platforms on the basis of extracted cell-membrane potential, and contractile force.

On the essence of beam's theory and electrostatic pull-in phenomenon, design syntheses and analyses of a highly sensitive cantilever-based biomass sensor are described in Chapter 5. It shall be further addressed analytically as well as experimentally that as the static DC pull-in potential is approached, the sensitivity of the cantilever is enhanced. Chapter 6, on the other hand, shall extend the beam's theory to study cell contractile force. In this chapter, microelectronics architecture, as well as dedicated controlling software are presented. Furthermore, in Chapter 6 literature discussion on contractile force mechanism and various conventional methods utilized to extract such force are addressed. Chapter 6 will investigate the hypothesis of this research: as the cancer cell progresses from an early stage towards highly metastasis, the magnitude of the cell membrane potential decreases, whereas the associated contractile force of the cell increases (i.e. higher contractile force signifies higher invasiveness); also, as a cell advances in the stage of the disease, cellular morphology gets steeper and sharper -- increase in the surface contact area between cell and flat substrate, as well as a decrease of cellular height. As a novel contribution in this chapter, the cellular contractile force is extracted based on a Heaviside step function  $H(s)$ , and pin-force model.

Chapter 7 shall provide concluding remarks, and address future works in advancing/enhancing the proposed systems, presented within this research. In this Ph.D. dissertation, analytical, empirical, microfabrication, and bio-experiments, links of video images, should all contribute in bridging the gap between biology and engineering field in tackling the subject of cellular medicine. This chapter briefly discusses the role of oncogenes (JAK and STAT3) on melanoma cell's motility, and proposes a method through immune-assay approach to analyze such role; this will be further addressed as an extension of this Ph.D. research. Figure 1.4 summarizes the structure, and interrelation of various chapters within this work.



**Fig. 1.4** Structure of the Ph.D. research in investigating cellular biophysics and mechanobiology.

## **1.7 Conclusion**

There are over 200 different types of cancer attacking over 60 human organs [46]; hence, a novel, non-invasive to the biological cell, cellular-based detection mechanism of this omnipresent intricate disease is highly demanded to save human lives. The analyses, presented in this chapter in terms of cancer-cell biology, characteristics of melanoma, the requirements of a living environment for cells to maintain their viabilities, cell's metastasis factors, routes of cancer cell migration, and limitations of conventional approaches in detecting cancer at a cellular level, should all provide a solid platform for general readers to be acquainted with the initiation of the disease, and these concepts should ease the process of understanding the topics presented in the subsequent chapters of this Ph.D. thesis dissertation.

Chapters 1 and 2 provide the essence to optimally model, design, and characterize miniaturized bio-mechatronic platforms, operating within an *in vitro* environment. For example, the requirements of oxygen, nutrients, and other vitamins, as well as disposal of wastes and carbon dioxide, expressed from the cellular domain, shall contribute in designing microfluidic chambers, channels, and pumping system that shall house cancer cells, and ensure their viability (living) status for enhanced experiments' throughputs. Moreover, the unique feature of some cancer cells in losing their adhesion characteristic should lead to surface treatment, if required, e.g., during microfabrication process of an effective layer of a mechanical interface with the biological cell through which a functionalized layer is created by coating the upper surface of the cantilever with a biocompatible layer to enhance fixation/seeding of the cell. Similarly, microchannels should be characterized as per the size of capillaries within the mammalian bodies; however, this is constrained with the limitations of

---

the microfabrication processes. Last but not least, published findings of cell-membrane potentials of different stages of cancer, which shall be illustrated in Chapter 3, would contribute in setting the range of detection within the written source code of the driving software for the bio-mechatronic system exhibited in Chapter 4.

The ability of cancer cells to trigger/activate the mitosis aspect of other cells should highlight the importance of cell's electrophysiology, which is the topic of Chapter 3. Moreover, understanding cellular biophysics would lead to an efficient design of a miniaturized bio-mechatronic platform that would swiftly, and faithfully carry each electronic signal emitted from a single or a population of cancer cells, trapped in a microfluidic-multi-electrode array module; this shall be further addressed in Chapter 4.

# **Chapter 2**

---

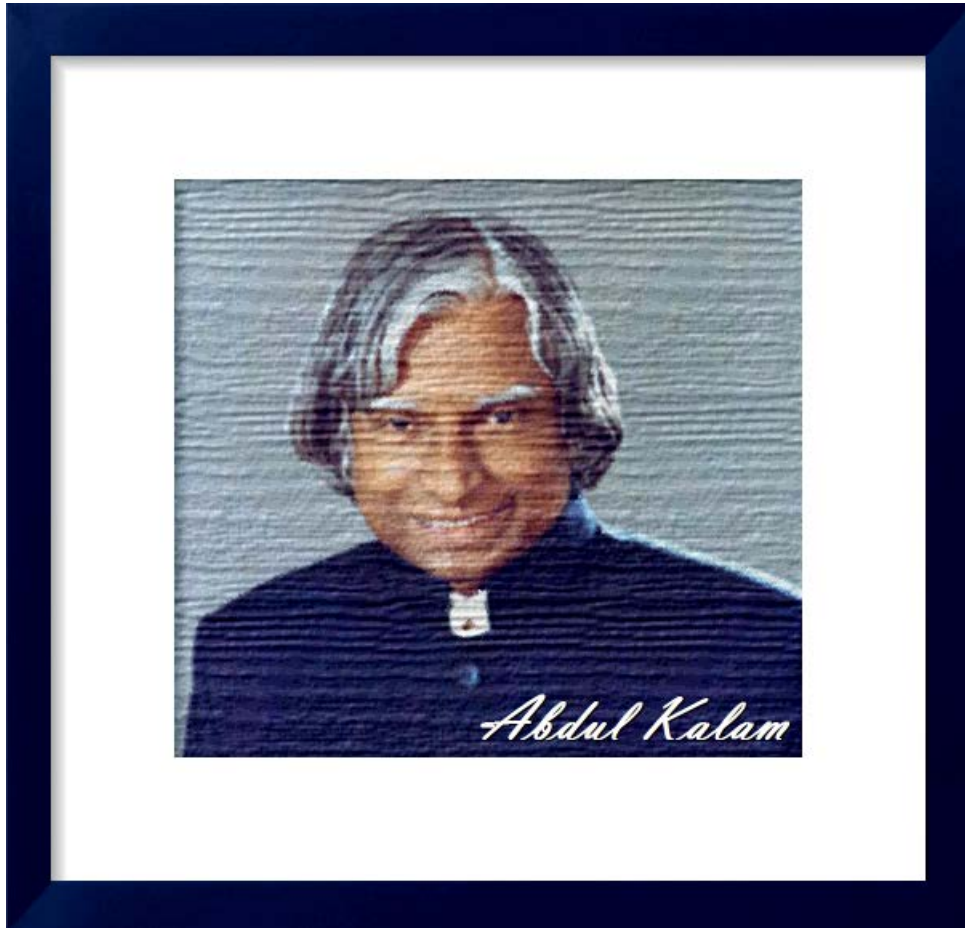
---

## **Lab-on-a-Chip (LoC)**

---

---





*"Learning gives creativity,  
Creativity leads to thinking,  
Thinking provides knowledge,  
Knowledge, makes you great."*

## **Chapter 2: Lab-on-a-Chip (LoC)**

### **2.1 System Overview**

It is of a growing interest among researchers in the Biotechnology field to acquire a reliable system that maintains the viability of a cell in an *in vitro* environment for a sufficient period of time, and provides multi-task analyses on a mammalian cell. Therefore, the Lab-on-a Chip (LoC) field, also referred to in literature as a micro-total-analytical system ( $\mu$ TAS), has been initiated to address such needs. However, it is astonishingly motivating to find that despite the infancy of the LoC field, it has grown massively in a very short time not only capturing biologists' attention, but also that of astrobiologists as well, for space travel bio-experiments by addressing constraints within different spectrum of science in a novel manner [47]. For instance, a major constraint faced by bio-researchers is the randomness of signals and noises experienced within a population of cells, which can be eliminated by sorting a single cell in a confined and controlled environment such as that of a microfluidic domain [1, 48].

It is important to comprehend the biology principle, merits of LoC, electrophysiology, and mechanobiology of cells, presented respectively in Chapters 1, 2, 3 and 5, prior to modeling, design, and fabrication of biomechatronic platform systems – in order to arrive at the biological consequences, and impacts on design aspects of an LoC domain, integrated within the biomechatronic platform. For example, as expressed in Chapter 1, some cells exhibit adhesive properties that can be considered as an added advantage in terms of fixation of the cell on an LoC surface for lab analyses, yet it might lead to clogging and poor controllability of cell

manipulation [48]. At the same time, disengaging cells from their adhesive state, could damage the cell membrane, and leads to random signal propagations [49].

This work highlights how nature, e.g., biology, defines, sets the parameters, and influences the design syntheses and analyses within the engineering field. Biotechnological miniaturized devices are just an illustration of how various elements of flow system components (e.g. brain neurons, immune cells, alveoli within lungs, etc.) are active with respect to each other in a background of a flow defining what the flow should carry (e.g. electrochemical signals, mechanical signals, etc.), and where should such each component of the flow system be optimally located to ensure durability, and high level performance with time [50, 51]. In line with this concept, the miniaturized platform that shall be further addressed in this study, e.g., array of microelectrodes patterned on a glass substrate should work hand in hand with another miniaturized component (microfluidic system) within the platform (the overall flow system) on the basis that the former flow system component's design (configurations and generated drawings prior to microfabrication) ensures faithful extraction of cellular electrochemical signals within a uniformly distributed electric current in a damage-free cell environment within a contained microfluidic system; such anticipated flow system should preserve cell's integrity throughout the conducted experiment. Therefore, the importance of flow systems (non-equilibrium systems) lies within the resultant efficient design that ensures durability and optimal utilization of any miniaturized system over time, shortens lead time by avoiding trial and error, and further enhances system components' performance; this is what defines the Constructal theory/law: *"For a finite-size flow system to persist in time (to live) it must evolve in such a way that it provides greater access to the currents that flow through it"* [50]. Driven by the two works in [50, 51], advocating Constructal law in justifying, in particular, the evolution of miniaturized devices on the essence of biology, and presenting design as science,

and optimizing a constructed platform, shall further assist in defining design boundaries as well as limitations (imperfections), where sources of enhancements could be allocated.

The objectives of this chapter are (1) to provide a review on how nature contributes in defining the design requirements of a miniaturized system for cell viability -- mimicking that of an *in vivo* domain, as well as extracting cellular electrophysiology at a molecular level, and (2) to translate such requirements into an engineering application of design syntheses and analyses of two main integrated components of an LoC platform: microfluidic ( $\mu$ F), and Multi-Electrode-Array (MEA) systems. Thus, this chapter highlights the optimal environment of a cell to live and grow for bioresearch, by acquiring an engineered system of nutrition supply and removal of wastes (perfusion), pH neutralization, sufficient supply of oxygen, thermal stability, elimination of air pockets, and a presence of a highly salted aqueous solution.

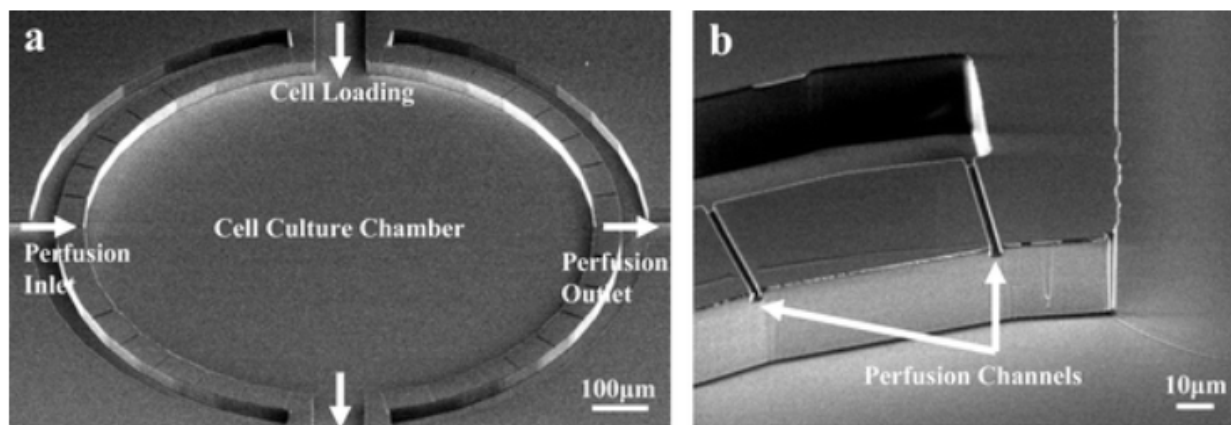
## **2.2 Integrated Microfluidic ( $\mu$ F) System**

### **2.2.1 Design Synthesis**

Microfluidics ( $\mu$ Fs) avail researchers the benefits of analyzing a single or a population of cells in a confined and controlled environment with a very high sensitivity [1, 52, 53]. Fragoso *et al.* [53] have fabricated an  $\mu$ F platform to detect breast cancer protein markers in a serum medium based on its electrochemical (electrophysiology) characteristics. They have designed their system to house two zones: (1) detection with  $\mu$ F chambers and their associated 16 working electrodes, and (2) fluidic storage zone of a cell sample and reagents, consisting of five reservoirs.

### 2.2.1.a System Perfusion

In mammalian bodies, **perfusion** is a process, in which, nutrients, oxygen, and cell growth factors are provided to cells, and wastes, such as  $CO_2$ , insoluble cell debris are removed from the system. Perfusion can be branched into (1) re-circulating (for large volume media: re-circulated through the system, where wastes are diluted and sent back to cells), and (2) non-re-circulating (media are perfused into the system and then sent entirely to waste) [54]; perfusion is an essential process of supplying nutrients to cells. Figure 2.1 shows microfluidic perfusion system [55].



**Fig. 2.1** A micrograph of 1-mm-diameter-culturing reservoir with perfusion channels prior to adherent to a glass substrate. High aspect ratio design. **(a)** SEM picture of a single unit of the arrayed device before bonding. Multiple perfusion channels surround the main culture chamber. The microchamber is 40  $\mu\text{m}$  in height with a diameter of 1 mm. Each culture unit has four fluidic access paths. **(b)** SEM image of perfusion channel dimensions. Each perfusion channel had a width and height of 2  $\mu\text{m}$  – Reproduced with text caption from [55] with permission from the Royal Society of Chemistry.

Kim *et al.* [56] have designed and fabricated a continuous perfused  $\mu\text{F}$  domain with a system of 3 and 4-way valves to culture murine adhesive embryonic stem cells (ESCs) for four days until **cell confluence**, where cellular dense culture has been reached and cells no longer proliferate. Their main objective was to model and design a variable flow rate initiated from a single input. They have noticed that slow flow rate environment didn't support cell growth as opposed to a constant higher flow rate, where cells have grown in a healthy-round-morphology shape. In the absence of neighboring cells, they have estimated the shear stress exerted on a single cell (cell's height  $(k)$ ), adhered to a channel of height  $h$ , to be three times the fluid shear stress experienced at the walls. However, they have concluded that shear stress has a minimal effect on the morphology of cell colonies, and that high flow rate plays an important role in terms of expediting the process of waste removal, nutrient delivery, and removal of proliferation (growth factor) concentration. Furthermore, continuous perfusion ensures non-evaporation of the contained fluid volume within the system, and multi-perfusion channels prevent the cell from being flushed away, and ensure uniform nutrient distribution [55].

Nevill *et al.* [57], on the other hand, have developed an on-chip- $\mu\text{F}$  system of a continuous perfusion cell culture and "on-demand-cell lysis." They have cultured HeLa, MCF7, Jurkat, and CHO-K1 cell over a 5-day-time period, and they have managed to lyse (break) cells in a lysing-reagent-free environment. In their device, the lysis process is achieved by imposing a DC potential that leads to the development of hydroxide within the proposed system, without the need for higher electric field development. The link in the footnote illustrates a form of cell breakage due to imposed external force, e.g., as in antibody<sup>1</sup>. The electrochemical cell lysis [58], on the other hand, is carried out by inducing a DC potential through an electrode neighboring the trapped cell, where hydroxide is initiated at the cathode upstream. In [58], Cr/Au as opposed to Ti/Pt configuration has been considered in their designed experiment as a robust electrode model.

<sup>1</sup> <http://www.youtube.com/watch?v=rPtCP7rR9y8&feature=youtu.be>

Hung *et al.* [55] have designed and fabricated a novel microenvironment for high throughput Human Carcinoma (HeLa) cell culture consisting of a circular  $\mu\text{F}$  chamber enclosed by a number of perfusion channels – cell culturing lasts for 8 days. The culturing was performed at  $37^{\circ}\text{C}$ , until cell confluency has been achieved. It is shown in [55] that high aspect ratio of the  $\mu\text{F}$  chamber to the multi-perfusion channels leads to a large fluidic resistance, which eventually contributes to having a uniform flow pattern (uniform nutrition distribution) for the cell. Similarly, Kim *et al.* [54] highlight the importance of optimal controllability on perfusion process: supply of nutrients and removal of wastes of adhesive cells.

### 2.2.1.b Mimicking *In Vivo* Environment

Prior to investigating the relevant literature on simulating *in vivo* domain within the *in vitro* environment, it is worth to draw a comparison, and highlight the merits associated with  $\mu\text{F}$  system in the *in vitro* environment to those of static Petri dish culturing, as well as humanized/nude mice [59, 60], where the latter are utilized in the *in vivo* model within biomedical research.  $\mu\text{Fs}$  provide high resolution and throughput in obtained measurement, real-time monitoring of the system, spatial and temporal controllability over the  $\mu\text{F}$  domain [61, 62].  $\mu\text{F}$  based-LoC reduces the usage of lysing reagents [57]. Furthermore, LoCs exhibit less evaporation rate and temperature variability than static petri-dish culturing. Their designed system allows the analyses of capillary morphogenesis as in tumor growth and wound healing [61]. Furthermore, static petri-dish-culturing approach experiences uncontrolled signaling, and accumulation of cell's waste. In addition, static culturing doesn't provide full spatial controllability over cell movements [63].  $\mu\text{Fs}$  provide a variety of flow gradient that allows

performance of complex bio-experiments, enabling prompt switching (continuous flow) or inclusion of cell-cell communication (no flow) [63].

µF-based LoC module can reduce the cost of robotic cell-culturing platform, especially in the case where a macro-level robot cannot conduct culturing at a miniaturized scale [64]. Also, µFs have a number of merits over static culturing by controlling the shear stress, which is advantageous for some types of cells, e.g., **vein endothelial**<sup>2</sup> [65]; also, controlling shear stress enhances perfusion process, once the system geometries are optimized [65]. The footnote provides a video link illustrating veins' endothelium cell [66].

µFs operate on a small culturing volume: providing most beneficial experimental environment, and hence eliminating labor intensive factor, as well as lessening the occurrence of experimental systematic errors [64]. It is reported in [67] that µF approach provides more sensitive analyses, and less utilized reagent volume than static culturing. Moreover, cross contamination is less likely to take place during µF experiments as opposed to static culturing processes.

*In vivo* mouse model approach is a process of nurturing tumors within mammalian bodies of animals such as mice [59, 60]; it is a very time consuming and tedious process that suffers from lack of legitimate model to perform the experiment. Also, it is quite expensive to maintain the *in vivo* model (i.e. animal technician would charge ~ US\$100/per day for mouse maintenance). Also, there is the issue of patenting and obtaining permission of utilizing a patented developed mouse model, as well as the monotonous/lengthy culturing procedures, and ethical obligations that the bio-experimentalists have to adhere to. Moreover, it acquires a lengthy lead time in obtaining approvals for certified protocols, when conducting the mouse model experiment. Thus, µF approach could provide a simulated *in vivo* model within the *in vitro* environment, without animal suffering.

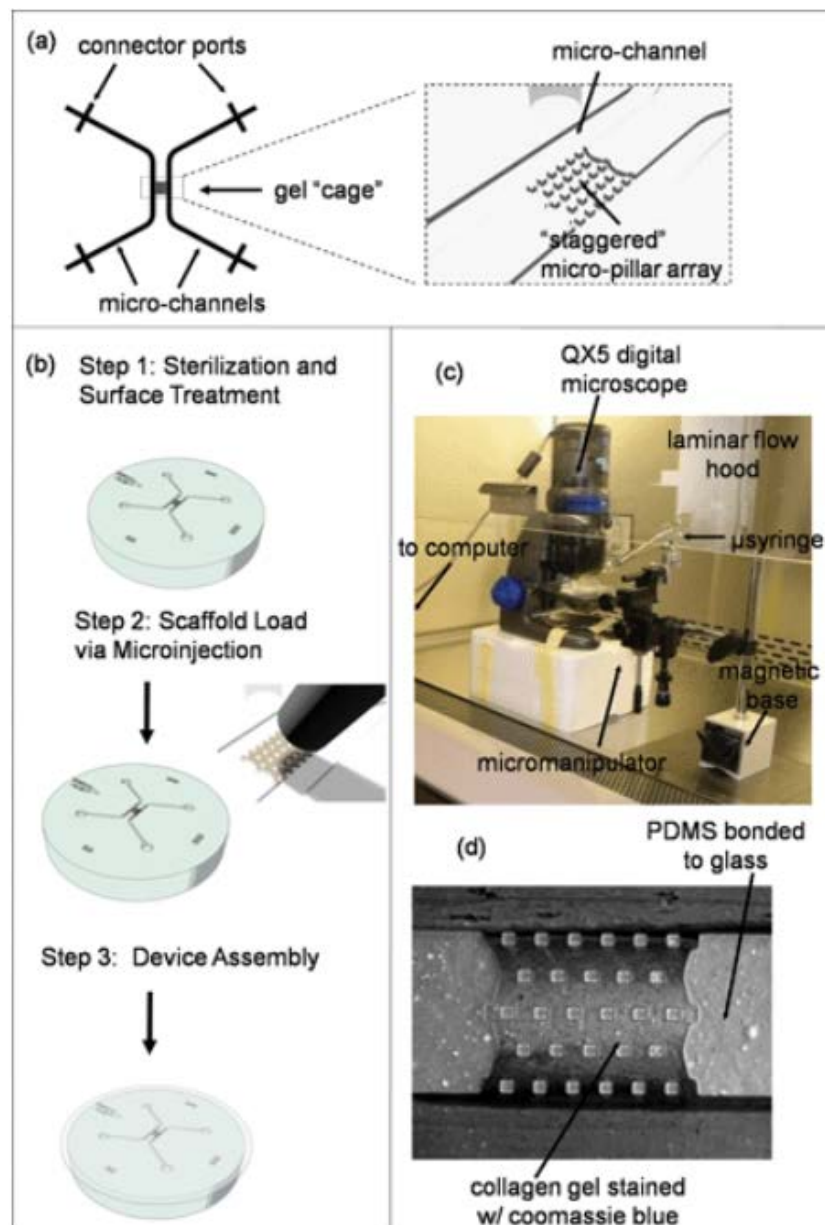
---

<sup>2</sup> <http://www.youtube.com/watch?v=0PU4FWwZaIg&feature=youtu.be>



---

In line with the merits of  $\mu\text{F}$  chamber over static culturing process, further research is geared towards mimicking the *in vivo* environment that in particular should benefit the tissue engineering field. Ziółkowska *et al.* [65] have provided a detailed review of utilizing  $\mu\text{F}$  to mimic *in vivo* environment. They have stated that a resemblance of *in vitro* to *in vivo* environment leads to a realistic cell growth, but on a slower rate than static culturing. Vickerman *et al.* [61] have developed a novel multi-parameter control of Polydimethylsiloxane (PDMS)  $\mu\text{F}$  platform, via soft lithography, for 3D-cell culturing in synthetic hydrogel, monitored through a QX5 digital microscope. This cell-scaffolding technique, of known pore size, density, and stiffness consisting of various cell types in a designed spatial arrangement, simulates tissue engineering in the *in vivo* environment. As shown in Figure 2.2, their proposed system consists of microfluidic channels with a central gel cage. In their work, gel cage micro-pillar array is utilized to provide a rigid platform when seeding cells into the scaffold. It should be noted that during perfusion flow, mechanical stresses are imposed on the 3D matrix cells entrapped in gel that requires a design for rigidity by embedding nano-pillars. The hydrogel scaffold is microinjected in a pre-set protocol with or without cell into the gel cage [61].



**Fig. 2.2** A 3D matrix of central gel cage for cell culturing illustrating *in vivo* tissue engineering. **(a)**  $\mu$ F domain consisting of two parallel channels and a central gel cage. **(b)** Scaffold loading protocol. **(c)** Microinjection station in sterile laminar flow cell culture hood. **(d)** Micrograph of assembled  $\mu$ F domain – Reproduced with summarized text caption from [61], with permission of Prof. Roger Kamm, Biological/Mechanical Engineering Dept., Massachusetts Institute of Technology (MIT), and with permission from the Royal Society of Chemistry.

Kim *et al.* [68] have also developed a 3D-cell-culturing platform for differentiating embryonic stem cells (ESCs) in an embryoid body. 3D culturing is more efficient within pharmaceutical industry in reporting results of drug screening than 2D culturing, as it provides the cell-cell mechanical and extracellular matrix (ECM) interaction resembling that of an *in vivo* tissue [68]. Cell interference with its in-range vicinity is normally accomplished by adhesion to another cell, and through ECM via its surface macromolecules [69]. Alternatively, Leclerc *et al.* [70] have uniquely designed and fabricated a 3D-PDMS- $\mu$ F device of two stacked layers for Hepatocarcinoma liver (Hep G2) cell culture for eight days until confluence has been reached. They have identified that glucose consumption, and albumin production are a manifestation of ongoing activity of viability of cells. To maintain viability of cultured cells, the culture medium has to be altered routinely to provide glucose (nutrients) on a 2-day basis to maintain cell viability [70]. They have estimated the oxygen consumption within the  $\mu$ F device based on the product of cell density, area of cell culture, and cell oxygen consumption per second; also they have illustrated that the permeability of oxygen (introduced  $O_2$  to the system) through PDMS compartment is based on the product of permeability of PDMS into the ratio of the oxygen gradient concentration to the thickness of PDMS walls. However, there are some constraints associated with PDMS permeability, where water vapor and organic solvent could enter the PDMS through its permeability feature [54]. Thus, for better experimental productivity, PDMS-based  $\mu$ F device should be placed in a vacuum chamber to remove all moisture prior to conducting an experiment.

Cheng *et al.* [71] have utilized a biocompatible 3D E-coli cell assembly within a  $\mu$ F domain with parallel sidewall Cr/Au electrodes, via spatially programmable gel formation, and controlled pH parameter. They have utilized calcium-responsive alginate hydrogel, which they have electrochemically deposited into the  $\mu$ F platform. Here, they've uniquely defined side-

wall electrodes, enabling trap of a cell within hydrogel, where cells are adhered to the calcium alginate gel on the anode for a 3D visualization of the cell growth on the gel substrate.

### 2.2.1.c Thermal Stability and pH Neutralization

$\mu$ F domain experiences high surface to volume ratio which should increase diffusion rate and heat conduction processes [52]. Therefore, high surface to volume ratio alarms for temperature built up, and hence designers should carefully investigate the approaches in thermally stabilizing the system [63]. Variability in temperature affects viscosity of the medium, and thus the overall velocity profile of the flow [72]. Many researchers maintain temperature stability by incorporating transparent indium-tin-oxide (ITO) heaters into their  $\mu$ F platform [53, 55]. It is reported in literature that stable temperature, and pH rate should respectively be 37°C, and 7.2-7.4 within 5%  $CO_2$  [54].  $CO_2$  oscillation rate, entrapped in a  $\mu$ F chamber, is interrelated to pH acidity within the system that affects any extracted electrophysiological characteristics out of a bio-system [73].

Eddington *et al.* [74] have developed an i $\mu$ F system, in which the pH is automatically controlled in a self-regulating mechanism of an input stream with respect to the output. In [75], a label-free, low-cost, and disposable polycrystalline silicon TFT have been utilized as a biological sensor of specific ions and analytes that could be extended to monitor pH concentration. It is demonstrated in [55] that after cells' settlements in the bottom of the  $\mu$ F chamber,  $CO_2$  independent medium was drawn through the perfusion channels; during the continuous perfusion, the whole system is placed into an incubator to control humidity and temperature, where  $O_2$  is permitted through the permeability feature of PDMS, and the

continuous feeding of perfused nutrition ensured a stabilized pH rate [55]; incubators are used to maintain cultured medium in a 5%  $CO_2$  rate.

Dimov *et al.* [58] have illustrated a novel  $\mu F$  array plate (iMAP) for gene expression, protein immunoassay, and cytotoxicity of real-time optical molecular analyses of adhesive cells (HeLa, MCF7), and non-adhesive cells (Plasma cells U266, macrophage J774). Their developed  $\mu F$  system consists of two-layer soft lithography with no requirement of alignment. By maintaining a channel to trench depth ratio of greater than 5, with an inlet fluid velocity of 100  $\mu m/s$ , they have successfully managed to trace a particle with a 100% efficiency in their obtained simulation.

#### 2.2.1.d Elimination of Air Pockets

Bubbles could lead to clogging (malfunction) of the  $\mu F$  system. A non-uniform flow leads to bubble formation and cell death [70]. Elimination of air pockets could be accomplished in different fashions. For example, from a practical experience, removal of air bubbles within a  $\mu F$  device is performed by filling the domain with DI water on a low pressure for about 30 minutes: not to break the bonding between the  $\mu F$  and glass substrate. Also, Phosphate Buffered Saline (PBS) flushing can be performed to ensure a bubble-free environment prior to cell culturing as in [57]. Furthermore, a bubble trap could be installed interconnecting the syringe pump, and first inlet valve. Vacuum chamber is utilized during fabrication for surface treatment, and removal of air bubbles. Also, a bubble tank is incorporated between culture medium tank, and the  $\mu F$ -peristaltic pump platform for a system in a loop. During sterilization, ethanol also removes air bubbles. From an electrode perspective, increasing potential may contribute to formation of air bubbles, and reducing the flow rate; this also could contribute to improper supply of nutrients to the cell, as well as generation of backflow.

Bubble accumulations on an electrode can degrade its performance by reducing its emitted current. Channels with slit, pit, and/or groove features and/or with sharp corners are a source of air-bubble-pocket formation, and flow resistance constraints [76]. Electric means, capillary force, ethanol can all be utilized to eliminate such bubble accumulation if they are well controlled.

### 2.2.1.e Sufficient Supply of Oxygen

Oxygen supply is indispensable for cells to maintain their viability. The mammalian cell metabolism mechanism is dependent on supply of oxygen and removal of carbon dioxide [63]. Thus, the system has to mimic the balance between supply and demand achieved in metabolism. However, cells' consumption of oxygen varies from one type to another. As an example, embryonic stem cells require low  $O_2$  consumption rate for better proliferation [77], whereas hepatocytes demand high oxygen consumption rate [78, 79]. As the cell density increases, the oxygen consumption proportionally increases [63].

The vast majority of  $\mu F$  devices are PDMS based, since it exhibits a unique feature of permeability that allows for gas exchange within the outside atmosphere. Thus, PDMS permeability permits oxygen to enter the system, which reduces the need for oxygen supply unit (oxygenator) [70]. Also, high surface to volume ratio experienced in  $\mu F$  devices contributes into an excess in oxygen supply, and less molecular dilution [65]. Leclerc *et al.* [70] have estimated the oxygen consumption within a  $\mu F$  domain by the product of cells' density in the  $\mu F$  compartment per  $cm^2$ , the consumption of  $O_2$  of a single cell per second, and cell culture area.

### 2.2.2 Anticipated Objectives of the $\mu$ F System

In light of the relevant literature described in this chapter in terms of the requirements of cell's viability, and microfabrication limitations, it is a pre-requisite to have the culture chamber sufficiently large for cell to grow and differentiate, as well as to consider tie-in-connection constraints (i.e. syringe pump, disposal capillary tube, etc.). However, dense tie-in  $\mu$ F environment of mixers, valves, pumps, and so forth, affects the throughput of the system by adding more mechanical constraints; this shall also deviate from one of the main objectives in designing the LoC system, which is acquiring simplicity of the structure and experimental setup.

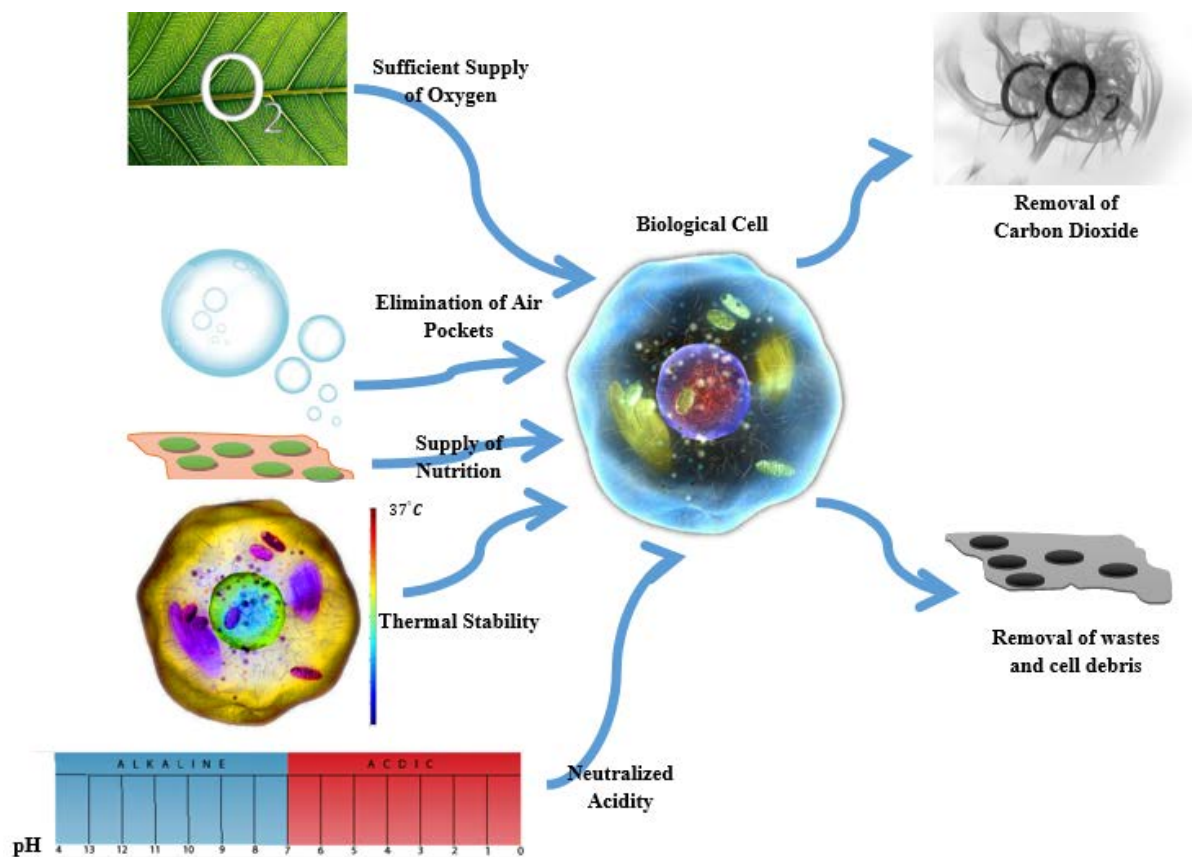
A uniform velocity profile is anticipated to ensure uniform distribution of nutrients (parabolic laminar flow profile). It is quite essential to design the channel breadth large enough to avoid adhesive cell accumulation (channel clogging). In order to prevent breakage of the glass-PDMS bonding, the channel has to be designed such that a pressure drop experienced within the channel is maintained at minimal during LoC system's normal performance. An essential design aspect of a rectangular channel is the hydrodynamic resistance factor that is directly proportional to channel length, and inversely proportional to channel width, and the third power of channel height [72]. From the biological perspective, **osmotic pressure**<sup>3</sup> [80] is essential for cell viability, and it should be considered that many cells do require attachments to solid surfaces prior to proliferation process to commence [73].

Figure 2.3 summarizes the aforementioned factors described in this research, which are required to maintain cell viability within a confined environment such as that of a  $\mu$ F and MEA

---

<sup>3</sup> Osmosis pressure is a force per unit area required to achieve a stabilized solute concentration resulted from solvent molecules' movement via partially permeable membrane to a higher solute concentration [80].

system. All these factors are quite essential during cell culturing, and preserving cell integrity (viability) prior to conducting *in vitro* experiments.



**Fig. 2.3** Requirements for cell viability by supplying sufficient oxygen rate and nutrition, elimination of air pockets, providing neutralized acidity and thermal stability environment, removal of wastes, insoluble cell debris, and carbon dioxide from the flow system.

As per the reviewed literature, controlling the flow within a  $\mu F$  domain is essentially important to gain a better controllability on cell trapping, manipulation, and distributing nutrition through growth medium to maintain cellular viability. This is achieved by analyzing the pressure and velocity profile of the flow. On the other hand, MEAs enhance the trapping of a cell as well, via imposed electric field. Furthermore, it is also important to maintain a uniform



current distribution, and avoid cross talk between two neighboring electrodes with a defined pitch distance, enabling faithful extraction of electrophysiological of cells, as well as allowing cell-line growth [1]. In the following subsections, Computational Fluid Dynamics (CFD), and Finite Element Method (FEM) are implemented as part of the design analysis approach. CFD helps in visualizing the flow pattern, and characterizing  $\mu\text{F}$  module building components (e.g., channel depth, length, etc.), whereas FEM analyses allocate a pitch distance between two adjacent electrodes to maintain uniform current distribution prior to microfabrication, and characterization of the LoC system that shall be introduced in Chapter 4.

### **2.2.3 System Level Design ( $\mu\text{F}$ Flow):**

As part of the detailed engineering analyses of the  $\mu\text{F}$  system, and the approach of utilizing a pressure difference via a syringe at the inlet and outlet ports to move fluids by inducing driven flow pressure, a Computational Fluid Dynamic (CFD) analysis, COMSOL Multiphysics 4.2a (Burlington, MA, USA), is performed to visualize and predict flow characteristics of the PBS medium. The objective of this analysis is to allocate optimal dimensions of the system that would contribute in sufficiently controlling pressure, and eventually injecting and ejecting medium solution to and out of the system at a uniform velocity rate. Furthermore, this first-hand empirical analysis will assist in analyzing the flushing process of PBS within the microsystem for several experimental uses, thus increasing system durability and usability.

In the  $\mu\text{F}$  system, the flow is laminar, and experiences a no-slip condition at walls; thus, this leads to a parabolic flow profile and limiting flow rate, which eventually yields a dispersion of sample plugs [81]. Laminar flow provides ease of controllability of the system [65].  $\mu\text{F}$  system exhibits a high surface to volume ratio (low characteristic length of the system), indicating a highly viscous laminar flow based on low Reynolds' number definition [81].

Accordingly, for an incompressible flow, the inertia term of the **Navier-Stokes equation**<sup>4</sup> drops out [82]. Another problematic design issue is flow resistance, which is found to be directly proportional to channel length, and inversely proportional to its width [81]. The size of the  $\mu\text{F}$  device should be selected such that it would hold an adequate amount of cell media (biological constraint), avoiding system clogging.

### 2.2.3.a $\mu\text{F}$ Model

The  $\mu\text{F}$  system analysis has been performed in several iterations, where depth and width of channels, dynamic viscosity and density of the PBS solution, and applied pressures are all held fixed, while the length of the channel varies (all resultant iteration graphs are not shown). The density and dynamic viscosity of the PBS buffer medium are  $1.06 \times 10^3 \text{ Kg/m}^3$ , and  $1.99 \times 10^{-3} \text{ Pa}\cdot\text{sec}$ , respectively [83, 84]. The analysis is conducted by considering a time domain (t). Therefore, the differential pressure injected into the system via a syringe mechanism in the inlet reservoir with respect to the outlet is timely controlled, as described in Equation (2.1). The pressure at the outlet reservoir is set to zero, where there will be no viscous stresses. Similarly, it is assumed that there will be no viscous stresses at pressure inlet exerted near the culturing reservoir upper edge, and it is defined in the following time-dependent equation:

$$P_{\text{applied}} = P_o + P_a \sin(wt) \quad (2.1)$$

Where, the pressures offset and amplitude are denoted as  $P_o$  and  $P_a$ , respectively, while applied pressure at the inlet is  $P_{\text{applied}}$  and  $w$  is angular velocity. The buffer medium flow within the  $\mu\text{F}$  system is laminar; thus, the flow pattern and characteristics are depicted by

<sup>4</sup> A mathematical formula that describes the kinematics and kinetics of a fluid flow [80]

solving the incompressible Navier-Stokes, Eq. (2.2), and continuity equation, Eq. (2.3), numerically within a 4-second-time domain to simulate fluid-injection time to the system.

$$\rho \frac{\partial u}{\partial t} - \nabla \cdot \eta (\nabla u + (\nabla u)^T) + \rho u \cdot \nabla u + \nabla P = 0 \quad (2.2)$$

$$\nabla \cdot u = 0 \quad (2.3)$$

$$(\nabla \cdot \eta (\nabla u + (\nabla u)^T)) \cdot n = 0 \quad (2.4)$$

$$P = P_{applied} \quad (2.5)$$

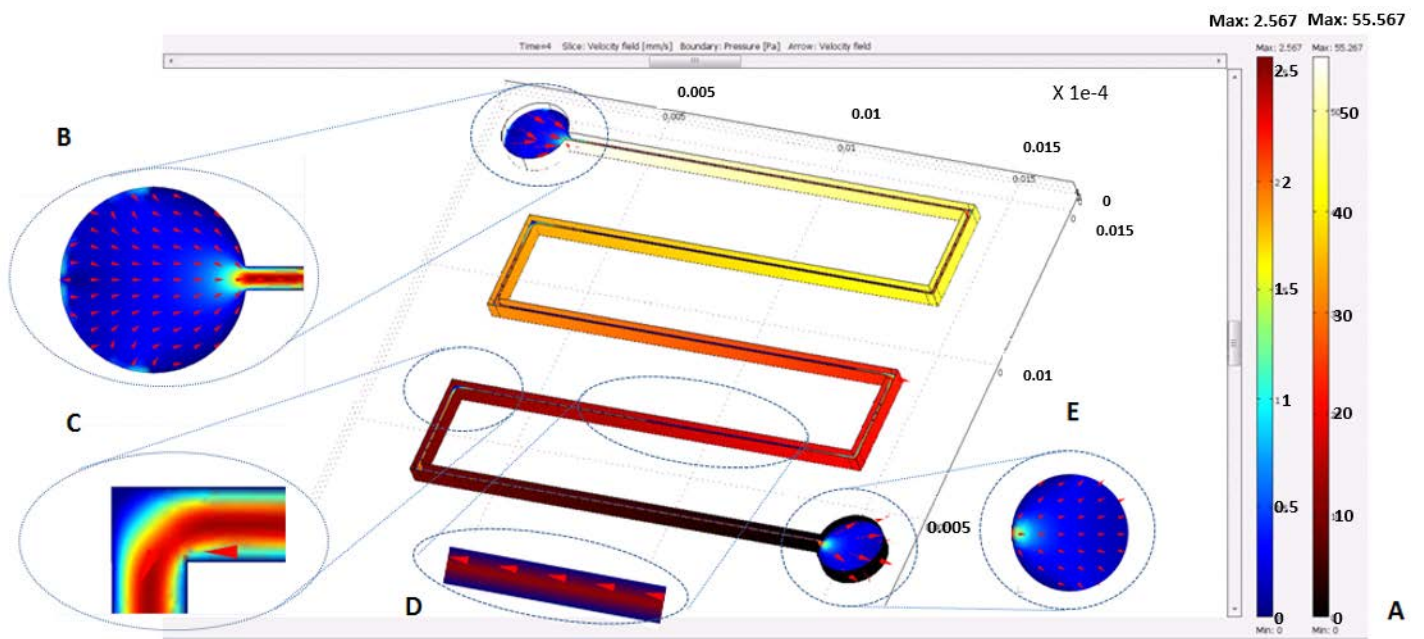
Where,  $u$  is the velocity,  $\rho$  is density,  $\eta$  is the dynamic viscosity of the solution, and  $n$  is the outward normal unit vector of the boundary. A no-slip condition is imposed, where velocity components at the walls are zero. The solution maintains a uniform density, and viscous stress effect diminishes at the inlet and outlet of the  $\mu$ F system.

### 2.2.3.b CFD: $\mu$ F System Characterization

Figure 2.4A depicts the velocity-field distribution and pressure at walls throughout the  $\mu$ F system. The right and left level indicators at the right side of Figure 2.4A, show pressure and velocity distribution, respectively. For pressure indicator, yellow indicates maximum pressure while dark red is minimum pressure experienced within the system. As for velocity distribution level indicator, red signifies maximum velocity, while blue is minimum. Figure 2.4D indicates that the streamlines (arrow velocities), within the microfluidic channel, are maximum

(squeezing) and experience a Gaussian velocity distribution across the width of the channel, where the maximum velocity is at the center of the channel. This result is anticipated as it depicts a typical Poiseuille (laminar) flow.

From the obtained results, a large pressure drop (pressure loss) would reduce the flow in the microchannels, and thus affecting the flushing process for proper maintenance of the system. This obtained optimal CFD result predicts flow pattern, and helps designers to reach a system that exhibits a uniform overall pressure distribution -- achieving better flow controllability over time.



**Fig. 2.4** (A) Pressure at walls and velocity field in the microchannel at  $t = 4$  sec, (B) Velocity profile distribution at the neck exit of the culturing reservoir and into the channel, (C) Built-up pressure at sharp edges, (D) Gaussian Poiseuille velocity profile within the microchannel, and (E) Pressure at minimum and velocity distribution at the exit reservoir.

From the obtained results of the several empirical iterations (just optimal case is shown), it has been demonstrated that in a longer channel case, the flow is slow due to a very large pressure drop caused by frictional losses. It should be noted that the larger the pressure loss, the slower the flow in the channels. On the other hand, shorter channels experience high pressure, and thus high velocities are being immediately experienced preceding the outlet, which will complicate the process of controlling the flow. However, the optimization process has yielded a system as shown in Fig. 2.4 with a uniform pressure gradient along the channel, and thus has a uniform parabolic velocity near the outlets, and offers a uniform flow controllability. In addition to the empirical analyses, the resultant size of the  $\mu\text{F}$  device as depicted in Fig. 2.4 meets the constraint/requirement of holding an adequate amount of cell media. The channel width is optimally chosen to fairly encapsulate the width of cell-line growths within a confined environment. As per the empirical analyses, the channel width is  $228\text{ }\mu\text{m}$ , and length varies on each side of the  $\mu\text{F}$  system. The diameter of the culturing and outlet reservoirs, where cell culturing is initiated and disposed from the system respectively, are of equal size of  $1.77\text{ mm}$  -- giving sufficient space for syringe tip to be injected into a feeding tube that is connected to a pin adaptor/connector. Based on the flow optimization analyses, the entire  $\mu\text{F}$  system has a uniform depth of  $20\text{ }\mu\text{m}$ .

### **2.3 Integrated Multi Electrode Arrays (iMEAs)**

In addition to the mechanical pressure driven flow exhibited in the previous section, the objective is to increase the versatility of the bio-mechatronic platform by considering a second driving force of the flow for future extension of this work: electroosmotic/electrokinetic, and electrophoresis. This is in line of the Constructal law in identifying the imperfection of a current

existing design, and arriving at enhancement tactics to elevate the existing flow system design. Thus, on the contrary to pressure-driven flow, electroosmotic/electrokinetic are utilizing electric field to induce fluid dynamics, whereas electrophoresis is used to cause motion of particles within the fluid [76]. In the study of [76], electrophoresis illustrates the movement of biological particles by electric fields, in which DNA for instance migrates towards a positive electrode, whereas electroosmotic flow is the fluid flow from a positive to a negative electrode [76]. Thus, the proposed system shall have the flexibility to switch between a simply operated-pressure-driven flow to an electro-kinetic flow: switching from the former to the latter mechanism enhances cell trapping and manipulation processes, and most importantly overcomes the deficiency of the pressure-driven flow with the incorporation of the no-slip condition at the  $\mu\text{F}$  walls, leading to a parabolic velocity distribution, and thus non-uniform distribution of nutrients, whereas electrokinetic driven flow exhibits a relatively uniform velocity distribution.

This added feature would contribute into cell trapping, deformation, and manipulation under a presence of an electric field. This is accomplished through integrated multi-electrode arrays (iMEAs), within the LoC/ $\mu\text{F}$  domain.

### **2.3.1 Electric Field Cell Manipulation**

A constant demand by bio-experimentalists working on cell manipulation is to optimally control the flow, and report changes in a real-time response. Although it is beyond the scope of this research in utilizing electric means in manipulating cells, it is worth re-stating that the limitations of pressure driven flow are overcome by utilizing an electric field to impose cell movements via electrophoresis mechanism, which is quite essential, and it is a very dense area

of research. Furthermore, it is worth stating that there is a third mechanism in manipulating cells, which is beyond the scope of this work as well, and that is the optical tweezers approach [85].

Issadore *et al.* [86] have comprehensively illustrated a method of cell manipulation through electric field frequency (i.e. dielectrophoresis, magnetophoresis, electrofusion): in a hybrid IC/ $\mu$ F chip. They have shown an ease of controllability of cell manipulation over a pico liter of volume. Their proposed system leads to a full automation in terms of deforming, trapping, and moving biological cells at potentials in MHz frequency, whereas mixing and fusion are achieved by electrofusion, and electroporation at potentials in a frequency range below 1 KHz. This is performed on the basis of dielectrophoresis (DEP) in a vast multi-electrode environment. Such system provides an automated multitask LoC platform that eliminates the bulky micromechanical tie-ins of the system, e.g., mixers, pumps, latches, and valves. They have also illustrated in their experiments that cell-membrane potential is dependent on the frequency of the imposed electric field, and it remains unharmed at frequencies below 1 KHz within a range of a utilized DEP. Furthermore, this shall open a new frontier in analyzing cell-cell communication without physical contact among cells, which is usually performed through a cellular gap-junction mechanism – **gap junction** is a physical biochemical connection among cell network [63]. Moreover, iMEAs contribute into extracting cell electrophysiological characteristics, which shall be further addressed in Chapter 4; hence, the obtained cell-membrane potential will be correlated with cancer cell contractile force (Chapter 6).

Cell manipulation and flow driven by electrical means are beyond the scope of this Ph.D. study, rather the main focus is on utilizing iMEAs in extracting the cell-membrane potential. MEAs contribute into high throughput of the LoC platform in terms of cell manipulation. As illustrated in Alqabandi *et al.* [1], multi-electrode arrays are acting as sensors in a passive mode

---

(recording electrode), and as a stimulator to the cell in an active mode, enabling the extraction of electrophysiology of cells.

### **2.3.2 Capturing Electrophysiology of Cells**

It has been reported that the electrophysiology/electrochemical characteristics of even a very diminutive building component of a cell such as a protein have been detected by utilizing MEAs [53]. Therefore, electrodes are utilized for electrochemical detection [1, 87], where such electrochemical changes at a molecular level contribute into the bio-signaling process [88].

On the same application, Dworak and Wheeler [89] have designed and fabricated a novel and highly stable MEA integrated within PDMS microtunnels to capture the speed and direction of cell-membrane action potential propagation, which was on the magnitude of a 300  $\mu\text{V}$  electric signal of isolated axon cells; they have developed a system consisting of four culturing wells, and one central interconnected by microtunnel arrays, where three configurations of varying Au/Cr microelectrode width (25  $\mu\text{m}$ , 50  $\mu\text{m}$ , and 75  $\mu\text{m}$ ), with a pitch distance of 200  $\mu\text{m}$  have been placed underneath the PDMS channel to investigate the dependence of signal amplitude on electrode size. The 50 and 75  $\mu\text{m}$  electrodes produce larger signals depending on their configuration and size within the channel. The theory behind having the MEA buried beneath the PDMS channel floor is to create a high amplification of the induced potential considering that the micro-size of the tunnel experiences a very high resistivity of 16  $\text{M}\Omega$  [89]. On an instrumentation aspect, current to voltage (I/V) convertor, and a system of digital-to-analog convertors (DACs) are utilized to assure controllability of induced potentials through gold patterned electrodes [90].



### 2.3.3 MEA Configuration

An overlap of neighboring electrodes could affect the performance of the entire MEA system. Freire *et al.* [91] have investigated the influence of the number of electrodes, their distribution pattern on the basis of gain of the signal-to-noise ratio (SNR), and overlap (cross talk) between adjacent electrodes due to diffusion layers. Based on their previous studies, the minimum maintained distance between two neighboring electrodes in MEA domain should be greater than six times their diameter of wire-shaped electrodes to eliminate overlap of diffusion layers. Also, they have investigated different variations of distances between electrodes on detection limit; the faradic current increases with distance, which negatively affect the detection limit. For their particular experiment, it is found that the distances between electrodes should be of 20 times the electrode diameter; also the detection limit resolution weakens, affecting the overall signal-to-noise ratio (SNR) of the system. Usually, the range of distance between two neighboring electrodes varies from 1-10  $\mu\text{m}$ , however, it is subject to microfabrication constraints, as well as the main desire of achieving high sensitivity by having a strong electric field [87]. A reduction in electrode surface area leads to a reduction in obtained signals [75].

### 2.3.4 System Level Design and Characterization: MEA

As for the MEA configuration, important findings for the design constraints associated with electrode cross talk, uniform stimulation threshold, heating of cell membranes, and electrode erosion have been extensively investigated and discussed by Planker *et al.* [92]. Their conclusion is that large-electrode cell displacement leads to a cross talk between adjacent

electrodes, and thus high charge density and power stimulation – eventually introducing heat to the system and causing electrodes to be eroded (poor resolution output). They have proven that the stimulating-threshold current is directly proportional to electrode-cell displacement, as well as electrode size. As a result of their findings, the optimal distance between neighboring electrodes should preserve a tenth of electric field of one electrode to a neighboring recording one.

In this research, a three-dimensional finite-element-method (FEM) model of two-upper-and-lower neighboring electrodes within a  $\mu\text{F}$  channel has been constructed, where the width of the electrode is held fixed at  $228\ \mu\text{m}$  (comparable to channel width), while the pitch distance between the stimulating and recording electrode was varied through several iterations. The electrodes used in the simulation are gold coated of rectangular shaped. The objective of the model is to visualize the current density distribution within the PBS buffer medium, and thus identify an optimal distance that provides a uniform current density distribution, and allows sufficient space for cell-line growth between two neighboring electrodes.

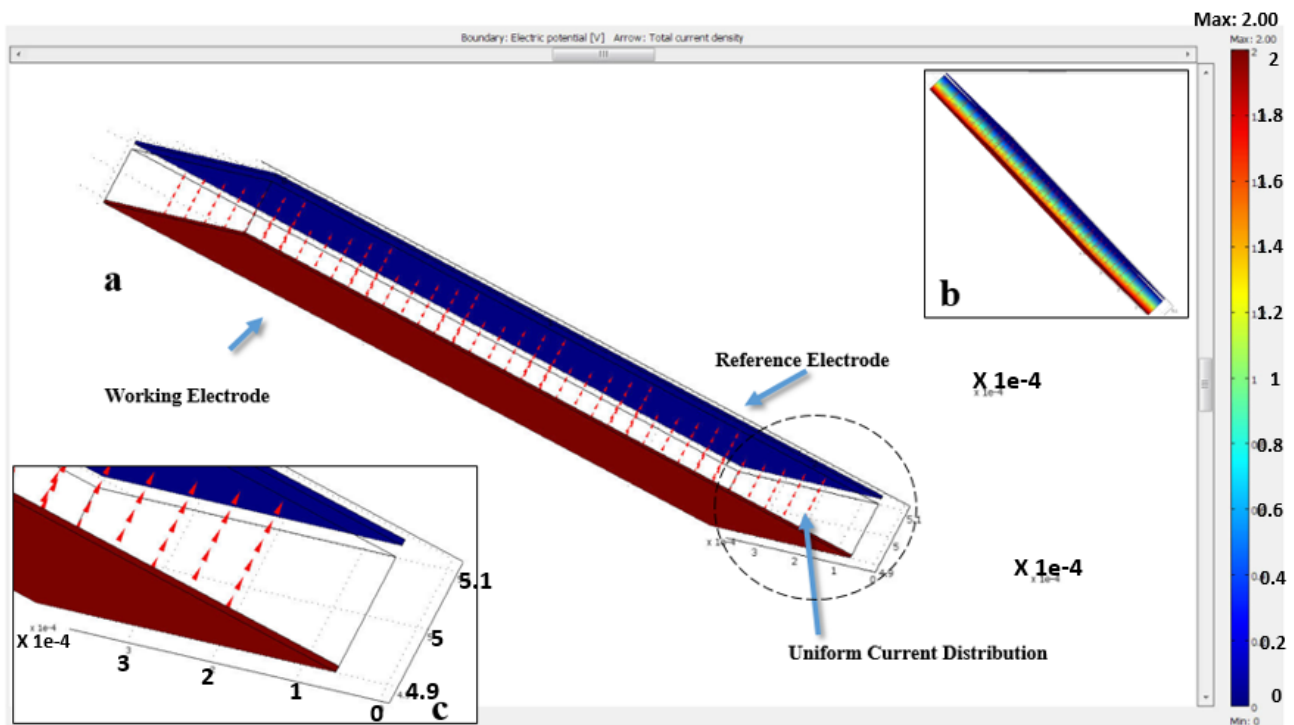
The principal physical relations are based on Maxwell's continuity equation (2.6), and two constitutive relations interrelating electric field, total current density, and electric potential of the system – Equations (2.7) and (2.8):

$$-\nabla \cdot (\sigma \nabla V) = 0 \quad (2.6)$$

$$E = -\nabla V \quad (2.7)$$

$$J = \sigma E \quad (2.8)$$

Where,  $E$  is the electrical field,  $V$  is the potential,  $J$  is current density, and  $\sigma$  is conductivity. The conductivity of the PBS and gold electrode are  $179 \times 10^{-3} \frac{S}{m}$ , and  $45.2 \times 10^6 \frac{S}{m}$ , respectively [93, 94]. Figure 2.5 shows the potential profile of electrodes as well as arrow representation of a total current density within the microchannel; the level indicator represents potential experienced within the system, and arrows illustrate current distribution between the active and passive electrode. After several iterations in COMSOL Multiphysics 4.2a, the current density distribution is relatively uniform at a pitch distance of  $20 \mu m$ . At this distance, the stimulating electrode doesn't experience comparatively high current density at its edges. High current density leads to a biofluidic coagulation, which will eventually affect the efficiency of cell electrophysiology measurements. Furthermore, reaching a uniform current distribution is desirable in designing an optimal distance between electrodes on the essence of providing stability of measurements over an extended period of time, and ensuring a damage-free cell membrane. Remarkably, the obtained optimal distance between the two neighboring electrodes that yielded a uniform total current distribution is in agreement with the obtained channel depth of the microfluidic system in achieving a proper pressure and velocity distribution, enabling better flow controllability (flow system integrity). The obtained optimal depth also complies with a biological constraint of entrapping cells, whose diameters are on average of  $8-10 \mu m$  [1].



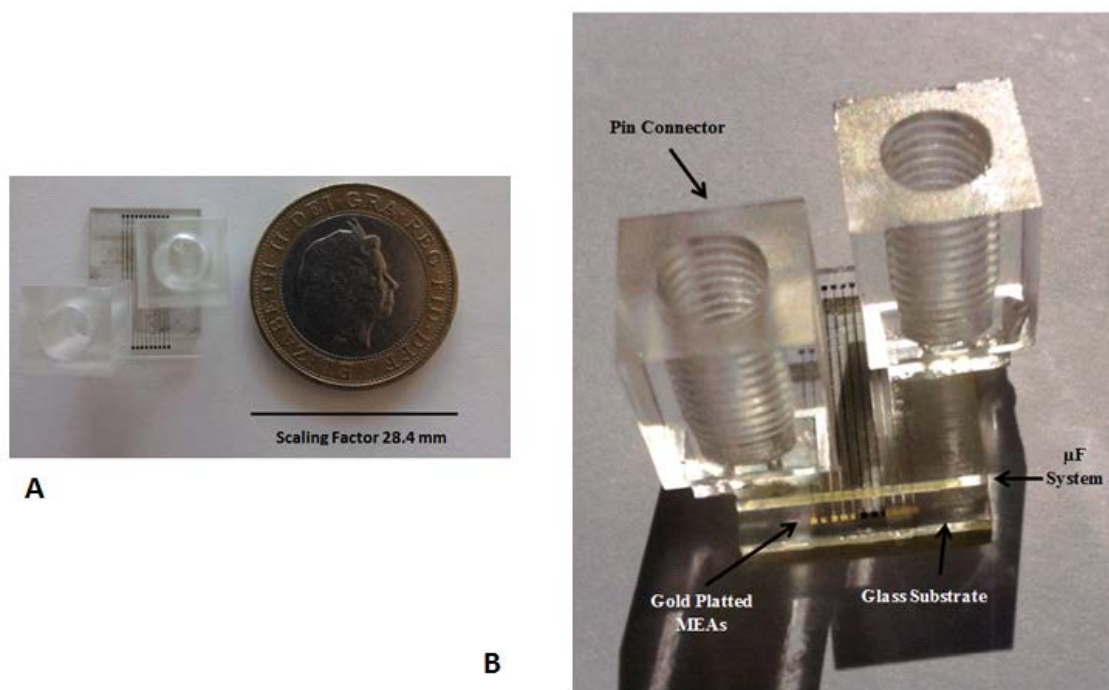
**Fig. 2.5** (a) Empirical analyses of a stimulated working electrode and recording reference electrode, (b) potential gradient distribution within the electrical field between working and reference electrode, and (c) enlargement of the small dotted circled section showing a uniform current distribution between the two electrodes within a  $\mu\text{F}$  channel.

## 2.4 Conclusion

This chapter has highlighted the dominant criteria for cell viability: sufficient supply of oxygen and nutrition, stabilized thermal system and pH rate, elimination of air pockets, and disposal of carbon dioxide, cell debris, and wastes. Furthermore, this chapter has shed light on extraction of cell electrophysiology, and has manifested the importance of *in vitro* testing as opposed to *in vivo* and petri-dish culturing. It is clearly illustrated how nature defines the engineering requirements of two important building blocks of LoC components –  $\mu\text{F}$  and MEAs. The

understanding of cellular biology requirements as a flow system defines a design strategy, on the basis of science, where spatial and temporal pattern, as well as system configuration of the major building components of LoC ( $\mu$ F and MEAs), are prominent. Such design approach shall save time, resources, and it shall avoid trial and error during microfabrication; it helps in understanding the cellular physical behavior when conducting *in vitro* experiments.

The design synthesis, in light of biological constraints, has yielded empirical analyses in terms of visualizing the flow within a  $\mu$ F domain that ensures uniform pressure gradient distribution, and uniform flow rate: ensuring controllability in flushing the system with PBS medium. This is accomplished through the constitutive relation sets forward in Navier Stokes, and continuity equations. From the MEA perspective, the FEM optimal result has illustrated a uniform current distribution between two adjacent electrodes. Such design syntheses on the essence of analyzing cellular viability, and design analyses of the CFD and FEM models should assist designers prior to microfabricating  $\mu$ F and iMEA LoC system. Such described design syntheses and analyses within this chapter have contributed in microfabricating the LoC shown in Figure 2.6, by controlling the microfabrication lithography and etching processes. The microfabrication and *in vitro* experiments shall be further elaborated on in Chapter 4.



**Fig 2.6 (A)** A top view of the LoC module placed next to a two-sterling British pound coin as a scaling factor **(B)** An image showing connecting pins of culturing and outlet reservoir, and gold plated upper and lower MEAs patterned on two glass substrates (upper and lower) which are crossing the microfluidic channels.

**Declaration:** This chapter appears in a peer-reviewed paper by the author -- Alqabandi, J. A., *Design syntheses and analyses of a lab on a chip (LoC) module based on biological cell requirements in nature. Design and Nature 2014: 7th International Conference on Comparing Design in Nature with Science and Engineering. WIT. 2014.*

# **Chapter 3**

---

---

## **Electrophysiology of Cells**

---

---



*"One cannot really argue  
with a mathematical  
theorem."*



## **Chapter 3: Electrophysiology of Cells**

### **3.1 Introduction: Electrochemical vs. SAW/Optical Approach**

Considerable research efforts are being geared towards finding new instrumentations and detection techniques of cancer at a cellular level that would overcome the problems and limitations of the currently existing ones, e.g., CT scan, X-Ray, MRI, PET and Bone scan [33-40, 42-45]. Cell's electrophysiology plays a pivotal role in cancer formation, which has initiated the necessities to develop a device that could detect the biophysics of cells [1, 2, 20, 95, 96]. Furthermore, electrophysiological cell-cell communication via ion and gap junction initiates different biological phenomena, such as cell's motility, apoptosis, mitosis, tissue reconstruction, and inflammation healing [1, 96, 97]. Moreover, it has defined two classes of cells: excitable (action potential propagating cells) such as neurons, muscle cells, and endocrine, as well as non-excitable cells (non-propagating action potential cells), such as fibroblast tissue cells, fat cell adipocytes, and endothelial cells within the boundary interior of veins, capillaries and arteries [96, 97]. Thus, the detection of such cellular phenomena can act as a label-free biomarker of cell status, type, and functionalities. However, it is fundamentally noteworthy to state that in order to optimally design, characterize, fabricate, and test a functionalized biosensor that would detect such cellular phenomena, is to initially necessary to understand the biophysics of cells, and investigate the controlling parameters of cellular electrophysiology. Therefore, this chapter sheds light on a vital aspect of research methodology, which is a mathematical modeling of electrophysiology of cells; understanding the dominant controlling parameters' role in shaping the physics associated with cellular

---

electrophysiology should shorten lead time, and alleviate costs and efforts prior to conducting bio-experiments -- enabling researchers to simulate and tentatively predict the outcomes of experiments without the suffer and cost associated with ordering, incubating, and culturing of cells. Furthermore, development of mathematical modeling would assist in effectively analyzing the obtained experimental results prior to microfabricating a customized biosensor, and hence efficiently validating the developed analytical model with the experimental findings.

To provide a comprehensive research on the subject of cellular electrophysiology, especially to novice readers, this chapter first highlights the merits, drawbacks, and mechanisms of different non-conventional methodologies utilized to analyze the characteristics of cells: Surface Acoustic Wave, Optical Fluorescence, and Electrochemical approach. By advocating the last approach, a vast literature review on experimental findings on cancer electrophysiology is provided to manifest the heterogeneity of tumorigenesis on the essence of biophysics of cells. This should provide a solid platform, and a sense of high appreciation to the importance of cellular biophysics role in cancer formation prior to invoking the subject of mathematical modeling with its detailed derivations, and presented empirical solutions. Hence, in addition to the aforementioned limitations, and constraints of conventional approaches in detecting cancer at a cellular level in Subsection 1.4, non-conventional techniques have been investigated, which include Surface Acoustic Wave (SAW) based sensors, lab-on-a-chip (LoC) optical fluorescence, and electrochemical-based approach.

SAW sensors are compact in size and can be wirelessly controlled [98-100]. The operation of SAW biosensors is based on placing a targeted biological specimen between two interdigital transducers (IDTs): input and output IDT [98-100]. The piezoelectric-based input IDT is stimulated by voltage means that consequently generates acoustic waves. The waves propagate crossing over a biological model towards the output IDT, where the acoustic waves are captured, and transduced by mechanical deflections of the output IDT fingers [98-100]. The

problems of acoustic-wave-based approach are in fourfold: (1) it requires lengthy calibration processes [101, 102]; (2) the wave propagation is difficult to control [103]; (3) a pre-knowledge of acoustic wave properties associated with the biological system is necessary that adds complexity to the detection feature of any biological phenomena in terms of reaching optimal sensitivity and specificity [104]; and (4) most importantly, acoustic waves could be invasive, and hence can endanger healthy cells [105].

Optical fluorescence based approach works by processing molecular images at various illumination wavelengths [96, 106-108]. This approach is non-invasive, yet it exhibits a “**dark**” **signal noise**<sup>1</sup> constraint [109]; like SAW approach, its sensitivity is dependent on species’ size [104, 110, 111]. Finally, electrochemical-based approach is established on sensing the electrophysiological potentials of biological cells. This approach, as manifested in Alqabandi *et al.* [1], relies on chemical potential experienced within a biological cell domain; it offers high resolution and sensitivity of measurements, where change rate of ionic concentration is dynamic, so is the biological system: reporting a close to a real-time response [1]. Thus, in this research, the electrochemical approach is highly advocated as a method in extracting the electrophysiology of cancer cells as one of two major factors that differentiate among cancer cell various stages. The other important factor lies within the field of Mechanobiology (contractile force), which shall be further addressed in Chapter 6.

### 3.2 Cell-Membrane Potential: The Electrochemical Approach

Typical methods of extracting the cell-membrane potential via electrochemical approach are classically pursued through three techniques: a patch clamp [2, 112, 113], voltage-sensitive fluorescent dyes [2, 96], and utilization of nano/micro electromechanical means [1, 2, 95]. A

---

<sup>1</sup> A dark noise is a current that is attributable to electric field sweeping of stochastically initiated electrons and holes in the depletion layer of photosensitive platforms.

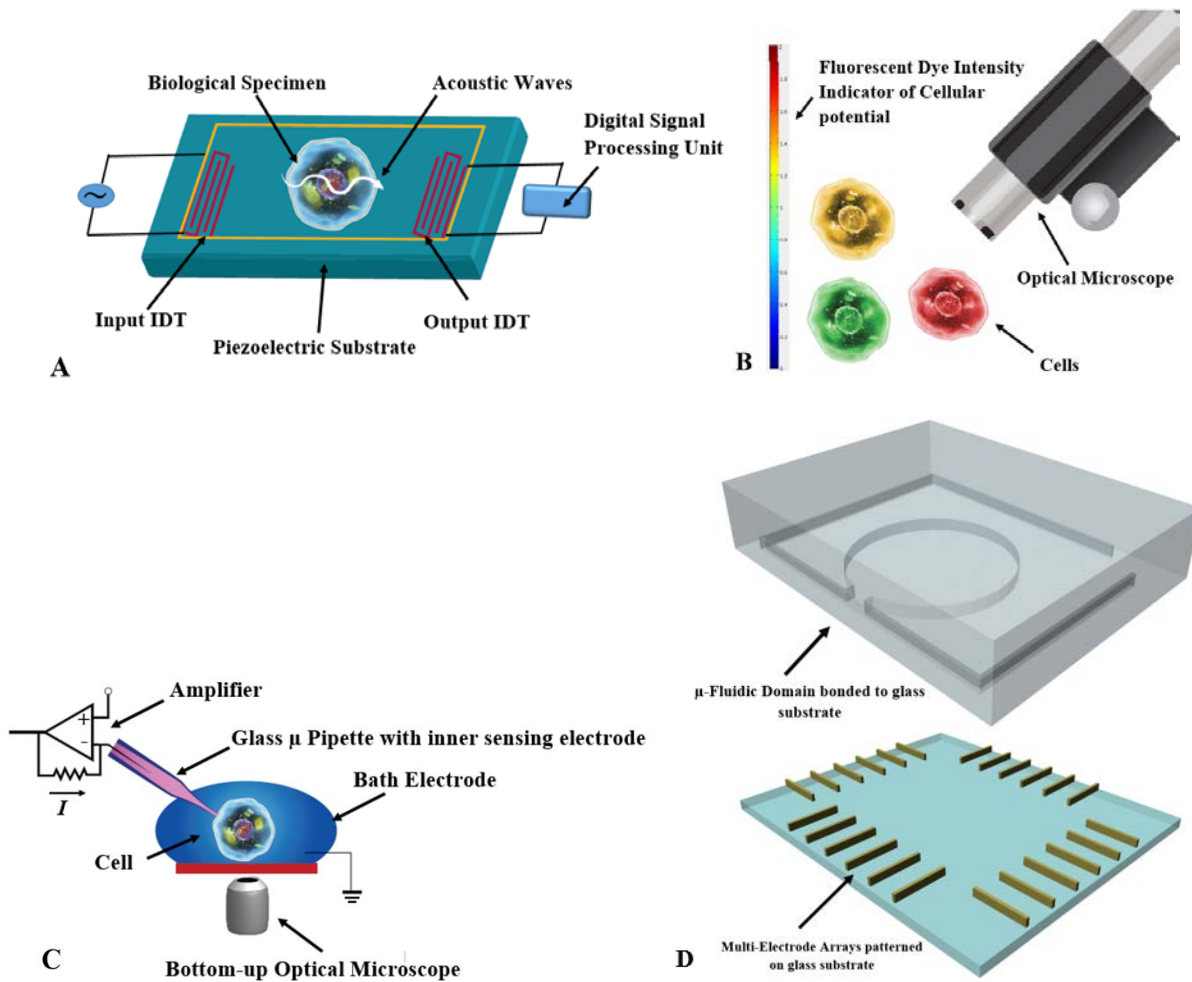
patch clamp could be invasive, and doesn't faithfully represent the cell-membrane potential in the cell's intended normal living environment [112]. The voltage clamp approach is described as fixing (clamping) the membrane potential at a fixed value, where a pipette and electrodes are used, which leads to no capacitive current flow of the cell membrane; thus, the total membrane current equals the ionic current [2, 112, 113]. On the other hand, voltage-sensitive fluorescent dye method is based on optical detection of the percentage difference experienced in fluorescence dye molecules, when interacted with the electric field of the cell membrane [2, 108]. It is worth re-stating that cell-membrane potential is also referred to in literature as transmembrane potential.

Despite the simplicity of the voltage-sensitive fluorescent dye approach in preparations, its unique feature of being implemented to a population of cells, applicability of analyzing the spatial profile of cell-membrane potential, and unlike patch clamp it can detect a minute change of cellular physics within a biological structure, yet it experiences major drawbacks [2, 96]. The deficiencies of dye optical detection method are mainly due to calibration constraints, limited sensitivity to capture various biological electrochemical phenomena at once, the extensive usages of such dye is limited in obtaining a confidence in the measured cell-membrane potential, and it experiences difficulty in attaining an absolute value of cell-membrane potential [2, 96, 114].

The third approach is an exponentially growing field in extracting the electrophysiology of cells, which is based on the utilization of nano/micro-electro-mechanical-system (N/MEMS) technology. It is demonstrated that by placing a cell between two electrodes in a microfluidic channel, the presence of the cell will generate a potential difference between the electrodes, upon a certain stimulation the cell-membrane potential can be obtained [1, 2, 95]. Moreover, this approach allows the registration of the biophysics of a single, as well as a population of cells; also, it analyzes signal propagation in temporal and spatial domains, lessens cross

---

contaminations, maintains cell viability due to the merits associated with the miniaturized LoC in terms of biocompatibility, thermal stability, neutralized acidity (pH), controlled supply of nutrients and oxygen, as well as disposal of wastes and carbon dioxide in a high throughput, less laborious, and cost effective working environment. Moreover, it avails the benefit of controlling signal propagation as opposed to the random propagations of signals experienced in a petri dish. In addition, this technique provides reusability for a number of experiments, and stability in obtained measurements. Therefore, in this research such approach concept is highly promoted. Figure 3.1 summarizes the various non-conventional methods addressed within this chapter in studying the biophysical characteristics of cells.



**Fig. 3.1** Non-conventional methods in studying the characteristics of cells: (A) SAW based sensor, (B) Optical Fluorescent Sensor, (C) Patch Clamp Method, and (D) N/MEMS technology consisting of a microfluidic and multi-electrode-array domain.

### 3.3 Relevant Literature on Cancer Electrophysiology

Electrochemical characteristics of a bio-cell are a manifestation of cell mitosis status, and DNA synthesis [2, 96]. Even proteins and their building components (amino acids) possess distinctive electrophysiology characteristics [115]. Remarkably, an enormous electric field is created within the vicinity of a biological cell [116, 117]. Marino *et al.* [118] have obtained the

electrochemical potential of a breast cancer cell collected from 110 female patients of different ages, races, and of different infected breast sides (right or left). Their analyses have considered 81 benign cases among which fibrosis, and fibroadenoma are analyzed, and 29 malignant of which ductal carcinoma is investigated [118]. Interestingly enough, they have exploited two cases in terms of cell potential: **Contralateral** and **Ipsilateral**. The former is defined in medical terms as the reoccurrence of cancer in “the opposite breast side,” whereas the latter is defined as the redevelopment of cancer “on the same breast side” [66]. Their findings on the magnitude of electrochemical potentials of cancer, and benign for Contralateral case are respectively  $16.8 \pm 15.3$  mV, and  $18.5 \pm 11.1$  mV (Mean  $\pm$  SD), where SD is the standard deviation [118]. On the other hand, the magnitude of electrochemical potentials of cancer and benign for Ipsilateral case are  $17.4 \pm 12.8$  mV, and  $16.9 \pm 8.9$  mV, respectively [118]. In their study, they have reached no conclusion in relating age of the patient to the associated electrical potential; furthermore, they have noticed an alteration in  $K^+$  cation concentration that manifests the activity of  $K^+$  ion-channel within the infected area [118].

In a publication by Cone and Tongier [119], it has been found that for Chinese hamster cells, the normal cells experience a membrane potential of -70 mV, while cancerous cells exhibit a potential of -10 mV, where DNA synthesis is imposed. On the other hand, Schaefer *et al.* [120] have measured the membrane potential of a rat Shay chloroleukemic tumor cell (leukemic cell), which was found to be  $-9.02 \pm 0.4$  mV (inside relative to the outside ground potential), by using a microelectrode of 10-30 M $\Omega$  tip resistance, and tip potential of -1 to -3 mV. Furthermore, they have measured the ion concentration of cells for  $K^+$  ion,  $Na^+$  ion,  $Cl^-$  ion, and water, which were  $122 \pm 9$  mEq/liter of cell water,  $48 \pm 4$  mEq/liter,  $72 \pm 7$  mEq/liter, and  $77.5\% \pm 0.5\%$  of cell wet weight, respectively. On the other hand, the external potassium

concentration was increased from 7 to 120 mEq/liter, where diffusion of external  $Na^+$  ion into the cell via ion channels didn't significantly change the internal concentration of  $K^+$ .

Marino *et al.* [121] have investigated the relation between cell-membrane potentials of breast tissue together with breast epithelial cells, and oncogenesis (progression toward malignancy and tumor formation) from one side, as well as electrical potentials of the surface of the breast from another perspective. They have recognized that presence of distinctive electrochemical potential of a cell is mainly attributable to diffusion (nutrient ionic concentration moving from high concentration to low); this highlights the depolarization feature of cancer cells as opposed to healthy ones, in which an increase of positive charges of the cancer cell is reached, and its polarity is eliminated or neutralized [121]. This is achieved by a reduction or a loss of intracellular potassium concentration ( $K^+$ ) to the extracellular region, as well as a built-up concentration of sodium ( $Na^+$ ) within the intracellular regime [121]. They have conducted their experiments on a criterion base of having a minimum of 20 cells for each studied case, where female-human subjects of different ages and races, as well as laboratory animals have been investigated. In general, it is found that cancer cell-membrane potential is less in magnitude than that of a healthy cell [121]. For instance, for 28 samples of MCF 10A cell (healthy epithelial cell line), the cell-membrane potential is  $-58.1 \pm 5.8$  mV; for 45 samples of MDA 435 L2 (Human breast carcinoma), the cell-membrane potential is  $-51.8 \pm 8$  mV; and for 33 samples of MCF7 (human breast adenocarcinoma cell line), the cell-membrane potential is  $-42.1 \pm 5.3$  mV [121]. Furthermore, they have reached a conclusion that cell-membrane potential is not related to patient's age [121].

On a liver-tissue scale, Sun *et al.* [108] have investigated the cell-membrane potential of four human malignant hepatocytes cell lines (Chang, HepG2, HuH-7, and PLC/PRF/5), and further studied the GABA<sub>A</sub> receptor mRNA expression within the same cell lines; interestingly, they have analyzed the consequences of restoring the cell-membrane potential of such



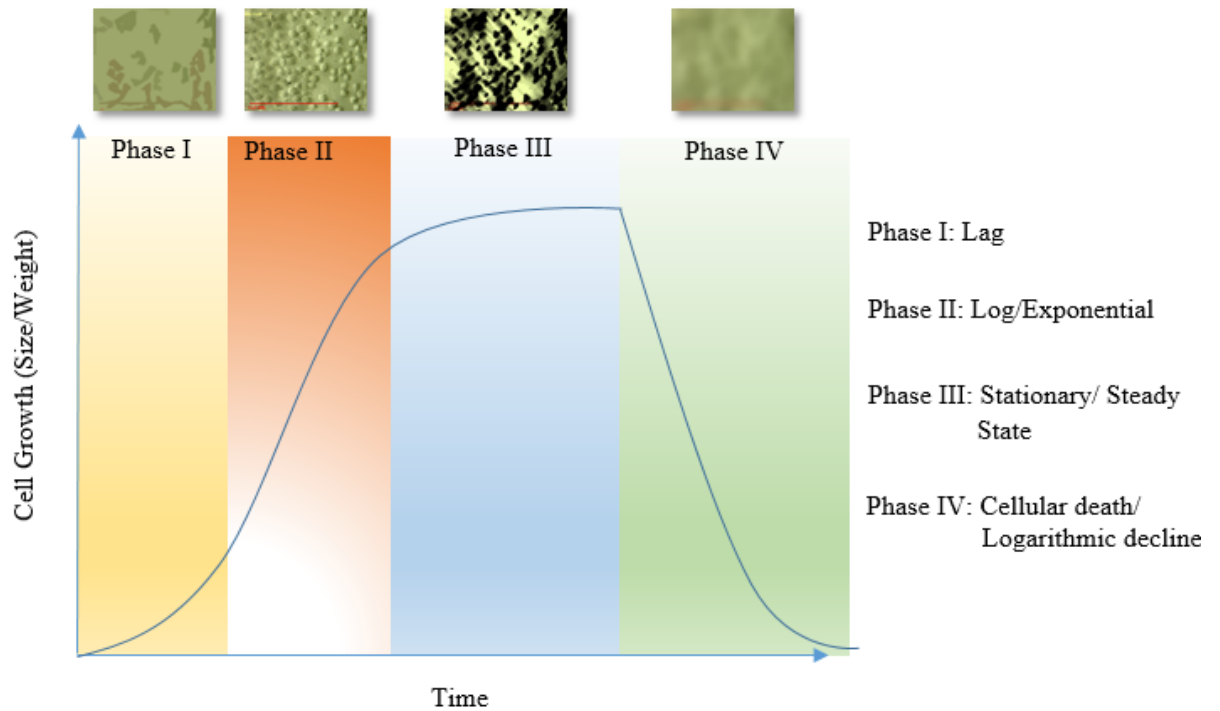
malignant cell lines to the vicinity of the resting potential of nonmalignant hepatocytes. Their potential measurement were carried out by optical fluorescent voltage-sensitive dye, and GABA<sub>A</sub> receptor expressions were monitored by RT-PCR screening together with performing Western blot (protein immunoblot) analyses, an extensively used analytical technique in the analysis of individual proteins. In their study, it has been proven that malignant cell lines as opposed to nonmalignant ones are substantially depolarized, and that elevating the trans-membrane potential, as well as GABAergic activity arrests malignant hepatocyte growth. They have concluded their analyses by showing that the studied four malignant hepatocyte cell lines are clearly depolarized (Chang:  $-7.5 \pm 1.0$  mV, Hep G<sub>2</sub>:  $-9.8 \pm 0.5$  mV, HuH-7:  $-4.2 \pm 0.3$  mV, and PLC/PRF/5:  $-3.2 \pm 0.4$  mV), as opposed to the resting and proliferating cell-membrane potentials of non-malignant hepatocytes, which were found respectively to be  $-25.1 \pm 1.5$  mV, and  $-20.1 \pm 1.6$  mV [108].

Pancrazio *et al.* [112] have allocated the presence of voltage-gated currents in the ionic channels of  $K^+$ ,  $Na^+$ , and  $Ca^{+2}$  in 3 lung-cancer-cell lines using a patch-clamp technique: NCI-H128, NCI-H69, and NCI-H146. The current-peak amplitude of  $Na^+$ ,  $K^+$ , and  $Ca^{+2}$  are found to be  $46 \pm 14$  pA for 5 cultured cells,  $58 \pm 6$  pA for 11 cultured cells, and  $93 \pm 16$  pA for 26 cultured cells, respectively. In their analyses, the voltage clamp approach is described as fixing (clamping) the membrane potential at a fixed value, where a pipette and electrodes are used, which leads to the elimination of the capacitive current of the cell membrane, and thus the total membrane current equals the ionic current [112, 122].

Nordenstrom [123] and Pekar [95] have extensively worked on the electrophysiology treatment by invasively inserting two platinum needles (two electrodes) into a tumor by DC means: anode into cancer cell, and cathode within a medium. The injection of direct current into a cancer cell has shown a reduction in DNA production, activation of the immune system, generation of electrolysis (breakage of chemical bonds via current), **electrophoresis**

(movement of particles within a medium due to electric field), **electroosmosis** (movement of polar fluid within cell membrane), and **electroporation** (increase in conductivity and dielectric property of cell membrane due to applied electric field) [124-126].

Hope and Iles [127] have highlighted the importance of impedance measurements; furthermore, they have reviewed major electrophysiological characteristics of breast cancer using an impedance analyzer. They have indicated that measurements taken at frequencies less than 1 KHz depict the ionic extracellular properties, where frequencies in the range of 30 KHz to 30 MHz are sufficient to characterize the cellular biophysics. They have drawn a distinction between impedance of dead and living tissues on the basis that impedance is dependent variable on time of which the permeability of cell membrane changes after a number of hours of cell death. Thus, to extract reliable information about the biological system within an *in vitro* experiment, measurements should be taken during cell viability period, and during constant cell growth commencement, illustrated in the division and cytoplasmic formation within the exponential phase of a cell growth versus time (Phase II) of the S-shaped curve (Figure 3.2).



**Fig. 3.2** S-Shaped curve (Phase I-III) together with logarithmic decline curve (Phase IV) illustrating the different phases of cell growth versus time. A microscopic image of A375 melanoma cell is taken during the exponentially growing logarithmic Phase II, where other images are just illustrative (non-real) of the different status of cell growth: initial cell growth (Phase I), steady state growth attributable to lack of nutrients (Phase III), and cellular death due to diminishing of cell viability requirements (Phase IV).

Han *et al.* [128] have also categorized different stages of breast cancer-cell lines through impedance analyses: MCF-10A (healthy cell), MCF7 (early-stage cancer), MDA-MB-231 (invasive-cell line), and MDA-MB-435 (late metastasized). They have measured the impedance magnitude of these cells, of which they have computed the membrane capacitance and resistance. They have shown that cell membrane specific capacitance at a frequency of 100 KHz for MCF-10A is  $1.94 \pm 0.14 \mu F / cm^2$ , MCF-7 is  $1.86 \pm 0.11 \mu F / cm^2$ , MDA-MB-231 is  $1.63 \pm 0.17 \mu F / cm^2$ , and MDA-MB-435 is  $1.57 \pm 0.12 \mu F / cm^2$ . Similarly, the resistance

values for the preceding cell lines are  $24.8 \pm 1.05 \text{ M}\Omega$ ,  $24.8 \pm 0.93 \text{ M}\Omega$ ,  $24.9 \pm 1.12 \text{ M}\Omega$ , and  $26.2 \pm 1.07 \text{ M}\Omega$ , respectively.

Yun *et al.* [129] have taken electrochemical impedance measurements of human prostate cancer cells (LNCaP) via the utilization of a nanotube within a microfluidic channel. The unique aspect of their experiment is measuring the electrochemical impedance in various buffer media at different incubation times: milli-Q water, di-ionized (DI) water, and electrical contacting electrodes. They have shown that phase angle increases with the increase of incubation time. They have illustrated a specific cell-membrane capacitance of  $20 \text{ pF/cm}^2$  [130].

Surowiec *et al.* [131] have indicated that permittivity and conductivity of different stages of breast-cancer cells within *in vitro* environment are discriminated in terms of frequency measurements between 20 KHz to 100 MHz [123]. Morimoto *et al.* [132], on the other hand, have arrived at the conclusion on the variation of impedance characteristics between healthy and breast-cancer cells within *in vivo* environment in a frequency range between 0-200 KHz as opposed to *ex vivo* regime. In addition, Chauveau *et al.* [133] have measured impedance in a frequency range of 10 KHz to 10 MHz; accordingly, their results also show a distinction between normal and cancerous cells.

Alqabandi *et al.* [1], have designed and microfabricated a device that measures the specific capacitance and resistance of a B16-F10 mouse melanoma in conjunction with a high impedance analyzer. A single extracted cell is trapped between two electrodes (stimulating and recording electrode) in a phosphate buffered saline (PBS) medium. It is concluded that a biological cell acts as a low pass filter, and that the electrical parameters of cell membrane are frequency dependent. The B16-F10 melanoma cancer cell does exhibit a very low specific capacitance ( $1.154 \pm 0.29 \text{ }\mu\text{F/cm}^2$ ), and a specific resistance of  $3.9 \pm 1.15 \text{ K}\Omega.\text{cm}^2$ , (mean  $\pm$  SEM, n = 14 Cells).

As per the reviewed literature, cells do exhibit unique cellular biophysics that can be utilized as a tool in discriminating various stages of cancer. However, it is essentially important that prior to microfabrication, design of microelectronics with a customized controlling software, and eventually extraction of cellular electrophysiology, the cellular biophysics and its associated controlling parameters should be first comprehended. Mathematical modeling unlocks the key of understanding the biophysics behavior of cells; furthermore, it assists in obtaining an efficient tool for design of experiment (DOE), and further it predicts and justifies obtained experimental findings. Therefore, mathematical modeling will be the main target of the next section.

### **3.4 Mathematical Modeling of a Biological Cell: Analytical Approach**

#### **3.4.1 Overview**

In Biochemistry, two anchor mathematical models are highly pronounced in literature, which have had enormous impacts on understanding the biophysics of cells: Nernst-Planck equation [134-138], and Hodgkin-Huxley cable model [139-142]. Those great scholars, Planck, Hodgkin, and Huxley, were all awarded the Nobel Prize, where Hodgkin and Huxley received the award in 1963 in Physiology or Medicine, whereas Planck received the Nobel Prize in Physics in 1919. Their findings have enriched the understanding of the mechanisms of electrophysiology, especially within the fields of neuroscience, cardiology, endocrinology, cellular functionalities, muscle tissue contractions, and neuroinformatics.

Nernst-Planck equation depicts electro-diffusion, mass transport phenomena, and chemical particles' kinematics within a medium [134-138]. Its applications are not just limited to free

ion kinematics, yet it extends to encounter the effect of pairing and clustering of multiple ion transport [134]; it can be coupled with other theorem, e.g., Poisson theorem, to extend its applicability [137]. Furthermore, it models the biological ion channels by considering ions in spatial and temporal domain as charged-hard spheres of excess of potentials [136]. Nernst equation describes the equilibrium potential of different ion concentrations, and thus it cannot depict cell-membrane potential; however, it can describe cell-membrane potential if one ion type concentration is evaluated excluding other ions' concentrations, which does not faithfully describe the biological system of various contributions of multiple ion channels [97].

It should have been noted in the aforementioned reviewed literature on cell-membrane potentials, the different magnitudes and signs of cell-membrane potential, which suggest that cell-membrane potentials in literature can have either negative or positive sign with a magnitude; this is justified mathematically by the natural logarithmic component of the Nernst-Planck equation in that the differences in signs are indications of higher or lower ion concentrations of intracellular to extracellular region, or vice versa, with respect to the cell membrane [97, 143]. Also, this is physically attributable to the hyperpolarization (an increase of cell membrane negative charges), and depolarization nature of cells due to the flux of specific nutrients out and in the cell [108, 112, 118, 119, 121, 144].

Many scholars in the field have successfully managed to link polarization/hyperpolarization, as well as depolarization to cellular various activities and nature of a disease. For example, it has been mostly found that cell mitosis (rapid division proliferation) is linked to depolarization [96]. This is evident in cancer cells, where cell-membrane potential is highly depolarized (low polarized characteristic); on the other hand, polarized/hyperpolarized cell-membrane potential cells such as somatic cells, which are the building cells of an organism, are quiescent and don't undergo mitosis, yet their malignant types are depolarized [145]; it is found that the intracellular concentration of  $Na^+$  leads to

depolarization of cell-membrane potential of the malignant somatic cells, and it regulates cell proliferation [145]. It is concluded that hyperpolarized (excess of cytoplasm negativity of a cell), and depolarized (excess of cytoplasm positivity of a cell) cell-membrane potential are respectively associated with non-proliferated, and cancerous cells, in which depolarization is linked to increasing intracellular activities of  $Na^+$  ion channels [108, 112, 118, 119, 121, 144, 146].

An interesting phenomenon is the ability of certain cells to transform from non-proliferating phase to a proliferating one, and vice versa, such as that experienced during inflammation, injury, restoration of skin in response to a certain electrochemical or environmental signaling, among those is the vascular smooth muscle cells (VSMCs) [96]. The following movie link in the footnote illustrates the movements of fibroblast to the wounded area to perform restoration<sup>2</sup>. This movie presentation raises many questions on the type of coded electrochemical signals that ordered specifically tasked cells to mobilize to a wounded area, coordinate among themselves to heal and restore the damaged tissue, terminate their performance after completing their tasks, and finally return to their initial stage.

The second standout mathematical model, Hodgkin-Huxley model, consists of a set of four nonlinear differential equations, which initially had exemplified the membrane potential of nerve impulse. This had placed their mathematical work at high rank in bridging the gap between theoretical and experimental approach [139, 140]. They measured membrane potential within a giant axon of a squid, by filling a capillary tube with seawater, and then inserting it into the axon to act as an electrode: enabling the extraction of potential difference in millivoltage within the membrane; this experimental setup has contributed in developing their mathematical modeling, and equivalent analogical electric circuit, and further predicting ion channels that modern technology have confirmed [139]. Thus, inspired by their approach, this chapter is structured in a manner presenting readers first with experimental findings of various

---

<sup>2</sup> [http://www.youtube.com/watch?v=\\_GtVWyt3lys&list=UU62EfCHc7cZBsYSUW-JY3Dw](http://www.youtube.com/watch?v=_GtVWyt3lys&list=UU62EfCHc7cZBsYSUW-JY3Dw)

---

scholars in the Biophysics field (literature review), together with different non-conventional methods used in extracting cellular physics, and at last arriving at full mathematical model derivations of the bio-system.

As in Nernst-Planck model, Hodgkin-Huxley model has opened new frontiers for researchers to extend its application by combining the cable model with other theories to suit their specific experimental setup. As an example, Roth and Basser [142] have developed a model of electromagnetic induction role on a passive (voltage independent) nerve fiber, where they have complemented their mathematical model with that of Hodgkin and Huxley.

Many scholars rely on models that are either discrete or lumped, however, a continuous system more efficiently mimics, to some extent, living structures, and hence it is considered more accurate in closely capturing cellular physics. Furthermore, many researchers in the bio-field don't encounter the resistivity of medium surrounding the biological cell (extracellular isopotentiality). In addition, the cell membrane is considered passive, which initiates the necessity of having active/passive cell membrane functionalities by inducing an active injected current at an effective node within an RC circuit in developing the mathematical model. In addition, a leakage factor illustrated by Warburg diffusion [1, 147] has to be present in a continuous model to closely capture, to a certain degree, the electrophysiology of a stimulated cell by encountering diffusion (leakage) of charges/ions. These are the objectives of the proposed extended mathematical model in this chapter.

### **3.4.2 Mathematical Model**

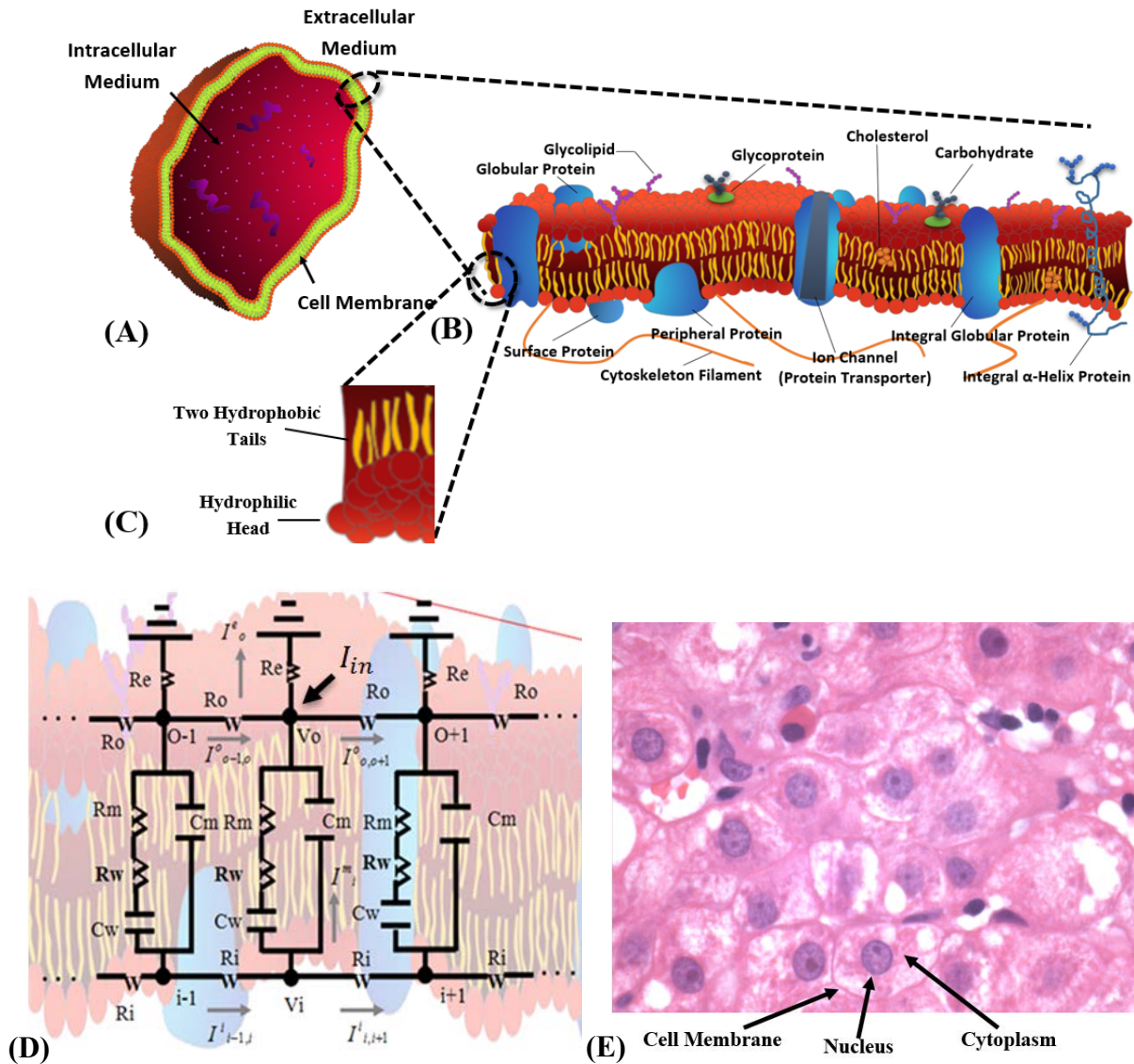
The biological cell is a complex and harsh system that can be further simplified and closely examined through mathematical representations [148]. This section is devoted to provide



novice readers an in-depth understanding of the physics and controlling parameters associated with the generation of cell-membrane potential. As partly depicted in Figure 3.3, cells consist of water, inorganic ions (i.e.  $Na^+$ ,  $Ca^{2+}$ ,  $Cl^-$ ,  $Mg^{2+}$ , etc.), macromolecules (DNA/RNA), and micro-organic molecules (i.e. vitamins, sugars, proteins, cholesterol, and fatty acids) [8, 97]. A mammalian biological cell consists of three main regions: extracellular, cell membrane, and intracellular medium (i.e. cytoplasm, nucleus, internal organelles, etc.) as shown in Figure 3.3A. The cell membrane, Figure 3.3 B, is of a closed boundary, its thickness varies from 65-100 Å m, and it is considered amphipathic, since it consists of arrays of phospholipid bilayer, Figure 3.3 C: hydrophilic (water loving) head, and 2 hydrophobic (water fearing) tails [97]. Accordingly, the cell membrane is then segregating two-conductive media, and it has a high dielectric property. Hence, cell membrane experiences a behavior of a capacitance. Similarly, there is a potential drop between the intracellular and extracellular domain, and such drop is resembled as a membrane resistance as shown in Figure 3.3D. As per the latter figure, cell membrane is considered in Biophysics as a series of parallel RC circuits, where the total capacitance is distributed into capacitive and resistive current. Finally, Figure 3.3E shows a microscopic image of a population of liver cells, illustrating the cell membrane, cytoplasm, and nucleus.

The electrochemical potential of a cell is attributable to the ion transfer between the intracellular and extracellular domains by diffusion via ion channels (voltage-gated channels ((Fig. 3.3B))), ATP pumping, and/or biological transporters [1, 2, 20, 136]. Therefore, the biophysics of a cell can be represented as a network of electrical circuitry, as depicted in Figure 3.3D, which explains the cell's distinctive electrophysiology that initiates various signal-transduction activities, such as mitosis and cell-cell communication [1, 2, 20]. This makes the field of Biophysics more pronounced within this study, where cell electrophysiology, and

cellular energy production play a dominant role in the formation of cancer that can be detected and quantified [1, 2, 20].



**Fig. 3.3** (A) A biological cell with its 3 distinctive regions: cell membrane, extracellular, and intracellular region (B) Exploded view of the cell membrane, where cellular arrays of phospholipid bilayer are shown in (C). In (D), an electric circuit representation of a series of parallel RC circuits experienced within a cell membrane, where cell-membrane resistance is denoted as  $R_m$  ( $\Omega$ ), cell-membrane capacitance is denoted as  $C_m$  (F),  $R_i$  is the longitudinal internal resistance ( $\Omega$ ),  $R_o$  is the

longitudinal resistance of current flow ( $\Omega$ ),  $R_e$  is the resistance of physiological medium ( $\Omega$ ),  $R_w$  is the Warburg resistance ( $\Omega$ ),  $C_w$  is the Warburg capacitance ( $F$ ), and  $I_{in}$  is the effective current injection from an electrode ( $A$ ). (E) A microscopic image of a population of liver cells showing cell membrane, cytoplasm, and nucleus, which is a very kind courtesy of Dr. John Patrick, Consultant and head of Histopathology, Amiri Hospital Clinical Laboratories.

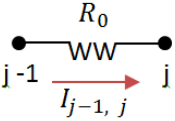
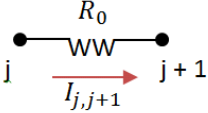
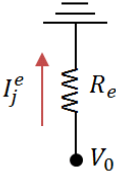
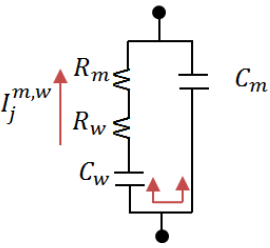
In order to effectively grasp the concept of electrophysiology of cells, this section provides detailed derivations, and extends the analytical model carried out in [144] by accounting for Warburg diffusion impedance (charge leakage) [1, 147], as shown in Fig. 3.3D. As experimentally proofed in Alqabandi *et al.* [1], Warburg diffusion plays an important role in justifying the phase angle shift for not reaching  $90^\circ$  in a typical potential current phase angle configuration, rather a  $45^\circ$  is being reached, implying ion diffusion of slow species/charge kinematics within the electrochemical domain. The mathematical representation of cell-membrane potential of Cable model is carried out based on Kirchhoff's Current Law, Laplace and Fourier Transforms, and their Invers Transforms.

It is assumed that a closed to a sphere-shaped cell is trapped between two electrodes (stimulating and recording) within a microfluidic chamber within an *in vitro* experimental setup. The assumptions are carried out such that (1) the biological cell is stimulated via injection of an effective current ( $I_{in}$ ) at a single external node (o) of a cell as shown in Fig. 3.3D, and (2) the direction of current flow is taken randomly, and it can also be assumed the opposite. The flow of current is longitudinal near cell interior boundary, and radial from the cell to the extracellular domain, and then to grounded recording electrode. There is a uniform resistivity of the extracellular medium. Also, the recording electrode potential is set with respect to ground. The following table summarizes the controlling parameters of circuit model representing the electrophysiological characteristics of a cell.

Symbol	Unit	Description
$C_m$	F (Farad)	Capacitance of cell membrane
$C_w$	F (Farad)	Capacitance of Warburg diffusion (leakage of charge)
$C_{me}$	F (Farad)	Equivalent capacitance of Warburg and cell membrane capacitors in parallel
$R_m$	$\Omega$ (Ohm)	Resistance of cell membrane
$R_w$	$\Omega$ (Ohm)	Resistance of Warburg diffusion (leakage of charge)
$R_{me}$	$\Omega$ (Ohm)	Equivalent resistance of Warburg and cell membrane resistors in series
$R_i$	$\Omega$ (Ohm)	Longitudinal intracellular resistance of the biological cell
$R_o$	$\Omega$ (Ohm)	Longitudinal resistance to current flow
$R_e$	$\Omega$ (Ohm)	Resistance of the buffered medium
$I_{in}$	A (Ampere)	Effective current injected from a stimulating electrode

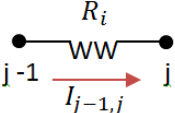
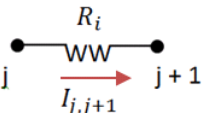
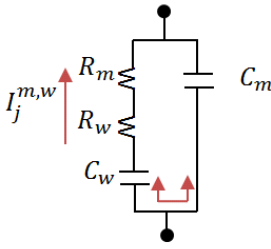
**Table 3.1** Controlling parameters of the electrical circuitry resembling a biological cell.

By examining the external node ( $j^0$ ), and applying Ohm's law, we arrive at the following constitutive relations that are illustrated in Table 3.2:

Circuit Diagram	Constitutive relation after applying Ohm's Law
	$I_{j-1,j}^o = \frac{V_{j-1}^o - V_j^o}{R_o}$
	$I_{j,j+1}^o = \frac{V_j^o - V_{j+1}^o}{R_o}$
	$I_j^e = \frac{V_o - (V_{earth} = 0)}{R_e}$
	$I_j^{m,w} = C_{me} \frac{dV_j^m}{dt} + \frac{V_j^m}{R_{me}}$ <p>Where, first term defines current via a capacitance (<math>Q</math> (charge) = <math>CV</math>; <math>dQ/dt = C dV/dt</math>; <math>I = C dV/dt</math>), whereas second term defines current via a resistance</p>

**Table 3.2** Ohm's representations at the external node characteristics of a biological cell.

The mathematical representations of capacitive and resistive current flow do exhibit the characteristics of outflow current experienced biologically within ATP pumps, and transporters in transferring charged ions. Next, in a similar manner at the internal node ( $j^i$ ), the constitutive relations are defined in the following table:

Circuit Diagram	Constitutive relation after applying Ohm's Law
	$I_{j-1,j}^i = \frac{V_{j-1}^i - V_j^i}{R_i}$
	$I_{j,j+1}^i = \frac{V_j^i - V_{j+1}^i}{R_i}$
	$I_j^{m,w} = C_{me} \frac{dV_j^m}{dt} - \frac{V_j^m}{R_{me}}$ <p>Where, first term defines current via a capacitance (Q (charge) = CV; <math>dQ/dt = C dV/dt</math>; <math>I = C dV/dt</math>), whereas second term defines current via a resistance.</p>

**Table 3.3** Ohm's representations at the internal node characteristics.

Where,  $I_{j-1,j}^o$ ,  $I_{j-1,j}^i$ ,  $I_j^o$ ,  $V_j^m$ ,  $V_j^i$ , and  $V_j^o$ , are respectively the exterior current from node (j - 1) to node (j), interior current from node (j - 1) to node (j), exterior current, membrane potential, intracellular potential, and extracellular potential. Appendix B contains nomenclature of all terms presented in this Chapter.

Applying Kirchhoff's Current Law (KCL) at external and internal node, where charge is conserved, and hence  $I$  is conserved ( $\sum I_{in\ node} = \sum I_{out\ node}$ ).

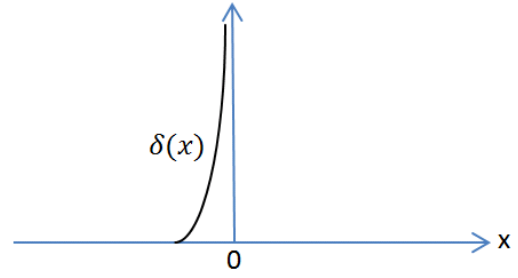
$$I_{j-1,j}^o - I_{j,j+1}^o + I_j^m - I_j^e + I_{in}\delta_{jo} = 0 \quad (3.1)$$

The Kronecker delta term,  $\delta(x)$ , is introduced into equation (3.1) to set current injection “On” or “Off,” and it is defined as:

$$\delta(x) = \begin{cases} 0 & x \neq 0 \\ \infty & x = 0 \end{cases}$$

$$\int_{-\infty}^{\infty} \delta(x) dx = \text{area} = 1$$

$$\int_{-\infty}^{\infty} f(x) \delta(x) dx = f(0)$$



At Internal Node:

$$I_{j-1,j}^i - I_{j,j+1}^i - I_j^m = 0 \quad (3.2)$$

Rewriting equations (3.1) and (3.2) in terms of potential at both external and internal nodes.

Therefore, the following terms are obtained:

At External Node:

$$\frac{V_{j-1}^o - V_j^o}{R_o} - \frac{V_j^o - V_{j+1}^o}{R_o} + C_{me} \frac{dV_j^m}{dt} + \frac{V_j^m}{R_{me}} - \frac{V_j^o}{R_e} + I_{in} \delta_{jo} = 0$$

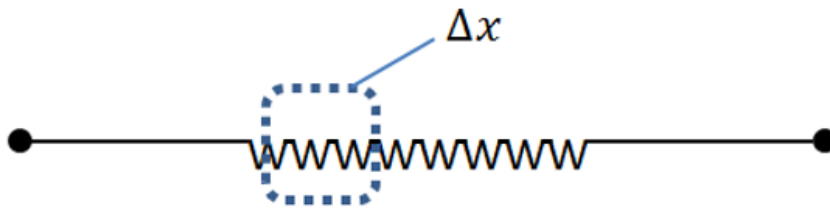
$$\frac{V_{j-1}^o - 2V_j^o + V_{j+1}^o}{R_o} + C_{me} \frac{dV_j^m}{dt} + \frac{V_j^m}{R_{me}} - \frac{V_j^o}{R_e} + I_{in} \delta_{jo} = 0 \quad (3.3)$$

At Internal Node:

$$\frac{V_{j-1}^i - V_j^i}{R_i} - \frac{V_j^i - V_{j+1}^i}{R_i} - C_{me} \frac{dV_j^m}{dt} - \frac{V_j^m}{R_{me}} = 0$$

$$\frac{V_{j+1}^i - 2V_j^i + V_{j-1}^i}{R_i} - C_{me} \frac{dV_j^m}{dt} - \frac{V_j^m}{R_{me}} = 0 \quad (3.4)$$

Equations (3.3) and (3.4) describe a lumped equivalent system, whereas a biological system is a continuous one. Thus, equations (3.3) and (3.4) shall be converted into continuous equations by taking a differential small element ( $\Delta x$ ), Figure 3.4. It should be noted that  $R_i$ 's and  $R_o$ 's are in series, while  $R_e$ 's,  $C_{me}$ 's, and  $R_{me}$ 's are in parallel. Therefore,



**Fig. 3.4** Differential Element of a resistor.

$$\frac{1}{R_{me,eqv}} = \frac{1}{R_{me}} + \frac{1}{R_{me}} + \dots + \frac{1}{R_{me}} = \frac{n}{R_{me}} = \frac{\Delta x}{r_{me}} \Rightarrow R_{me} = \frac{r_{me}}{\Delta x}$$

$$\frac{1}{R_{e,eqv}} = \frac{1}{R_e} + \frac{1}{R_e} + \dots + \frac{1}{R_e} = \frac{n}{R_e} = \frac{\Delta x}{r_e} \Rightarrow R_e = \frac{r_e}{\Delta x}$$

$$C_{me,eqv} = C_{me} + C_{me} + \dots + C_{me} = nC_{me} = \Delta x c_{me}$$

$$R_{o,eqv} = R_o + R_o + \dots + R_o = nR_o = \Delta x r_o$$

$$R_{i,eqv} = R_i + R_i + \dots + R_i = nR_i = \Delta x r_i$$

As for  $\delta(x)$

$$\delta(x) \rightarrow \frac{1}{c} \delta(x)$$

$$x = cX$$

$$\int_{-\infty}^{\infty} \delta(x) f(x) dx = \int_{-\infty}^{\infty} \frac{1}{c} \delta(x) f(cX) dX \quad \text{by definition.}$$

Also by definition,

$$\int_{-\infty}^{\infty} \delta(x) dx = 1 \quad \text{and since} \quad x = cX$$



$$= \int_{-\infty}^{\infty} \delta(cX) d(cX) = c \int_{-\infty}^{\infty} \delta(cX) dX = 1$$

$$\delta(cX) = \frac{1}{c} \delta(x)$$

$$\int_{-\infty}^{\infty} \delta(x) f(x) dx = f(0) \quad \text{by definition and since } x = cX$$

$$c \int_{-\infty}^{\infty} \delta(cX) f(cX) dx = \int_{-\infty}^{\infty} \delta(x) f(cx) dx$$

$$= \frac{1}{c} \delta(x) = f(cx0) = f(0)$$

$$\therefore \delta(cX) = \frac{1}{c} \delta(x) \text{ where, } c \text{ is some constant.}$$

Thus, the following terms are defined to transform the discrete circuit to a continuous one:

$$\left. \begin{aligned} R_{me} &\rightarrow \frac{r_{me}}{\Delta x} & ; & & C_{me} &\rightarrow C_{me} \Delta x \\ R_i &\rightarrow r_i \Delta x & ; & & R_o &\rightarrow r_o \Delta x \\ \delta_{jo} &\rightarrow \delta(x) \Delta x \end{aligned} \right\} \quad (3.5)$$

Substituting terms of (3.5) into (3.3) and (3.4)

For equation (3.4)

$$\frac{V_{j+1}^i - 2V_j^i + V_{j-1}^i}{R_i} - C_{me} \frac{dV_j^m}{dt} - \frac{V_j^m}{R_{me}} = 0$$

$$\frac{V_{j+1}^i - 2V_j^i + V_{j-1}^i}{r_i(\Delta x)} - c_{me} \Delta x \frac{dV_j^m}{dt} - \frac{V_j^m}{r_{me}} \Delta x = 0 \quad (3.6)$$

Multiplying equation (3.6) by  $\frac{1}{\Delta x}$

$$\boxed{\frac{V_{j+1}^i - 2V_j^i + V_{j-1}^i}{r_i(\Delta x)^2}} - c_{me} \frac{dV_j^m}{dt} - \frac{V_j^m}{r_{me}} = 0$$

The above dotted-circled term represents the definition of a second derivative, and by taking the limit  $\Delta x \rightarrow 0$ , the following term is obtained.

$$\begin{aligned}
 V''(x) &= \lim_{\Delta x \rightarrow 0} \frac{V'(x) - V'(x - \Delta x)}{\Delta x} \\
 &= \lim_{\Delta x \rightarrow 0} \frac{\frac{V(x + \Delta x) - V(x)}{\Delta x} - \frac{V(x) - V(x - \Delta x)}{\Delta x}}{\Delta x} \\
 V''(x) &= \lim_{\Delta x \rightarrow 0} \frac{V(x + \Delta x) - 2V(x) + V(x - \Delta x)}{(\Delta x)^2}
 \end{aligned}$$

$$\text{As } \lim_{\Delta x \rightarrow 0} \quad \frac{1}{r_i} \frac{\partial^2 V_i}{\partial x^2} - c_{me} \frac{\partial V_m}{\partial t} - \frac{V_m}{r_{me}} = 0 \quad (3.7)$$

For equation (3.3)

$$\begin{aligned}
 \frac{V_{j-1}^o - 2V_j^o + V_{j+1}^o}{R_o} + c_{me} \frac{dV_j^m}{dt} + \frac{V_j^m}{R_{me}} - \frac{V_j^o}{R_e} + I_{in} \delta_{jo} &= 0 \\
 \frac{V_{j-1}^o - 2V_j^o + V_{j+1}^o}{\Delta x r_o} + c_{me} \Delta x \frac{dV_j^m}{dt} + \frac{V_j^m}{r_{me}} \Delta x - \frac{V_j^o}{r_e} \Delta x + I_{in} \Delta x \delta(x) &= 0
 \end{aligned}$$

Multiplying the above term by  $\frac{1}{\Delta x}$ , the following term is obtained:

$$\frac{V_{j-1}^o - 2V_j^o + V_{j+1}^o}{(\Delta x)^2 r_o} + c_{me} \frac{dV_j^m}{dt} + \frac{V_j^m}{r_{me}} - \frac{V_j^o}{r_e} + I_{in} \delta(x) = 0$$

As in equation (3.4), the above dotted circled term is a definition of the second derivative.

$$\frac{1}{r_o} \frac{\partial^2 V_o}{\partial x^2} + c_{me} \frac{\partial V_m}{\partial t} + \frac{V_m}{r_{me}} - \frac{V_o}{r_e} + I_{in} \delta(x) = 0 \quad (3.8)$$

To simplify equations (3.7) and (3.8), time and distance are rescaled [144], which yields:

$$X = x \sqrt{\frac{r_i}{r_{me}}} \rightarrow x = X \sqrt{\frac{r_{me}}{r_i}}$$

$$T = \frac{t}{\tau_{me}} \rightarrow t = T \tau_{me} = T r_{me} C_{me}$$

$$k = \frac{r_o}{r_i} ; \quad \mu = \frac{r_{me}}{r_e} ; \quad v = \sqrt{r_{me} r_i} ; \quad \tau_{me} = r_{me} C_{me}$$

Since  $\delta(x) = \delta\left(X \sqrt{\frac{r_{me}}{r_i}}\right) = \sqrt{\frac{r_i}{r_{me}}} \delta(X)$ , and with the above expressions, equation (3.8)

becomes:

$$\frac{1}{r_o} \frac{\partial^2 V_o}{\frac{r_{me}}{r_i} \partial X^2} + c_{me} \frac{\partial V_m}{\tau_{me} \partial T} + \frac{V_m}{r_{me}} - \frac{V_o}{r_e} + I_i \sqrt{\frac{r_i}{r_{me}}} \delta(X) = 0$$

$$\frac{r_i}{r_o r_{me}} \frac{\partial^2 V_o}{\partial X^2} + \frac{\partial V_m}{r_{me} \partial T} + \frac{V_m}{r_{me}} - \frac{V_o}{r_e} + I_i \sqrt{\frac{r_i}{r_{me}}} \delta(X) = 0$$

Multiplying both sides by  $r_{me}$

$$\frac{r_i}{r_o} \frac{\partial^2 V_o}{\partial X^2} + \frac{\partial V_m}{\partial T} + V_m - V_o \frac{r_{me}}{r_e} + I_i \sqrt{\frac{r_{me}^2 r_i}{r_{me}}} \delta(X) = 0$$

$$\frac{1}{k} \frac{\partial^2 V_o}{\partial X^2} + \frac{\partial V_m}{\partial T} + V_m - V_o \mu + I_i v \delta(X) = 0$$

$$\frac{\partial V_m}{\partial T} + V_m = -\frac{1}{k} \frac{\partial^2 V_o}{\partial X^2} + \mu V_o - v I_{in}(T) \delta(X) \quad (3.9)$$

Similarly for equation (3.7),

$$\frac{1}{\frac{r_{me}}{r_i}} \frac{\partial^2 V_i}{\frac{r_{me}}{r_i} \partial X^2} - c_{me} \frac{\partial V_m}{r_{me} \partial T} - \frac{V_m}{r_{me}} = 0$$

Multiplying both sides by  $r_{me}$

$$\frac{\partial^2 V_i}{\partial X^2} = \frac{\partial V_m}{\partial T} + V_m \quad (3.10)$$

The cell-membrane potential is defined as the difference between the intracellular to extracellular potential:  $V_m = V_i - V_o$

Equations (3.9) and (3.10) are two coupled partial differential equations (PDEs), and they both depict the physics of the biological system; they are in a second order within a spatial domain (X variable). Therefore, 2 boundary conditions are required. Also, they are first order PDEs, and hence one initial condition is required in the temporal domain (T variable). Proper boundary and initial conditions are important to describe the bio-environment.

#### Boundary Conditions (Finite Biological System):

$V_i(X, T) \rightarrow 0, V_o(X, T) \rightarrow 0$  as  $|X| \rightarrow \pm L$ , where L is length of the cell.

Or

$$\frac{dV}{dX} = 0, \text{ When } X = \pm L$$

#### Initial Condition

$$V_m(X, T = 0) = 0$$

For a step current injection:

$$I_{in}(T) = \begin{cases} 0 & T < 0 \\ -I_o & T \geq 0 \end{cases}$$

For a rectangular pulse input:

$$I_{in}(T) = \begin{cases} -I_o & 0 \leq T \leq T_o \\ 0 & \text{Otherwise} \end{cases} \quad \text{Where, } I_o \text{ and } T_o \text{ are constants}$$

**Rearranging the finally obtained terms:**

$$\frac{\partial V_m}{\partial T} + V_m = -\frac{1}{k} \frac{\partial^2 V_o}{\partial X^2} + \mu V_o - v I_{in}(T) \delta(X) \quad (3.9)$$

$$\frac{\partial^2 V_i}{\partial X^2} = \frac{\partial V_m}{\partial T} + V_m \quad (3.10)$$

Where,

$$V_m(X, T) = V_i(X, T) - V_o(X, T)$$

$$k = \frac{r_o}{r_i} ; \quad \mu = \frac{r_{me}}{r_e} ; \quad v = \sqrt{r_{me} r_i} ; \quad X = x \sqrt{\frac{r_i}{r_{me}}} ; \quad T = \frac{t}{\tau_m} ; \quad \tau_m = r_{me} C_{me}$$

The injected current is taken to be sinusoidal, where  $w$  is angular frequency (angular velocity)

$$I_{in}(T) = I_o \sin(wt) \quad 0 \leq T < \infty$$

The partial differential equations shall be solved by utilizing Fourier and Laplace Transform method that is widely used in feedback control theory, electronic circuit, and heat mass transfer.

The tedious calculus problems are transformed into algebraic ones, and the Laplace and Fourier Inverse Transforms allow shifting between spatial and temporal variables to a parameter 's' domain and vice versa. The parameter 's' can be considered as a conditional constant. The Laplace Transform complements the shortage of obtaining a definition of a function that Fourier Transform failed to have.

Applying Laplace Transform with respect to (T), the Laplace transform is defined as,

$$\bar{V}(s) = \mathcal{L}\{V(t)\} = \int_0^{\infty} e^{-st} V(t) dt$$

The Laplace transform of a derivative of a function is defined as:

$$\mathcal{L}\left[\frac{df}{dt}\right][s] = s\mathcal{L}f(s) - f(0)$$

Thus, respectively equations (3.9) and (3.10) become,

$$s\bar{V}_m + \bar{V}_m = -\frac{1}{k} \frac{\partial^2}{\partial x^2} \bar{V}_o + \mu\bar{V}_o - v\mathcal{L}[I_{in}(T)]\delta(x)$$

$$s\bar{V}_m + \bar{V}_m = \frac{\partial^2}{\partial x^2} \bar{V}_i$$

Now since,

$$\mathcal{L}[I_{in}(T)] = \int_0^{\infty} e^{-sT} I_{in}(T) dT = I_o \int_0^{\infty} e^{-sT} \sin(wT) dT$$

$$\therefore \sin(wT) = \frac{e^{iwT} - e^{-iwT}}{2i} \quad (\text{Euler's definition})$$

$$\therefore \mathcal{L}[I_{in}(T)] = I_o \int_0^{\infty} e^{-sT} \frac{e^{iwT} - e^{-iwT}}{2i} dT = \frac{I_o}{2i} \int_0^{\infty} [e^{(iw-s)T} - e^{-(iw+s)T}] dT$$

$$= \frac{I_o}{2i} \left\{ \frac{1}{iw-s} e^{(iw-s)T} \Big|_0^{\infty} + \frac{1}{iw+s} e^{-(iw+s)T} \Big|_0^{\infty} \right\} = \frac{I_o}{2i} \left[ \frac{1}{s-iw} - \frac{1}{s+iw} \right]$$

$$= \frac{I_o}{2i} \frac{s+iw-s+iw}{s^2+w^2} = \frac{I_o}{2i} \frac{2iw}{s^2+w^2} = \frac{I_o w}{s^2+w^2}$$

It should be noted that the same result could have been obtained for  $\mathcal{L}[I_{in}(T)]$ , if the following definition is used:

$$e^{iwT} = \cos(wT) + i \sin(wT)$$

$$\mathcal{L}[I_{in}(T)] = I_o \int_0^{\infty} e^{-sT} \sin(wT) dT = I_m \left[ I_o \int_0^{\infty} e^{-sT} e^{iwT} dT \right] = I_m \left[ I_o \frac{1}{iw-s} e^{(iw-s)T} \Big|_0^{\infty} \right]$$

$$= I_m \left[ I_o \frac{1}{s-iw} \right] = I_m \left[ I_o \frac{s+iw}{s^2+w^2} \right] = I_o \frac{w}{s^2+w^2}$$

Thus, equations (3.10) and (3.9) would respectively become,

$$s\bar{V}_m + \bar{V}_m = \frac{\partial^2}{\partial x^2} \bar{V}_i \quad (3.11)$$

$$s\bar{V}_m + \bar{V}_m = -\frac{1}{k} \frac{\partial^2}{\partial x^2} \bar{V}_o + \mu \bar{V}_o - v \left[ \frac{I_o w}{s^2 + w^2} \right] \delta(x) \quad (3.12)$$

Applying Fourier Transform to equations (3.11) and (3.12) with respect to X, by utilizing the definition of Fourier Transform:

$$\bar{\bar{V}} = F\{f(x)\} = \hat{f}(w) = \int_{-\infty}^{\infty} f(x) e^{-iwx} dx$$

Revising Fourier Transform properties is essential for the following derivations. Therefore, if Fourier Transform is defined as per the following,

$$F(w) = F\{f(t)\} = \frac{1}{\sqrt{2\pi}} \int_{-\infty}^{\infty} f(t) e^{-iwt} dt$$

and, if the function  $f(t)$  is defined as a differential function with Fourier Transform (FT)  $F(w)$ , then FT of its derivative is given by  $iwF(w)$ , which can be used to transform differential equations into algebraic ones. It is important to note that such approach is only applicable to problems whose domain consists of a set of real numbers. Accordingly, the FT of a Kronecker delta function ( $\delta$ ) is,

$$F\{\delta(x)\} = \frac{1}{\sqrt{2\pi}} \int_{-\infty}^{\infty} \delta(x) e^{ixy} dx = \frac{1}{\sqrt{2\pi}}$$

As a result, equations (3.11) and (3.12) respectively become

$$s\bar{\bar{V}}_m + \bar{\bar{V}}_m = -y^2\bar{\bar{V}}_i \quad (3.13)$$

$$\text{And since } F\left\{\frac{\partial}{\partial x}\right\} = -iy \rightarrow \therefore F\left\{\frac{\partial^2}{\partial x^2}\right\} = [-iy]^2$$

$$\therefore i = \sqrt{-1} \rightarrow \therefore F\left\{\frac{\partial^2}{\partial x^2}\right\} = -y^2$$

$$s\bar{\bar{V}}_m + \bar{\bar{V}}_m = \frac{y^2}{k} \bar{\bar{V}}_o + \mu\bar{\bar{V}}_o - \frac{v}{\sqrt{2\pi}} \frac{I_o w}{s^2 + w^2} \quad (3.14)$$

Since the cell-membrane potential is defined as  $\bar{\bar{V}}_m = \bar{\bar{V}}_i - \bar{\bar{V}}_o$ , hence equations (3.13) and (3.14) respectively become,

$$\begin{aligned} s[\bar{\bar{V}}_i - \bar{\bar{V}}_o] + [\bar{\bar{V}}_i - \bar{\bar{V}}_o] &= -y^2\bar{\bar{V}}_i \\ [s + 1][\bar{\bar{V}}_i - \bar{\bar{V}}_o] &= -y^2\bar{\bar{V}}_i \end{aligned} \quad (3.15)$$

$$\begin{aligned} s[\bar{\bar{V}}_i - \bar{\bar{V}}_o] + [\bar{\bar{V}}_i - \bar{\bar{V}}_o] &= \frac{y^2}{k} \bar{\bar{V}}_o + \mu\bar{\bar{V}}_o - \frac{v}{\sqrt{2\pi}} \frac{I_o w}{s^2 + w^2} \\ [s + 1][\bar{\bar{V}}_i - \bar{\bar{V}}_o] &= \frac{y^2}{k} \bar{\bar{V}}_o + \mu\bar{\bar{V}}_o - \frac{v}{\sqrt{2\pi}} \frac{I_o w}{s^2 + w^2} \end{aligned} \quad (3.16)$$

Rearranging equation (3.15):

$$\begin{aligned} (1 + s + y^2)\bar{\bar{V}}_i - (1 + s)\bar{\bar{V}}_o &= 0 \\ \text{Thus, } \bar{\bar{V}}_o &= \frac{1+s+y^2}{1+s} \bar{\bar{V}}_i \end{aligned} \quad (3.17)$$

Plugging equation (3.17) into equation (3.16)

$$[s + 1]\bar{\bar{V}}_i - [s + 1]\bar{\bar{V}}_o = \frac{y^2}{k} \bar{\bar{V}}_o + \mu\bar{\bar{V}}_o - \frac{v}{\sqrt{2\pi}} \frac{I_o w}{s^2 + w^2}$$



$$[s + 1]\bar{V}_i - \left(1 + s + \frac{y^2}{k} + \mu\right)\bar{V}_o = \frac{-v}{\sqrt{2\pi}} \frac{I_o w}{s^2 + w^2}$$

$$\bar{V}_i \left(1 + s - \left(1 + s + \frac{y^2}{k} + \mu\right) \frac{1+s+y^2}{1+s}\right) = \frac{-v}{\sqrt{2\pi}} \frac{I_o w}{s^2 + w^2}$$

$$\bar{V}_i = -\frac{v}{\sqrt{2\pi}} \frac{I_o w}{s^2 + w^2} \frac{1+s}{(1+s)^2 - (1+s + \frac{y^2}{k} + \mu)(1+s+y^2)}$$

$$\bar{V}_i = -\frac{v}{\sqrt{2\pi}} \frac{I_o w}{s^2 + w^2} \frac{1+s}{1 + 2s + s^2 - 1 - s - \frac{y^2}{k} - \mu - s - s^2 - s \frac{y^2}{k} - s\mu - y^2 - y^2 s - \frac{y^4}{k} - y^2 \mu}$$

$$\bar{V}_i = -\frac{v}{\sqrt{2\pi}} \frac{I_o w}{s^2 + w^2} \frac{1+s}{\left(-\frac{y^2}{k} - \mu - s \frac{y^2}{k} - s\mu - y^2 - y^2 s - \frac{y^4}{k} - y^2 \mu\right)}$$

$$\bar{V}_i = -\frac{v}{\sqrt{2\pi}} \frac{I_o w}{s^2 + w^2} \frac{1+s}{\left(\frac{-y^2 - sy^2 - \mu k - sk\mu - y^2 k - y^2 sk - y^4 - y^2 \mu k}{k}\right)}$$

$$\bar{V}_i = -\frac{v}{\sqrt{2\pi}} \frac{I_o w}{s^2 + w^2} \frac{1+s}{\left(\frac{-s(y^2 + \mu k + y^2 k) - y^2 - \mu k - y^2 k - y^4 - y^2 \mu k}{k}\right)}$$

$$\bar{V}_i = -\frac{v}{\sqrt{2\pi}} \frac{I_o w}{s^2 + w^2} \frac{1+s}{-\left(\frac{s(y^2 + \mu k + y^2 k) + y^2(y^2 + 1) + k(\mu + y^2 + y^2 \mu)}{k}\right)}$$

$$\bar{V}_i = -\frac{v}{\sqrt{2\pi}} \frac{I_o w}{s^2 + w^2} \frac{1+s}{-\left(\frac{s(y^2 + \mu k + y^2 k) + y^2(y^2 + 1) + ky^2 + k\mu(y^2 + 1)}{k}\right)}$$

$$\bar{V}_i = -\frac{v}{\sqrt{2\pi}} \frac{I_o w}{s^2 + w^2} \frac{1+s}{-\left(\frac{s(y^2 + \mu k + y^2 k) + ky^2 + (y^2 + 1)(y^2 + \mu k)}{k}\right)}$$

In order to simplify the expression, the following terms are defined:

$$P = ky^2 + (y^2 + k\mu)(1 + y^2)$$

$$Q = ky^2 + y^2 + \mu k$$

Thus,

$$\bar{V}_i = -\frac{v}{\sqrt{2\pi}} \frac{I_o w}{s^2 + w^2} \frac{1+s}{-\left(\frac{P+sQ}{k}\right)}$$

$$\bar{V}_i = \frac{vk}{\sqrt{2\pi}} \frac{I_o w}{s^2 + w^2} \frac{1+s}{(P+sQ)} \quad (3.18)$$

Substituting (3.18) into (3.17)

$$\begin{aligned}\bar{\bar{V}}_o &= \frac{vk}{\sqrt{2\pi}} \frac{I_o w}{s^2 + w^2} \frac{(1+s)}{(P+sQ)} \frac{(1+s+y^2)}{(1+s)} \\ \bar{\bar{V}}_o &= \frac{vk}{\sqrt{2\pi}} \frac{I_o w}{s^2 + w^2} \frac{(1+s+y^2)}{(P+sQ)}\end{aligned}\quad (3.19)$$

At this stage, double transformed  $(\bar{\bar{V}}_i, \bar{\bar{V}}_o)$  as functions of  $y$  and  $s$ , e.g.,  $\bar{\bar{V}}_i(y, s), \bar{\bar{V}}_o(y, s)$ , are obtained. Therefore, Laplace Inverse Transform is required to move from spatial domain parameter ( $s$ ) to a temporal domain( $t$ ). In order to perform Inverse Laplace Transform, partial fractions are implemented with the exclusion of constant terms, and by just evaluating the "s" term.

$$\begin{aligned}\bar{\bar{V}}_i &: \frac{1+s}{(s^2+w^2)(P+Qs)} = \frac{1+s}{(s-iw)(s+iw)(P+Qs)} \\ &= \frac{A}{s-iw} + \frac{B}{s+iw} + \frac{C}{P+SQ} \\ &= \frac{A(s+iw)(P+sQ)+B(s-iw)(P+sQ)+C(s^2+w^2)}{(s-iw)(s+iw)(P+sQ)} \\ &= \frac{(AQ+BQ+C)s^2+(AP+BP-BiwQ+AiWQ)s+iwPA-iwPB+w^2C}{(s-iw)(s+iw)(P+sQ)}\end{aligned}$$

Equating coefficients:

$$s^2: AQ + BQ + C = 0 \rightarrow C = -AQ - BQ \quad (3.20)$$

$$s: PA + iwAQ + BP - iwBQ = 1 \quad (\text{Multiplying both sides by } iw)$$

$$APiw - w^2AQ + iwBP + w^2BQ = iw \quad (3.21)$$

$$\text{Constant: } APiw - BPiw + Cw^2 = 1 \quad (3.22)$$

Plugging equation (3.20) into (3.22), the following term is obtained

$$APiw - BPiw - w^2AQ - w^2BQ = 1 \quad (3.23)$$

Adding equation (3.21) to (3.23), and solving for A, this yields

$$2iwAP - 2w^2AQ = iw + 1$$

$$A = \frac{1+iw}{2iwP-2w^2Q} = \frac{1+iw}{2w(iP-wQ)}$$

Subtracting equation (3.21) from (3.23), and solving for B

$$2iwBP + 2w^2BQ = iw - 1$$

$$B = \frac{iw-1}{2w(iP+wQ)}$$

Finally,

$$\begin{aligned} C &= -Q[A + B] = \frac{-Q}{2w} \left[ \frac{1+iw}{iP-wQ} + \frac{iw-1}{iP+wQ} \right] = \frac{-Q}{2w} \left[ \frac{iP+wQ-wP+iw^2Q-wP-iw^2Q-iP+wQ}{-P^2-w^2Q^2} \right] \\ &= \frac{Q}{2w} \left[ \frac{2wQ-2wP}{P^2+w^2Q^2} \right] = \frac{Q(Q-P)}{P^2+w^2Q^2} \end{aligned}$$

Reconsidering constants by referring to the table of Inverse Laplace Transform ( $\frac{1}{s-a} \rightarrow e^{at}$ ).

Thus, the Inverse Laplace Transform of  $\bar{V}_i$  with respect to "s" is given by

$$\bar{V}_i(y, T) = \frac{vk}{\sqrt{2\pi}} I_o w \left[ \frac{1+iw}{2w(iP-wQ)} e^{iwT} + \frac{iw-1}{2w(iP+wQ)} e^{-iwT} + \frac{Q(Q-P)}{(P^2+w^2Q^2)Q} e^{-\frac{P}{Q}T} \right] \quad (3.24)$$

Similarly, same process is applied for  $\bar{V}_o$

$$\begin{aligned} \bar{V}_o: \frac{1+s+y^2}{(s^2+w^2)(P+sQ)} &= \frac{1+s+y^2}{(s-iw)(s+iw)(P+sQ)} = \frac{A}{s-iw} + \frac{B}{s+iw} + \frac{C}{P+sQ} \\ &= \frac{A(s+iw)(P+sQ) + B(s-iw)(P+sQ) + C(s^2+w^2)}{(s^2+w^2)(P+sQ)} \end{aligned}$$

$$= \frac{(AQ+BQ+C)s^2 + (AP+iwQA+BP-iwBQ)s + iwAP-iwBP+cw^2}{(s^2+w^2)(P+sQ)}$$

Equating coefficients

$$s^2: AQ + BQ + C = 0$$

$$C = -AQ - BQ \quad (3.25)$$

$$s: AP + iwQA + BP - iwBQ = 1 \quad (\text{Multiplying both sides by } iw)$$

$$iwAP - w^2AQ + iwBP + w^2BQ = iw \quad (3.26)$$

$$\text{Constant: } APiw - iwBP + Cw^2 = 1 + y^2 \quad (3.27)$$

Plugging equation (3.25) into (3.27), this results in,

$$iwAP - iwBP - w^2AQ - w^2BQ = 1 + y^2 \quad (3.28)$$

Adding equation (3.26) to (3.28), the following term is obtained:

$$2iwAP - 2w^2AQ = 1 + y^2 + iw$$

Finally, subtracting (3.26) from (3.28)

$$2iwBP + 2w^2BQ = iw - 1 - y^2$$

Therefore,

$$A = \frac{1+y^2+iw}{2w(ip-wQ)} \quad ; \quad B = \frac{iw-1-y^2}{2w(ip+wQ)} \quad (3.29)$$

And for C:

$$C = -Q(A + B)$$

$$= \frac{-Q}{2w} \left[ \frac{1+y^2+iw}{ip-wQ} + \frac{iw-1-y^2}{ip+wQ} \right]$$

$$= \frac{-Q}{2w} \frac{(1+y^2+iw)(ip+wQ) + (iw-1-y^2)(ip-wQ)}{-P^2-w^2Q^2}$$

$$= \frac{Q}{2w} \frac{ip+wQ+ipy^2+wQy^2-wP+iw^2Q-wP-iw^2Q-ip+wQ-ipy^2+wQy^2}{P^2+w^2Q^2}$$

$$C = \frac{Q}{2w} \frac{2wQ + 2wQy^2 - 2wP}{P^2 + w^2Q^2}$$

$$C = \frac{Q(Q - P + Qy^2)}{P^2 + w^2Q^2} \quad (3.30)$$

Similarly, constants for  $\bar{V}_o$  are considered, and by referring to the Inverse Laplace Transform table ( $\frac{1}{s-a} \rightarrow e^{at}$ ), the Inverse Laplace Transform of  $\bar{V}_o$  with respect to "s," is defined as,

$$\bar{V}_o(y, T) = \frac{vk}{\sqrt{2\pi}} I_o w \left[ \frac{1+y^2+iw}{2w(ip-wQ)} e^{iwT} + \frac{iw-1-y^2}{2w(iP+wQ)} e^{-iwT} + \frac{Q(Q-P+Qy^2)}{(P^2+w^2Q^2)Q} e^{-\frac{P}{Q}T} \right] \quad (3.31)$$

Multiplying each denominator and numerator of equations (3.24) and (3.31) by denominator's complex conjugate ( $a + ib \rightarrow a - ib$ ) in order to eliminate the "i" from the denominator -- putting over a common denominator:

For equation (3.24)

$$\bar{V}_i(y, T) = \frac{vk}{\sqrt{2\pi}} I_o w \left[ e^{iwT} \frac{(1+iw)(-wQ-iP)}{2w(-wQ+iP)(-wQ-iP)} + e^{-iwT} \frac{(iw-1)(wQ-iP)}{2w(wQ+iP)(wQ-iP)} + e^{-\frac{P}{Q}T} \frac{(Q-P)}{(P^2+w^2Q^2)} \right]$$

$$\bar{V}_i(y, T) = \frac{vk}{\sqrt{2\pi}} I_o w \left[ e^{iwT} \frac{(-wQ-iP-iw^2Q+wP)}{2w(w^2Q^2+P^2)} + e^{-iwT} \frac{(iw^2Q+wP-wQ+iP)}{2w(wQ^2+P^2)} + e^{-\frac{P}{Q}T} \frac{(Q-P)}{(P^2+w^2Q^2)} \right]$$

Using the Euler's formulas:

$$e^{+iwT} = \cos(wT) + i \sin(wT)$$

$$e^{-iwT} = \cos(wT) - i \sin(wT)$$

$$\bar{V}_i(y, T) = \frac{vk}{\sqrt{2\pi}} I_o w \left[ \frac{(\cos(wT) + i \sin(wT))(-wQ-iP-iw^2Q+wP)}{2w(w^2Q^2+P^2)} + (\cos(wT) -$$

$$i \sin(wT)) \frac{(iw^2Q+wP-wQ+iP)}{2w(wQ^2+P^2)} + e^{-\frac{P}{Q}T} \frac{(Q-P)}{(P^2+w^2Q^2)} \right]$$

$$\begin{aligned}\bar{V}_i(y, T) = \frac{vk}{\sqrt{2\pi}} I_o w \left[ \frac{1}{2w(w^2Q^2 + P^2)} \right. & \left[ -wQ \cos(wT) - iP \cos(wT) - iw^2Q \cos(wT) + \right. \\ & \left. wP \cos(wT) - iwQ \sin(wT) + P \sin(wT) + w^2Q \sin(wT) + iwP \sin(wT) + \right. \\ & \left. iw^2Q \cos(wT) + wP \cos(wT) - wQ \cos(wT) + iP \cos(wT) + w^2Q \sin(wT) - \right. \\ & \left. iwP \sin(wT) + iwQ \sin(wT) + P \sin(wT) \right] + \left[ e^{-\frac{P}{Q}T} \frac{(Q-P)}{(P^2 + w^2Q^2)} \right] \end{aligned}$$

$$\begin{aligned}\bar{V}_i(y, T) = \frac{vk}{\sqrt{2\pi}} I_o w \left[ \frac{1}{2w(w^2Q^2 + P^2)} \right. & \left[ -2wQ \cos(wT) + 2wP \cos(wT) + 2P \sin(wT) + \right. \\ & \left. 2w^2Q \sin(wT) \right] + \left[ e^{-\frac{P}{Q}T} \frac{(Q-P)}{(P^2 + w^2Q^2)} \right] \end{aligned}$$

$$\begin{aligned}\bar{V}_i(y, T) = \frac{vk}{\sqrt{2\pi}} I_o w \left[ \frac{1}{w(w^2Q^2 + P^2)} \right. & \left[ -wQ \cos(wT) + wP \cos(wT) + P \sin(wT) + \right. \\ & \left. w^2Q \sin(wT) \right] + \left[ e^{-\frac{P}{Q}T} \frac{(Q-P)}{(P^2 + w^2Q^2)} \right] \end{aligned}$$

This is an even function of 'y' since only embedded 'y<sup>2</sup>' within the equation appears. Similarly, after multiplication of the complex conjugate of the numerator and denominator of equation (3.31), and using the same identities used for  $\bar{V}_i$ , the following term is obtained for  $\bar{V}_o$ :

$$\begin{aligned}\bar{V}_o(y, T) = \frac{vk}{\sqrt{2\pi}} I_o w \left[ \frac{(1+y^2+iw)(-wQ-iP)(\cos(wT)+isin(wT))}{2w(w^2Q^2 + P^2)} + \right. \\ \left. \frac{(iw-1-y^2)(wQ-iP)(\cos(wT)-isin(wT))}{2w(w^2Q^2 + P^2)} + \frac{(Q-P+Qy^2)}{(P^2 + w^2Q^2)} e^{-\frac{P}{Q}T} \right] \end{aligned}$$

$$\bar{V}_o(y, T) = \frac{vk}{\sqrt{2\pi}} I_o w \left[ \frac{1}{2w(w^2 Q^2 + P^2)} [-wQ \cos(wT) - y^2 wQ \cos(wT) - iw^2 Q \cos(wT) - iP \cos(wT) - iy^2 P \cos(wT) + wP \cos(wT) - iwQ \sin(wT) - iy^2 wQ \sin(wT) + w^2 Q \sin(wT) + P \sin(wT) + y^2 P \sin(wT) + iwP \sin(wT) + iw^2 Q \cos(wT) - wQ \cos(wT) - y^2 wQ \cos(wT) + wP \cos(wT) + iP \cos(wT) + iy^2 P \cos(wT) + w^2 Q \sin(wT) + iwQ \sin(wT) + iy^2 wQ \sin(wT) - iwP \sin(wT) + P \sin(wT) + y^2 P \sin(wT)] + \frac{(Q-P+Qy^2)}{(P^2+w^2Q^2)} e^{-\frac{P}{Q}T} \right]$$

$$\bar{V}_o(y, T) = \frac{vk}{\sqrt{2\pi}} I_o w \left[ \frac{1}{2w(w^2 Q^2 + P^2)} [-2wQ \cos(wT) - 2y^2 wQ \cos(wT) + 2wP \cos(wT) + 2w^2 Q \sin(wT) + 2P \sin(wT) + 2y^2 P \sin(wT)] + \frac{(Q-P+Qy^2)}{(P^2+w^2Q^2)} e^{-\frac{P}{Q}T} \right]$$

$$\bar{V}_o(y, T) = \frac{vk}{\sqrt{2\pi}} I_o w \left[ \frac{w(P-Q-y^2Q) \cos(wT) + (P+w^2Q+y^2P) \sin(wT)}{w(w^2 Q^2 + P^2)} + \frac{(Q-P+Qy^2)}{(P^2+w^2Q^2)} e^{-\frac{P}{Q}T} \right]$$

$\bar{V}_o(y, T)$ , also appears to be an even function in 'y,' and by taking the Inverse Fourier Transform with respect to 'y'

$$V_i(X, T) = \frac{1}{\sqrt{2\pi}} \int_{-\infty}^{\infty} e^{-iyX} \bar{V}_i(y, T) dy$$

$$V_o(X, T) = \frac{1}{\sqrt{2\pi}} \int_{-\infty}^{\infty} e^{-iyX} \bar{V}_o(y, T) dy$$

Knowing that:

- $e^{-iyX} = \cos(yX) - i \sin(yX)$
- -  $\cos(y, X)$  is an even function.
- $\bar{V}_i(y, T)$  and  $\bar{V}_o(y, T)$  are also even functions as per the obtained derivations.
- $\sin(y, T)$  is an odd function.

- Integration of an odd function over a symmetric interval = 0

$$\int_{-a}^a f(x) dx = 0 \quad \text{if } f(x) \text{ is odd.}$$

$$\int_{-a}^a f(x) dx = 2 \int_0^a f(x) dx \quad \text{if } f(x) \text{ is an even function.}$$

- Even x Odd Function = Odd Function

Even x Even Function = Even Function

Odd x Odd Function = Even Function

Therefore,

$$V_i(X, T) = \frac{1}{\sqrt{2\pi}} \int_{-\infty}^{\infty} \underset{\substack{\uparrow \\ \text{Even}}}{\cos(yX)} \underset{\substack{\uparrow \\ \text{Even}}}{\bar{V}_i(y, T)} dy - i \frac{1}{\sqrt{2\pi}} \int_{-\infty}^{\infty} \overset{\substack{\nearrow 0 \\ \text{Odd}}}{\sin(y, X)} \underset{\substack{\uparrow \\ \text{Even}}}{\bar{V}_i(y, T)} dy$$

$$V_i(X, T) = \sqrt{\frac{2}{\pi}} \int_0^{\infty} \cos(yX) \bar{V}_i(y, T) dy \quad (3.32)$$

$$V_o(X, T) = \sqrt{\frac{2}{\pi}} \int_0^{\infty} \cos(yX) \bar{V}_o(y, T) dy \quad (3.33)$$

Hence, the two-coupled-partial differential equations, Equations (3.9) and (3.10), are transformed into two integrals, where,

The cell-membrane potential is defined as:

$$V_m = V_i - V_o \quad (3.34)$$

Where,

$$\bar{V}_i(y, T) = \frac{vk}{\sqrt{2\pi}} I_o w \left[ \frac{1}{w(w^2 Q^2 + P^2)} [-wQ \cos(wT) + wP \cos(wT) + P \sin(wT) + w^2 Q \sin(wT)] + \left[ e^{-\frac{P}{Q}T} \frac{(Q-P)}{(P^2 + w^2 Q^2)} \right] \right] \quad (3.35)$$



$$\bar{V}_o(y, t) = \frac{vk}{\sqrt{2\pi}} I_o w \left[ \frac{w(P-Q-y^2Q) \cos(wT) + (P+w^2Q+y^2P) \sin(wT)}{w(w^2Q^2+P^2)} + \frac{(Q-P+Qy^2)}{(P^2+w^2Q^2)} e^{-\frac{P}{Q}T} \right] \quad (3.36)$$

$$P = ky^2 + (y^2 + k\mu)(1 + y^2)$$

$$Q = ky^2 + y^2 + k\mu$$

$$k = \frac{r_o}{r_i} \quad \mu = \frac{r_{me}}{r_e} \quad v = \sqrt{r_{me}T_i} \quad r_{me} = r_m + r_w$$

When setting the Warburg impedance to nil (zero), the obtained results are in agreement of the findings of the peer-reviewed work in [144]; this validates the full derivations carried out in this chapter. As per the obtained results, all capacitance terms have explicitly vanished from the fully derived cell-membrane potential, which could mislead the general reader by suggesting that the capacitive factor does not play a role in shaping the cell-membrane potential. However, as shall be further elaborated on this issue in the next section, in short, the capacitive term does play a role, and mathematically, such role is implicit.

### 3.5 Empirical Solution

The transformed equations, (3.32) and (3.33), are respectively the intracellular and extracellular potential, and their difference gives the membrane potential of a cell ( $V_m$ ). The two integral equations are evaluated numerically using symbolic Maple 16 (Maplesoft, Ontario, Canada), and resultant figures of cell-membrane potential with respect to time and space are obtained via an M-File command processed through Matlab 7.12 (The Mathworks Inc., Natick, MA). Appendix C.1 provides numerical algorithms, evaluating the derived expression of cell-membrane potential. The numerical algorithms shall allow different scenarios to be drawn, and

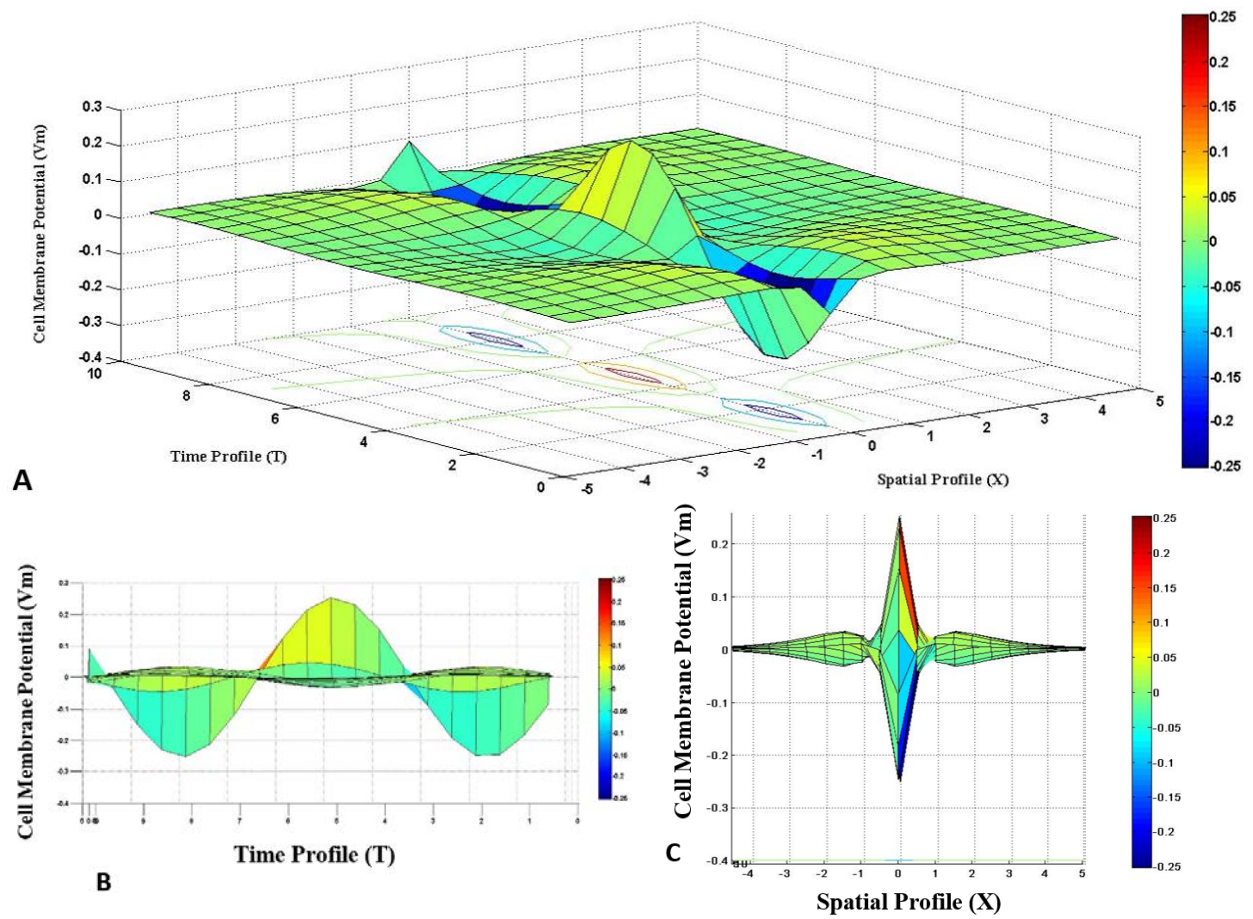
hence the dependencies among controlling physical parameters in shaping the cell-membrane potential can be analyzed.

One of the main objectives of this chapter is to provide a solid review on cellular biophysics, and to investigate the electrophysiology of cells. Furthermore, understanding the theory introduced in this chapter would assist in interpreting the experimental findings of Chapter 4. The derived mathematical expression of cell-membrane potential would be evaluated numerically, resulting into a number of graphs (Figures 3.5-3.11), which would highlight the electrophysiology phenomena of cells. Due to lack of experimental findings of intracellular, as well as extracellular physical parameters, the values of the rescaled parameters are assigned arbitrarily as in [144], considering that the main objective is to investigate and interpret the theory of cellular biophysics. Furthermore, different scenarios are considered to investigate the variations of the controlling parameters, and study their dependencies among each other. As in [144], the first intuitive scenario is to set all resistive parameters equal to unity. The other two scenarios would be varying either  $k$  or  $\mu$ . It should be noted that setting  $\mu$  to nil is not physically possible, as this implies that injecting current via stimulating electrode is going through a completely sealed biological system, which contradicts with the physical phenomena of cellular charge leakage.

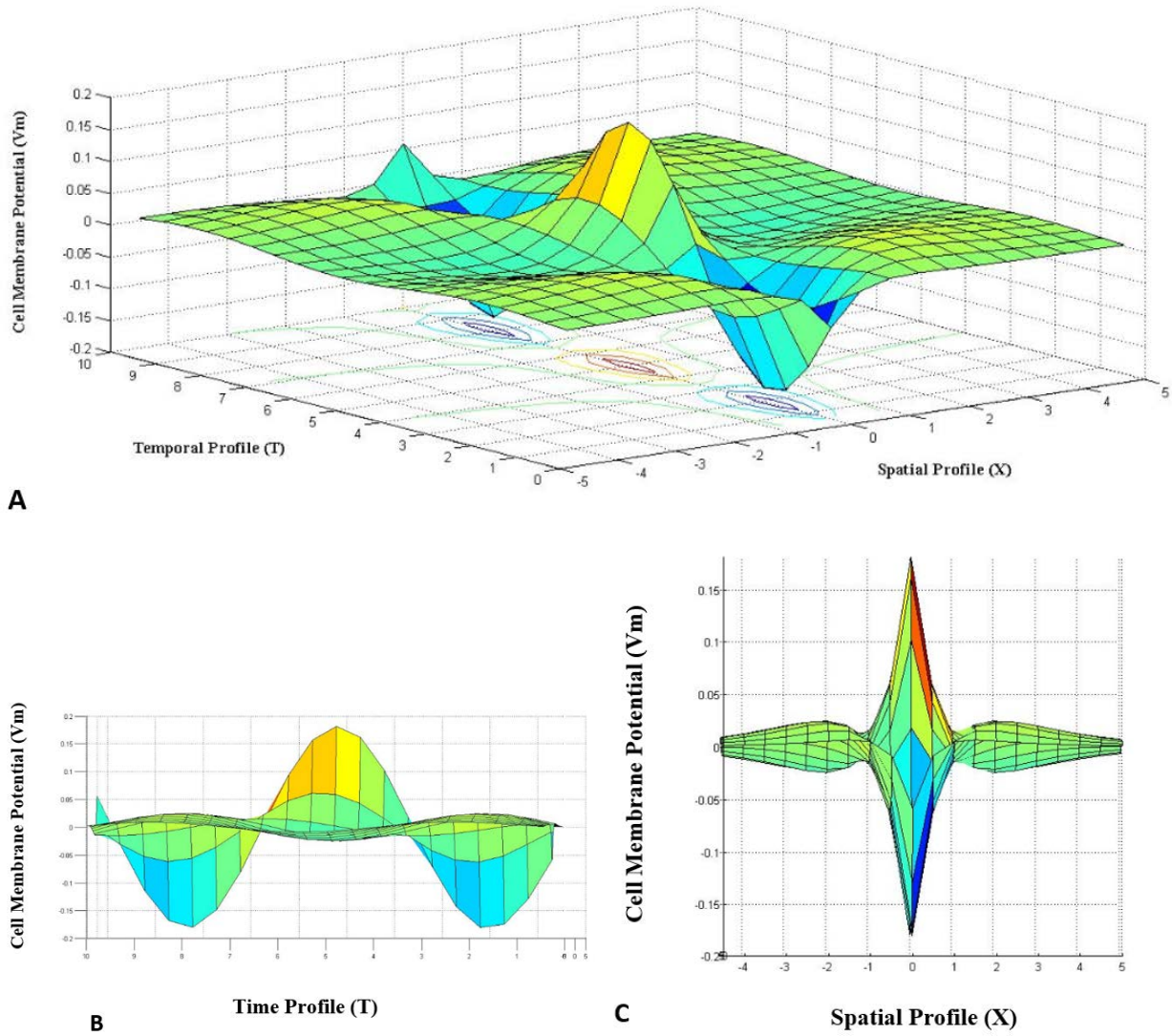
The empirical results should provide in-depth analyses in presenting the concept of electrophysiology of cells, and this shall further investigate the dependencies among controlling parameters of the analogical circuit of the biological cell. The following table summarizes three different scenarios that are evaluated numerically, where generated graphs (Figures 3.5-3.11) are discussed in Section 3.6.

Scenarios	Case	$r_o$	$r_i$	$\kappa$	$r_m$	$r_w$	$r_{me}$	$r_e$	$\mu$	$v$	$I_o$	$w$
<b>I</b>	all = unity	1	1	1	1	1	2	1	2	$\sqrt{2}$	1	1
<b>II</b>	$\kappa$ = variable	1	4	0.25	1	1	2	1	2	$2\sqrt{2}$	1	1
	$\mu$ = fixed	1	2	0.5	1	1	2	1	2	2	1	1
	$v$ = variable	6	3	2	1	1	2	1	2	$\sqrt{6}$	1	1
<b>III</b>	$\kappa$ = fixed	1	1	1	2	1	3	1	3	$\sqrt{3}$	1	1
	$\mu$ = variable	1	1	1	4	2	6	1	6	$\sqrt{6}$	1	1
	$v$ = variable	1	1	1	6	3	9	1	9	3	1	1

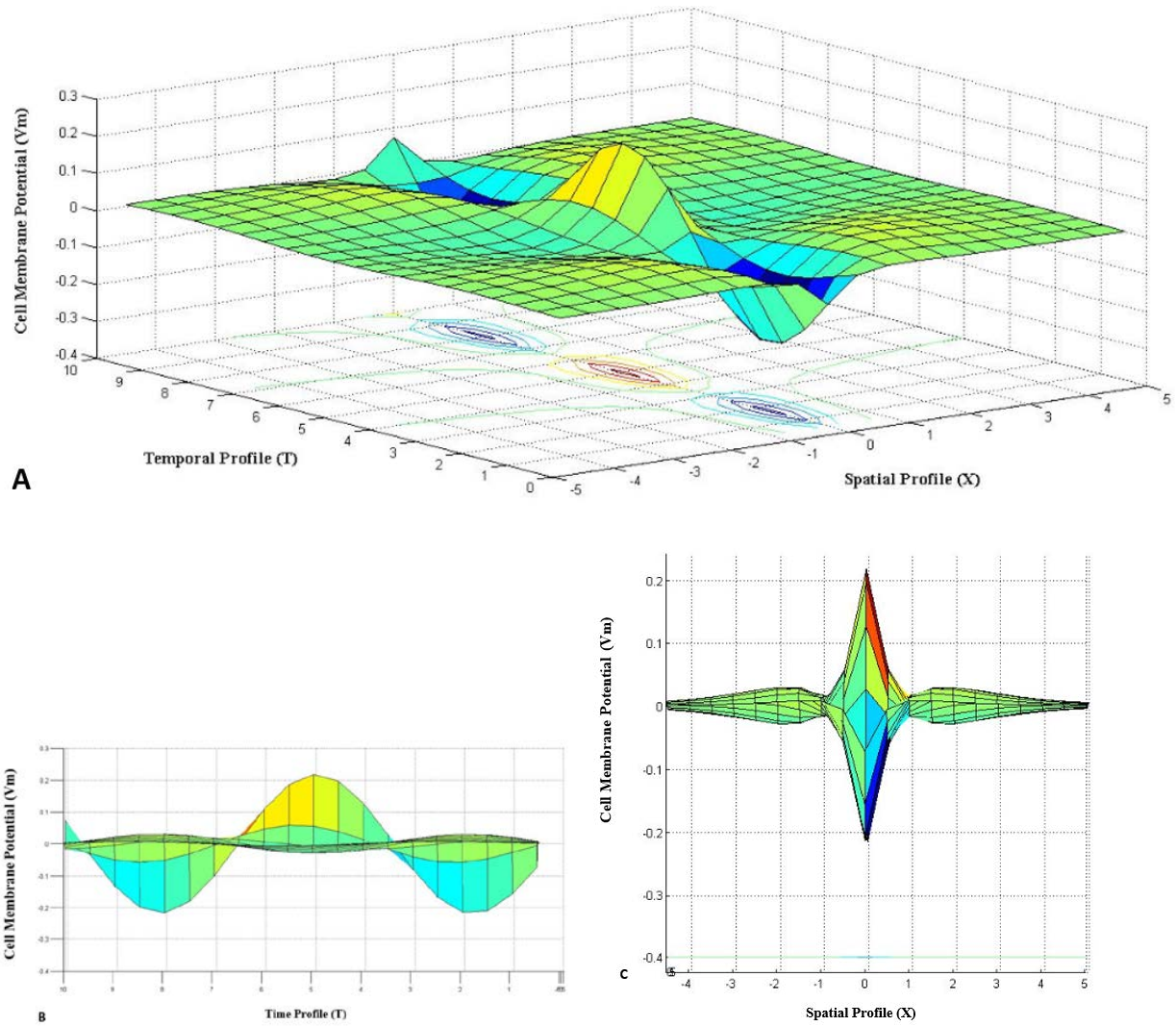
**Table 3.4** Numerical solution of arbitrarily selected parameters: three different scenarios.



**Fig. 3.5** Case I. All essential parameters equal to unity, (A-C) cell-membrane potential ( $V_m$ ) with respect to spatial (X) and time (T) profiles.

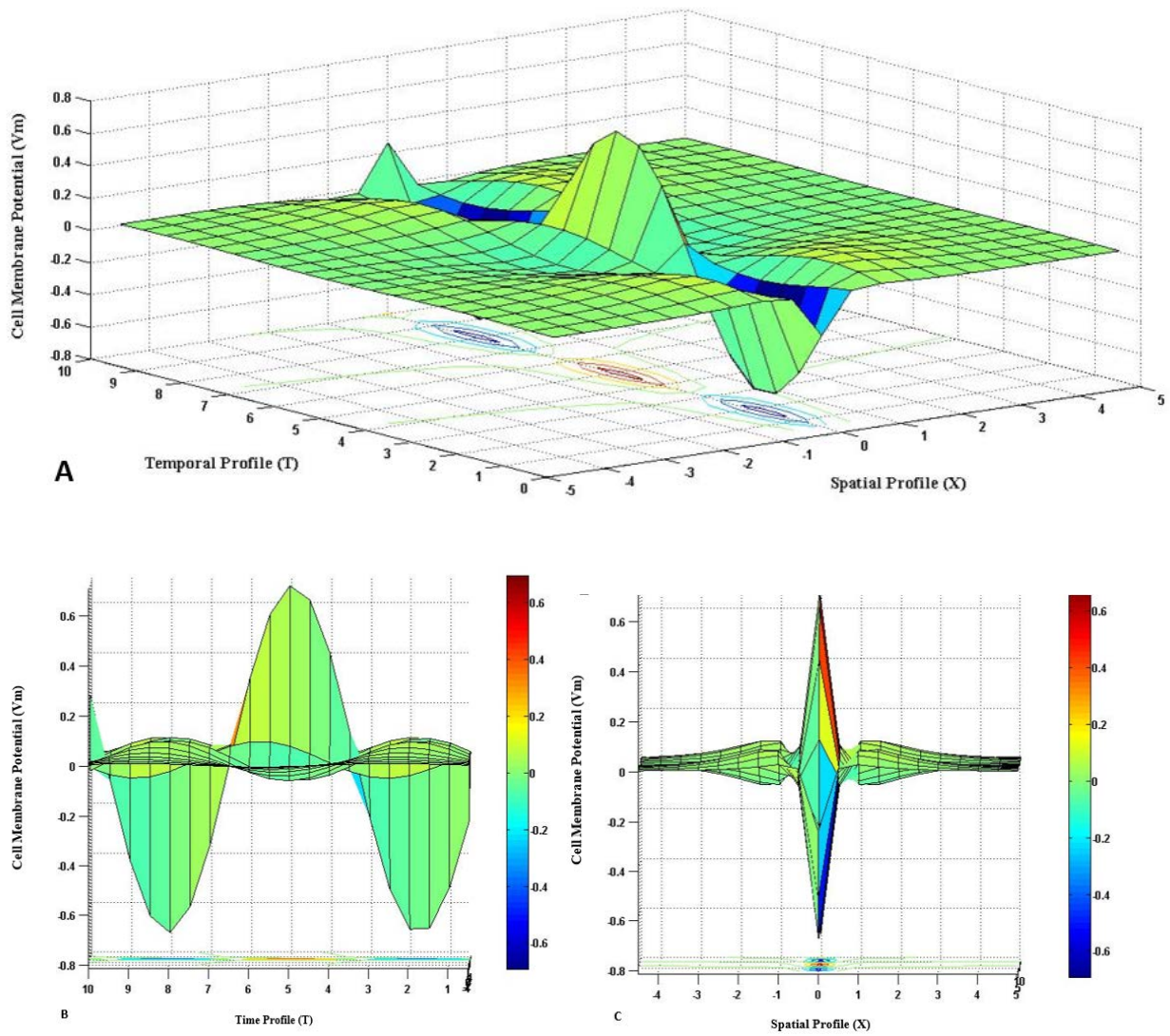


**Fig. 3.6** Case II. ( $\kappa = 0.25$ ,  $v = 2\sqrt{2}$ ,  $\mu$  is fixed), (A-C) cell-membrane potential ( $V_m$ ) with respect to spatial (X) and time (T) profiles.

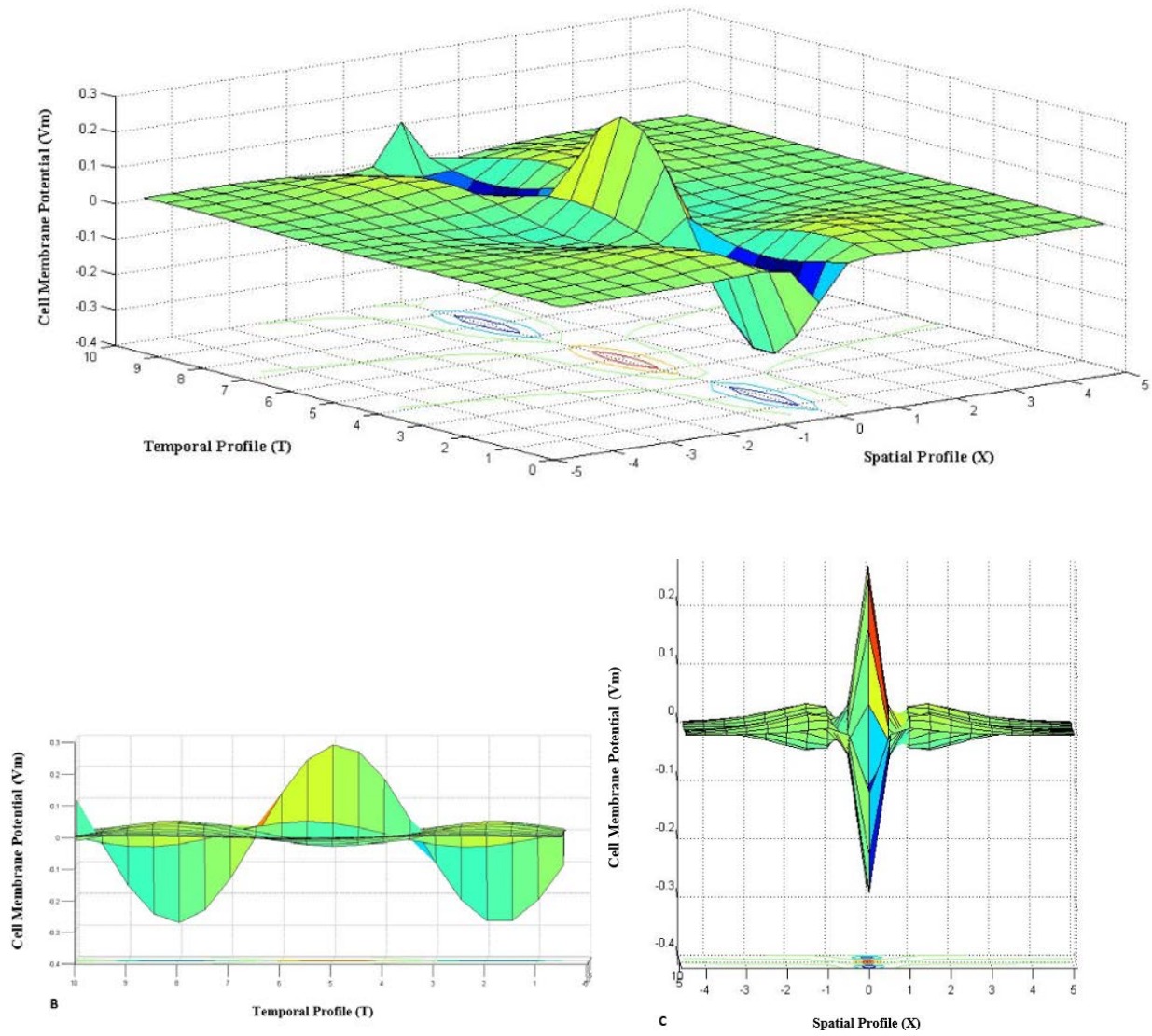


**Fig. 3.7** Case II. ( $\kappa = 0.5$ ,  $v = 2$ ,  $\mu$  is fixed), (A-C) cell-membrane potential ( $V_m$ ) with respect to spatial ( $X$ ) and time ( $T$ ) profiles.



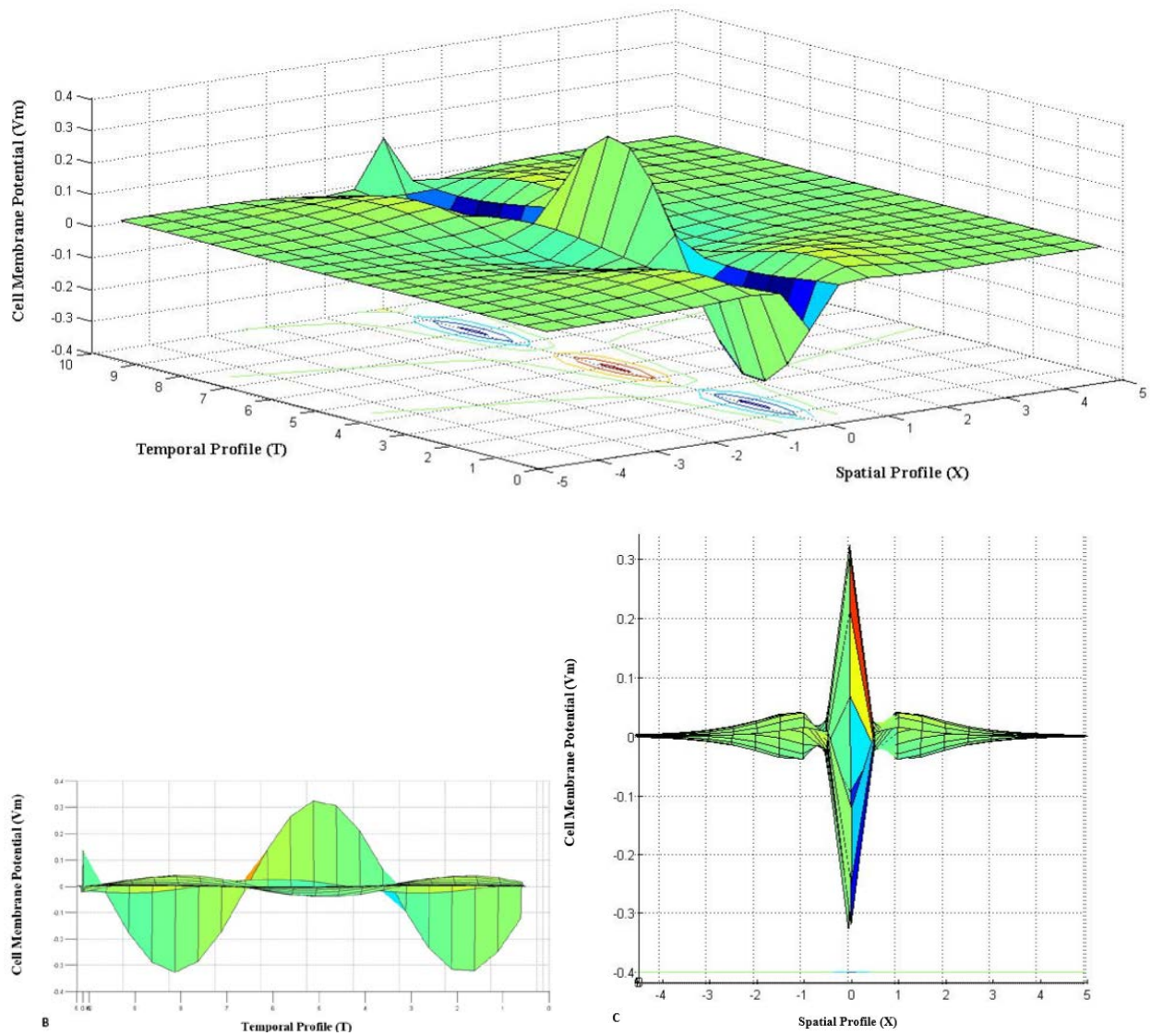


**Fig. 3.8** Case II. ( $\kappa = 2$ ,  $v = \sqrt{6}$ ,  $\mu$  is fixed), (A-C) cell-membrane potential ( $V_m$ ) with respect to spatial (X) and time (T) profiles.

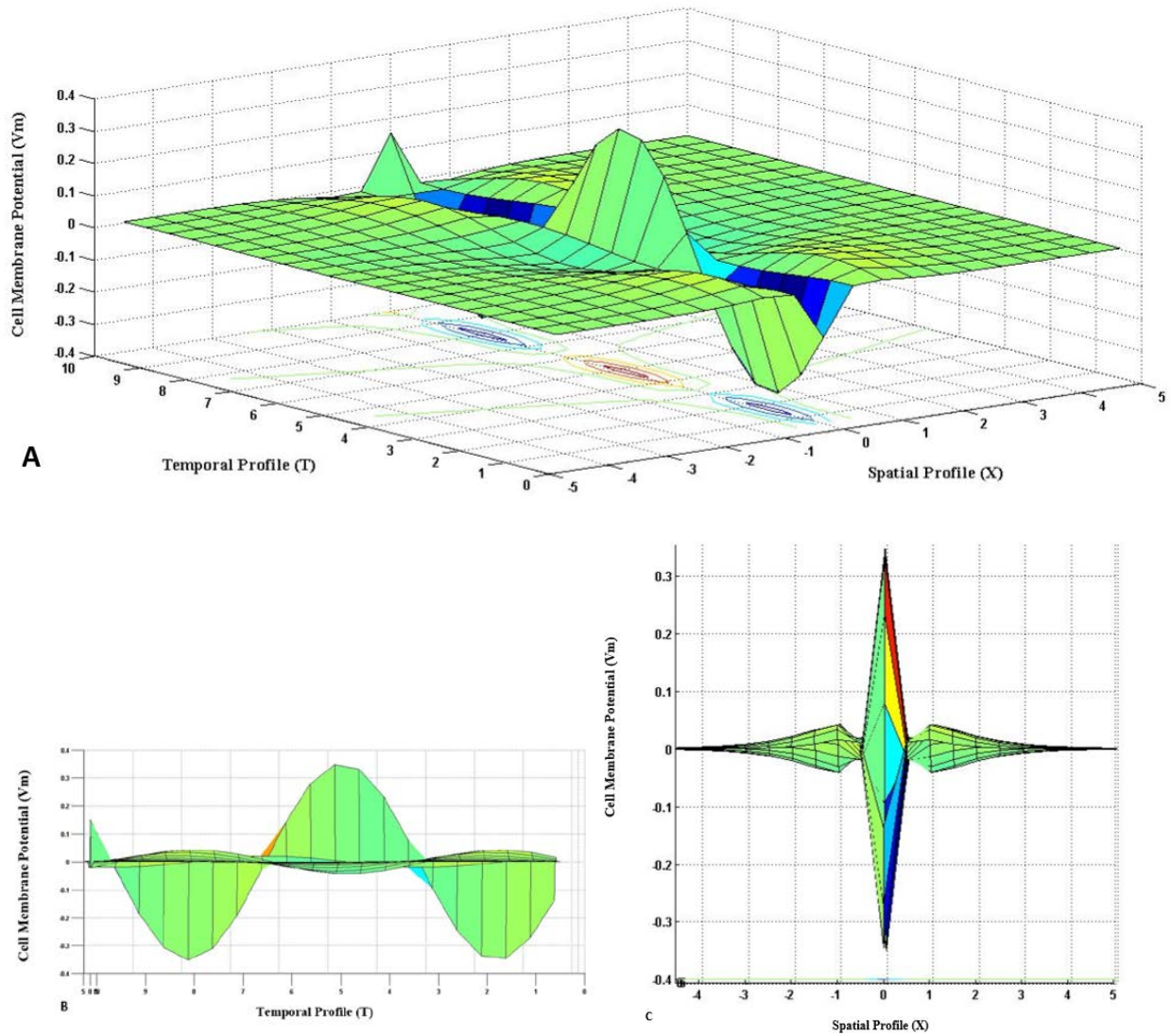


**Fig. 3.9** Case III. ( $\mu = 3$ ,  $v = \sqrt{3}$ ,  $\kappa$  is fixed), (A-C) cell-membrane potential ( $V_m$ ) with respect to spatial (X) and time (T) profiles.





**Fig. 3.10** Case III. ( $\mu = 6$ ,  $v = \sqrt{6}$ ,  $\kappa$  is fixed), (A-C) cell-membrane potential ( $V_m$ ) with respect to spatial ( $X$ ) and time ( $T$ ) profiles.



**Fig. 3.11** Case III. ( $\mu = 9$ ,  $\nu = 3$ ,  $\kappa$  is fixed), (A-C) cell-membrane potential ( $V_m$ ) with respect to spatial (X) and time (T) profiles.

### 3.6 Discussion of Results

The cyclic events of rise and drop of cell-membrane potential of any type of mammalian cells, as shown in the numerically generated figures (Figures 3.5-3.11), are the initiation of numerous events of cell-cell communication, as well as intracellular activities that would lead to cell motility and contractile forces, where the latter are of a particular interest in cell

mechanobiology that shall be further addressed in Chapter 6. Slightly deviating from the main topic of this research, investigating such electrophysiology of cells is quite beneficial within cardiology field by understanding the mechanisms of defibrillation in case of a cardiac heart arrest medical emergency, ECG monitoring, and configuration of pacemaker electrodes [149]. Also, this aids in understanding the staging of neuron diseases such as that of multiple sclerosis (MS) [150].

The generated figures (Figure 3.5 – 3.11) illustrate that cell-membrane potential is a function of time and space. The subfigures B, of Figures 3.5-3.11, clearly demonstrate that the slope of the cell-membrane potential to unit time defines power of the amount of work performed in moving charged ions within cell membrane from intracellular to extracellular domain (or vice versa): the intracellular to extracellular potential difference defines cell-membrane potential resembled as an exerted work per unit charge of any moving charged nutrients/ions against an electric field. This is important that despite the vanished capacitive terms in the finally obtained equation of cell-membrane potential, yet the overall implicit capacitive nature of cell is still present. This also illustrates the active characteristic of the developed circuit, on the essence of the injected effective current, and in the presence of the passive components of the system: resistors and capacitors.

In nature, moving of ions/charges within a cell membrane is not ideally in a straight line parallel to the generated electric field, rather it could take a curved infinitesimal path within a cell membrane as a generalized form; this is mathematically depicted in the proposed model by the integral and cosine term; this is again in a great harmony of the biological kinematics of ions within the cellular domain described earlier by the term ‘diffusion:’ stochastic movements of ion molecules from high to low concentration.

The mathematically implicit effective cell-membrane capacitive factor, sum of paralleled capacitors (Warburg and cell membrane), plays a dominant role in shaping the overall cell-

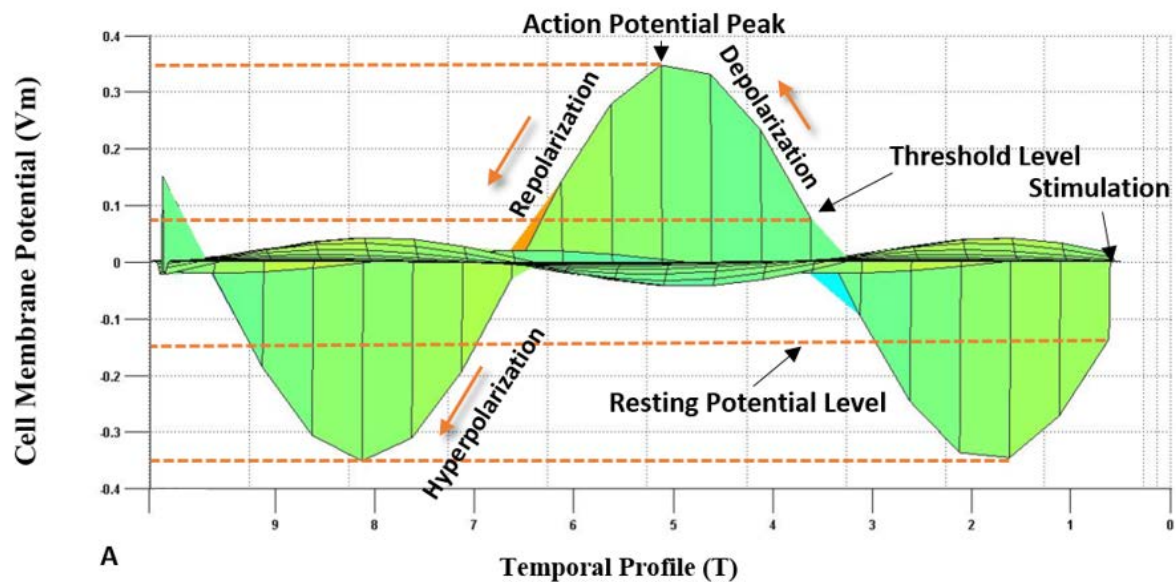
membrane potential, despite its explicit absence from the finally obtained expression. In a similar manner, the slope of the C subfigures of 3.5-3.11 gives energy (work required) to transfer charges between the two domains segregated by the cell membrane – a lipid bilayer that impedes the kinematics of one way movement of charged ions.

The three drawn scenarios, (1) fixation of the ratio of effective cell-membrane potential (the sum of the serial resistors consisting of cell membrane and Warburg diffusion) to physiological medium resistance, which defines  $\mu$ , and then varying  $\kappa$  and  $\nu$ ; (2) fixation of the ratio of longitudinal resistance of current flow to longitudinal internal resistance of the cell cytoplasm, which defines  $\kappa$ , and then varying  $\mu$  and  $\nu$ ; and finally (3) equating all independent generalized parameters/resistors (i.e.,  $r_i$ ,  $r_o$ ,  $r_m$ ,  $r_w$ , and  $r_e$ ) to unity, all yield same configuration pattern of cell-membrane potential profile against time and space in a cyclic manner, but with varying amplitudes and ratios of maximum hyperpolarization to maximum depolarization.

Considering that biological cell-membrane potential in nature starts at a negative cytoplasm (negative resting potential) in a stage of polarization: resting potential is an invariant time potential at which ionic equilibrium is maintained, and electrochemical kinetics driving the ion kinematics are balanced [96]. Then upon stimulation, cell membrane starts to polarize from negative; this is denoted as stage (I), moving to a swift depolarization stage (stage II: negative to positive), then to repolarization stage towards resting potential (stage III: positive to negative), and finally more negative passing resting potential in a stage denoted as hyperpolarization (stage IV). After stage (IV) is elapsed and re-initialization of stage (I) recommenced, such period is termed in biophysics as refractory period; this entire process goes into a cycle along the cell membrane, where specific types of ion-channels are open and close in an orchestrated manner, led by an electrochemical signaling maestro: producing a prominent pattern of hyper/depolarization. Such pattern of the constant initiations of signal peaks (action potentials) are representations of excitable cells. To better visualize the travelled signals,

imagine the belly of a snake as our cell membrane, and that the digested prey moving along the belly is our travelled signal of cell membrane. Thus, the obtained numerical findings (Figure 3-12) are in agreement with the physical cellular potential going into cycle events of polarization, depolarization, and hyperpolarization [96, 108, 112, 118, 119, 121, 144].

It should be re-stressed on the point that the values set for the controlling parameters are arbitrary, and only utilized to investigate the theory of cell-membrane potential, as well as to study the dependency of the controlling parameters of the illustrated analogical circuit of the biological cell on each other: shaping the overall electrophysiology of a cell. To closely examine the various stages that cell potential goes through, Figure 3.11B has been enlarged into the following figure (Figure 3.12), illustrating the different phases of cellular potential.



**Fig. 3.12** Numerical result of cell-membrane potential ( $V_m$ ) vs. temporal profile (T) based on non-ideal/arbitrarily selected parameters ( $\mu = 9$ ,  $v = 3$ ,  $\kappa$  is fixed) due to lack of experimental findings of intracellular and extracellular resistive values to illustrate the different phases of cellular potentials: polarization, depolarization, repolarization, and hyperpolarization.



The cyclic analog wave signaling of cell-membrane potential, as shown in Figures 3.5-3.11, justify the polarity of cells; imagine a cell, close to a spherical shape, contracts and extracts due to ‘firing/overshooting’ of action potential (depolarization), opening of voltage-gated channel, and undershooting (hyperpolarization), closure of certain voltage-gated channel. If an initial stimulation takes place, when the cell is at a resting potential (time invariant potential) of  $-0.15$  V as depicted in Figure 3.12, then the cell for some short period of time (about 0.7-1.6 T) shall maintain a minor increase in its negativity (negative cytoplasm) that could be attributable to either an increase or decrease in outward or inward current flow from of the cell, respectively.

At around 1.7 T the cell starts to depolarize by having a few number of either  $Na^+$  or  $Ca^{2+}$  channels open, where the respective cations start to flow into the intracellular domain. The stimulation reaches a threshold value, where the cell-membrane potential steeply increases in a depolarization stage of either increase or decrease of inward or outward current flow from the cell respectively, suggesting an increase in the number of influx cations of  $Na^+$  and/or  $Ca^{2+}$  into the intracellular domain. The cell membrane reaches a peak at 5.2 T of an action potential of 0.35 V, which is also the equilibrium potential, e.g., of  $Na^+$ . At this stage the cation of  $K^+$  starts to repel against the similarly charged cation of, e.g.,  $Na^+$ , occupying the  $K^+$  initial territory within the intracellular domain. The cytoplasm starts to gradually lose its positivity in a repolarization process by gradually opening  $K^+$  ion channels, permitting efflux of  $K^+$  cations out of the cell. This is followed by a hyperpolarization passing the initial resting potential of the cell, as the negativity of the cytoplasm starts to increase. The hyperpolarization stage could be attributable to an increase in the number of voltage-gated channels, e.g., of  $K^+$  and/or  $Cl^-$ , allowing either efflux or influx of  $K^+$  cations or  $Cl^-$  anions, out and in the cell, respectively. Finally, the ionic ATP pumps restore the initial concentrations of  $K^+$  and  $Na^+$ , where cell membrane goes back to resting potential before starting a new cycle. As a summary, and for

better illustration, the diffusion of  $K^+$  and  $Na^+$  are animated in this link<sup>3</sup>, which summarizes the different phases of cellular potentials.

It should be re-stressed on the importance of identifying all different phases of cellular potentials; for example, knowing resting potential of cells, which is typically ranges from -10 mV to -90 mV [96], is beneficial in identifying cell-membrane potential, and then link  $V_m$  to a nature of a disease and/or to specific functionalities performed by a cell.

The three different scenarios of the arbitrarily selected values of the controlling parameters, investigating the theory of cell-membrane potential resulted in Figures 3.5 to 3.11, manifest that the term  $v$ , describing the ratio of longitudinal resistance to current flow to intracellular resistance, cannot be held fixed if either  $\mu$  or  $\kappa$  is changing due to the resistor coupling with these two terms. It has been found that by fixing  $\mu$ , and varying  $\kappa$  and  $v$  (scenario II),  $\kappa$  and  $v$  are inversely proportional to each other; also, it is found that as the ratio of longitudinal resistance of cell membrane to its intracellular increases ( $\kappa$  increases), the cell-membrane potential amplitude increases. Furthermore, by fixing  $\kappa$ , and varying  $\mu$  and  $v$  (scenario III),  $\mu$  and  $v$  are appeared to be directly proportional to each other; moreover, as the ratio of effective cell-membrane resistor, which is the sum of Warburg diffusion and cell-membrane resistors in series, to buffer medium resistance increases ( $\mu$  increases), the cell-membrane potential amplitude increases. Therefore, measuring cell-membrane potential is affected by the resistivity of the medium, in which it is placed in; it is eventually reflected on its intracellular and extracellular potentials. Moreover, the amplitude of the cell-membrane potential is more pronounced at the external node, where the effective current is injected, and it is gradually depleting, when moving away from the injected effective node along the spatial profile as depicted in sub-figures C of Figures 3.5-3.11.

<sup>3</sup> <http://www.youtube.com/watch?v=FjOVYHQ1upM&list=TLRsuMhW1tJSpl6OvgKnGQQWW9sKbiDPEX>

### **3.7 Conclusion and Future Outlook**

Description of various non-conventional methods utilized to study the characteristics of cells have been presented (SAW, optical fluorescence, and electrochemical), and their mechanisms have been highlighted. By advocating the electrochemical technique, different tactics within this approach have been investigated: a patch clamp method, optical fluorescence, and N/MEMS. Vast literature review is illustrated mainly on the subject of cancer cell's biophysics. This is followed by the development of a mathematical modeling of the electrophysiology mechanisms of cells.

This chapter provides in-depth analyses in understanding the biophysics of cell, and its equivalent analogical electric circuit that captures cellular electrophysiology. Furthermore, the outcome of this analytical study is to investigate the cell-membrane potential spatial and temporal dependence, when stimulated by a current. This analytical approach simulates, to some extent, an experimental case where a cell is trapped in a buffered medium, and then stimulated by an electrode, and cell-membrane potential is finally recorded by another adjacent electrode; this will be the target subject of next chapter.

The mathematical modeling has shown that the contributed factor of Warburg diffusion impedance is essential in shaping the overall cell-membrane potential, just as it has been justified experimentally in [1]. Furthermore, the presented model could have been extended to encounter injection of currents at various locations within a cell membrane, either simultaneously or consecutively.

The contribution of this work presented within this chapter in encountering the Warburg diffusion impedance factor in the constructed analogical circuit of the cellular biophysics pays



off in the overall effective cell-membrane signature. Such impedance diffusion accounts for a charge leakage that could be physically interpreted, e.g., to a charge leakage of nutrients via cells' pore. This is in line of one of the main objectives of this work through the detailed mathematical derivations of the cell-membrane potential expression presented in this chapter to the general reader, by first familiarizing him or her of the controlling parameters of the cellular biophysics, as well as enabling the future extension of this research by encountering the subject of cellular pore specificity. Such subject, to the author's best knowledge, has not yet been legitimately justified mathematically, giving a certain pore on a cell, of a size ranges from 7-10 Åm [97], to specifically open or close (flux/efflux) with respect to a distinctive nutrient, e.g., sodium ( $Na^+$ ) and not to other nutrient types (i.e.,  $Mg^{2+}$ ,  $Ca^{2+}$ , etc.), yet another pore on the same cell would have specificity for opening and closing for, e.g., chlorine ( $Cl^-$ ) anion. Such biophysics phenomena could be interpreted, mathematically, as a conditional current passing through an array of logic switches on the exterior of the cell membrane (combination of logical gate arguments), which also can ignite a switch of a gap junction of a cell-cell communication on a global mathematical modeling of a cluster of cells..

The main objective of this chapter is to provide a solid understanding of cellular biophysics through the proposed detailed mathematical model of cellular physics. One approach of utilizing the findings of this chapter could be during the analyses of experimental findings, and based on an obtained signature of the extracted cell-membrane potential (e.g., positive ((depolarization)) vs. negative ((hyperpolarization))), one could predict which specific ion channel is more dominant than the other within a particular cell of a disease type.

This work, within this chapter, assists researchers in sensor technology, molecular biophysics, analytical chemistry, as well as biologists to investigate the response of a cell subjected to an injected current. The ability to unlock the coding of electrochemical language/signaling of cells could be beneficial in allocating a novel approach in directing cells,

including stem cells, toward performing a specific task, modifying intracellular ionic concentrations within a cancer cell, e.g.,  $Na^+$ , via electrochemical stimulation to stop depolarization, and hence perform mitotic arrest, effectively delivering medicine by up/down regulating the performance of specific ion channels, and finally repairing disrupted genes, e.g., PTEN, TSGp53, that are respectively responsible for Autism [151], and the dual role of p53 in Parkinson and cancer diseases [152], by stimulating cells via electrochemical means to activate/code proteins that are responsible for the repair of such genes. Furthermore, the electrochemical approach could provide a novel technique in identifying the different phenotypes of stem cells, which are hard to be segregated by using Fluorescence Activated Cell Sorting (FACS) machine, arriving at their heterogeneity, manipulating them, and finally analyzing their subpopulation dependencies and their interconnections with their niche.

As a step forward in appreciating the science behind cellular electrophysiology, the next chapter addresses the electrochemical profiling of cell membrane of well-established melanoma cell-line models, which to the author's best knowledge, such characteristics have not been yet extracted experimentally in distinguishing the different stages of the melanomagensis.

# **Chapter 4**

---

---

**Electrophysiology**

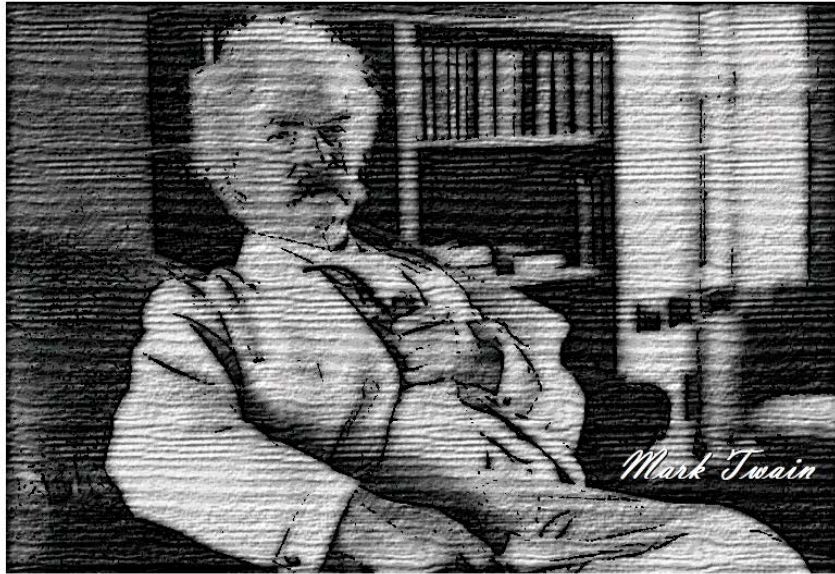
---

---

**Biomechatronic-Based  
Platform**

---

---



*"Keep away from people who try  
to belittle your ambitions.  
Small people always do that,  
but the really great make you  
feel that you, too, can become  
great."*

---

## **Chapter 4: A Miniaturized Biomechatronic Electrophysiology Based Platform – Characterizing the Biophysical Heterogeneity of Melanoma Cell Lines**

### **4.1 Related Work**

Due to the complexity of melanoma pattern and texture, it requires a well-experienced dermatologist to clinically diagnose, and classify the skin lesion as benign, suspicious, or malignant. Sometimes physicians require further histological analyses that are time and cost consuming, which requires further analyses to be performed by a pathologist. Furthermore, visual inspection results in a high tendency of false diagnosis of the disease that puts higher risks on the patient, and may lead to unnecessary invasive surgical involvement. Many noises are present within the dermatological images such as variable lighten conditions, thick hair, image overlapping, skin pores, and sharp edges [153-163]. Also, it is a cumbersome task for most dermatologists to distinguish between malignant melanoma, and a typical nevus (mole) [153-162]. Furthermore, melanoma can form in any area in the human body, including those that are hard to be discovered visually such as the vagina, or within the retinal area (ocular melanoma), as shown in Figure 1.2 [21, 24, 164].

Biopsies may result in contaminating neighboring healthy tissues and organs with melanoma cells [41]. Lead time to properly diagnose the disease is on average a month. Therefore, a requirement for accurate, fast, and cost-effective detection and further biological characterization of melanoma at a cellular level is demanded that could lead to an effective

treatment of the disease, especially if it is discovered at a very early stage. In this chapter, a review is given on two approaches followed generally by dermatologists on the essence of prognosis that are categorized as conventional and nonconventional approach. The former is an image-pattern-recognition based that is processed through computer aided diagnosis (CAD) system, whereas the latter describes tools that detects the disease based on its physical characteristics in a real-time-diagnosis setup. Driven by the merits of nano/microtechnology (LoC), and electrochemical approach described respectively, in Chapters 2 and 3, a miniaturized biomechatronic platform is thoroughly developed, and experimentally tested to characterize the heterogeneity of the biophysical characteristics of eight melanoma cell lines of different genetic complexities.

#### **4.1.1 Dermatological Conventional Prognosis Approach: Pattern Recognition and CAD System for Melanoma Detection**

An image-pattern-recognition approach, which contributes to the early clinical detection of melanoma, is based on conventional “ABCD” method [153-162]: Asymmetry, Border, Color, and Diameter/Dermatoscopic features. The physician studies the tumor’s asymmetric feature, its stochastic-border interaction with neighboring healthy tissues/organs, and homogeneity of the pigmentation, and its diameter. However, this approach poorly describes the fine boundary segregating healthy from infected tissues. This may mislead the physician in invasively taking off more regions than what is required. On the border recognition aspect, this approach has been enhanced by using a Six-Sigma threshold, together with region connectivity concepts to study the availabilities of red-green-blue (RGB) spectrum of skin lesions, and its directional propagation [153]. The Six-Sigma threshold is a  $\pm 3\sigma$  segmentation process based on color

variability emitted from the skin [153]. The modified approach takes into consideration the breakage of the obtained image into a number of rectangular regions, in order to reach a homogenous color deformation, increase sensitivity of pattern recognition, and detect the boundaries of the tumor. However, the modified approach does not obtain satisfactory results in case of presence of thick hair on the skin (image noise).

On the basis of textures and color parameters, Di Leo *et al.* [154] have defined a new set of 7-checklist-scoring mechanism for the usage of Epiluminescence microscopy (ELM) at a sub-surface level, a technique using oil immersion, and intense light beamed on the pigmented lesion, in which beamed light reflects back to the viewer. This approach claimed to have a better accuracy, and less effort than the ABCD scoring method. On this perspective, the ELM-7-checklist mechanism differentiates between melanoma (a score of 3 or more), and benign (a score less than 3) [154]. The method consists of two criteria: major (atypical pigmented network, blue-whitish veil, atypical vascular pattern), and minor (irregular streaks, irregular pigmentation, irregular dots/globules, and regression structures), where 1 major and 1 minor criterion, or 3 minors are required to sufficiently detect melanoma using this approach [155].

Computer Aided Diagnosis (CAD) is a vital tool for early detection of melanoma [156-161]. Thus, an independent component analysis (ICA) has been created to analyze the dermatological images of skin lesions based on vector principle, a linear mixture of independent source of signals of a vector [156]. The method is unique in terms of its algorithm that contains a preprocessing stage of removing image noises, such as hair from the identified infected boundary using a MATLAB platform, followed by a segmentation of the infected region, extraction of targeted region color and structure, and finally performing a classification iteration to diagnose the malignancy of skin cancer [156]. Qin *et al.* [157] utilize local fractal dimension (local FD) in analyzing the irregularity of cancer deformed pattern, as well as

contour irregularities. As a result of their findings, benign possesses a smoother and an oval shape, while melanoma contour distribution is irregular. Also, the former has a contour size that is much smaller than the latter one [157]. In their work, they have found that during the implementation of Gaussian filtering of the extracted features, different features' parameters (max, variance, and entropy), drop gradually for melanoma case, while they remain constants for benign.

A new approach on skin lesion pigment, by visualizing and empirically quantifying its asymmetry, has been presented by Clawson *et al.* [158]. In their findings, they have conservatively claimed that there might be a case where two infected lesions coincide, forming an overall asymmetry index, which they have considered as an added feature in their developed algorithm by generating additional contours. From the noise perspective, and in order to alleviate the image interferences within the system, a segmentation hybrid approach is integrated using active dynamic contours that move as per the internal and external forces generated from (1) within the contour, and (2) from the obtained image data, respectively [159]. At another end, efforts have been made to eliminate system noises using median filtering, and contrast enhancement [160]. Another approach in detection of melanoma, within the CAD system, is the “Bag-of-Features,” among which are texture, color, and boarder that are defined, and evaluated in a patch manner within an image [161].

#### **4.1.2 Non-Conventional Dermatological Approaches in Detecting Melanoma**

Based on the combination of ABCD approach and ELM concept, a mechatronic device (Bluetooth-enabled-handled device) has been designed, and further developed to detect melanoma at an early stage, process images in a real-time domain, and determine whether a



lesion is malignant or benign [162]. In their work, the ELM Transillumination (TLM), in which a ring light generates a focal point beneath the skin (enhanced visualization of the subsurface pigmentation of a nevus), results in a generation of more blood flow and achieves high sensitivity in detecting the infected tissues. In their hardware architecture, they consider the usage of microprocessing -- enabling low power consumption, as well as low noise complementary metal oxide semiconductor (CMOS) image sensor for data processing.

On the wave dynamic aspect, Surface Acoustic Wave (SAW) concept has contributed in early detection of cancer [163]. Based on tumor's distinctive mass density, the SAW propagating velocity, and operating frequency will be altered due to such tumor presence. SAW technology acts as a biosensor, in which a piezoelectric plate is actuated by an electric signal transmitted to an input/output transducer that produces the propagating surface acoustic waves. An experiment of the usage of SAW technology in the field of cancer detection and immunology, has been constructed to have a protein-A (cross linker) placed at the bio-layer, and adjacent to the sensing element (SAW unit) [163]. When antibodies are placed in the system, with specific and non-specific target antigens, adhesion to the associated protein takes place. Thus, a mass loading alteration takes place, generating a frequency shift back to the I/O transducer. As proposed in their work [163], the frequency shift is allocated by a radio frequency identification via I/O antenna installed in the I/O transducer component – the proposed work claims a detection within minutes; however, solid and sufficient experimental findings haven't been presented to support such claim.

On a different detection regime, melanoma circulating tumor cells (CTCs) have been detected in human blood circularity (lymph system) via photoacoustic flowmetry [164]. Despite the immaturity of such research field in terms of obtaining a confidence in experimental findings, the utilization of laser induced ultrasound (photoacoustics), in which a

mechanical wave is generated due to photon optical energy, does lead to perturbation, and thus the development of acoustic waves [165]; the photon energy results in prompt heating and expansion that generates mechanical perturbation, detected as photoacoustic waves. Such mechanical acoustic perturbation is transformed as a voltage signal signature via a piezoelectric copolymer transducer. However, the limitation for such method is a major issue in addressing its applicability in detecting other types of cancer cells, considering the fact that melanoma cells (originating from melanocytes) produce melanin that interacts with light wavelength, while other cells are colorless and don't possess such feature [21, 24]. However, what researchers in the engineering field failed to fully grasp that melanoma can also be generated without the production of melanin, which is referred to as "acromic melanomas" [21, 24]; this certainly wouldn't possess the desirable light absorption feature, which makes this approach inapplicable.

Mehta *et al.* [166] investigate the applicability of using a microwave reflectometry in differentiating among normal, benign, and malignant skin lesions based on their distinctive skin tissue microwave/dielectric properties. The study uses an open-ended coaxial probe in extracting the dielectric properties, given that a healthy skin differs significantly in water, and nutrient contents than a malignant one, in which the former is less in water and sodium content than the latter. However, such solid dielectric properties of the complex structure of a skin are not available. Also, there are a lot of factors need to be controlled to ensure a faithful extraction of data (e.g. acceptable applied pressure on skin, probe size, condition(s) of the skin while taking the measurements, fat, muscle, blood vessels, etc.) [166]. Thus, it is a cumbersome to faithfully extract the skin dielectric features after filtering all noises within the biological system.

On a nano-scale level, a carbon-nanotube-based biosensor system has been designed, and further developed for an early detection of melanoma [167]. The research distinctively measures the response of melanoma cancer biomarkers: MART-1 (Melan A) for *in situ* melanoma diagnosis, and Ki-67 (monoclonal antibody) for mitosis aspect of melanoma: sensing the electrochemical characteristics of the biological system. Remarkably, since sidewalls of the carbon nanotube adhere to the melanoma distinctive protein (not confirmed for all stages of melanoma), it has been considered as an additional biomarker of the disease [167].

As manifested in Chapter 3, the merits associated with the electrochemical approach with the utilization of nano/micro electromechanical system (N/MEMS) technology shall be further investigated and implemented in this chapter. As illustrated above, the conventional, image based, dermatological approaches are limited to melanoma developed on the skin tissue, leaving the internal melanoma development at a cellular level undetected.

## **4.2 Research Specific Approach**

In this study, the findings of the previous chapters are aggregated, and embodied into a robust biomechatronic platform that would capture the electrophysiology of cells, and thus identify melanomagenesis. The biology of cancer, and cellular viability requirements together with computational fluid dynamics (CFD), and finite element method (FEM) analyses, represented respectively in Chapters 1 and 2, as well as understanding the biophysics of cells in Chapter 3, would all contribute in further developing, and reaching an optimal design of experiment (DOE) of the proposed biomechatronic platform presented in this chapter. Accordingly, a microfluidic ( $\mu\text{F}$ ) domain is integrated with multi-electrode arrays (MEAs) to form an

integrated lab on a chip (iLoC). The proposed iLoC together with customized microelectronics, and controlling software provide a hybrid biomechatronic structure that would extract cellular biophysics, and hence identify the different stages of the disease.

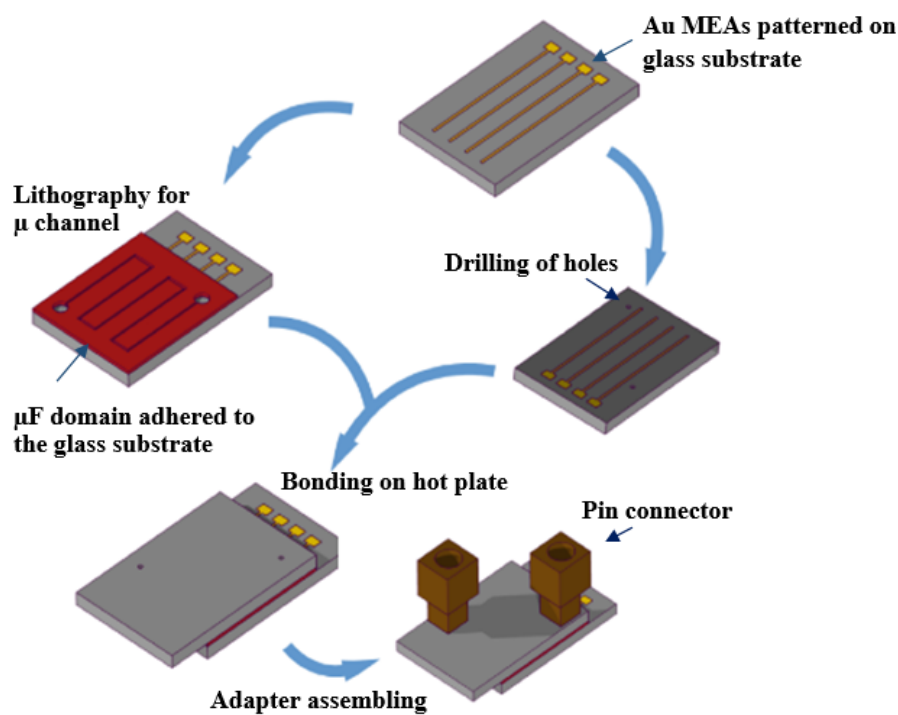
### **4.3 Construction of the Electrophysiology Biomechatronic Based Platform**

In light of the findings of previous chapters, a biomechatronic system is constructed with customized controlling software and microelectronics to trap a biological cell within a microfluidic domain. Upper and lower multi-electrode arrays are integrated within the microfluidic system to stimulate, and faithfully record cell-membrane potential of each melanoma cell-line model. The objectives are to have a biocompatible, and robust system that would also preserve cell's integrity throughout a sufficient number of *in vitro* experiments, and attain repeatability in the obtained readings.

#### **4.3.1 Microfabrication of the Mechanical Structure**

As presented in Chapter 2, detailed empirical analyses have been performed in COMSOL Multiphysics 4.2a (Burlington, MA, USA) prior to microfabrication, to visualize the flow pattern, arrive at a sensible flow speed that would ease the process of flushing the microfluidic ( $\mu\text{F}$ ) system in a controlled applied pressure manner, and achieving repeatable and durable usages of the proposed system. Furthermore, such empirical analyses assist in attaining an optimal pitch distance between two adjacent electrodes (stimulating and recording), upon which uniform current distribution is maintained.

In light of cells' physical characteristics, discussed in Chapter 1, the microfluidic channels are characterized to accommodate the size of biological cells, avoid clogging, and allow system maintenance. The proposed miniaturized mechanical structure consists of a  $\mu$ F domain, sandwiched between upper and lower glass substrates, consisting of gold (Au) patterned multi-electrode arrays (MEAs), Figure 4.1.



**Fig. 4.1** 3D illustrations and assembling of the proposed  $\mu$ -structure consisting of two upper and lower glass substrates and a microfluidic domain. An array of gold electrodes are patterned on the glass substrates. The upper glass substrate is drilled at two locations in line of the two inlet and outlet reservoir. The connecting pin adaptors are adhered to the upper glass by UV adhesion method. The 3 domains ( $\mu$ F system and lower and upper MEA glass substrates) are thermally adhered on a hot plate.

The materials for the  $\mu$ F domain has been chosen to serve three criteria: ease of machinability, biocompatibility, and high dielectric resistivity (acting as an insulator). Such characteristics are found in AZ related family of polymers that are widely used in biological applications [168]. Thus, AZ EXP 125nXT photoresist material is a negative working-photoresist-polymer binder, which is utilized in the proposed  $\mu$ F system.

The MEAs were patterned on two-glass substrates of 1mm thick. The transparent glass substrate allowed accessible view of cell manipulation and trapping under a microscope. First, Piranha cleaning was carried out on the glass substrates. This was followed by optical photolithography to pattern the gold electrodes in a standard lift-off process. The glass substrates were coated with positive photoresist, AZ 1518 (Microresist, Berlin, Germany), and spun at 3000 rpm (forming a layer of 1.8  $\mu$ m thick), followed by a prebake process on a hotplate for 1 min at 115°C. High-resolution exposure dose of 60 mJ together with patterned mask were performed. The glass substrates were developed using a resist developer AZ 400 K 1:4 in a beaker for 6 minutes, where no post bake process was carried out. The developed glass substrate was examined under the microscope to verify design specifications. Ar sputter metallization was performed, where an adhesive layer of 5 nm Ti, and 300 nm of functional layer of Au were sputtered/deposited on the AZ1518 resist structure. This was followed by a lift-off process using Dimethylsulfoxide (DMSO), performed at 80 °C for 4 hours; the glass substrate was then cleaned using Isopropyl Alcohol (IPA) and acetone. Prior to deicing,  $\sim$  2  $\mu$ m photoresist for backside protection was added. Diesaw was utilized to cut different MEAs on the glass substrates of 17 x 20 mm; the  $\mu$ F channel area (reddish component of Fig. 4.1) is 10 x 20 mm.

The AZ 125nXT based  $\mu$ F system (channels and reservoirs) was developed on top of the bottom glass substrate as shown in Figure 4.1, where optical photolithography process was

performed. The bottom glass substrate was coated with negative photo resist AZ 125nXT (Microresist, Berlin, Germany), forming a layer of 17  $\mu\text{m}$ . A soft baked process on a hotplate at 140°C for 8 minutes was carried out; this was followed by hard-contact exposure dose of 6 J/cm<sup>2</sup>. The microfluidic features were developed in 6 minutes using AZ MIF 814 with no post-baked process to be performed. The developed system was examined under the microscope for any microfabrication deficiencies in the developed process. Also, Dektak 3 was utilized to confirm that the developed channel depth (photoresist height) is within design specification: ~ 20  $\mu\text{m}$ .

Two 1-mm holes were drilled into the top glass substrate in line with inlet and outlet reservoirs, followed by glass substrate cleaning process using IPA. The miniaturized mechanical structure of the two (upper and lower) glass substrates together with  $\mu\text{F}$  domain were bonded on hot plate at 100 °C for 5 minutes. A microscope was utilized to confirm the alignment of the upper and lower electrode arrays, and to examine the intersection of the MEAs with the microfluidic channels. The two connecting adaptors were adhered to the clean upper surface of the glass substrate via UV adhesion method.

### **4.3.2 Microelectronics Architecture**

The continuous numerical analog cyclic signal propagations of cellular potential, obtained in Chapter 3, initiates the need for analog-to-digital convertor (ADC) in order to arrive at the cell-membrane potential experimentally, and to eventually analyze the collected data. Therefore, on the essence of understanding the cellular biophysics covered in the previous chapter, the microelectronic architecture has been designed and constructed. Furthermore, as per the microfabricated mechanical components of the overall biomechatronic platform in the previous

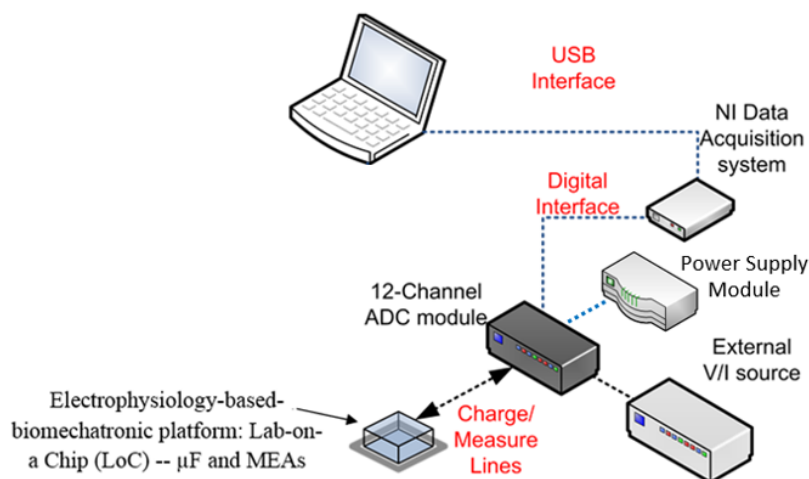
section, there are 11 pairs of electrodes (upper and lower); therefore, 12-channel-ADC module (Microsystems Ltd., Varna, Bulgaria) has been constructed, where one channel is dummy (12<sup>th</sup> channel). The ADC module is of a fully differential input type, with a resolution of 24 bits. The maximum full-scale error is  $\pm 0.01\%$ , with the ability to generate maximum internal and external voltages up to  $\pm 10\text{V}$ , and  $\pm 100\text{ V}$ , respectively. Furthermore, the input common mode voltage is  $\pm 2\text{V}$ , with input impedance of 20 Mohm, and bias current of 30 pA. The ADC module has 8-input ranges of potentials:  $\pm 1\text{mV}$ ,  $\pm 2\text{mV}$ ,  $\pm 4\text{mV}$ ,  $\pm 8\text{mV}$ ,  $\pm 16\text{ mV}$ ,  $\pm 32\text{ mV}$ ,  $\pm 64\text{ mV}$ , and  $\pm 128\text{ mV}$ . The selection of such input ranges shall be further justified in the next section.

In addition, a biasing voltage can be applied to the electrodes, with the ability to generate maximum internal and external voltages up to  $+10\text{V}$ , and  $+100\text{ V}$ , respectively. The ADC module provides the option of reversing the biasing polarity – switching the role of stimulating and recording between the upper and lower electrodes. Hence, this is quite beneficial in terms of extracting the cell-membrane potential of adhesive and non-adhesive cells, in which the former could be adhered to either upper or lower electrode, whereas the latter is floating within the vicinity of either one. The ADC module is connected to a National Instrument multi-function data acquisition card (NI USB-6009, 14-Bit, 48 KS/s) via a customized DB M15 pin cable. A shield cover is dedicated to protect the underlying circuitry (wires, pads, etc.) from any electromagnetic emissions.

An MS7212 multi-function process calibrator (MASTECH, Guangdong, China) is utilized to generate potential/current: charging electrodes; also, it acts as a multi-meter to investigate whether electrodes, and other connections of the micro system are faithfully transmitting signals. A BNC-pin cable is interconnecting the multifunction process calibrator together with the 12-channel ADC module. A dedicated power supply module (Microsystems Ltd., Varna,



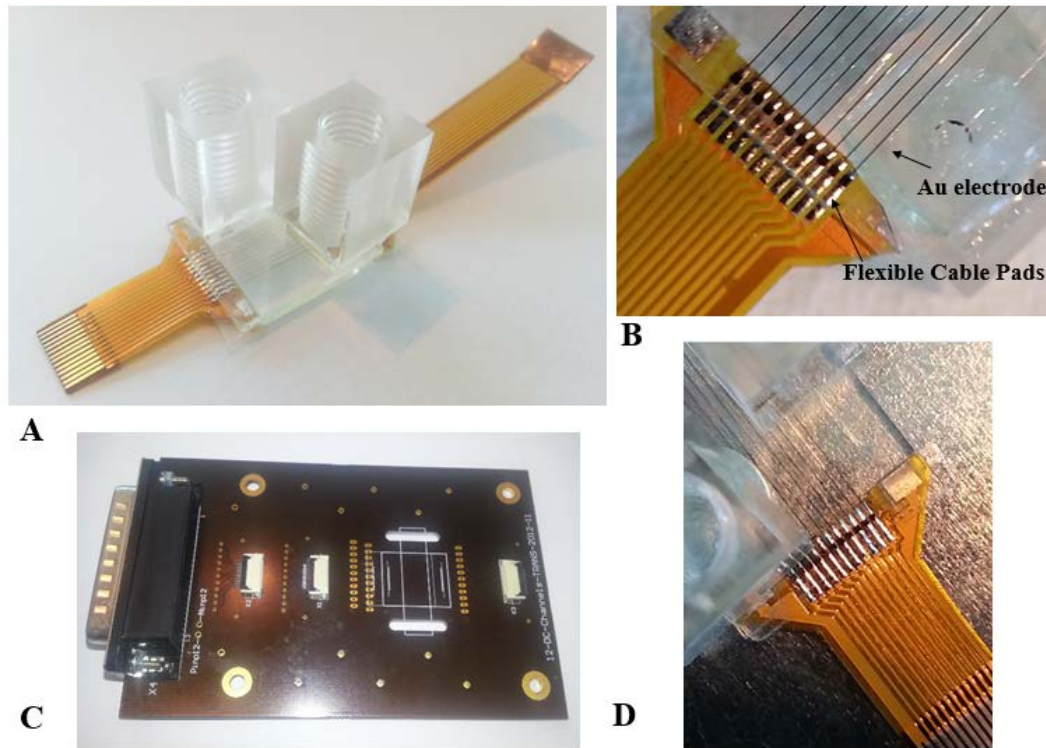
Bulgaria) is energizing the 12-channel-ADC platform. Figure 4.2 shows the microelectronics hardware architecture of the electrophysiology biomechatronic based platform. Appendix D.1 presents detailed hardware installation, and wire connection to the NI-DAQ card and PC.



**Fig. 4.2** Microelectronic hardware architecture of the electrophysiology-based biomechatronic platform connected to a 12-channel-ADC module through NI card, and multifunction voltage/current generator. The system is connected to a PC to collect and analyse experimental data.

In order to capture the polarity of a biological cell by recording the differential voltage between the upper and lower electrode, where the cell is trapped, a passive (no active components) transition printed circuit board (PCB) has been fabricated. Furthermore, a flexible cable is uniquely customized to connect the miniaturized electrophysiology-based biomechatronic platform with the transition board. The customized flexible cable pads are soldered to the patterned gold electrodes on the glass substrate (upper and lower), and final

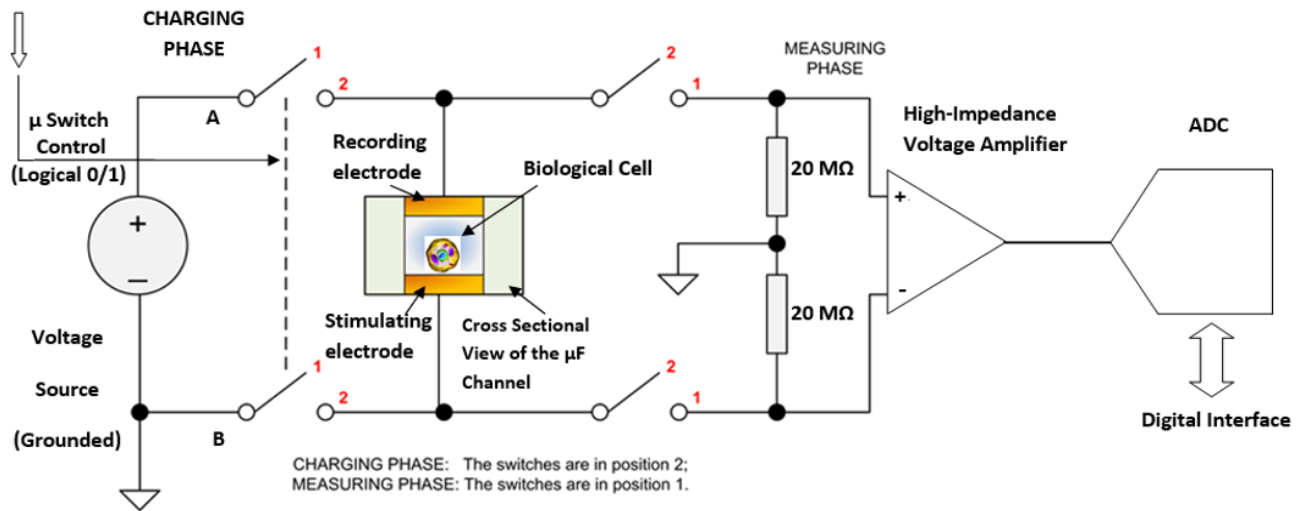
connection is examined under the microscope, and signal was checked through the multifunction multi-meter, Figure 4.3.



**Fig 4.3** (A) Assembled flexible cable to upper and lower multi-electrode arrays. (B) Soldering of bottom gold electrodes patterned on glass substrate to flexible electrode pads. (C) Transition-printed-circuit board (PCB) showing passive components: input connector pin out, pins and cables. (D) Soldering upper gold electrodes, patterned on a glass substrate, to flexible cable pads.

The ADC module consists of four ADC blocks, each having 3 parallel channels, thus forming twelve parallel measurement channels. The 12<sup>th</sup> channel is a dummy one, since only 11 pairs of electrodes can be active, when conducting the *in vitro* experiments. Figure 4.4 illustrates the electronic circuit schematic diagram of the injection/measurement principle of operation for the electrophysiology biomechatronic based platform. One channel of the ADC

is presented for illustration purpose only, and it applies to all channels. The schematic diagram of a multiplexer (MUX), which processes the multi-input signal to a single output, is not shown. The system works in two phases, which are switched by a microswitch control block driven by a digital circuit of 0/1 logical value. The microswitches A and B, in Figure 4.4, work synchronously; it should be noted that there are two phases: charging and measuring phase to the left and right of the miniaturized biomechatronic platform. The system consists of two microswitches A and B -- taking either position '1' or '2'. Therefore, if the microswitches are at position '2' in both sides, this is considered the charging phase (potential injection mode) of the electrodes; alternatively, if the microswitches are at position '1' on both sides, this is considered the measuring potential phase, where the electrodes are disconnected from the voltage source. The high impedance-voltage amplifier is utilized to measure charges, and to prevent discharging of microelectronic regime on a fast rate. The resistors are biasing the amplifier inputs to ground if there is no signal present. Finally, the polarity of the voltage source can be reversed, giving the flexibility of reversing the role of upper and lower electrode to be either recording or stimulating (injecting) electrode, and vice versa.



**Fig. 4.4** Schematic diagram illustrating the working principle of the electrophysiology biomechatronic platform of one channel of an ADC. Position 1 and 2 respectively show measuring and charging regime of the microelectronic characteristics of the platform. A cross-sectional view of the  $\mu\text{F}$  system with a biological cell entrapped between upper and lower electrodes is illustrated.

### 4.3.3 The Electrochemical Bio-Mechatronic Platform Operating Software

The controlling software of the electrophysiology biomechatronic platform has been coded in DELPHI application programming language, and it is operating under Microsoft Windows platform. This program has been customized to serve the experimental needs of the miniaturized electrochemical bio-mechatronic device (Figure 4.5). Furthermore, the pre-set controlling parameters are in line of the reviewed literature in terms of biophysics of cells, and various scholars' findings in the field of cellular electrophysiology that were presented in Chapter 3.

This design-of-experiment (DOE) oriented program operates within up to 12 channels; only 11 channels are used in the current setup -- allowing collection of data from various pairs of 11 electrodes: stimulating and recording electrode. Thus, this shall allow extraction of electrophysiology of cells, and further analyze their biophysics. Before commencing the program, all experimental microelectronic hardware components have to be connected (Appendix D.1).

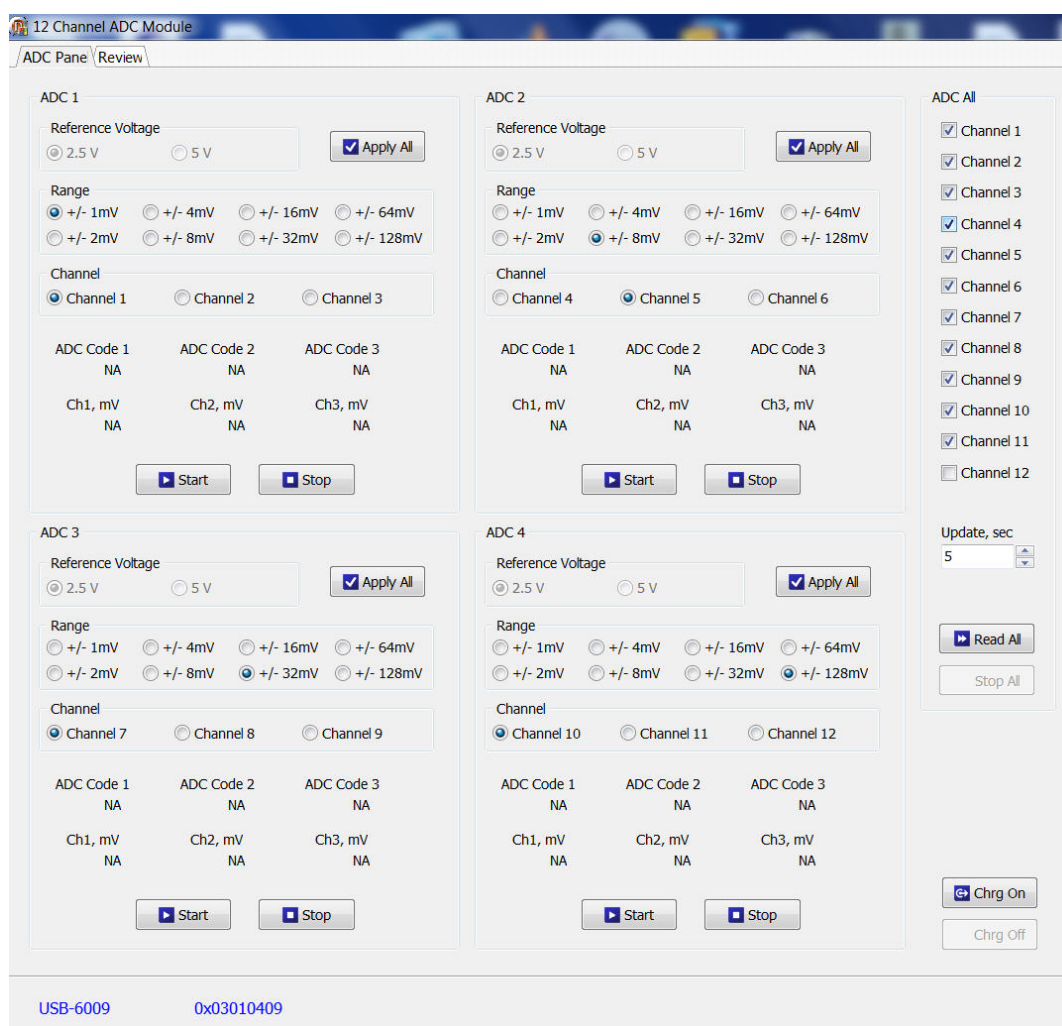


Fig. 4.5 Electrochemical biomechatronic platform operating software control panel.

The hardware system consists of a 12-channel-Analog-to-Digital-Convertor (ADC) module in order to account for the 11 pairs of electrodes (upper and lower electrode) embedded within the microfluidic domain. The objective is to capture polarity of a cell, and extract the cell-membrane potential. The ADC convertors are slow and precise. The maximal update rate for collecting data from all 11 channels is 5 updates per second. Each ADC hardware component has 3 channels, and hence there are 4 ADCs to accommodate the 11 pairs of electrodes, which leaves channel 12 as a dummy one.

The user starts by charging on the electrodes either via internal or external source. The former charge-voltage approach takes up to  $\pm 10$  V as a maximum charge, whereas the latter approach takes up to  $\pm 100$  V. It should be noted that when internal charging is in active mode within the biomechatronic system, there is an internal amplifier gain of 2 within the ADC module. Hence, the maximum voltage generator that is connected to the 12-channel-ADC module shouldn't exceed 5V; the internal generation of voltage doubles the potential, and that is attributable to the usage of power operational amplifier (OPAM). The OPAM is utilized to enhance system performance in case of lack of high voltage source to be fed to the electrodes. As for the external charging, the upper and lower electrode can be both charged, or one is charged and the other is grounded. The charging starts once the user clicks on the “Charge on” command.

Each ADC by default has a fixed reference voltage to ensure its operation. Furthermore, each ADC is on one circuit, and hence its associated 3 channels must all have one value of voltage difference range. The ADC microelectronics measure the differential voltage between the upper, and lower electrode. For example, if a voltage range is selected to be  $\pm 4$  mV, then voltage measurements between  $-4$  mV and  $+4$  mV is possible. All voltages exceeding 4 mV will cause ADC saturation, i.e., the program will show the upper limit of the range as 4 mV.

Respectively, all voltages below - 4 mV, will cause the program to show the lower limit as - 4 mV. Thus, the user can recognize the saturation by the obtained readings; if all obtained readings are constantly + 4 mV or constantly - 4 mV, this means the chosen range is too small, so it has to be increased.

The detection regime range of voltages is in line of potential of cell-membrane findings within the published literature [115-121], illustrated in Chapter 3. Each channel corresponds to a pair of electrodes: bottom and upper. The software provides flexibility in terms of assigning the same detection range value to all ADCs' channels by a single click on "Apply All" button, or it allows user to perform different experiments by assigning different detection ranges for different ADCs. Furthermore, the developed software allows the user to obtain the readings for a single ADC module. Finally, as shown in Figure 4.4, the user has the ability to select which channel(s) to obtain readings from, as well as to choose the update time, e.g., every 5 seconds the system registers a reading. Appendix E.1 provides detailed-step-by-step operational manual of the developed software.

#### **4.4 The Biological Model: The Rationale Behind the Selection of the Melanoma Cell Lines**

Well-established, eight melanoma cancer cell lines have been prudently selected with distinctive genetic complexities, and genomic mutations; they were categorized into three groups: Group I (SK-MEL-1, A-375, G-361, WM-115), Group II (NM2C5, M4A4, M4A4 LM3-4 CL16 GFP ((CL 16)), M4A4 LM3-2 GFP ((LM3))), and Group III (MDA-MB-231, MCF7). The cell lines have been procured from the American Type Culture Collection (ATCC, Maryland, USA), all cell culture plastic ware were supplied by Corning (Corning Life Sciences,



Leicestershire, UK). The melanoma cell lines, grouped in II, clearly illustrate the genetic complexities, and intensity of metastasis among all cell lines within this cluster; on the other hand, Group I exhibits four cell lines that are closely related in terms of malignancy severity, yet this would manifest the notable merit of the proposed biomechatronic platform in allocating the fine distinction of malignancy grade/intensity among these four cell lines in particular, based on their electrophysiological heterogeneity. Group III contains two breast cancer cell-line models that their cell-membrane potentials are well documented in literature, and thus they will be utilized as calibration models for testing the proposed biomechatronic platform.

As per the ATCC specifications, SK-MEL-1 cell line [169, 170] is a primary tumor source, extracted from a lymphatic metastatic system of a widely spread malignant melanoma skin tissue within a human Homo sapiens organism. The cell line has been acquired from a thoracic duct of a 29-year-old Caucasian male patient. The A-375 is an adherent primary malignant cell line, which was derived from a 54-year-old female's skin tissue within Homo sapiens organism of 62 chromosomes that shows a rapid growth [171, 172]. The primary malignant melanoma, G-361 cell line [173-175], was extracted from a skin tissue within Homo sapiens of a 31-year-old Caucasian male. The fourth cell line encompassed in Class I group is WM-115 [176], which is an adherent primary melanoma skin cancer of Homo sapiens organism extracted from a 58-year-old female.

The 4-cell lines within Group II are **isogenic** (genetically alike) that are derived via serial dilution of polyclonal, and metastatic human breast cancer cell line MDA-MB-435 [177]. As per ATCC, they are all adherent cells, and are derived from a 31-year-old Caucasian female. The 4- cell lines within Group II possess distinctive degree of metastatic intensity. NM2C5 is a non-metastatic cell line, M4A4 is an early stage metastatic (lungs and lymph nodes), LM3 is an intermediate metastatic initiated from a second generation lung metastasis, and finally CL16



is a highly metastatic melanoma, and it has initiated from a third-generation-lung metastasis [177].

It is a debatable issue among scholars, within the cellular biology field, of the initiation of the cell lines within Group II, whether they represent breast cancer or melanoma, since cell lines within Group II are derived from a parental breast ductal carcinoma cell line, MDA-MB-435. Ross *et al.* [178] have identified the systematic variation within gene expression in characterizing MDA-MB-435, and they concluded that its gene expression pattern is closer to melanoma as opposed to breast cancer. Furthermore, it is found that MDA-MB-435 is of melanocytic origin based on immunohistochemical staining [179]. Finally, MDA-MB-435 shares the same origin as melanoma cell line, M14, as per a single nucleotide polymorphism (SNP) array analysis [180]. Therefore, it is concluded that such four-cell lines within Group II do represent melanoma. Table 4.1 summarizes the three groups of cell-line models, together with their properties and sources.

Group	Cell	Organism/ Tissue	Adherent/ Non-adherent	Comments	Source
<b>I</b>	SK-MEL-1	Skin	Non-adherent	Malignant melanoma derived from metastatic site (lymphatic system) of a 29-year-old male patient	ATCC
	A375	Skin	Adherent	Malignant melanoma derived from Homo sapiens organism of a 54-year-old female patient	ATCC
	G361	Skin	Adherent	Malignant melanoma derived from Homo sapiens of a 31-year-old male patient	ATCC
	WM115	Skin	Adherent	Primary melanoma derived from Homo sapiens of a 58-year-old female patient	ATCC
<b>II</b>	NM2C5	Homo sapiens epithelial	Adherent	Non-metastatic cell line derived from Homo sapiens of a 31-year-old female patient	ATCC
	M4A4	Homo sapiens epithelial	Adherent	Early stage cancer cell line derived from Homo sapiens of a 31-year-old female patient	ATCC
	M4A4 LM3-4CL16GFP (CL16)	Homo sapiens epithelial	Adherent	Highly metastatic cell line derived from a third generation lung metastasis of a 31-year-old female patient	ATCC
	M4A4 LM3-2GFP (LM3)	Homo sapiens epithelial	Adherent	Intermediate metastatic cell line derived from a second generation lung metastasis of a 31-year-old female patient	ATCC
<b>III</b>	MDA-MB-231	Breast (epithelial)	Adherent	Adenocarcinoma derived from a 51-year-old female patient	ATCC
	MCF7	Mammary gland/breast (epithelial)	Adherent	Adenocarcinoma derived from a 69-year-old female patient	ATCC

**Table 4.1** Three groups of cell line models' properties and sources.

## **4.5 Materials and Methods**

### **4.5.1 Cell Culturing Protocol and Growth Inhibition**

All cell lines, within Group I and II, as well as the calibrating cancer cell line models (MCF7 ((early stage breast cancer cell)), and invasive breast cancer cell line ((MDA-MB-231))), were all cultured as per the protocol set forward by ATCC. This includes multiple washing processes, staining, suspension, filtering, centrifugation, and aspiration. The design constraints associated with cell culturing microenvironment are highlighted in [15].

The calibrating cancer-cell-line models, MCF7 and MDA-MB-231, are utilized since their cell-membrane potentials are well documented in peer-reviewed literature [121, 181-183]; hence, they shall both act as calibrating tools, to check the applicability of our proposed miniaturized biomechatronic platform. All cell lines were harvested at logarithmic (Log) growth phase to arrive at the maximum viability of cells, and highly active proliferation kinetics; the genetic stability were maintained by not exceeding ten times of culture passages from frozen stock.

SK-MEL-1 Cell line of Group (I) were cultured in Eagle's Minimum Essential Medium (EMEM) (ATCC 30-2003, Middlesex, UK) as a growth medium, supplemented at 10% concentration with fetal bovine serum (FBS), and streptomycin plus penicillin (100 µg/ml and 100 u/ml, respectively). During SK-MEL-1 culturing process, non-essential amino acids, and 1 mM of sodium pyruvate were added. The entire process was conducted in a laminar flow chamber, where the culture is conditioned to a humidified atmosphere of 98% relative humidity and 5% CO<sub>2</sub>, at a 37°C temperature. The medium was renewed 2-3 times a week, or when

acidification took place, as per the pH indicator (phenol red). Within the same group, the lightly pigmented human melanoma cell line, G-361 (ATCC, Middlesex, UK), is cultured in an ATCC-formulated McCoy's 5a medium modified (ATCC 30-2007), supplemented with 10% FBS and 1% penicillin streptomycin (10,000 U/ml and 10,000 µg/ml, respectively) in 5% CO<sub>2</sub>, at 37 °C culture conditions.

The adherent epithelial primary melanoma cell lines, WM115, were cultured in ATCC-formulated Eagle's Minimum Essential Medium (EMEM, ATCC: 30-2003), containing 10% concentration of Fetal Bovine Serum (FBS). The cultured conditions were maintained at 34 °C in 5% CO<sub>2</sub> atmosphere. Finally within this batch, A-375, was maintained in a growth medium of ATCC-formulated Dulbecco's Modified Eagle's Medium (DMEM, ATCC: 30-2002), supplemented with fetal bovine serum (10%) at 37 °C in CO<sub>2</sub> incubator (95% relative humidity, 5% CO<sub>2</sub>).

The early stage breast adenocarcinoma cell, MCF-7 of Group III, was cultured in a growth base medium of ATCC-formulated Eagle's Minimum Essential Medium (EMEM, ATCC: 30-2003), supplemented with fetal bovine serum to a final concentration of 10%, and 0.01 mg/ml human recombinant insulin, at 37 °C in CO<sub>2</sub> incubator (95% relative humidity, 5% CO<sub>2</sub>).

An adhesive human breast cancer cell line (MDA-MB-231) of Group III, procured from ATCC, was extracted from a 51-year-old Caucasian female. The cell was cultured in Leibovitz's L-15 medium (ATCC, Middlesex, UK), supplemented with 10% fetal bovine serum (FBS). The cell layer was rinsed with 0.25% (w/v) Trypsin – 0.53 mM EDTA solution, to eliminate traces of serum (trypsin inhibitor). The cell lines were harvested by trypsinization by adding 2-3 mL of trypsin-EDTA solution. Growth medium, and an appropriate amount of aliquots of cell suspension were then added, and finally cultures were incubated at 37°C without CO<sub>2</sub>.

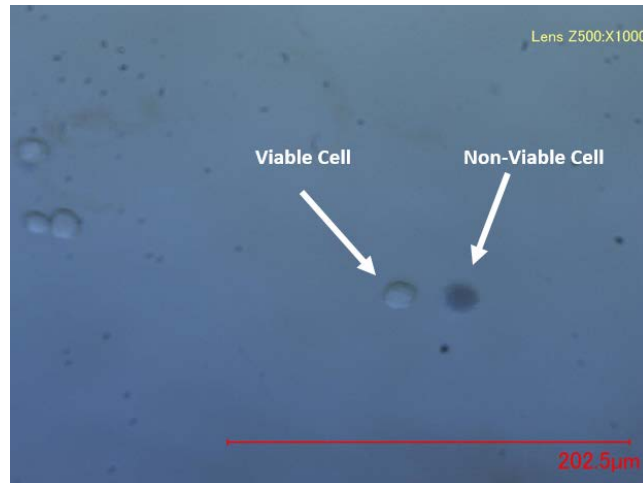
The cell lines of Group II were derived from the triple negative human breast cancer cell line, MDA-MB-435, and were maintained in Dulbecco's Modified Eagle's Medium (DMEM) (ATCC 30-2002, Middlesex, UK), supplemented with 10% fetal bovine serum (FBS), and 5% penicillin/streptomycin (P/S). Cultures were propagated, and conditioned in a humidified atmosphere of 5% CO<sub>2</sub>, at a temperature of 37°C.

#### **4.5.2 Cell Viability Check, Serial Dilution, and System Sterilization**

The culturing process is proceeded by a viability test. The cell viability and cell counting are investigated through Moxi Z mini automated cell counter (ORFLO Technologies, WA, USA). A sample of 75 µL of the cultured cell medium is extracted via a micropipette, and then injected into one of the two-fill ports of the Moxi Z device. The Moxi Z cassette consists of microfluidic culturing reservoir, and channels crossed by an array of micro-electrodes. The Moxi Z device basically utilizes gold standard Coulter Principle in conjunction with a patented thin-film sensor technology to report accurate results of cell's viability, numbers, and mechanobiology in 8 seconds. The gold standard counter is based on cell impedance [1], where passing batches of cells, through the microchannel, leads to escalation of resistivity; thus by Ohm's law (i.e.  $V$  ((voltage)) =  $I$  ((current)) x  $R$  ((resistance))), this yields an increase in voltage that are exemplified as spikes of each passing cell; equally sized spikes are aggregated into a curve-fitting histogram.

Acquiring the number of cells per unit volume via Moxi Z enables extraction of a single cell through serial dilution in a 96-well plate. The dilution factor was 0.1 (e.g., each subsequent well is 10 folds diluted). Keyence VHX-2000ES digital microscope (Keyence, Milton Keynes, UK) was utilized to allocate the extracted single cell. A trypan blue dye is used to confirm cell

viability during serial dilution stage, where dead cells lose their integrity, and absorb the blue dye. Figure 4.6 shows a serially diluted sample with extracted viable, and non-viable cell through a trypan blue marker.



**Fig. 4.6** Serially diluted media showing viable and non-viable LM3 intermediate stage melanoma of a second lung metastasis.

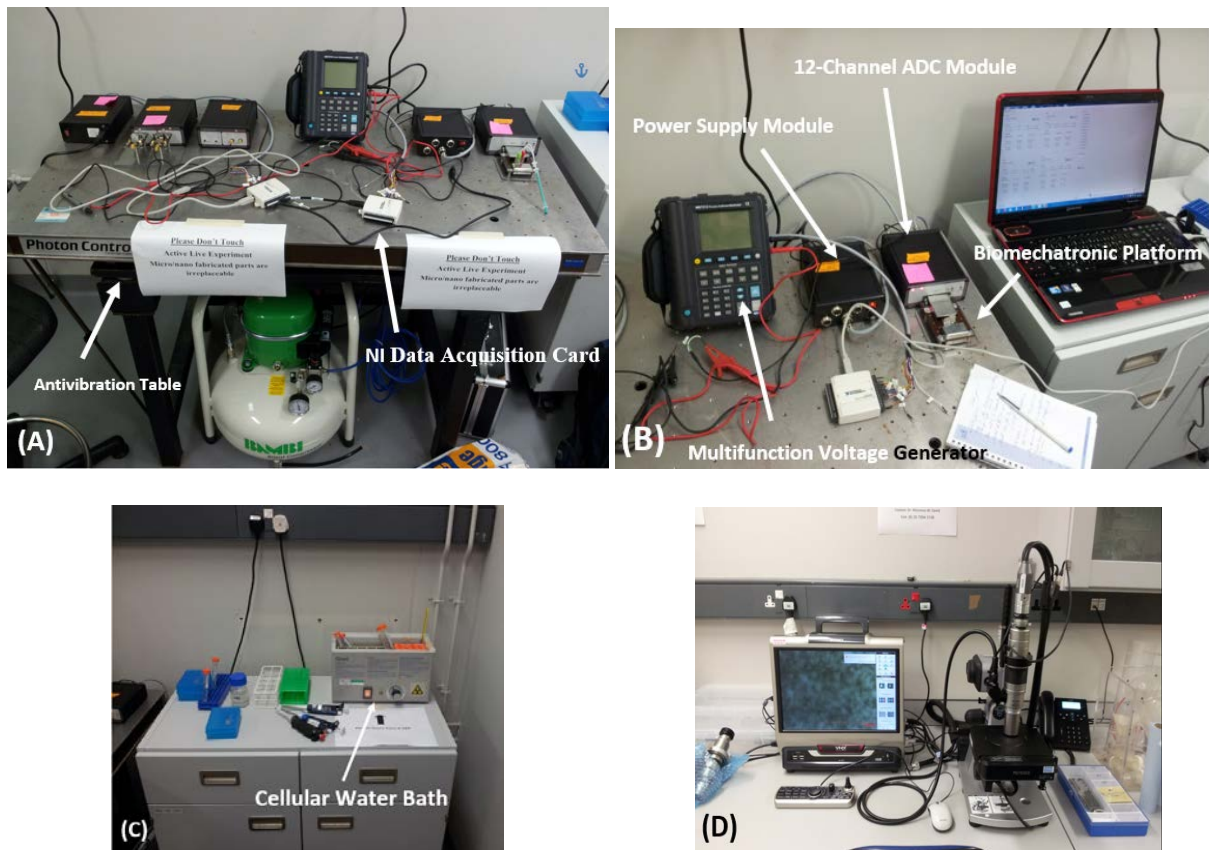
The entire system could be sterilized by different means; it can be performed by pumping ethanol into the  $\mu\text{F}$  chamber. Also, sterilization can be carried out by exposing the device to UV light as in [55]. Furthermore, plasma can be used for patterning features on the substrate, strengthen bonding, surface treatment to the microfluidic structure, as well as sterilization of the  $\mu\text{F}$  device as in [68]. The microfluidic surface treatment is performed by inducing  $\text{O}_2$  plasma to its mechanical structure, which makes the hydrophilic characteristic of the  $\mu\text{F}$  surface more pronounced, and enhance cell adhesion on the microfluidic polymer layer [70]. On the contrary, to prevent cell from adhering to the channel surfaces, a 5% w/v bovine serum albumin (BSA, Sigma) could be induced into the microchannel, and incubated overnight as in [68].

### 4.5.3 *In Vitro* Experiments

The microfluidic-multi-electrode module (LoC) was first fully filled with DI water to remove any resultant debris from the microfabrication processes, and measures were taken to avoid forming air pockets within the system. Then a sterilization process was performed with ethanol. At last, a Phosphate Buffered Saline (PBS) wash was implemented to enhance biocompatibility of the structure, and then system was left to dry. At the termination of the experiment, trypsin was utilized to detach the cell from the LoC domain, followed by DI water filling, sterilization, and PBS wash for miniaturized device reusability.

The *in vitro* experiments have been conducted under clean room conditions, where the entire experimental microelectronic hardware, and micromechanical structure components are placed on an anti-vibration table to eliminate noises, and damp any residual vibrational energy into the experimental system; the experimental setup is shown in Figure 4.7.

The electromagnetic field radiation within the immediate vicinity of the miniaturized system, has been measured by an EMF meter, which was negligible:  $12 \times 10^{-14}$  Tesla. This assures that electromagnetic interferences with the *in vitro* experimental setup are minimal. The connecting pads and patterned electrodes were examined by the multifunction meter, to investigate the faithfulness of the proposed miniaturized device in registering signals.



**Fig. 4.7** Experimental setup (A) Anti-vibration table and NI data acquisition card, (B) Miniaturized biomechatronic platform, multifunction voltage generator, 12-channel-ADC module, and power supply module, (C) Cellular water bath to maintain a temperature of  $37^{\circ}\text{C}$  for cultured cells, and (D) VHX-2000ES Keyence Digital Microscope.

The experiments have been conducted at various stages. At stage (-1) measurements were taken directly from the miniaturized device without adding any biological substances nor liquid. Stage (0) is followed by adding a buffer medium (PBS) to the microfluidic culturing reservoir, and then readings were registered; stage (1) is injecting trypan blue dye to investigate viability of cells, and then measurements were collected. The trypan blue dye is utilized for the subsequent stage in investigating the cell viability. Finally, a single cell is extracted from the serial dilution process by a micropipette, and then injected into the iLoC domain. Breaking the



experiments into stages critically assists in allocating, and eliminating noises within the system, and eventually arriving at the distinctive potential of the cancer cell. Furthermore, the developed customized driving software has an embedded triangle smoothing algorithm (a statistical noise reduction algorithm of the obtained signals based on weighted smoothing function), which contributes in enhancing signal-to-noise ratio, and ultimately reduces noises. Syringes were used to trap cells within the microfluidic/MEA domain, and Keyence flexible microscope was utilized to monitor cell position. Different values of potential stimulations, through the working electrode, were used, and over 200 recording points were registered in a number of trials for each melanoma cell type, as well as, the well-documented MCF7 and MDA-MB-231 cell line model: achieving a repeatability in the obtained registered data.

### 4.6 Results and Discussion

On the basis of cellular electrophysiology, the cell-line models have been selected to investigate the heterogeneity of melanoma cells, which are exhibiting different genetic complexities. First, a number of *in vitro* experiments were conducted on well-documented-cell-line models in Biophysics' literature: poorly invasive human breast **adenocarcinoma** (MCF7) cell line, and human breast cancer cell line (MDA-MB-231). The resultant electrophysiology potential of MCF7 was found to be  $-43.34 \pm 0.85$  mV (Mean  $\pm$  SD,  $n = 14$  trials ((single cell per trial))), whereas the cellular potential of MDA-MB-231 was  $-25.95 \pm 1.05$  mV (Mean  $\pm$  SD,  $n = 17$  cells), where SD is the standard deviation.

The obtained results have placed confidence in the proposed biomechatronic platform, developed within this chapter, as the extracted cell-membrane potential of MCF 7 and MDA-MB-231 were within the range of peer-reviewed findings within literature, in which they were

obtained through different methods, e.g., the standard patch clamp method or fluorescence method. It's reported in [181, 182] that MDA-MB-231 possesses a cell-membrane potential of  $-29.2 \pm 1.6$  mV, while MCF7 has a cell-membrane potential of  $-42.1 \pm 5.3$  mV [121].

As per the obtained experimental findings, it is found that as the stage of metastasis ascends, the magnitude of cell-membrane potential drops. The highly invasive metastatic melanoma cell, CL16, experiences the lowest cell-membrane potential in magnitude ( $-9.39 \pm 0.32$  mV,  $n = 12$ ), as opposed to non-metastatic (NM2C5), and early stage (M4A4) cell-line melanoma, whose cell-membrane potentials are respectively,  $-52.62 \pm 1.53$  mV ( $n = 17$ ), and  $-46.67 \pm 0.64$  mV ( $n = 15$ ). Similarly, by examining the metastases of WM115 (low), LM3 (intermediate), A375 (Late), they show distinctive variation of cell-membrane potentials in a descending order of magnitude:  $-42.28 \pm 0.26$  mV ( $n = 10$ ),  $-32.03 \pm 1.25$  mV ( $n = 12$ ), and  $-17.25 \pm 0.38$  mV ( $n = 17$ ), respectively. Interestingly, the proposed miniaturized biomechatronic platform has managed to discriminate between the closely comparable melanoma cell lines in terms of metastasis, based on their extracted electrophysiology: G361, and SK-MEL-1. The former exhibits a cell-membrane potential of  $-34.32 \pm 0.86$  mV ( $n = 14$ ), while the latter has a cell-membrane potential of  $-32.23 \pm 1.81$  mV ( $n = 12$ ).

The relatively small spread of measurements could be attributable to instrumentation errors due to weak soldering of the flexible cable with some patterned gold electrodes on glass substrate, and/or external noise interferences to the experimental setup. However, as illustrated earlier, the microfabricated components, soldered connections, and measurements of electromagnetic interferences were closely examined, to keep source of errors as minimal as possible. Furthermore, the micro-device was extensively sterilized and cleaned after each *in vitro* experimental trial to avoid any cross contaminations. The resultant cell-membrane

potentials ( $V_m$ ) of the melanoma, as well as breast cancer cell line models are summarized in Table 4.2.

Cell-Line Model	Description of Metastatic Potential	$V_m$ (mV) Mean $\pm$ SD	$n$
<b>MCF 7</b>	Poorly invasive human breast adenocarcinoma	- 43.34 $\pm$ 0.85	14
<b>MDA-MB-231</b>	Invasive metastasis	- 25.95 $\pm$ 1.05	17
<b>NM2 C5</b>	Non-metastatic	- 52.62 $\pm$ 1.53	17
<b>M4A4</b>	Early stage melanoma	- 46.67 $\pm$ 0.64	15
<b>WM115</b>	Low metastasis	- 42.28 $\pm$ 0.26	10
<b>G361</b>	Primary metastasis	- 34.32 $\pm$ 0.86	14
<b>SK-MEL-1</b>	Primary metastasis	- 32.23 $\pm$ 1.81	12
<b>M4A4LM3-2GFP</b>	Intermediate metastasis	- 32.03 $\pm$ 1.25	12
<b>A375</b>	Late invasive malignant	- 17.25 $\pm$ 0.38	17
<b>M4A4LM3-4CL16 GFP</b>	Highly invasive metastasis	- 9.39 $\pm$ 0.32	12

**Table 4.2** Resultant extracted electrophysiology potential of melanoma and breast cancer cell lines in mV (healthy, early stage metastasis, intermediate, late, and highly invasive metastasis).

As it has been illustrated in Alqabandi *et al.* [1], cancer cells differ from healthy ones by having an increase in their permeability (fusion pore size), leading to an influx of water and  $Na^+$ , and efflux of  $K^+$ ,  $Mg^{2+}$ , and  $Ca^{2+}$  ions out of the cell. As discussed in Chapter 3, this ultimately leads to a drastic reduction of cell-membrane capacitive characteristic in storing ion charges, a decrease in depolarization and hyperpolarization time, as well as a drop in-cell

membrane potential. Also, this sheds light on the interrelated effect of cellular electrophysiology, and mechanobiology of cells, such that the physical characteristic of cells affect its permeability, and thus its biophysics; the mechanobiology of cells will be deliberately addressed in the upcoming chapters. Therefore, as a cell progresses in the cancer stage, its permeability increases, and hence its electrophysiological potential drops in magnitude. This is also consistent with the theory introduced in Chapter 3, where the advancement of cancer stage is allocated by the drop of the cell-membrane potential, and this is a manifestation of depolarization process taking place [96, 108, 112, 118, 119, 121, 144]. The depolarization could be attributable to a reduction in the intracellular activities of  $K^+$  ion, and/or an increase in the intracellular activities of  $Na^+$  [96]. Thus, depolarization is experienced with melanoma cells as they ascend in the stage of their tumorigenesis. It is worth exploring the depolarization process during cell cycling, particularly in  $G_1$  and S-phase; however, this is beyond the scope of this research.

## 4.7 Conclusion

Electrophysiology of cells plays a major role in many biological activities within mammalian bodies<sup>1</sup>. This Chapter has illustrated different conventional and non-conventional prognosis procedures, followed by dermatologists in detecting melanoma. Furthermore, it has described a detailed process in constructing a biomechatronic electrophysiology-based platform. Detailed microfabrication processes, associated microelectronics, and development of a customized driving software have been extensively presented. One section of this chapter is fully devoted for justifying the rationale behind the selection of melanoma cell-line models exhibited within this research. To the best of the author's knowledge, this is the first time the characterization

---

<sup>1</sup> Importance of cellular biophysics in cell communication: <http://youtu.be/rRVQZydmqH0>

of the electrophysiology of the different stages of melanoma has been achieved, leaving the cell-membrane cytoplasmic component intact as opposed to other invasive methods in extracting cell-membrane potential, e.g., patch clamp method.

The novelty presented in this chapter is the extraction of the cell-membrane potential of well-established melanoma cell-line models, showing different genetic complexities and metastatic potential, via biomechatronic platform with customized microelectronic and controlling software. To the author's best knowledge, such biophysical characteristics of such melanoma cells have not been yet extracted experimentally -- enabling the distinction of the various stages of the melanomagensis.

The outcomes of this chapter with the proposed device, could assist bio-researchers in analyzing the biophysics of cells, and draw a correlation between cell proliferation/cancer metastasis and depolarization of cell-membrane potential. Also, this could contribute in identifying a pharmaceutical drug compound that has the electrochemical characteristics to deactivate certain ion channel activities, e.g.,  $Na^+$ , of cancer cells.

# **Chapter 5**

---

---

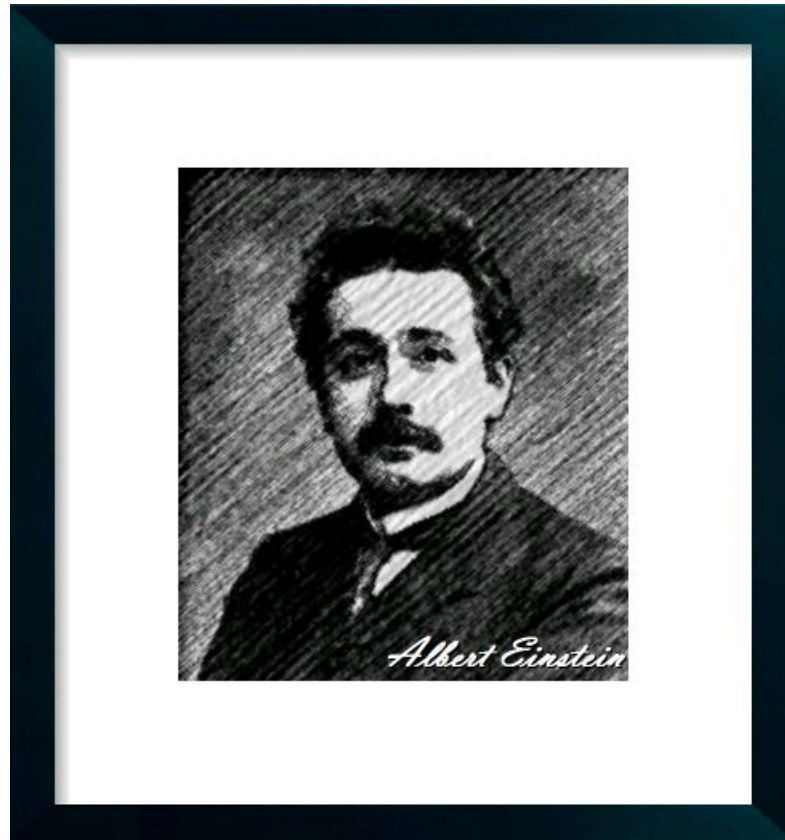
## **A Cantilever-Based Biomass Sensor: Pull- In Phenomena**

---

---

---

---



*"Look deep into nature, and  
then you will understand  
everything better."*

---

## **Chapter 5: Experimental Setup of a Label-Free Microcantilever-Based-Biomass Sensor: Investigating the Effect of Pull-In Phenomena on Sensitivity**

### **5.1 Introduction: Versatility Applications of Cantilever-Based Sensors**

Many cantilever-based sensors have been utilized by scholars in various fields, in which other physical phenomena are transduced into mechanical energy, and/or further transmitted into other physical domains: awarding the cantilever a versatility characteristic [184-186]. Cantilever-based sensors have been widely implemented in Atomic Force Microscopy (AFM), in which cantilevers are the essential elements in performing surface profile topology (imaging metrology), and minute-force measurements, upon which interactive forces, such as electrostatic, Casimir, and van der Waals' forces, are quantified by the deflection of the beam's tip (mechanical signals) [1, 187]; ultimately, these signals are quantified by the deflection of an optical laser beam into a set of photodiodes that electrically transform the collected readings via a control-data-acquisition unit to produce electronic readout signals [188, 189]. Alqabandi *et al.* [1] have obtained an image of a melanoma B16-F10 cancer cell on a scale of few microns using an AFM-cantilever-based system.

On a different application regime, cantilever-based devices are extensively used in mass and gas sensing applications, reaching a sensitivity of Pico, Femto, Atto, and Zepto gram per hertz,  $10^{-12}$ ,  $10^{-15}$ ,  $10^{-18}$ , and  $10^{-21} gHz^{-1}$ , respectively [190-201]. Here, the static



configurations of the beam, as well as its dynamic-time-dependent deflection mode, of which the latter accounts for a shift in the harmonic resonant frequency attributable to a loaded mass, while the former describes bending, and associated surface stresses upon mass loading; they both define the cantilever's sensitivity in measuring even a very diminutive molecular masses, such as those of hemoglobin protein at the order of 0.109 Atto gram (ag) [192].

Cantilever gas and mass sensors have broadened their scope of work to encounter the detection of a change in density experienced within a liquid domain [202]. Furthermore, the material and geometry (length) of the cantilever play a dominant role in extending its applications. For example, an array of varying cantilevers' lengths, where each cantilever possess a distinctive coating at its effective layer, make the cantilever system array a valuable tool to respond, and detect compounds of different chemicals, upon which each cantilever with its distinctive length and coating layer shall respond differently – achieving specificity and selectivity as well as high sensitivity [203, 204]. On the other hand, an array of cantilevers, sharing the same nominal length, shall contribute in system repeatability, and robustness of the obtained results. The two last stated arrays of cantilevers with distinctive coating effective layers have led to the capability of cantilever-based sensors to detect chemical explosives [203]; also, it has defined a novel field in Mechatronics denoted as robotic artificial nose application [204].

On a power harvesting and conversion scale, a cantilever system is used to transform vibrational energy into an electrical one [205]. Moreover, cantilevers find their way in robotic microgrippers for handling hazardous materials [206], and performing minimally invasive operations [207]. It is considered the building block of microvalves [208], sound emitters [209], comb-drives [210], microswitches [211], micropumps [212], and calorimeter for heat source and sink sensor [213].

In an aerospace application domain, cantilevers are utilized within microgyroscope system [214], and as a microactuation instrument for precise satellite structural positioning [215]. It is an essential tool in Micro-Opto-Electro Mechanical Systems (MOEMS) for micromirror scanning, and laser printing applications [216]. Furthermore, it is employed in high contact-probe force applications [217, 218]. Last but not least, a cantilever beam is also considered an efficient modeling tool. For example, in an actuated underwater vehicle, the vibration of a robotic fish propulsion unit is analyzed as a cantilever model [219, 220]. Moreover, cantilevers can capture the instability of ship-mounted crane dynamics [221]; also, they can model the steady-state characteristics of nonlinear piping systems, with their associated nonlinear boundary conditions, and collision features, which is extensively utilized in nuclear engineering applications [222]. Therefore, by examining the numerous interrelated disciplines with the associated versatility usages of cantilevers, it is found that this subject has captured different spectrums of science. In this study, the main focus is on experimentally testing a highly sensitive microcantilever-based biomass sensor, where sensitivity is enhanced by electrostatic force: the essence of pull-in phenomena.

## **5.2 Merits of Cantilever-Based Sensors in Cancer Research**

Cellular medicine with the utilization of micro/nanotechnology has captured the attention of medical practitioners, as well as engineers to combat life-threatening diseases [3, 30-32, 93, 224, 225]. Wu *et al.* [223] have employed a microcantilever array of different geometries to detect prostate-specific antigen (PSA), within a background of human-serum albumin (HSA), as well as human plasminogen (HP). Their analysis is based on antigen-antibody (Ag-Ab) binding on the upper surface of a cantilever, coated with a biocompatible and adhesive material,

e.g., Au/Cr or SU8; the biocompatible upper surface coating would firmly hold the Ab. Upon such binding, an optical/resistive mechanism detects the bending of the cantilever that distinctively signifies the presence of the disease [223]. Also within the label-free detection regime, where no biomarkers are used, a p53 antibody in human sera has been detected using a cantilever-based biosensor, where bending of the beam has been registered by integrated piezoresistors [3].

A biosensor of a cantilever base has also found its way in detecting lung cancer via breath examination [224]; this is accomplished by implementing an exponentially growing field within biotechnology mechatronic sensing mechanism, denoted as artificial/electronic nose-detection approach [224, 225]. The analyses in [224, 225] are based on quantifying the gaseous elements of patient's exhaled breath, which are directed to an array of cantilevers of different geometries and distinctive coated polymer layers at the upper surface of each cantilever: forming the artificial nose mechanism [224, 225]. Therefore, the differences in geometry and coated materials from one cantilever to the other within an array, lead to a unique response (bending) of each cantilever in the electronic nose system – enabling not only high sensitivity, but also high specificity in allocating a distinctive gaseous element within a compound of cancer patient's breath smell<sup>1</sup> [224, 225]. Therefore, exploiting microcantilever applications within cancer detection field is essential to arrive at sensitivity limitations within the biosensor regime, which requires a well-defined design stage based on analytical theory to better understand the physics associated with the sensitivity of the device prior to microfabrication, and system characterization.

It is worth stating that cantilever approach has a number of merits as opposed to a clamped-clamped microbeam (bridge) approach [199, 226], in which the former experiences minimal power consumption (power scavenging), simplicity in structural setup, less microfabrication

---

<sup>1</sup> A 2 and 3D Cantilever-Based Artificial Nose Illustration:  
<http://www.youtube.com/watch?v=656uKaAKGDA&feature=youtu.be>  
<http://www.youtube.com/watch?v=iZtUr6p1ioY&feature=youtu.be>

time, and higher dynamical range than the latter; most importantly, the mid-plane stretching and pre-stress experienced in the bridge structure are not exhibited in cantilevers that mostly leads to system failure [227].

It is worth mentioning that Micro-Electro-Mechanical System (MEMS) based sensors are categorized based on their actuated mechanisms: extrinsic, intrinsic, or both. Thus, the cantilever beam may bend intrinsically via intrinsic stress initiated, e.g., from thermal-load cycling in relation to material characteristics [228]. Also, the bending might be attributable to several extrinsic mechanisms: electromagnetic [229], electrostatic [189, 194, 203, 210, 226], nuclear radiation (mere mass) [230], pneumatic [231], piezoelectric [188, 232], optical [233], bimaterial effect [234], as well as mechanical deformation due to uploaded, e.g., Ag/Ab, on the effective cantilever surface layer that is extensively utilized in immunoassay applications [235, 236]. Finally, bending may occur due to a combination of intrinsic, and extrinsic factors imposed to the system, such as joule heating for Shape Memory Alloy (SMA), or Shape Memory Polymer (SMP), accompanied with an extrinsic electrostatic actuation to achieve further strain of the mechanical system [237, 238].

This chapter sheds light on an important mechanobiology characteristic of cells, which is mass. Extracting cellular mass is vital, in analyzing mass changes as cells ascend into different stages of cancer. It is reported in literature that cellular mass, density, and size hold a physiological key towards indicating the different stages/phases that the cell would possess during cycle, e.g., DNA synthesis, and protein accumulation [239, 240]. The main objectives of this chapter are summarized in fourfold: (1) develop a cantilever-based-biomechatronic platform of an enhanced sensitivity, on the essence of electrostatic force to extract cellular mass, (2) investigate experimentally the theory of static pull-in phenomenon, and its impact on sensitivity, (3) acquire cellular mass, and (4) investigate the cellular mass change as cell is

progressing in the stage of cancer by adopting two cell-line models: MCF7 (early stage breast cancer), and MDA-MB-231 (late metastasis breast cancer).

### **5.3 Physical Phenomena (Theoretical Background)**

Prior to microfabricating a cantilever-based biosensor, and exploiting the governing equation of motion with its associated dynamic as well as geometric boundary conditions, various physical phenomena experienced within the MEMS domain that contribute into system damping, and thus affecting the overall mechanical quality factor, “Q factor,” of the entire mechanical system, should be first addressed and highlighted. This should ensure a highly sensitive, and stable sensor with optimal dynamic range.

Damping is a critical issue to system reliability, and optimal control of any sensor applications. Since in this present study, the focus is on sensitivity, which implies a high Q-factor magnitude. This requires a low damping experienced within the system; hence, the task is to design for experiment and lessen, as much as possible, any form of energy emitted to the surrounding, as well as any form of noises invoking the experimental setup. In this subsection, such phenomena are briefly highlighted, considering that detail elaboration on each phenomenon is laborious, and thus it will lead to a loss of main aim of this chapter: constructing and testing a biomechatronic platform that detects a cellular mass, and study the impact of electrostatic force on sensitivity. However, analyzing such damping effects, in a general term, shall enrich the robustness of the proposed design syntheses and analyses, and eventually produce a highly sensitive, and stable cantilever-based biosensor.

The squeeze-film-damping phenomenon is prominent in case of fluid presence within the vicinity (gap) that segregates the geometrically alike exciting stationary electrode, and rigid

body portion of a cantilever [198]. By performing a control volume (CV) analysis between the rigid body (tip of a microcantilever), and the stationary gold electrode, the squeeze film phenomenon is a damping force that varies with time, and it is a function of fluid velocity and gap displacement [197, 241]. As the mechanical structure starts to bend or/and torsion at the same time, the gap distance is deduced forcing the fluid to move, ‘squeeze,’ out the CV [241]. As the fluid molecules are escaping the CV, they are constrained with the viscosity of the fluid that delays the escaping process, which leads to viscous shear that eventually contributes into system damping, upon which the kinetic energy gets partially depleted. Thus, a pressure distribution per unit area, of a spatial and temporal function, is generated under the effective mass of the rigid body [241]. Mathematically, there are 3 approaches in modeling squeeze film damping: thermodynamical approach, incompressible Reynolds’s (Re) flow, and compressible Reynolds’s equation [241]. In terms of the main objective of this study, it has been shown in [241] that sensitivity increases by minimizing the gap distance, and enlarging stationary electrode area, but this may induce squeeze-film damping to the system. Generally, alleviating the squeeze film damping effect is achieved by perforating the cantilever effective mass (rigid body) [242], placing the structural system in a high vacuum chamber [241, 242], and/or enlarging the distance between the stationary electrode and rigid body [241].

Thermoelastic damping (internal friction) is an internal phenomenon of energy dissipation (intrinsic characteristic) [243]. It is initiated from an irreversible heat flow through the cyclic load experienced by the mechanical structure [241]. During elastic deformation, a volume change takes place leading to an increase in potential energy, and hence a free oscillation of the cantilever beam, until a gradual decay in potential energy is experienced by the dynamical system [244]; this is attributable to energy transformation to the surrounding, or forced by an external factor such as frictional fluid drag, upon which the system subsequently attains its

stable equilibrium configurations [244]; thermoelastic damping is more pronounceable as a form of dissipated heat from an elastic deformation. The physics of thermoelastic damping can be examined by two phenomena: mechanical energy dissipation, and entropy [244]. In the former, the non-homogeneity in stress distribution within a cantilever beam leads to a thermoelastic coupling with thermal gradient, and hence a generation of heat flow. This yields an out-of-phase stress and strain field [244]. Thermoelastic damping respectively decreases with an increase in residual stresses, and increases with an increase of the attractive electrostatic forces [241].

In addition to the aforementioned limitations and damping experienced within the electrostatic sensing applications, there are other physical phenomena that greatly affect the static bending, and frequency-based detection method, which are referred to static and dynamic pull-in phenomena, respectively. Static and dynamic pull-in phenomena play a vital role in not only defining the biosensor system stability, and dynamical range, but also they contribute into allocating system's highest sensitivity detection operating range, which shall be further discussed in the following section.

## **5.4 Pull-In Phenomena**

At a miniaturized scale, another form of system instability, which causes the mechanical structure to collapse and malfunction, is known as pull-in phenomenon [198, 226], which has been regrettably over looked by many researchers when designing a miniaturized cantilever-based biosensor. In theory, pull-in phenomena illustrate instability within the cantilever system, after which no analytical equilibrium solution exists [198, 226]. Furthermore, exceeding the static pull-in potential value, an unbounded increase in the slope takes place, and hence there

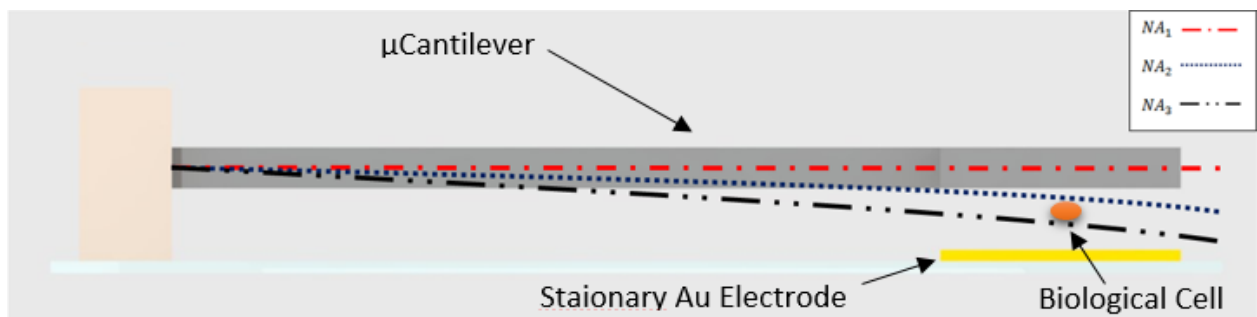
is no equilibrium solution beyond this range, where the tip of the biosensor snaps into the stationary electrode, leading to a structural collapse [198, 226]. On the other hand, in a dynamic mode, the pull-in potential is harmonic, and hence time dependent, where the harmonic response is no longer periodic rather it is unstable [226, 245].

The phenomenon gained its name on the basis that at certain modes/regions, resonance compelled to ‘pull in’ the system dynamical energy from a potential state by boosting its initial velocity (escape-phenomenon), which is a remark of system malfunction [246]. Thus in literature, dynamic pull-in is also denoted as escape-from-potential-well phenomenon, or escape phenomenon [247].

The name originated from the fact that at high energy rate, the dynamic system goes beyond its potential energy boundary, and tends to escape due to an increase of the system’s kinetic energy (velocity at transient phase) leading to instability: hysteresis or jumps to another stable or unstable attractor [247]. Therefore, such phenomena are physically interpreted as kinetic co-energy, and they are amplified by the presence of noises within the system that impose more nonlinearity. Accordingly, Alsaleem *et al.* [247] have categorized and quantified pull-in phenomena as dynamic ( $V_{AC}$ ), and static pull in ( $V_{DC}$ ), in which the former takes place first at a lower potential than the latter threshold (i.e.  $V_{Pull\ in-AC} < V_{Pull\ in-DC}$ ), if dynamic mode is superimposed to a system already experiencing a DC potential. In the static mode, non-uniform surface stresses along the beam’s thickness lead to bending [241], while in dynamic mode, shifting of the center of mass leads to a resonant frequency of the vibrating microcantilever beam, which is electronically quantifiable [248, 249]. They found that increasing  $V_{DC}$  would deduce  $V_{Pull\ in-AC}$  threshold. The allocation of static pull-in voltage infers the designer to construct a microcantilever system to resonate in a bandwidth not exceeding static pull-in potential, and hence deviating from system instability (collapse). Figure 5.1 illustrates three



configurations of the miniaturized mechanical structure. First, the microcantilever is at its neutral axis ( $NA1$ ) non-deformed equilibrium position; then after injecting DC potential through the stationary gold electrode patterned on a glass substrate, the microcantilever starts to bend to a new equilibrium position of  $NA2$ ; finally, a biological cell is loaded on top of the microcantilever, where the microcantilever is reaching a third equilibrium position of  $NA3$ , after a short transient time: the system in static mode deflects, and as it reaches a new equilibrium configuration, the cantilever resonates within a small amplitude in a transient state, until it gradually reaches steady state (new equilibrium stage) due to damping.



**Fig. 5.1** Three configurations of the  $\mu$ cantilever system:  $NA1$  is the non-deformed configuration,  $NA2$  defines a new static configuration after inducing a DC potential and development of electrostatic force is reached, and  $NA3$  illustrates a third equilibrium configuration after loading a cell.

## 5.5 Analytical Representation of the DC Pull-In Phenomenon

Mathematical modeling of the microcantilever kinematics and kinetics is an essential tool to unfold the physical behavior of the system, and better understand the concept of pull-in phenomena. Moreover, it allows the understanding of the main controlling parameters' effects

on sensitivity, which define the shape and geometry of a miniaturized cantilever. However, without losing the overall flow of the main objective of this chapter in developing, and experimentally testing a functional biomass sensor, this section is briefly depicting the work carried out by Nayfeh *et al.* [198], where they have dynamically described the physics associated with pull-in phenomena experienced by a microcantilever gas sensor: modeled as a beam coupled to a plate.

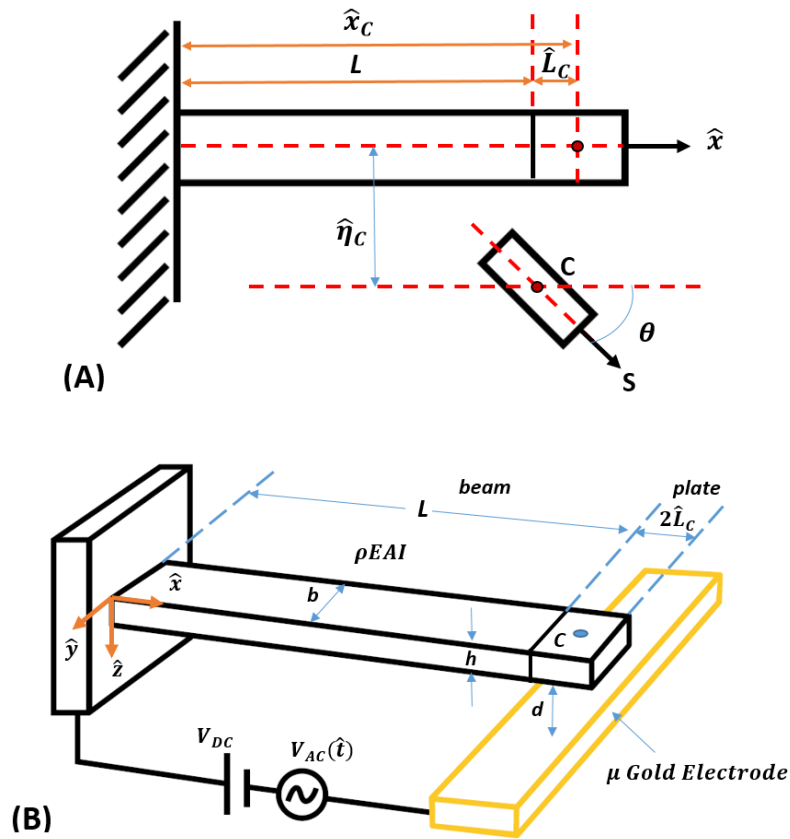
In this section, the analytical model of [198] is adopted as an approximation model in examining the dynamical behavior of the characterized cantilever-based biosensor, which shall be presented in Section 5.7. The aim is to investigate the possibility of having the proposed analytical model, developed in [198], as an approximation model of the tip deflection of the microfabricated cantilever within the biomechatronic system.

For brevity and without losing the overall flow of this chapter, the detailed mathematical derivations are omitted in this section, and are extensively carried out in Appendix F. The detailed step-by-step regeneration of the work by Nayfeh *et al.* [198], shall significantly assist in future extension of this research study in developing a better approximation algorithm, embedded within the developed software, which would act as an indication of system instability prior to conducting an *in vitro* experiment. Thus, this will save money and efforts associated with refabricating a new device to replace the damaged one in case of system failure. As a contribution to [198], mathematical expression of sensitivity ( $\frac{\text{meter}}{\text{volt}}$ ), together with optimization analyses are generated in Appendix F. The optimization investigates the dependency among the controlling parameters of the miniaturized cantilever system.

### 5.5.1 System Kinematics and Kinetics

The governing equation of motion of the MEMS structure is derived first by defining the potential energy, system kinetic co-energy, and non-conservative force(s) imposed to the system. As in the developed model by Nayfeh *et al.* [198], an effective damping coefficient ( $C_{eff}$ ) is introduced to account for all damping effects experienced within the system (e.g. viscous film damping, sound, air resistance, etc.).

The proposed modified cantilever system, Figure 5.2, is Holonomic, which justifies the utilization of Lagrangian formula [198, 250]. Therefore, by applying Hamilton's principle variation indicator approach (V.I.) [198, 250], all terms can be represented and converted into a geometrically admissible form. By collecting alike terms (i.e.,  $\delta\hat{\eta}(\hat{x}, \hat{t})$ ,  $\delta\hat{\eta}(L, \hat{t})$ ,  $\frac{\partial}{\partial \hat{x}} \delta\hat{\eta}(L, \hat{t})$ ), the nonlinear governing partial differential equation of flexural motion (Equation 5.1), and its associated natural (force-dynamic) boundary conditions (Equations 5.2 and 5.3), as well as the geometric boundary conditions (Equations 5.4 and 5.5) are obtained.



**Fig. 5.2** (A) Cross sectional view of cantilever beam-plate structure (not drawn to scale), and (B) Perspective view of the cantilever and patterned gold electrode on a glass substrate showing all controlling parameters.

The controlling parameters of the proposed analytical model above are described in Table 5.1. The assigned values are based on the characterized cantilever in Section 5.7.

Length of the beam ( $\mu\text{m}$ )		Uniform Width ( $\mu\text{m}$ )		Uniform Thickness ( $\mu\text{m}$ )		Gap distance ( $\mu\text{m}$ )		Rigid body total length ( $\mu\text{m}$ )	
$L$	250	$b$	120	$h$	3	$D$	4	$2\hat{L}_C$	100
Density ( $\frac{\text{Kg}}{\text{m}^3}$ )		Modulus of Elasticity (GPa)		Relative permittivity (F/m)		Moment of Inertia ( $\text{m}^4$ )		Area ( $\text{m}^2$ )	
$\rho$	2330	$E$	160	$\varepsilon$	$8.9 \times 10^{-12}$	$I$	$2.7 \times 10^{-22}$	$A$	$3.6 \times 10^{-10}$

**Table 5.1** Controlling parameters of the miniaturized-cantilever-based-biomass sensor.

The nonlinearity of the re-derived equations in Appendix F, arise in a general term from inertia, material, geometry, discontinuity of the structure, imposed external forces to the system (e.g. electrostatic force vs. gap distance), static and harmonic potentials, as well as dynamical boundary conditions. Furthermore, the nonlinearities, within the proposed system in Appendix F, may also arise from nonlinear interactions of molecular charges with those at the surface of the cantilever and rigid body, and/or from the impurity of material microstructure (system topology, and various composite mechanical structures). Elimination of the influence of nonlinearities, on the basis of controlling a number of design parameters, should enhance the performance of the cantilever-based-biomass sensor to reach higher amplitude (more sensitivity) in a linear manner. It should be noted that miniaturization makes softening nonlinearities more pronounceable, in which spring softening takes place, as the resonance frequency increases and amplitude of oscillation decreases when the miniaturized device is subjected to electrostatic force [251].

Normalization holds the key to simplify the evaluation of the derived nonlinear equation of motion. Moreover, it balances force and damping terms with nonlinear ones. Also, normalization enables a better understanding of the parameters' effects on the overall biosensor dynamical system, and on each other. Therefore, by introducing non-dimensional terms in Appendix F, the normalized system dynamics can be obtained.

$$\frac{\partial^2 \eta(x,t)}{\partial t^2} + \frac{\partial^4 \eta(x,t)}{\partial x^4} + C_{eff} \frac{\partial \eta(x,t)}{\partial t} = 0 \quad (5.1)$$

$$\left[ \frac{\partial^2 \eta(1,t)}{\partial x^2} \right] = -L_C(M) \left[ \frac{\partial^2 \eta(1,t)}{\partial t^2} \right] - \left( \frac{4}{3} M L_C^2 \right) \left[ \frac{\partial^3 \eta(1,t)}{\partial t^2 \partial x} \right] + \frac{L^4 \varepsilon b (V_{DC} + V_{AC}(t))^2}{2EI d^3 \left( \frac{\partial \eta(1,t)}{\partial x} \right)^2} \left\{ \ln \left( \frac{1 - \eta(1,t) - \frac{\partial \eta(1,t)}{\partial x} 2L_C}{1 - \eta(1,t)} \right) + \frac{\frac{\partial \eta(1,t)}{\partial x} 2L_C}{1 - \eta(1,t) - \frac{\partial \eta(1,t)}{\partial x} 2L_C} \right\} \quad (5.2)$$

$$\left[ \frac{\partial^3 \eta(1,t)}{\partial x^3} \right] = (M) \left[ \frac{\partial^2 \eta(1,t)}{\partial t^2} \right] + (L_C(M)) \left[ \frac{\partial^3 \eta(1,t)}{\partial t^2 \partial x} \right] - \frac{L^4 \varepsilon b (V_{DC} + V_{AC}(t))^2}{2EI d^3 \frac{\partial \eta(1,t)}{\partial x}} \left\{ \frac{1}{1 - \eta(1,t) - \frac{\partial \eta(1,t)}{\partial x} 2L_C} - \frac{1}{1 - \eta(1,t)} \right\} \quad (5.3)$$

$$\eta(0,t) = 0 \quad (5.4)$$

$$\frac{\partial \eta(0,t)}{\partial t} = 0 \quad (5.5)$$

Where, each term parameter is defined in nomenclature of Appendix B, as well as table 5.1. Equation 5.1 represents the normalized governing equation of motion of the system, whereas the normalized natural dynamic boundary conditions, Equation 5.2 and 5.3, respectively depict bending moment, and shear force experienced within the beam. The normalized geometric boundary conditions for a clamped (fixed) end, are resembled in displacement (Equation 5.4), and slope (Equation 5.5).

### 5.5.2 Static Mode Analysis

The steady-state mode of the system, where the beam-rigid body deflection is constant in time, can be found by setting the time, and AC voltage terms to zero in Equations (1-5). This leads

to the static response of the system. Thus, by evaluating the resultant normalized static equation of motion subject to the boundary conditions, the general solution reduces to:

$$\eta_{Static}(x) = Ax^3 + Bx^2 \quad (5.6)$$

Where,  $\eta_{Static}$  represents the static deflection of the microcantilever beam. The two unknown coefficients, A and B, can be evaluated by applying the boundary conditions, which yield two nonlinear algebraic equations, Equation (5.7), and Equation (5.8):

$$f_1(V_{DC}, A, B) = \frac{L^4 \epsilon b}{2EI d^3} \frac{(V_{DC})^2}{(3A+2B)^2} \left\{ \ln \left( \frac{1-A-B-(3A+2B)2L_C}{1-A-B} \right) + \frac{(3A+2B)2L_C}{1-A-B-(3A+2B)2L_C} \right\} - (6A + 2B) = 0 \quad (5.7)$$

$$f_2(V_{DC}, A, B) = -6A - \frac{\epsilon b L^4}{2EI d^3} \frac{(V_{DC})^2}{3A+2B} \left\{ \frac{1}{1-A-B-(3A+2B)2L_C} - \frac{1}{1-A-B} \right\} = 0 \quad (5.8)$$

For a known static induced potential ( $V_{DC}$ ), Equations 5.7 and 5.8 are evaluated numerically to obtain solutions for the constants A and B. Hence, the deflection is obtained. The theoretical results of tip deflections with respect to imposed DC voltage are drawn, and compared to the experimental findings in Section 5.10. Thus, this shall verify experimentally, whether the developed model by Nayfeh *et al.* [198] could be utilized as an approximation tool of the dynamics of the *in vitro* experimental setup of this study.

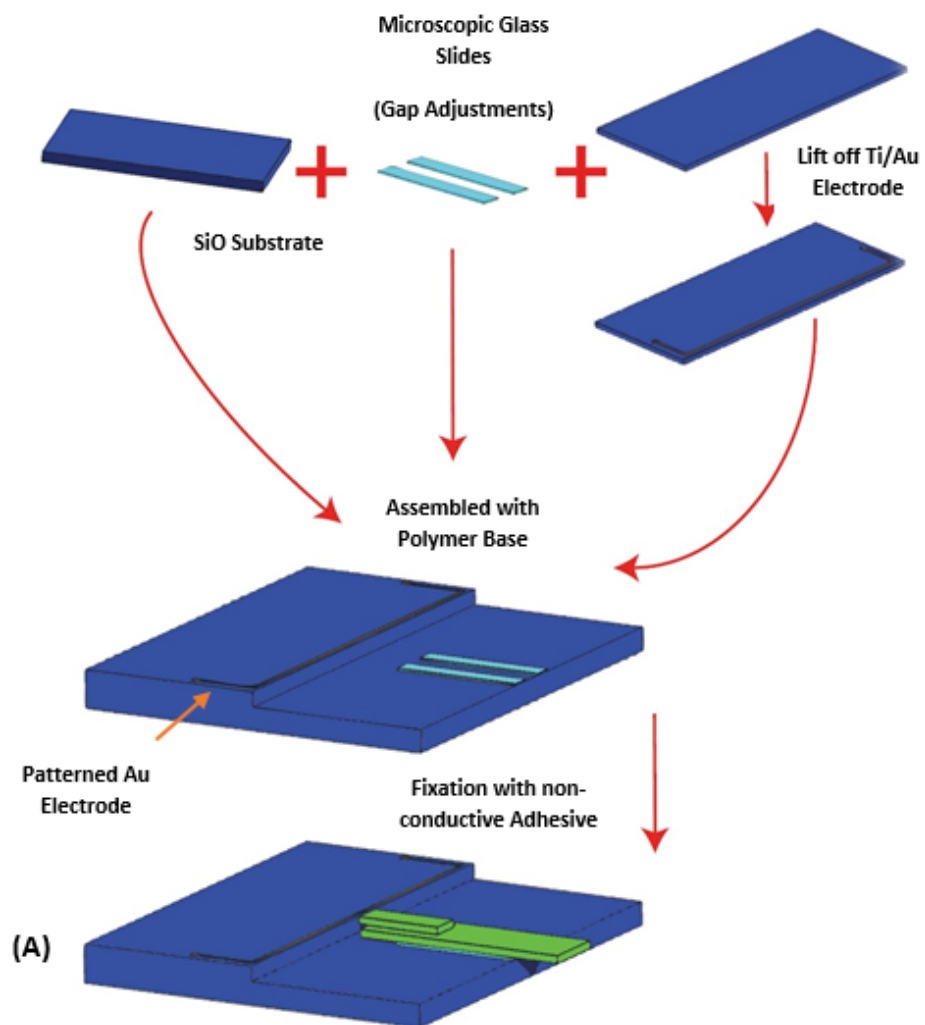
## **5.6 Microfabrication of the Biomass Sensor Mechanical Structure**

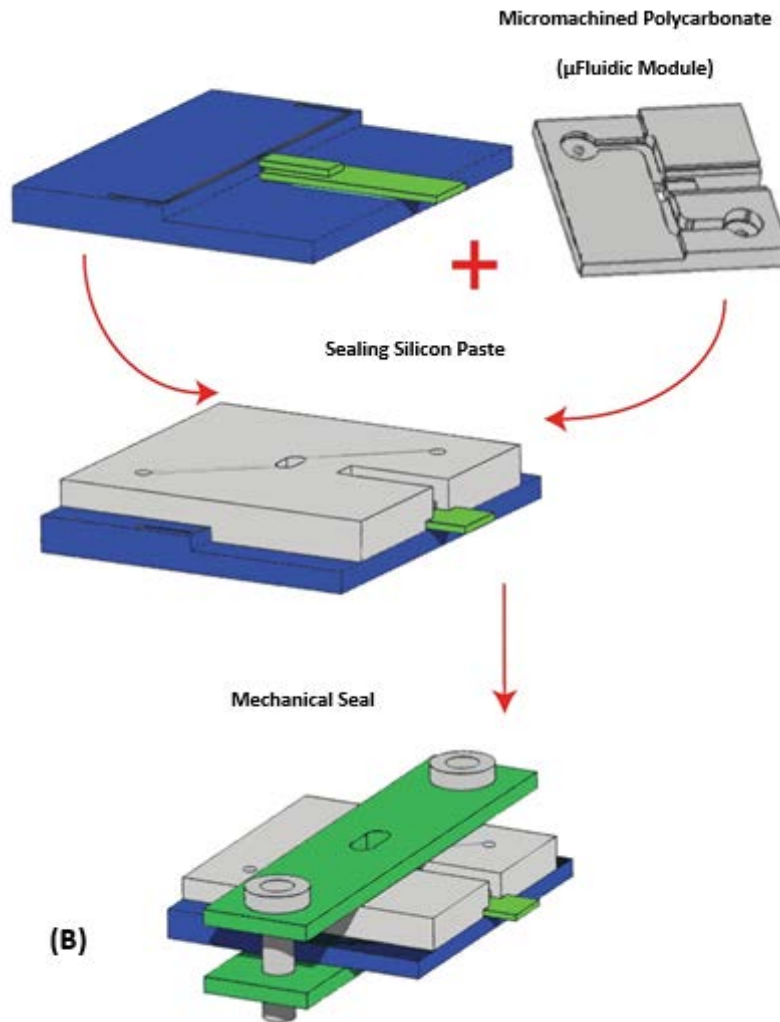
As per the theoretical essence of electrostatic force, illustrated in the previous sections, and the anticipated pivotal role of such phenomenon in enhancing the sensitivity of biomass sensor, microfabrication processes are carried out to construct a biomechatronic platform of a cantilever base that captures cellular mechanobiology, such as mass. The sensitivity is based on a correlation between static deflections of the microcantilever beam due to induced static DC potentials, as well as change of mass. In this chapter an investigation is made to explore one of the versatility characteristics of the proposed platform by extracting the mass of a cell, whereas Chapter 6 will extend the application of the proposed microdevice to obtain cellular contractile force.

As shown in Figure 5.3, the proposed miniaturized mechanical structure consists of a  $\mu$ cantilever,  $\mu$ fluidic domain, a gold electrode patterned on a glass substrate, mechanical seal, and copper connection arms, where the Cu arms are later shown in Figure 5.7.

The copper spring arms are utilized to transmit DC potential to the patterned gold electrode, creating electrostatic force in conjunction with the  $\mu$ cantilever. The gold electrode is intentionally patterned symmetrically on the glass substrate to accommodate the two copper springs, and thus ensures faithful, and smooth transition of charges in case of any default in fabrication that might have yielded a partially developed electrode pattern on the glass substrate.







**Fig. 5.3** 3D drawings of the proposed miniaturized mechanical structure consisting of (A) The mechanical assembly of the patterned gold electrode on a glass substrate, microcantilever, microscopic glass slides, and the diced glass steps. (B) Assembly of the polycarbonate (PC) microfluidic domain with the mechanically assembled components in (A).

The microfabrication processes had started by Piranha cleaning, performed on glass substrates. This was followed by a backside protection through spin coating, adding  $\sim 2 \mu\text{m}$  photoresist film as a post process to deicing. Photoresist/polymer layers protect surfaces from dicing dust (Silicon Oxide particles); if such dust particles touch the glass surface, they form

van der Waals' force, and they couldn't be removed easily. Then a die saw was utilized to cut the two glass upper and lower step: 10 x 20 mm and 17 x 20 mm, respectively. The die-sawed-glass substrates are then cleaned by Isopropyl Alcohol (IPA), and acetone. The development of the patterned gold electrode is carried out through a standard lift-off process via optical photolithography.

A positive photoresist, AZ 1518 (Microresist, Berlin, Germany), had been utilized to coat the glass substrate; then it was spun at 3000 rpm (forming a layer of 1.8  $\mu$ m thick); this was proceeded by a prebake process on a hotplate for 1 min at 115°C. A dosage of 60 mJ high-resolution exposure, together with patterned mask, were performed. Finally, the glass substrates were developed using a resist developer AZ 400 K 1:4 in a beaker for 6 minutes, where no post-bake process was carried out. Metallization process was performed by Argon sputtering, where an adhesive layer of 5 nm Ti, and 300 nm of functional layer of Au were deposited on the AZ1518 resist structure. A 4-hour-lift-off process was then performed at 80 °C using Dimethylsulfoxide (DMSO). This was followed by a cleaning process using IPA and acetone.

The die-sawed glass substrates were spin coated using AZ1518 photoresist structure as an adhesive layer. The 20 x 10 mm glass substrates, on which the Au/Ti electrode is patterned, and 2 microscopic glass slides of a 2 x 1 mm in size, were both aligned, and then all were bonded to the 17 x 20 mm glass substrate through a polymer on a hot plate, for 1 minute at a temperature of 115°C. The 2 microscopic glass slides were used to ensure alignment, equally spaced gap, and leveling of the microcantilever structure, when it is finally bonded to the overall structure through a non-conductive adhesive substance (Henkel, Düsseldorf, Germany).

The Wheatstone Piezoresistive microcantilever was fabricated through a process of wet etching, and double side polished of n-type <100> silicon wafer, with ground doping n-type,

following the process previously described [187, 252]. A wafer oxidation, and silicon-oxide-dot-patterning method, together with dry plasma etching, and thermal oxidation, were all utilized to define the sharp features of the microcantilever. This was followed by optical lithography, and phosphorus implementation to form the electrical shielding lines that efficiently eliminated electrical crosstalk between actuation and sensing elements. The Piezoresistive set of Wheatstone bridge were fabricated by ion and post-annealing process for 30 minutes, at a temperature of 850°C [187, 252].

Plasma enhanced chemical vapor deposition (PECVD) was utilized to deposit silicon nitrides as an insulating protection film, followed by a standard metallization process. Notably, the microcantilever was insulated (electric passivation) by depositing low-stress PECVD silicon nitride, empowering the microcantilever to perform in different environments, experiencing various conductive buffered media [187, 252].

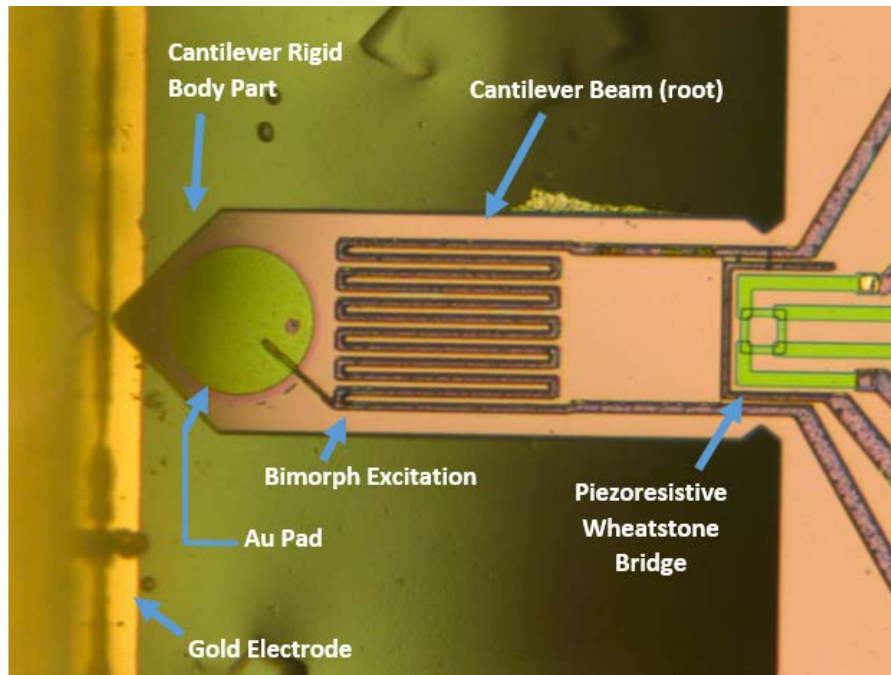
An optimized annealing process with controlled doping condition were carried out to produce highly sensitive Piezoresistive elements [187, 252, 253]; the Wheatstone piezoresistors were insulated with silicon nitrides; hence, the microelectronic components would be protected from any fluid contact, as well as it would diminish electrical noises attributable to crosstalk among electronic components. Moreover, the Piezoresistive elements were formed at the microbeam (root) support anchor, where thermal stability was achieved, and hence enhanced sensitivity. The Piezoresistive elements of the Wheatstone bridge are located in the longitudinal direction of the beam, and it is of full symmetrical bridge configuration, resulting in four order of magnitude higher signal than a single piezoresistor configuration (more thermal stability, and controllability over offset compensation) [253].

A functionalized layer of a circular gold (Au) pad was deposited within the cantilever rigid body portion. This would ensure biological chemical interaction of the loaded cell with the

cantilever active surface: achieving an affinity of molecular level interaction between the targeted analyte (biological specimen), with the thin layer of gold pad. Finally, gas plasma and wet etching were used to release the microcantilever mechanical structure.

Due to its robustness in micromachining, and extensive use as a biocompatible material, polycarbonate (PC) [254, 255] was micromachined to form the microfluidic reservoirs and channels. The two connecting adaptors, shown later in Figure 5.7, were adhered to the clean upper surface of the polycarbonate substrate through ultra violet adhesion process. An opening window was made through the polycarbonate structure for cell loading via a micropipette.

The entire miniaturized mechanical components were assembled, and mechanically sealed. The assembled components were examined under the microscope to verify design specifications, investigate any microfabrication deficiencies, and to analyze the overlap of the tip of the microcantilever with the patterned gold electrode on the glass substrate, as shown in Figure 5.4. The integrated Aluminium bimorph [256] is allowing the extension of this research study to encounter a second driving excitation, which is beyond the scope of this work. Thus, awarding the microcantilever an additional feature, next for being a self-registering (sensing) mechanism, and that is a self-actuating microprobe for future extension of this work.



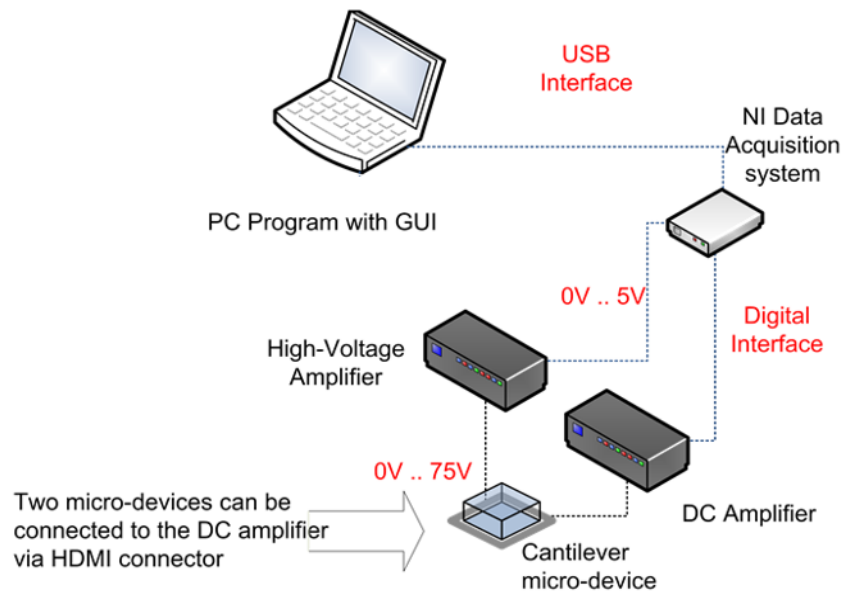
**Fig. 5.4** A microscopic image of the miniaturized mechanical component of the biomechatronic platform featuring the microcantilever (root, and rigid body), patterned gold electrode on glass substrate, Piezoresistive Wheatstone bridge, and bimorph excitation element for future extension of this research study.

## 5.7 Microelectronic Architecture

The system architecture of the miniaturized-biomechatronic-cantilever-based platform, Figure 5.5, consists of a DC-Microbalance-ADC module, and High Voltage Amplifier (Microsystems Ltd., Varna, Bulgaria), as well as a multifunction data acquisition card (National Instruments, Berkshire, UK), together with a transition printed circuit board (PCB) module, accommodating the microfabricated mechanical device. The DC-Microbalance-ADC module comprises of a high precision, low-noise, preamplifier, and a supply of DC potential to the Wheatstone bridge

(1V, 2V, 4V, and 4.5V). It can operate in two channels, allowing two experiments to be conducted simultaneously.

In order to reduce electronic components within the voltage supplier source (design simplicity), as well as to eliminate additional source of electronic noises, the bridge supply of DC potential is set manually by a jumper, implying that the two channels would have the same feeding DC potential to the Wheatstone bridge piezoresistors. Moreover, two biomechatronic platforms can be connected directly, or via HDMI cables, to the DC-Microbalance-ADC module, where the former approach eliminates electronic noises experienced with long cable connections. The transition PCB design, housing the miniaturized biomechatronic platform, is in agreement with a prerequisite of the anticipated *in vitro* experiments, in provisionally having a transparent space beneath the microfluidic chamber: allowing visual inspection under the microscope.



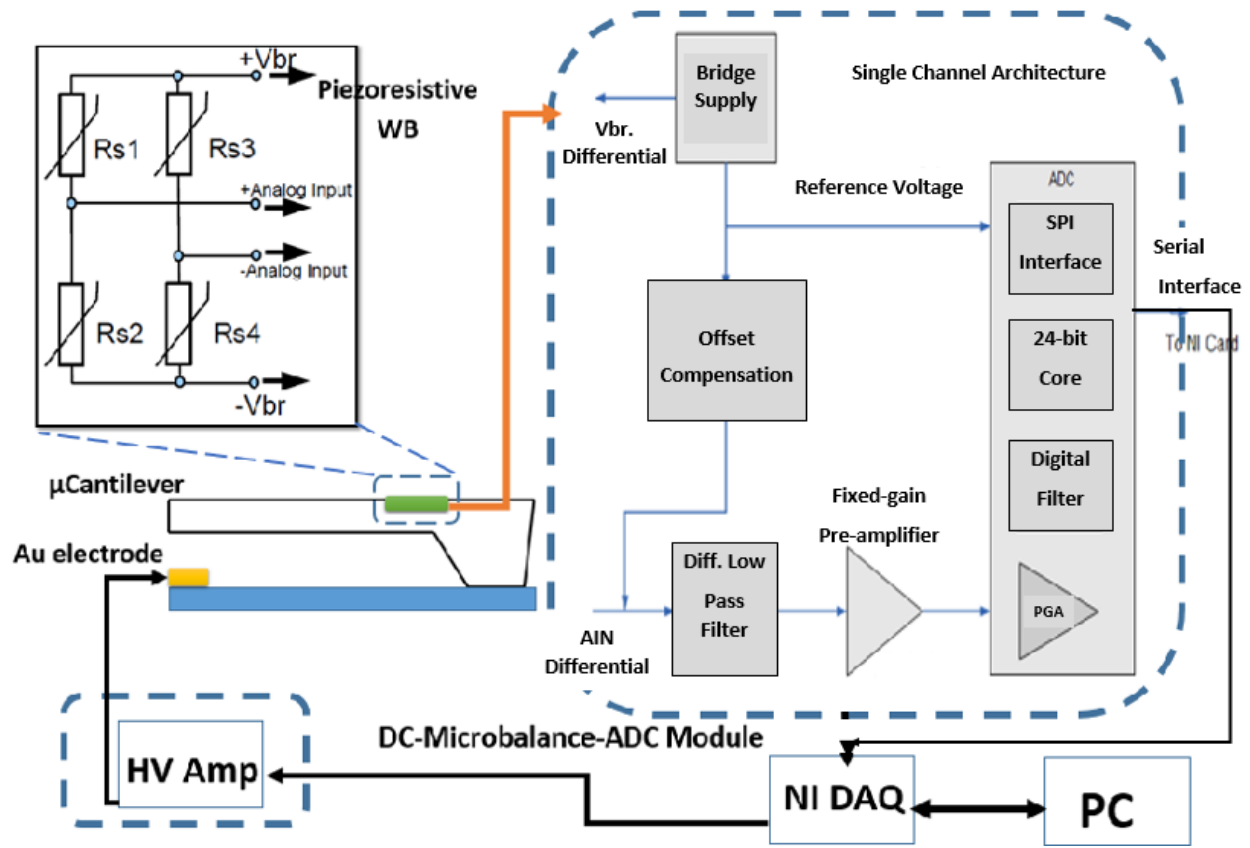
**Fig. 5.5** Microelectronic hardware architecture of the microcantilever-based biomechatronic platform connected to a DC-Microbalance-ADC module, and High Voltage (HV) Amplifier. The system is connected to a PC to collect, and analyse experimental data, through NI card.

The high precision, low-noise, preamplifier, with a fixed effective gain of 102, amplifies the output Wheatstone bridge voltage signal. The system bandwidth of 5 Hz allows the obtaining of up to 5 samples per second. The driving software allows collected data to be exported in a comma-separated-value (CSV) format, which eventually permits further data import to be widely processed by other software programs, e.g., Excel, Matlab, etc., and hence subsequent averaging can be carried out. The built-in ADC-signal module within the Microbalance unit, allows further signal amplification, and low-pass filtering. The signal processing is digitized through 24-bit resolutions for precise DC measurements.

The DC-Microbalance-ADC module has a bipolar input detection range that allows allocating high, and low registered signals:  $\pm 98 \mu\text{V}$ ,  $\pm 196 \mu\text{V}$ ,  $\pm 392 \mu\text{V}$ , and  $\pm 784 \mu\text{V}$ . Furthermore, the module has a maximum effective resolution of  $0.5 \mu\text{V}$ , and a full scale error of  $\pm 0.01\%$ . It has two digitally controlled offset compensation potentiometers (256 rough/fine steps for offset compensation); such feature provides the voltage offset compensation, which is due to the microfabrication tolerances experienced within the Wheatstone bridge piezoresistors. The digitized output from the built-in ADCs is fed to the NI-DAQ card, using virtual Serial Peripheral Interface (SPI), and then it is processed to the host PC.

On the other hand, the high voltage (HV) module receives a signal from NI-DAQ card, up to 1V, which is programmable from the PC software; then such signal is amplified via HV module to a maximum output of 75 V; therefore, this module will induce DC potential to the patterned gold electrode on the glass substrate via fabricated copper arms (spring probes), generating the electrostatic potential -- investigating the static pull-in phenomenon.





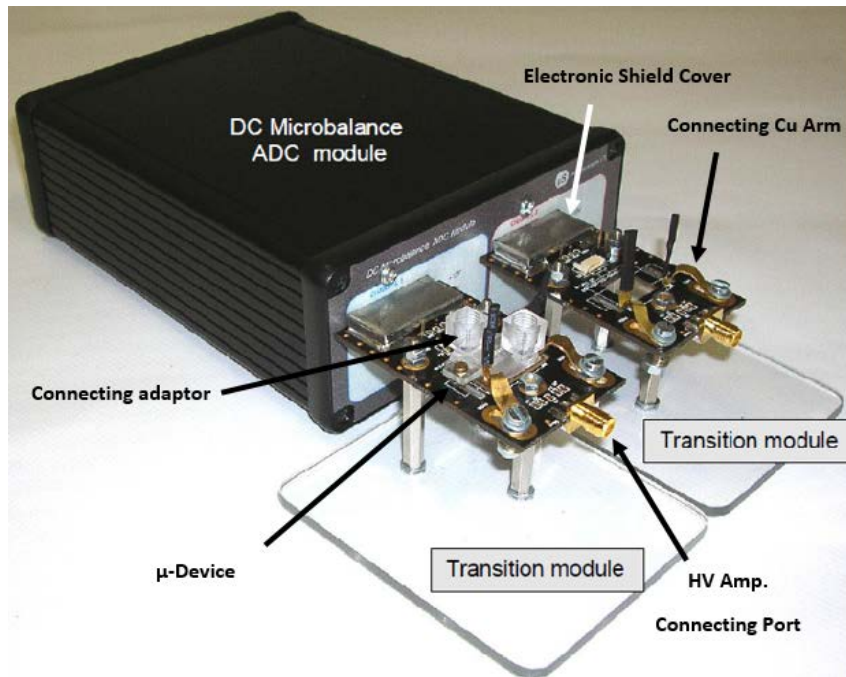
**Fig. 5.6** Microelectronic setup in probing deflection(s) of a microcantilever due to an induced DC potential to the stationary gold electrode patterned on a glass substrate via HV Amplifier module. The exploded view illustrates the Piezoresistive Wheatstone bridge (sensor scheme), where is the manually selected voltage bridge. The DC-Microbalance-ADC module consists of an input differential filter, fixed-gain preamplifier, ADC with integrated programmable gain amplifier (PGA), bridge supply module, and offset compensation block.

## 5.8 The $\mu$ -Cantilever Based Bio-Mechatronic Platform Operating Software

A design-of-experiment (DOE) oriented program, operating within two channels, has been customized, and coded in DELPHI application programming language; it is operating under Microsoft Windows, and it consists of three tabs: control panel (assigning experimental

parameters), experiment execution tab, and data registry tab. The developed driving software allows collecting data from two different experimental setups (two bio-mechatronic platforms operating in parallel). The software is connected to NI-DAQ card, which controls two hardware modules: DC-Microbalance-ADC module, and high voltage (HV) amplifier. First, the feeding potential value to the Wheatstone bridge has to be assigned in agreement with the manually set value in the DC-Microbalance-ADC module.

In light of the premise of this chapter in investigating the static pull-in phenomenon, and its impact on sensitivity, both channels having the same bridge supply of potential, can differ in terms of the imposed DC potential range that feeds the stationary gold electrode patterned on the glass substrate. Hence, having two channels running simultaneously, as shown in Figure 5.7, shall give flexibility to perform two different experiments in parallel, under two different conditions: analyzing two different biological phenomena at once; furthermore, having two experiments running at the same conditions in both channels shall investigate repeatability in the obtained results, shorten lead time, and enhance productivity in performing a number of experiments in one trial. Also, such configuration can have one experimental setup through one channel running as a reference with respect to the other. The customized software also provides a wide variety of detection input ranges, allowing readings of minute changes experienced within the microcantilever kinematics throughout the *in vitro* experiments.



**Fig. 5.7** DC-Microbalance-ADC module 2-channel configurations, showing two platforms (active, and reference) with HV amplifier feeding port, microdevice, transition PCB module, and 2 connecting copper arms.

A crucial factor in microfabricating cantilevers is tolerance, where Wheatstone bridge resistors experience offset. Thus, the customized software is empowered with a feature to fine tune the offset, alleviating tolerances to the vicinity of zero tolerance. Appendix E.2 provides in detail a step-by-step operational manual of the developed software, where electronic hardware should be connected first. Figure 5.8 illustrates a sample of registered data of one of the conducted trials.

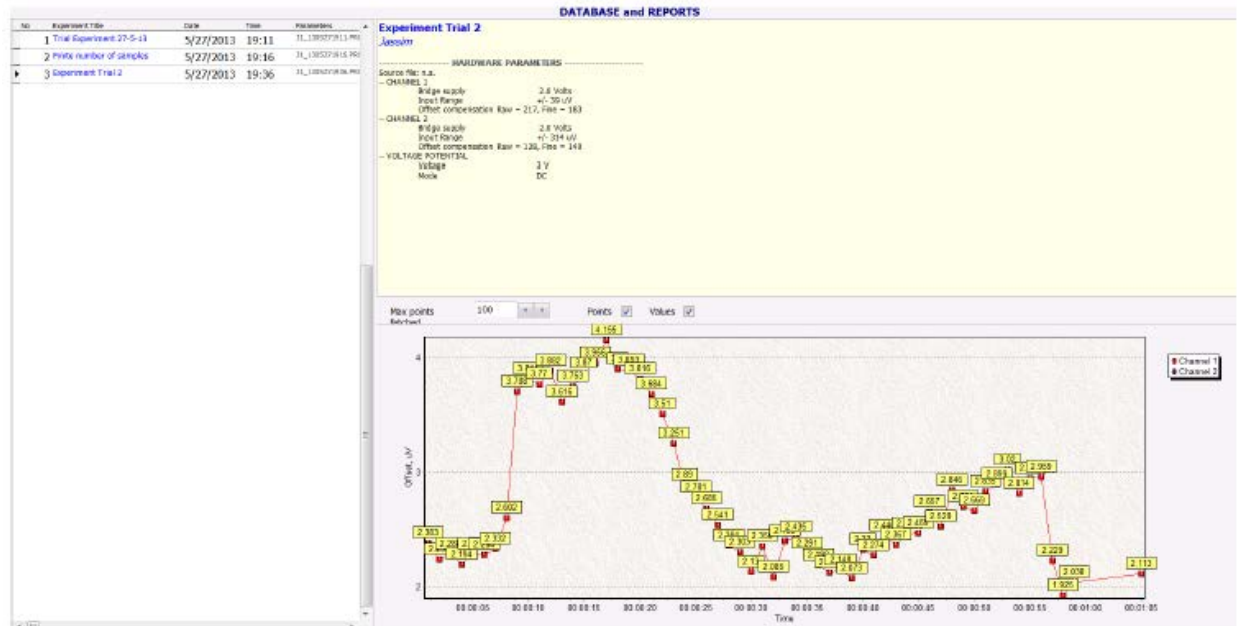


Fig. 5.8 Registered report of an *in vitro* trial experiment of the cantilever-based biomass sensor.

## 5.9 *In Vitro* Experiments: Materials and Methods

As extensively addressed in Chapter 2 in terms of the merits associated with LoC and maintaining efficiency of the miniaturized device performance, the microfluidic chamber was first filled with DI water to remove any resultant debris within the miniaturized mechanical structure in an air-bubble-free environment, followed by a sterilization process carried out with ethanol for both microfluidic and cantilever; finally, a Phosphate Buffered Saline (PBS) wash was performed to enhance biocompatibility of the structure, and then system was left to dry.

Human breast adenocarcinoma cell lines, MDA-MB-231 and MCF 7, were cultured as per the protocols set by the American Type Culture Collection (ATCC), which is addressed in Section 4.5.1. The cell's viability, concentration within a given volume medium, diameter, and cellular volume were extracted via Moxi Z device (ORFLO Technologies, WA, USA). The

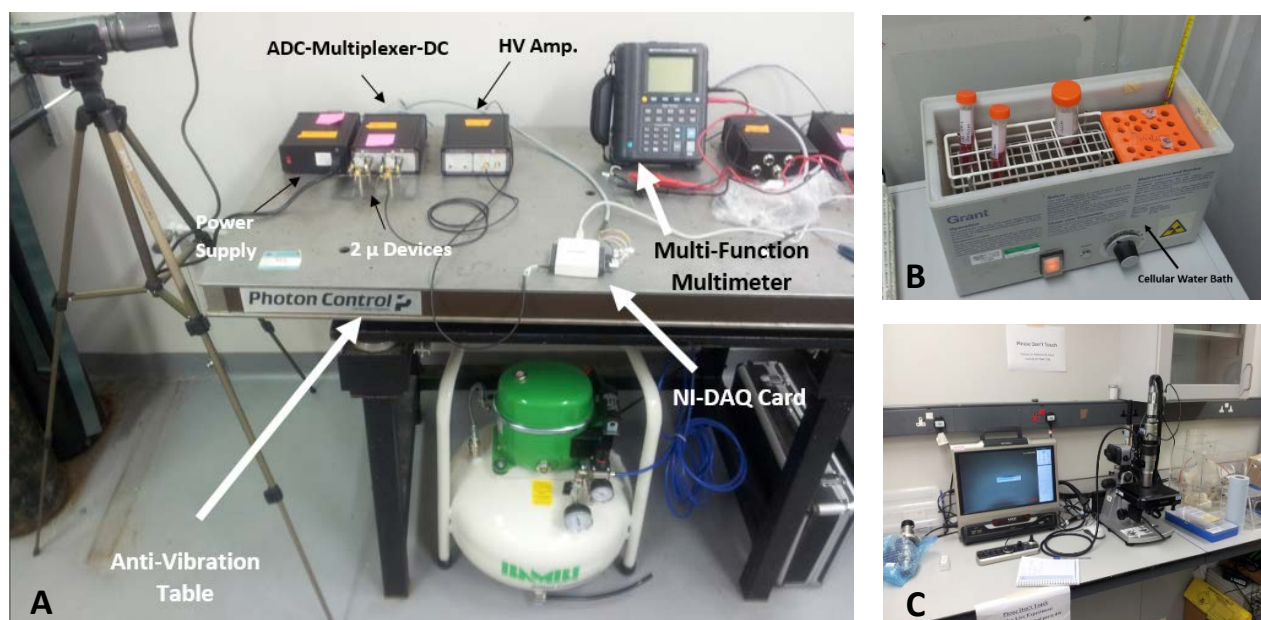
PCB connecting pads of the biomechatronic cantilever-based platform, and Wheatstone bridge piezoresistors, were all examined via a multifunction multi-meter (MASTECH, Guangdong, China): investigating whether all transition lines were faithfully transferring signals, and that the piezoresistors were damaged free. Furthermore, the copper arms were checked against a received signal initialized by the HV amplifier as pre-set in the customized software.

A single cell is extracted via serial dilution process, as discussed in Chapter 4 with registered locations via VHX 2000 Keyence microscope coordinate control positioning registry algorithm (Keyence, Milton Keynes, UK). Furthermore, through Keyence change focus lens mechanism, the air gap displacement between the tip portion of the microcantilever system (rigid body), and the patterned gold electrode on glass substrate was found to be  $\sim 4 \mu\text{m}$ . Accordingly, the microcantilever is characterized to have a total length of  $350 \mu\text{m}$ , width  $120 \mu\text{m}$ , and a thickness of  $\sim 3 \mu\text{m}$ . The cantilever structure is mainly composed of silicon ( $3 \mu\text{m}$ ), and  $300 \text{ nm SiO}_2$ , with a density of  $2330 \text{ kg.m}^{-3}$ , and modulus of elasticity ( $E$ ) of  $160 \text{ GPa}$  [187, 253, 256-258].

All microelectronic hardware were first connected, then the driving software was initialized. The software potentiometer capability was first utilized to account for the drift in the Piezoresistive tolerance. The experiments were conducted under clean room conditions. Electromagnetic wave interferences within the vicinity of the experimental setup were monitored via an EMF, and it was found to be negligible ( $10^{-10}$  Tesla). The entire experimental setup was placed on an anti-vibration table to refrain any entrances of vibrational noises to the system, as shown in Figure 5.9.

The cantilever was housed inside a microfluidic module, which would eliminate any optical intervention to bend the miniaturized beam mechanical structure. It's crucially important that during injection of DC potential to the gold electrode patterned on glass substrate, the two-

copper arms are not touching the circuit as this could lead to circuit damage. Furthermore, a shield cover is used to insulate the microelectronic noises from entering the cantilever-based biomass domain, also to protect the underlying circuitry (e.g., wires, pads, etc.) from any electromagnetic emissions.



**Fig. 5.9** (A) Experimental setup consisting of an anti-vibration table, NI data acquisition card, ADC-Multiplexer-DC, HV Amplifier, power supply, and Multi-function multi-meter. (B) Cellular water bath to maintain a temperature of 37°C for cultured cells, and (C) VHX-2000ES Keyence Digital Microscope.

A single cell was extracted via serial dilution process, re-examined for its viability through trypan blue dye marker, and then was loaded to the cantilever functionalized surface through the opening window on top of the microfluidic domain. The *in vitro* experiments were performed at different stages: reference stage, where the cantilever was first in a non-deformed equilibrium configuration (reference stage), followed by loading cell stage. The cell would

adhere to the functional gold pad near the tip of the cantilever. Finally at the termination of the experiment stage, trypsin was utilized to detach cell from the cantilever functionalized surface followed by DI water filling, sterilization, and PBS wash for miniaturized device reusability.

Two channels were operating throughout the *in vitro* experiments, where one channel with no-loaded mass was left as a reference. A number of trials have shown that the static potential, where the cantilever breaks, is within 15-Volt range. More precisely, since the developed software source code is programmed such that the initialized command to the HV Amplifier module has a resolution increment of 1V, the experimental static potential could be in the range exceeding 14 V, but less than 15 V ( $14\text{ V} < V_{DC-breakage} \leq 15\text{ V}$ ).

The registered data of output voltage signals from the Wheatstone bridge are correlated to cantilever's static deflection by the following equation [253, 256-258]:

$$V_{out} = V_{in} \frac{\Delta R}{R} = V_{in} \sigma \pi = V_{in} \frac{3Et}{2L^2} \eta \pi \quad (5.9)$$

Where,  $V_{in}$  is the supply potential to the Wheatstone bridge (1 V),  $V_{out}$  is the output voltage signal of the bridge,  $\Delta R$  is the strain gauge (Piezoresistive change) of the Wheatstone bridge,  $\sigma$  stress component,  $\pi$  is Piezoresistive coefficient ( $70 \times 10^{-11} \frac{m^2}{N}$ ),  $E$  is the modulus of elasticity,  $t$  is thickness,  $L$  is total length of cantilever, and  $\eta$  is beam's deflection. All output bridge voltage signals were registered, and exported in a CSV-file format, where triangle filtering algorithm was applied to obtain smoother curves, allowing simplicity in reading the generated signals.

The cellular mass is obtained by correlating the deflection of the non-loaded to the loaded mass case. The cantilever is first deflected in response to a static bias DC voltage (not exceeding the voltage the cantilever breaks at during the experiments). At the static



configuration, the deflection of the miniaturized mechanical structure is registered. The cell is then loaded, where a transient time is allowed for system to stabilize, and reach equilibrium at the same DC bias potential. Fixing the static potential at that value, the system body force is more dominant; the cantilever beam effective mass in the unloaded case, with its associated static deflection, is related to the deflection of the loaded mass case by  $F = \delta K_{eff}$  [259], where  $K_{eff}$ ,  $\delta$ , and  $F$ , respectively represent the constant stiffness, registered deflection, and body force. Therefore, the following mathematical definition (Equation 5.10) illustrates the correlation of cellular mass ( $m_{cellular}$ ) to effective beam mass ( $M_{eff}$ ), loaded deflection  $\delta_m$ , and unloaded deflection  $\delta$  at a targeted imposed DC potential [259].

$$m_{cellular} = 0.23 M_{eff} \frac{(\delta_m - \delta)}{\delta} \quad (5.10)$$

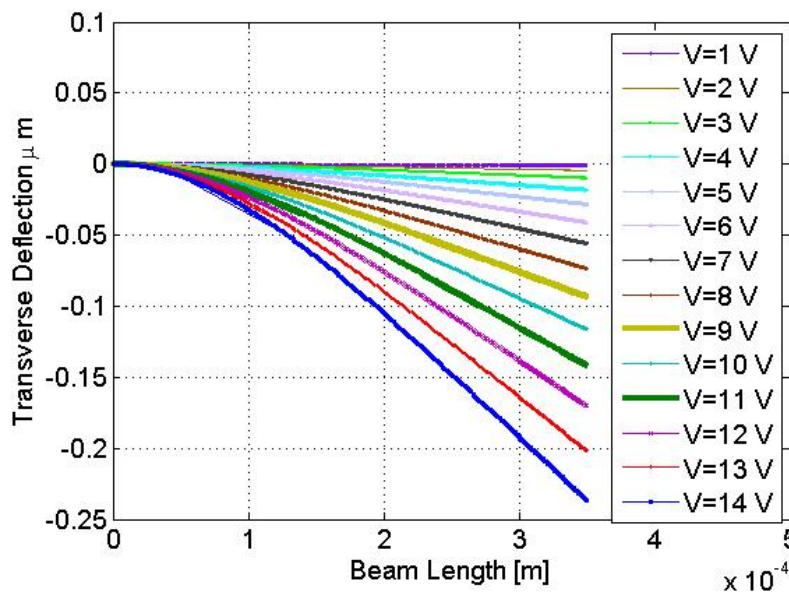
## 5.10 Results and Discussion

The microfabricated cantilever is assumed to have a uniform rectangular cross section; furthermore, the dominant material is considered to be silicon, and hence the effective modulus of elasticity ( $E$ ), and effective density ( $\rho$ ), are respectively, 160 GPa, and  $2330 \text{ kg.m}^{-3}$  [253, 256-258]; the microfabricated mechanical structure of the cantilever is characterized to have a total length of 350  $\mu\text{m}$ , 120  $\mu\text{m}$  width, and a uniform thickness of 3  $\mu\text{m}$ .

The imposed static DC potential, through the patterned gold electrode on the glass substrate, generates an electrostatic force: resulting in a transverse deflection of the cantilever structure. As the static force increases the cantilever transverse deflection increases (Figure 5.10), reducing the air gap between the cantilever, and stationary gold electrode. Various



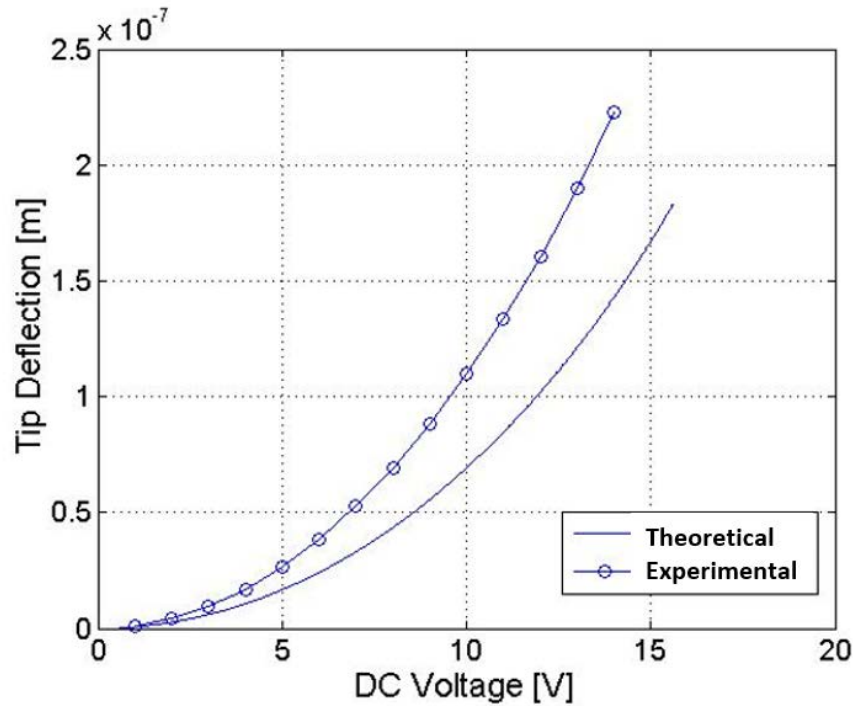
equilibrium configurations are achieved along the transverse deflections of the beam, until instability takes place at a certain DC potential, where the mechanical system fails -- breakage of the cantilever occurs. The Wheatstone bridge provides readings of the output voltage signals corresponding to the transverse deflections of the miniaturized beam, and since the supply voltage to the Wheatstone bridge is known, the transverse deflection is obtained through Equation 5.9.



**Fig. 5.10** Experimental results of static transverse deflections of the microcantilever beam corresponding to various induced DC potentials prior to cantilever breakage at 15 V.

Prior to reaching a breakage point, the cantilever maintains equilibrium by balancing the developed beam's surface stress forces with the imposed electrostatic ones, and upon reaching a point, where the electrostatic forces overcome the stress forces, equilibrium cease to take place, and mechanical failure of the systems occurs. The experimental findings manifest that as the DC voltage increases, the bending curvature of the mechanical deflection increases

(Figure 5.10). However, a number of *in vitro* experiments illustrate the inapplicability of the static pull-in phenomenon for the proposed developed system, since the miniaturized mechanical structure fractures (system failure at  $\sim 0.24 \mu\text{m}$  deflection), without approaching pull-in potential as proposed by the mathematical model in [198]. However, the analytical model, as manifested in Figure 5.11, could be considered as an approximation of the dynamical behavior of the *in vitro* experiments in regards to the microcantilever tip deflection.



**Fig. 5.11** A comparison between experimental and analytical model results of tip deflection (m) with respect to induced DC potential (V).

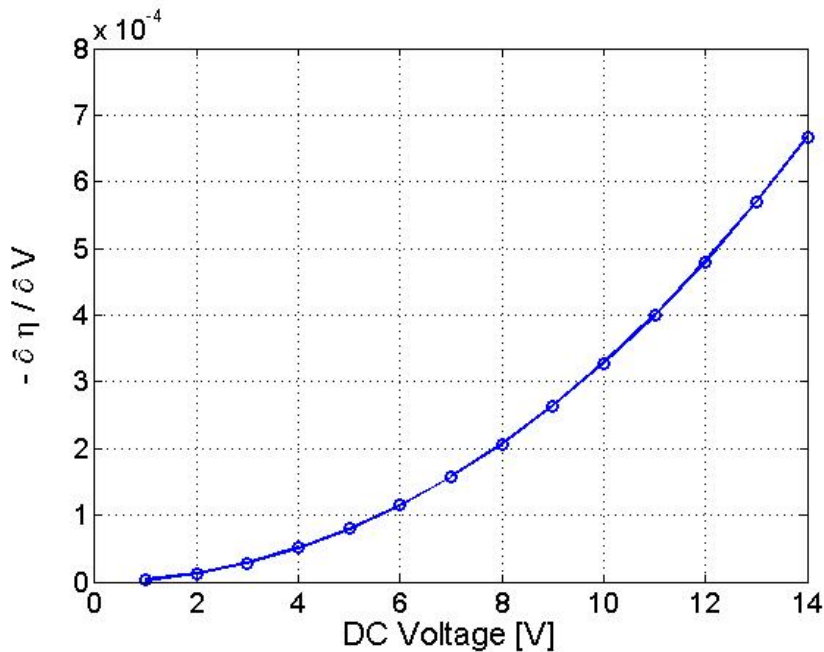
It should be re-emphasized, as it has been earlier stated in this chapter, that the main objectives are (1) to construct a biomechatronic platform of a cantilever base that is able to detect cellular mass, and later to be utilized to extract contractile force of cells (Chapter 6):

manifesting the versatility feature of the proposed system; (2) investigate the variation in mass as the cell is ascending in mitosis stage; (3) utilize static pull-in phenomenon as an approximation tool to estimate the failure state of the miniaturized mechanical system, considering that microfabrication is a tedious process and not straight forward, and (4) further to use the phenomenon in enhancing sensitivity of the cantilever. The intention is not to derive and validate an analytical approach describing the configuration of the manufactured mechanical system as this is beyond the scope of this chapter, and will be left for future extension of this work. Figure 5.11 investigates the theory of the static pull-in phenomenon, and provides approximation of the dynamical behavior of the cantilever-based biomechatronic platform; moreover, based on Figure 5.11, the analytical model developed by Nayfeh *et al.* [198] is considered a good approximation for low induced static potential not exceeding 4.5 V.

Such differences between theoretical and experimental tip deflections could be attributable to a number of factors: parallel plate electrostatic definition in the theoretical model differs from the triangle tip configuration in the *in vitro* experiments; the microfabricated triangle tip would anticipate to possess higher electrostatic force than a rectangular one; there is a shifting in the rigid body center of mass between the theoretical and experimental case; the assumption of complete overlap of the rigid portion of the beam with patterned gold electrode on the glass is not fully captured experimentally; at last, the assumption of considering an effective dominant modulus of elasticity and density of silicon, and the assumption of uniform thickness of the microfabricated mechanical structure, all contribute of having such differences. In addition to the aforementioned factors justifying the differences between theoretical and experimental findings, the effective damping coefficient in the analytical model doesn't explicitly illustrate the effect of thermoelastic damping, which increases as the electrostatic force increases.

As thoroughly discussed in Section 5.1, the beam-plate cantilever [198] is considered as an effective modeling tool [219-222]. Figure 5.11 illustrates that the beam's analytical model could be utilized to approximate the deflection of the tip with respect to induced DC voltage of the proposed experimental setup in this chapter, especially at lower values of the injected DC potentials.

The change of transverse deflections with respect to induced potentials defines a slope, which gives the sensitivity in  $\mu\text{m}/\text{Volt}$ . According to Figure 5.12, as the static bias voltage increases, the sensitivity enhances (increases); this is in agreement with the developed analytical model in [198]. Therefore, investigating the electrostatic effect on sensitivity has been proven experimentally.



**Fig. 5.12** The sensitivity in  $\frac{m}{V}$  (negative slope) of the *in vitro* experimental findings of the cantilever's tip with respect to the induced DC potential (V).

The main objective of this chapter is to design, and develop a cantilever-based biomechatronic platform that is able to quantify the mechanobiology (mass) of a cell. It has proven experimentally that sensitivity increases proportionally with the increase of electrostatic forces. Therefore, in this work such effect is utilized in favor of enhancing the sensitivity of a cantilever-based-biomass sensor in static mode. By fixing the static DC potential, and correlating the deflection of the cantilever with, and without loading a mass as per Equation (5.10) [259], the late metastasis (MDA-MB-231), and early stage breast cancer (MCF7) cellular masses were characterized to be  $1.2 \pm 0.00165$  ng (Mean  $\pm$  SD,  $n = 3$ ), and  $0.921 \text{ ng} \pm 0.00223$  ng (Mean  $\pm$  SD,  $n = 3$ ), respectively. This is within the same order of magnitude of cellular mass within the published works [184, 239, 260]. As per the obtained findings, the cell mass increases, as cell advances in the metastasis stage. Furthermore, as per the obtained readings of the respective volumes of these cell lines extracted via Moxi Z device, the average volume of MDA-MB-231 is  $3.09 \times 10^{-15} \text{ m}^3$ , whereas the average volume of MCF 7 is  $3.35 \times 10^{-15} \text{ m}^3$ . Therefore, the density of MDA-MB-231 cell is  $0.4 \pm 0.028 \frac{\text{g}}{\text{cm}^3}$ , whilst the density of MCF 7 is  $0.275 \pm 0.0067 \frac{\text{g}}{\text{cm}^3}$  (Mean  $\pm$  SD,  $n = 3$ ). Accordingly, the density of a cell does increase as the cell progresses in the cancer stage. This might suggest that intracellular activities, as well as organelle contents within a cell, at an advanced stage of proliferation, are correlated to the increase in cell mass; on another scale, this suggests that mass might not be uniformly distributed within a cell. Generally, as cell advances in the malignancy stage, the mechanobiology of cells could be an indication of the nature of the disease, mechanism of cell mutation cycle, mitosis, and apoptosis [260, 261]. From another perspective, cellular mass could be correlated to the cancerous activities of DNA synthesis, DNA content, lipid content, and protein accumulation [239].

## 5.11 Conclusions and Future Prospective

In this study, measuring cellular mechnobiology (mass) in a non-invasive manner, without detaching a cell from a contact surface, has been achieved via a self-registering-cantilever-based biomechatronic platform as opposed to confocal microscopy, and flow cytometry [239]. The work of this chapter is going to be extended to conduct more *in vitro* experiments, achieving high repeatability, and robust results; also, a study of local stiffness of cancer cells at different stages shall be considered. A Focused Ion Beam (FIB) shall be utilized to remove a known deposited mass on the cantilever's tip, to efficiently calibrate mass sensor mechanism.

Dynamic pull-in phenomenon stimulation, and its impact on sensitivity will be further explored. This will also be accompanied with static deflection, and bimorph excitation to achieve the highest possible deflection of the beam structure (highest sensitivity). In line of this future prospective, a detailed analytical approach, based on Bernoulli-Euler beam theory, is pursued to predict the dynamical behavior of such system excited statically, dynamically, as well as thermally, where the analytical model of such system will be verified experimentally. Furthermore, the future objective is to extend the work of Nayfeh *et al.* [198], by encountering the viscoelasticity characteristics of cells, as well as the fringing field factor of electrostatic force.

Despite the extensive measures taken to minimize effect of noises during the static deflections of the beam, it is crucially important to investigate, in great detail, the impact of noises on sensitivity (e.g. Hooke, Johnson,  $1/f$ , etc.) [256, 257, 262, 263]. Noise is defined as time-dependent-stochastic phenomena [256, 257, 262]; hence, such detailed analyses shall

achieve better sensitivity by quantifying the effect of presence of such noises within the experimental domain.

The developed cantilever-based biomechatronic platform highlights the importance of a miniaturized lab-on-a-chip (LoC) field, the premise of Chapter 2. The developed system is compact in size as opposed to hospital-based cytology laboratories; also, it is more cost effective, noninvasive to the biological cells, can be mass produced, reusable, and it doesn't require highly trained technician to run the experiments. Most importantly, it achieves real-time *in situ/in vitro* analyses, giving that cellular density, and thus mass are variants with respect to stage of cancer.

Based on the design syntheses and experimental analyses illustrated in this chapter, electrostatic bending of the beam would aid researchers to consider enhancing the sensitivity of their already developed cantilever based sensors without the adversity, and cost associated with optimizing the microelectronic of the system, reducing thickness of the cantilever through lengthy and complex micro/nanofabrication processes, modifying the cantilever's geometrical shape configurations, enhancing material properties, placing it into a vacuum chamber to lessen noise and obtain high quality factor, which is inapplicable to biological testing (cell will burst in vacuum), perforating the effective mass of the cantilever, enlarging stationary gold area, and/or reducing gap distance. The sensitivity of the cantilever-based biosensor would sufficiently increase, if a dynamic potential ( $V_{AC}$ ) is superimposed into a static potential ( $V_{DC}$ ). Invoking the dynamic excitation, as well as exploring combined stimulation would contribute in increasing the dynamical range of cantilevers, and enhancing their sensitivities. This could lead to exploring the differences in mass of not only cancerous cells, but any altered cells, undergoing oncogene transformation, or being infected by viruses or intracellular parasites.

# **Chapter 6**

---

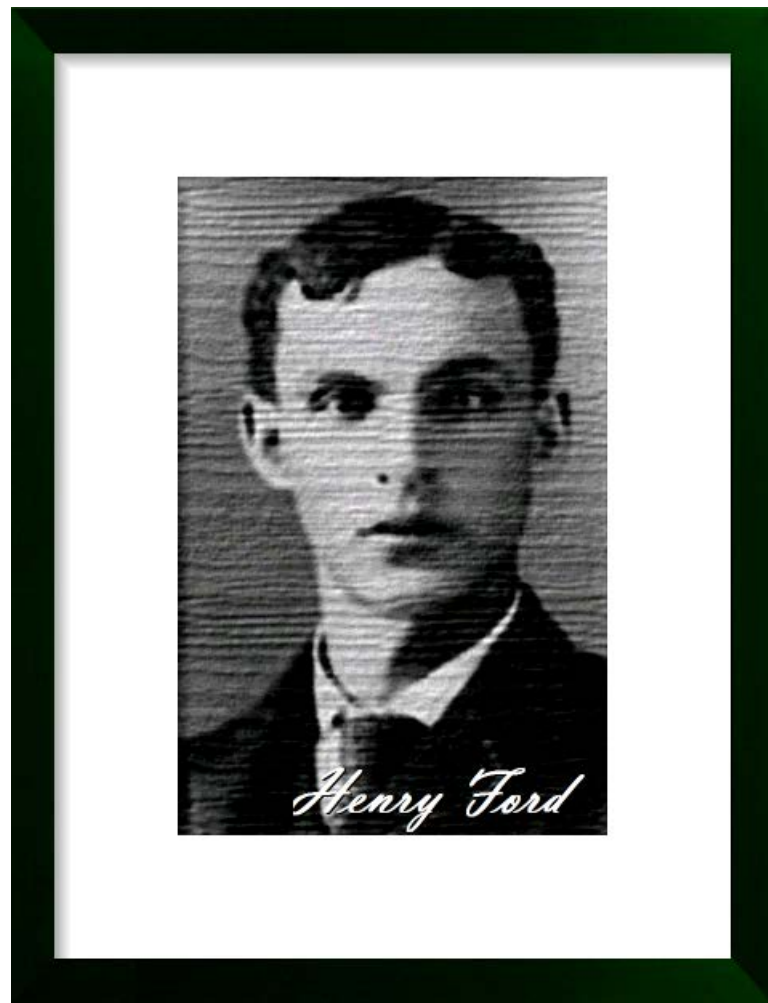
---

## **Contractile Force**

---

---





*"When everything seems to be going  
against you, remember that the  
airplane takes off against the wind,  
not with it..."*

## Chapter 6: *In Vitro* Real-Time Characterization of Melanoma Contractile Force via a Self-Probing Cantilever-Based Biomechatronic Platform

### 6.1 Introduction

Biological cells are the building blocks of life, they come in different forms, perform different tasks, and they experience different motility (movement) mechanisms [264-270]. Most sperm cells swim [266], whereas cancer cells generally crawl<sup>1</sup> [267]. Furthermore, some bacteria exhibit a unique motility by rotating flagellar motors, in which a generated torque within the flagellum-ion-driven motor is passed to helical propelled flagellar filaments via a hook-shaped joint<sup>2</sup> [268]. A fourth motility mechanism, experienced mostly by parasites, is known as gliding<sup>3</sup>, which is driven by overlaying transmembrane proteins on a given substrate [271]; it differs from crawling motility, in which the morphology of a cell is unaltered during cell migration [271].

Cellular motility is responsible about numerous biological events. It plays a dominant role in constructing tissues and organs through dividing cells in a process denoted as **morphogenesis** [264]. Moreover, wound healing is a remarkable process that involves three biological phenomena: cell migration (movement), diversified assigned cellular physiological tasks, and unique morphological shapes of each cell type: all collaborate in tissue reconstruction [272, 273]. In wound healing, distinctive electrochemical/mechanical signaling,

---

<sup>1</sup>Crawling mechanism: <http://www.youtube.com/watch?v=kQKXvOufeGg&feature=youtu.be> 214

<sup>2</sup>Flagella motility: [http://youtu.be/eqD8aX\\_Yfps](http://youtu.be/eqD8aX_Yfps) (vorticella motility) <http://youtu.be/hDfBpQHnsio>

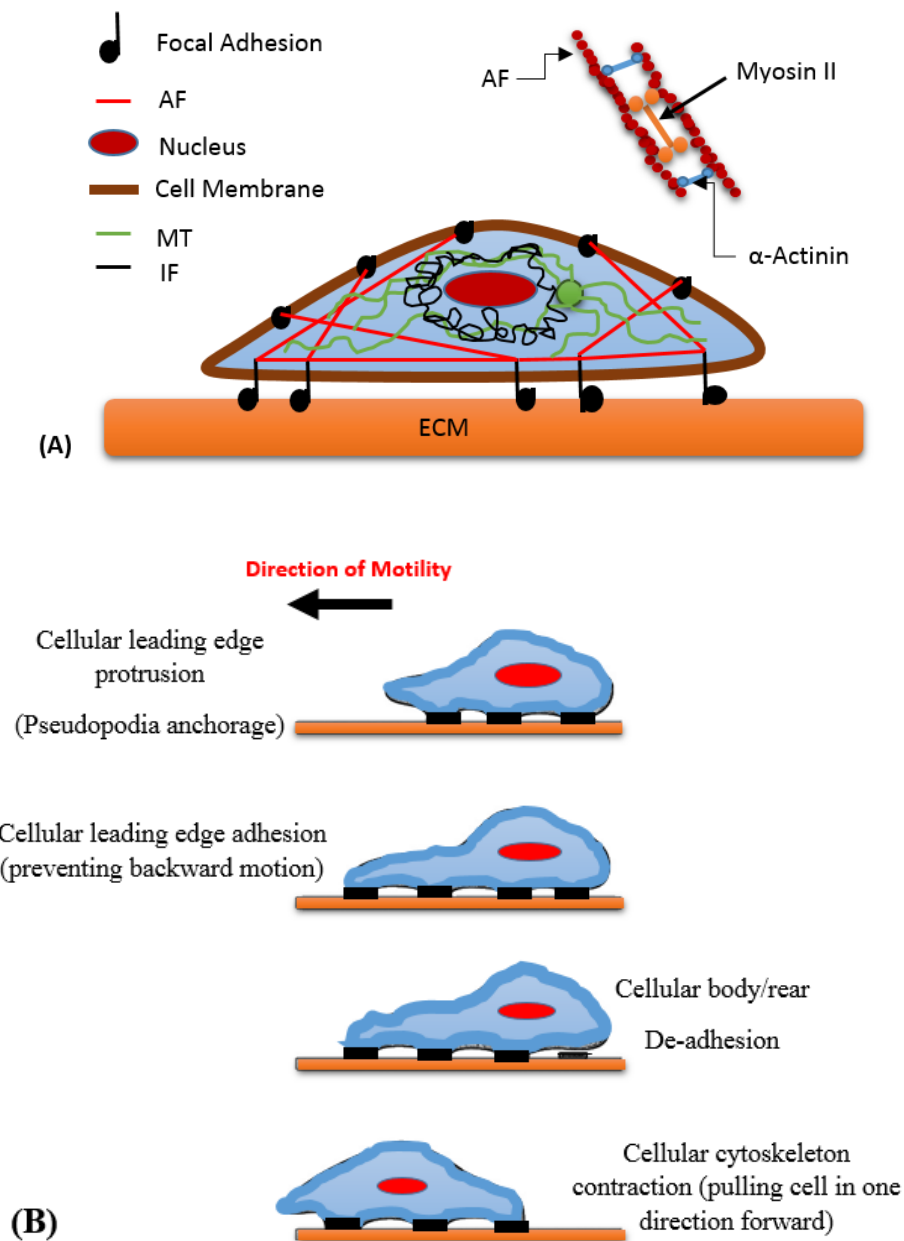
<sup>3</sup>Gliding: <http://youtu.be/x0RNjE65Ygw>

received by the gene receptors of certain cells, would initiate the cellular movements, and orchestrate the motilities of white blood cells, **neutrophils**, and digesting-bacterium defensive cells, known as **macrophages**, to terminate microorganisms responsible for infection, and at the same time connective tissue cells, **fibroblasts**, engineer and reconstruct damaged tissues [272, 273]. Furthermore, the importance of cellular force lies within the nature of a disease; for instance, some bone diseases are attributable to a change of bone and endothelium cellular forces within their normal physiological environment [265]. Similarly, heart failure is due to a loss of contractile force of heart cells [274-276].

Parasites with their unique gliding motility yield human malaria through *Plasmodium* parasite, as well as human related immunocompromised disease via *Toxoplasma* and *Cryptosporidium* [271]. Tumorigenesis is a manifestation of cellular motility through the formation of a secondary tumor due to the development of cancer cell in a metastasized distant tissue/organ [23, 277, 278]. It has been reported that melanoma cells have the highest occurrence in developing brain metastasis as opposed to other cancer cell types, where they migrate through brain capillary endothelial cell layer, the blood-brain barrier [23].

In this chapter, melanoma cancer cells' crawling motility is thoroughly investigated, together with the morphological changes of these cell lines based on their level of metastases. The cellular crawling migration goes into four segments<sup>4</sup>: cellular leading edge protrusion (pseudopodia anchorage), cellular leading edge adhesion (preventing backward motion), cellular body/rear de-adhesion, and finally cellular cytoskeleton contraction (pulling cell in one direction forward) [264, 269, 271]; this process is depicted in Figure 6.1. As shown, cell consists of nucleus, cell membrane, microtubules (MT), myosin motors, intermediate filaments (IF), focal adhesion, extracellular matrix substrate, and actin filaments (AFs) within the intracellular domain [1, 264, 269].

<sup>4</sup> Animated cell crawling motility: <http://youtu.be/vNlasSiQIM0>



**Fig. 6.1** (A) Illustration of cell's cytoskeleton, (B) Four stages of cellular motility.

As shown in Figure 6.1A, the cell is bounded by a membrane that segregates the intracellular cytoskeleton region from the extracellular one [1, 264, 269]. The cytoskeleton is

a scaffolding network, consisting of three-main-filament types based on their rigidity: actin filament (semi-flexible distinctive pairs of monomers), microtubules (stiffest rod-shaped polymer with functionalized treadmill motion), and intermediate filaments (most flexible, non-polarized ((static))) [264, 269]. At the cellular periphery, the radial extensions of microtubules (Figure 6.1A), from the center to the AF network where the positive ends are in the direction of cellular edge, assist in selecting the direction of cell's movements [269, 279].

The two distinctive (+/-) ends of an actin filament play a dominant role in cell's motility, where the (-) actin monomer concentration is higher than that of a (+) end, and if the end of the AF is exposed to a higher monomeric concentration, polymerization takes place, where monomers grow, and bind [264, 269]; alternatively, if the concentration is lower, de-attachment and shrinkage (de-polymerization) takes place, where AFs extend asymmetrically [264, 269]. Therefore, **polymerization**, a higher rate extension process of the positive end than the negative end based on actin monomer concentration, is a key factor in understanding motility (forward momentum/treadmilling) of cells [264, 269].

The subject of polymerization is analogous in a similar manner to Engineering Material Science, which again brings to the surface one of the aims of this research study: analyzing a biological system through the interpretation of various physical characteristics and/or behavior(s) of cells in an engineering manner. In addition to polymerization, cellular motility can be generated through the interactions between AFs and **myosin motors** -- a molecular motor converting chemical energy ( $\text{ATP} \rightarrow \text{ADP}$ ) to a mechanical work exerted on AFs, yielding a contractile force pushing a biological cell forward [264, 275].

## 6.2 Different Approaches in Quantifying the Contractile Force of Cells

Cellular mobility initiates due to received electrochemical, mechanical, and/or diffusible/non-diffusible signals, picked by receptor proteins on cell membrane<sup>5</sup> [1, 265]. During mobilization, cells form extracellular matrix (ECM) via focal adhesion complexes with the surrounding environment, and as they move, they do experience external forces, e.g., viscous forces, interaction forces, as well as cellular cytoskeleton internal forces [264, 265, 280]. It is, therefore, the dominant cellular contractile force that overcomes other external, and interaction forces to push the cell forward, which has been experimentally characterized through invasive, and non-invasive manners; this can be grouped into three categories: local point probing, entire cell probing, and a population of cells probing [265, 281].

Figure 6.2 shows different methods in extracting cellular contractile force. Exposing a cell or a population of cells to a shear flow in a cone-and-plate viscometer (Figure 6.2A), and then by applying Navier Stoke's equation, the cellular contractile force with respect to the shear stress exerted on cells would be estimated [264, 282]. Similarly, extracting contractile force of a cell or a population of cells<sup>6</sup> can be achieved by forcing a cell or a group of cells to be adhered to a thin polymer substrate, e.g., Si, coated with ECM-cell-molecular adhesion (Figure 6.2B), and then cells would experience tensile or compression test [265]. However, such approaches extract the mechanobiology of cells in an imposed/forced manner, which raises the question: whether the findings of such approaches would genuinely represent the contractile force of a cell or not? Atomic Force Microscopy (AFM) [283], Figure 6.2C, and Magnetic Twisting Cytometry (MTC) [2, 284, 285], Figure 6.2D, both perform a local point deformation on a cell, where in the former approach, the tip needle deflection of the AFM cantilever can be correlated

<sup>5</sup> Movie presentation of neutrophil chasing bacteria: <http://youtu.be/LYP8MUK3Iqk>

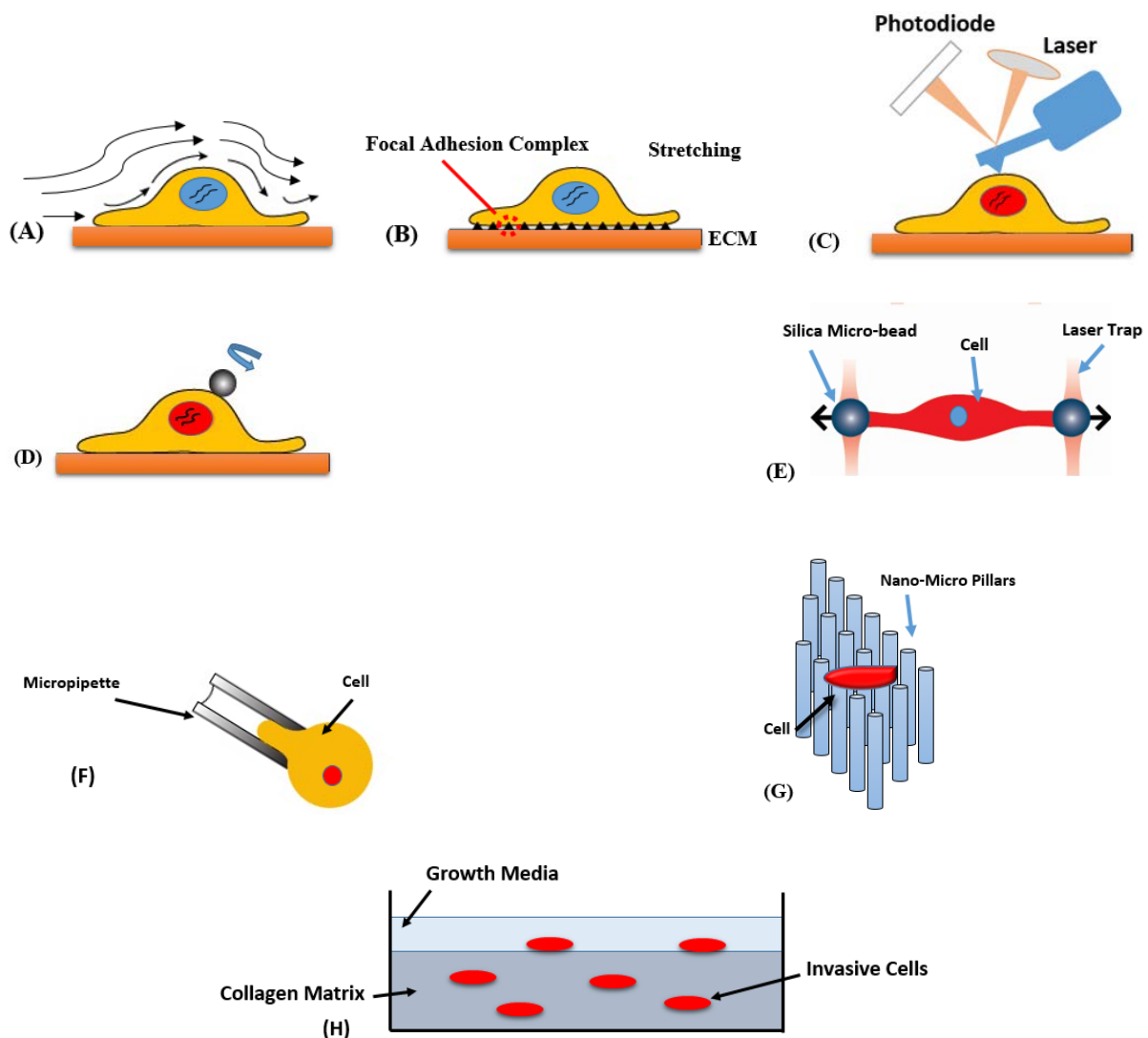
<sup>6</sup> Cell crawling in a group: [http://youtu.be/WzLQ0\\_mKaiU](http://youtu.be/WzLQ0_mKaiU)

to the cellular force, whereas the latter approach utilizes magnetic field to force a magnetic bead to deform the cell, and eventually such elastic/viscoelastic deformation is correlated to cellular contractile force. MTC method is similar to hardness test in Solid Mechanics. These last stated two methods are invasive, and cannot be applied to a population of cells.

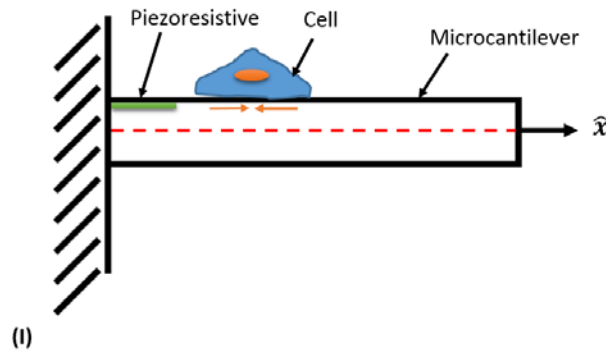
Optical tweezers or laser-trap approach [286] uses a laser beam to attract a high refractive dielectric silica bead into a cell, and hence forces a whole cell to deform (Figure 6.2E). In a similar manner, but with mechanical deformation, micropipette aspiration technique [2, 284, 285] imposes suction of a cell, and by ignoring the frictional forces between cell and internal surface of the micropipette, the changes in cellular geometry (elasticity) are correlated to cellular force (Figure 6.2F). However, both approaches are invasive, and can endanger the viability of a cell. A seventh approach is culturing a cell in an array of nano/micropillars [287, 288], where cell is then exerting additional force, when migrating to a new location (Figure 6.2G). This again rises the paradox question whether the resultant forces, correlated to those deflected pillars, are again genuinely representing the cellular contractile force or not? Also, such approach requires optical imaging to record deflection of the nano/micropillars, which adds to the cost and complexity of experimental setup; this would be constrained with the optical resolution. Also, cells do differ in their morphology, when experiencing micropillar environment during their migration, as opposed to flat surfaces. Another approach is named a 3D-ECM-invasion assay (Figure 6.2H), where cells are spread on collagen, and then their surface indentations are measured after cell de-attachments [289]. However, such approach requires a time consuming experimental preparation and setup.

A cantilever-based micro-electro-mechanical system (MEMS) [281, 290] is used to record the deflection of the beam in response to exerted cellular surface compressions on the functional layer of the beam via Piezoresistive elements, where such deflection is then

correlated mathematically to cellular contractile force (Figure 6.2I). This approach is non-invasive, can be applied on a single, as well as a population of cells, has a self-registering mechanism, can operate in a controlled microfluidic environment to maintain cell viability, is cost effective, and most importantly reports dynamics of a cell in real time. Therefore, such approach is highly advocated in this research to extract the contractile forces of melanoma cells.







**Fig. 6.2** Various approaches in extracting cellular contractile force (A) Shear flow analysis method, (B) Substrate focal adhesion complex approach, (C) AFM approach, (D) MTC approach, (E) Laser trap approach, (F) Micropipette approach, (G) Micropillar approach, (H) 3D-ECM-invasion assay method, and (I) Piezoresistive cantilever-based approach.

### 6.3 Cantilever-Based N/MEMS platform

Despite the infancy of the nano/micro-electro-mechanical-system field in probing the contractile force of cells, yet it has grown massively among biotechnologists for the past decade to explore the mechanobiology of cells [269]. Yin *et al.* [281] have micofabricated a cantilever within a microfluidic channel to measure the contractile force of a cell. An embedded Piezoresistive mechanism, forming a Wheatstone bridge, has been utilized to capture the deflections of a beam. They have implemented the negative dielectrophoretic (nDEP) to trap a cell. Similarly, Yang and Yin [4] have designed and analyzed a Piezoresistive microcantilever, utilized to sense surface stresses generated from a biological loading on the cantilever. They propose improvements on sensitivity by modifying the dimensions, and at the same time they have allocated source of noises within the system. On the other hand, Goericke and King [291] investigate different configurations of a microcantilever sensor, as well as its embedded Piezoresistive elements, to enhance the sensitivity of the microdevice.

Raorane *et al.* [292] have utilized an Au/SiN<sub>x</sub>-based-coated-microcantilever-paddle array configuration to quantify protein enzymes that are associated with a disease. In their work, the minute mechanical structure acts as a transducer of biological intermolecular forces.

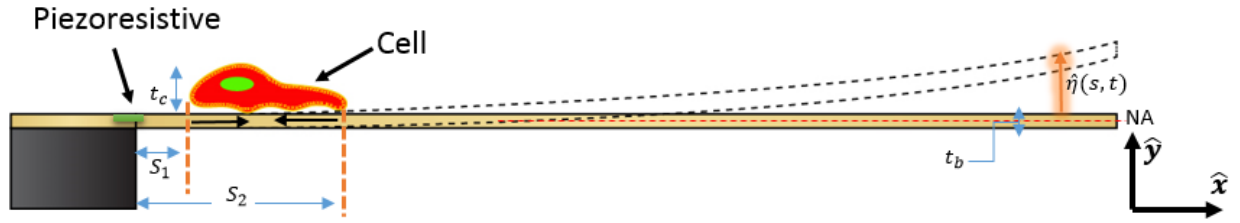
Ricciardi *et al.* [293] have proposed a label-free-microfluidic cantilever array in an immunoassay application within a liquid domain. They have uniquely utilized Pyrex material instead of the conventional PDMS in fabricating their microfluidic channel. Their proposed system can be utilized for progression of cancer cell mutation. They highlight the merits of performing experiments in liquid as opposed to vacuum or air, in which it reduces the false and positive negative response in measured data, and most importantly considering that cell membrane and proteins change their morphology status, depending on the domain they are in: liquid or vacuum/air domain.

Park, *et al.* [275] have quantified the contractile forces of self-organized cardiomyocytes by utilizing a flexible, transparent, and biocompatible microcantilever array. Their technique in seeding cells on the cantilever array, ensure damage-free-cell structure.

## 6.4 Mathematical Modeling

The majority of scholars, in the field of cantilever-based probing contractile forces, employ the discrete model of Stoney's equation [294], in which the cantilever's deflection is correlated to mechanical stresses. However, such discrete model requires the knowledge of modulus of elasticity ( $E$ ), as well as Poisson's ratio ( $\nu$ ) of the investigated biological model, whose values are most often missing experimentally, forcing biologists to make rough assumptions on such values; this would question the reliability of their obtained contractile force findings.

In this chapter, and as a new contribution in mathematically expressing the contractile force of a cell on a microcantilever-beam structure (Figure 6.3), a Heaviside step function  $H(s)$  [295], as well as pin-force model [296] are utilized in formulating a mathematical term representing the contractile force of a cell.



**Fig. 6.3** Schematic illustration of a deflected beam due to exerted contractile force (compressive surface stresses) of a biological cell experiencing motility.

Beam's theory describes a relationship between deflection of the cantilever and applied load, where stiffness factor ( $EI$ ) is mostly considered constant [221, 295, 297]. As illustrated in Figure 6.3, a biological cell is defined by two coordinates with respect to the clamped end of the cantilever:  $S_1$  (starting coordinate), and  $S_2$  (ending coordinate of the cell). The beam is assumed to be inextensible isotropic beam. The thickness of the beam is denoted as  $t_b$ , whereas the thickness of the cell (height) is denoted as  $t_c$ . The transverse deflection of the beam is expressed as  $\hat{\eta}(s, t)$ . Biological cell's cytoskeletal forces generate surface compression on the functional surface of the cantilever. The resultant force of rear and front of the cell, yields a net force pushing cell forward: leading to a transverse deflection of the beam upward. The equation of motion describing the system is given by [221, 295, 297]

$$\rho A \ddot{\eta} + EI \eta^{iv} = q(s, t) \quad (6.1)$$

Where,  $q(s, t)$ , is the total resultant distributed load on the beam, and since load is moment; thus,

$$q(s, t) = \frac{\partial^2 M}{\partial s^2} \quad (6.2)$$

Where,  $M$  defines the uniformly distributed bending moment acting on the beam, and it is expressed as in [221, 295-297]

$$M = \frac{F(t_b + t_c)}{2} [H(s - s_1) - H(s - s_2)] \quad (6.3)$$

The associated geometrical, as well as dynamic force boundary conditions of the system [295] are defined as

$$\begin{aligned} \eta = 0 \quad \text{and} \quad \eta' = 0 & \quad \text{at } s = 0 \\ \eta'' = 0 \quad \text{and} \quad \eta''' = 0 & \quad \text{at } s = L \end{aligned} \quad (6.4)$$

Generating a reduced-order model of the system, by expressing beam's deflection,  $\eta$ , in terms of Galerkin expansion, yields

$$\eta = \sum w(s)u(t) \quad (6.5)$$

Where,  $u(t)$  are generalized temporal coordinates, and  $w(s)$  represent orthonormal mode shapes of the cantilever beam, defined as in [221, 295, 297]

$$w(s) = \sum_1^n A \cos(r_n s) + B \sin(r_n s) + C \cosh(r_n s) + D \sinh(r_n s) \quad (6.6)$$

By substituting the boundary conditions (6.4), and considering only the first mode shape, the deflection term can be simplified as,

$$w(s) = C [\cosh(r_n s) - \cos(r_n s) - \sigma(\sinh(r_n s) - \sin(r_n s))] \quad (6.7)$$

The frequency,  $r_n$ , is obtained by the characteristic Equation (6.8), whereas  $\sigma$  is defined by Equation (6.9), and  $C$  is obtained by normalizing the mode shapes through Equation (6.10) [295].

$$1 + \cosh(r_n L) \cos(r_n L) = 0 \quad (6.8)$$

$$\sigma = \frac{\cosh(r_n L) + \cos(r_n L)}{\sinh(r_n L) + \sin(r_n L)} \quad (6.9)$$

$$\int_0^L w(s)^2 ds = 1 \quad (6.10)$$

By substituting Equations 6.5 and 6.10, into the Equation of motion (6.1), multiplying by mode shape  $w(s)$ , integrating over the entire domain length of the beam, and utilizing the orthonormal properties of the linear mode shapes, the following term is obtained

$$EI r_n^4 u = \frac{F(t_b+t_c)}{2} [w'(s_1) - w'(s_2)]$$

$$u = \frac{F(t_b+t_c)}{2EI r_n^4} [w'(s_1) - w'(s_2)] \quad (6.11)$$

Where ‘ $u$ ,’ is the normalized deflection of the system, and by applying Equation (5.9) in Chapter 5, defining the dimensional experimental deflection of the beam,  $\hat{\eta}$ , as per the obtained output voltage signals from the Piezoresistive elements,  $u$  is then obtained. [253, 256-258]:

$$V_{out} = V_{in} \frac{\Delta R}{R} = V_{in} \sigma \pi = V_{in} \frac{3Et}{2L^2} \hat{\eta} \pi \quad (6.12)$$

$$\hat{\eta} = u w(L) \quad (6.13)$$

The deflection at length  $L$  of the beam is defined by  $w(L)$ . Obtaining the experimental reading of the deflection of beam due to cellular motility, would give the contractile force,  $F$ , experienced by the beam (Equation 6.11); hence, the effective contractile force of the cell,  $F_C$ , is obtained by

$$F_C = \frac{2F\pi\left(\frac{d_C}{2}\right)^2}{b(s_2-s_1)} \quad (6.14)$$

Where,  $d_c$  and  $b$  respectively represent cellular diameter, and width of the beam. A numerical algorithm in Appendix C.3.1 is developed in Maple (Maplesoft, Ontario, Canada) to solve for  $F_C$  with respect to the experimentally obtained deflections of the beam.

## 6.5 Materials and Methods

As thoroughly described in Chapter 4, all cells were cultured as per the American Type Culture Collection (ATCC) protocols. Cells were examined in Moxi Z (ORFLO Technologies, WA, USA), a mini-automated-cell counter utilized to investigate viability, volume, and size of a cell, as well as cell's concentration within a given fluid medium. The cantilever-based biomechatronic platform was filled with DI water to eliminate any resultant biological or microfabrication related debris from the system. A sterilization process was performed with ethanol for the entire microdevice. At last, PBS wash was carried out to improve system's biocompatibility, and then the platform was left to dry.

Keyence VHX-2000ES digital microscope (Keyence, Milton Keynes, UK) was employed to investigate the topography, and heights of each cell line via the built-in change-of-focus mechanism featured in the Keyence microscope. A serial dilution approach was carried out as described in Chapter 4, where the digital microscope was used to register the coordinate location of each viable cell within a culturing well, allowing flexibility in extracting a single cell via a micropipette. A trypan blue dye marker was applied to investigate cell's viability. The Keyence VHX-2000ES was employed through its change of focus mechanism to investigate the deflection of the tip of the beam, and compare the results with the obtained deflections from the Wheatstone bridge reading. The results were in good agreement, which

added confidence to the microfabricated cantilevers' Piezoresistive elements in registering the deflection of the beam.

Scanning Electron Microscopy (SEM) has been performed in low vacuum chamber (avoiding cellular burst), where cells were fixed in 6% (w/v) paraformaldehyde (sigma) for 25 minutes, and washed in phosphate buffered medium, whereas typical protocol of dehydration, fixation, and gold sputtering were eliminated [275]. SEM images of cells were obtained, to investigate their morphology in terms of their heights, and maximum contact surface area with a flat substrate.

The *in vitro* experiments were carried out under clean room conditions. Electromagnetic wave interferences were measured via EMF meter, and was found negligible ( $10^{-13}$  Tesla). The experimental setup was the same as the one described in the previous chapter. However, on the contrary to Chapter 5, gold electrode patterned on glass substrate with associated copper springs were not employed (no DC voltage injection), since in Chapter 5 the aim was to enhance sensitivity of the beam by imposing electrostatic force (pulling cantilever downward), whereas Chapter 6 addresses cell contractile force which is causing a transverse deflection upward (Figure 6.3). All signals of the electronic connections were examined via a multi-meter device. The experiments were performed on an anti- vibration table to eliminate any source of vibrational noises to be induced to the measurement domain.

The measurements were recorded at various stages: biomechatronic platform without media and cell (stage 1), biomechatronic platform with media only (stage 2), and biomechatronic platform with media and cell (stage 3). Such process allowed arriving at the distinctive cellular motility signals; furthermore, such methodology has eliminated noises, and by using triangle smoothing algorithm, the obtained voltage signals were clearly read. A culturing and growth medium was added to the microfluidic chamber culturing reservoir inlet.



A viable cell extracted from the serially diluted process was then loaded to the functional layer of the microcantilever via the opening window on top of the microfluidic domain. When a cell was loaded on the functional layer of the microcantilever, the cell got attached, and then adhered to the functional surface of the cantilever, and finally initiated motility signals at different time intervals were recorded, which varied from one cell line to the other. Some cell lines within the microdevice were kept in incubators for one-full day. At a final stage, trypsin was injected into the system to detach the cell from the cantilever functionalized surface, followed by DI water filling, sterilization, and PBS wash, for miniaturized device reusability.

## **6.6 Results and Discussions**

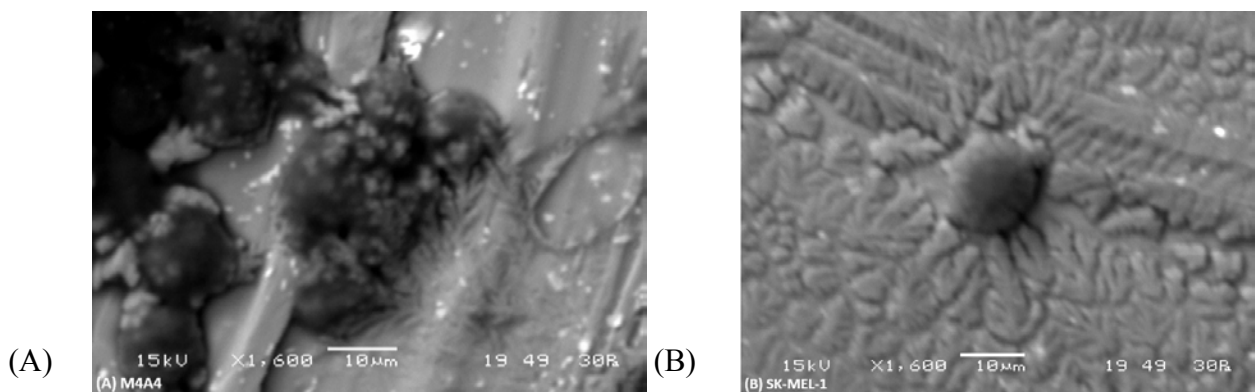
Well-established-eight-melanoma cancer cell-line models of unique genetic complexities, and genomic mutations have been investigated in terms of their morphologies, as well as their cellular contractile forces: SK-MEL-1, A-375, G-361, WM-115, NM2C5, M4A4, M4A4 LM3-4 CL16 GFP (CL 16), and M4A4 LM3-2 GFP (LM3). In addition, a well-documented breast cancer adenocarcinomas, MDA-MBA-231 (late metastasis), has been utilized as a calibration model, when extracting the cellular contractile force, as a resultant correlation with the deflection of a microcantilever beam.

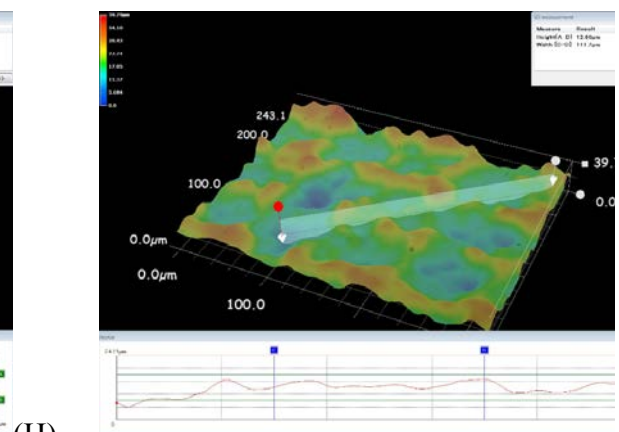
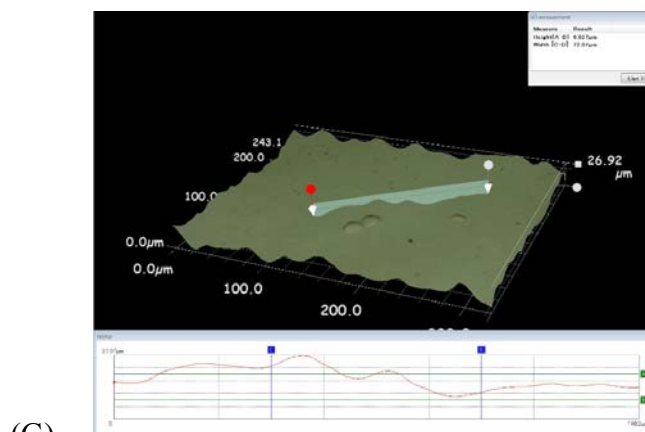
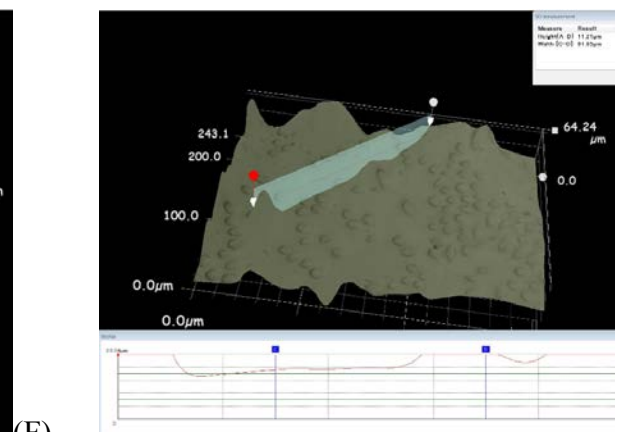
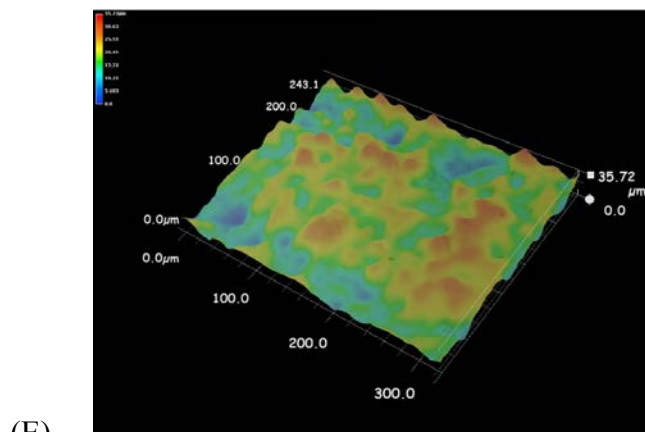
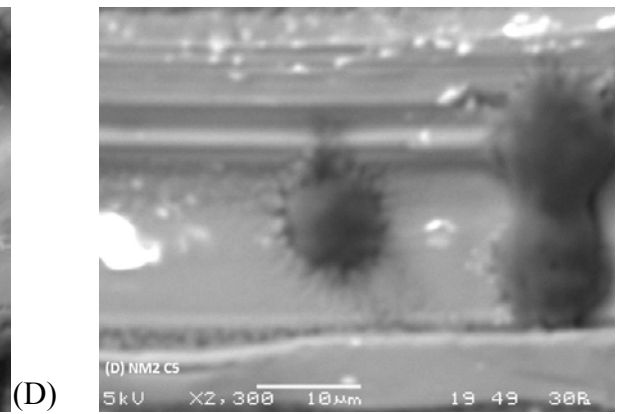
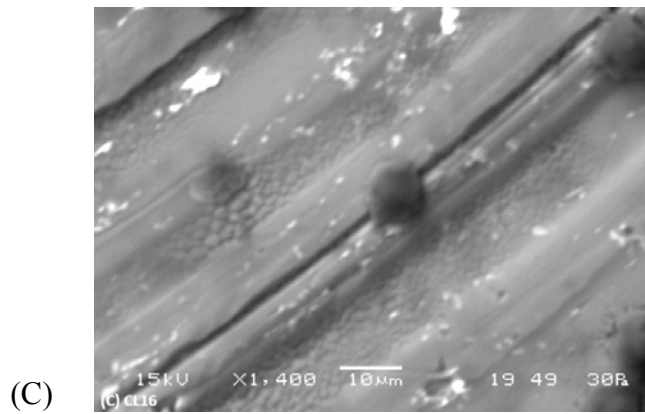
As the cell is loaded on the functional surface of the miniaturized cantilever, extracellular matrix (ECM) is developed between the cell, and cantilever's functional surface substrate. After that, the cell is adhered, then active polymerization, as well as cellular AF-myosin motor (actomyosin) interaction, contribute in cell's motility. The experimental analyses in Chapter 5, in terms of cantilever's bending due to electrostatic force, have greatly contributed into allocating signals that correspond to negative slope (bending downward), as opposed to signals

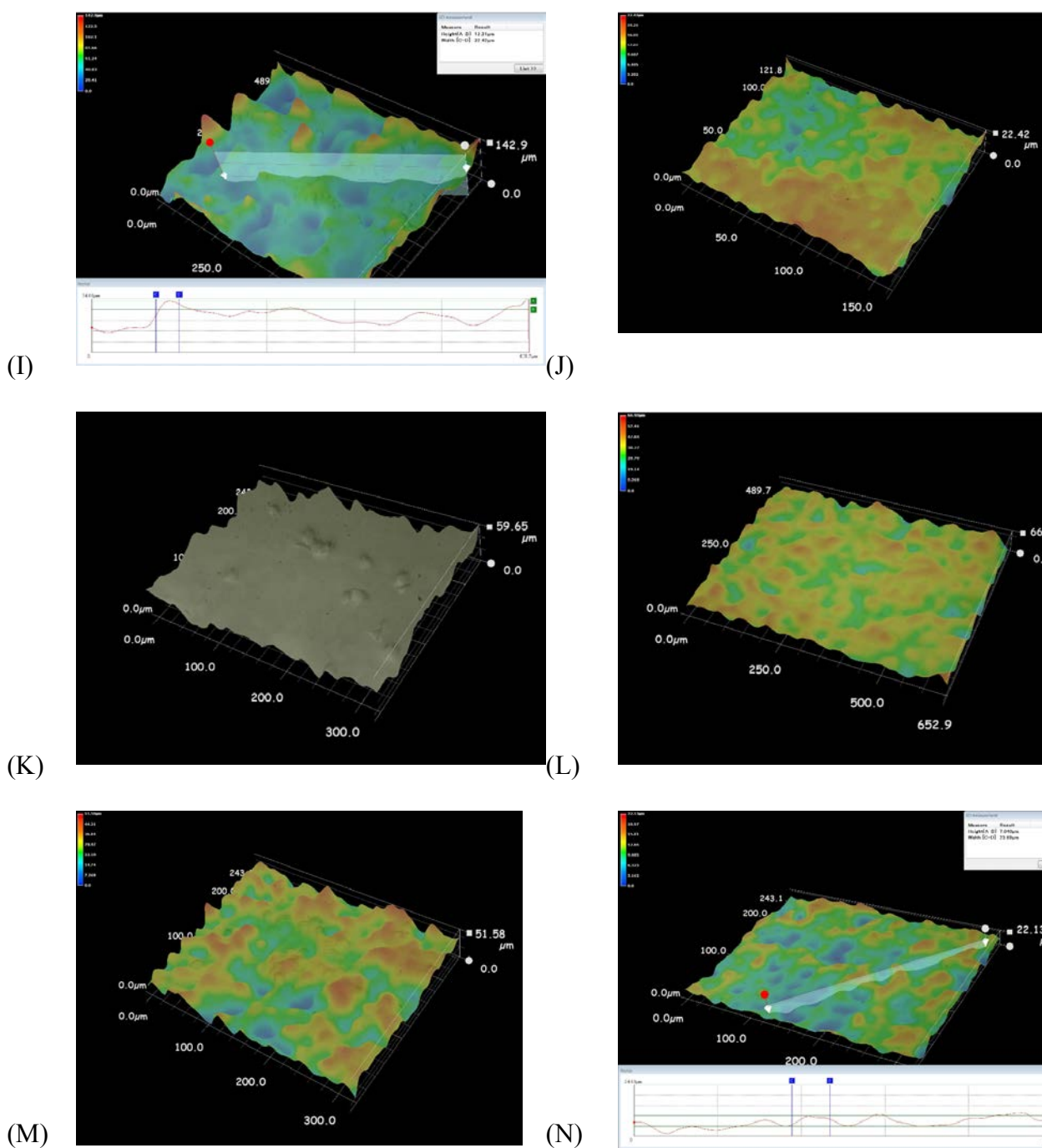
associated with positive slope due to cellular compressive surface stresses, imposed on the cantilever functional surface (upward transverse deflection).

Prior to discussing the findings on cellular contractile forces at different stages of melanoma, morphology analyses have been carried out by SEM and Keyence microscope. The cellular morphology has been evaluated in terms of its steepness that is in terms of its height (thickness), and contact surface area. As in [64], it has been demonstrated experimentally that having a considerable contact surface area, where the cell is spreading over, shall favour cell's viability, growth, and motility, whereas smaller area would lead to cell's apoptosis. This is also in agreement of the premise of Chapter 2 (LoC) in assuring exchange of oxygen and nutrients for cells, and disposing carbon dioxide out of the system, within a sufficient space to maintain cell viability. Figure 6.4 illustrates the depth compositions, and 3D pattern configurations, generated by Keyence microscope, as well as SEM images of melanoma cells.

The aims of the morphology analyses are to investigate cellular contact surface areas with flat substrate, and heights of cells; also the objective is to examine the status of these two geometrical factors as cells differ in their heterogeneities (advancement in the stage of metastasis).












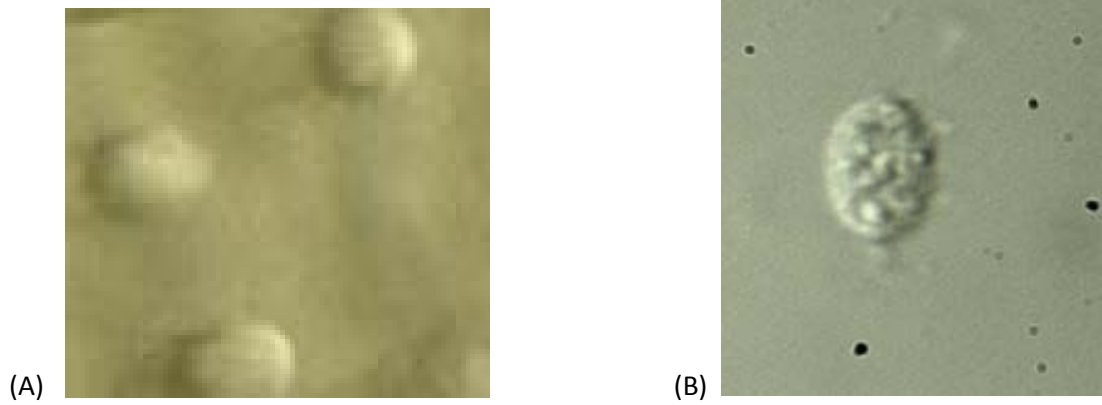
**Fig. 6.4** Investigation of cellular heights and their contact surface areas via the analyses of SEM images of (A) M4A4, (B) SK-MEL-1, (C) CL16, and (D) NM2C5, as well as depth compositions, and 3D pattern generated microscopic images of (E) LM3, (F) A375, (G) MDA-MB-231, (H) CL16, (I) NM2C5, (J) MCF7, (K) WM115, (L) SK-MEL-1, (M) G361, and (N) M4A4.

The metastasis heterogeneity of the eight melanoma cell lines, as well as breast adenocarcinoma cell (MDA-MB-231) have been thoroughly discussed in Chapter 4. Through SEM, microscopic depth composition analyses, and results obtained from Moxi Z, cell-line models have been characterized in terms of their average diameters, thicknesses (heights), and contact surface areas with the flat substrate. It has been noticed that cells' morphologies get steeper and steeper, as the level of metastasis increases that is cells spread more as they are at an advanced stage than if they were at an early one. The average cells' diameter get comparatively larger and larger as cells advance from a non-metastatic stage towards a highly metastatic phase. On the contrary, the average thickness (height) of the cells decreases as they progress in the metastatic stages. Accordingly, the cellular contact surface area with a flat substrate increases, as cells progress throughout the stages of non-metastatic, early, intermediate, late, and highly metastatic stage. Table 6.1 summarizes the morphology characteristics of the different stages of melanoma cellular metastasis.

					<b>Morph.</b>
Non-Metastatic	Early Stage Metastasis	Intermediate Metastasis	Late Metastasis	Highly Metastasis	Stage
NM2 C5	Averaged for M4A4, WM115, G361, SK-MEL-1	M4A4LM3-2GFP (LM3)	A375	M4A4LM3-4CL16GFP (CL16)	Cell-Line
13.400 $\mu\text{m}$	17.2 $\mu\text{m}$	17.7 $\mu\text{m}$	19.80 $\mu\text{m}$	20.25 $\mu\text{m}$	$d_{avg}$
18.200 $\mu\text{m}$	16.4 $\mu\text{m}$	14.2 $\mu\text{m}$	11.21 $\mu\text{m}$	7.308 $\mu\text{m}$	$t_c$
0.141 $\text{nm}^2$	0.232 $\text{nm}^2$	0.246 $\text{nm}^2$	0.308 $\text{nm}^2$	0.322 $\text{nm}^2$	$A_{avg}$

**Table. 6.1** Characterization of different stages of cancer metastasis based on their morphology, where  $d_{avg}$  is average diameter,  $t_c$  is average thickness/height of a cell, and  $A_{avg}$  is average contact surface area.

The obtained findings of cellular morphology confirm the viscoelastic characteristics of cells. As shown in Figure 6.5, the morphology varies from one stage to the other, as cells mostly experience smooth round shape at early stages of the metastasis, and then they elongate at late stages. Yin *et al.* [298] have developed high throughput imaging, and computational methods in analyzing cells' morphologies, and they have investigated the role of subset genes in cellular configurations; they were successful in allocating a subset of genes, among them tumor suppressor gene *PTEN*, within human metastatic melanoma cells, which would provide a better understanding of the role of genes on defining cellular shape. They have managed to categorize various cellular configurations: normal rounded, elongated, bipolar, spindle-shaped, small tear-drop shapes, large with smooth edges, and very large flat cells of irregular/non uniform edges.



**Fig. 6.5** (A) Non-metastatic NM2C5 smooth rounded morphology, and (B) Elongated late invasive malignant melanoma, A375.

Analyzing cell's configurations, in conjunction with its associated contractile force, would significantly assist in understanding the metastatic aspect of the cancer disease **pathogenesis**: contributing in cell's motilities and penetrations through other tissues and organs. Equations 6.11-6.14 are utilized to obtain the contractile force of a cell based on the obtained voltage signals from the Piezoresistive elements of the Wheatstone bridge. The developed numerical algorithm in Appendix C.3.1 provides a solution of the compressive force developed on the cantilever with respect to the normalized deflection.

The contractile force, of well-documented cell-line model in literature, MDA-MB-231, is first measured, and found to be  $-3.87 \pm 0.4 \mu\text{N}$  (Mean  $\pm$  SD,  $n = 3$ ), which is within the range of magnitude of the published finding of the contractile force for this cell line in literature ( $5 \mu\text{N}$ ) [281]. The MDA-MB-231 cell-line model has been used as a calibration model: testing the reliability of the proposed microcantilever based biomechatronic system. The discrepancy could be attributable to the constant changes in the viscoelastic form of the cell with time, and the different mathematical approach that had been pursued in arriving at the contractile force

by considering the surface stress loading on the cantilever surface [281]. However, considering the surface stress loading experienced by the beam accounts for the entire compressive surface stresses exerted at the entire width, and effective length of the beam. Therefore, in this study, the cellular contractile force is measured as per the area the cell occupies, where the effective cellular compressive surface stresses are applied. This is achieved by utilizing the Heaviside step function [295].

The obtained results of the contractile force of MDA-MB-231 has added confidence in the methodology pursued, and the performance of the developed biomechatronic system. The contractile forces of the eight-melanoma-cancer-cell lines of different genomic mutations have been characterized, and summarized in table 6.2. It has been demonstrated that the higher the diameter of the cell, the higher the contractile force exerted on the cantilever surface. The negative sign of the obtained contractile force indicates the compressive force characteristic experienced by the cell during its migration, upon which cellular motility is invariant in time from one cell to the other. The output voltage signal from the Piezoresistive elements of the Wheatstone bridge, after cell attachment and reaching steady state, confirms that beam has experienced a positive transverse deflection due to cell migration. It has been noted that the output voltage signal has increased considerably for the late and highly metastatic melanoma cell lines. However, it has been illustrated that there is a slight change between early stage and intermediate in terms of contractile force magnitude.



Cell-Line Model	Level of Metastasis	$F_c$ ( $\mu\text{N}$ ) Mean $\pm$ SD	$n$	$V_m$ (mV) Mean $\pm$ SD	$n$
MDA-MB-231	Invasive metastasis	$-3.870 \pm 0.400$	3	$-25.95 \pm 1.05$	17
NM2 C5	Non-metastatic	$-0.268 \pm 0.006$	5	$-52.62 \pm 1.53$	17
M4A4	Early stage melanoma	$-0.314 \pm 0.010$	5	$-46.67 \pm 0.64$	15
WM115	Low metastasis	$-0.329 \pm 0.005$	4	$-42.28 \pm 0.26$	10
G361	Primary metastasis	$-0.347 \pm 0.002$	3	$-34.32 \pm 0.86$	14
SK-MEL-1	Primary metastasis	$-0.376 \pm 0.001$	4	$-32.23 \pm 1.81$	12
M4A4LM3-2GFP	Intermediate metastasis	$-0.428 \pm 0.003$	5	$-32.03 \pm 1.25$	12
A375	Late invasive malignant	$-3.000 \pm 0.003$	3	$-17.25 \pm 0.38$	17
M4A4LM3-4CL16 GFP	Highly invasive metastasis	$-4.830 \pm 0.150$	4	$-9.390 \pm 0.32$	12

**Table 6.2** Contractile force and cell-membrane potential of different stages of cancer.

As demonstrated in Table 6.2, the cellular contractile force of a cell increases, as the cell advances in the metastatic stage – cell is becoming more aggressive and invasive. Furthermore, in correlation with the obtained results of Chapter 4, the increase of the contractile force accompany a decrease in the magnitude of the associated cell-membrane potential. From the morphological analyses described in this chapter, a cell becomes steeper; its contact surface area increases and its thickness decreases: if it is at a very late metastasis stage than if it were at an early one. Therefore, these experimental findings have investigated the raised hypothesis at the early chapters, which demonstrate that as cells progress in the metastasis stages, they become more aggressive/more invasive, and their motility and eventually their contractile forces increase. This would yield, on the other hand, a decrease in the cell-membrane potential. Furthermore, such approach in extracting the cellular contractile force has succeeded in differentiating in terms of the degree of metastasis severity between the closely related G361, and SK-MEL-1 primary metastasis cell line.

As per the analyses carried out in Chapter 3, as cells ascend in their metastatic potential, their depolarized activities increase: resulting in an excess of cytoplasm positivity of a cell, which is also interlinked to increase activities of  $Na^+$  ion channels [108, 112, 118, 119, 121, 144, 146]. This could justify the highly active polymerization process, experienced within advanced-stage-cancerous cells as opposed to less aggressive ones that would yield cellular motility. However, this requires in-depth analyses on the oncogene mutation of these cell-line models, which would be the target of future extension of this work.

## 6.7 Conclusion and Future Trends

In this chapter, different mechanisms of cell's motilities have been discussed; cell's migration contributes into many human diseases, among them is cancer. To clearly present the cellular motility stages, a description of cell's cytoskeleton is presented. Furthermore, various approaches of quantifying cellular contractile force has been illustrated.

Driven by the merits associated with the Piezoresistive cantilever-based sensor, a biomechatronic platform is designed, and further developed to extract the contractile force of eight-melanoma-cell-line models. This chapter presents a novel contribution in computing the contractile force of a cell based on a Heaviside step function  $H(s)$ , and pin-force model. Furthermore, to the best of the author's knowledge, this is the first time that the heterogeneity of eight melanoma cell lines are being characterized based on their contractile forces, and then such forces are correlated to their associated cell-membrane potentials, as well as cellular morphologies.

It has been demonstrated that as a cell advances in metastatic stages, its contractile force increases, and its associated morphology changes by becoming steeper with higher contact

surface area. Therefore, this chapter concludes the investigation of the hypothesis that as a cell progresses in metastatic stage, its contractile force increases and its morphology becomes steeper, whereas its cell-membrane potential decreases.

Understanding the physics of cellular contractile force could assist in allocating a pharmaceutical substance that would inhibit cellular motility: refrain cancer metastasis in forming a secondary tumor at a distant metastatic organ or tissue. In a general term, comprehending the physics associated with the loss of contractile force, e.g., in cardio diseases, could contribute in developing a miniaturized cell-driven motor system as proposed in [275]. The findings of this chapter would be extended to study the effect of substrate surface topography and rigidity, and their impact on cellular mechanobiology [299]. Furthermore, cellular modulus of elasticity, a measure of cellular resistance to elastic deformation, and its impact on nature of the disease will be thoroughly examined.

# Chapter 7

---

---

## Conclusion

---

---



*Young Stephen Hawking*

*"The whole history of science has been the gradual realization that events do not happen in an arbitrary manner, but that they reflect a certain*

*underlying order, which may or may not be divinely inspired."*



*A young adult Stephen Hawking*



*Stephen Hawking*

## Chapter 7: Summary, Conclusion, and Future Work

Two novel, highly versatile, biomechatronic platforms have been designed, modeled, and further developed to characterize the electrophysiology and mechanobiology of cells. Dedicated microelectronics together with customized software have been attained to functionalize, and empower the two biomechatronic systems. Furthermore, detailed microfabrication processes are illustrated to construct the miniaturized mechanical components of the biomechatronic platforms. A number of *in vitro* experiments were conducted to extract the cell-membrane potential, mass, and cellular contractile force. The first biomechatronic platform consists of a microfluidic and multi-electrode arrays (MEAs) module to characterize the biophysics of cells, whereas the second platform, of a microcantilever base with an embedded Piezoresistive Wheatstone bridge and microfluidic module, is utilized to quantify the mass and contractile forces of cells.

Various well-characterized melanoma cancer cell lines, with varying degrees of genetic complexities have been utilized: SK-MEL-1 (primary malignant metastatic melanoma), A375 (late invasive malignant melanoma), G-361 (primary malignant melanoma), WM-115 (low metastasis melanoma), NM2C5 (weakly/virtually non-metastatic melanoma), M4A4 (early stage metastatic), M4A4 LM3-2 GFP (intermediate stage second lung metastasis), and M4A4 LM3-4 CL16 GFP (highly metastatic third generation lung metastasis). In addition, well-documented cell models within literature, breast cancer adenocarcinoma human (*homo sapiens* MDA-MB-231), and early stage breast cancer (MCF7) have been used as calibration-cell

models for the microfabricated biomechatronic platforms on the basis of extracted cell-membrane potential and contractile force.

Contractile force is mainly responsible about cell motility, and it is initiated by cell signaling, where cell-membrane potential plays a dominant role in instructing cells to mobilize via electrochemical signals. It has been concluded in this study that as cancer cell progresses to ascending metastatic stages (healthy to late metastasis), the cell contractile force increases, while its associated cell-membrane potential decreases in magnitude, and its morphology gets steeper (higher surface contact area and lower cellular height). Additional *in vitro* experiments will be conducted on other types of cancer as well to confirm such findings. Furthermore, it has been illustrated that higher metastatic cells are more massive than those at early stages of metastasis.

The proposed versatile bio-mechatronic platforms could be utilized in various fields such as cardiology, immunotherapy, astrobiology, and biophysics. The novelties flourished within this work are manifested in fivefold: (1) developing a mathematical model that utilizes a Heaviside step function, as well as pin-force model to compute the contractile force of a biological cell, (2) deriving an expression of cell-membrane potential based on Laplace and Fourier Transform and their Inverse Transform functions by encountering Warburg diffusion impedance factor, (3) microfabricating novel biomechatronic platforms with associated microelectronics and customized software that extract cellular physics and mechanics, (4) developing a label-free biomarker, (5) to the first time in literature, and to the best of the author's knowledge, discriminating different stages and morphology of cancer cell melanoma based on their cell-membrane potentials, and associated contractile forces.

In addition to the investigated applications of the developed biomechatronic platforms within this research, the fabricated miniaturized devices are designed and developed to be

highly versatile; therefore, this could easily extend the work within this research to perform cell manipulation, facilitate *in vitro* stem-cell proliferation, identify cell signal propagation, and examine cell-cell communication via electrical means through MEAs patterned on glass substrate. Furthermore, the microfluidic chamber will be enhanced to provide an optimal environment of cell incubation throughout the experiment based on the requirements of cell's viability illustrated in Chapter 2. Furthermore, the effective functional layer of the microcantilever will be coated to analyze antibody/antigen binding mechanism, and correlate the mechanical deflection of the beam to the identification of a vaccine based on such binding. Finally, driven by the work of Nayfeh *et al.* [198], the claimed enhancement of sensitivity of the miniaturized deflection of the beam by injecting harmonic AC potential, superimposed to a static DC voltage, will be investigated experimentally.

To comprehensively conclude the findings of this research in drawing the correlations among electrophysiology, morphology, and contractile forces of cells, this research study will be extended to investigate and discuss the interrelation of oncogenes' mutations within each stage of melanoma cells, experiencing different metastases, which are mainly responsible about melanoma cells' motilities. Two oncogenes are of a great interest to examine: JAK and STAT3 [276, 300-302].

The Janus Kinase (JAK) family of non-receptor tyrosine kinases (NRTKs) is responsible for actomyosin contractility force for cell's migration [300]. STAT3 is a downstream signal transduction resulted from the activation of JAK [300, 301]. STAT3 is part of the signal transducer and activator transcription 3 family, and it plays a major role in cell's motility, immune response, anti-apoptosis, and proliferation [302]. It is also believed that JAK/STAT preserves tumorigenesis, and at some events stimulates tumor angiogenesis [276]. Thus,



---

inhabitation of JAK/STAT signal pathway could arrest cellular mitosis, and thus prevent cancer from invading tissues and others organs.

An immune assay approach shall be utilized to investigate the role of JAK/STAT on the proposed 8 melanoma-cell lines' motilities, by measuring their activities, functions, inhibitions, and knockdowns. A proposed ELISA assay (eBioscience, SD, USA) will be utilized to capture the phosphorylated human STAT3 within cell lysates. The STAT3 activity will be correlated to the extracted electrophysiology of the melanoma cell, and its associated contractile force measurement.

---

# References

- [1] Alqabandi, J. Abdul Mottal, U., and Youcef-Toumi, K., "Extracting cancer cell line electrochemical parameters at the single cell level using a microfabricated device," *Biotechnology Journal*, Vol. 4, pp. 216-223, 2009.
- [2] Suresh, S., "Biomechanics and biophysics of cancer cells." *Acta Biomaterialia*. Vol. 3, pp. 413-438, 2007.
- [3] Zhou, Y., Wang, Z., Yue, W., Tang, K., Ruan, W., Zhang, Q., and Liu, L., "Label-free Detection of p53 Antibody Using A Microcantilever Biosensor With Piezoresistive Readout," *IEEE Sensors Conference*., pp. 819-822, 2009.
- [4] Graeber, T. G., Osmanian, C., Jacks, T., David, H., Cameron, J. Koch, Scott, W. Lowe, Amato, and J. Giaccia, "Hypoxia-mediated selection of cells with diminished apoptotic potential in solid tumors," *Nature*, Vol. 379, pp. 88-91, 1996.
- [5] Pellman, D., "Cell biology: Aneuploidy and cancer," *Nature*, Vol. 446, pp. 38-39, 2007.
- [6] Dale W., and Laird, D. W., "The gap junction proteome and its relationship to disease," *Trends in Cell Biology*, Vol. 20, No. 2, pp. 92-101, 2010.
- [7] Lodish, H., Berk, A., Zipursky, L. S., Matsudaira, P., Baltimore, D., and J. Darnell, W. H. (Eds.), "Molecular Cell Biology," New York, 4<sup>th</sup> ed., 2000.
- [8] Sims, C. E., Allbritton, N. L., "Analysis of single mammalian cells on-chip," Vol. 7, pp. 423-440, 2007.
- [9] Kraus, T., Verpoorte, E., Linder, V., Franks, W., Hierlemann, A., Heer, Flavio, Hafizovic, S., Fujji, T., de Rooij, N. F., and Koster, S., "Characterization of a microfluidic dispensing system for localized stimulation of cellular networks," Vol. 6, pp. 218-229, 2006.
- [10] ASHMORE, J. F., "A fast motile response in guinea-pig outer hair cells: the cellular basis of the cochlear amplifier," *J. Physiol.*, 388, pp. 323-347, 1987.
- [11] Yang D., Welm, A., and Bishop, J. M., "Cell division and cell survival in the absence of surviving," *Proc. Natl. Acad. Sci. U S A*. 2004, Vol. 101, No. 42, pp. 15100-15105, 2004.
- [12] Kim, H. S. *et al.*, "Metastasis of hepatocellular carcinoma to the small bowel manifested by intussusception," *World J. Gastroenterology*. 12 (12), pp. 1969-197, 2006.
- [13] Mihaljevic, A. L., Michalski, C. W., Friess, H., and Kleeff, J., "Molecular mechanism of pancreatic cancer - understanding proliferation, invasion, and metastasis," Vol. 395, No. 4, pp. 295-308, 2010.

- 
- [14] Zarghooni, M., *et al.*, “Whole-Genome Profiling of Pediatric Diffuse Intrinsic Pontine Gliomas Highlights Platelet-Derived Growth Factor Receptor  $\alpha$  and Poly (ADP-ribose) Polymerase As Potential Therapeutic Targets,” *JCO*, Vol. 28, No. 8, pp. 1337-1344, 2010.
- [15] Meyvantsson, I., and Beebe, D. J., “Cell Culture Models in Microfluidic Systems,” *Annu. Rev. Anal. Chem.*, Vol. 1, pp. 423-449, 2008.
- [16] Turner, N., and Grose, R., “Fibroblast growth factor signaling: from development to cancer,” *Nature Reviews Cancer*, Vol. 10, pp. 116-129, 2010.
- [17] Feldmann, G., *et al.*, “Inhibiting the Cyclin-Dependent Kinase CDK5 Blocks Pancreatic Cancer Formation and Progression through the Suppression of Ras-Ral Signaling,” *Cancer Res*, Vol. 70, pp. 4460-4469, 2010.
- [18] Delia, M., “miRNA control of apoptotic programs: focus on ovarian cancer, *Expert Review of Molecular Diagnostics*,” Vol. 11, No. 3, pp. 277-286, 2011.
- [19] Frago, A., Latta, D., Laboria, N., Germar, F., Hansen-Hagge, T. E., Kemmner, W., Gärtner, C., Klemm, R., Drese, K. S., and O'Sullivan, C. K., “Integrated microfluidic platform for the electrochemical detection of breast cancer markers in patient serum samples,” *Lab Chip*, Vol. 11, pp. 625-631, 2011.
- [20] Sundelacruz, S., Levin, M., Kaplan, D. L., “Role of Membrane Potential in the Regulation of Cell Proliferation and Differentiation,” *Stem Cell Rev and Rep.* 2009, 5, 231-246.
- [21] American Cancer Society. *Cancer Facts & Figures*. Atlanta: American Cancer Society; 2010.
- [22] Wright, C. J. E., “Prognosis in cutaneous and ocular malignant melanoma: A study of 222 cases,” *The Journal of Pathology and Bacteriology*, Vol. 61, Issue 4, pp. 507–525, 1949.
- [23] Wilhelm, I., Molnár, J., Fazakas, C., Haskó, J., Krizbai, I. A., “Role of the Blood-Brain Barrier in the Formation of Brain Metastases,” *Int. J. Mol. Sci.*, Vol. 14, pp. 1383-1411, 2013.
- [24] Kioi, M., *et al.*, “Inhibition of vasculogenesis, but not angiogenesis, prevents the recurrence of glioblastoma after irradiation in mice,” *J Clin. Invest.* Vol. 120, No. 3, pp. 694–705, 2010.
- [25] Wang, B. *et al.*, “E-Cadherin Expression Is Regulated by miR-192/215 by a Mechanism That Is Independent of the Profibrotic Effects of Transforming Growth Factor- $\beta$ . Diabetes,” Vol. 59, No. 7, pp. 1794-1802, 2010.
- [26] Folkman, J., “The vascularization of tumours,” *Sci. Am.*, Vol. 234, pp. 58–64, 1976.
- [27] American Cancer Society. *Cancer Facts & Figures*. Atlanta: American Cancer Society; 2013.
-

- 
- [28] Li, H., "Cancer-Expanded Myeloid-Derived Suppressor Cells Induce Anergy of NK Cells through Membrane-Bound TGF- $\beta$ 1," *The Journal of Immunology*, pp. 240-249, 2008.
- [29] Schatton, T. *et al.*, "Identification of cells initiating human melanomas," *Nature*, Vol. 451, pp. 345-349, 2008.
- [30] Choi, Y.-E., Kwak, J.-W., Park, J. W., "Nanotechnology for Early Cancer Detection," *Sensors*. 2010, 10, 428-455.
- [31] Ferrari, M. (Ed.), "Cancer Nanotechnology: Opportunities and Challenges," *Nature Reviews*. 2005, 5, 161-171.
- [32] Datar, R., Kim, S., Jeon, S., Hesketh, P., Manalis, S., Boisen, A., Thundat, T., "Cantilever Sensors: Nanomechanical Tools for Diagnostics," *MRS bulletin*. 2009, 34, 449-454.
- [33] Kim, S.-K., Kang, K. W., Lee, J. S., Kim, H. K., Chang, H. J., Choi, J. Y., Lee, J. H., Ryu, W., Kim, Y.-W., Bae, J.-M. "Assessment of lymph node metastases using  $^{18}\text{F}$ -FDG PET in patients with advanced gastric cancer," *Eur. J. Nucl. Med. Mol. Imaging*. 2006, 33, no. 2, 148-155.
- [34] Trojan, J., Schroeder, O., Raedle, J., Baum, R. P., Hermann, G., Jacobi, V., Zeuzem, S. "Fluorine-18 FDG positron emission tomography for imaging of hepatocellular carcinoma," *The American Journal of Gastroenterology*. 1999, 94, no. 11, 3314-3319.
- [35] Kitajima, K., Murakami, K., Yamasaki, E., Fukasawa, I., Inaba, N., Kaji, Y., Sugimura, K, "Accuracy of  $^{18}\text{F}$ -FDG PET/CT in Detecting Pelvic and Paraaortic Lymph Node Metastasis in Patients with Endometrial Cancer," *AJR Women's Imaging*. 2008, 190, no. 6, 1652-1658.
- [36] Kinkel, K., Lu, Y., Both, M., Warren, R. S., Theoni, R.F., "Detection of Hepatic Metastases from Cancers of the Gastrointestinal Tract by Using Noninvasive Imaging Methods (US, CT, MR Imaging, PET): A Meta-Analysis," *Radiology*. 2002, 224, 748-756.
- [37] Bonomo, L., Ciccotosto, C., Guidotti, A., Storto, M. L. "Lung cancer staging: the role of computed tomography and magnetic resonance imaging," *European Journal of Radiology*. 1996, 23, 35-45.
- [38] Pisano, E. D., Gatsonis, C., Hendrick, E., Yaffe, M., Baum, J. K., Acharyya, S., Conant, E. F., Fajardo, L. L., Basset, L., D'Orsi, C., Jong, R., Rebner, M., "Diagnostic performance of digital versus film mammography for breast-cancer screening," *N. Engl. J Med.*, 353, no. 17, pp. 1773-1783, 2005.
- [39] Deguchi, T., Yang, M., Ehara, H., It, S., Nishino, Y., Takahashi, Y., Ito, Y., Shimokawa, K., Tanaka, T., Imaeda, T., Doi, T., Kawada, Y., "Detection of micrometastatic prostate cancer cells in the bone marrow of patients with prostate cancer," *Br J. Cancer*. 1997, 75, no.5, 634-638.
-

- 
- [40] Salomon, G., Köllerman, J., Thederan, I., Chun, F. K.H., Budäus, L., Schlomm, T., Isbarn, H., Heinzer, H., Huland, H., Graefen, M., “Evaluation of Prostate Cancer Detection with Ultrasound Real-Time Elastography: A Comparison with Step Section Pathological Analysis after Radical Prostatectomy,” *European Urology*. 2008, 54, no. 6, 1354-1362.
- [41] Lotan, Y., Roehrborn, C. G., “Sensitivity and specificity of commonly available bladder tumor markers versus cytology: results of a comprehensive literature review and meta-analyses,” *Urology*. 2003, 61, no. 1, 109-118.
- [42] Hamaoka, T., Madewell, J. E., Podoloff, D. A., Hortobagyi, G. N., and Ueno, N. T., “Bone Imaging in Metastatic Breast Cancer,” *Journal of Clinical Oncology*. 2004, 22, no. 14, 2942-2953.
- [43] Robbins, E., “Radiation risks from imaging studies in children with cancer,” *Pediatric Blood and Cancer*. 2008, 51, no. 4, 453-457.
- [44] Gimbel, J. R., Kanal, E. (Eds.). “Can Patients With Implantable Pacemakers Safely Undergo Magnetic Resonance Imaging?,” *Journal of the American College of Cardiology Foundation*. 2004, 43, no. 7, 1325-1327.
- [45] Teissl, C., Kremser, C., Hochmair, E. S., Hochmair-Desoyer, I. J., “Magnetic Resonance Imaging and Cochlear Implants: Compatibility and Safety Aspects,” *Journal of Magnetic Resonance Imaging*. 1999, 9, 26-38.
- [46] Rasooly, A., and Jacobson, J., “Development of biosensors for cancer clinical testing. Biosensors and Bioelectronics,” Vol. 21, No. 10, pp. 1851-1858, 2006.
- [47] Skelley, A. M., Cleaves, H. J., Jayarajah, C. N., Bada, J. L., and Mathies, R. A., “Application of the mars organic analyzer to nucleobase and amine biomarker detection,” *Astrobiology*, Vol. 6, No. 6, pp. 824-837, 2006.
- [48] Sims, C. E., and Allbritton, N. L., “Analysis of single mammalian cells on-chip,” *Lab Chip*, Vol. 7, pp. 423-440, 2007.
- [49] Seidl, J., Knuechel, R., and Kunz-Schughart, L. A., “Evaluation of membrane physiology following fluorescence activated or magnetic cell separation,” *Cytometry*, Vol. 36, pp. 102-111, 1999.
- [50] A. Bejan and S. Lorente, “Design with Constructal Theory,” Wiley, Hoboken, 2008.
- [51] A. Bejan and J. P. Zane, “Design in Nature,” Doubleday, New York, 2012.
- [52] Breslauer, D. N., Lee, P. J., and Lee, L. P., “Microfluidics-based systems biology,” *Mol. BioSyst.*, Vol. 2, pp. 97-112, 2006.
- [53] Fragoso, *et al.*, “Integrated microfluidic platform for the electrochemical detection of breast cancer markers in patient serum samples,” *Lab Chip*, Vol. 11, pp. 625-631, 2011.
-

- 
- [54] Kim, L., Toh, Y.-C., Voldman, J., and Yu, H., “A practical guide to microfluidic perfusion culture of adherent mammalian cells,” *Lab Chip*, Vol. 7, pp. 681-694, 2007.
- [55] Hung, P. J., Lee, P. J., Sabounchi, P., Aghdam, N., Lin, R., and Lee, L. P., “A novel high aspect ratio microfluidic design to provide a stable and uniform microenvironment for cell growth in a high throughput mammalian cell culture array,” *Lab Chip*, Vol. 5, pp. 44-48, 2005.
- [56] Kim, L., Vahey, M. D., Lee, H.-Y., Voldman, J., “Microfluidic arrays for logarithmically perfused embryonic stem cell culture,” *Lab Chip*, Vol. 6, pp. 394-406, 2006.
- [57] Nevill, J. T., and Cooper, R., Dueck, M., Breslauer, D. N., and Lee, L. P., “Integrated microfluidic cell culture and lysis on a chip,” *Lab Chip*, Vol. 7, pp. 1689-1695, 2007.
- [58] Dimov, I. K., Kijanka, G., Park, Y., Ducrée, J., Kang, T., and Lee, L. P., “Integrated microfluidic array plate (iMAP) for cellular and molecular analysis,” *Lab Chip*, Vol. 11, pp. 2701-2710, 2011.
- [59] María José Escámez, Marta García, Fernando Larcher, Alvaro Meana, Evangelina Muñoz, Jose Luis Jorcano, and Marcela Del Río, “An *In Vivo* Model of Wound Healing in Genetically Modified Skin-Humanized Mice,” *Journal of Investigative Dermatology*, Vol. 123, pp. 1182–1191, 2004.
- [60] Shultz, L. D., Ishikawa, F., and Greiner, D. L., “Humanized mice in translational biomedical research,” *Nature Reviews Immunology*, Vol. 7, pp. 118-130, 2007.
- [61] Vickerman, V., Blundo, J., Chung, S., and Kamm, R., “Design, fabrication and implementation of a novel multi-parameter control microfluidic platform for three-dimensional cell culture and real-time imaging,” *Lab Chip*, Vol. 8, pp. 1468-1477, 2008.
- [62] Gómez-Sjöberg, R., Leyrat, A. A., Pirone, D. M., Chen, C. S., and Quake, S. R., “Versatile, Fully Automated, Microfluidic Cell Culture System,” *Anal. Chem.*, Vol. 79, pp. 8557-8563, 2007.
- [63] Meyvantsson, I., and Beebe, D. J., “Cell Culture Models in Microfluidic Systems,” *Annu. Rev. Anal. Chem.*, Vol. 1, pp. 423-449, 2008.
- [64] El-Ali, J., Sorger, P. K., and Jensen, K. F., “Cells on chips,” *NATURE*, Vol. 442, pp. 403-411, 2006.
- [65] Ziolkowska, K., Kwapiszewski, R., and Brzózka, Z., “Microfluidic devices as tools for mimicking the *in vivo* environment,” *New J. Chem.*, Vol. 35, pp. 979-990, 2011.
- [66] *Dorland’s Medical Dictionary for Health Consumers*. 2007 by Saunders, an imprint of Elsevier, Inc.
- [67] Rhee, S. W., Taylor, A. M., Tu, C. H., Cribbs, D. H., Cotman, C. W., and Jeon, N. L., “Patterned cell culture inside microfluidic devices,” *Lab Chip*, Vol. 5, pp. 102-107, 2005.
-

- 
- [68] Kim, C., Lee, K. S., Bang, J. H., Kim, Y. E., Kim, M.-C., Oh, K. W., Lee, S. H., and Kang, J., Y., “3-Dimensional cell culture for on-chip differentiation of stem cells in embryoid body,” *Lab Chip*, Vol. 11, pp. 874-882, 2011.
- [69] Romer, L. H., Konstantin, G. B., and Garcia, J. G. N., “Circ. Res.,” Vol. 98, pp. 606-616, 2006.
- [70] Lecrec, E., Sakai, Y., and Fujii, T., “Cell Culture in 3-Dimensional Microfluidic Structure of PDMS (polydimethylsiloxane),” *Biomedical Microdevices*, Vol. 5, No. 2, pp. 109-114, 2003.
- [71] Cheng, Y. Luo, X., Tsao, C.-T., Wu, H.-C., Betz, J., Payne, G. F., Bentley, W. E., and Rubloff, G. W., “Biocompatible multi-address 3D cell assembly in microfluidic devices using spatially programmable gel formation,” *Lab Chip*, Vol. 11, pp. 2316-2318, 2011.
- [72] Stone, H. A., “Introduction to fluid dynamics for microfluidic flows,” *CMOS Biotechnology*, Springer, pp.5-30, 2007.
- [73] Prakash, S. B., and Abshire, P., “Tracking cancer cell proliferation on a CMOS capacitance sensor chip,” *Biosensors and Bioelectronics*, Vol. 23, pp. 1449-1457, 2008.
- [74] Eddington, D. T., Liu, R. H., Moore, J. S., and Beebe, D. J., “An organic self-regulating microfluidic system,” *Lab Chip*, Vol. 1, pp. 96-99, 2001.
- [75] Estrela, P., and Miglirato, P., “Chemical and biological sensors using polycrystalline silicon TFTs,” *J. Mater. Chem.*, Vol. 17, pp. 219-224, 2007.
- [76] Cross, J. D., and Craighead, H. G., “Micro- and nanofluidics for biological separations,” *CMOS Biotechnology*, Springer, pp.31-75, 2007.
- [77] Ezashi, T., Das, P., and Roberts, R. M., “Low  $O_2$  tensions and the prevention of differentiation of human embryonic stem cells,” *Proc. Natl. Acad. Sci. U. S. A.*, Vol. 102, pp. 4783-4788, 2005.
- [78] Allen, J. W., Khetani, S. R., and Bhatia, S. N., “In vitro zonation and toxicity in a hepatocyte bioreactor,” *Toxicol. Sci.*, vol. 84, pp. 110-119, 2005.
- [79] Tilles, A. W., Baskaran, H., Roy, P., Yarmush, M. L., and Toner, M., “Effects of oxygenation and flow on the viability and function of rat hepatocytes cocultured in a microchannel flat-plate bioreactor,” *Biotechnol. Bioeng.*, Vol. 73, pp. 379-389, 2001.
- [80] Lee, K.L., Baker, R.W., and Lonsdale, H.K., “Membranes for power generation by pressure-retarded osmosis,” *Journal of Membrane Science*, Elsevier B.V., Volume 8, Issue 2, Pages 141–171, 1981.
- [81] Seger, U., “Electrical Cell Manipulation in Microfluidic Systems,” Ph.D. Dissertation, Ecole Polytechnique Fereale Lausanne, EPFL 2006.
-



- 
- [82] Body JP, Yager P, Goldstein RE and Austin RH, "Biotechnology at low Reynolds numbers," *Biophysical Journal*, Vol. 71: 2, 44, pp. 3430-3441. 1996.
- [83] Basalo, I., Chahine, N., Kaplun, M., Chen, F., Hung, T., Ateshian, G., "Chondrotini sulfate reduces the friction coefficient of articular cartilage," *Journal of Biomechanics*, 40, pp. 1847-1854, 2007.
- [84] Oren, A., Pri-El, N, Shapiro, O, and Siboni, N., "Buoyancy studies in natural communities of square gas-vacuolate archea in saltern crystallizer ponds," *Saline Systems*, 2:4, 2006.
- [85] Hellmich, W., Greif, D., Pelargus, C., Anselmetti, D., and Ros, A., "Improved native UV laser induced fluorescence detection for single cell analysis in poly(dimethylsiloxane) microfluidic devices," *J. Chromatogr. A*, Vol. 1130, pp. 195-200, 2006.
- [86] Issadore, D., Franke, T., Brown, K. A., and Westervelt, R. M., "A microfluidic microprocessor: controlling biomimetic containers and cells using hybrid integrated circuit/microfluidic chips," *Lab Chip*, Vol. 10, pp. 2937-2943.
- [87] Lisdat, F., and Schafer, D., "The use of electrochemical impedance spectroscopy for biosensing," *Anal. Bioanal. Chem.*, Vol. 391, pp. 1555-1567, 2008.
- [88] Ficher, N. O., Tarasow, T. M., and Tok, J. B.-H., "Heightened sense for sensing: recent advances in pathogen immunoassay sensing platforms," *Analyst*, Vol. 132, pp. 187-191, 2007.
- [89] Dworak, B. J., and Wheeler, B. C., "Novel MEA platform with PDMS microtunnels enables the detection of action potential propagation from isolated axons in culture," *Lab Chip*, Vol. 9, pp. 404-410, 2009.
- [90] Rohwedder, J. J. R., and Pasquini, C., "Multi-electrode detection in voltammetry Part I. A versatile multi-channel voltammetric instrument," *Analyst*, Vol. 123, pp. 1641-1648, 1998.
- [91] Freire, R. S., Rohwedder, J. J. R., and Pasquini, C., "Multi-electrode detection in voltammetry Part 3. Effects of array configuration on the Hadamard multiplexed voltammetric technique," *Analyst*, Vol. 124, pp. 1657-1660, 1999.
- [92] Palanker, D., Vankov, A., Huie, P., Baccus, S., "Design of high-resolution optoelectronic retinal prosthesis," *Journal of Neural Engineering*, 2, pp.105-120, 2005.
- [93] Johnson, A. Sadoway, D, Cima, M, and Langer, R., "Design and Testing of an Impedance-Based Sensor for Monitoring Drug Delivery," *Journal of the Electrochemical Society*, 2005.
- [94] Environmental, Chemistry & Hazardous Materials News, Careers & Resources: <http://environmentalchemistry.com>.
-



- 
- [95] Pekar R., "Percutaneous Bio-Electrotherapy of Cancerous Tumors: A Documentation of Basic Principles and Experiences with Bio-Electrotherapy," Munich, Germany: Verlag Wilhelm Maudrich, 1997.
- [96] Sundelacruz, S., Levin, M., and Kaplan, D. L., "Role of Membrane Potential in the Regulation of Cell Proliferation and Differentiation." *Stem Cell Rev and Rep.* 2009, 5, pp 231–246.
- [97] Ashrafuzzaman, M., and Tuszynski, J., "Membrane Biophysics (Structure of Membranes), Biological and Medical Physics, Biomedical Engineering," Springer-Verlag Berlin Heidelberg, 2012.
- [98] Tigli, O., Bivona, L., Berg, P., Zaghloul, M. E., "Fabrication and Characterization of a Surface-Acoustic-Wave Biosensor in CMOS Technology for Cancer Biomarker Detection," *IEEE Transactions on Biomedical Circuits and Systems.* 4, no. 1, pp. 62-73, 2010.
- [99] Tigli, O., Zaghloul, M. E., "A Novel Saw Device in CMOS: Design, Modeling, and Fabrication," *IEEE Sensors Journal*, 7, no. 2, pp. 219-227, 2007.
- [100] Sharma, P., "Highly sensitive ultraviolet detector based on ZnO/LiNbO<sub>3</sub> hybrid surface acoustic wave filter," *Appl. Phys. Lett.* 2003, 83, no. 17, pp. 3617-3619.
- [101] Ho, C. K., Lindgren, E. R., Rawlinson, K. S., McGrath, L. K., Wright, J. L., "Development of a Surface Acoustic Wave Sensor for In-Situ Monitoring of Volatile Organic Compounds," *Sensors.* 2003, 3, 236-247.
- [102] Clorennec, D., Royer, D., "Analysis of surface acoustic wave propagation on a cylinder using laser ultrasonics," *Appl. Phys. Lett.* 2003, 82, no. 25, 4608-4610.
- [103] Yeo, L. Y., Friend, J. R., "Ultrafast microfluidic using surface acoustic waves," *Biomicrofluidics.* 2009, 3, 012002-1-23.
- [104] Vellekoop, M. J. "Acoustic wave sensors and their technology," *Ultrasonics.* 1998, 36, no. 1-5, 7-14.
- [105] Wang, X. Ellis, J. S., Kan, C.-D., Li, R.-K., Thompson, M., "Surface immobilization and properties of smooth muscle cells monitored by on-line acoustic wave detector," *Analyst.* 2008, 133, 85-92.
- [106] Chin, W. WL., Thong, P. SP., Bhuvaneswari, R., Soo, K. C., Heng, P. WS., Olivo, M., "In-vivo optical detection of cancer using chlorine e6-polyvinylpyrrolidone induced fluorescence imaging and spectroscopy," *BMC Medical Imaging.* 2009, 9:1, 1-13.
- [107] Pierce, M. C., Richard-Kortum, R., "Low-Cost Portable Optical Imaging Systems for Cancer Diagnosis," *32<sup>nd</sup> Annual International Conference of the IEEE EMBS.* 2010, 1093-1096.
-

- 
- [108] Sun, D., Gong, Y., Kojima, H., Wang, G., Ravinsky, E., Zhang, M., Minuk, G. Y., "Increasing cell membrane potential and GABAergic activity inhibits malignant hepatocyte growth," *Am J Physical Gastrointest Liver Physiol.* 2003, 285, 12-19.
- [109] Pais, A., Banerjee, A., Klotzkin, D., Paputsky, I., "High-sensitivity, disposable lab-on-a-chip with thin-film organic electronics for fluorescence detection," *Lap Chip.* 2008, 8, 794-800.
- [110] Gronewold, T. M. A., "Surface acoustic wave sensors in the bioanalytical field: Recent trends and challenges," *Analytical Chemica ACTA.* 2007, 603, 119-128.
- [111] Shin, K.-S., Lee, S. W., Han, K.-C., Kim, S. K., Yang, E. K., Park, J. H., Ju, B.-K., Kang, J. Y., Kim, T. S. "Amplification of fluorescence with packed beads to enhance the sensitivity of miniaturized detection in microfluidic chip," *Biosensors and Bioelectronics.* 2007, 22, 2261-2267.
- [112] Pancrazio, J., Viglione, M., Tabbara, I., Kim, Y., "Voltage-dependent Ion Channels in Small-Cell Lung Cancer Cells," *Cancer Research.* 1989, 49, 5901-5906.
- [113] DeFelice, L., "Electrical Properties of Cells: Patch Clamp for Biologists," Plenum Press. New York, 1997, 49-121.
- [114] Stuart, G. J., & Palmer, L. M. (2006), "Imaging membrane potential in dendrites and axons of single neurons." *Pflugers Archive*, 453, pp. 403–410.
- [115] Cross, J. D., and Craighead, H. G., "Micro and Nano Fluidics for Biological Separations," *CMOS Biotechnology*, Springer, pp. 31-75, 2007.
- [116] Brown, G., "The Energy of Life: The Science of What Makes Our Minds and Bodies Work," The Free Press, New York 1999.
- [117] Reilly, J. P., "Applied Bioelectricity: From Electrical Stimulation to Electropathology," Springer, New York 1998.
- [118] Marino, A. A., Morris, D. M., Schwalke, M. A., Iliev, I. G., Rogers, S., "Electrical Potential Measurements in Human Breast Cancer and Benign Lesions," *Tumor Biol.* 1994, 15, 147-152.
- [119] Cone, C. D., Jr., Tongier, M., Jr., "Control of Somatic Cell Mitosis by Simulated Changes in Transmembrane Potential Level," *Oncology.* 1971, 25, Issue no. 2, 168-182.
- [120] Schaefer, A., Hempling, H., Handler, E. E., Handler E. S., "Measurement of the Electrical Potential Difference and the Distribution of Ions in the Shay Chloroleukemic Tumor Cell," *Cancer Res.* 1972, 32, 1170-1176.
- [121] Marino, A. A., Iliev, I. G., Schwalke, M. A., Gonzalez, E., Marler, K. C., Flanagan, C. A., "Association between Cell Membrane Potential and Breast Cancer," *Tumor Biol.* 1994, 15, 82-89.
-

- 
- [122] Ashcroft, F., "Ion Channels and Disease," Academic Press SD California. 2000.
- [123] Nordenstrom BEW. "Biologically Closed Circuit: Clinical, Experience and Theoretical Evidence for an Additional Circulation," Stockholm, Sweden: Nordic Medical Publications, 1983.
- [124] Chou CK, Vora N, Li JR, *et al.*, "Development of electrochemical treatment at the City of Hope," In proceedings of the Fourth International Symposium on Biologically Closed Electric Circuits. Bloomington, MN: International Association for Biologically Closed Electric Circuits in Biomedicine, pp. 100-103, October 26-29, 1997.
- [125] Dousaw FR, Szasz A., "Electrochemical therapy of cancer. A new treatment modality for cancer destruction. Clinical use and experience," Proceedings of the Fourth International Symposium on Biologically Closed Electric Circuits. Bloomington, MN: International Association for Biologically Closed Electric Circuits in Biomedicine, pp. 75-99, October 26-29, 1997.
- [126] Li KH, Xin YL, Gu B, *et al.*, "Effects of direct electric current on dog liver: possible mechanisms for tumor electrochemical treatment," Bioelectromagnetics 1997; 18:2.
- [127] Hope, A, and Lles S., "Technology review: The use of electrical impedance scanning in the detection of breast cancer," Breast cancer research, Vol. 6, pp 69-74, 2003.
- [128] Han, A., Yang, L., and Fraizer A., "Quantification of the Heterogeneity in Breast Cancer Cell Lines Using Whole-Cell Impedance Spectroscopy," Imaging, Diagnosis, Prognosis. Jan 2007.
- [129] Yun, Y., Dong, Z, Shanov, Vesselin, and Schulz, M., "Electrochemical impedance measurement of prostate cancer cells using carbon nanotube array electrodes in a microfluidic channel," Nanotechnology 18 (2007) 465505 (7pp).
- [130] Sverre, G., and Orjan, M., "Bioimpedance and Bioelectricity: Basic." (New York: Academic), 2000.
- [131] Surowiec A., Stainslaw S. S., Barr JR, and Swarup, A., "Dielectric properties of breast carcinoma and the surrounding tissues," IEEE Trans. Biomed. Eng., 1988, 35:257-263.
- [132] Morimoto T, Kinouchi Y, Iritani T, Kimura S, Konishi Y, Mitsuyama N, Komaki K, Monden Y., "Measurement of the electrical bio-impedance of breast tumors," Eur. Surg. Res 1990, 22: 86-92.
- [133] Chauveau N, Hamzaoui L, Rochaix P, Rigaud B, Voigt JJ, Morucci JP, "Ex vivo discrimination between normal and pathological tissues in human breast surgical bioimpedance spectroscopy," Ann. NY Acad. Sci. 1999, 873:42-50.
-

- 
- [134] BUCK, R. P., "Kinetics of bulk and interfacial ionic motion: microscopic bases and limits for the Nernst-Planck equation applied to membrane systems," *Journal of Membrane Science*, 17 (1984) 1-62.
- [135] NEUMCKE, B., and LAUGER, P., "Nonlinear electrical effects in lipid bilayer membranes II. Integration of the generalized Nernst-Planck equations," *Biophysical Journal*, Vol. 9, pp. 1160-1170, 1969.
- [136] Gillespie, D., Nonner, W., and Eisenberg, R. S., "Coupling Poisson–Nernst–Planck and density functional theory to calculate ion flux," *J. Phys.: Condens. Matter* **14** (2002) 12129–12145.
- [137] Sokalski, T., and Lewenstam, A., "Application of Nernst-Planck and Poisson equations for interpretation of liquid-junction and membrane potentials in real-time and space domains," *Electrochemistry Communications*, Vol. 3, 2001, pp. 107-112.
- [138] BRUMLEVE, T. R., and BUCK, R. P., "Numerical solution of the Nernst-Planck and poisson equation system with applications to membrane electrochemistry and solid state physics," *J. Electroanal. Chem.*, 90 (1978) pp. 1-31.
- [139] RINZEL, J., "Discussion: electrical excitability of cells, theory of cells, theory and experiment: review of the Hodgkin-Huxley foundation and an update," *Bulletin of Mathematical Biology* Vol. 52, No. 1/2, pp. 5-23, 1990.
- [140] Kistler, W. M., Gerstner, W., and Leo van Hemmen, J., "Reduction of the Hodgkin-Huxley Equations to a Single-Variable Threshold Model," *Neural Computation* 9, pp. 1015-1045 (1997).
- [141] Izhikevich, E. M., "Simple Model of Spiking Neurons," *IEEE Transactions on Neural Networks*, VOL. 14, NO. 6, NOVEMBER 2003, pp. 1569-1572.
- [142] ROTH, B. J., AND BASSER, P. J., "A Model of the Stimulation of a Nerve Fiber by Electromagnetic Induction," *IEEE Transactions on Biomedical Engineering*, Vol. 37. No. 6. JUNE 1990.
- [143] Fain, G. L., "Molecular and Cellular Physiology of Neurons," Harvard University Press, 1999.
- [144] Bennet, M. R., "Cable Analysis of a Motor-nerve Terminal Branch in a Volume Conductor," *Bulletin of Mathematical Biology*, Vol. 61, pp. 1-17, 1999.
- [145] Cone, C. D., Jr. (1971). "Unified theory on the basic mechanism of normal mitotic control and oncogenesis," *Journal of Theoretical Biology*, 30, 151–181.
- [146] Binggeli, R., and Weinstein, R. C. (1986), "Membrane potentials and sodium channels: Hypotheses for growth regulation and cancer formation based on changes in sodium channels and gap junctions," *Journal of Theoretical Biology*, 123, 377–401.
-

- 
- [147] Scholz, F. (ed.), “Electroanalytical Methods: Guide to Experiments and Applications,” 2<sup>nd</sup> revised and extended edition. Springer, 2010.
- [148] Baker, S. G., Kramer, B. S., “Systems biology and cancer: Promises and perils,” *Progress in Biophysics and Molecular Biology*. 2011, *106*, 410-413.
- [149] Clayton, R. H., “Computational models of normal and abnormal action potential propagation in cardiac tissue: linking experimental and clinical cardiology,” *Physiol. Meas.* 22 (2001) R15-R34.
- [150] Sheen, G. L., Murray, N. M. F., Rothwell, J. C., Miller, D. H., and Thompson, A. J., “An open-labelled clinical and electrophysiological study of 3,4 diaminopyridine in the treatment of fatigue in multiple sclerosis,” *Brain* (1998), 121, 967-975.
- [151] Butler, M. G., Dasouki, M. J., Zhou, X-P., Talebizadeh, Z., Brown, M., Takahashi, T. N., Miles, J. H., Wang, C. H., Stratton, R., Pilarski, R., Eng, C., “Subset of individuals with autism spectrum disorders and extreme macrocephaly associated with germline PTEN tumour suppressor gene mutations,” *J Med Genet.* 2005; 42: 318-321.
- [152] Clements, C. M., McNally, R.S., Conti, B. J., Mak, T. W., and Ting, J. P.-Y. DJ-1, “a cancer and Parkinson’s disease associated protein, stabilizes the antioxidant transcriptional master regulator Nrf2,” *PNAS* (2006). Vol. 103, no. 41, pp. 15091-15096.
- [153] Sethumadhavan, G., and Sankaran, S., “Border Detection and Cancer Propagation on Spectral Bands of Malignant Melanoma Using Six Sigma Threshold,” *Computer and Information Science, 2009. ICIS 2009. Eighth IEEE/ACIS International Conference on*, pp.586-592, 1-3 June 2009.
- [154] Di Leo, G., Paolillo, A., Sommella, P., and Fabbrocini, G., “Automatic Diagnosis of Melanoma: A Software System Based on the 7-Point Check-List,” *System Sciences (HICSS), 2010 43rd Hawaii International Conference on*, pp.1-10, 5-8 Jan. 2010.
- [155] Di Leo, G., Paolillo, A., Sommella, P.; Fabbrocini, G.; Rescigno, O., “A software tool for the diagnosis of melanomas,” *Instrumentation and Measurement Technology Conference (I2MTC), 2010 IEEE*, pp.886-891, 3-6 May 2010.
- [156] Tabatabaie, K., and Esteki, A., “Independent Component Analysis as an Effective Tool for Automated Diagnosis of Melanoma,” *Biomedical Engineering Conference, 2008. CIBEC 2008. Cairo International*, pp.1-4, 18-20 Dec. 2008.
- [157] Bo Qin, Li Ma, and Weidong Xu, “Comparative Study on Boundary Structural Irregularity Using Local FD and Curvature Analysis for Melanoma Detection,” *Bioinformatics and Biomedical Engineering (iCBBE), 2010 4th International Conference on*, pp.1-4, 18-20 June 2010.
- [158] Clawson, K.M., Morrow, P.J., Scotney, B.W., McKenna, D.J., and Dolan, O.M., “Computerised Skin Lesion Surface Analysis for Pigment Asymmetry Quantification,”
-

---

*Machine Vision and Image Processing Conference, 2007. IMVIP 2007. International*, pp.75-82, 5-7 Sept. 2007.

- [159] Taouil, K., Ben Romdhane, N., Bouhlel, M.S., "A New Automatic Approach for Edge Detection of Skin Lesion Images," *Information and Communication Technologies, 2006. ICTTA '06. 2nd*, vol.1, pp.212-220.
- [160] Chiem, A., Al-Jumaily, A., Khushaba, R.N., "A Novel Hybrid System for Skin Lesion Detection," *Intelligent Sensors, Sensor Networks and Information, 2007. ISSNIP 2007. 3rd International Conference on*, pp.567-572, 3-6 Dec. 2007.
- [161] Situ, Ning, Yuan, Xiaojing, Chen, Ji, and Zouridakis, George, "Malignant melanoma detection by Bag-of-Features classification," *Engineering in Medicine and Biology Society, 2008. EMBS 2008. 30th Annual International Conference of the IEEE*, pp.3110-3113, 20-25 Aug. 2008.
- [162] Wu, Y., Stotzer, E., Chen, J., Yuan, X., Mullani, N., and Zouridakis, G., "A Programmable DSP Development Platform for Automated Detection of Melanoma," *Engineering in Medicine and Biology Workshop, 2007 IEEE Dallas*, pp.106-109, 11-12 Nov. 2007.
- [163] Wafa Soofi, William D. Hunt, and Christopher Corso, "Nanoscale Surface Acoustic Wave Sensors for Early Cancer Detection," NNIN REU Research Accomplishments, 2005.
- [164] Weight, R.M., Dale, P.S., and Viator, J.A., "Detection of circulating melanoma cells in human blood using photoacoustic flowmetry," *Engineering in Medicine and Biology Society, 2009. EMBC 2009. Annual International Conference of the IEEE*, pp.106-109, 3-6 Sept. 2009.
- [165] J. Viator, J. Komadina, L. Svaasand, G. Aguilar, B. Choi, and J. Nelson, "A comparative study of photoacoustic and reflectance methods for determination of epidermal melanin content," *J. Invest. Derm.* (122), 1432-1439 (2004).
- [166] Mehta, P., Chand, K., Narayanswamy, D., Beetner, D.G., Zoughi, R., and Stoecker, W.V., "Microwave reflectometry as a novel diagnostic tool for detection of skin cancers," *Instrumentation and Measurement, IEEE Transactions on*, vol.55, no.4, pp. 1309- 1316, Aug. 2006.
- [167] Kierk, I., Bockrath, M., and Landi, M., "Novel nano-biosensors for life science systems and their applications in early, accurate, and non-invasive melanoma and other types of cancer detection," *Life Science Systems and Applications Workshop, 2007. LISA 2007. IEEE/NIH*, pp.128-131, 8-9 Nov. 2007.
- [168] Joshua S. Marcus, "Single Cell Gene Expression Analysis Using Microfluidics," Ph.D. dissertation, California Institute of Technology, 2006.
- [169] Rodriguez, J., Yáñez, J., Vicente, V., Alcaraz, M., Benavente-Garcia, O., Castillo, J., Lorente, J., and Lozan, J. A., "Effects of several flavonoids on the growth of B16F10 and



---

SK-MEL-1 melanoma cell lines: relationship between structure and activity,” *Melanoma Research*, **12**, pp. 99-107, 2002.

- [170] Sheridan, C., Brumatti, G., Martin, S. J., “Molecular Basic of Cell and Developmental Biology: Oncogenic B-RafV600E Inhibits Apoptosis and Promotes ERK-dependetn Inactivationof Bad and Bim,” *J. Biol. Chem*, 283, 22128-22135, 2008.
- [171] Giard, D. J., Aaronson, S. A., Todaro, G. J., Arnstein, P., Kersey, J. H., Dosik, H., and Parks, W. P., “In Vitro Cultivation of Human Tumors: Establishment of Cell Lines Derived From a Series of Solid Tumors,” *Journal of the Cancer Institute*, Vol. 51, No. 5, pp. 1417-1423, 1973.
- [172] Dejana *et al.*, “Interleukin 1 Promotes Tumor Cell Adhesion to Cultured Human Endothelial Cells,” *J. Clin. Invest.* Vol. 82, pp. 1466-1470, 1988.
- [173] Wieland, B. M. *et al.*, “Is There a Human Homologue to the Murine Proteolysis-Inducing Factor?,” *Clin. Cancer Res.*, 13 (17), pp. 4984 - 4992, 2007.
- [174] Shepard, H. M., and Lewis, G. D., “Resistance of Tumor Cells to Tumor Necrosis Factor,” *Journal of Clinical Immunology*, Vol. 8, No. 5, pp. 333-341, 1988.
- [175] Blesch, A., *et al.*, “Cloning of a Novel Malignant Melanoma-derived Growth-Regulatory Protein,” *MIA. Cancer Research*, 54, pp. 5695-5701, 1994.
- [176] MacDougall, J. R., Bani, M. R., Lin, Y., Muschel, R. J., and Kerbel, R. S., ‘Proteolytic switching’: opposite patterns of regulation of gelatinase B and its inhibitor TIMP-1 during human melanoma progression and consequences of gelatinase B overexpression. *British Journal of Cancer* (1999), 80 (3/4), pp. 504–512.
- [177] Terp, M. G., *et al.*, “Identification of Markers Associated with Highly Aggressive Metastatic Phenotypes Using Quantitative Comparative Proteomics,” *Cancer Genomics & Proteomics*, 9, pp. 265-274, 2012.
- [178] Ross, D. T., *et al.*, “Systematic variation in gene expression patterns in human cancer cell lines,” *Nat. Genet.*, 24(3), pp. 227-35, 2000.
- [179] Ellison, G. *et al.*, “Further evidence to support the melanocytic origin of MDA-MB-435,” *Mol. Pathol.*, 55(5):294-299, 2002.
- [180] Garraway, L. A., *et al.*, “Integrative genomic analyses identify MITF as a lineage survival oncogene amplified in malignant melanoma,” *Nature*, 436(7047), pp. 117-122.
- [181] Wu, C.-C., *et al.*, “Pristimerin includes caspase-dependent apoptosis in MDA-MB-231 cells via direct effects on mitochondria,” *Mol. Cancer Ther.*, 4, pp. 1277-1285, 2005.
- [182] Roger, S., *et al.*, “Involvement of a novel fast inward sodium current in the invasion capacity of a breast cancer cell line,” *Biochimica et. Biophysica Acta*. 1616, pp. 107-111, 2003.

- 
- [183] Kirschmann, D. A., *et al.*, “Differentially expressed genes associated with the metastatic phenotype in breast cancer,” *Breast Cancer Research and Treatment*, 55, pp. 127-136, 1999.
- [184] Raiteri, R., Grattarola, M., Butt, H.-J., Skládal, P., “Micromechanical cantilever-based biosensors,” *Sensors and Actuators, B* 79, pp. 115-126, 2001.
- [185] Johnson, B. N., and Mutharasan, R., “Biosensing using dynamic-mode cantilever sensors: A review,” *Biosensors and Bioelectronics*, 32, pp. 1-18, 2012.
- [186] Alvarez, M., and Lechuga, L. M., “Microcantilever-based platforms as biosensing tools,” *Analyst*, 135, pp. 827-836, 2010.
- [187] Michaels, T., Guliyev, E., Klukowski, M., Rangelow, I. W., “Micromachined self-actuated Piezoresistive cantilever for high speed SPM,” *Microelectronic Engineering*, 97, pp. 265-268, 2012.
- [188] S. Jesse, A. P. Baddorf, and S. V. Kalinin, “Dynamic behavior in piezo response force microscopy,” *Nanotechnology* 17, pp. 1615-1628, 2006.
- [189] S. Rana, P. M. Ortiz, A. J. Harris, J. S. Burdess, and C. J. McNeil, “An electrostatically actuated cantilever device capable of accurately calibrating the cantilever on-chip for AFM-like applications,” *Journal of Micromechanics and Microengineering*, Vol. 19, pp. 1-11, 2009.
- [190] Y. C. Li, M.H. Ho, S. J. Hung, M. H. Chen, and M. S. C. Lu, “CMOS micromachined capacitive cantilevers for mass sensing,” *Journal of Micromechanics and Microengineering*, VOL. 16, pp. 2659-2665, 2006.
- [191] S. J. Kim, T. Ono, and M. Esashi, “Capacitive resonant mass sensor with frequency demodulation detection based on resonant circuit,” *Applied Physics Letters*, 88, 053116-0, 2006.
- [192] M. Villarroya, J. Verd, J. Teva, G. Abadal, E. Forsen, F. P. Murano, A. Uranga, E. Figueras, J. Montserrat, J. Esteve, A. Boisen, and N. Barniol, “System on chip mass sensor based on polysilicon cantilevers arrays for multiple detection,” *Sensors and Actuators, A* 132, pp. 154-165, 2006.
- [193] M. Villarroya, J. Verd, J. Teva, G. Abadal, F. Pérez, J. Esteve, and N. Barniol, “Cantilever based MEMS for multiple mass sensing,” *Research in Microelectronics and Electronics*, Vol.1, pp. 197- 200, 2005.
- [194] J. Teva, G. Abadal, F. Torres, J. Verd, F. Pérez-Murano, and N. Barniol, “A femtogram resolution mass sensor platform based on SOI electrostatically driven resonant cantilever. Part II: Sensor calibration and glycerine evaporation rate measurement,” *Ultramicroscopy*, VOL. 106, pp. 808-814, 2006.
-



- 
- [195] B. Llic, H. G. Craighead, S. Krylov, W. Senaratne, C. Ober, and P. Neuzil, "Attogram detection using nanoelectromechanical oscillators," *Journal of Applied Physics*, Vol. 95, NO. 7, pp. 3694-3703, 2004.
- [196] N. Lobontiu, L. Lupea, R. Llic, and H. G. Craighead, "Modeling, design, and characterization of multisegment cantilevers for resonant mass detection," *Journal of Applied Physics*, 103, pp. 064306 1-10, 2008.
- [197] C. Li, M. H. Miller, "Optimization Strategy for Resonant Mass Sensor Design in the Presence of Squeeze Film Damping," *Micromachines Manuscript*, 1, pp. 112-118, 2010.
- [198] A. H. Nayfeh, H. M. Ouakad, F. Najjar, S. Choura, and E. M. Abdul-Rahman, "Nonlinear dynamics of resonant gas sensor," *Nonlinear Dynamics*, VOL. 59, pp. 607-618, 2010.
- [199] N. Kacem, J. Arcamone, F. Pérez-Murano, and S. Hentz, "Dynamic range enhancement of nonlinear nanomechanical resonant cantilevers for highly sensitive NEMS gas/mass sensor applications," *Journal of Micromechanics and Microengineering*, 20, pp. 045023 1-9, 2010.
- [200] J. Zhou, P. Li, S. Zhang, F. Zhou, Y. Huang, P. Yang, and M. Bao, "A novel MEMS gas sensor with effective combination of high sensitivity and high selectivity," *IEEE*, pp. 471-474, 2002.
- [201] M. Nishio, S. Sawaya, S. Akita, Y. Nakayama, "Carbon nanotube oscillators toward zeptogram detection," *Appl. Phys. Lett.* 86, pp. 133111-1-133111-3, 2005.
- [202] K. Rijal, and R. Mutharasan, "Piezoelectric-excited millimeter-sized cantilever sensors detect density differences of a few micrograms in liquid medium," *Sensors and Actuators, B* 124, pp. 237-244, 2007.
- [203] I. Voiculescu, M. E. Zaghloul, R. A. McGill, E. J. Houser, and G. K. Fedder, "Electrostatically Actuated Resonant Microcantilever Beam in CMOS Technology for the Detection of Chemical Weapons," *IEEE Sensors Journal*, Vol. 5, NO. 4, pp. 641-647, AUGUST 2005.
- [204] M.K. Baller, H. P. Lang, et al, "A cantilever array-based artificial nose," *Ultramicroscopy* 82, pp. 1-9, 2000.
- [205] A. M. Paracha, P. Basset, D. Galayko, A. Dudka, F. Marty, and T. Bourouina, "MEMS DC/DC converter for 1D and 2D vibration-to-electricity power conversion," *IEEE, Transducers*, pp. 2098-2101, 2009.
- [206] Chu Due, T., Wei, J., Sarro, P.M., Lau, G.K., "Integrated Silicon-Polymer Laterally Stacked Bender for Sensing Microgrippers," *Sensors, 2006. 5th IEEE Conference*, pp.662-665, 2006.
- [207] Yongqing Fu, Weimin Huang, Hejun Du, Xu Huang, Junping Tan, Xiangyang Gao, "Characterization of TiNi shape-memory alloy thin films for MEMS applications, *Surface and Coatings Technology*," Vol. 145, Issues 1-3, pp. 107-112, 2001.
-

- 
- [208] Ohnstein, T.; Fukiura, T.; Ridley, J.; Bonne, U., "Micromachined silicon microvalve," Micro Electro Mechanical Systems, 1990. Proceedings, An Investigation of Micro Structures, Sensors, Actuators, Machines and Robots. IEEE, pp.95-98, 1990.
- [209] Eddie C. Burt, Alvin C. Bailey, Randall K. Wood, "Effects of soil and operational parameters on soil-tire interface stress vectors," Journal of Terramechanics, Volume 24, Issue 3, 1987, Pages 235-246.
- [210] M. Boutaayamou, K.H. Nair, R. V. Sabariego, and P. Dular, "Finite Element Modeling of Electrostatic MEMS Including the Impact of Fringing Field Effects on Forces," 7<sup>th</sup>. Int. Conf. on Thermal, Mechanical and Multiphysics Simulation and Experiments in Micro-Electronics and Micro-Systems, EuroSimE, pp. 1-5, 2006.
- [211] S. Ertl, M. Adamschik, P. Schmid, P. Gluche, A. Flöter, E. Kohn, "Surface micromachined diamond microswitch," Diamond and Related Materials, Volume 9, Issues 3-6, 2000, Pages 970-974.
- [212] W. L. Bernard, H. Khan, A. H. Heuer, and M. A. Huff, "Thin-Film Shape Memory Alloy Actuated Micropumps," Journal of Microelectromechanical Systems, VOL. 7, NO. 2, pp. 245-251, JUNE 1998.
- [213] R. Berger, Ch. Gerber, H.P. Lang, J.K. Gimzewski, "Micromechanics: A toolbox for femtoscale science: 'Towards a laboratory on a tip'," Microelectronic Engineering, Volume 35, Issues 1-4, February 1997, Pages 373-379.
- [214] Mehdi Esmaeili, Nader Jalili, Mohammad Durali, "Dynamic modeling and performance evaluation of a vibrating beam microgyroscope under general support motion," Journal of Sound and Vibration, Volume 301, Issues 1-2, 20 March 2007, Pages 146-164.
- [215] Syms, R. R. A., 2002, "Long-Travel Electrothermally Driven Resonant Cantilever Microactuators," J. Micromech. Microeng., **12**(3), pp. 211–218.
- [216] M. F. Daqaq, E. M. Abdel-Rahman, and A. H. Nayfeh, "Two-tone internal resonance in microscanners," Nonlinear Dynamics, Vol. 57, pp. 231-251, 2009.
- [217] T. Namazu, Y. Tashiro, and S. Inoue, "Ti-Ni shape memory alloy film-actuated microstructures for a MEMS probe card," Journal of Micromechanics and Microengineering, VOL. 17, pp. 154-162, 2007.
- [218] T.Namazu, Y. Okamura, Y. Tashiro, and S. Inoue, "Ti-Ni Shape Memory Alloy Film Cantilever Actuator for Micro-Probing," Materials Science Forum, Vols. 539-543, pp. 3213-3218, 2007.
- [219] M. Aureli, V. Kopman, and M. Porfiri, "Free-Locomotion of Underwater Vehicles Actuated by Ionic Polymer Metal Composites," IEEE/ASME Transactions on Mechatronics, Vol. 15, No.4, pp. 603-614, AUGUST 2010.
-

- 
- [220] Z. Chen, S. Shatara, and X. Tan, "Modeling of Biomimetic Robotic Fish Propelled by An Ionic Polymer-Metal Composite Causal Fin," *IEEE/ASME Transactions on Mechatronics*, Vol. 15, No.3, pp. 448-459, JUNE 2010.
- [221] Khaled A. Alhazza, Ali H. Nayfeh, Mohammed F. Daqaq, "On utilizing delayed feedback for active-multimode vibration control of cantilever beams," *Journal of Sound and Vibration*, Volume 319, Issues 3-5, 23 January 2009, Pages 735-752.
- [222] S. Aoki, and T. Watanabe, "Various Aspects of Response of the Cantilever Beam with Hysteresis Damping," *Transactions, SMIRT*, Vol. 16, No. 1277, pp. 1-8, 2001.
- [223] Wu, G., Datar, R. H., Hansen, K. M., Thundat, T., Cote, R. J., Majumdar, A., "Bioassay of prostate-specific antigen (PSA) using microcantilevers," *Nature Biotechnology*. 2001, 19, 856-860.
- [224] Tran, V. H., Chan, H. P., Thurston, M., Jackson, P., Lewis, C., Yates, D., Bell, G., Thomas, P. S., "Breath Analysis of Lung Cancer Patients Using an Electronic Nose Detection System," *IEEE Sensors Journal*. 2010, 10, Issue no. 9, 1514-1518.
- [225] Lang, H. P., Ramseyer, J., P., Grange, W., Braun, T., Schmid, D., Hunziker, P., Jung, C., Hegner, M., Gerber, C., "An Artificial Nose Based on Microcantilever Array Sensors," *Journal of Physics: Conference Series*. 2007, 61, 663-667.
- [226] G. Rezazadeh, M. Fathalilou, K. Shirazi, and S. Talebian, "A Novel Relation between Pull-in Voltage of the Lumped and Distributed Models in Electrostatically-Actuated Microbeams," *MEMSTECH, Polyana-Svalyava (Zakarpattya)*, Ukraine, pp. 31-35, 2009.
- [227] S. Gutschmidt, V. Rochus, and J.-C. Golinval, "Static and dynamic experimental investigations of a micro-electromechanical cantilever in air and vacuum," *10<sup>th</sup> Int. Conf. on Thermal, Mechanical, and Multiphysics Simulation and Experiments in Micro-Electronics and Micro-Systems*, EuroSimE, pp. 1-6, 2009.
- [228] T. Hauke, H. Beige, M. Giersbach, S. Seifert, and D. Sporn, "Mechanical and electric fatigue of PZT(53/47) films on metallic substrates," Vol. 35, Iss. 1-4, 2001.
- [229] Venstra, W.J., van der Velden, M., Spronck, J.W., van Eijk, J., and Sarro, P.M., "Versatile wire configuration for independent actuation of bending and torsion displacements of microcantilevers," *Sensors, 2005 IEEE*, pp.585-587, 2005.
- [230] Bhatti, M. A., Xi, L. C., Zhong, L. Y., and Abdalla, A. N., "Design and Finite Element Analysis of Piezoresistive Cantilever with Stress Concentration Holes," *2007 Second IEEE Conference on Industrial Electronics and Applications*, pp. 1171-1174, 2007.
- [231] Kusuda, S., Sawano, S., and Konishi, S., "Fluid-resistive bending sensor having perfect compatibility with flexible pneumatic balloon actuator," *Micro Electro Mechanical Systems, 2007. MEMS. IEEE 20th International Conference*, pp.615-618, 2007.
-

- 
- [232] S. M. Mahmoodi, N. Jalili, and M. F. Daqaq, "Modeling, Nonlinear Dynamics, and Identification of a Piezoelectrically Actuated Microcantilever Sensor," *IEEE/ASME Transactions on Mechatronics*, Vol. 13, No. 1, pp. 58-65, February 2008.
- [233] Pham, S.V.; Kauppinen, L.J.; Dijkstra, M.; van Wolferen, H.A.G.M.; de Ridder, R.M.; Hoekstra, H.J.W.M.; , "Read-Out of Cantilever Bending With a Grated Waveguide Optical Cavity," *Photonics Technology Letters, IEEE* , vol.23, no.4, pp.215-217, 2011.
- [234] Zhao, J., Berger, R., and Gutmann, J. S., "Thermal contributions to the bending of bimaterial cantilever sensors," *Appl. Phys. Lett.*, Vol. 89, Issue No. 3, 2006.
- [235] Karolyn M. Hansen, Thomas Thundat, "Microcantilever biosensors," *Methods*, Volume 37, Issue 1, 2005.
- [236] C Grogan, R Raiteri, G.M O'Connor, T.J Glynn, V Cunningham, M Kane, M Charlton, D Leech, "Characterisation of an antibody coated microcantilever as a potential immuno-based biosensor," *Biosensors and Bioelectronics*, Vol. 17, Issue 3, pp. 201-207, 2002.
- [237] H. Irschik, "A review on static and dynamic shape control of structures by piezoelectric actuation," *Engineering Structures*, Volume 24, Issue 1, Pages 5-11, 2002.
- [238] Ken Gall, Martin L. Dunn, Yiping Liu, Dudley Finch, Mark Lake, Naseem A. Munshi, "Shape memory polymer nanocomposites," *Acta Materialia*, Vol. 50, Issue 20, pp. 5115-5126, 2002.
- [239] Park, K. *et al.*, 'Living cantilever arrays' for characterization of mass of single live cells in fluids. *Lab Chip*, 8, pp. 1034-1041, 2008.
- [240] Baniyash, M., Netanel, T., and Witz, I. P., "Differences in Cell Density Associated with Differences in Lung-colonizing Ability of B16 Melanoma Cells," *Cancer Res*, 41, pp. 433-437, 1981.
- [241] M. I. Younis, "Modeling and Simulation of Microelectromechanical Systems in Multi-Physics Fields," Ph.D. Dissertation, Virginia Polytechnic Institute and State University, June 2004.
- [242] Minhang Bao, Heng Yang, Yuancheng Sun, and Paddy J French, "Modified Reynolds' equation and analytical analysis of squeeze-film air damping of perforated structures," *J. Micromech. Microeng.* Vol. 13, No. 6, pp. 795-800, 2003.
- [243] Roszhart, T.V., "The effect of thermoelastic internal friction on the Q of micromachined silicon resonators," *Solid-State Sensor and Actuator Workshop, IEEE 1990. 4th Technical Digest.*, pp.13-16, 4-7, 1990.
- [244] J. Rajagopalan, M. Taher, and A. Saif, "Single Degree of Freedom Model for Thermoelastic Damping," *Journal of Applied Mechanics*, Vol. 74, pp. 461-468, May 2007.
-

- 
- [245] S. Chowdhury, M. Ahmadi, and W. C. Miller, "A closed-form model for the pull-in voltage of electrostatically actuated cantilever beams," *Journal of Micromechanics and Microengineering*, Vol. 15, pp 756-763, 2005.
- [246] J.A. Gottwald, L.N. Virgin, E.H. Dowell, "Routes to escape from an energy well," *Journal of Sound and Vibration*, Vol. 187, Issue 1, pp. 133-144, 1995.
- [247] F. M. Alsaleem, M. I. Younis, and L. Ruzziconi, "An Experimental and Theoretical Investigation of Dynamic Pull-In in MEMS Resonators Actuated Electrostatically," *Journal of Microelectromechanical Systems*, Vol. 19, No. 4, pp. 794-806, 2010.
- [248] H. Tobushi, A. Ikai, S. Yamada, K. Tanaka, and C. LExcellent, "Thermomechanical Properties of TiNi Shape Memory Alloy," *Journal de Physique IV*, Volume 6, pp. C1-385-393, 1996.
- [249] H. N Arafat, "Nonlinear Response of Cantilever Beams," Ph.D. Dissertation, Virginia Polytechnic Institute and State University, 1999.
- [250] Aboelkassem, Y., Nayfeh, A. H., Ghommam, M., "Bio-mass sensor using an electrostatically actuated microcantilever in a vacuum microchannel," *Microsyst Technol*, 16, pp. 1749-1755, 2010.
- [251] Agarwal, M., Mehta, H., Candler R. N., *et al.*, "Impact of miniaturization on the current handling of electrostatic MEMS resonators," in *2007 Proceedings of the IEEE International Conference on Micro Mechanical Systems (MEMS)*, pp. 783-786.
- [252] Ivanov, Tzv., Gotszalk, T., Grabiec, P., Tomerov, E., and Rangelow, I. W., "Thermally driven micromechanical beam with Piezoresistive deflection readout," *Microelectronic Engineering*, Vol. 67-68, pp. 550-556, 2003.
- [253] Gotszalk, T., Grabiec, P., and Rangelow, I. W., "Piezoresistive sensors for scanning probe microscopy," *Ultramicroscopy*, 82, pp. 39-48, 2000.
- [254] Manhee Han, Dong-Hun Hyun, Hyoun-Hyang Park, Seung S Lee, Chang-Hyeon Kim, and ChangGyou Kim, "A novel fabrication process for out-of-plane microneedle sheets of biocompatible polymer." *J. Micromech. Microeng.*, 17, pp. 1184-1191, 2007.
- [255] Wang, G. J., Chen, C. L., Hsu, S. H., Chiang, Y. L., "Bio-MEMS fabricated artificial capillaries for tissue engineering," *Microsyst Technol*, 12, pp. 120-127, 2005.
- [256] Tzvetan Ivanov, "Piezoresistive cantilevers with an integrated bimorph actuator," Ph.D. Dissertation, University of Kassel, 2004.
- [257] Woszczyna, M., *et al.*, "Quantitative force and mass measurements using the cantilever with integrated actuator and deflection detector," *Microelectronic Engineering*, 86, pp. 1043-1045, 2009.
-

- 
- [258] Fielenko, D., *et al.*, “Experimental setup for characterization of self-actuated microcantilevers with Piezoresistive readout for chemical recognition of volatile substances,” *Review of Scientific Instruments*, 79, 094101, 2008.
- [259] Rao, S. S., *Mechanical Vibrations*, 4<sup>th</sup> edition, Prentice-Hall, Inc., Singapore, 2004.
- [260] Groover, W. H., *et al.*, “Measuring single-cell density,” *PNAS*, vol. 108, no. 27, pp. 10992-10996, 2011.
- [261] Park, K., *et al.*, “Measurement of adherent cell mass and growth,” *PNAS*, vol. 107, no. 48, pp. 20691-20696, 2010.
- [262] Chaudhary, M., and Gupta, A., “Microcantilever-based sensors,” *Defense Science Journal*, Vol. 59, No. 6, pp. 634-641, 2009.
- [263] Zhang, W., and Turner, K. L., “A mass sensor based on parametric resonance,” In *Proc. Of the solid-state sensor, actuator, and microsystems workshop*, pp. 49-52, 2004.
- [264] Ananthakrishnan, R., and Ehrlicher, A., “The Forces Behind Cell Movement,” *Int. J. Biol. Sci.*, 3, pp. 303-317, 2007.
- [265] Bao, G., and Suresh, S., “Cell and molecular mechanics of biological materials,” *Nature materials*, Vol. 2, pp. 715-725, 2003.
- [266] Quill, T. A., Wang, D., and Garbers, D. L., “Insights into sperm cell motility signaling through sNHE and CatSper,” *Molecular and Cellular Endocrinology*, 250, pp. 84-92, 2006.
- [267] Oslen, M. F., and Sahai, E., “The actin cytoskeleton in cancer cell motility,” *Clin. Exp. Metastasis*, 26, pp. 273-287, 2009.
- [268] Turner, L., Ryu, W., and Berg, H. C., “Real-Time Imaging of Fluorescent Flagellar Filaments,” *Journal of Bacteriology*, Vol. 182, No. 10, pp. 2793-2801, 2000.
- [269] Eyckmans, J., Boudou, T., Yu, X., and Chen C. S., “A Hitchhiker’s Guide to Mechanobiology,” *Developmental Cell* 21, pp. 35-47, 2011.
- [270] Franziska van Zijl, Krupitza, G., and Mikulits, W., “Initial steps of metastasis: Cell invasion and endothelial transmigration,” *Mutation Research*, 728, pp. 23–34, 2011.
- [271] Sibley, L. D., Håkansson, S., and Carruthers, V. B., “Gliding motility: An efficient mechanism for cell penetration,” *Current Biology*, Vol. 8, No.1, R-12-R-14, 1998.
- [272] Alberts, B., Johnson A., Lewis J., *et al.* “*Molecular Biology of the Cell*,” 4e. Garland Science. 2002.
- [273] Li, W. *et al.*, “Extracellular heat shock protein-90 $\alpha$ : linking hypoxia to skin cell motility and wound healing,” *The EMBO Journal*, 26, pp. 1221-1233, 2007.
-

- 
- [274] Fung, Y. C., “Biomechanics: Mechanical Properties of Living Tissues,” 2nd ed. (Springer, New York, 1993).
- [275] Park, J., *et al.*, “Real-Time Measurement of the Contractile Forces of Self-Organized Cardiomyocytes on Hybrid Biopolymer Microcantilevers,” *Anal. Chem.*, 77, pp. 6571-6580, 2005.
- [276] Chen, M. H., KerKelä, R, and Force, T., “Mechanisms of Cardiac Dysfunction Associated with Tyrosine Kinase Inhibitor Cancer Therapeutics,” *Journal of the American Heart Association*, 118, pp. 84-95, 2008.
- [277] Mireke, C. T., *et al.*, “Contractile forces in tumor cell migration,” *European Journal of Cell Biology*, 87, pp. 669-676, 2008.
- [278] Sahai, E., “Mechanisms of cancer cell invasion,” *Current Opinion in Genetics & Development*, 15, pp. 87–96, 2005.
- [279] Euteneuer, U., and Schliwa, M., “The Function of Microtubules in Directional Cell Movement,” *Annals of the New York Academy of Sciences*. 1986; 466 (1): 867–886.
- [280] Jalali, S. *et al.*, “Integrin-mediated mechanotransduction requires its dynamic interaction with specific extracellular matrix (ECM) ligands,” *Proc. Natl. Acad. Sci. USA* **98**, 1042–1046 (2001).
- [281] Yin, T. I., Zhao, Y., Lin, C. F., Tsai, H. H., Juang, Y. Z., and Urban, G. A., “Development of A Microfluidic Device with Microcantilever Sensor Array for Probing Single Cancer Cells Mechanics,” *IEEE Transducers’11.*, pp. 1216-1219, 2011.
- [282] Usami, S., Chen, H. H., Zhao, Y., Chien, S. and Skalak, R., “Design and construction of a linear shear stress flow chamber,” *Ann. Biomed. Eng.* 21, 77–83 (1993).
- [283] Chaudhuri, O., Parekh, S. H., Lam, W. A., and Fletcher, D. A., “Combined atomic force microscopy and side-view optical imaging for mechanical studies of cells,” *Nature Methods*, Vol.6, No.5, pp. 383-388, 2009.
- [284] Lim, C.T., Zhou, E.H., and Quek, S. T., “Mechanical models for living cells - a review. *Journal of Biomechanics*,” 39, pp. 195–216, 2006.
- [285] Sun, Y., and Nelson, B. J., “MEMS for Cellular Force Measurements and Molecular Detection,” *International Journal of Information Acquisition*, Vol. 1, No. 1, pp. 23–32, 2004.
- [286] Lee, G. H., and Lim, T. C., “Biomechanics approaches to studying human diseases,” *TRENDS in Biotechnology*, Vol.25, No.3, pp. 111-118, 2007.
-



- 
- [287] Berry, C. C., Gordon, C., Antonio, S., Robertson, M., and Curtis, A. S. G., “The influence of microscale topography on fibroblast attachment and motility,” *Biomaterials*, 25, pp. 5781–5788, 2004.
- [288] Ghibaudo, M., Di Meglio, J.-M., Hersen, P., Ladoux, B., “Mechanics of cell spreading within 3D-micropatterned environments,” *Lab Chip*, 11, pp. 805-812, 2011.
- [289] Mierke, C. T., Bretz, N., Altevogt, P., “Contractile Forces Contributed to Increased Glycosylphosphatidylinositol-anchored Receptor CD24-facilitated Cancer Cell Invasion,” *J. Biol. Chem*, 286, pp. 34858-34871, 2001.
- [290] Yang, S. M., and Yin, T. I., “Design and analysis of piezoresistive microcantilever for surface stress measurement in biochemical sensor,” *Sensors and Actuators*, Vol. B 120, pp. 736-744, 2007.
- [291] Goericke, F. T., and King, W. P., “Modeling Piezoresistive Microcantilever Sensor Response to Surface Stress for Biochemical Sensors,” *IEEE Sensors Journal*, Vol. 8, No. 8, pp. 1404-1410, 2008.
- [292] Raorane, D. A., Lim, M. D., Chen, F. F., Craik, C. S., and Majumdar, A., “Quantitative and Label-Free Technique for Measuring Protease Activity and Inhibition using a Microfluidic Cantilever Array,” *Nano Lett*, Vol. 8, No. 9, 2008.
- [293] Ricciardi, C., Canavese, G., Castagna, R., Ferrante, I., Ricci, A., Marasso, S. L., Napione, L., and Bussolino, F., “Integration of microfluidic and cantilever technology for biosensing application in liquid environment,” *Biosensors and Bioelectronics*, Vol. 26, pp. 1565-1570, 2010.
- [294] Lin, G., Pister, K., Roos, K., “Surface micromachined polysilicon heart cell force transducer.” *IEEE J. MEMS*, Vol. 9, pp. 9-17, 2000.
- [295] Alhazza, K. A., Masoud, Z. N., and Alajmi, M., “Nonlinear free vibration control of beams using acceleration delayed-feedback control,” *Smart Mater. Struct.*, 17, 015002, pp1-10, 2008.
- [296] Wang, B.-T., and Rogers, C. A., “Modeling of Finite-Length Spatially-Distributed Induced Strain Actuators for Laminate Beams and Plates,” *AIAA-91-1258-CP*, pp. 1511-1520, 1991.
- [297] Daqaq, M. F., Alhazza, K. A., and Arafat, H. N., “Non-linear vibrations of cantilever beams with feedback delays,” *International Journal of Non-Linear Mechanics*, 43, pp. 962-978, 2008.
- [298] Yin, Z., *et al.*, “A screen for morphological complexity identifies regulators of switch-like transitions between discrete cell shapes,” *Nature Cell Biology*, pp. 1-16, 2013.
-



- 
- [299] Frey, M. T., Tsai, I. Y., Russell, T. P., Hanks, S. K., and Wang, Y-L., “Cellular Responses to Substrate Topography: Role of Myosin II and Focal Adhesion Kinase,” *Biophysical Journal*, Vol. 90, pp.3774–3782, 2006.
- [300] Sanz-Moreno, V. *et al.*, “ROCK and JAK1 Signaling Cooperate to Control Actomyosin Contractility in Tumor Cells and Stroma,” *Cancer Cell*, 20, pp. 229–245, 2011.
- [301] Gui, Y. *et al.*, “Cytokine-Generated Contractility Drives Tumor Cell Migration,” *Cancer Discovery*, 1:284, 2011.
- [302] Teng, T. S., *et al.*, “Stat3 promotes directional cell migration by regulating Rac1 activity via its activator  $\beta$ PIX,” *Journal of Cell Science* 122, pp. 4150-4159, 2009.
- [303] Sheeparamatti, B. G., Hebbal, M. S., Sheeparamatti, R. B., Math, V. B., Kadadevaramath, J. S., “Simulation of Biosensor using FEM,” *Journal of Physics: Conference Series*, 34, pp. 241-246, 2006.
- [304] Moghimi Zand, M., Ahmadian, M. T., “Dynamic pull-in instability of electrostatically actuated beams incorporating Casimir and van der Waals forces,” *Proceedings of the Institution of Mechanical Engineers, Part C: Journal of Mechanical Engineering Science*, 224, pp. 2037-2047, 2010.
- [305] Batra, R. C., Porfiri, M., Spinello, D., “Vibrations of narrow microbeams predeformed by an electric field,” *Journal of Sound and Vibration*, 309, pp. 600-612, 2008.
- [306] Wang, Y.-G., Lin, W.-H., “Pull-in voltage analysis for an electrostatically actuated extensional microbeam with large deflection,” *Math. Mech.*, 90, Issue no. 3, pp. 211-218, 2010.

---

## Appendix A: Glossary

### A.

<b>Adenocarcinoma</b>	Initiation of cancer within the glandular tissues.
<b>Angiogenesis</b>	A new formation of blood vessels.
<b>Antigen</b>	A substance that forces an immune system to produce an antibody against it.
<b>Apoptosis</b>	Programmed cell death.
<b>Arteries</b>	Blood stream flow from heart towards other parts of the mammalian body.

### B.

<b>Benign cancer</b>	Neoplastic growth that does not metastasize – no invasive capacity.
<b>Biomarker</b>	A biological marker.

### C.

<b>Carcinomas</b>	Malignant cancer initiates within the epithelial tissues lining the entire human body skin, internal structure, and cavities and mostly diagnosed with adults and rarely with children; it has 5 different types: basal (skin outer layer), squamous (skin and other organs), renal (kidney origin), ductal (originates in the breast milk duct non-invasive 'in situ' in its place of origin), invasive ductal (migrates to outside tissue of breast duct).
<b>Cell confluence</b>	Cellular dense culture that no longer proliferates.
<b>Contralateral cancer</b>	The reoccurrence of cancer in “the opposite breast side.”

## D.

**Dark signal noise** A current that is attributable to electric field sweeping of stochastically initiated electrons and holes in the depletion layer of photosensitive platforms.

## E.

**E-cadherin** Cell-cell adhesion protein.

**Electroosmosis** Movement of polar fluid within cell membrane.

**Electrophoresis** Movement of particle molecules within a medium due to electric field.

**Electroporation** Increase in conductivity and dielectric property of a cell membrane due to applied electric field.

**Endometrial cancer** Cancer within the tissue lining the uterus.

**Extracellular matrix (ECM)** Extracellular component of the cellular domain and between cells.

## F.

**Fibroblasts** Connective tissue cells that can engineer and reconstruct damaged tissues.

## G.

**Gap junction** A physical biochemical connection among cell networks.

**Gastric carcinoma** A malignant tumor initiated from the epithelium of the stomach.

## H.

**Hematogenous**                      Spreading mechanism through blood.

**Hepatocellular carcinoma**                      A liver cancer.

## I.

**Ipsilateral**                      Redevelopment of cancer “on the same side.”

**Isogenic**                      Genetically alike.

## L.

**Lymphatic vessels**                      Hair-like capillaries, thin walled of a valve structure that functionalize as storage, filter, and transporter of lymph (fluid), containing plasma and cells: maintaining normal blood pressure and volume.

## M.

**Macrophages**                      Phagocytic cells.

**Malignant Cancer**                      A cancer that replicates and invades, attacking neighboring cells and tissues through blood vessels, and incursion of lymph nodes.

**Minuscule**                      Interconnecting capillaries between veins and arteries, which are comparable to the size of a cell.

**Mitosis**                      The cell proliferation mechanism.

**Morphogenesis**                      The process of forming an organism where proliferated cell is marching toward forming a tissue or organ.

**Myosin motors**                      A molecular motor converting chemical energy (ATP to ADP) to mechanical work exerted on AFs, yielding a contractile force pushing cell forward.

## N.

Navier-Stokes equation	A mathematical formula that describes the kinematics and kinetics of a fluid flow.
Neutrophils	Phagocytic white blood cells.

## O.

<b>Oncogene</b>	A mutated form of a normal proto-oncogene that promotes the malignant phenotype.
<b>Osmotic pressure</b>	A force per unit area required to achieve a stabilized solute concentration resulted from solvent molecules' movement via partially permeable membrane to a higher solute concentration.

## P.

<b>p53</b>	A protein responsible for the apoptosis process of cells, in which a single allele damage is sufficient.
<b>Pathogenesis</b>	The initiation of a disease.
<b>Perfusion</b>	A process in which nutrients, oxygen, and cell growth factors are provided to cells, and wastes such as $CO_2$ , insoluble cell debris are removed from the system.
<b>Polymerization</b>	Actin polymerization is a process of extension of the positive end in a higher rate than the negative one based on actin monomer concentration.
<b>Proto-oncogene</b>	Normal gene.

## S.

<b>Sarcomas</b>	A fleshy growth malignant tumor initiated from soft tissue and bone.
<b>Serosal surfaces</b>	A fine membrane consisting of layers of cells to reduce friction among organs.

## T.

<b>Transcoelomic</b>	Across the peritoneal cavity which is the space within the two membranes segregating the organs in the abdominal cavity from the abdominal wall.
<b>Tumor Suppressor Gene (TSp53)</b>	Genes encoding proteins required for regulation of normal cell growth and differentiation. Deletion or inactivation promotes the neoplastic phenotype.

## V.

<b>Vein endothelial</b>	A type of cell initiated from endothelium (cellular thin layer) of veins [66].
<b>Veins</b>	Backward blood flow stream from body towards heart.

# Appendix B: Nomenclature

## B.1 Electrophysiology of Cells

$C_m$	Capacitance of cell membrane
$C_w$	Capacitance of Warburg diffusion (leakage of charge)
$C_{me}$	Equivalent capacitance of Warburg and cell membrane capacitors in parallel
$R_m$	Resistance of cell membrane
$R_w$	Resistance of Warburg diffusion (leakage of charge)
$R_{me}$	Equivalent resistance of Warburg and cell membrane resistors in series
$R_i$	Longitudinal intracellular resistance of the biological cell
$R_o$	Longitudinal resistance to current flow
$R_e$	Resistance of the buffered medium
$I_{in}$	Effective current injected from a stimulated electrode
$I_{j-1,j}^o$	Exterior current from node ( j -1) to node ( j )
$I_{j-1,j}^i$	Interior current from node ( j - 1 ) to node ( j )
$I^o$	Exterior current
$V_j^m$	Membrane potential
$V_j^i$	Intracellular potential
$V_j^o$	Extracellular potential

**B.2 Beam's Theory (Pull-In Phenomena)**

$V_{DC}$	Dc induced potential
$V_{AC}$	Harmonic force excitation
$L$	Equilibrium length of the beam
$\hat{L}_C$	Length of the paddle
$\hat{x}_C$	Inertial reference frame defining the center of mass of the paddle
$\varepsilon$	Permittivity of free space (vacuum)
$C$	Center of mass of the paddle, which is distanced at $\hat{L}_C = \hat{x}_C - L$
$S$	Body fixed coordinate: intermediate reference frame fixed to the rigid body
$(\hat{x}, \hat{y}, \hat{z})$	Inertial (reference frame) coordinates
$E$	Modulus of elasticity of the beam
$\rho$	Density
$D$	Gap distance separating the paddle and stationary electrode
$H$	Thickness of the beam and paddle (plate)
$b$	Width of the beam
$A_{beam}$	Cross-sectional area of the beam = $bh$
$\rho A_{beam}$	Mass per unit length of the beam
$\hat{M}$	Mass of the paddle is considered to be the effective mass of the system
$J$	Mass moment of inertia of paddle = $\frac{1}{3} \hat{M} \hat{L}_C^2$
$b_p$	Width of the paddle
NA	Neutral axis



---

$I$	Second moment of cross-sectional area about NA $= \frac{bh^3}{12}$
$\hat{\eta}(\hat{x}, \hat{t})$	Transverse (lateral) displacement: independent and complete generalized coordinate of beam depicting temporal and spatial transverse displacement
$\hat{\eta}_C(\hat{x}_C, \hat{t})$	Spatial and temporal displacement of the center of mass of the paddle
$\theta_C$	Transverse rotational angle about neutral axis = slope of the tip of the continuous beam $= \frac{\partial \hat{\eta}(\hat{x}, \hat{t})}{\partial \hat{x}}$
$\hat{\xi}$	Dimensional parameter
$\xi$	Normalized parameter

### **B.3 Contractile Force**

$H(s)$	Heaviside step function
$EI$	Stiffness factor
$S_1$	Starting coordinate of a cell with respect to the beam's fixed end
$S_2$	Ending coordinate of a cell with respect to the beam's fixed end
$t_b$	Thickness of a beam
$t_c$	Thickness of a cell (height)
$\hat{\eta}(s, t)$	Transverse deflection of a beam
$q(s, t)$	Total resultant distributed load on a beam
$M$	Uniformly distributed bending moment acting on a beam
$\eta$	Beam's deflection
$u(t)$	Generalized temporal coordinates
$w(s)$	Orthonormal mode shapes of a cantilever beam
$r_n$	Frequency (1/meter)

---

---

$w(s)$	Mode shape
$u$	Normalized deflection
$w(L)$	Deflection at length $L$ of the beam
$F$	Beam's contractile force
$F_C$	Effective contractile force of a cell

# Appendix C

## Numerical Algorithms

---

# **C.1.1**

## **Cell-Membrane Potential (Maple Algorithm)**

restart;

$k := 1; \mu := 1; \nu := 1; w := 1; I0 := 1;$

$P := k \cdot y^2 + (y^2 + k \cdot \mu) \cdot (1 + y^2);$

$Q := k \cdot y^2 + y^2 + k \cdot \mu;$

1

1

1

1

1

$y^2 + (y^2 + 1)^2$

$2 y^2 + 1$

[>

$k y^2 + (y^2 + k \mu) (1 + y^2)$

$k y^2 + y^2 + k \mu$

(2)

$$Vi := \frac{I0 \cdot w \cdot \nu \cdot k}{\text{sqrt}(2 \cdot \text{Pi})} \cdot \left( \frac{1}{w \cdot (w^2 \cdot Q^2 + P^2)} (-w \cdot Q \cdot \cos(w \cdot T) + w \cdot P \cdot \cos(w \cdot T) + P \cdot \sin(w \cdot T) + w^2 \cdot Q \cdot \sin(w \cdot T)) + \frac{\exp\left(-\frac{P}{Q} \cdot T\right) \cdot (Q - P)}{(P^2 + w^2 \cdot Q^2)} \right);$$

$$\frac{1}{2} \frac{1}{\sqrt{\pi}} \left( \sqrt{2} \left( \frac{1}{(2 y^2 + 1)^2 + (y^2 + (y^2 + 1)^2)^2} (- (2 y^2 + 1) \cos(T) + (y^2 + (y^2 + 1)^2) \cos(T) + (y^2 + (y^2 + 1)^2) \sin(T) + (2 y^2 + 1) \sin(T)) \right. \right. \quad (3)$$

$+ 1)^2) \cos(T) + (y^2 + (y^2 + 1)^2) \sin(T) + (2 y^2 + 1) \sin(T))$

$+ \frac{e^{-\frac{(y^2 + (y^2 + 1)^2) T}{2 y^2 + 1}} (y^2 + 1 - (y^2 + 1)^2)}{(2 y^2 + 1)^2 + (y^2 + (y^2 + 1)^2)^2} \Bigg)$

$$Vo := \frac{\nu \cdot k \cdot I0 \cdot w}{\text{sqrt}(2 \cdot \text{Pi})} \cdot \left( \frac{(w \cdot (P - Q - y^2 \cdot Q) \cdot \cos(w \cdot T) + (P + w^2 \cdot Q + y^2 \cdot P) \cdot \sin(w \cdot T))}{w \cdot (w^2 \cdot Q^2 + P^2)} + \frac{(Q - P + Q \cdot y^2)}{(P^2 + w^2 Q^2)} \cdot \exp\left(-\frac{P}{Q} \cdot T\right) \right);$$

$$\frac{1}{2} \frac{1}{\sqrt{\pi}} \left( \sqrt{2} \left( \frac{1}{(2 y^2 + 1)^2 + (y^2 + (y^2 + 1)^2)^2} ((- (2 y^2 + 1) y^2 - y^2 + (y^2 + 1)^2) \right. \quad (4)$$

$$-1) \cos(T) + ((y^2 + (y^2 + 1)^2) y^2 + 3 y^2 + 1 + (y^2 + 1)^2) \sin(T) \\ + \frac{((2 y^2 + 1) y^2 + y^2 - (y^2 + 1)^2 + 1) e^{-\frac{(y^2 + (y^2 + 1)^2) T}{2 y^2 + 1}}}{(2 y^2 + 1)^2 + (y^2 + (y^2 + 1)^2)^2} \Bigg)$$

```
fd := fopen("figu2", WRITE);
N := 20;
for i from 1 to N do;
for j from 1 to N do;
X := -5 +  $\frac{j}{N}$  · 10;
T :=  $\frac{i}{N}$  · 3;
Vii[i,j] := evalf( sqrt( $\frac{2}{\text{Pi}}$ ) · (int( (cos(y·X) · Vi), y = 0 .. 1000, numeric) ) );
Voo[i,j] := evalf( sqrt( $\frac{2}{\text{Pi}}$ ) · (int( (cos(y·X) · Vo), y = 0 .. 1000, numeric) ) );
Vm[i,j] := Vii[i,j] - Voo[i,j];
fprintf( fd, "%g    %g    %g\n", evalf(X), evalf(T), evalf(Vm[i,j]) );

od;
od; fclose(fd);
```

0

20

(5)

---

# **C.1.2**

## **Cell-Membrane Potential (Matlab M-File)**

```
clear all
load figu1
[n,m]=size(figu1);
h=0;
[-] for i=1:sqrt(n)
[-]     for j=1:sqrt(n)
        h=h+1;
        X(j)=figu1(h,1);
        T(i)=figu1(h,2);
        F(i,j)=figu1(h,3);
        end
    end
figure(1)
surf(X,T,F)
```



# **C.2**

## **Pull-In Phenomena**

### **(Regeneration of the results obtained in [198])**

```
> restart;
```

```
> V[dc]=7;
```

$$V_{dc}=7$$

(1)

```
> a[b]:=5E-6;b[b]:=1.5E-6;d:=4E-6;L[l]=250E-6;L[p]:=1/5*L[l];a[p]:=
20E-6;b[p]:=1.5E-6;rho:=2300;E:=160E9;epsilon:=8.85E-12;A[b]:=a
[b]*b[b];II:=1/12*a[b]*b[b]^3;L[c]:=1/2*L[p];M:=a[p]*b[p]*rho*L
[p];J:=1/3*M*L[c]^2;
```

$$a_b := 0.000005$$

(2)

$$b_b := 0.0000015$$

$$d := 0.000004$$

$$L_l = 0.000250$$

$$L_p := \frac{1}{5} L_l$$

$$a_p := 0.000020$$

$$b_p := 0.0000015$$

$$\rho := 2300$$

$$E := 1.60 \cdot 10^{11}$$

$$\epsilon := 8.85 \cdot 10^{-12}$$

$$A_b := 7.5 \cdot 10^{-12}$$

$$II := 1.406250000 \cdot 10^{-24}$$

$$L_c := \frac{1}{10} L_l$$

$$M := 1.380000000 \cdot 10^{-8} L_l$$

$$J := 4.600000000 \cdot 10^{-11} L_l^3$$

```
> alpha[1]:=epsilon*a[p]*L[l]^4/(2*E*II*d^3);ah:=a[b]/d;Lh[c]:=L[c]
/L[l];Gamma:=2*Lh[c];Mh:=M/(rho*A[b]*L[l]);
```

$$\alpha_1 := 6.145833335 \cdot 10^{12} L_l^4$$

(3)

$$ah := 1.250000000$$

$$Lh_c := \frac{1}{10}$$

$$\Gamma := \frac{1}{5}$$

$$Mh := 0.8000000000$$

```
> eq1:=6*A+2*B=alpha[1]/(3*A+2*B)^2*V[dc]^2*(Gamma*(3*A+2*B)/(1-A-
```

$$\text{B-Gamma}*(3*A+2*B)) - \ln((1-A-B)/(1-A-B-\text{Gamma}*(3*A+2*B))) ;$$

$$\text{eq1} := 6 A + 2 B \quad (4)$$

$$= \frac{6.145833335 \cdot 10^{12} L_l^4 V_{dc}^2 \left( \frac{3A+2B}{5 \left( 1 - \frac{8A}{5} - \frac{7B}{5} \right)} - \ln \left( \frac{1-A-B}{1 - \frac{8A}{5} - \frac{7B}{5}} \right) \right)}{(3A+2B)^2}$$

$$> \text{eq2} := 6*A = -(\text{alpha}[1]*V[\text{dc}]^2)/(3*A+2*B)*(1/(1-A-B-\text{Gamma}*(3*A+2*B)) - 1/(1-A-B));$$

$$\text{eq2} := 6 A = - \frac{6.145833335 \cdot 10^{12} L_l^4 V_{dc}^2 \left( \frac{1}{1 - \frac{8A}{5} - \frac{7B}{5}} - \frac{1}{1-A-B} \right)}{3A+2B} \quad (5)$$

$$> \text{Digits} := 20;$$

$$\text{Digits} := 20 \quad (6)$$

$$> \text{S22} := \{A = -.29609108669429914117\text{e-}3, B = .97710690337665423008\text{e-}3\};$$

$$\text{S22} := \{A = -0.00029609108669429914117, B = 0.00097710690337665423008\} \quad (7)$$

$$> \text{S22} := \{A = -.29609108669429914117\text{e-}3, B = .97710690337665423008\text{e-}3\};$$

$$L[1] := 250\text{E-}6;$$

$$V1 := .6;$$

$$\text{S22} := \text{fsolve}(\{\text{subs}(V[\text{dc}] = V1, \text{eq1}), \text{subs}(V[\text{dc}] = V1, \text{eq2})\}, \{A = \text{subs}(\text{S22}, A), B = \text{subs}(\text{S22}, B)\});$$

$$\text{for kk from 1 to 25 do}$$

$$L[1] := L[1] + 10\text{E-}6;$$

$$V1 := .6; N1 := 1000;$$

$$S1 := \text{fsolve}(\{\text{subs}(V[\text{dc}] = V1, \text{eq1}), \text{subs}(V[\text{dc}] = V1, \text{eq2})\}, \{A = \text{subs}(\text{S22}, A), B = \text{subs}(\text{S22}, B)\});$$

$$\text{for i from 1 to N1 do};$$

$$V1 := i/N1 * 7.8 + .6;$$

$$A1 := \text{subs}(S1, A);$$

$$B1 := \text{subs}(S1, B);$$

$$S1 := \text{fsolve}(\{\text{subs}(V[\text{dc}] = V1, \text{eq1}), \text{subs}(V[\text{dc}] = V1, \text{eq2})\}, \{A = A1, B = B1\});$$

$$A2[i] := A1;$$

$$B2[i] := B1;$$

$$V2[i] := V1;$$

$$\text{if } (i > 1) \text{ then}$$

$$\text{if } (0.5 < \text{abs}((A2[i] + B2[i]) - (A2[i-1] + B2[i-1]))) \text{ then}$$

$$VV[kk] := V1;$$

$$LL[kk] := L[1];$$

$$\text{end if};$$

```

end if;
A2k[i,k]:=A1;
B2k[i,k]:=B1;
V2k[i,k]:=V1;
od;
plot({seq([V2[j],A2[j]+B2[j]],j=1..1000)},style=point);
od;

```

$S22 := \{A = -0.00029609108669429914117, B = 0.00097710690337665423008\}$

$L_I := 0.000250$

$VI := 0.6$

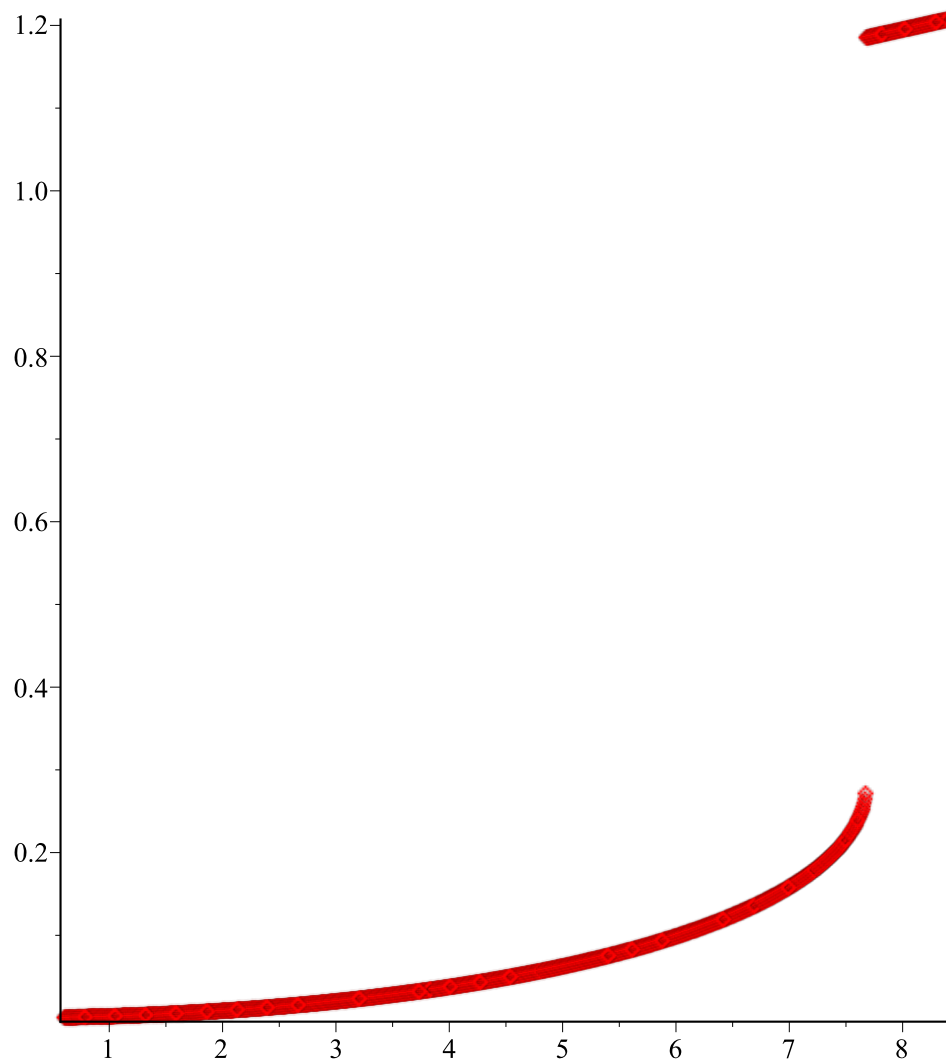
$S22 := \{A = -0.00028852865843372249679, B = 0.00095215057141704801556\}$

$L_I := 0.000260$

$VI := 0.6$

$NI := 1000$

$SI := \{A = -0.00033762597311927654923, B = 0.0011141739261557412836\}$

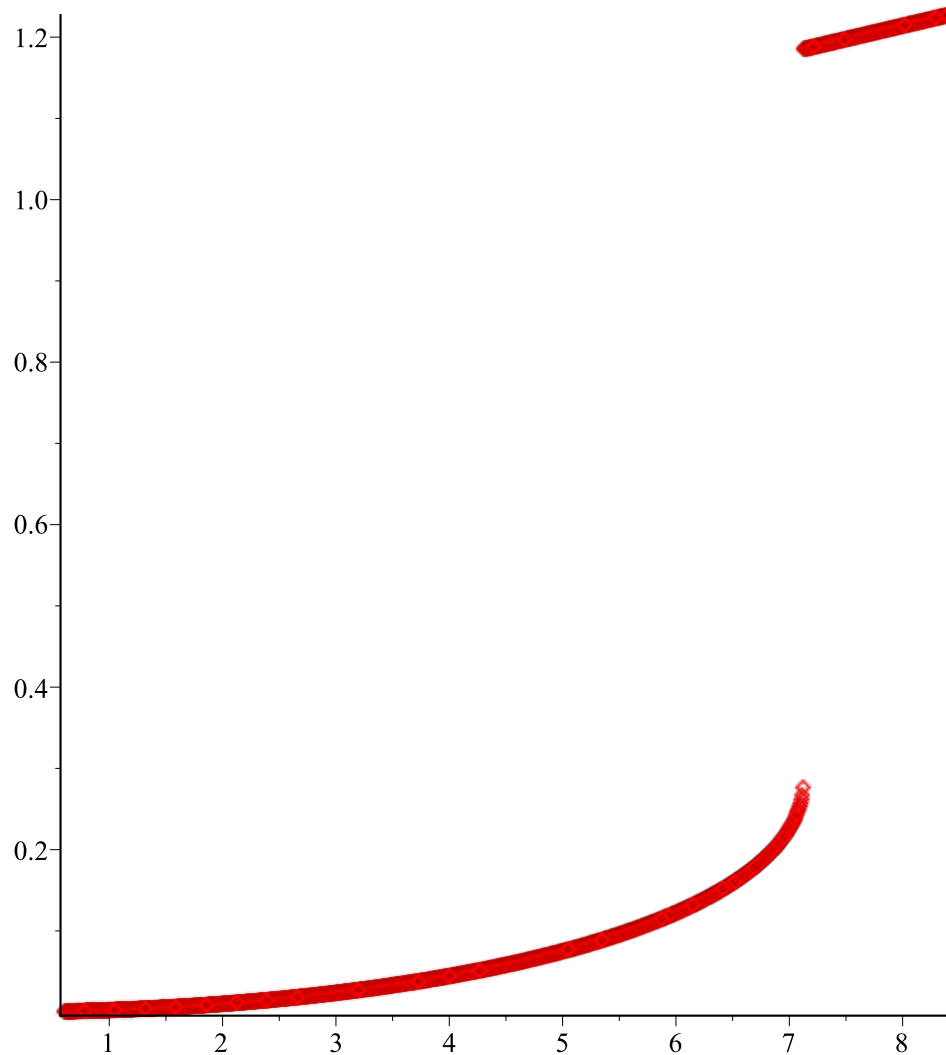


$$L_t := 0.000270$$

$$VI := 0.6$$

$$NI := 1000$$

$$SI := \{A = -0.00039275798424083535005, B = 0.0012961124664215081896\}$$

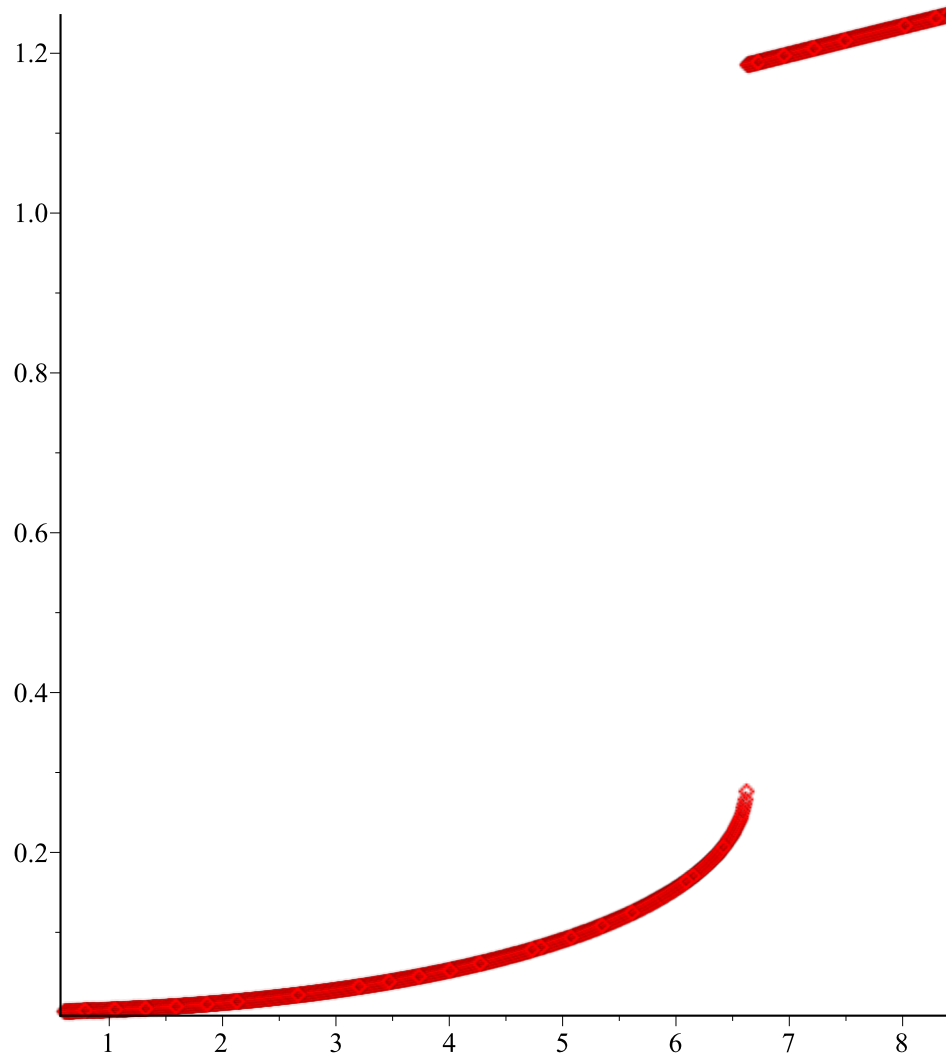


$$L_t := 0.000280$$

$$VI := 0.6$$

$$NI := 1000$$

$$SI := \{A = -0.00045440666703480471356, B = 0.0014995568864280107582\}$$

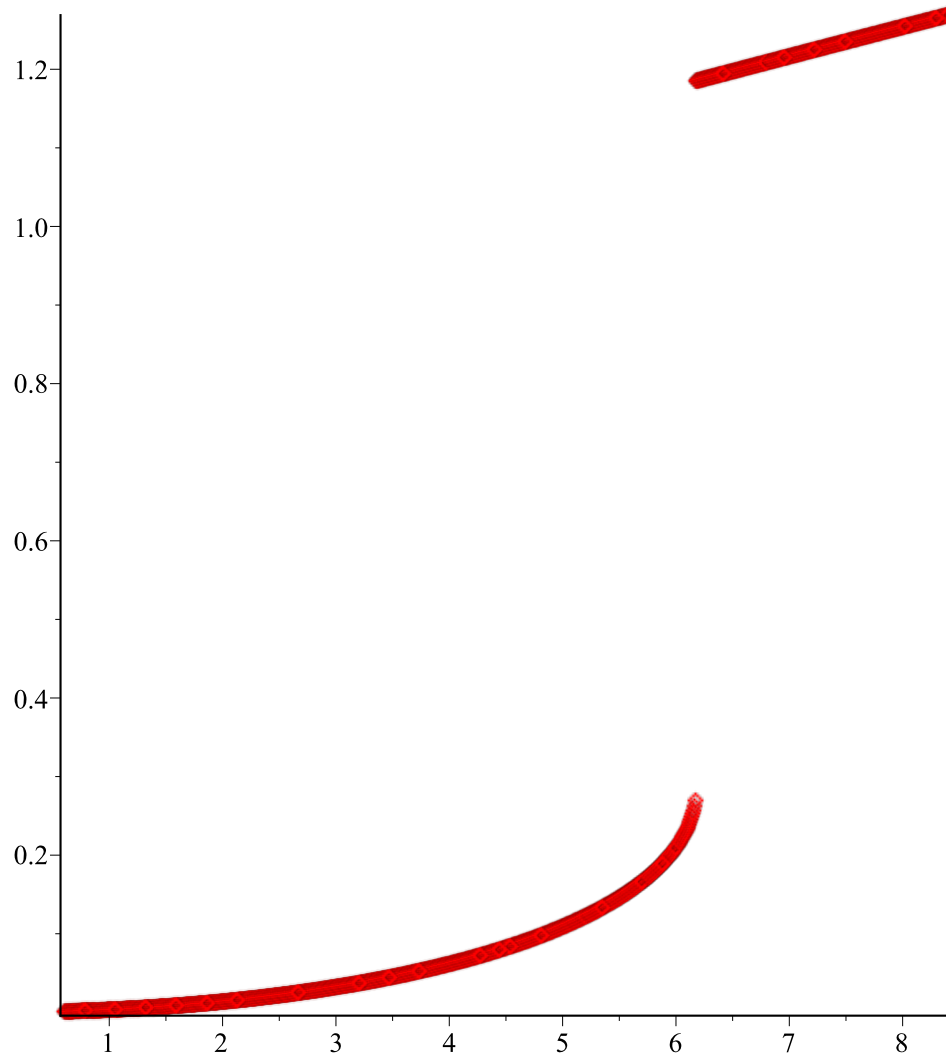


$$L_t := 0.000290$$

$$VI := 0.6$$

$$NI := 1000$$

$$SI := \{A = -0.00052307435636655059614, B = 0.0017261651035597829770\}$$



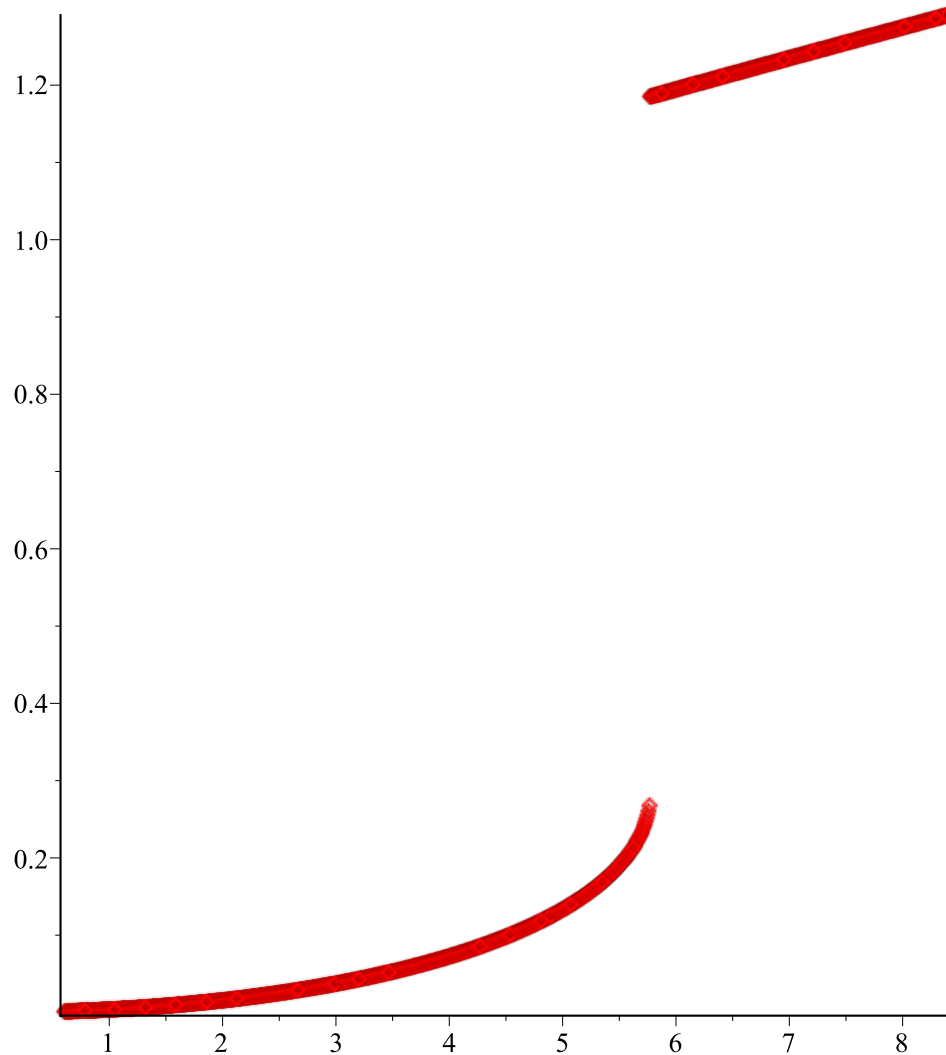
$$L_t := 0.000300$$

$$VI := 0.6$$

$$NI := 1000$$

$$SI := \{A = -0.00059928417528409501256, B = 0.0019776636785362999470\}$$



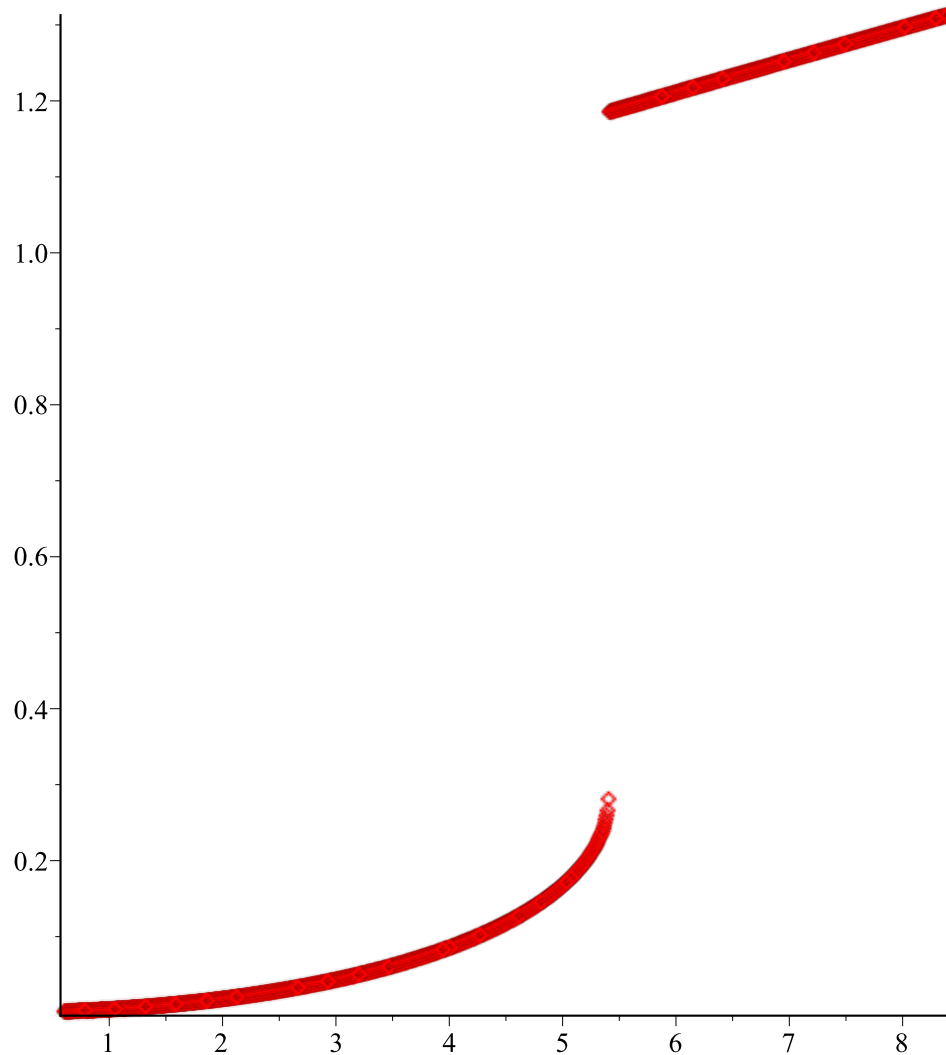


$$L_t := 0.000310$$

$$VI := 0.6$$

$$NI := 1000$$

$$SI := \{A = -0.00068358051611153974194, B = 0.0022558494097080999110\}$$

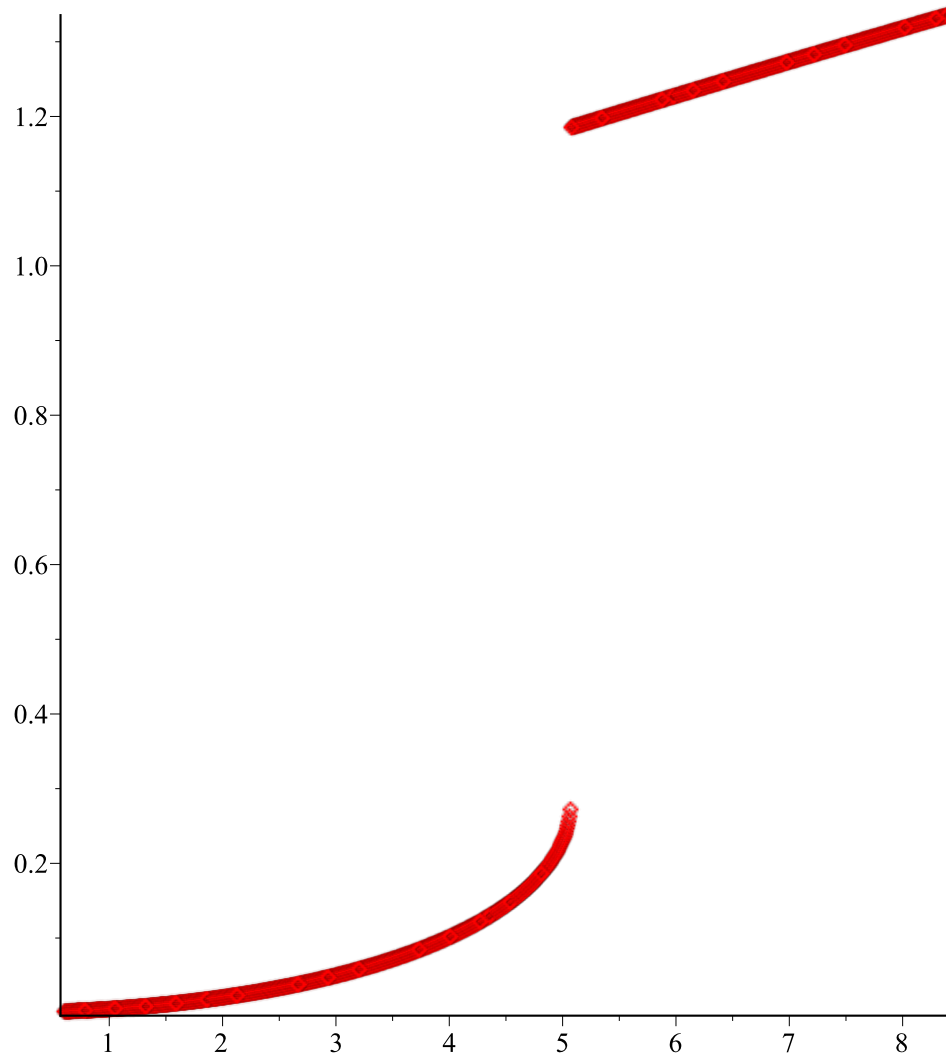


$$L_t := 0.000320$$

$$VI := 0.6$$

$$NI := 1000$$

$$SI := \{A = -0.00077652957904826071245, B = 0.0025625911179499527159\}$$

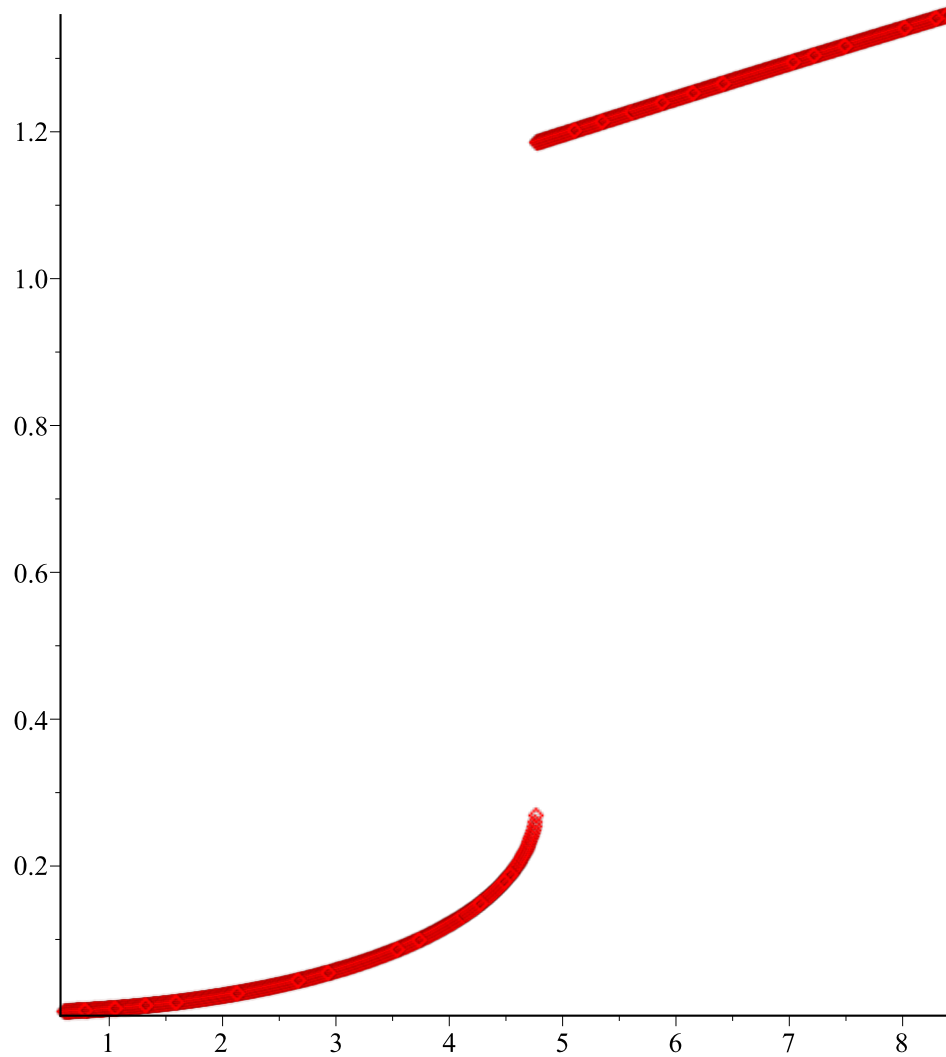


$$L_t := 0.000330$$

$$VI := 0.6$$

$$NI := 1000$$

$$SI := \{A = -0.00087871997368821929690, B = 0.0028998316401035990300\}$$

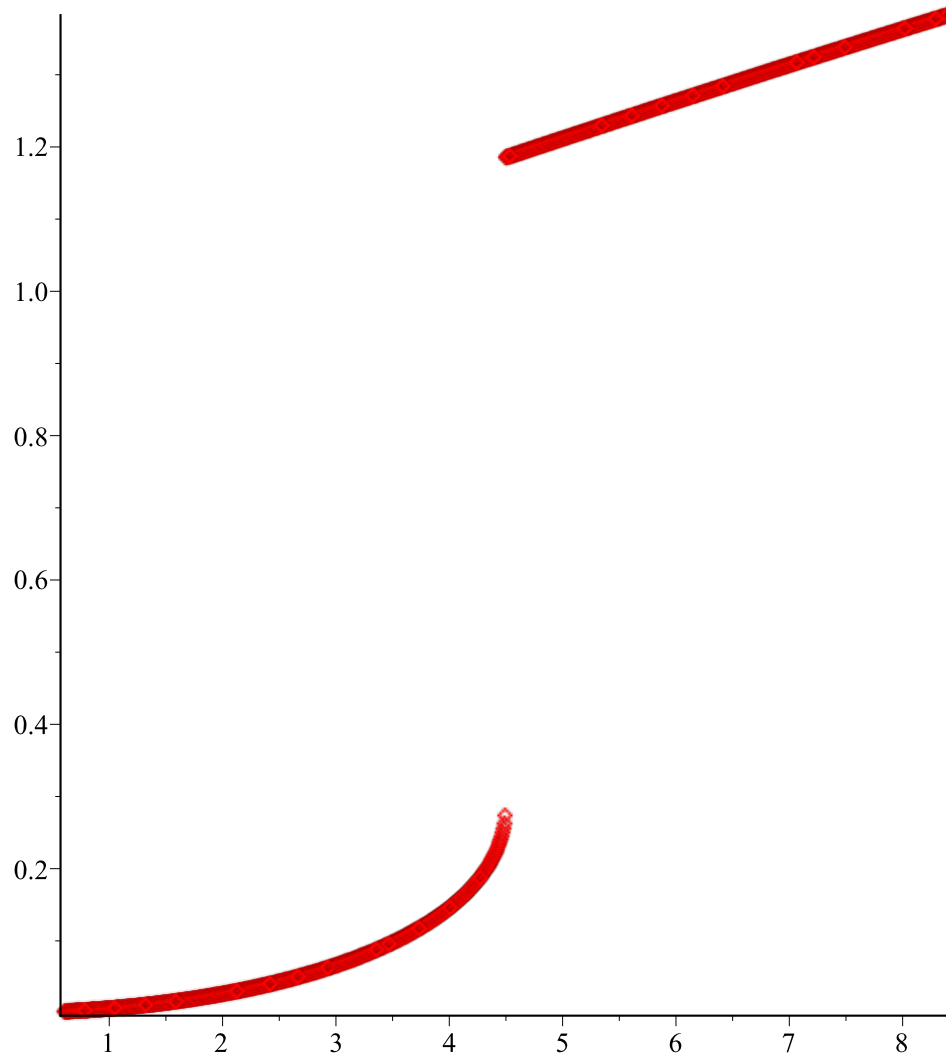


$$L_t := 0.000340$$

$$VI := 0.6$$

$$NI := 1000$$

$$SI := \{A = -0.00099076338937863811637, B = 0.0032695900505980321981\}$$

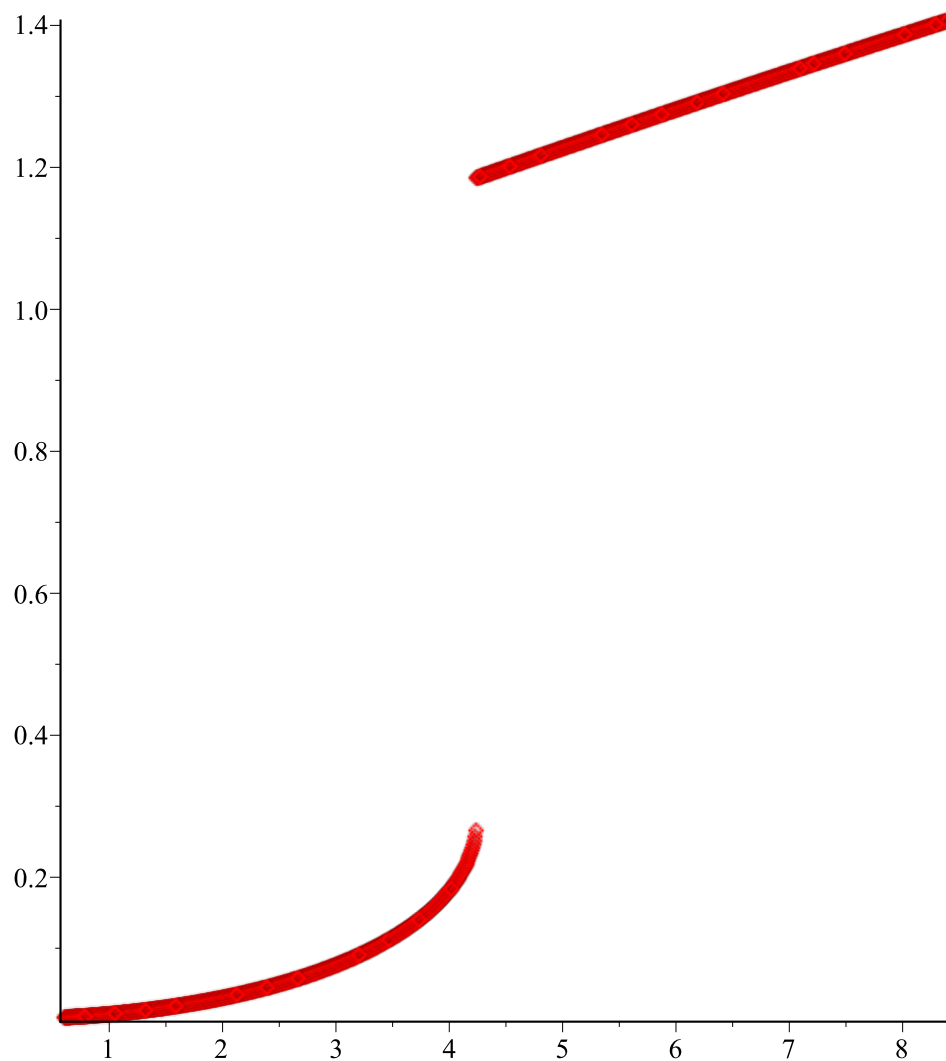


$$L_t := 0.000350$$

$$VI := 0.6$$

$$NI := 1000$$

$$SI := \{A = -0.0011132953409074630083, B = 0.0036739641327674679178\}$$

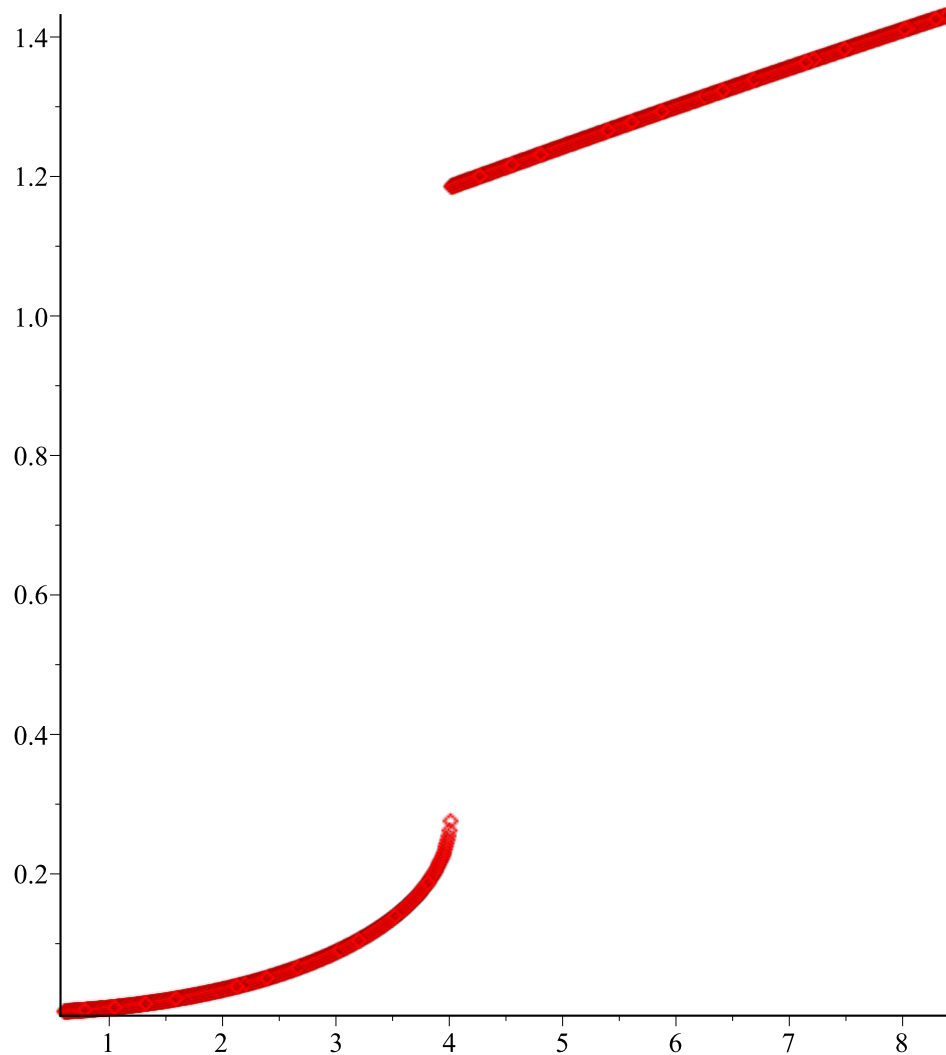


$$L_t := 0.000360$$

$$VI := 0.6$$

$$NI := 1000$$

$$SI := \{A = -0.0012469759966545244583, B = 0.0041151331235294070848\}$$

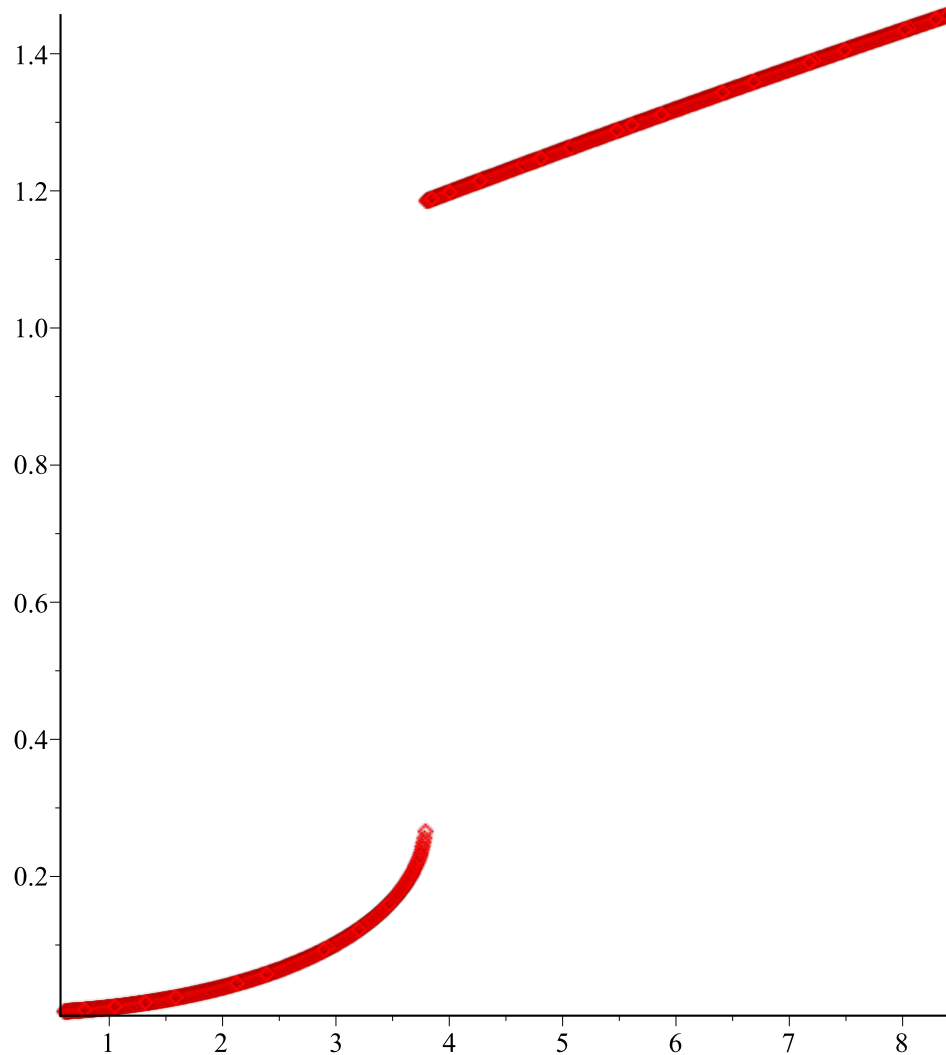


$$L_t := 0.000370$$

$$VI := 0.6$$

$$NI := 1000$$

$$SI := \{A = -0.0013924910970737874558, B = 0.0045953607575162926977\}$$



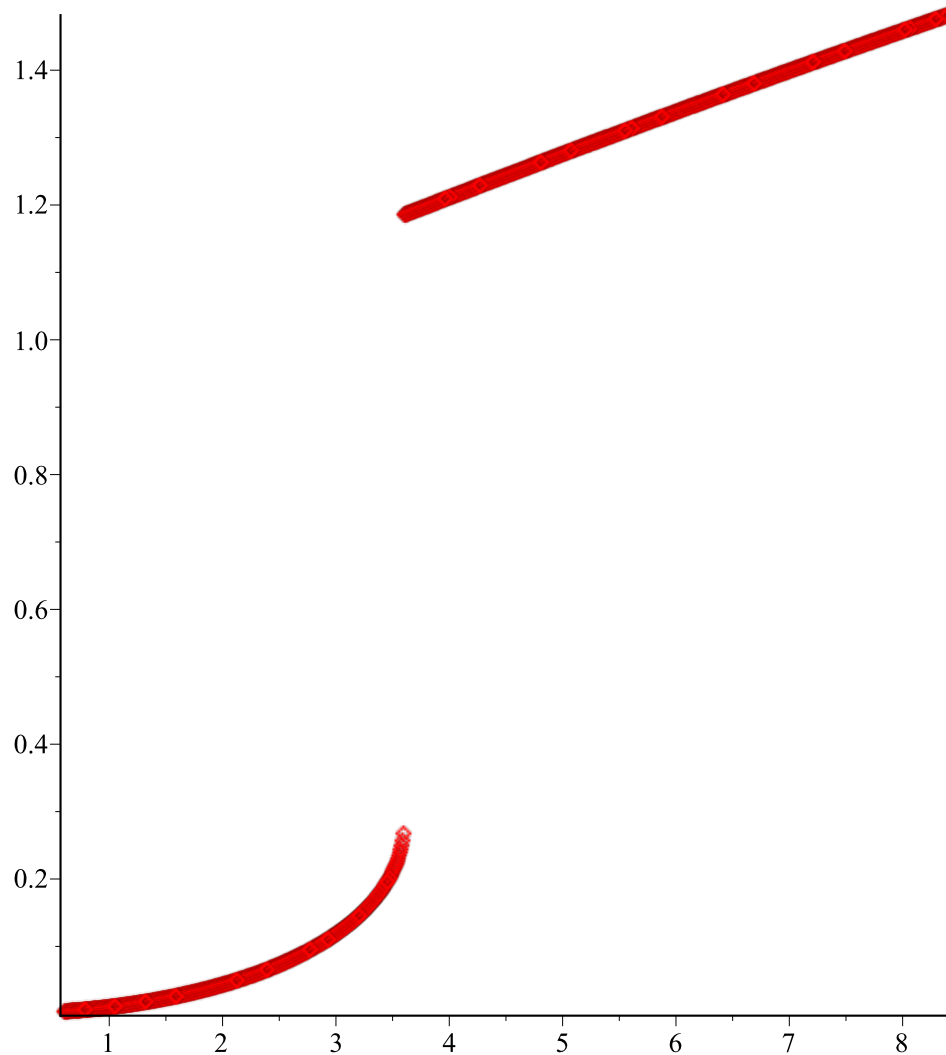
$$L_t := 0.000380$$

$$VI := 0.6$$

$$NI := 1000$$

$$SI := \{A = -0.0015505529722071300617, B = 0.0051169986395193377660\}$$



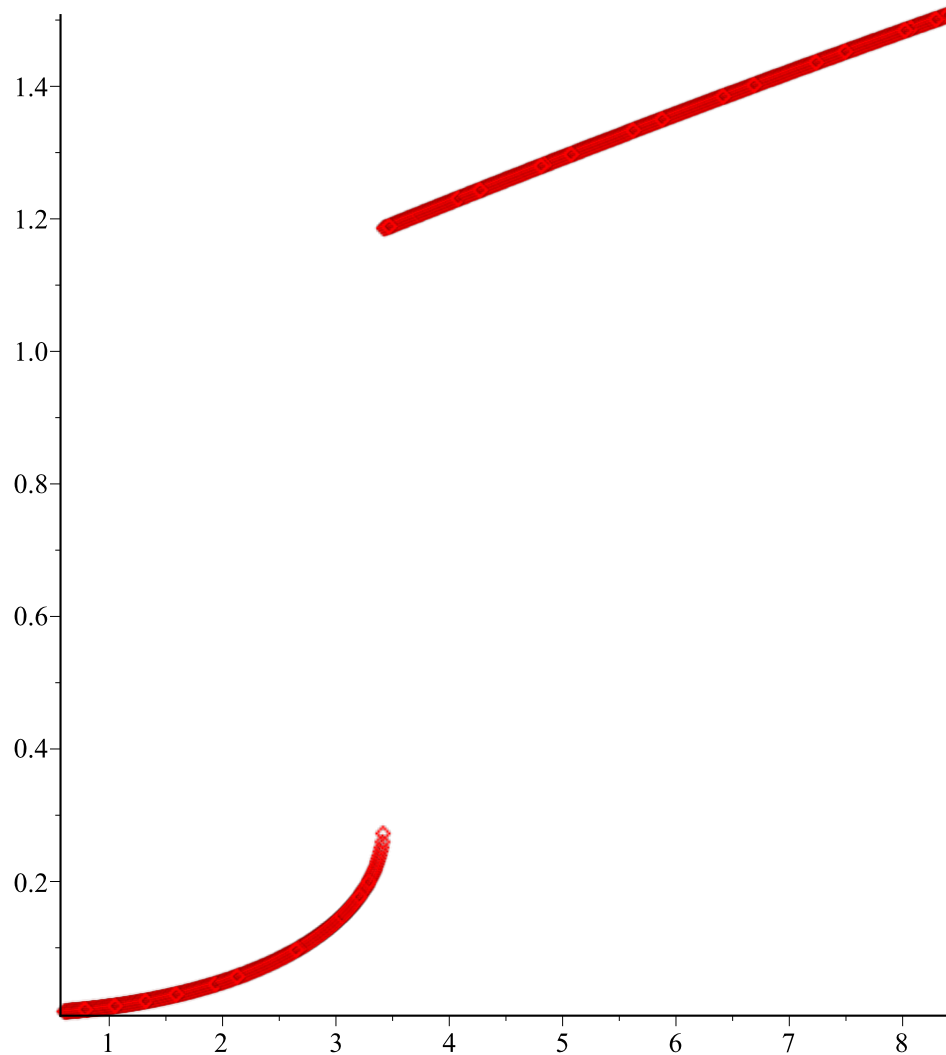


$$L_t := 0.000390$$

$$VI := 0.6$$

$$NI := 1000$$

$$SI := \{A = -0.0017219016678796027521, B = 0.0056824899772549222574\}$$

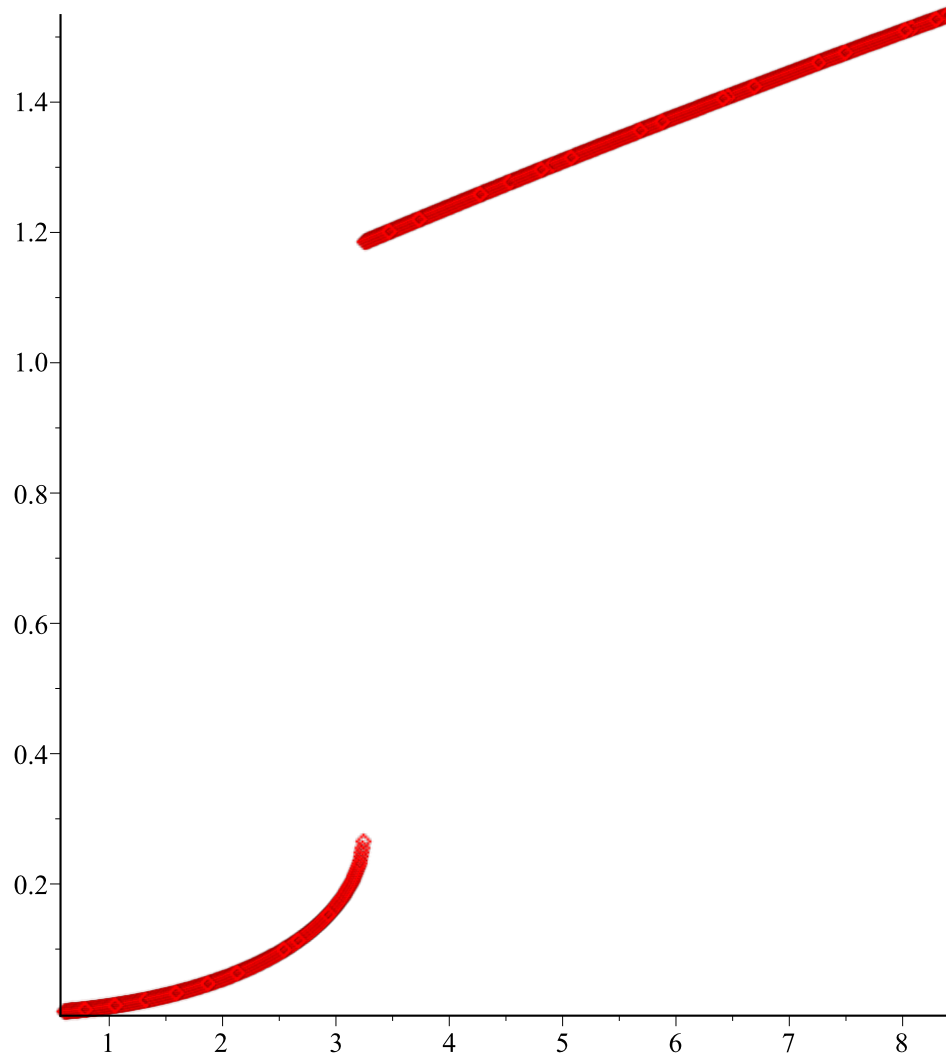


$$L_t := 0.000400$$

$$VI := 0.6$$

$$NI := 1000$$

$$SI := \{A = -0.0019073061913107177228, B = 0.0062943737100643928109\}$$

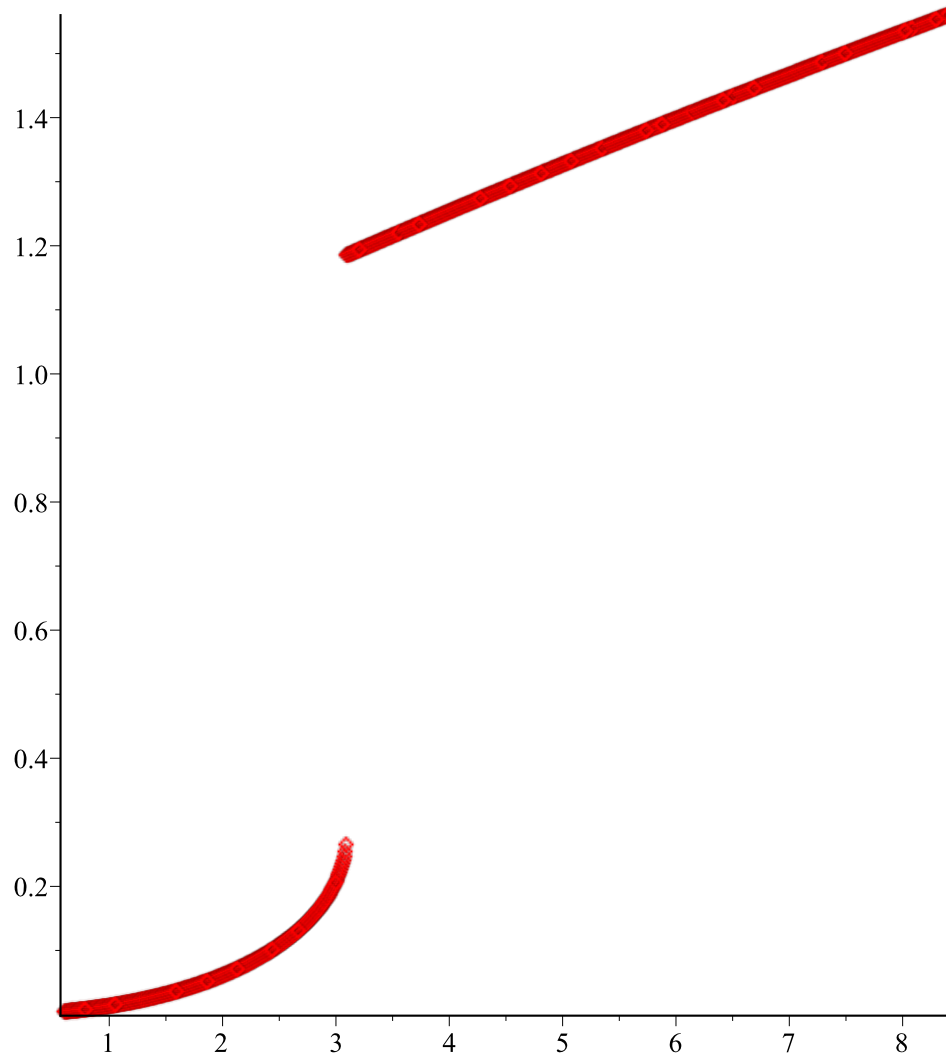


$$L_t := 0.000410$$

$$VI := 0.6$$

$$NI := 1000$$

$$SI := \{A = -0.0021075658881179095684, B = 0.0069552890732799343890\}$$

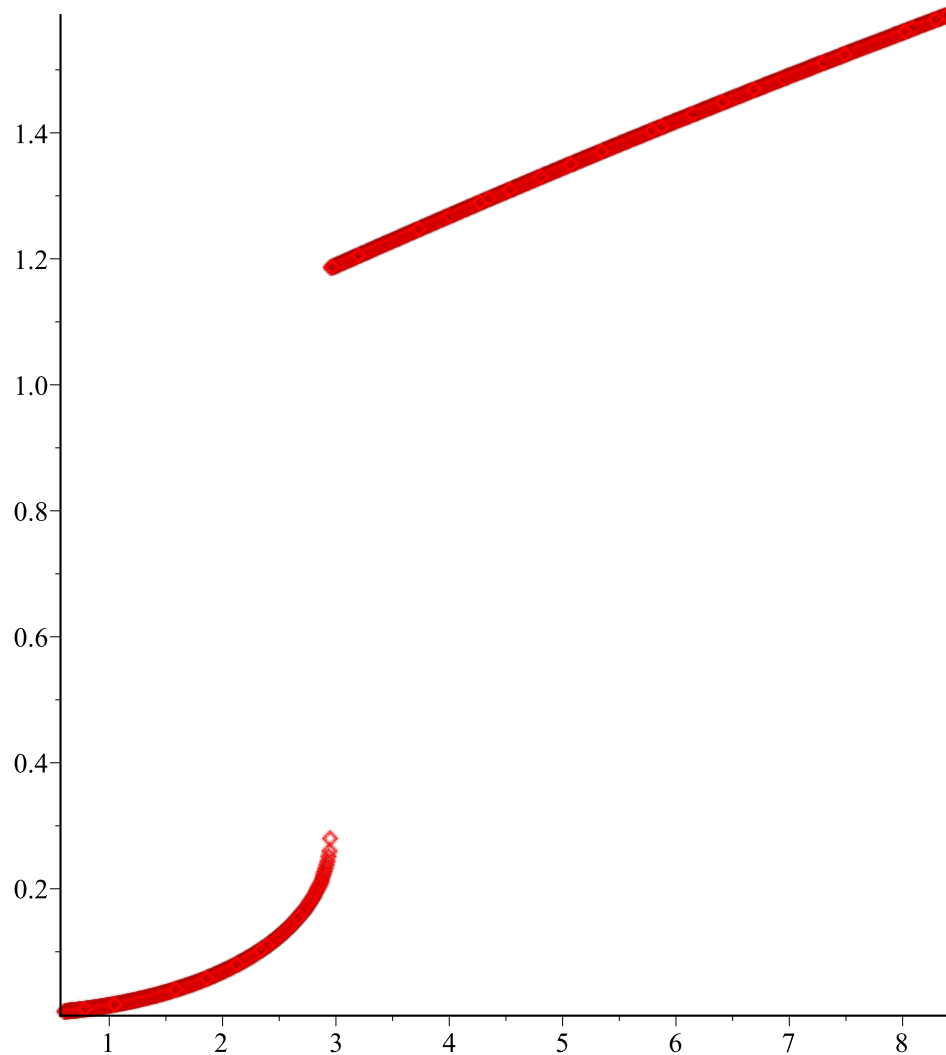


$$L_t := 0.000420$$

$$VI := 0.6$$

$$NI := 1000$$

$$SI := \{A = -0.0023235119641127566244, B = 0.0076679806427183325798\}$$

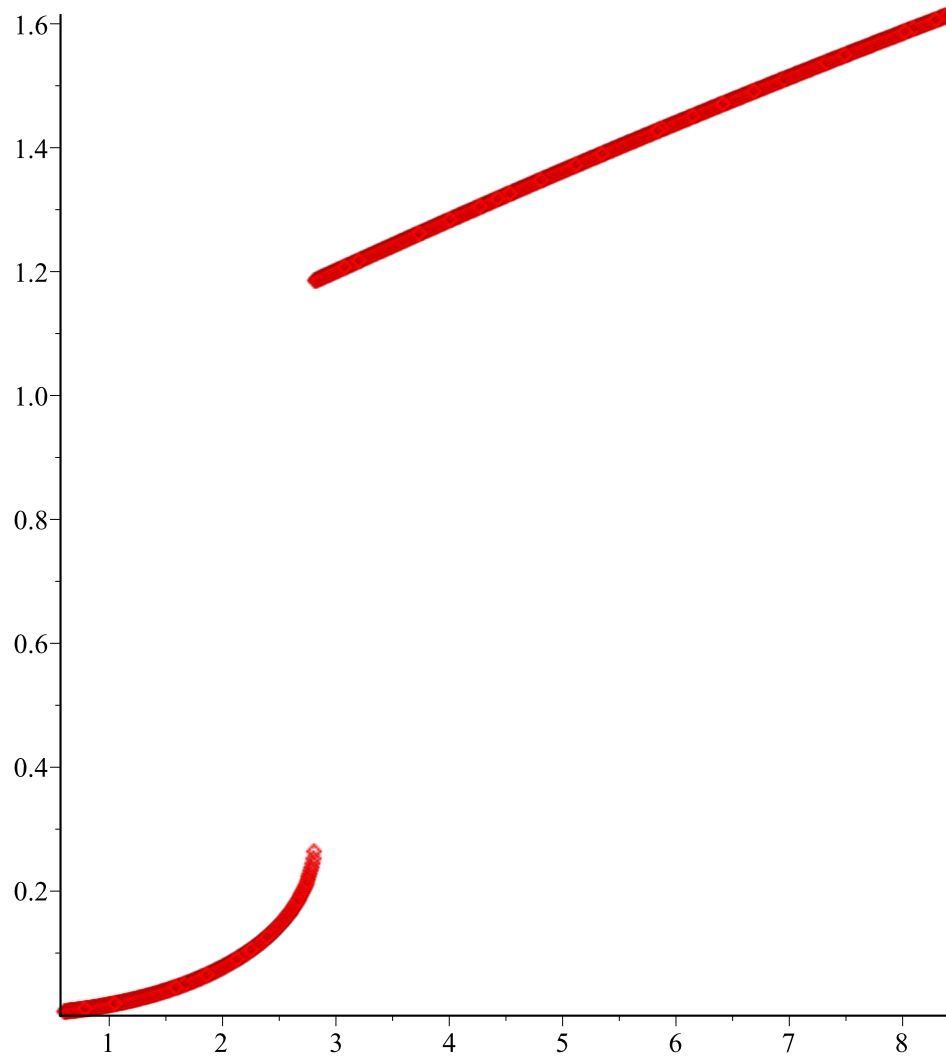


$$L_t := 0.000430$$

$$VI := 0.6$$

$$NI := 1000$$

$$SI := \{A = -0.0025560091669284840532, B = 0.0084353039092026677853\}$$

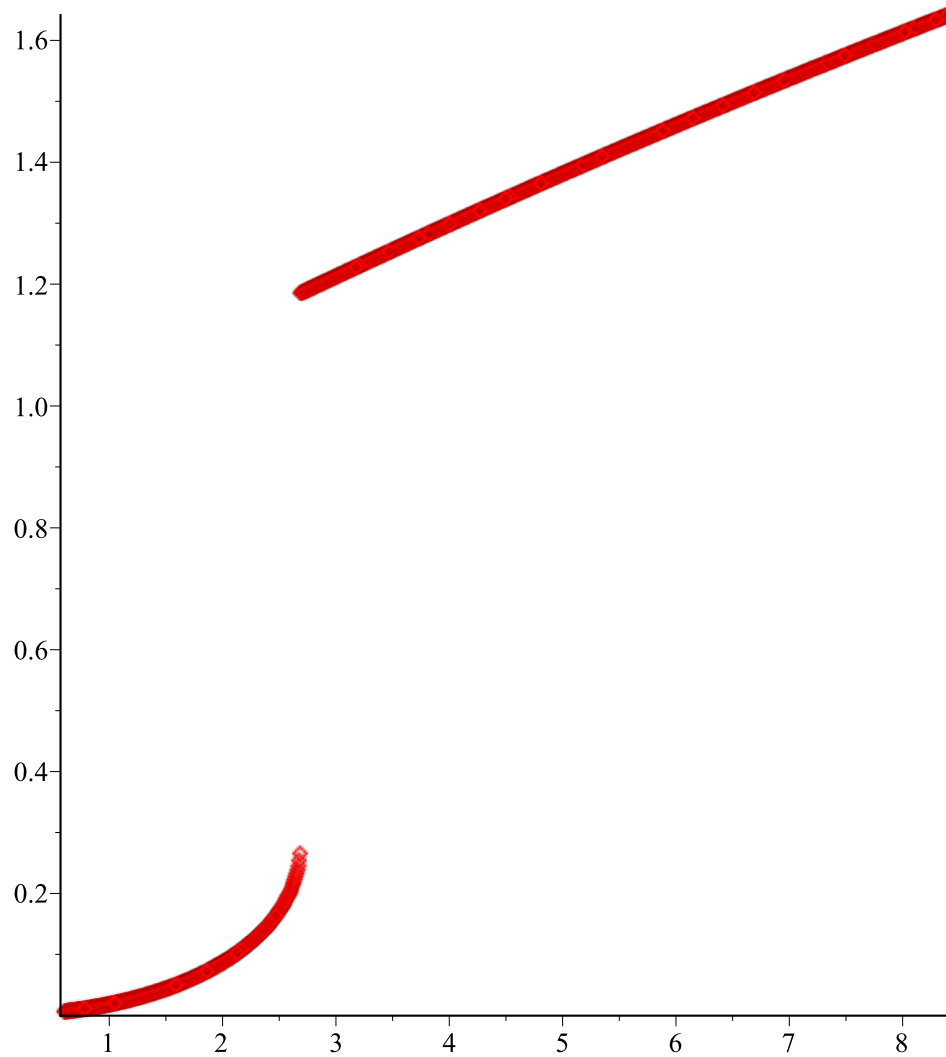


$$L_t := 0.000440$$

$$VI := 0.6$$

$$NI := 1000$$

$$SI := \{A = -0.0028059576444050870285, B = 0.0092602314392802244636\}$$

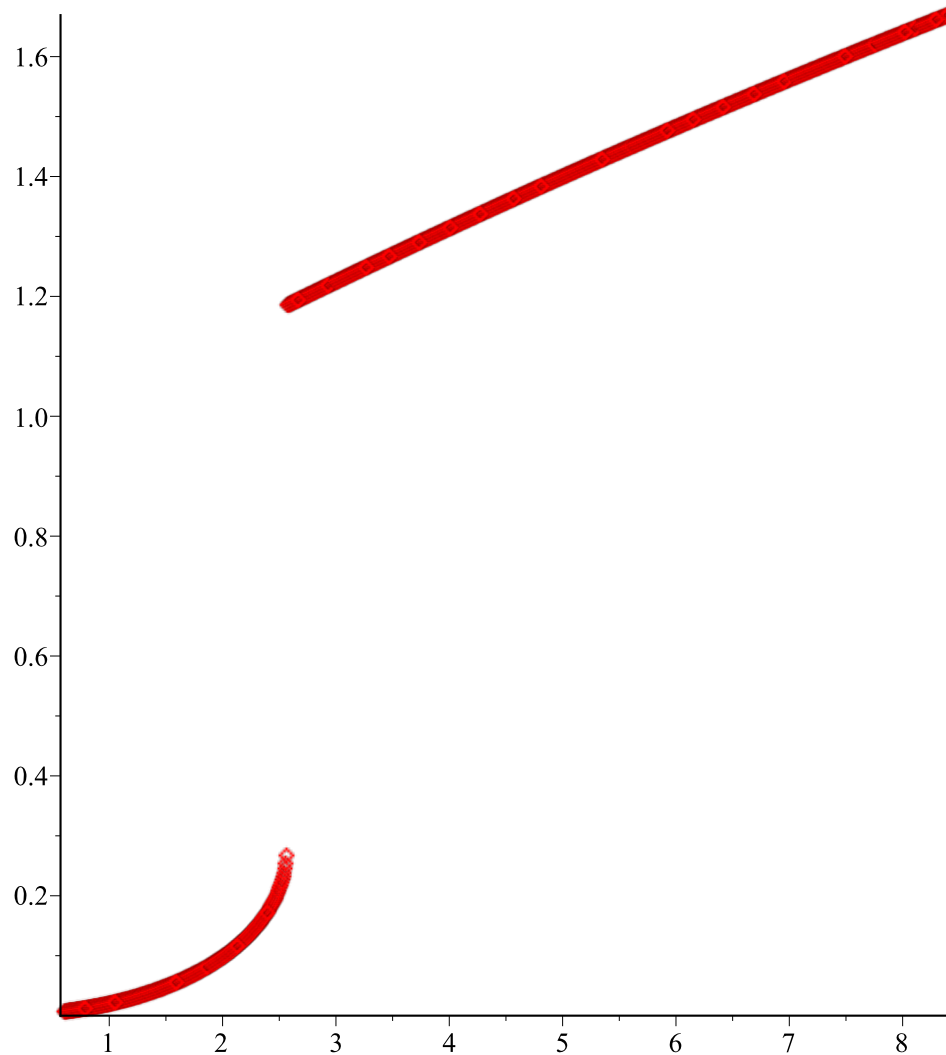


$$L_t := 0.000450$$

$$VI := 0.6$$

$$NI := 1000$$

$$SI := \{A = -0.0030742949988395326566, B = 0.010145859685547424636\}$$



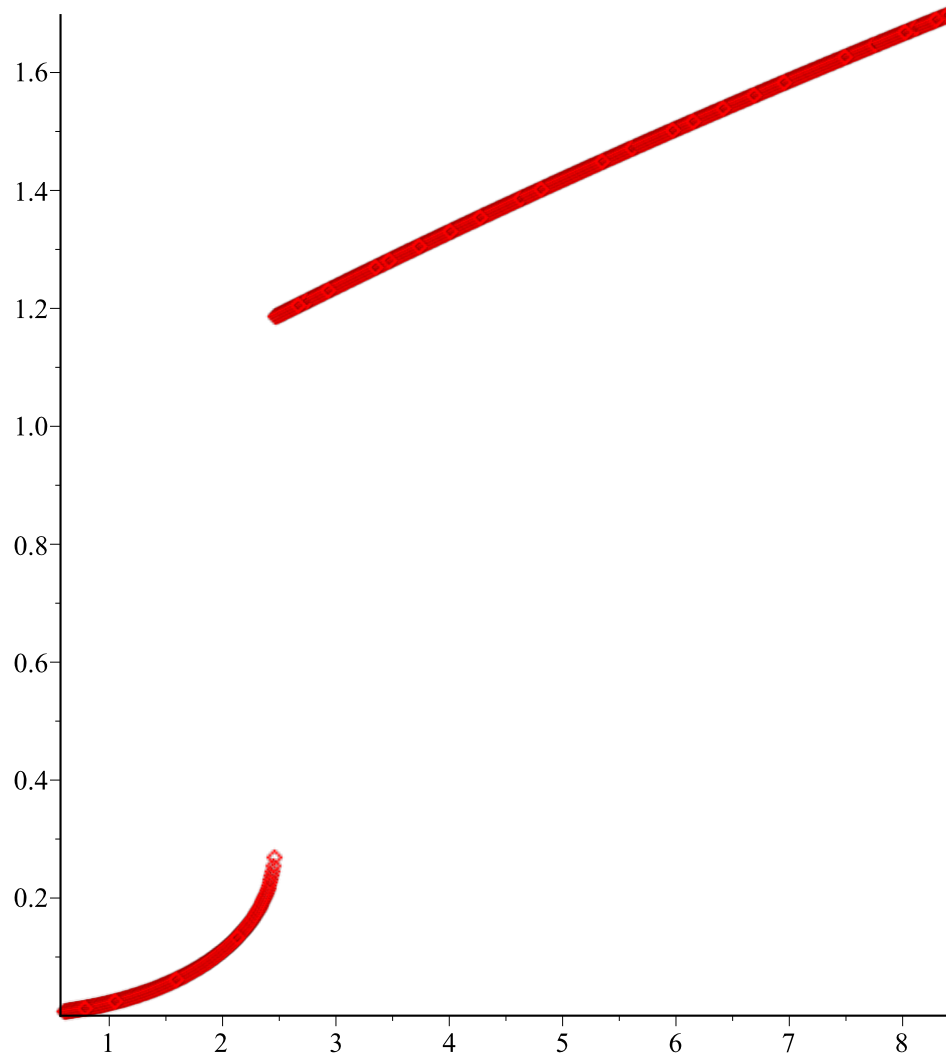
$$L_t := 0.000460$$

$$VI := 0.6$$

$$NI := 1000$$

$$SI := \{A = -0.0033619985587348973879, B = 0.011095416518382112409\}$$



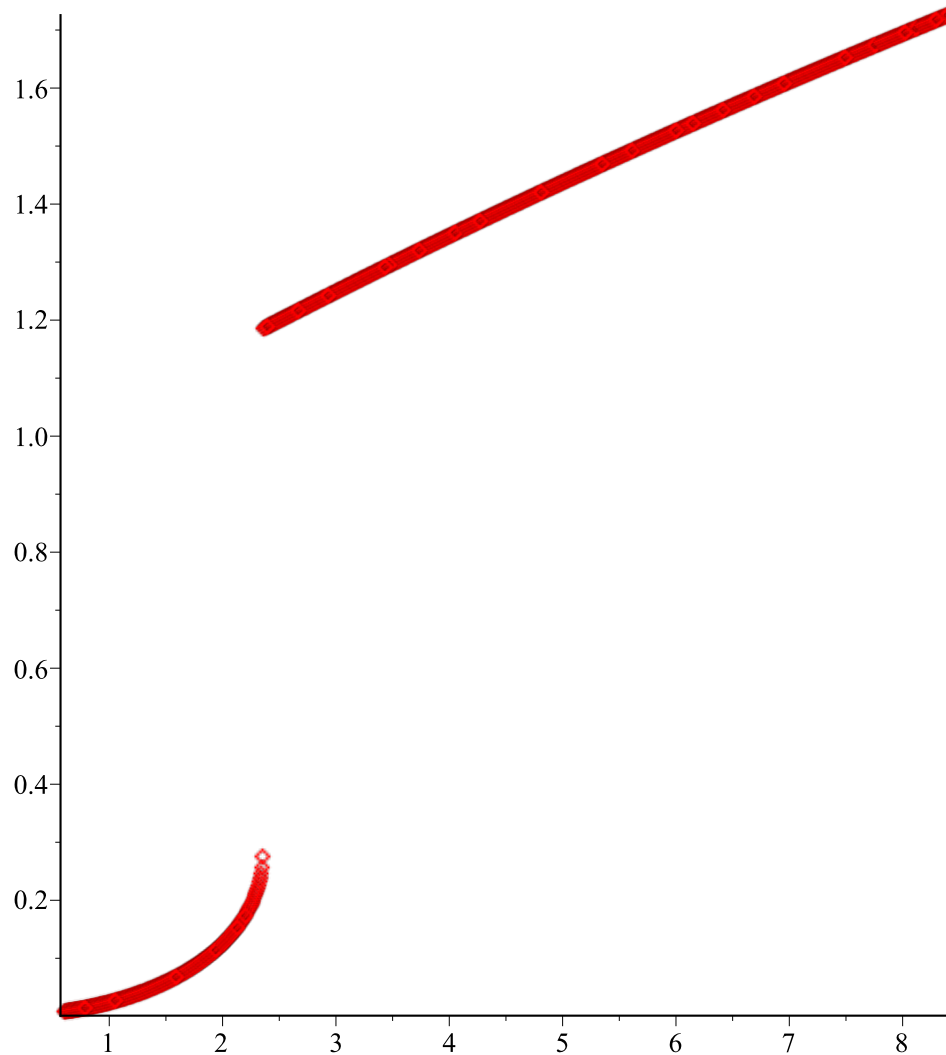


$$L_t := 0.000470$$

$$VI := 0.6$$

$$NI := 1000$$

$$SI := \{A = -0.0036700878926164246908, B = 0.012112269560627558196\}$$

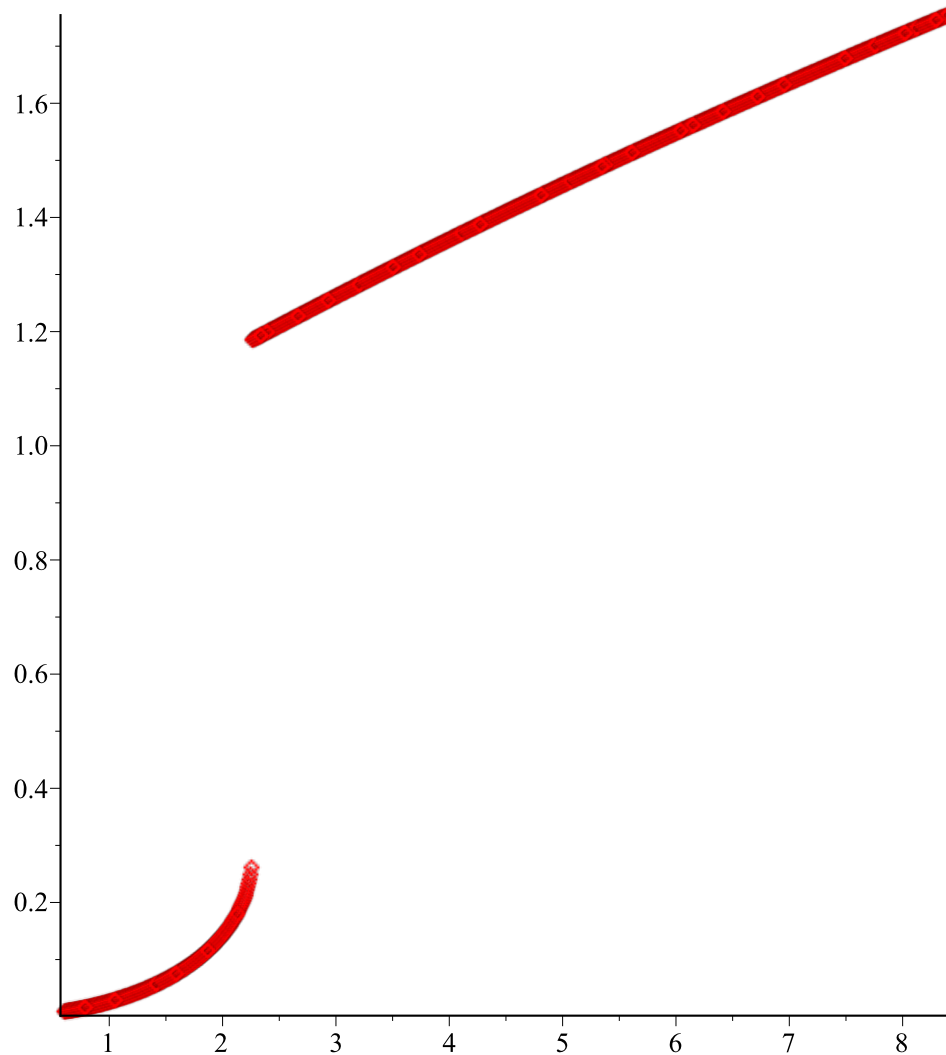


$$L_t := 0.000480$$

$$VI := 0.6$$

$$NI := 1000$$

$$SI := \{A = -0.0039996275928996764984, B = 0.013199935418121460829\}$$

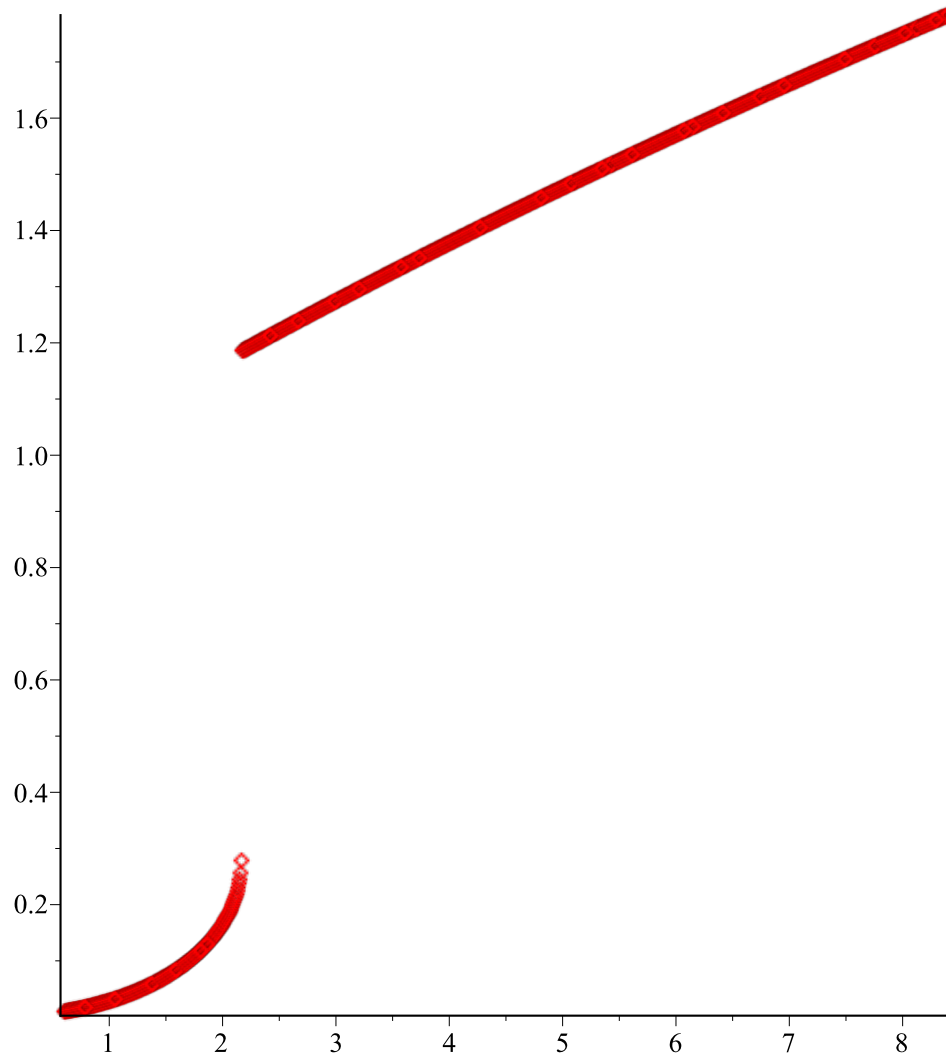


$$L_t := 0.000490$$

$$VI := 0.6$$

$$NI := 1000$$

$$SI := \{A = -0.0043517303617874285074, B = 0.014362089912220188841\}$$

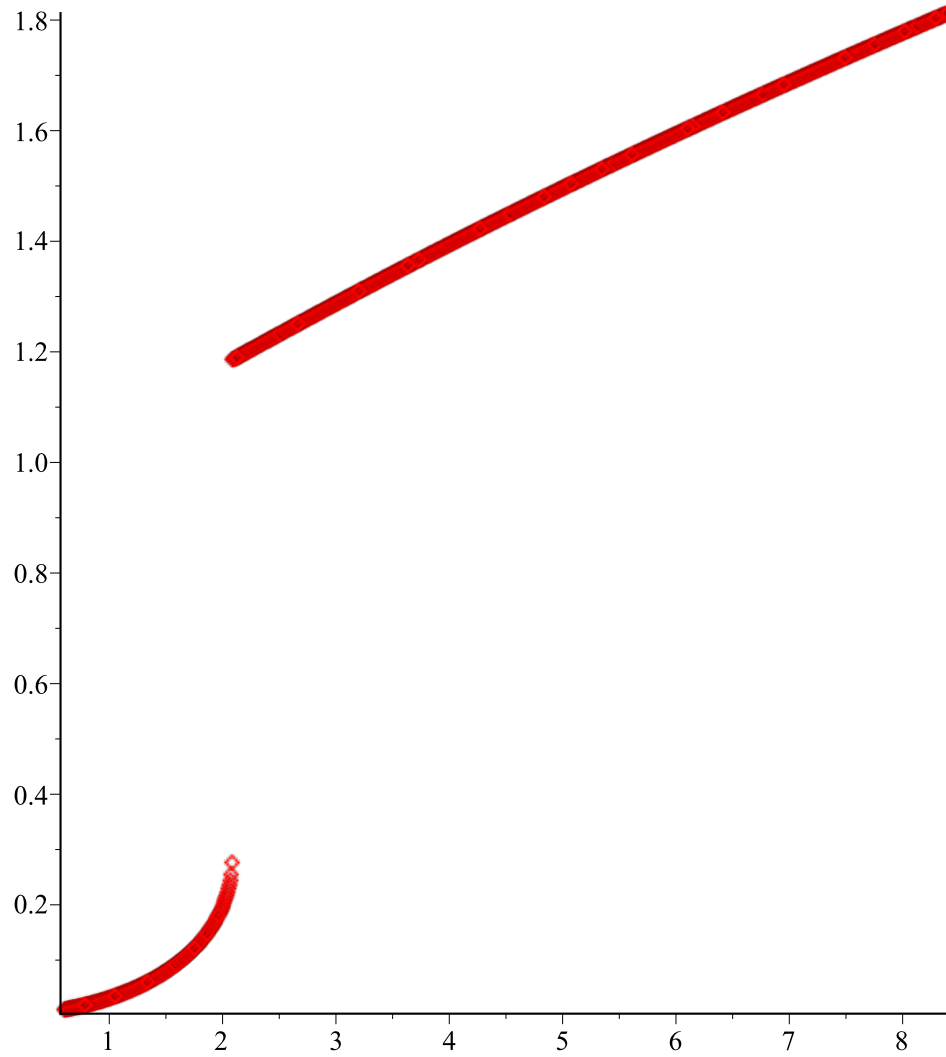


$$L_t := 0.000500$$

$$VI := 0.6$$

$$NI := 1000$$

$$SI := \{A = -0.0047275604358486562030, B = 0.015602579436002213440\}$$

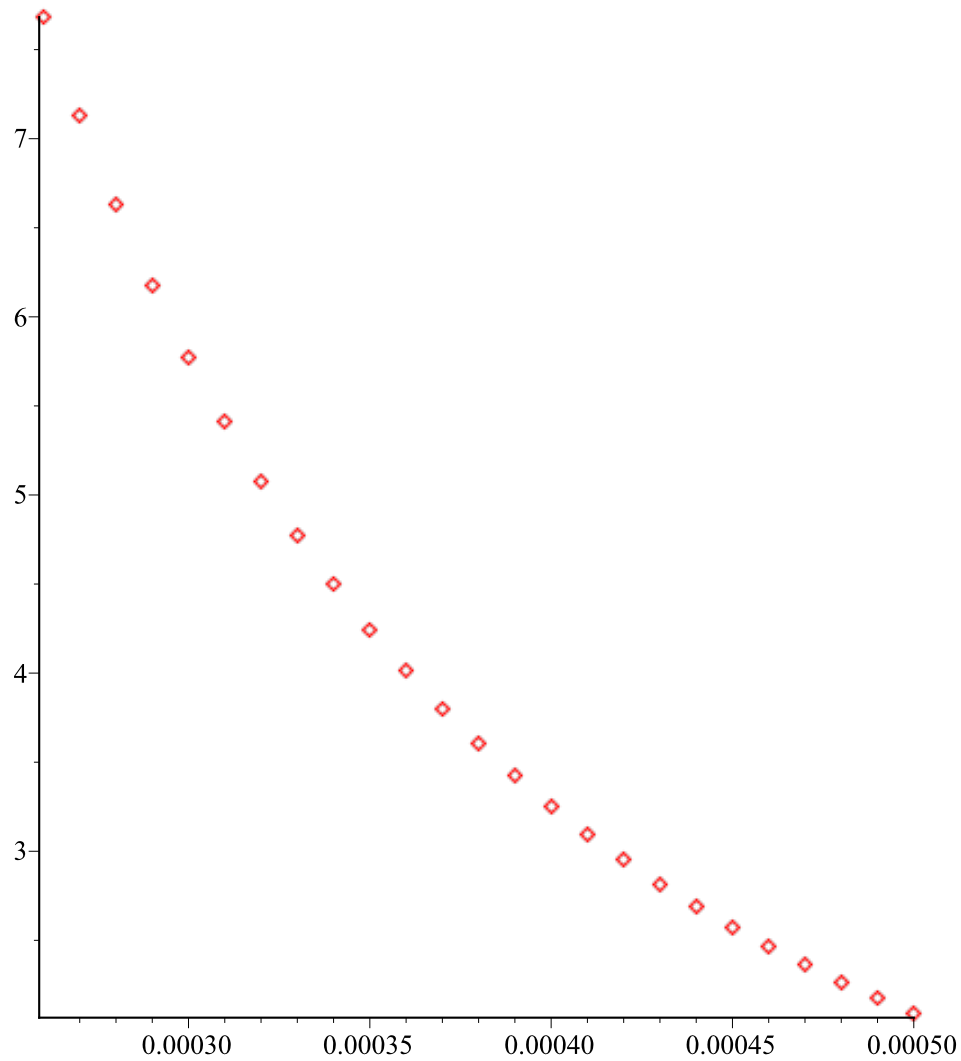


```
> seq(KK[i],i=1..10);
```

$KK_1, KK_2, KK_3, KK_4, KK_5, KK_6, KK_7, KK_8, KK_9, KK_{10}$

(8)

```
> plot({seq([LL[j],VV[j]],j=1..25)},style=point);
```



```
> V2[3000];
```

20.6

(9)

```
> i;
SS2:=fsolve({subs(V[dc]=V1,eq1),subs(V[dc]=V1,eq2)},{A=subs(S22,
A),B=subs(S22,B)});
```

1

(10)

$SS2 := \{A = -0.00019907330466001133955, B = 0.00065694476028556223363\}$

```
> V1;
```

```

> S22:={A = -.29609108669429914117e-3, B =
.97710690337665423008e-3};
L[1]:=250E-6;
V1:=1;
S22:=fsolve({subs(V[dc]=V1,eq1),subs(V[dc]=V1,eq2)},{A=subs(S22,
A),B=subs(S22,B)});
S1:={A=subs(S22,A),B=subs(S22,B)};
for kk from 1 to 25 do
L[1]:=L[1]-5E-6;
V1:=1+.05*kk;N1:=5000;
S1:=fsolve({subs(V[dc]=V1,eq1),subs(V[dc]=V1,eq2)},{A=subs(S1,A),
B=subs(S1,B)});
for i from 1 to N1 do;
V1:=i/N1*20+.8;
A1:=subs(S1,A);
B1:=subs(S1,B);
S1:=fsolve({subs(V[dc]=V1,eq1),subs(V[dc]=V1,eq2)},{A=A1,B=B1});
A2[i]:=A1;
B2[i]:=B1;
V2[i]:=V1;
A2km[i,k]:=A1;
B2km[i,k]:=B1;
V2km[i,k]:=V1;
od;
plot({seq([V2[j],A2[j]+B2[j]],j=1..N1)},style=point);
od;

```

$$S22 := \{A = -0.00029609108669429914117, B = 0.00097710690337665423008\}$$

$$L_l := 0.000250$$

$$V_l := 1$$

$$S22 := \{A = -0.00080367132165642297035, B = 0.0026521619665051582070\}$$

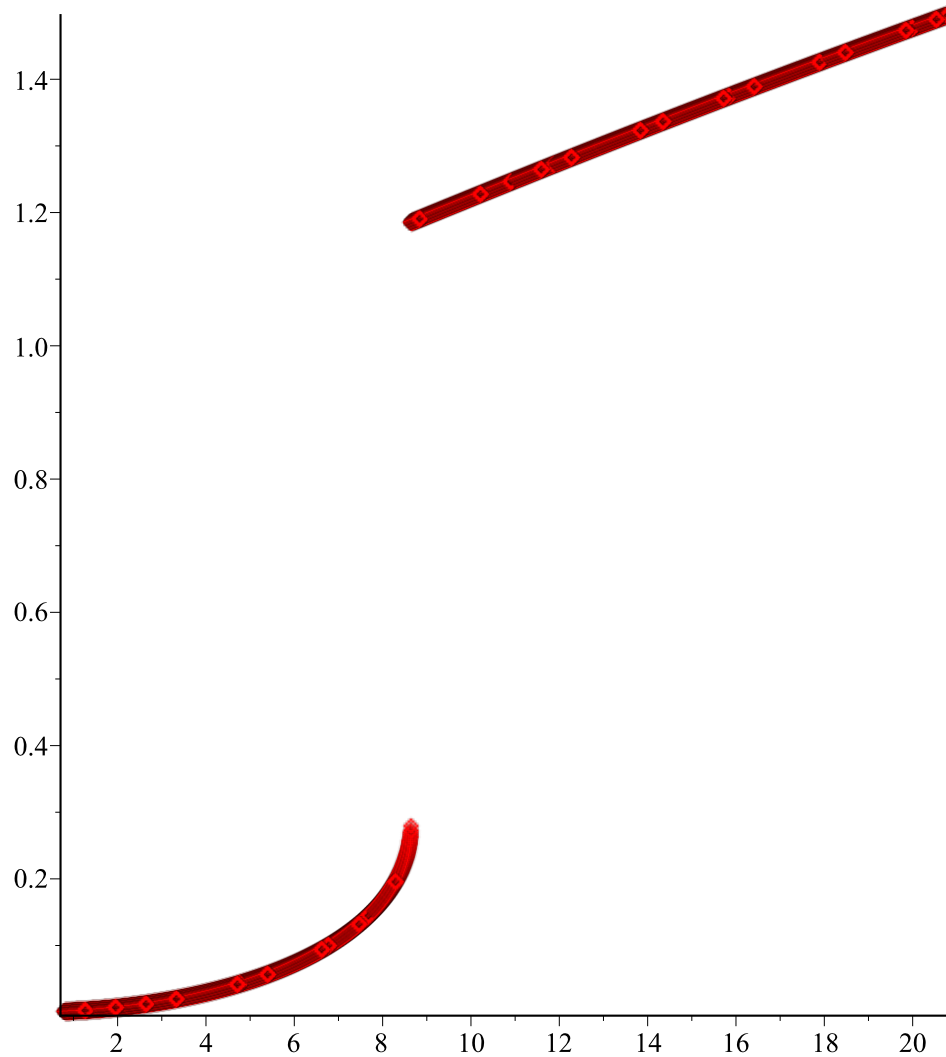
$$S1 := \{A = -0.00080367132165642297035, B = 0.0026521619665051582070\}$$

$$L_l := 0.000245$$

$$V_l := 1.05$$

$$N1 := 5000$$

$$S1 := \{A = -0.00081732160920546209808, B = 0.0026972095138075791177\}$$



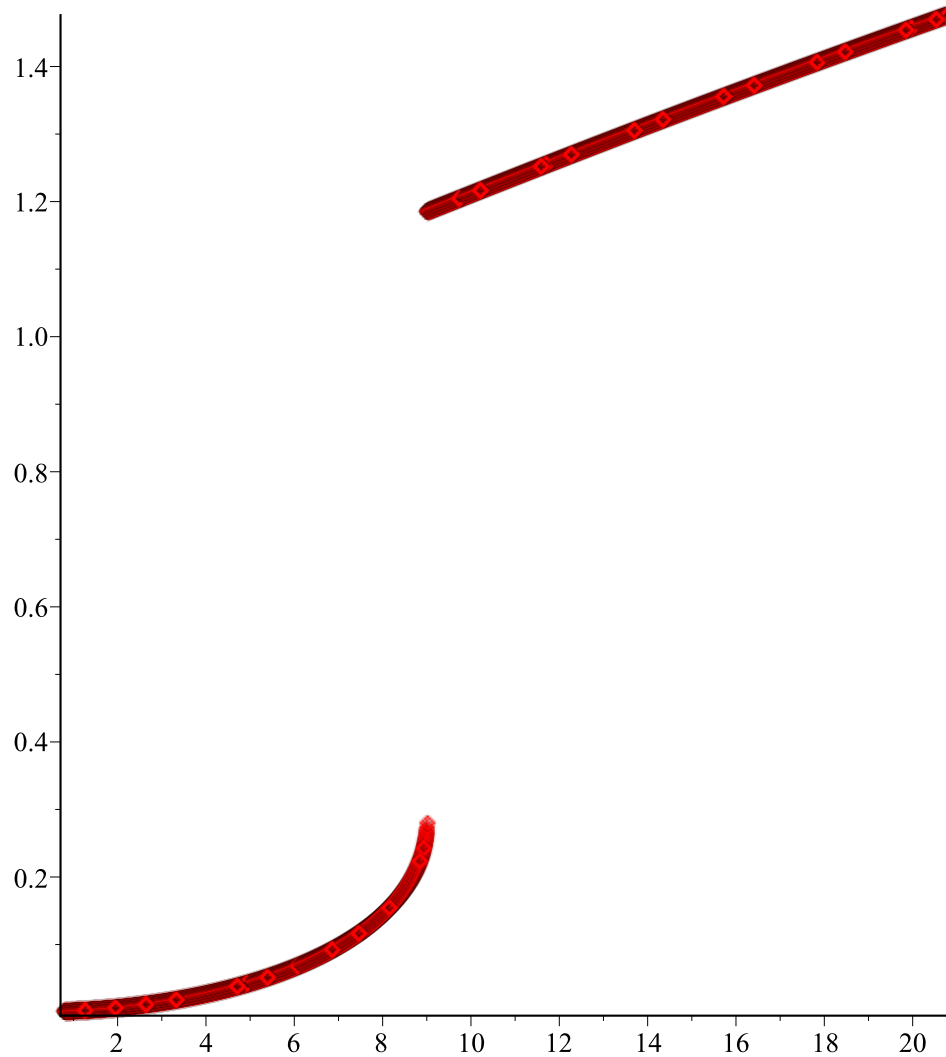
$$L_t := 0.000240$$

$$VI := 1.10$$

$$NI := 5000$$

$$SI := \{A = -0.00082603903396909785203, B = 0.0027259780504332957874\}$$



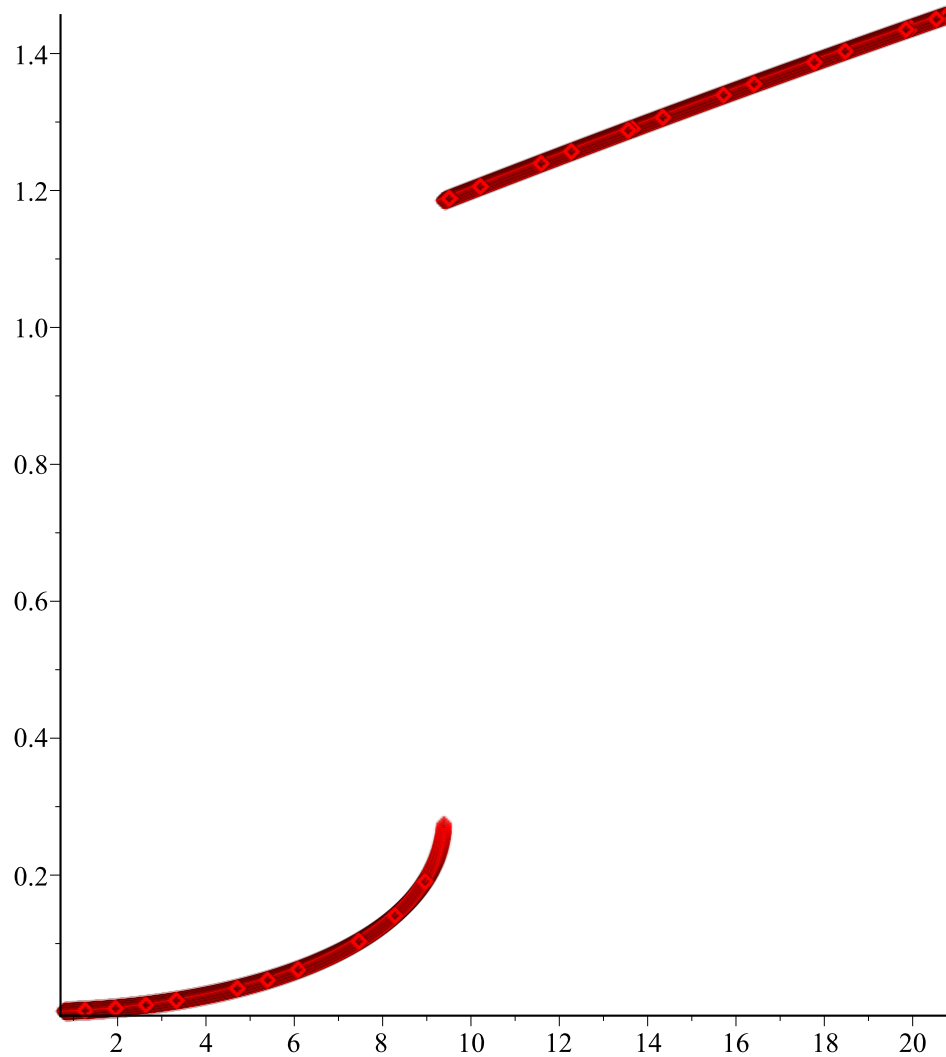


$$L_t := 0.000235$$

$$VI := 1.15$$

$$NI := 5000$$

$$SI := \{A = -0.00082993942418705857766, B = 0.0027388498047620421843\}$$

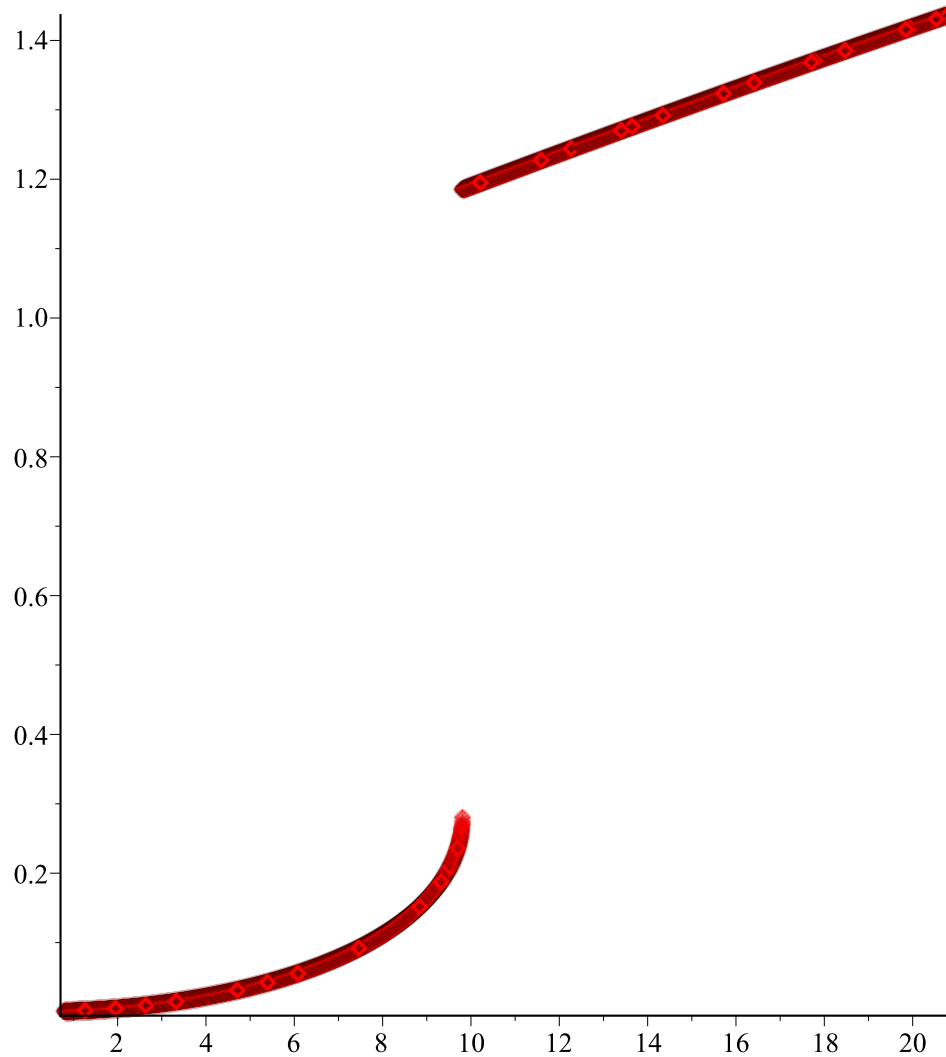


$$L_t := 0.000230$$

$$VI := 1.20$$

$$NI := 5000$$

$$SI := \{A = -0.00082918484151128818498, B = 0.0027363595914880898047\}$$

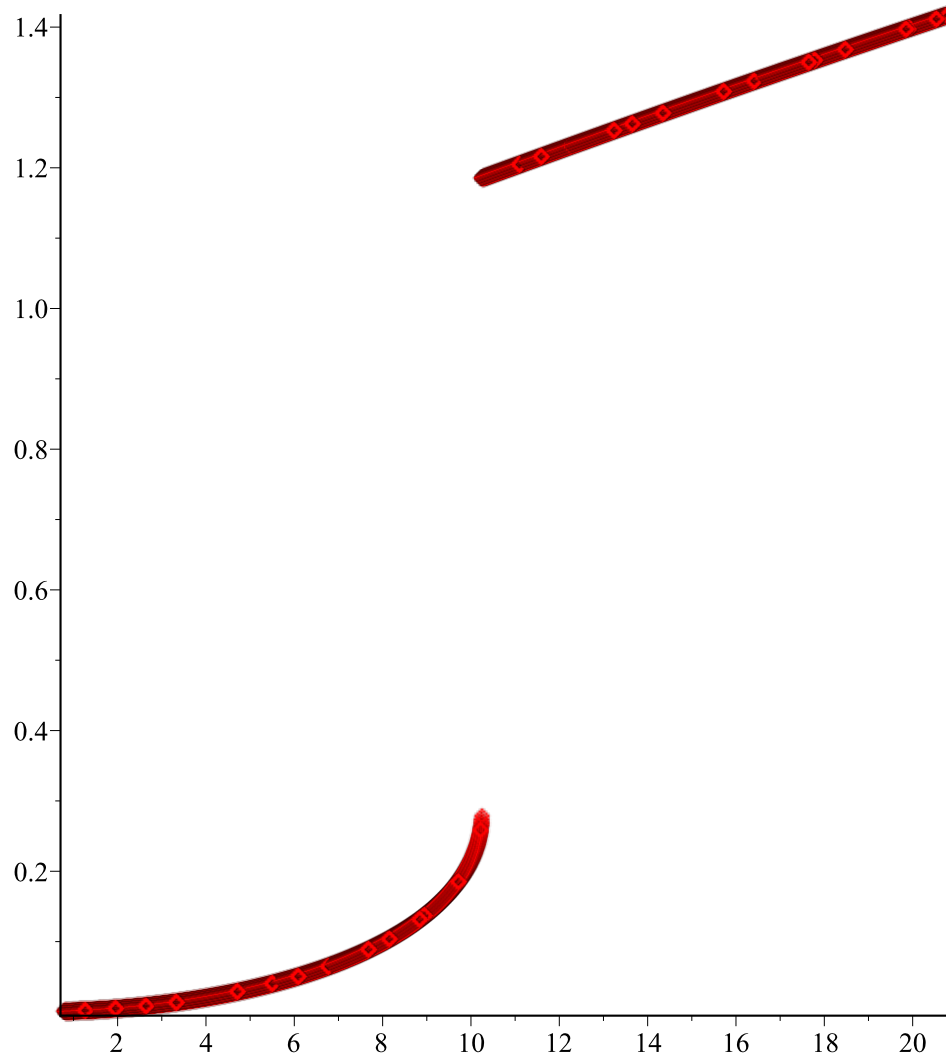


$$L_t := 0.000225$$

$$VI := 1.25$$

$$NI := 5000$$

$$SI := \{A = -0.00082397789002662190184, B = 0.0027191760297360699810\}$$

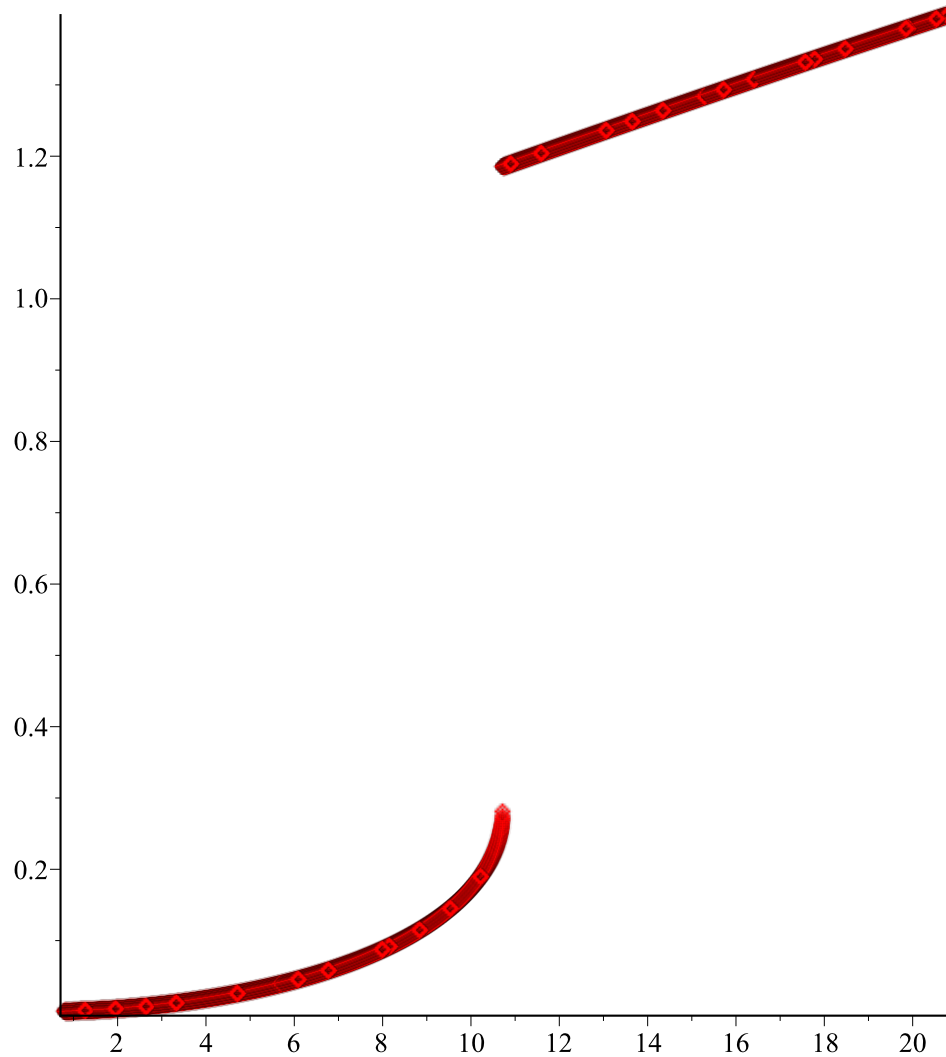


$$L_t := 0.000220$$

$$VI := 1.30$$

$$NI := 5000$$

$$SI := \{A = -0.00081455623055448389926, B = 0.0026880834382636973656\}$$

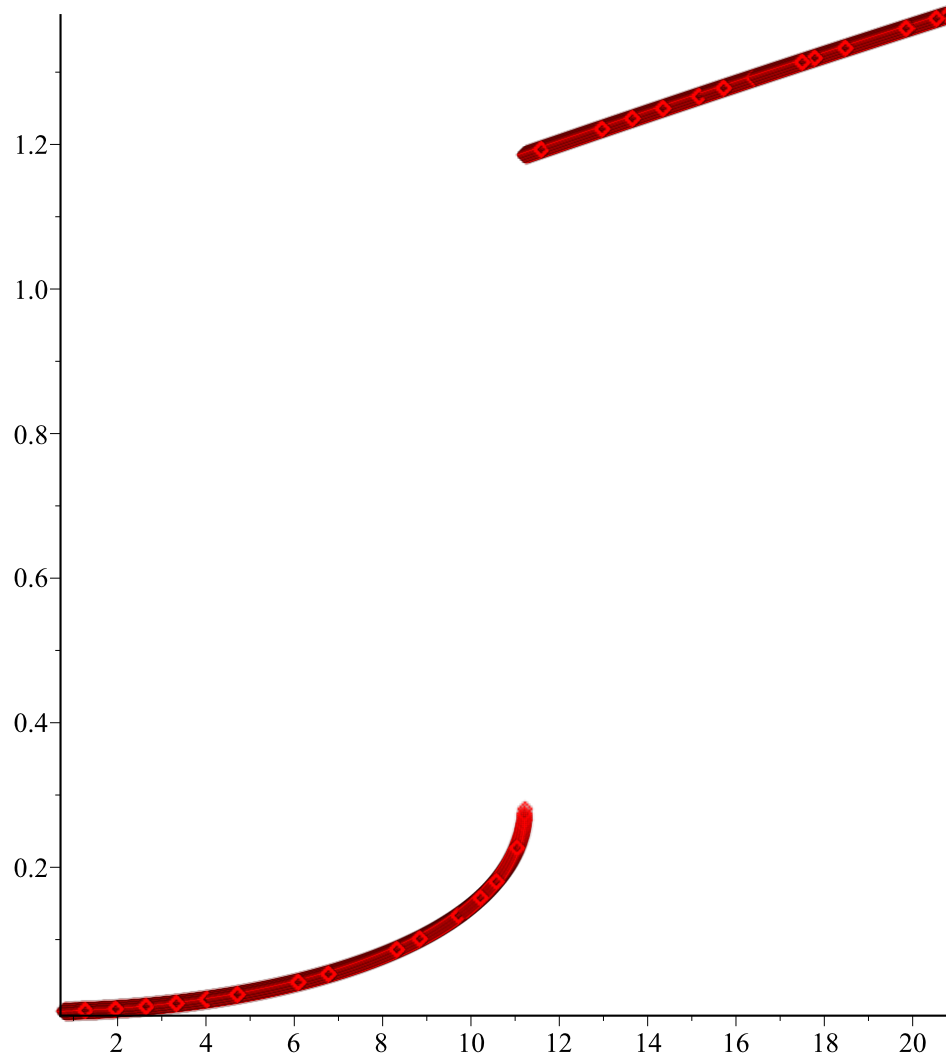


$$L_t := 0.000215$$

$$VI := 1.35$$

$$NI := 5000$$

$$SI := \{A = -0.00080118730863331074681, B = 0.0026439644355660899083\}$$

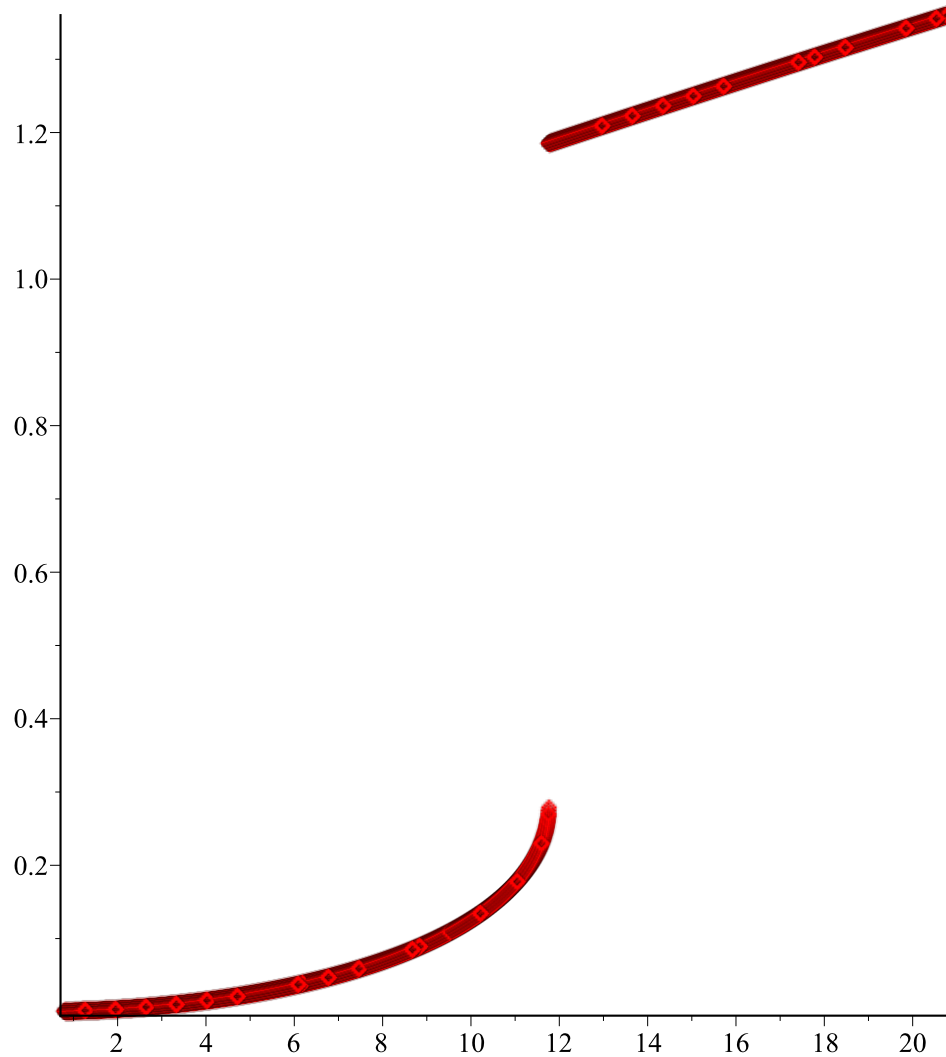


$$L_t := 0.000210$$

$$VI := 1.40$$

$$NI := 5000$$

$$SI := \{A = -0.00078416330404390748915, B = 0.0025877832709551790824\}$$

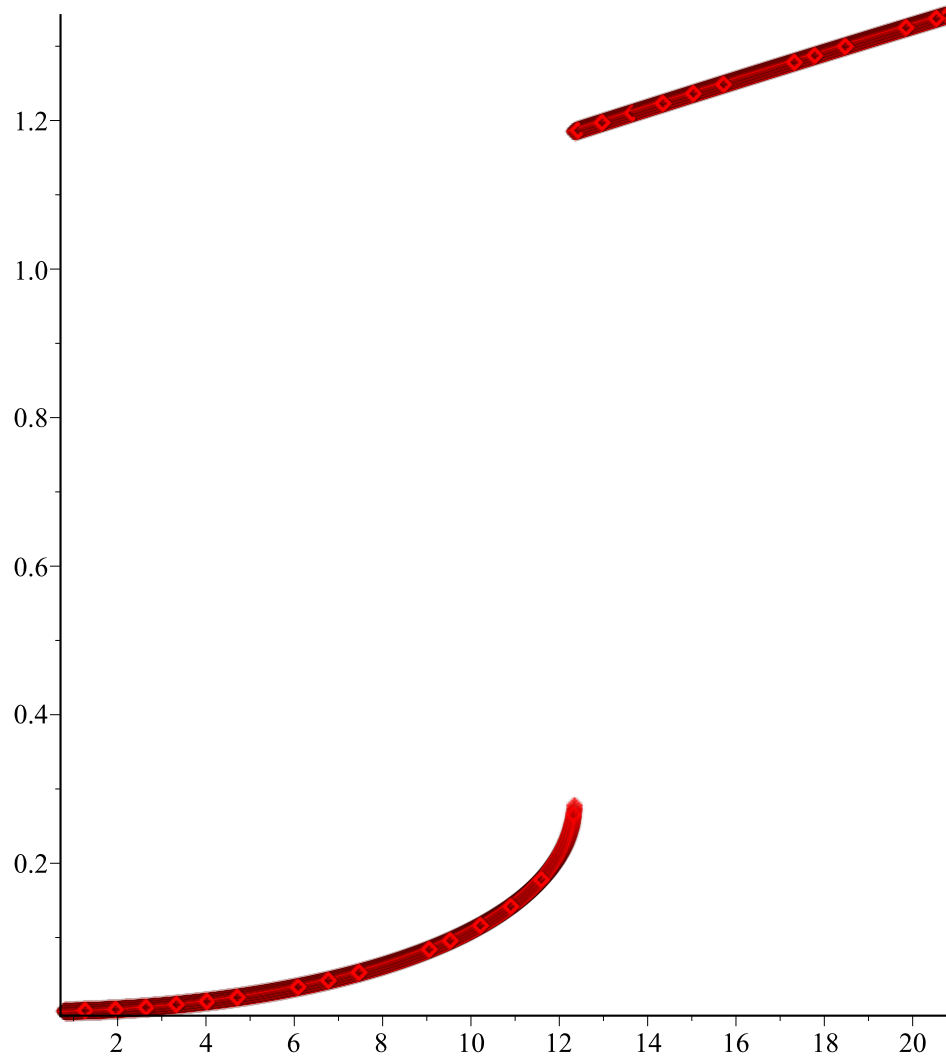


$$L_t := 0.000205$$

$$VI := 1.45$$

$$NI := 5000$$

$$SI := \{A = -0.00076379630902734125643, B = 0.0025205699102998660635\}$$



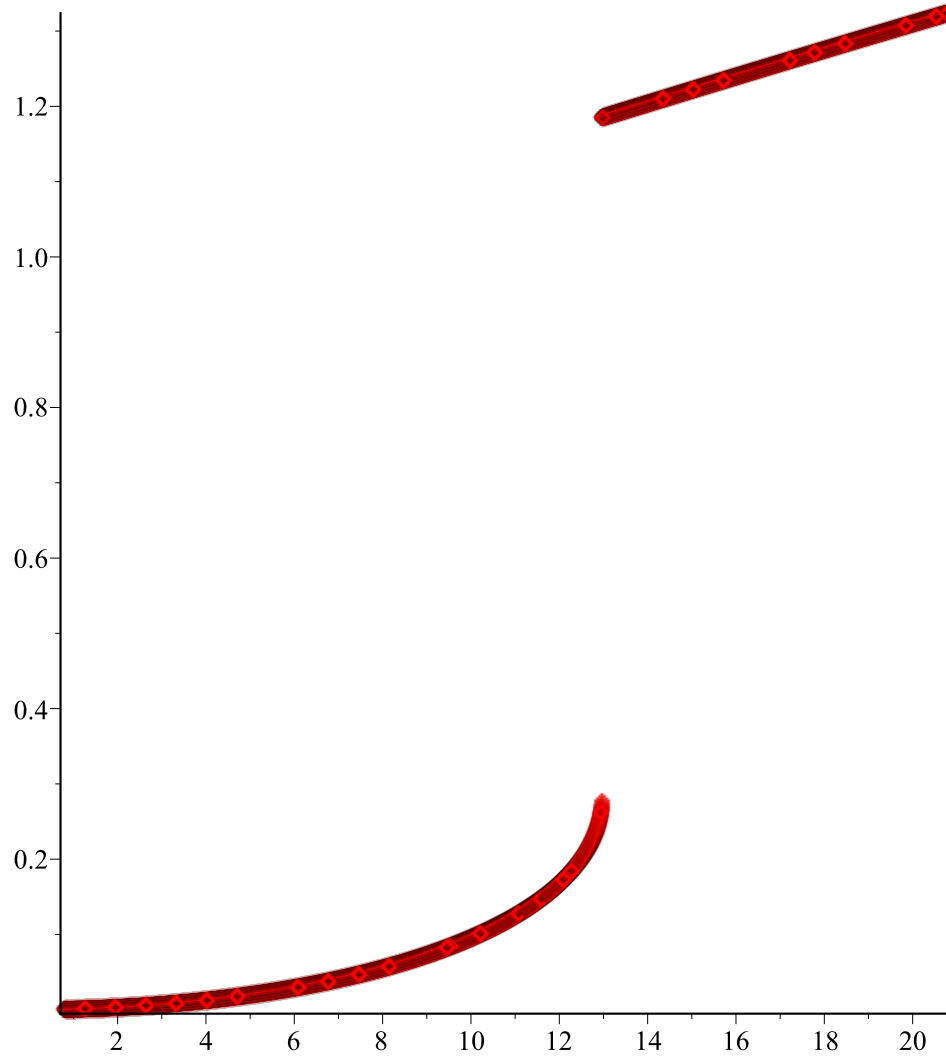
$$L_t := 0.000200$$

$$VI := 1.50$$

$$NI := 5000$$

$$SI := \{A = -0.00074041374148134413511, B = 0.0024434048972573120322\}$$





$$L_t := 0.000195$$

$$VI := 1.55$$

$$NI := 5000$$

$$SI := \{A = -0.00071435399846752950319, B = 0.0023574050076654426284\}$$

Error, invalid input: subs received fsolve( $\{6*A = -.59169723752546026776e-2 / (3*A+2*B) * (1/(1-8/5*A-7/5*B) - 1/(1-A-B))$ ,  $6*A+2*B = .59169723752546026776e-2 / (3*A+2*B)^2 * (1/5 * (3*A+2*B) / (1-8/5*A-7/5*B) - \ln((1-A-B)/(1-8/5*A-7/5*B)))\}$ ,  $\{A = -.19550679599813650999e-3, B = .64517518029667356519e-3\}$ ), which is not valid for its 1st argument

```
> i;
```

5

(12)

```
> V1:=8.2;N1:=1000;  
A5:=-1.2;  
S1:=fsolve({subs(V[dc]=V1,eq1),subs(V[dc]=V1,eq2)},{A=-.17...1,  
B=.4...0.5});
```

$V1 := 8.2$

(13)

$N1 := 1000$

$A5 := -1.2$

$S1 := \{A = -0.14476734761234273894, B = 0.48022542501132651269\}$

```
> V1:=8.2;N1:=1000;  
for i from 1 to N1 do;  
V1:=-i/N1*8.4+8.2;  
A1:=subs(S1,A);  
B1:=subs(S1,B);  
S1:=fsolve({subs(V[dc]=V1,eq1),subs(V[dc]=V1,eq2)},{A=A1,B=B1});  
A3[i]:=A1;  
B3[i]:=B1;  
V3[i]:=V1;  
od;
```

$V1 := 8.2$

(14)

$N1 := 1000$

```
> V1:=8.2;N1:=1000;  
A5:=-1.2;  
S1:=fsolve({subs(V[dc]=V1,eq1),subs(V[dc]=V1,eq2)},{A=-.17...1,  
B=.4...0.5});
```

```
> V1:=8.2;N1:=1000;  
for i from 1 to N1 do;  
V1:=i/N1*8.4+8.2;  
A1:=subs(S1,A);  
B1:=subs(S1,B);  
S1:=fsolve({subs(V[dc]=V1,eq1),subs(V[dc]=V1,eq2)},{A=A1,B=B1});  
A4[i]:=A1;  
B4[i]:=B1;  
V4[i]:=V1;  
od;
```

$V1 := 8.2$

(15)

$NI := 1000$

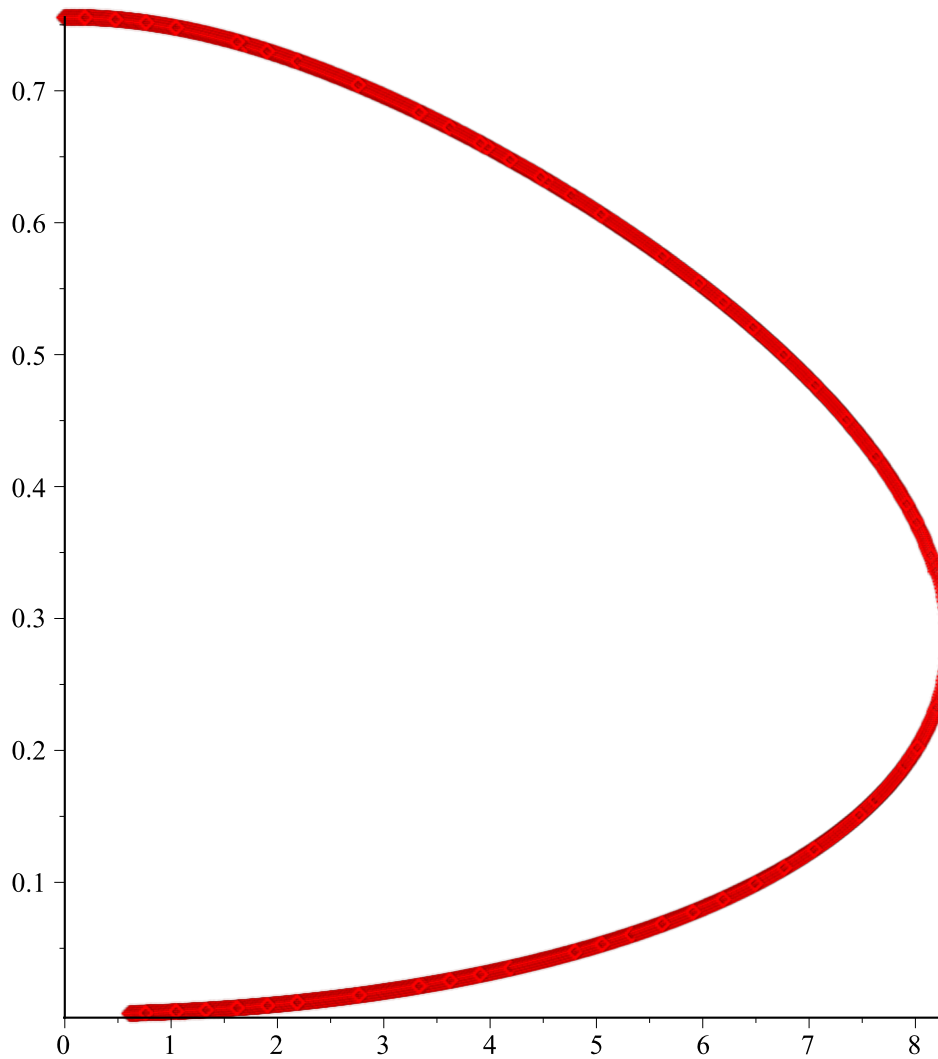
$A5 := -1.2$

$SI := \{A = -0.14476734761234273894, B = 0.48022542501132651269\}$

$VI := 8.2$

$NI := 1000$

```
> plot({seq([V3[j], A3[j]+B3[j]], j=1..977), seq([V2[j], A2[j]+B2[j]],  
j=1..988), seq([V4[j], A4[j]+B4[j]], j=1..12)}, style=point);
```



```

> Digits:=10;
  fd := fopen("jassem1.txt", WRITE);
  for k from 1 to 988 do;
> fprintf(fd, "%g,%g\n",V2[k],evalf(B2[k]+A2[k]));
  od:
  fd := fopen("jassem2.txt", WRITE);
  for k from 1 to 977 do;
  fprintf(fd, "%g,%g\n",V3[k],evalf(B3[k]+A3[k]));
  od:
  fd := fopen("jassem3.txt", WRITE);
  for k from 1 to 12 do;
  fprintf(fd, "%g,%g\n",V4[k],evalf(B4[k]+A4[k]));
  od:
> fclose(fd);

```

*Digits := 10*

(1.1)

Error, (in fopen) file "jassem1.txt" already open

*fd:=1*

*fd:=2*

```

> V1;

```

16.6

(1.2)

```

> OS2:=fsolve({eq1,eq2},{A,B}, avoid = {S1});
Error, missing operator or `;`

> S3:=fsolve({eq1,eq2},{A,B}, avoid = {S1,S2});
Error, (in fsolve) avoid = {S2, {A = -.63295564018497416334, B =
2.0436233966617796306}} is an invalid option

> Ws(x):=A*x^3+B*x^2;

```

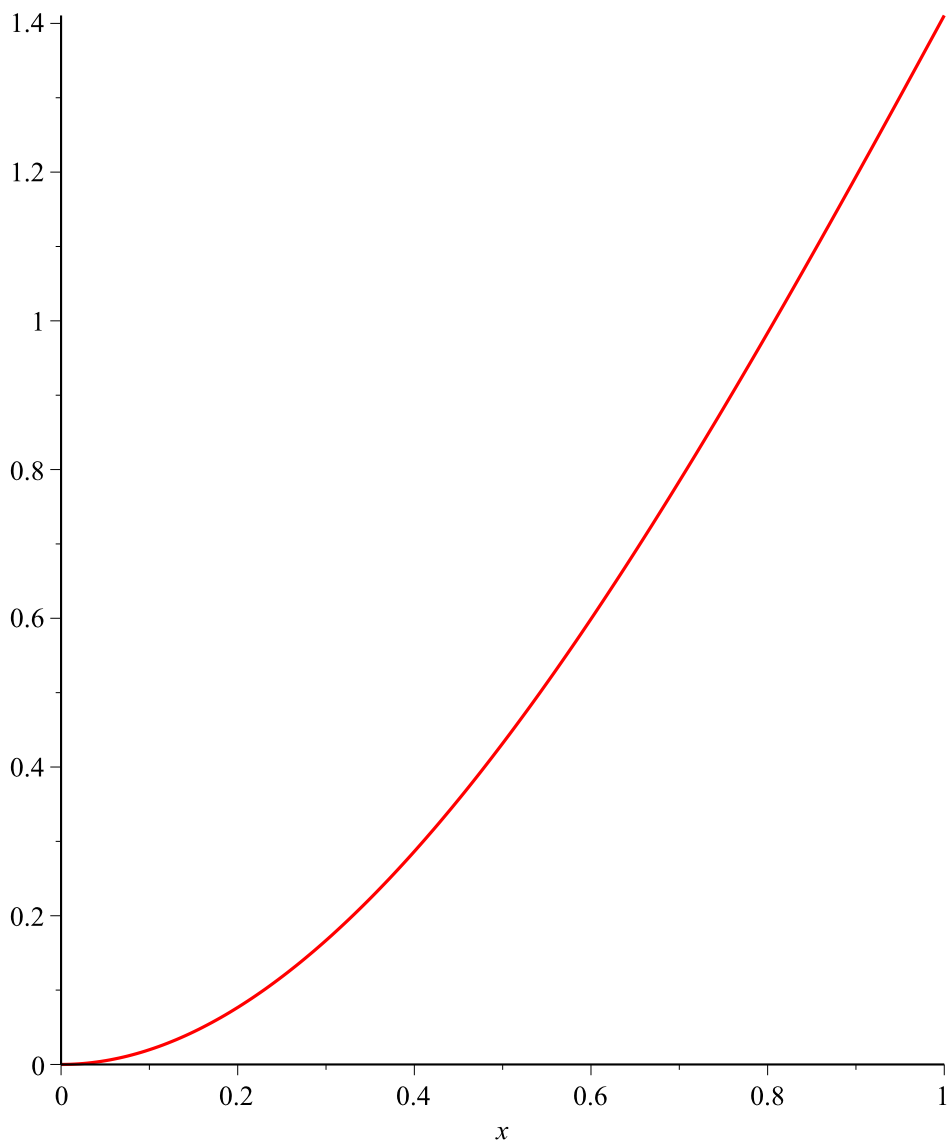
$Ws(x) := Ax^3 + Bx^2$

(16)

```

> plot(subs(S1,Ws(x)),x=0..1);

```



```
> dis:=subs(x=1,subs(S1,Ws(x)));
dis := 1.4106677564768054673 (17)
```

```
> Xi:=1-Ws(x);
Xi := 1 - Ax^3 - Bx^2 (18)
```

```
> kappa:=1-Ws(x)-Gamma*diff(Ws(x),x);
kappa := 1 - Ax^3 - Bx^2 - 0.6000000000 Ax^2 - 0.4000000000 Bx (19)
```

```
> C[1]:=Gamma^2/(Xi*kappa);
```

$$C_1 := \frac{0.0400000000000000000000000000000000}{(1 - A x^3 - B x^2) (1 - A x^3 - B x^2 - 0.6000000000 A x^2 - 0.4000000000 B x)} \quad (20)$$

$$> C[2] := (-\text{Gamma} * \text{diff}(Ws(x), x) * (2 * Xi - 3 * \text{Gamma} * \text{diff}(Ws(x), x)) + 2 * \text{kappa}^2 * \ln(Xi / \text{kappa})) / (\text{kappa}^2 * \text{diff}(Ws(x), x)^3);$$

$$C_2 := \left( -0.2000000000 (3 A x^2 + 2 B x) (2 - 2 A x^3 - 2 B x^2 - 1.8000000000 A x^2 - 1.2000000000 B x) + 2 (1 - A x^3 - B x^2 - 0.6000000000 A x^2 - 0.4000000000 B x)^2 \ln \left( \frac{1 - A x^3 - B x^2}{1 - A x^3 - B x^2 - 0.6000000000 A x^2 - 0.4000000000 B x} \right) \right) / \left( (1 - A x^3 - B x^2 - 0.6000000000 A x^2 - 0.4000000000 B x)^2 (3 A x^2 + 2 B x)^3 \right) \quad (21)$$

$$> C[3] := \text{Gamma} * (2 * Xi - \text{Gamma} * \text{diff}(Ws(x), x)) / (Xi^2 * \text{kappa}^2);$$

$$C_3 := \frac{0.2000000000 (2 - 2 A x^3 - 2 B x^2 - 0.6000000000 A x^2 - 0.4000000000 B x)}{(1 - A x^3 - B x^2)^2 (1 - A x^3 - B x^2 - 0.6000000000 A x^2 - 0.4000000000 B x)^2} \quad (22)$$

$$> \text{phi}(x) := b[1] * \cos(\text{beta} * x) + b[2] * \sin(\text{beta} * x) + b[3] * \cosh(\text{beta} * x) + b[4] * \sinh(\text{beta} * x);$$

$$\phi(x) := b_1 \cos(\beta x) + b_2 \sin(\beta x) + b_3 \cosh(\beta x) + b_4 \sinh(\beta x) \quad (23)$$

$$> E1 := \text{eval}(\text{subs}(x=0, \text{phi}(x))) = 0;$$

$$b[3] := \text{solve}(E1, b[3]);$$

$$E1 := b_1 + b_3 = 0 \quad (24)$$

$$b_3 := -b_1$$

$$> E2 := \text{eval}(\text{subs}(x=0, \text{diff}(\text{phi}(x), x))) = 0;$$

$$b[4] := \text{solve}(E2, b[4]);$$

$$E2 := b_2 \beta + b_4 \beta = 0 \quad (25)$$

$$b_4 := -b_2$$

$$> \text{phi}(x) := \text{eval}(\text{phi}(x));$$

$$\phi(x) := b_1 \cos(\beta x) + b_2 \sin(\beta x) - b_1 \cosh(\beta x) - b_2 \sinh(\beta x) \quad (26)$$

$$> E3 := -\text{subs} \left( x=1, SI, \frac{d^2}{dx^2} \phi(x) \right) + \text{subs} \left( x=1, SI, Lh_c Mh \omega^2 \phi(x) + \frac{4 Lh_c^2 Mh \omega^2 \left( \frac{d}{dx} \phi(x) \right)}{3} \right. \\ \left. + \alpha_1 V_{dc}^2 \left( C_1 \phi(x) + C_2 \left( \frac{d}{dx} \phi(x) \right) \right) \right)$$

$$E3 := b_1 \cos(\beta) \beta^2 + b_2 \sin(\beta) \beta^2 + b_1 \cosh(\beta) \beta^2 + b_2 \sinh(\beta) \beta^2 \quad (27)$$

$$\begin{aligned}
& + 0.08000000000000000000 \omega^2 (b_1 \cos(\beta) + b_2 \sin(\beta) - b_1 \cosh(\beta) - b_2 \sinh(\beta)) \\
& + 0.01066666666666666667 \omega^2 (-b_1 \sin(\beta) \beta + b_2 \cos(\beta) \beta - b_1 \sinh(\beta) \beta \\
& - b_2 \cosh(\beta) \beta) + 0.02400716146 V_{dc}^2 (0.11481470936550287481 b_1 \cos(\beta) \\
& + 0.11481470936550287481 b_2 \sin(\beta) - 0.11481470936550287481 b_1 \cosh(\beta) \\
& - 0.11481470936550287481 b_2 \sinh(\beta) \\
& + 0.13258309559720402648 (0.93415959717222220660 \\
& + 1.4393741719576100328 \ln(0.48408179545093506944)) (-b_1 \sin(\beta) \beta + b_2 \cos(\beta) \beta \\
& - b_1 \sinh(\beta) \beta - b_2 \cosh(\beta) \beta)
\end{aligned}$$

$$\begin{aligned}
> E4 := \text{subs}\left(b_3 = -b_1, b_4 = -b_2, \text{simplify}\left(-\text{subs}\left(x = 1, SI, \frac{d^3}{dx^3} \phi(x)\right) + \text{subs}\left(x = 1, SI, \right.\right. \\
\left.\left.- Mh \omega^2 \phi(x) - Lh_c Mh \omega^2 \left(\frac{d}{dx} \phi(x)\right) - \alpha_1 V_{dc}^2 \left(C_3 \phi(x) + C_1 \left(\frac{d}{dx} \phi(x)\right)\right)\right)\right)
\end{aligned}$$

$$E4 := -1. b_1 \sin(\beta) \beta^3 + b_2 \cos(\beta) \beta^3 + b_1 \sinh(\beta) \beta^3 + b_2 \cosh(\beta) \beta^3 \quad (28)$$

$$\begin{aligned}
& - 0.80000000000000000000 \omega^2 b_1 \cos(\beta) - 0.80000000000000000000 \omega^2 b_2 \sin(\beta) \\
& + 0.80000000000000000000 \omega^2 b_1 \cosh(\beta) + 0.80000000000000000000 \omega^2 b_2 \sinh(\beta) \\
& + 0.08000000000000000000 \omega^2 b_1 \sin(\beta) \beta \\
& - 0.08000000000000000000 \omega^2 b_2 \cos(\beta) \beta \\
& + 0.08000000000000000000 \omega^2 b_1 \sinh(\beta) \beta \\
& + 0.08000000000000000000 \omega^2 b_2 \cosh(\beta) \beta + 0.049805302324949157635 \\
& V_{dc}^2 b_1 \cos(\beta) + 0.049805302324949157635 V_{dc}^2 b_2 \sin(\beta) - 0.049805302324949157635 \\
& V_{dc}^2 b_1 \cosh(\beta) - 0.049805302324949157635 V_{dc}^2 b_2 \sinh(\beta) \\
& + 0.0027563752657206016697 V_{dc}^2 b_1 \sin(\beta) \beta - 0.0027563752657206016697 \\
& V_{dc}^2 b_2 \cos(\beta) \beta + 0.0027563752657206016697 V_{dc}^2 b_1 \sinh(\beta) \beta \\
& + 0.0027563752657206016697 V_{dc}^2 b_2 \cosh(\beta) \beta
\end{aligned}$$

> with(linalg):

MM:=array(1..2,1..2);

Warning, computation interrupted

> omega:=beta^2;

$$\omega := \beta^2 \quad (29)$$

**> MM[1,1]:=coeff(expand(E3),b[1]);;**

$$MM_{1,1} := \cos(\beta) \beta^2 + \cosh(\beta) \beta^2 + 0.08000000000 \beta^4 \cos(\beta) - 0.08000000000 \beta^4 \cosh(\beta) \\ - 0.01066666667 \beta^5 \sin(\beta) - 0.01066666667 \beta^5 \sinh(\beta) + 0.06395953006 \cos(\beta) \\ - 0.06395953006 \cosh(\beta) - 0.01028161163 \sin(\beta) \beta - 0.01028161163 \sinh(\beta) \beta \quad (30)$$

**> MM[1,2]:=coeff(expand(E3),b[2]);;**

$$MM_{1,2} := \sin(\beta) \beta^2 + \sinh(\beta) \beta^2 + 0.08000000000 \beta^4 \sin(\beta) - 0.08000000000 \beta^4 \sinh(\beta) \\ + 0.01066666667 \beta^5 \cos(\beta) - 0.01066666667 \beta^5 \cosh(\beta) + 0.06395953006 \sin(\beta) \\ - 0.06395953006 \sinh(\beta) + 0.01028161163 \cos(\beta) \beta - 0.01028161163 \cosh(\beta) \beta \quad (31)$$

**> MM[2,1]:=coeff(expand(E4),b[1]);**

$$MM_{2,1} := -1. \sin(\beta) \beta^3 + \sinh(\beta) \beta^3 - 0.8000000000 \beta^4 \cos(\beta) + 0.8000000000 \beta^4 \cosh(\beta) \\ + 0.08000000000 \beta^5 \sin(\beta) + 0.08000000000 \beta^5 \sinh(\beta) - 0.7458794475 \cos(\beta) \\ + 0.7458794475 \cosh(\beta) + 0.06395953006 \sin(\beta) \beta + 0.06395953006 \sinh(\beta) \beta \quad (32)$$

**> MM[2,2]:=coeff(expand(E4),b[2]);**

$$MM_{2,2} := \cos(\beta) \beta^3 + \cosh(\beta) \beta^3 - 0.8000000000 \beta^4 \sin(\beta) + 0.8000000000 \beta^4 \sinh(\beta) \\ - 0.08000000000 \beta^5 \cos(\beta) + 0.08000000000 \beta^5 \cosh(\beta) - 0.7458794475 \sin(\beta) \\ + 0.7458794475 \sinh(\beta) - 0.06395953006 \cos(\beta) \beta + 0.06395953006 \cosh(\beta) \beta \quad (33)$$

**> Ed:=det(MM)=0;**

$$Ed := -0.0205632233 \beta^4 \cosh(\beta) \sin(\beta) + 1.600000000 \cos(\beta) \beta^6 \sinh(\beta) \\ - 0.0205632233 \beta^4 \cos(\beta) \sinh(\beta) - 1. \cdot 10^{-10} \beta^4 \cosh(\beta) \sinh(\beta) \\ - 0.007156042630 \cos(\beta) \cosh(\beta) \beta + 0.003578021317 \cos(\beta)^2 \beta \\ + 1.005947812 \cos(\beta)^2 \beta^5 + 1.005947812 \cosh(\beta)^2 \beta^5 + 0.002133333336 \beta^9 \cos(\beta)^2 \\ + 0.002133333336 \beta^9 \cosh(\beta)^2 + 0.002133333336 \beta^9 \sin(\beta)^2 + 1.005947812 \beta^5 \sin(\beta)^2 \\ - 0.002133333336 \beta^9 \sinh(\beta)^2 - 1.005947812 \beta^5 \sinh(\beta)^2 \\ + 0.003578021317 \cosh(\beta)^2 \beta + 0.003578021317 \sin(\beta)^2 \beta \\ - 0.003578021317 \sinh(\beta)^2 \beta - 5. \cdot 10^{-12} \beta^5 \sin(\beta) \sinh(\beta) \\ - 1.600000000 \cosh(\beta) \beta^6 \sin(\beta) + 1. \cdot 10^{-10} \beta^4 \cos(\beta) \sin(\beta) \\ - 1.491758895 \cosh(\beta) \beta^2 \sin(\beta) + 1.988104375 \cos(\beta) \beta^5 \cosh(\beta) \\ + 1.491758895 \cos(\beta) \beta^2 \sinh(\beta) - 0.00426666667 \beta^9 \cos(\beta) \cosh(\beta) \quad (34)$$



$$\begin{aligned}
 & -0.02133333334 \beta^8 \cos(\beta) \sinh(\beta) - 0.02133333334 \beta^8 \cosh(\beta) \sin(\beta) \\
 & -0.3200000000 \sin(\beta) \beta^7 \sinh(\beta) - 0.2558381203 \sin(\beta) \beta^3 \sinh(\beta) = 0
 \end{aligned}$$

```

> B1:=fsolve(Ed,beta=1.7);
O1:=(B1)^2;
B1:=1.118117072
O1:=1.250185787

```

(35)

```

> B2:=fsolve(Ed,beta=4.2);
O2:=(B2)^2;
B2:=3.629579092
O2:=13.17384439

```

(36)

```

> B3:=fsolve(Ed,beta=6.8);
O3:=(B3)^2;
B3:=6.287241843
O3:=39.52940999

```

(37)

```

> B4:=fsolve(Ed,beta=9);
O4:=(B4)^2;
B4:=8.975757762
O4:=80.56422740

```

(38)

```

> B5:=fsolve(Ed,beta=12);
O5:=(B5)^2;
B5:=11.79001205
O5:=139.0043841

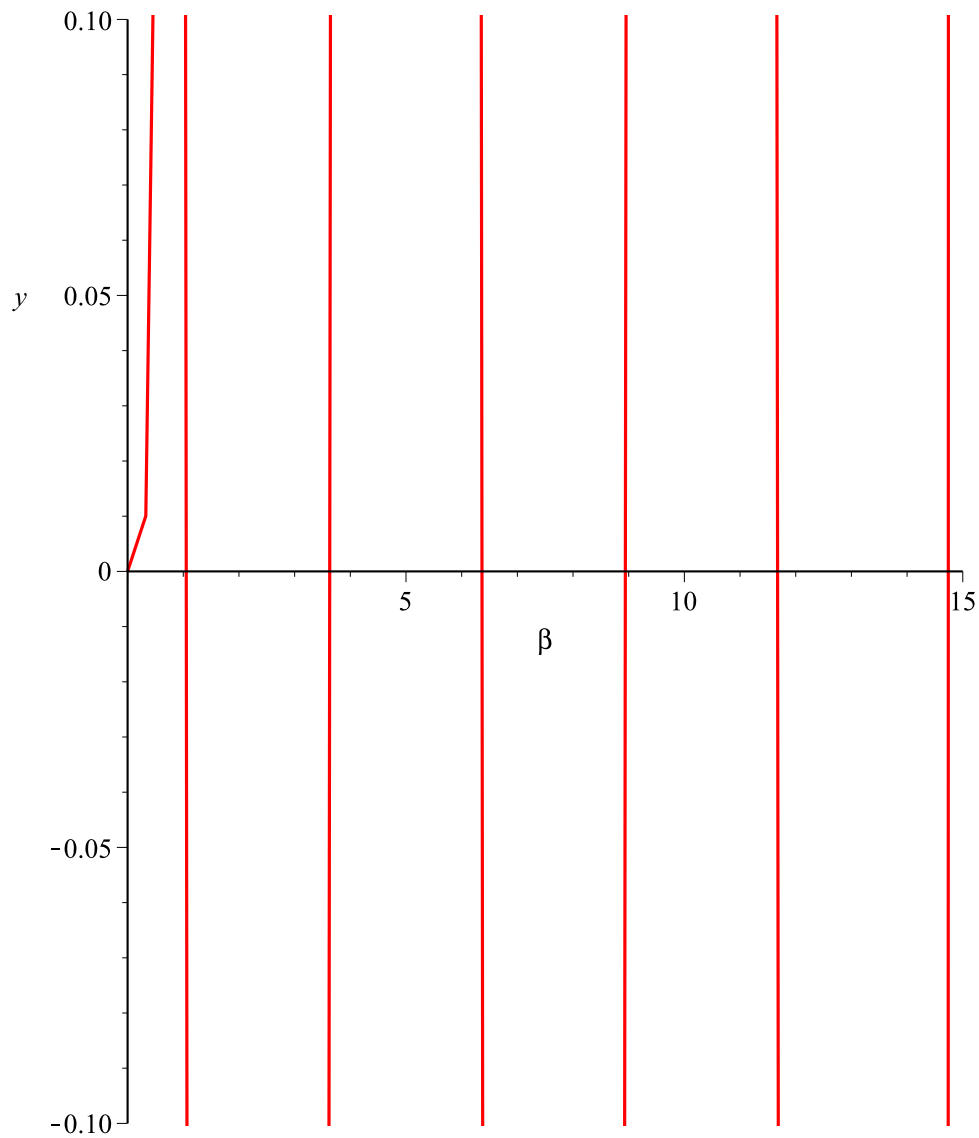
```

(39)

```

> plot(det(MM),beta=0..15,y=-.1..0.1);

```



```

> EF1:=eval(subs(beta=B1,MM[1,1]))*b[1]+eval(subs(beta=B1,MM[1,2]))
  *b[2];
S2:={b[1]=solve(EF1,b[1])};
S3:={b[2]=solve(int(subs(S2,beta=B1,phi(x))^2,x=0..1)=1,b[2])[1]}
;
S21:={b[1]=solve(EF1,b[1])}:
S31:={b[2]=solve(int(subs(S2,beta=B1,phi(x))^2,x=0..1)=1,b[2])[1]}
}:

```

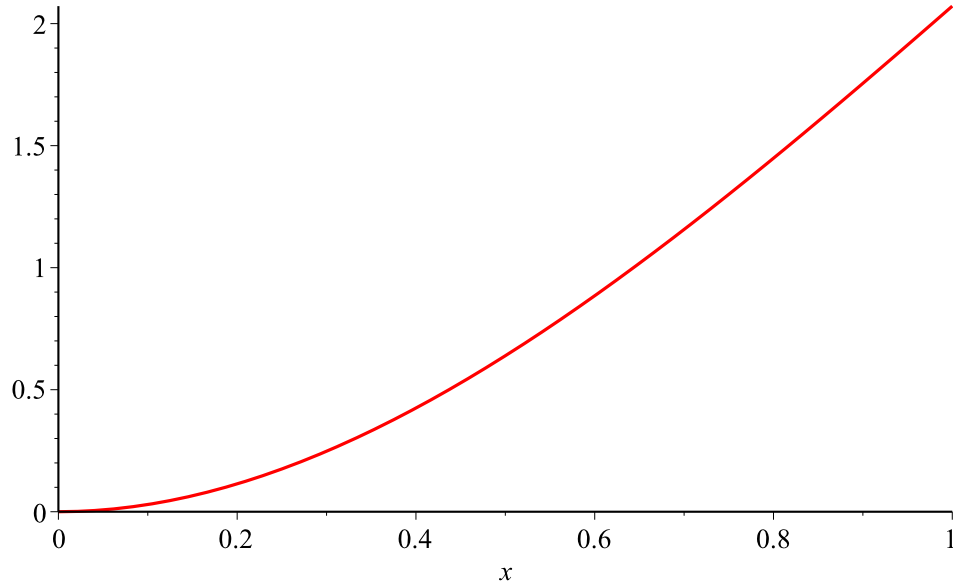
$$EF1 := 2.357777633 b_1 + 2.706072770 b_2$$

$$S2 := \{b_1 = -1.147721792 b_2\}$$

$$S3 := \{b_2 = 2.126420913\}$$

```
> plot(subs(S2,S3,beta=B1,phi(x)),x=0..1);
```

```
Phi[1]:=subs(S2,S3,beta=B1,phi(x));
```



$$\Phi_1 := -2.440539621 \cos(1.118117072 x) + 2.126420913 \sin(1.118117072 x) \\ + 2.440539621 \cosh(1.118117072 x) - 2.126420913 \sinh(1.118117072 x)$$

```
> EF1:=eval(subs(beta=B2,MM[1,1]))*b[1]+eval(subs(beta=B2,MM[1,2]))
*b[2];
```

```
S2:={b[1]=solve(EF1,b[1])};
```

```
S3:={b[2]=solve(int(subs(S2,beta=B2,phi(x))^2,x=0..1)=1,b[2])[1]};
```

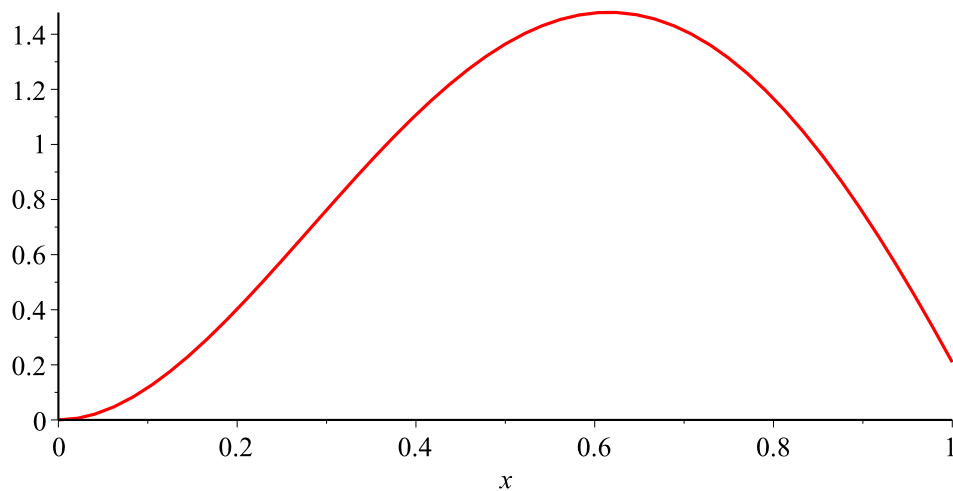
```
plot(subs(S2,S3,beta=B2,phi(x)),x=0..1);
```

```
Phi[2]:=subs(S2,S3,beta=B2,phi(x));
```

$$EF1 := -162.6480569 b_1 - 160.7021578 b_2$$

$$S2 := \{b_1 = -0.9880361368 b_2\}$$

$$S3 := \{b_2 = 1.022679997\}$$



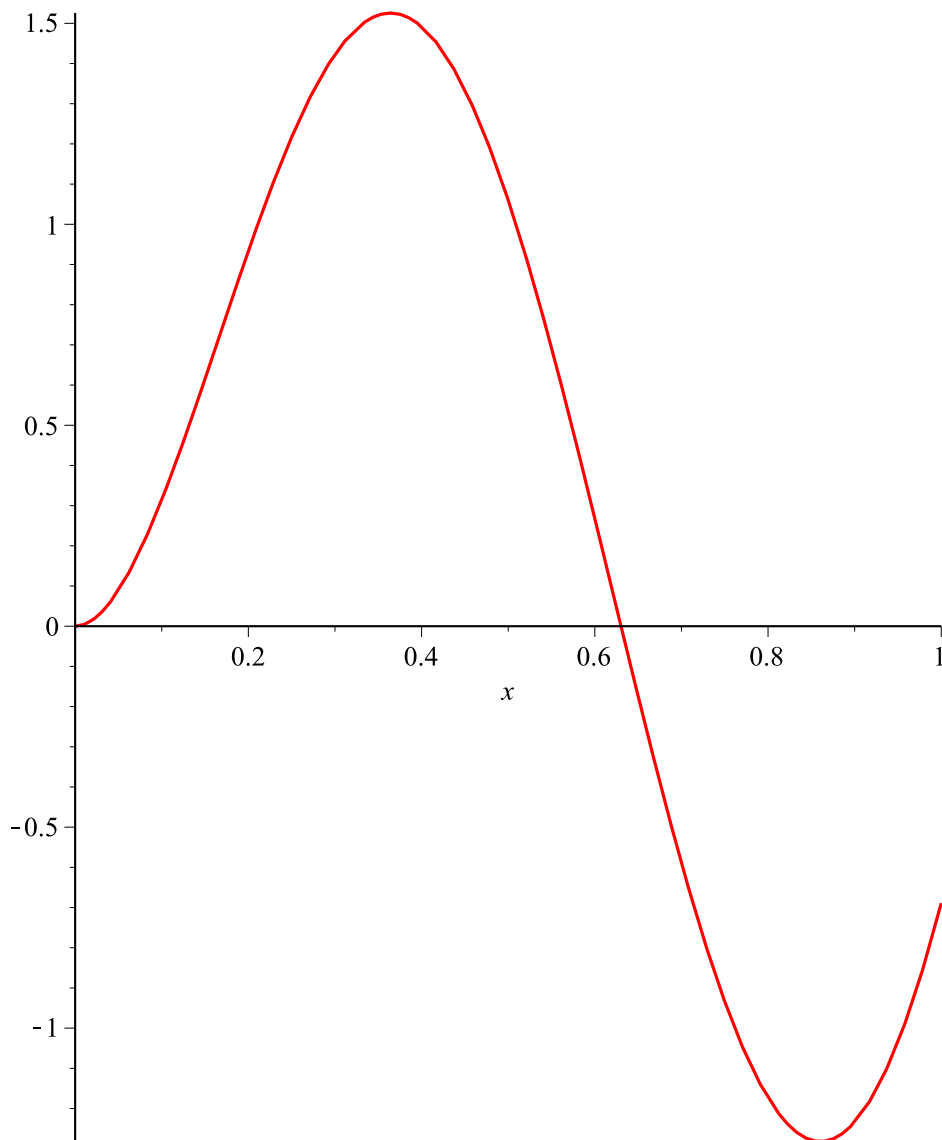
$$\Phi_2 := -1.010444793 \cos(3.629579092 x) + 1.022679997 \sin(3.629579092 x) \\ + 1.010444793 \cosh(3.629579092 x) - 1.022679997 \sinh(3.629579092 x)$$

```
> EF1:=eval(subs(beta=B3,MM[1,1]))*b[1]+eval(subs(beta=B3,MM[1,2]))
    *b[2];
S2:={b[1]=solve(EF1,b[1])};
S3:={b[2]=solve(int(subs(S2,beta=B3,phi(x))^2,x=0..1)=1,b[2])[1]};
;
plot(subs(S2,S3,beta=B3,phi(x)),x=0..1);
Phi[3]:=subs(S2,S3,beta=B3,phi(x));
```

$$EF1 := -51021.15406 b_1 - 51079.83877 b_2$$

$$S2 := \{b_1 = -1.001150204 b_2\}$$

$$S3 := \{b_2 = 1.004479682\}$$



$$\Phi_3 := -1.005635039 \cos(6.287241843 x) + 1.004479682 \sin(6.287241843 x) \\ + 1.005635039 \cosh(6.287241843 x) - 1.004479682 \sinh(6.287241843 x)$$

```
> EF1:=eval(subs(beta=B4,MM[1,1]))*b[1]+eval(subs(beta=B4,MM[1,2]))
    *b[2];
S2:={b[1]=solve(EF1,b[1])};
S3:={b[2]=solve(int(subs(S2,beta=B4,phi(x))^2,x=0..1)=1,b[2])[1]}
;
```

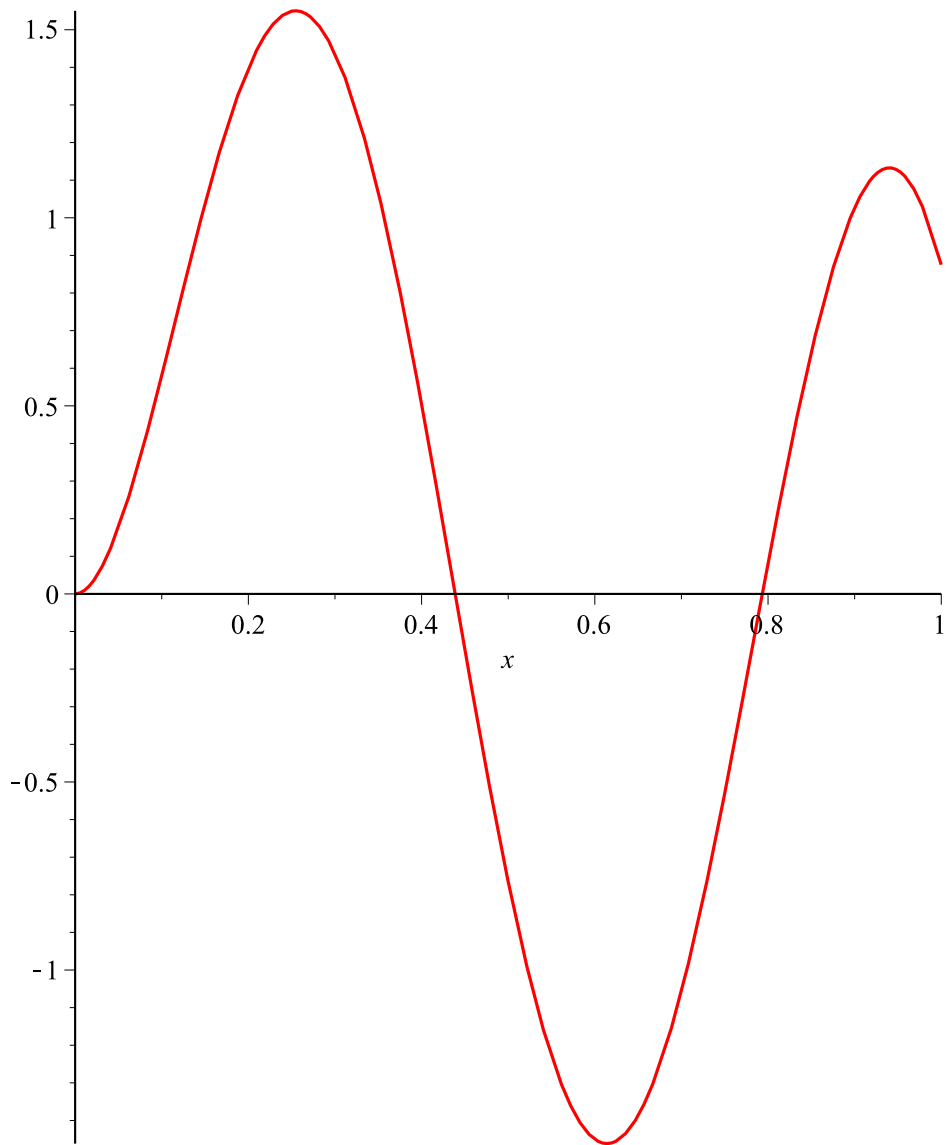
```
plot(subs(S2,S3,beta=B4,phi(x)),x=0..1);
```

```
Phi[4]:=subs(S2,S3,beta=B4,phi(x));
```

$$EF1 := -4.193606491 \cdot 10^6 b_1 - 4.193095821 \cdot 10^6 b_2$$

$$S2 := \{b_1 = -0.9998782265 b_2\}$$

$$S3 := \{b_2 = 1.025592899\}$$



$$\Phi_4 := -1.025468009 \cos(8.975757762 x) + 1.025592899 \sin(8.975757762 x)$$

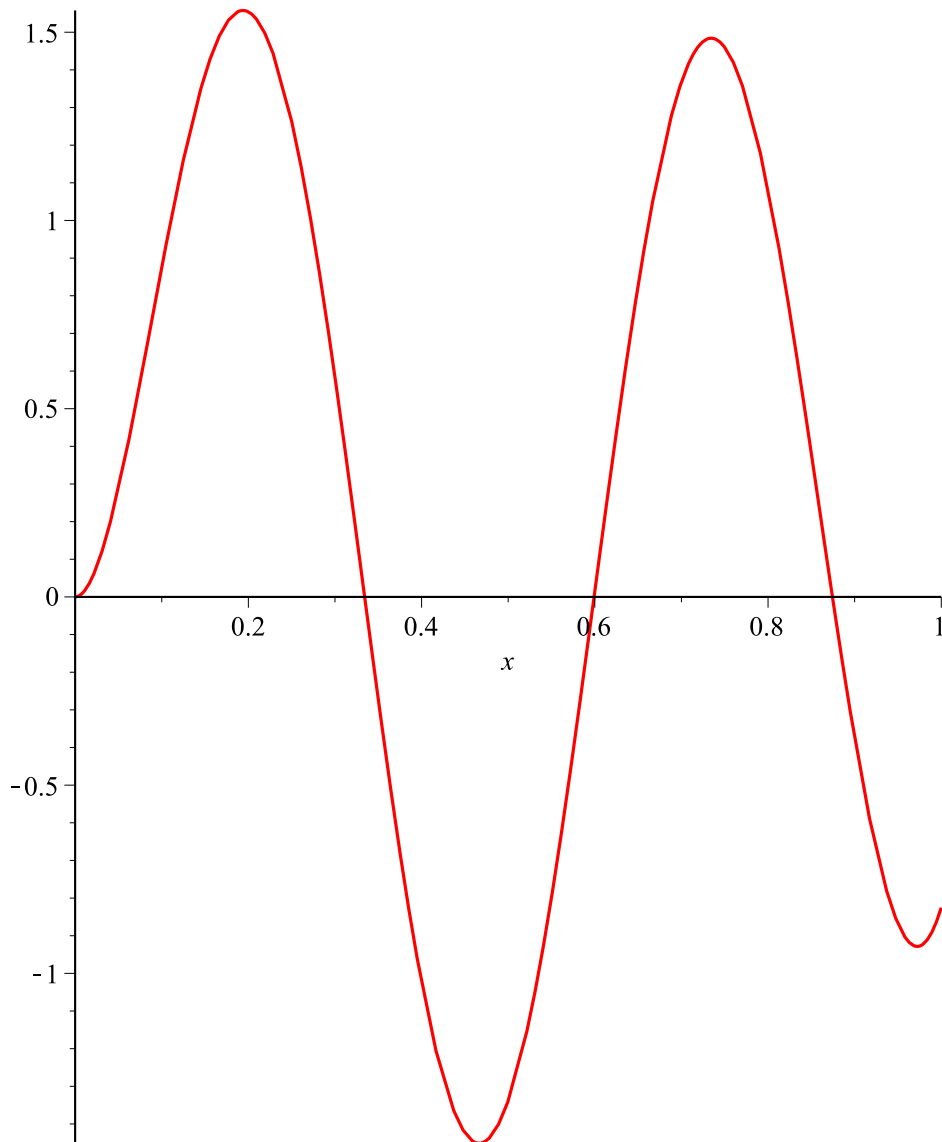
$$+ 1.025468009 \cosh(8.975757762 x) - 1.025592899 \sinh(8.975757762 x)$$

```
> EF1:=eval(subs(beta=B5,MM[1,1]))*b[1]+eval(subs(beta=B5,MM[1,2]))
    *b[2];
S2:={b[1]=solve(EF1,b[1])};
S3:={b[2]=solve(int(subs(S2,beta=B5,phi(x))^2,x=0..1)=1,b[2])[1]};
;
plot(subs(S2,S3,beta=B5,phi(x)),x=0..1);
Phi[5]:=subs(S2,S3,beta=B2,phi(x));
```

$$EF1 := -2.530959998 \cdot 10^8 b_1 - 2.530983513 \cdot 10^8 b_2$$

$$S2 := \{b_1 = -1.000009291 b_2\}$$

$$S3 := \{b_2 = 1.030030864\}$$



$$\Phi_5 := -1.030040434 \cos(3.629579092 x) + 1.030030864 \sin(3.629579092 x) \\ + 1.030040434 \cosh(3.629579092 x) - 1.030030864 \sinh(3.629579092 x)$$

$$\begin{aligned} &> R[1] := 12 * \epsilon * a[p] * L[1]^4 / (E * a[b] * b[b]^3 * d^3); \\ &R_1 := 0.04801432292 \end{aligned} \quad (41)$$

$$\begin{aligned} &> \theta := \text{eval}(\text{subs}(x=1, \Phi[1] + \Gamma * \text{diff}(\Phi[1], x))); \\ &\theta := 2.711014477 \end{aligned} \quad (42)$$



```

> n:=1;
  for i from 1 to n do;
    for j from 1 to n do;
      DD[i,j]:=c*int(expand(Phi[i]*Phi[j]),x=0..1);
    od;
  od;

```

$$n := 1 \quad (43)$$

```

> for i from 1 to n do;
  for j from 1 to n do;
    KK[i,j]:=int(expand(diff(Phi[i],x$2))*expand(diff(Phi[j],x$2)),x=
      0..1);
  od;
od;

```

```

> for i from 1 to n do;
  for j from 1 to n do;
    MN[i,j]:=int(expand(Phi[i]*Phi[j]),x=0..1)+subs(x=1,1/3*Mh*Lh[c]
      ^2*diff(Phi[i],x)*diff(Phi[j],x)+Mh/4*(2*Phi[i]+Gamma*diff(Phi
      [i],x))*(2*Phi[j]+Gamma*diff(Phi[j],x)));
  od;
od;

```

Single Mode Approximation Linear Equation

```

> T0:=MN[1,1]*diff(q(t),t$2)+DD[1,1]*diff(q(t),t)+KK[1,1]*q(t);

```

$$T0 := 5.602167446 \left( \frac{d^2}{dt^2} q(t) \right) + 1.000000004 c \left( \frac{d}{dt} q(t) \right) + 12.90948917 q(t) \quad (44)$$

```

> sqrt(KK[1,1]/MN[1,1]);

```

$$1.518016479 \quad (45)$$

```

> 1.5179088150;

```

$$1.5179088150 \quad (46)$$

```

> Phi[1];subs(S1,Ws(x));

```

$$\begin{aligned} & -2.440539621 \cos(1.118117072 x) + 2.126420913 \sin(1.118117072 x) \\ & + 2.440539621 \cosh(1.118117072 x) - 2.126420913 \sinh(1.118117072 x) \\ & - 0.05329960835 x^3 + 0.1761277362 x^2 \end{aligned} \quad (47)$$

```

> T1:=-int(diff(subs(S1,Ws(x)),x$2)*diff(Phi[1],x$2),x=0..1);

```

$$T1 := -0.7662826794 \quad (48)$$

```

> T2:=R[1]*(V[dc]+V[ac])^2*evalf(subs(S1,x=1,ln((kappa-theta*q(t))/
  (Xi-q(t)*subs(x=1,Phi[1]))))/2/evalf(subs(x=1,S1,(diff(Phi[1],x)

```

```
*q(t)+diff(Ws(x),x)^2));
```

$$T2 := \frac{0.02400716146 (7 + V_{ac})^2 \ln\left(\frac{0.8387005423 - 2.711014477 q(t)}{0.8771718718 - 2.071726090 q(t)}\right)}{(3.196441929 q(t) + 0.1923566474)^2} \quad (49)$$

$$T3 := \frac{0.03075163001 (7 + V_{ac})^2}{3.119826058 q(t) - 24.14971262 q(t)^2 + 0.2830276174 + 35.90550064 q(t)^3} \quad (50)$$

```
> T33:=simplify(expand(T3));
```

$$T33 := \left(1.53758150 \cdot 10^8 (49. + 14. V_{ac} + V_{ac}^2)\right) / \left(1.559913029 \cdot 10^{10} q(t) - 1.207485631 \cdot 10^{11} q(t)^2 + 1.415138087 \cdot 10^9 + 1.795275032 \cdot 10^{11} q(t)^3\right) \quad (51)$$

```
> c:=0;
```

$$c := 0 \quad (52)$$

```
> EOM:=T0/MN[1,1]=T1/MN[1,1]+T2/MN[1,1]+T3/MN[1,1];
```

$$EOM := 0.9999999999 \left(\frac{d^2}{dt^2} q(t)\right) + 2.304374029 q(t) = -0.1367832516 + \frac{0.004285334505 (7 + V_{ac})^2 \ln\left(\frac{0.8387005423 - 2.711014477 q(t)}{0.8771718718 - 2.071726090 q(t)}\right)}{(3.196441929 q(t) + 0.1923566474)^2} + \frac{0.005489237926 (7 + V_{ac})^2}{3.119826058 q(t) - 24.14971262 q(t)^2 + 0.2830276174 + 35.90550064 q(t)^3} \quad (53)$$

## Damping

```
C[15]:= .15;
```

$$C_{15} := 0.15 \quad (54)$$

```
> C[1]:=KK[1,1]/MN[1,1];
```

$$C_1 := 2.304374029 \quad (55)$$

```
> C[2]:=T1/MN[1,1];
```

$$C_2 := -0.1367832516 \quad (56)$$

```
> C[3]:=R[1]/2/MN[1,1];
```

$$C_3 := 0.004285334505 \quad (57)$$

```
> C[4]:=subs(x=1,S1,kappa);
```

```

|                                      $C_4 := 0.8387005423$  (58)
|=
| > C[5] := -eval (subs (x=1, theta) );
|                                      $C_5 := -2.711014477$  (59)
|=
| > C[6] := subs (x=1, S1, Xi) ;
|                                      $C_6 := 0.8771718718$  (60)
|=
| > C[7] := -eval (subs (x=1, Phi [1] ) ) ;
|                                      $C_7 := -2.071726090$  (61)
|=
| > C[8] := eval (subs (x=1, diff (Phi [1] , x) ) ) ;
|                                      $C_8 := 3.196441929$  (62)
|=
| > C[9] := subs (x=1, S1, diff (Ws (x) , x) ) ;
|                                      $C_9 := 0.1923566474$  (63)
|=
| > C[10] := eval (Gamma*R[1]*subs (x=1, S1, (Xi*diff (Phi [1] , x) +diff (Ws (x) ,
| x)*Phi [1] ) ) ) /MN[1,1] ;
|                                      $C_{10} := 0.005489237926$  (64)
|=
| > aa:=C[6] ;bb:=-C[7] ;cc:=C[8] ;dd:=C[9] ;ee:=C[4] ;ff:=-C[5] ;
|                                      $aa := 0.8771718718$  (65)
|                                      $bb := 2.071726090$ 
|                                      $cc := 3.196441929$ 
|                                      $dd := 0.1923566474$ 
|                                      $ee := 0.8387005423$ 
|                                      $ff := 2.711014477$ 
|=
| > C[11] := eval (2*aa*cc*ee-2*aa*dd*ff-2*bb*dd*ee) ;
|                                      $C_{11} := 3.119826057$  (66)
|=
| > C[12] := eval (-2*aa*cc*ff-2*bb*cc*ee+2*bb*dd*ff) ;
|                                      $C_{12} := -24.14971263$  (67)
|=
| > C[13] := eval (2*aa*dd*ee) ;
|                                      $C_{13} := 0.2830276174$  (68)
|=
| > C[14] := eval (2*bb*cc*ff) ;
|                                      $C_{14} := 35.90550064$  (69)
|=
| > C[16] := V[dc] ;
|                                      $C_{16} := 7$  (70)
|=
| > C[17] := subs (S1, A) ;
|                                      $C_{17} := -0.05329960835$  (71)
|=
| > C[18] := subs (S1, B) ;
|                                     ---

```

$$C_{18} := 0.1761277362 \quad (72)$$

```
> C[19] := subs(S21, b[1]/b[2]);
```

$$C_{19} := -1.147721792 \quad (73)$$

```
> C[20] := subs(S21, S31, b[2]);
```

$$C_{20} := 2.126420913 \quad (74)$$

```
> C[21] := B1;
```

$$C_{21} := 1.118117072 \quad (75)$$

```
> collect(expand((aa-bb*q)*(cc*q+dd)*(ee-ff*q)*2), q);
```

$$3.119826058 q - 24.14971262 q^2 + 0.2830276174 + 35.90550064 q^3 \quad (76)$$

```
> collect(expand((aa1-bb1*q)*(cc1*q+dd1)*(ee1-ff1*q)*2), q);
```

$$2 bb1 q^3 cc1 ff1 + (-2 aa1 cc1 ff1 - 2 bb1 cc1 ee1 + 2 bb1 dd1 ff1) q^2 + (2 aa1 cc1 ee1 - 2 aa1 dd1 ff1 - 2 bb1 dd1 ee1) q + 2 aa1 dd1 ee1 \quad (77)$$

```
> fd := fopen("data_jassim_7.txt", WRITE);
  for i from 1 to 21 do;
    fprintf(fd, "%10.7f\n", C[i]);
  > od;
  fclose(fd);
```

$$fd := 0 \quad (78)$$

11

11

11

11

11

11

11

11

11

11

11

12

11

11

11

11

11

11

L

11  
11  
11

# **C.3**

# **Cellular Contractile Force**

```

> restart;
This is a proof of the derivation carried out in Ref. [295] -- Assuming a Solution For Mode Shape
> W(x) := A*cos(rn*x)+B*sin(rn*x)+C*cosh(rn*x)+D1*sinh(rn*x);
      A cos(rn x) + B sin(rn x) + C cosh(rn x) + D1 sinh(rn x)
(1)
> E1:=diff(W(x),x);
      -A sin(rn x) rn + B cos(rn x) rn + C sinh(rn x) rn + D1 cosh(rn x) rn
(2)
> E2:=diff(W(x),x$2);
      -A cos(rn x) rn^2 - B sin(rn x) rn^2 + C cosh(rn x) rn^2 + D1 sinh(rn x) rn^2
(3)
> E3:=diff(W(x),x$3);
      A sin(rn x) rn^3 - B cos(rn x) rn^3 + C sinh(rn x) rn^3 + D1 cosh(rn x) rn^3
(4)
> eq1:=eval(subs(x=0,W(x))=0);
      A + C = 0
(5)
> eq2:=eval(subs(x=0,E1)=0);
      B rn + D1 rn = 0
(6)
> eq3:=eval(subs(x=L,E2)=0);
      -A cos(rn L) rn^2 - B sin(rn L) rn^2 + C cosh(rn L) rn^2 + D1 sinh(rn L) rn^2 = 0
(7)
> eq4:=eval(subs(x=L,E3)=0);
      A sin(rn L) rn^3 - B cos(rn L) rn^3 + C sinh(rn L) rn^3 + D1 cosh(rn L) rn^3 = 0
(8)
> C:=solve(eq1,C);
      -A
(9)
> D1:=solve(eq2,D1);
      -B
(10)
> with(linalg):
Looking for non trivial solution -- putting equation in matrix form
> M:=array(1..2,1..2);
      table([ ])
(11)
> collect(eq3,{A,B});
      (-cos(rn L) rn^2 - cosh(rn L) rn^2) A + (-sin(rn L) rn^2 - sinh(rn L) rn^2) B = 0
(12)
> M[1,1]:=-cos(rn*L)*rn^2-cosh(rn*L)*rn^2;
      -cos(rn L) rn^2 - cosh(rn L) rn^2
(13)
> M[1,2]:=-sin(rn*L)*rn^2-sinh(rn*L)*rn^2;
      -sin(rn L) rn^2 - sinh(rn L) rn^2
(14)
> collect(eq4,{A,B});
      (sin(rn L) rn^3 - sinh(rn L) rn^3) A + (-cos(rn L) rn^3 - cosh(rn L) rn^3) B = 0
(15)
> M[2,1]:=sin(rn*L)*rn^3-sinh(rn*L)*rn^3;
      sin(rn L) rn^3 - sinh(rn L) rn^3
(16)
> M[2,2]:=-cos(rn*L)*rn^3-cosh(rn*L)*rn^3;
      -cos(rn L) rn^3 - cosh(rn L) rn^3
(17)
> Q1:=simplify(det(M)/rn^5)/2=0;
      cos(rn L) cosh(rn L) + 1 = 0
(18)
> fsolve(subs(rn=r[n]/L,Q1),r[n]);
(19)

```

$$1.875104069 \quad (19)$$

Since we are in static mode, we take first mode solution; B stands for sigma in Ref. [295]

**> B:=solve(eq3,B);**

$$-\frac{A(\cos(rnL) + \cosh(rnL))}{\sin(rnL) + \sinh(rnL)} \quad (20)$$

Mode Shape

**> W1:=collect(eval(W(x)),{A,sin(rn\*x),cos(rn\*x)});**

$$\left( \cos(rn x) - \frac{(\cos(rn L) + \cosh(rn L)) \sin(rn x)}{\sin(rn L) + \sinh(rn L)} - \cosh(rn x) + \frac{(\cos(rn L) + \cosh(rn L)) \sinh(rn x)}{\sin(rn L) + \sinh(rn L)} \right) A \quad (21)$$

A is C in Ref[295]

**> A:=subs(rn=1.875104069/L,solve(subs(rn\*L=1.875104069,simplify(subs(rn\*L=1.875104069,int(W1^2,x=0..L)))=1),A)[1]);**

$$1.000000000 \sqrt{\frac{1}{L}} \quad (22)$$

Deflection at L

**> WL:=eval(subs(x=L,subs(rn=1.875104069/L,W1)));**

$$-2.000000000 \sqrt{\frac{1}{L}} \quad (23)$$

Normalized Deflection

**> E7:=u=F[com]\*(t[b]+t[c])/2/E/II/rn^4\*(Wx1-Wx2);**

$$u = \frac{1}{2} \frac{F_{com} (t_b + t_c) (Wx1 - Wx2)}{E I I r n^4} \quad (24)$$

Derivative of Mode Shape

**> Wx1:=eval(subs(x=x1,subs(rn=1.875104069/L,diff(W1,x))));**

$$1.000000000 \left( -\frac{1.875104069 \sin\left(\frac{1.875104069 x1}{L}\right)}{L} - \frac{1.376505485 \cos\left(\frac{1.875104069 x1}{L}\right)}{L} - \frac{1.875104069 \sinh\left(\frac{1.875104069 x1}{L}\right)}{L} + \frac{1.376505485 \cosh\left(\frac{1.875104069 x1}{L}\right)}{L} \right) \sqrt{\frac{1}{L}} \quad (25)$$

**> Wx2:=eval(subs(x=x2,subs(rn=1.875104069/L,diff(W1,x))));**

$$1.000000000 \left( -\frac{1.875104069 \sin\left(\frac{1.875104069 x2}{L}\right)}{L} - \frac{1.376505485 \cos\left(\frac{1.875104069 x2}{L}\right)}{L} - \frac{1.875104069 \sinh\left(\frac{1.875104069 x2}{L}\right)}{L} \right) \quad (26)$$



$$+ \frac{1.376505485 \cosh\left(\frac{1.875104069 x_2}{L}\right)}{L} \sqrt{\frac{1}{L}}$$

Assigning variables based on in vitro experimental parameters

Enter Beams length

$$> L := 350 \text{E-}6; \quad 0.000350 \quad (27)$$

Insert the Piezoresistive coefficient

$$> Q := 70 \text{E-}11; \quad 7.0 \cdot 10^{-10} \quad (28)$$

Insert the feeding DC potential as per the jumper setting -- feedign the Wheatstone Bridge

$$> U[i] := 1; \quad 1 \quad (29)$$

Solution of r (n) as obtained above

$$> rn := 1.875104069/L; \quad 5357.440197 \quad (30)$$

Enter modulus of elasticity

$$> E := 160 \text{E}9; \quad 1.60 \cdot 10^{11} \quad (31)$$

Enter beam's width

$$> b1 := 120 \text{E-}6; \quad 0.000120 \quad (32)$$

Enter beam's thickness

$$> t[b] := 3 \text{E-}6; \quad 0.000003 \quad (33)$$

Enter Cell's height

$$> t[c] := 7.2 \text{E-}6; \quad 0.0000072 \quad (34)$$

Enter moment of inertia expression

$$> II := 1/12 * b1 * t[b]^3; \quad 2.700000000 \cdot 10^{-22} \quad (35)$$

Enter the first displacement coordinate of the rear of the cell to the clamped side of the cantilever

$$> x1 := 100 \text{E-}6; \quad 0.000100 \quad (36)$$

Enter the second displacement coordinate of the front of the cell to the clamped portion of the cantilever

$$> x2 := 121 \text{E-}6; \quad 0.000121 \quad (37)$$

Now solve for equation 7 to obtain the surface compressive force generated on cantilever with respect to normalized deflection

$$> E7; \quad u = 0.000005264913745 F_{com} \quad (38)$$

Then substitute with the definition of the dimensionlized deflection in Equation 7 to obtain Equation 8

$$> E8 := \{v = rhs(E7) * WL\}; \quad (39)$$

$$\{v = -0.0005628429546 F_{com}\} \quad (39)$$

Now solve Equation 8 for F(compressive) with respect to dimensionized deflection

$$\begin{aligned} &> F[com] = \text{solve}(E8, F[com]); \\ &F_{com} = \{F_{com} = -1776.694532 v\} \end{aligned} \quad (40)$$

What is the output voltage signal obtained from the bridge

$$\begin{aligned} &> U[out] := 42E-6; \\ &0.000042 \end{aligned} \quad (41)$$

Obtaining the dimensionized deflection based on Equation 5.9 in Chapter 5, Where v stands for dimensionized deflection

$$\begin{aligned} &> E11 := U[out] = U[i] * 3 * E * t[b] / (2 * L^2) * v * Q; \\ &0.000042 = 4114.285714 v \end{aligned} \quad (42)$$

Therefore the normalized deflection v is

$$\begin{aligned} &> v = \text{solve}(E11, v); \\ &v = 1.020833333 \cdot 10^{-8} \end{aligned} \quad (43)$$

Therefore the Compressive forces generated on the surface of the beam is

$$\begin{aligned} &> E12 := U[out] = \text{subs}(E8, U[i] * 3 * E * t[b] / (2 * L^2) * v * Q); \\ &0.000042 = -2.315696727 F_{com} \end{aligned} \quad (44)$$

$$\begin{aligned} &> F[com] := \text{solve}(E12, F[com]); \\ &-0.00001813709002 \end{aligned} \quad (45)$$

What is the diameter of the biological cell?

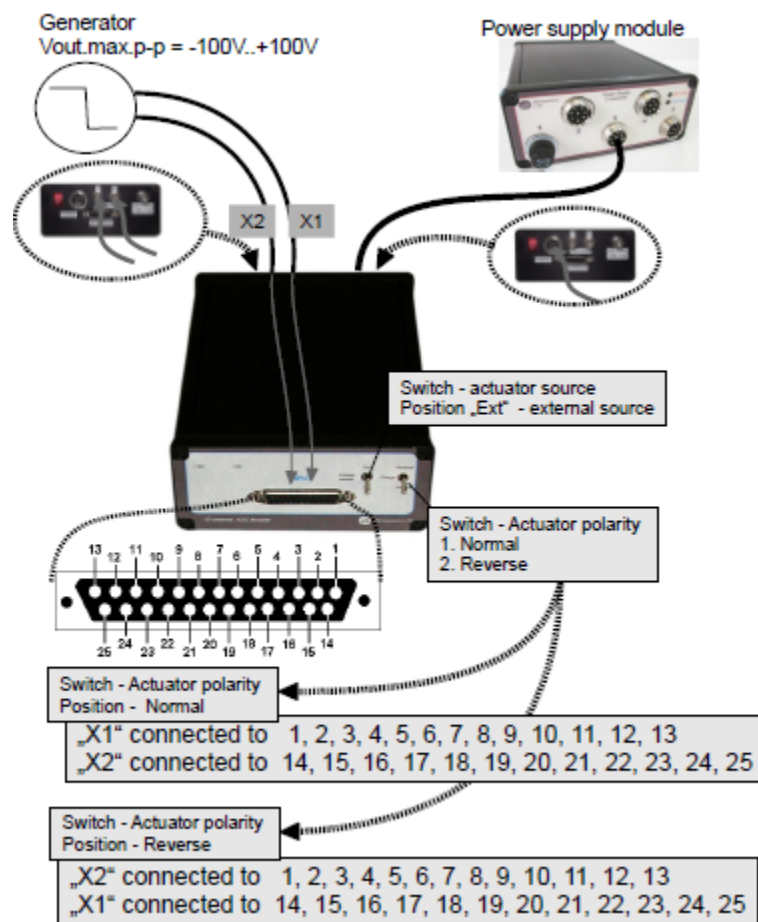
$$\begin{aligned} &> d[c] := 21E-6 \\ &0.000021 \end{aligned} \quad (46)$$

Therefore the cellular contractile force of a cell is obtained by

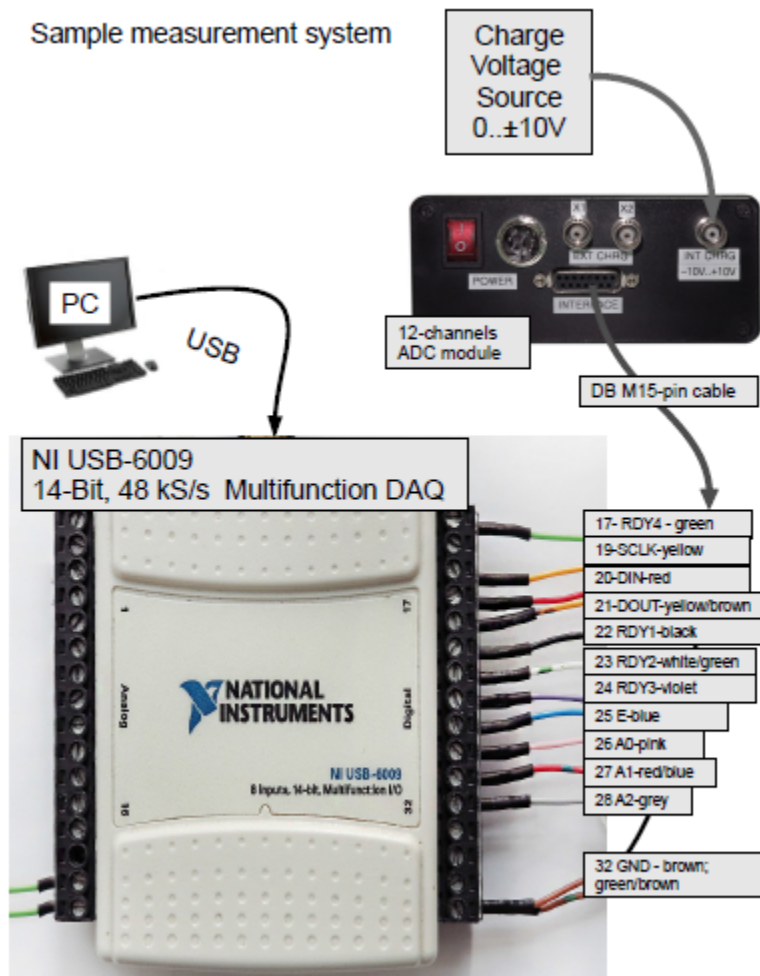
$$\begin{aligned} &> E13 := F[con] = \frac{\left( F[com] \cdot 2 \cdot 3.14 \cdot \left( \frac{d[c]}{2} \right)^2 \right)}{(b1 \cdot (x2 - x1))}; \\ &F_{con} = -0.000004983165482 \end{aligned} \quad (47)$$

$$\begin{aligned} &? \\ &> ? \end{aligned} \quad (48)$$

# **D.1 Microelectronic Hardware Arch.: Electrochemical Biomechatronic Platform**



(A)

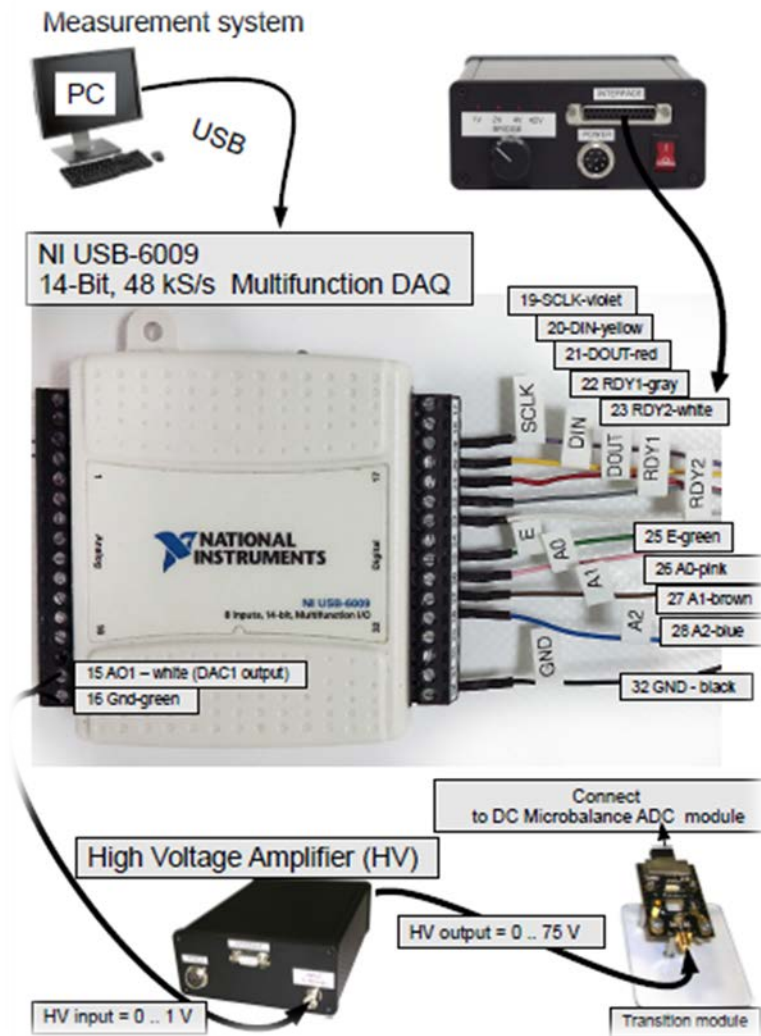


(B)

**Fig. D.1** Microelectronic Hardware Architecture of the 12-Channel-ADC module (Jassim Alqabandi, Imperial College London, All Rights Reserved).

---

# **D.2 Microelectronic Hardware Arch.: Mechanobiology Biomechatronic Platform**



**Fig. D.2** Microelectronic Hardware Architecture of the DC-Microbalance-ADC module (Jassim Alqabandi, Imperial College London, All Rights Reserved).

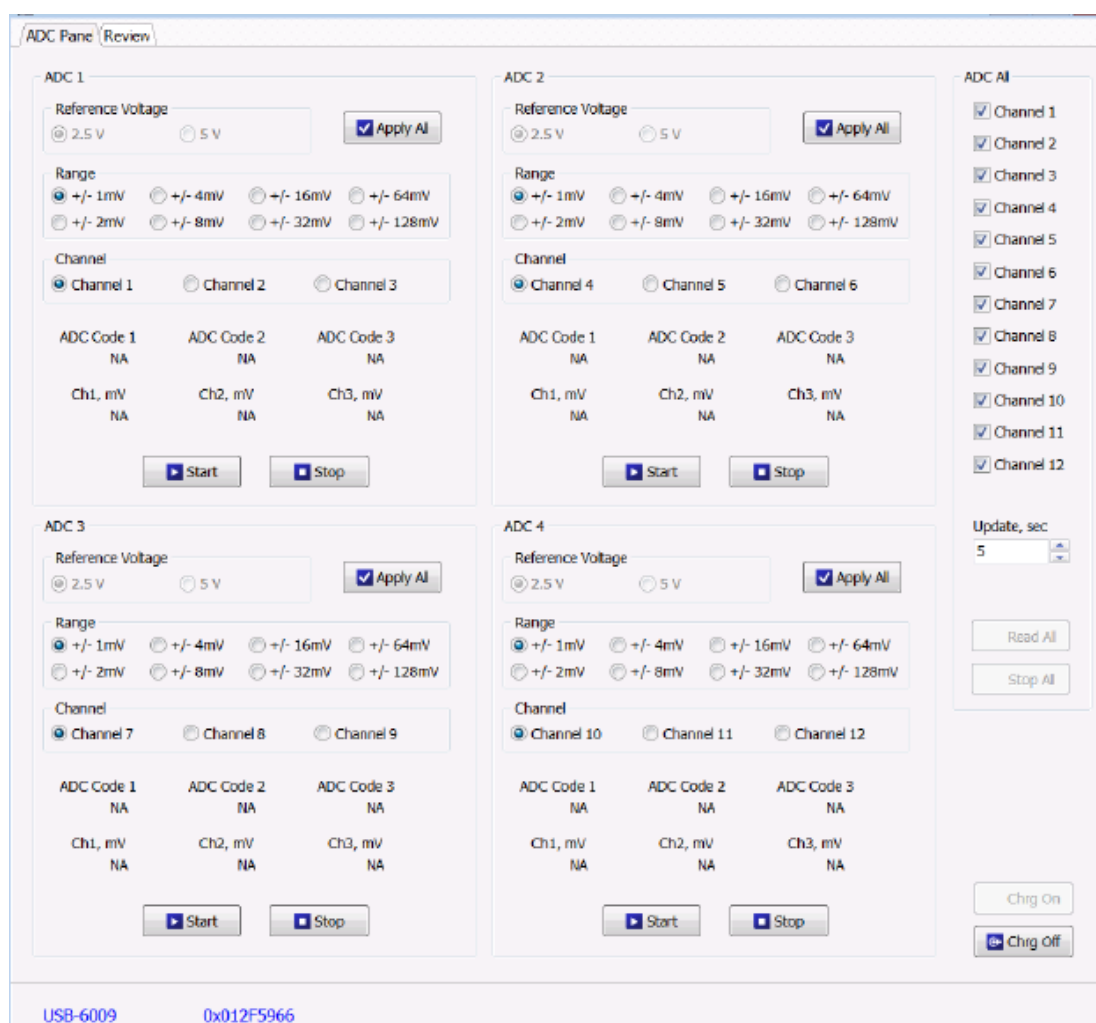
---

# **E.1 Customized Controlling Software Manual -- Electrochemical Biomechatronic Platform**



## Manual of the Electrochemical Bio-Mechatronic Platform Operating Software

The software has been coded in DELPHI application programming language, and it is operating under Microsoft Windows. This program has been customized to serve the experimental needs of the miniaturized electrochemical bio-mechatronic device. Furthermore, the pre-set controlling parameters are in line of the reviewed literature in terms of biophysics of cell, and various scholars' findings in the field. This design-of-experiment (DOE) oriented program operates within up to 12 channels; 11 channels used in the current setup -- allowing collection of data from various pairs of 11 electrodes: stimulating and recording electrode embedded within the microfluidic domain. Thus, this shall allow extracting electrophysiology of cells, and further analyze their biophysics. Before commencing the program, all experimental hardware has to be connected.



**Fig. E.1.1** Electrochemical biomechatronic platform operating software control panel.

The hardware system consists of a 12-channel-Analog-Digital-Convertor (ADC) module, to account for the 11 pair of electrodes (upper and lower electrode) embedded within the

microfluidic domain. The objective is to capture polarity of cells, and extract its cell-membrane potential. The ADC convertors are slow and precise. The maximal update rate for collecting data from all 12 channels is 5 updates per second. Each ADC hardware component has 3 channels, and hence there are 4 ADCs to accommodate the 11 pair of electrodes, which leaves channel 12 as a dummy channel.

The user starts by charging on the electrodes either via internal or external source. The former charge voltage approach takes up to  $\pm 10$  V as a maximum charge, whereas the latter approach takes up to  $\pm 100$  V. It should be noted that when internal charging the biomechatronic system, there is an internal amplifier gain of 2. Hence, the maximum voltage generator that is connected to the 12-channel-ADC module shouldn't exceed 5V; the internal generation of voltage doubles the potential, which is attributable to the usage of power operational amplifier (OPAM). The OPAM is utilized to enhance the system performance in case of lack of high voltage source to be fed to the electrodes. As for the external charging, the upper and lower electrode can be both charged or one is charged, and the other is grounded. The charging starts once the user clicks on the "Charge on" command.

When the time required as per the experiment to charge the electrodes is reached, the user clicks on "Charge off" button; this will activate "Read All" and "Charge On" buttons as shown in Figure E.1.2.



**Fig. E.1.2** (A) Charging and discharging the pair of electrodes (B) The serial number of NI data acquisition card.

Each ADC by default has a fixed reference voltage to ensure its operation. Therefore, as shown in Fig. 3A, such fixed value of 2.5 V doesn't play any role in the experiment, and user cannot modify it. Furthermore, Each ADC is on one circuit, and hence its associated 3 channels must all have one value of voltage difference range. The ADC module is measuring the differential voltage between the two electrodes. If a range is selected, e.g.,  $\pm 4$  mV, then

voltages between  $-4\text{mV}$  and  $+4\text{ mV}$  can be measured. All voltages  $> 4\text{mV}$  will cause the saturation of the ADC, i.e. the program will show the upper limit of the range:  $4\text{mV}$ . Respectively, all voltages  $< -4\text{mV}$  will cause the program to show the lower limit:  $-4\text{mV}$ . Thus, the user can recognize, if it is in saturation by the readings: if all readings are constantly  $+4\text{mV}$  or constantly  $-4\text{mV}$ , which means the chosen range is too small, so you have to increase it.

The detection regime range of voltages (Fig. E.1.3) is in line of cell-membrane findings within published literature. Each channel corresponds to a pair of electrodes: bottom and upper. The software provides flexibility in terms of assigning the same detection range value to all ADCs' channels by a single click on "Apply All" button, or it allows user to perform different experiments by assigning different range of values for different ADCs.

The software allows the user to obtain the readings for a single ADC module by clicking on "Start" to collect data, and terminating the reading process by selecting "Stop" command as shown in Figure E.1.2. The ADC Codes are internal electronics references, and they don't interfere with the experiment. The readings for each channel is shown in Figure E.1.3D, while user can switch between channels by ticking the circle in front of channel designation (Figure E.1.3C).

The screenshot shows the 'ADC Pane' with a 'Review' tab. It is divided into several sections:

- ADC 1**: The main configuration area.
- Reference Voltage**: Two radio buttons for '2.5 V' (selected) and '5 V'. An 'Apply All' button is to the right.
- Range**: Eight radio buttons for different voltage ranges: '+/- 1mV' (selected), '+/- 4mV', '+/- 16mV', '+/- 64mV', '+/- 2mV', '+/- 8mV', '+/- 32mV', and '+/- 128mV'.
- Channel**: Three radio buttons for 'Channel 1' (selected), 'Channel 2', and 'Channel 3'.
- ADC Code 1, 2, 3**: Each has a label 'NA' below it.
- Ch1, mV, Ch2, mV, Ch3, mV**: Each has a label 'NA' below it.
- Buttons**: 'Start' and 'Stop' buttons at the bottom.

Red dashed lines and letters A, B, C, and D are overlaid on the image to highlight specific areas: A points to the Reference Voltage section, B points to the Range section, C points to the Channel section, and D points to the ADC Code and Channel mV sections.

**Fig. E.1.3** (A) Reference internal assigned voltage for ADC performance (B) Voltage range to assigned experiments (C) Selection of Channel (D) Displaying of values extracted from each channel (pair of electrodes) in mV.

Finally, as shown in Figure E.1.4A, the user has the ability to select which channels to obtain readings from, as well as to choose the update time (Figure E.1.4B), e.g., every 5 seconds the system registers a reading and saves it, where system “Busy” is shown at the bottom of the screen.

The screenshot shows a software window titled "ADC All". It contains a list of 12 channels, each with a checked checkbox, indicating they are all selected. Below the list is a section labeled "Update, sec" with a text box containing the value "5" and up/down arrow buttons. At the bottom are two buttons: "Read All" (with a play icon) and "Stop All".

**A** points to the list of channels, and **B** points to the "Update, sec" field.

**Fig.E.1.4** (A) Selection of channels of which the readings shall be obtained, (B) The timer period to collect samples and save them.

---

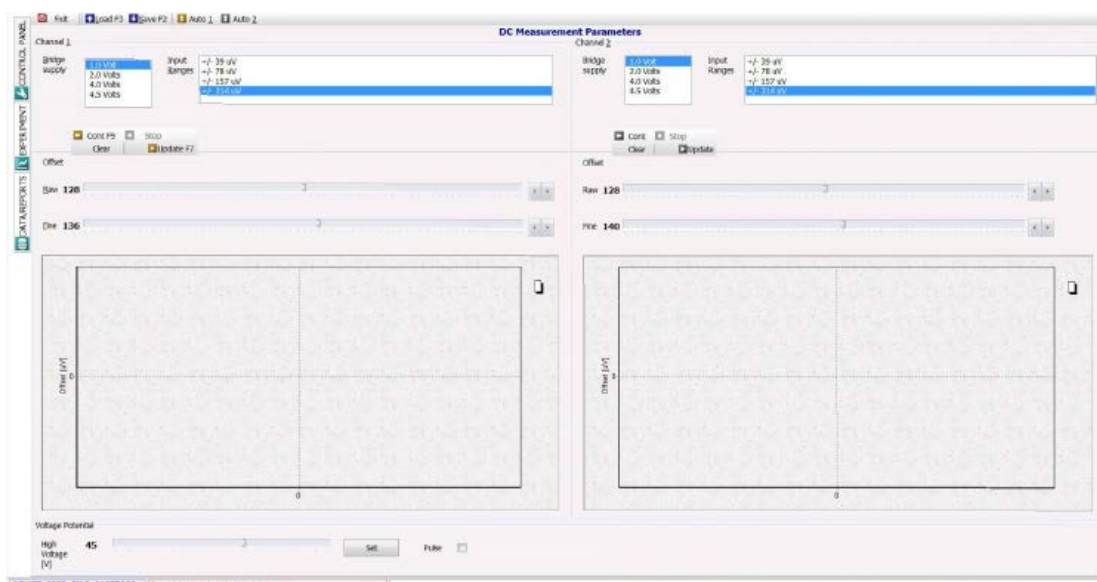
# **E.2 Customized Controlling Software Manual -- Mechanobiology Biomechatronic Platform**

## Manual of the $\mu$ -Cantilever Based Bio-Mechatronic Platform Operating Software

The software has been coded in DELPHI application programming language, and it is operating under Microsoft Windows. This program has been customized to serve the experimental needs of the miniaturized cantilever-based bio-mechatronic device. Furthermore, the pre-set controlling parameters are in line of the reviewed literature in terms of bio cell characteristics, and various scholars' findings in the field. This design-of-experiment (DOE) oriented program operates within two channels -- allowing collecting data from two different experimental setups (two bio-mechatronic platforms operating in parallel).

The PC software is connected to NI DAQ card, which controls two hardware modules: "DC-Microbalance-ADC module" and "High-Voltage (HV) Amplifier". As illustrated in Figure E.2.1, the program consists of 3 major tabs/panels: Control Panel, Experiment, and Data Reports. Before commencing the program, all experimental hardware has to be connected. The software has been designed to be a user friendly by providing instructions when moving the mouse cursor on each term on the screen, where a display message at the bottom of the page provides information on each parameter through Graphical User Interface (GUI). Thus, it is always essential that users start with setting/loading their experimental parameters in control panel tab prior to visiting other panels.

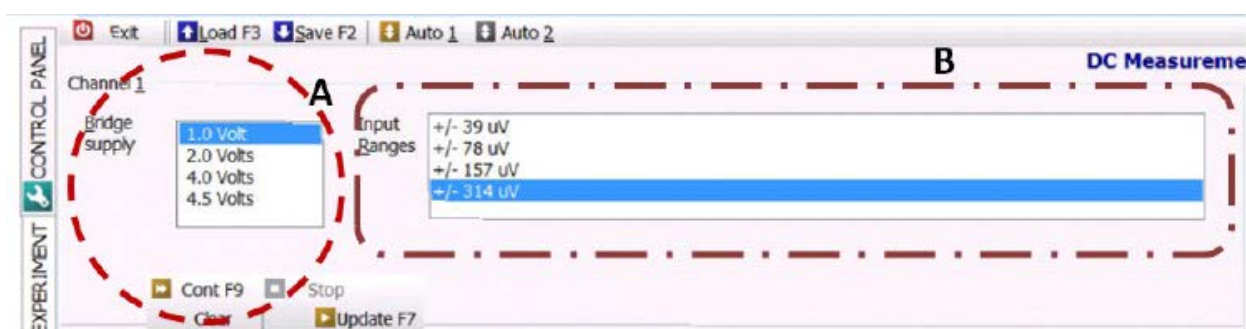
### Part 1: Setting Experimental Parameters in Control Panel:



**Fig. E.2.1** A screen image of the customized software to operate the  $\mu$ cantilever-based bio-mechatronic platform.

The user has to initiate the program by manually selecting from the DC-Microbalance-ADC module value to feed the bridge as depicted in Figure E.2.2.A. The selection must be the same as the value manually set in the DC Microbalance ADC module jumper. This manual operation

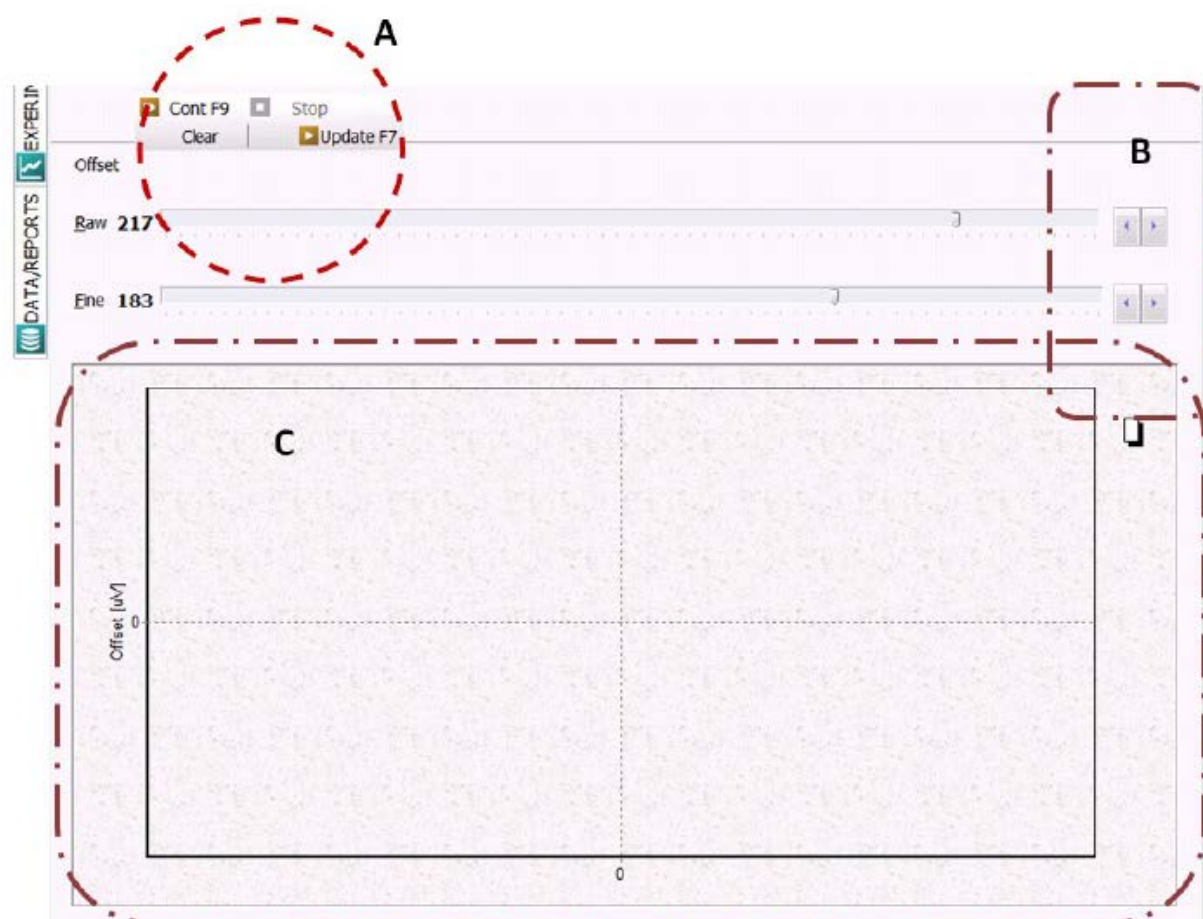
is taken place to reduce the electronic components within the voltage supplier source (simplicity of the design), as well as to eliminate additional source of electronic noises. Therefore, both devices (channels) would have the same bridge supply value.



**Fig.E.2.2** (A) Bridge voltage supply and (B) input range initiation under control panel tab.

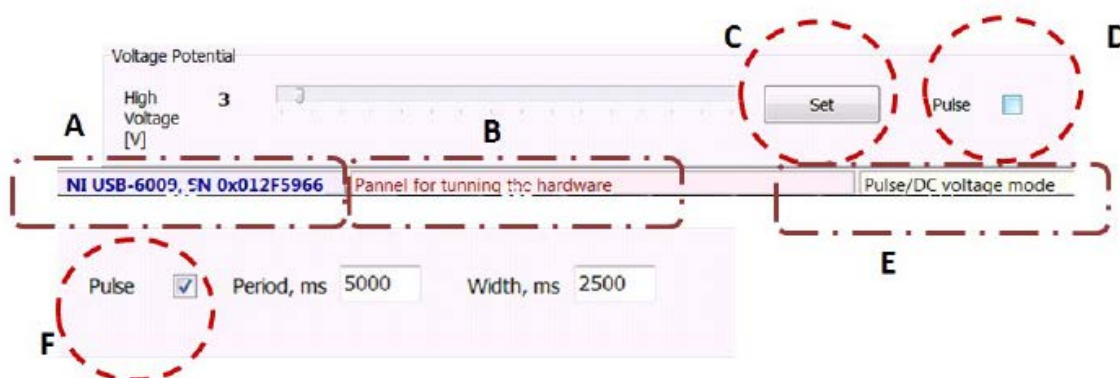
The user can determine the input ranges based on the reading measurements; e.g., if the reading measurements experience minute changes, then small input ranges should be selected. As shown in Fig. E.2.2A, each channel has to have the same bridge supply of potential, but they can differ in terms of DC potential input range (Fig E.2.2.B). Hence, this shall give flexibility to the user to perform 2 different experiments in parallel, under 2 different conditions (analyzing two different biological phenomena), or have them both running at the same conditions for repeatability, shorten lead time in performing a number of experiments, or setting one experimental setup as a reference to the other. It should be noted that by switching from one input range selection to the other, a delay time period is taken to have such values set in the attached hardware. During the hardware initialization, the controls on the Control Panel becomes inactive.





**Fig. E.2.3** (A) executing/terminating the program to obtain readings from the NI data acquisition card, and clearing and updating obtained graph (B) Fine and coarse tuning of the offset, and (C) Display of the graph.

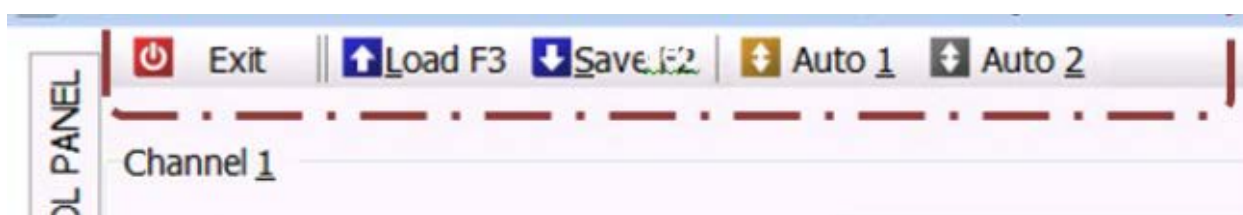
Due to the microfabrication tolerances while developing the microcantilevers, their Wheatstone Bridge resistors are experiencing offsets. Thus, this software enables users to adjust the offset of the obtained readings. In Fig. E.2.3.A, the user selects the command "Cont" or hits F9 to execute the reading command, and extract data from the NI data acquisition card. If the obtained readings are off range (i.e. far from zero line), the user has to terminate the reading process by pressing the "Stop" in order to fine/coarse tune the offset to be within the vicinity of zero (Fig. E.2.3B). Once the desired offset is obtained, the user can re-run the command by pressing on F9, clearing previous graphs obtained from previous readings through the "Clear" command, and/or updating the graph based on new parameters by selecting "update F7". Within the graph area of Fig E.2.3.C, users can zoom in or out, by pressing on left mouse button, and simultaneously draw a diagonal inward or downward respectively on their mouse pad. Also, user can shift graph upward or downward by pressing on the right mouse button, and then simultaneously moving his/her index finger upward or downward.



**Fig. E.2.4** (A) Software recognition of the serial number of the NI USB card, (B) Message indicating the purpose of this segment of the software upon moving the mouse cursor, (C) Setting values for injecting a DC voltage to a stationary electrode to generate electrostatic forces, (D) Setting the injected potential to be in the pulse mode, (E) Display message familiarizing user of the command upon moving the mouse cursor, and (F) New display upon ticking the pulse box that allows setting period and width in milli second.

The user has the option to induce electrostatic force, by setting the DC voltage value: feeding the stationary electrode patterned on the glass substrate (Fig. E.2.4C). Also, a choice of setting pulse injection mode of potential with a specified period and width can be achieved (Fig. E.2.4 D, F).

As a final stage in setting the parameters in the control panel tab, the user can, save the pre-set parameters, and load them for other experiments (shortening lead time in preparation), Fig E.2.5. Furthermore, upon exiting the program the user is prompted to save the file.



**Fig. E.2.5.** Upper left menu of the Control Panel tab.

## Part 2: Performing the Experiments (Experiment Tab)

After finalizing all steps in Part 1, and selecting all controlling parameters, the user can proceed to experiment tab (Fig. E.2.6) to start performing the experiments and collecting data.

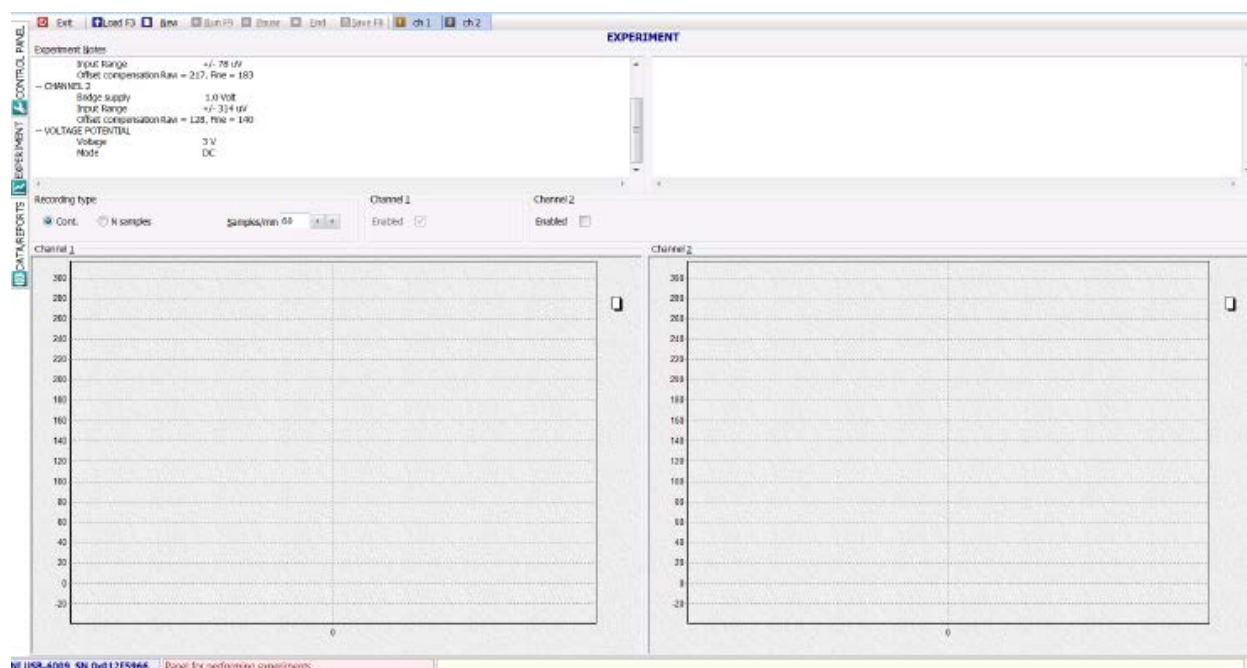


Fig. E.2.6 Experiment tab to collect data

The Experiment tab starts by displaying the experimental pre-selected parameters in control panel tab (Figure E.2.7B). First, the user has to click on “New” (Figure E.2.7A), to commence a new experiment, where a message “Put your notes here” is displayed (Figure E.2.7C); here the user can place a description of this particular experiment. As shown in Figure E.2.7. A, the user can decide to exit the program, run the experiment, and choose to show or hide the obtained results received from Channel 1 and Channel 2.

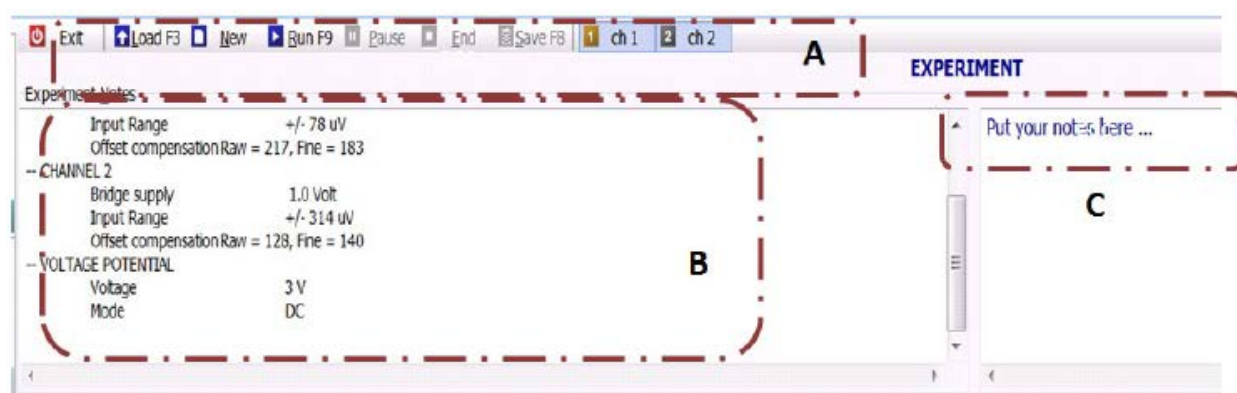


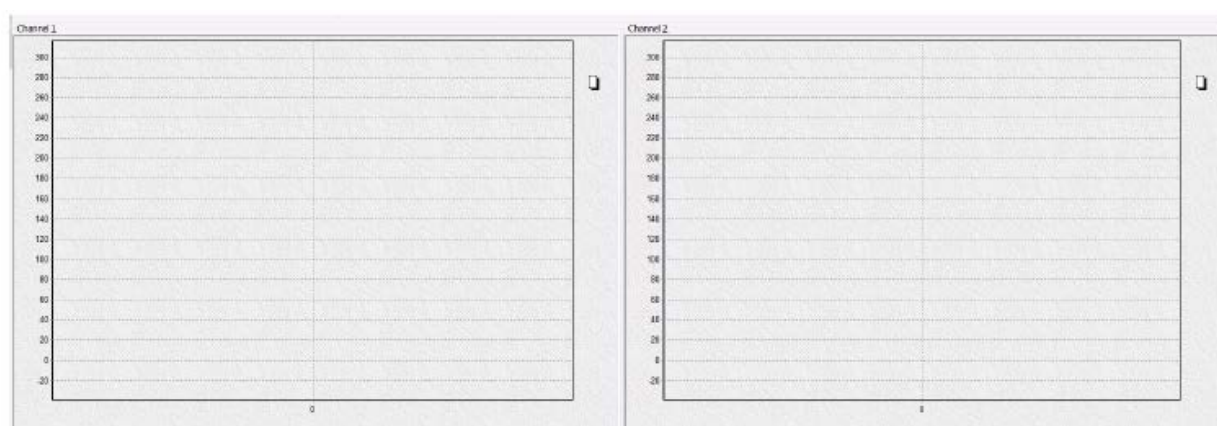
Fig. E.2.7 (A) Upper left menu of the Experiment tab (B) Assigned controlling parameters, (C) Adding text notes during experiments.

The user can then select the recording mode: either by continuous data recording with assigned number of samples (Figure E.2.8A), or by selecting N samples option (Figure E.2.8B) to specify the number of samples to be taken before the experiment terminated. Also, the user can enable which channel's result to be displayed on graph during recording.



**Fig. E.2.8** (A) Selecting recording type mode, (B) Recording in N-sample mode.

The results are displayed on channel 1 and 2 as shown in Figure E.2.9. The user can perform zoom in and out as well as shifting the graph upwards or downwards as indicated in Part I. Finally, the user can save, end, or pause the collection of reading data through the controlling commands in the upper left menu (Figure E.2.7A). Upon saving the obtained results, the data files are saved in a local database.



**Fig. E.2.9** Display window of the experimental results.

### Part 3: Data Reports Tab

At a final stage, the Data Reports tab provides the final obtained results (Figure E.2.10). The upper left menu (Figure E.2.11) provides the user the option of exiting the program with a

reminder to save, scroll through first to last reports, search for particular reports by period, search by key words through the filter command, print or delete a report.

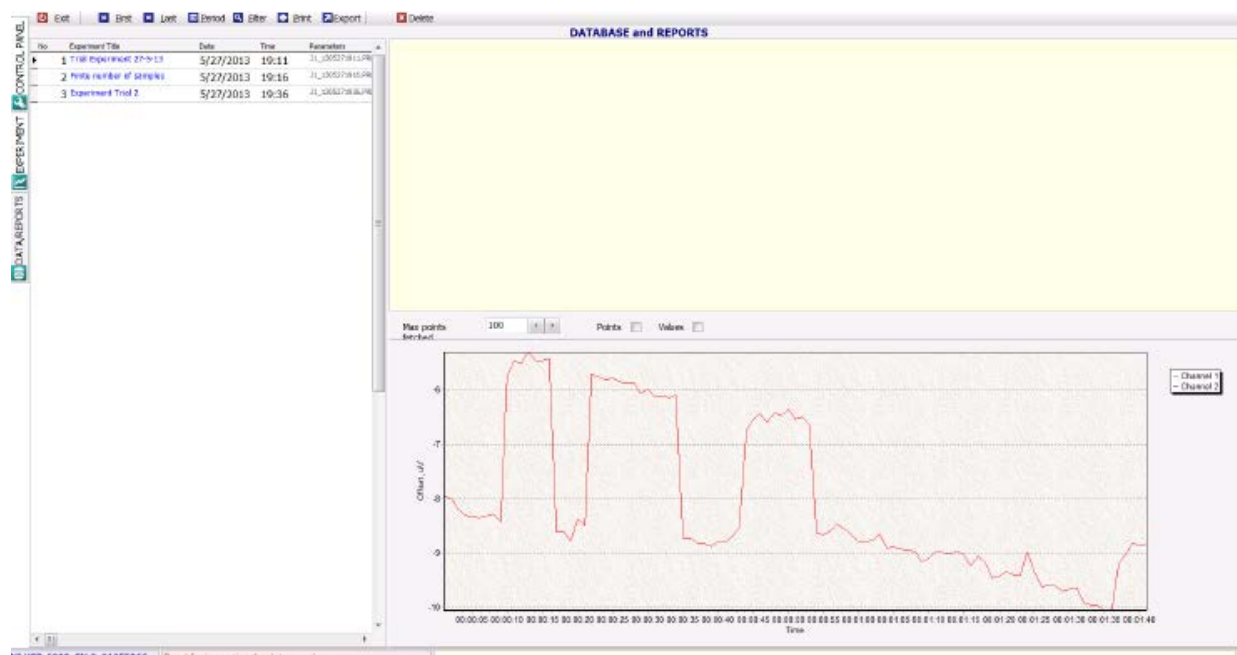


Fig. E.2.10 Data Reports tab.

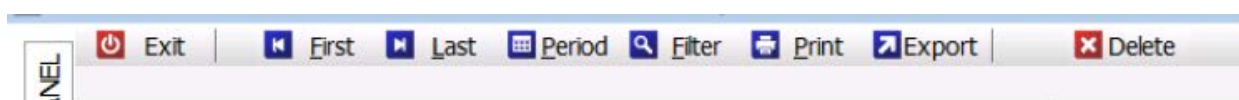


Fig. E.2.11 Upper left menu of the Data Report screen.

By selecting any of the generated experiments, reports are displayed as shown in Figure E.2.12, where hardware pre-set parameters are displayed, and associated figure is shown with the option of showing all/part/nil of points and values on graph. Also, user can still zoom in and out, shift the graph upward and downward as explained in Part 1, as well as fetching points to shows more results on the graph.



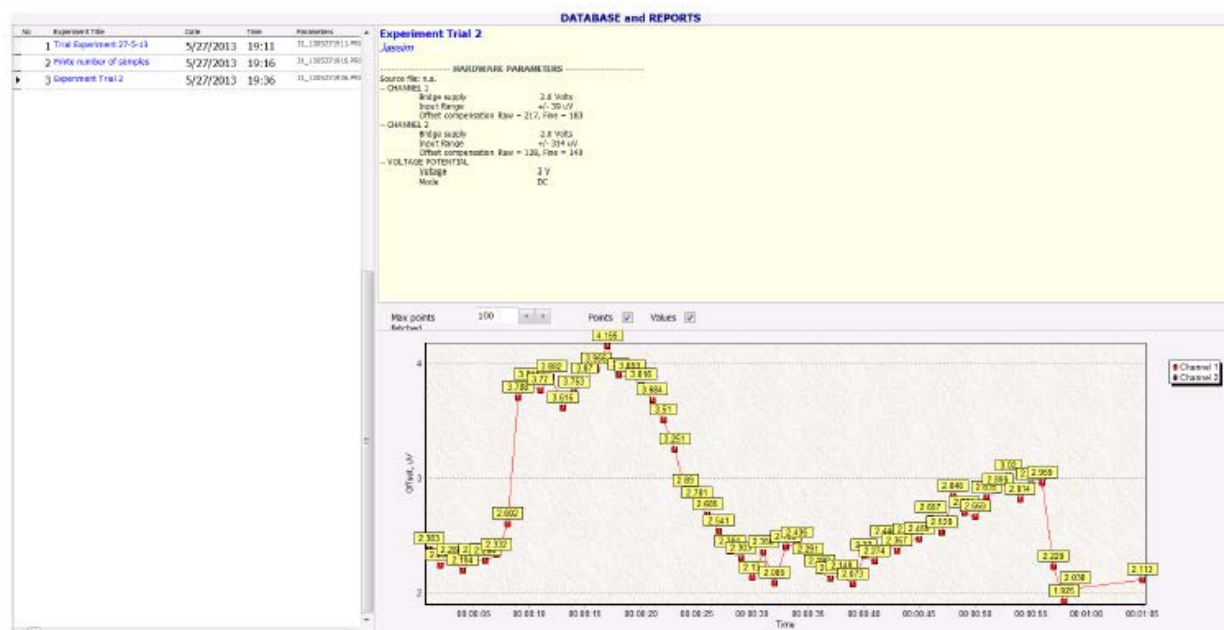


Fig. E.2.12 Retrieved database and reports on saved experiment.

# **Appendix F**

## **Pull-In Phenomena**

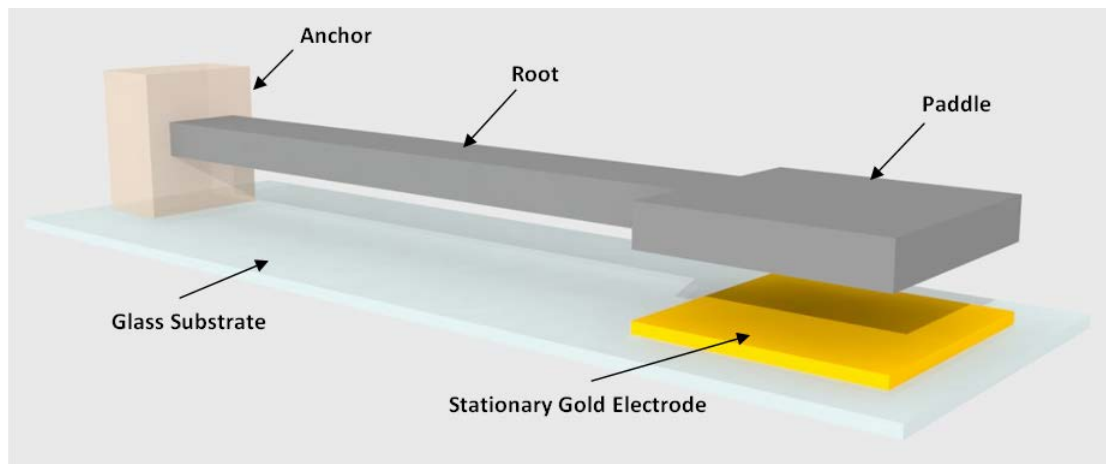
### **(Detailed Derivations)**

## Appendix F: Pull-In Phenomena

### F.1 Model Formulation

A cantilever-based biosensor system, depicted in Figure F.1, is of a single-polysilicon structure that has been used by Nayfeh *et al.* [198] as a resonant gas sensor. It consists of a root (continuous beam) coupled with a paddle (plate). The entire cantilever structure is anchored (clamped) at the end. The anchor is made of an insulating material (PDMS). A stationary gold electrode, comparable to the size of the effective mass paddle, is patterned on a glass substrate. The beam-plate structure is electrostatically stimulated through the induction of a potential on the stationary gold electrode. Furthermore, this system can be extended for future analyses to consider dynamic mode by superimposing harmonic AC potential,  $V_{AC}$ , within the fixed induced DC voltage,  $V_{DC}$ . Appendix F highlights the work of Nayfeh *et al.* [198], and it extends the study to provide a definition of sensitivity, and optimization.

The paddle is modeled as a rigid body due to the assumption of a uniform overlap of the attractive electrostatic force between the paddle, and the stationary electrode. Moreover, deformation of the paddle is of a minimal effect as opposed to the overall system kinematics; thus, the paddle is simply modeled as a rigid body. The miniaturized mechanical system is assumed to have a uniform structure with a constant cross-sectional area, density, modulus of elasticity, and second moment of cross-sectional area throughout the one dimensional length continuum. Furthermore, the mechanical structure is assumed to be isotropic (directionally uniform); the effective mass of the rigid-body paddle is invariant with respect to time, and it has a non-extensible neutral axis (NA).



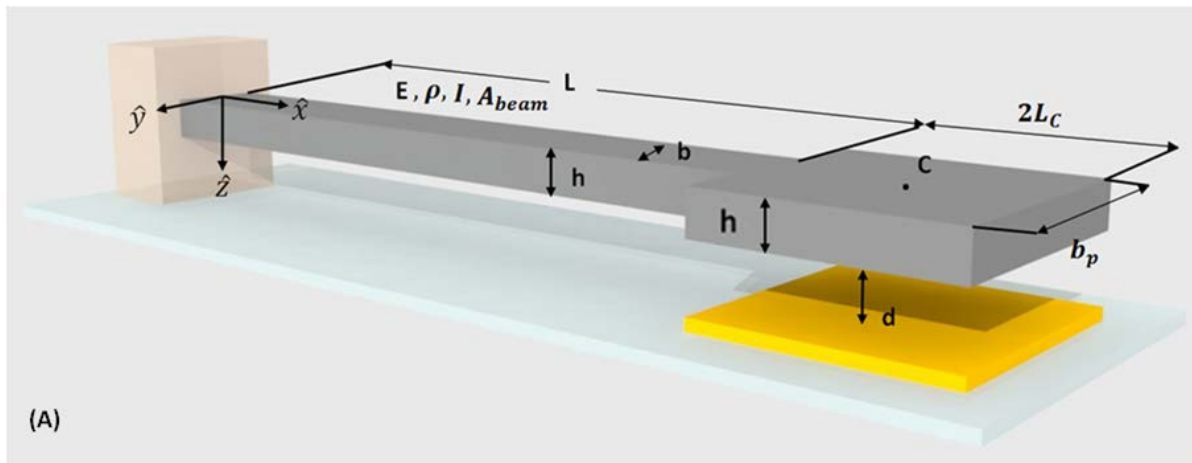
**Fig. F.1** MEMS System: Paddle (plate), Root (cantilever), Anchor (insulating material), and Stimulating Stationary Electrode.

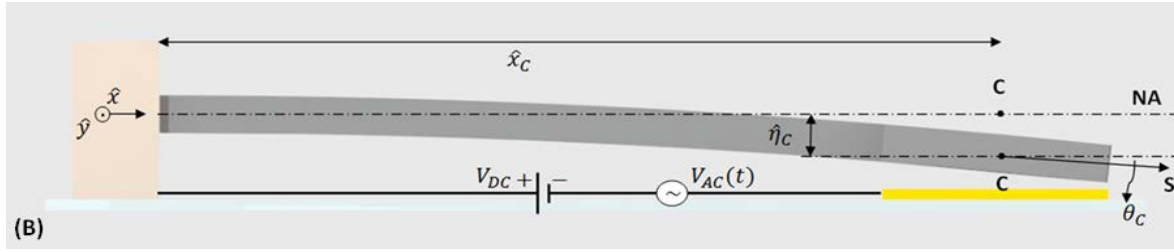
The proposed design of the microcantilever beam coupled with the microplate is long and thin. Thus, a Bernoulli-Euler beam is adopted, in which shear strain and all its variations are set to zero, and where normal to mid-surface plane is invariant prior to or after deformation (non-extensional beam). The mathematical relationship relating the deformation of a continuous linear prismatic Bernoulli-Euler microbeam with an electrostatic effect has been



investigated in [198]. In their work, it was found that the electrostatic force is nonlinearly dependent on the distance between the plate and the stationary electrode, and on the applied potential beneath the plate as well. In the static mode, non-uniform surface stresses along the beam's thickness lead to bending [303], while in dynamic mode, shifting in the center of mass leads to a resonant frequency of the vibrating microcantilever beam, which is electronically quantifiable [198, 304]. The following analysis will focus on the static mode, re-deriving the equation of motion previously developed in [198], and further account for the effective mass of the paddle.

The controlling parameters of the MEMS device depicted in Figure F.2 are a source of static and alternating potential,  $V_{DC}$  and  $V_{AC}$ , respectively;  $L$  the equilibrium length of the beam;  $\hat{L}_C$  is the length of the paddle;  $\hat{x}_C$  is the center of mass (C) of the paddle (where  $\hat{x}_C = \hat{L}_C + L$ );  $S$  is the body fixed coordinate;  $(\hat{x}, \hat{y}, \hat{z})$  is the inertial (reference frame) coordinates;  $E$  is the modulus of elasticity of the beam;  $\rho$  is density;  $d$  is the distance between the paddle and stationary electrode;  $b$  is the width of the beam;  $b_p$  is the width of the paddle; and  $h$  is the thickness of the beam and paddle. The cross-sectional area of the beam is denoted as  $A_{beam}$  (where  $A_{beam} = bh$ ). The mass moment of inertia of the paddle is  $J = \frac{1}{3} \hat{M} \hat{L}_C^2$ ; and the second moment of cross-sectional area about the neutral axis (NA) is  $I = bh^3/12$ . The independent and complete generalized coordinate of the beam depicting temporal and spatial transverse displacement is  $\hat{\eta}(\hat{x}, \hat{t})$ . The spatial and temporal displacement of the center of mass is  $\hat{\eta}_C(\hat{x}_C, \hat{t})$ .  $\theta_C$  represents the transverse rotational angle about neutral axis (where  $\theta_C = \frac{\partial \hat{\eta}(\hat{x}, \hat{t})}{\partial \hat{x}}$ ). It should be noted that  $\hat{\xi}$  and  $\xi$  respectively denote a dimensional and its corresponding normalized parameter. It should also be noted that the paddle mass ( $\hat{M}$ ) is considered the effective mass of the system.





**Fig. F.2** Analytical model of the MEMS structure (A) Design parameters of the microcantilever, (B) Representation of a transversely deformed beam due to a DC electrostatic actuation.  $s$  is a body fixed coordinate, and  $\theta_C$  is the transverse rotational angle about NA.

## F.2 Analytical Representation: A Quantitative Approach

The governing equation of motion of the MEMS structure is derived first by defining the potential, system kinetic co-energy, and non-conservative force(s) imposed into the system. The proposed system is Holonomic that justifies the utilization of Lagrangian formula.

### System kinetic co-energy function

$$T^* = \int_0^L \frac{1}{2} \rho A_{beam} \left[ \frac{\partial \hat{\eta}(\hat{x}, \hat{t})}{\partial \hat{t}} \right]^2 d\hat{x} + \frac{1}{2} (\hat{M}) \left[ \frac{\partial \hat{\eta}(L, \hat{t})}{\partial \hat{t}} + \hat{L}_C \frac{\partial^2 \hat{\eta}(L, \hat{t})}{\partial \hat{t} \partial \hat{x}} \right]^2 + \frac{1}{2} J \left[ \frac{\partial^2 \hat{\eta}(L, \hat{t})}{\partial \hat{t} \partial \hat{x}} \right]^2 \quad (F.1)$$

Equation (F.1) represents system's kinetic co-energy. The three terms in Eq. (F.1) account for the energy associated with the total transverse velocity across the length of the beam, the energy associated with the translational motion of the rigid body mass, as well as energy associated rotational motion of the mass of the rigid body. On the other hand, the total potential energy of the system is a sum of the energy of beam elastic deformation, gravitational force, and electrostatic between stationary electrode and rigid body.

### Overall system potential energy

$$V_{Total} = V_{beam \text{ elastic deformation}} + V_{gravitational \text{ force}} + V_{electrostatic \text{ field}}$$

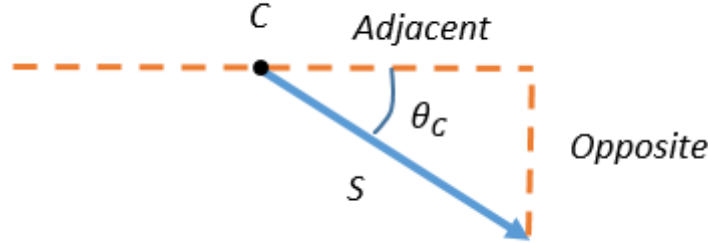
Where,  $V_{beam}$  is defined as,

$$V_{beam} = \int_0^L \frac{1}{2} EI \left[ \frac{\partial^2 \hat{\eta}(\hat{x}, \hat{t})}{\partial \hat{x}^2} \right]^2 d\hat{x}$$

The potential energy due to conservative gravitational force exerted on a rigid body of mass ( $\hat{M}$ ) is expressed as,

$$V_g = -\hat{M}g \hat{\eta}(\hat{L}_C, \hat{t})$$

The electrostatic potential energy within the system is defined as per a capacitive effect, which is a nonlinear function of the gap between the stationary electrode and rigid body. Therefore, referring to Figure F.3, and considering a parallel-plate approximation, the time varying gap is obtained.



**Fig. F.3** A small angle approximation of the time varying gap.

$$\frac{\text{Opposite}}{S} = \sin\theta_c = \theta_c \quad \text{by small angle approximation, where } \frac{\partial\hat{\eta}}{\partial\hat{x}} = \theta_c$$

$$\therefore \text{Opposite} = \text{Time Varying Gap} = S \sin\theta_c = S\theta_c = S \frac{\partial\hat{\eta}}{\partial\hat{x}}$$

Thus, the potential energy associated with electrostatic force, where  $\epsilon$  is the permittivity of air, and where  $\mathcal{F}$  is the fringing field effect calibrating constant [210, 245, 304-306], is described mathematically as follows,

$$V_{\text{electro}} = -\frac{1}{2}\epsilon b\mathcal{F}(V_{DC} + V_{AC}(\hat{t}))^2 \left[ \int_0^{2\hat{L}_C} \frac{1}{d - \hat{\eta}(L, \hat{t}) - \frac{\partial\hat{\eta}}{\partial\hat{x}}(L, \hat{t})\hat{S}} d\hat{S} \right]$$

Evaluating the integral term of the electrostatic potential energy:

$$-\int_0^{2\hat{L}_C} \frac{d\hat{S}}{d - \hat{\eta}(L, \hat{t}) - \frac{\partial\hat{\eta}}{\partial\hat{x}}(L, \hat{t})\hat{S}}$$

$$u = d - \hat{\eta}(L, \hat{t}) - \frac{\partial\hat{\eta}}{\partial\hat{x}}(L, \hat{t})\hat{S} \quad du = -\frac{\partial\hat{\eta}}{\partial\hat{x}}(L, \hat{t})d\hat{S} \quad d\hat{S} = \frac{1}{-\frac{\partial\hat{\eta}}{\partial\hat{x}}(L, \hat{t})} du$$

Thus,

$$\begin{aligned} & -\int_0^{2\hat{L}_C} \frac{1}{u} \frac{du}{-\frac{\partial\hat{\eta}}{\partial\hat{x}}(L, \hat{t})} \\ &= \frac{1}{\frac{\partial\hat{\eta}}{\partial\hat{x}}(L, \hat{t})} \ln(u) \Big|_0^{2\hat{L}_C} = \frac{1}{\frac{\partial\hat{\eta}}{\partial\hat{x}}(L, \hat{t})} \ln(d - \hat{\eta}(L, \hat{t}) - \frac{\partial\hat{\eta}}{\partial\hat{x}}(L, \hat{t})\hat{S}) \Big|_0^{2\hat{L}_C} \\ &= \frac{1}{\frac{\partial\hat{\eta}}{\partial\hat{x}}(L, \hat{t})} \left( \ln(d - \hat{\eta}(L, \hat{t}) - \frac{\partial\hat{\eta}}{\partial\hat{x}}(L, \hat{t})2\hat{L}_C) - \ln(d - \hat{\eta}(L, \hat{t})) \right) \\ &= \frac{1}{\frac{\partial\hat{\eta}}{\partial\hat{x}}(L, \hat{t})} \left( \ln \left( \frac{d - \hat{\eta}(L, \hat{t}) - \frac{\partial\hat{\eta}}{\partial\hat{x}}(L, \hat{t})2\hat{L}_C}{d - \hat{\eta}(L, \hat{t})} \right) \right) \end{aligned}$$

Therefore,

$$V_{Total} = V_{beam\ elastic\ deformaion} + V_{gravitational\ force} + V_{electrostatic\ field}$$

$$V_{total} = \int_0^L \frac{1}{2} EI \left[ \frac{\partial^2 \hat{\eta}(\hat{x}, \hat{t})}{\partial \hat{x}^2} \right]^2 d\hat{x} + \frac{1}{2} \epsilon \mathcal{F} b (V_{DC} + V_{AC}(\hat{t}))^2 \left[ \frac{1}{\frac{\partial \hat{\eta}(L, \hat{t})}{\partial \hat{x}}} \left( \ln \left( \frac{d - \hat{\eta}(L, \hat{t}) - \frac{\partial \hat{\eta}(L, \hat{t})}{\partial \hat{x}} 2 \hat{L}_C}{d - \hat{\eta}(L, \hat{t})} \right) \right) \right] - (\hat{M}) g \hat{\eta}(\hat{L}_C, \hat{t}) \quad (F.2)$$

Equation (F.2) represents the total potential energy. The three terms in the equation respectively account for the contributions of the elastic strain energy from the flexural deformation of the beam (bending strain), the electrostatic field initiated within the vicinity of the stationary electrode, and effective paddle, as well as the conservative gravitational force. On the other hand, Equation (F.3) represents the contributions of non-conservative forces, among which is the viscous film damping effect. Therefore,  $C_{eff}$  is an effective damping coefficient that is introduced to account for various damping factors experienced within the system environment (e.g. viscous film damping, thermoelastic damping ((internal friction)), sound, air resistance, etc.). The damping force is a non-conservative force that is distributed along the mechanical structure of the MEMS domain. Therefore, the non-conservative virtual work is defined as:

$$\delta w^{nc} = \sum_{j=1}^n \Xi_j \delta \zeta_j = -\hat{C}_{eff} \frac{\partial \hat{\eta}(\hat{x}, \hat{t})}{\partial \hat{t}} \quad (F.3)$$

This is a Holonomic system that justifies the utilization of Lagrangian formula. Therefore, by applying Hamilton's principle variation indicator approach (V.I.), as defined in Eq. (F.4), all terms can be represented and converted into a geometrically admissible form.

$$V.I. = \int_{\hat{t}_1}^{\hat{t}_2} [\delta(T^* - V) + \sum_{j=1}^n \Xi_j \delta \zeta_j] d\hat{t} \quad (F.4)$$

$$= \int_{\hat{t}_1}^{\hat{t}_2} \left[ \delta \left( \int_0^L \frac{1}{2} \rho A_{beam} \left[ \frac{\partial \hat{\eta}(\hat{x}, \hat{t})}{\partial \hat{t}} \right]^2 d\hat{x} + \frac{1}{2} (\hat{M}) \left[ \frac{\partial \hat{\eta}(L, \hat{t})}{\partial \hat{t}} + \hat{L}_C \frac{\partial^2 \hat{\eta}(L, \hat{t})}{\partial \hat{t} \partial \hat{x}} \right]^2 + \frac{1}{2} J \left[ \frac{\partial^2 \hat{\eta}(L, \hat{t})}{\partial \hat{t} \partial \hat{x}} \right]^2 - \int_0^L \frac{1}{2} EI \left[ \frac{\partial^2 \hat{\eta}(\hat{x}, \hat{t})}{\partial \hat{x}^2} \right]^2 d\hat{x} - \frac{1}{2} \epsilon \mathcal{F} b (V_{DC} + V_{AC}(\hat{t}))^2 \left[ \frac{1}{\frac{\partial \hat{\eta}(L, \hat{t})}{\partial \hat{x}}} \left( \ln \left( \frac{d - \hat{\eta}(L, \hat{t}) - \frac{\partial \hat{\eta}(L, \hat{t})}{\partial \hat{x}} 2 \hat{L}_C}{d - \hat{\eta}(L, \hat{t})} \right) \right) \right] + (\hat{M}) g \hat{\eta}(\hat{L}_C, \hat{t}) \right) - \hat{C}_{eff} \frac{\partial \hat{\eta}(\hat{x}, \hat{t})}{\partial \hat{t}} \right] d\hat{t} \quad (F.5)$$

And by evaluating term by term of Eq. (F.5) using the Hamilton's variation indicator method,

### Term 1

$$= \int_{\hat{t}_1}^{\hat{t}_2} \left[ \delta \left( \int_0^L \frac{1}{2} \rho A_{beam} \left[ \frac{\partial \hat{\eta}(\hat{x}, \hat{t})}{\partial \hat{t}} \right]^2 d\hat{x} \right) \right] d\hat{t}$$

$$= \int_0^L d\hat{x} \int_{\hat{t}_1}^{\hat{t}_2} \frac{1}{2} \rho A_{beam} 2 \frac{\partial \hat{\eta}(\hat{x}, \hat{t})}{\partial \hat{t}} \delta \frac{\partial \hat{\eta}(\hat{x}, \hat{t})}{\partial \hat{t}} d\hat{t}$$

$$u = \rho A_{beam} \frac{\partial \hat{\eta}(\hat{x}, \hat{t})}{\partial \hat{t}} \quad dv = \frac{\partial}{\partial \hat{t}} \delta \hat{\eta}(\hat{x}, \hat{t}) d\hat{t} \quad du = \rho A_{beam} \frac{\partial^2 \hat{\eta}(\hat{x}, \hat{t})}{\partial \hat{t}^2} \quad v = \delta \hat{\eta}(\hat{x}, \hat{t})$$

Performing integration by parts:  $\int u dv = uv - \int v du$

$$= \int_0^L d\hat{x} \left\{ \rho A_{beam} \frac{\partial \hat{\eta}(\hat{x}, \hat{t})}{\partial \hat{t}} \delta \hat{\eta}(\hat{x}, \hat{t}) \Big|_{\hat{t}_1}^{\hat{t}_2} - \int_{\hat{t}_1}^{\hat{t}_2} \rho A_{beam} \frac{\partial^2 \hat{\eta}(\hat{x}, \hat{t})}{\partial \hat{t}^2} \delta \hat{\eta}(\hat{x}, \hat{t}) d\hat{t} \right\}$$

The first term vanishes as per Hamilton's principle that the variations vanish at time  $\hat{t}_1$  and  $\hat{t}_2$ .

$$= - \int_{\hat{t}_1}^{\hat{t}_2} d\hat{t} \int_0^L \rho A_{beam} \frac{\partial^2 \hat{\eta}(\hat{x}, \hat{t})}{\partial \hat{t}^2} \delta \hat{\eta}(\hat{x}, \hat{t}) d\hat{x} \quad (F.6)$$

## Term 2

$$\begin{aligned} &= \int_{\hat{t}_1}^{\hat{t}_2} \left[ \delta \left( \frac{1}{2} (\hat{M}) \left[ \frac{\partial \hat{\eta}(L, \hat{t})}{\partial \hat{t}} + \hat{L}_C \frac{\partial^2 \hat{\eta}(L, \hat{t})}{\partial \hat{t} \partial \hat{x}} \right]^2 \right) \right] d\hat{t} \\ &= \int_{\hat{t}_1}^{\hat{t}_2} \left[ \left( \frac{2}{2} (\hat{M}) \right) \left( \frac{\partial \hat{\eta}(L, \hat{t})}{\partial \hat{t}} + \hat{L}_C \frac{\partial^2 \hat{\eta}(L, \hat{t})}{\partial \hat{t} \partial \hat{x}} \right) \delta \left( \frac{\partial \hat{\eta}(L, \hat{t})}{\partial \hat{t}} + \hat{L}_C \frac{\partial^2 \hat{\eta}(L, \hat{t})}{\partial \hat{t} \partial \hat{x}} \right) \right] d\hat{t} \end{aligned}$$

Where,  $\delta(\dot{\xi})^2 = 2\dot{\xi}\delta\dot{\xi}$

$$\begin{aligned} &= \int_{\hat{t}_1}^{\hat{t}_2} \left[ \left( (\hat{M}) \right) \left( \frac{\partial \hat{\eta}(L, \hat{t})}{\partial \hat{t}} \right) \delta \left( \frac{\partial \hat{\eta}(L, \hat{t})}{\partial \hat{t}} \right) \right] d\hat{t} + \int_{\hat{t}_1}^{\hat{t}_2} \left[ \left( (\hat{M}) \right) \left( \frac{\partial \hat{\eta}(L, \hat{t})}{\partial \hat{t}} \right) \delta \left( \hat{L}_C \frac{\partial^2 \hat{\eta}(L, \hat{t})}{\partial \hat{t} \partial \hat{x}} \right) \right] d\hat{t} + \\ &\int_{\hat{t}_1}^{\hat{t}_2} \left[ \left( (\hat{M}) \right) \left( \hat{L}_C \frac{\partial^2 \hat{\eta}(L, \hat{t})}{\partial \hat{t} \partial \hat{x}} \right) \delta \left( \frac{\partial \hat{\eta}(L, \hat{t})}{\partial \hat{t}} \right) \right] d\hat{t} + \int_{\hat{t}_1}^{\hat{t}_2} \left[ \left( (\hat{M}) \right) \left( \hat{L}_C \frac{\partial^2 \hat{\eta}(L, \hat{t})}{\partial \hat{t} \partial \hat{x}} \right) \delta \left( \hat{L}_C \frac{\partial^2 \hat{\eta}(L, \hat{t})}{\partial \hat{t} \partial \hat{x}} \right) \right] d\hat{t} \end{aligned}$$

Evaluating each sub-term of the above resultant equation:

### Sub-term 2.1

$$= \int_{\hat{t}_1}^{\hat{t}_2} \left[ \left( (\hat{M}) \right) \left( \frac{\partial \hat{\eta}(L, \hat{t})}{\partial \hat{t}} \right) \delta \left( \frac{\partial \hat{\eta}(L, \hat{t})}{\partial \hat{t}} \right) \right] d\hat{t}$$

Integrating by parts:  $\int u dv = uv - \int v du$

$$\begin{aligned} u &= (\hat{M}) \frac{\partial \hat{\eta}(L, \hat{t})}{\partial \hat{t}} \quad dv = \frac{\partial \delta \hat{\eta}(L, \hat{t})}{\partial \hat{t}} \quad du = (\hat{M}) \frac{\partial^2 \hat{\eta}(L, \hat{t})}{\partial \hat{t}^2} \quad v = \delta \hat{\eta}(L, \hat{t}) \\ &= (\hat{M}) \frac{\partial \hat{\eta}(L, \hat{t})}{\partial \hat{t}} \frac{\partial}{\partial \hat{t}} \delta \hat{\eta}(L, \hat{t}) \Big|_{\hat{t}_1}^{\hat{t}_2} - \int_{\hat{t}_1}^{\hat{t}_2} (\hat{M}) \frac{\partial^2 \hat{\eta}(L, \hat{t})}{\partial \hat{t}^2} \delta \hat{\eta}(L, \hat{t}) d\hat{t} \\ &= - \int_{\hat{t}_1}^{\hat{t}_2} (\hat{M}) \frac{\partial^2 \hat{\eta}(L, \hat{t})}{\partial \hat{t}^2} \delta \hat{\eta}(L, \hat{t}) d\hat{t} \quad (F.7) \end{aligned}$$

**Sub-term 2.2**

$$= \int_{\hat{t}_1}^{\hat{t}_2} \left[ \left( (\hat{M}) \right) \left( \frac{\partial \hat{\eta}(L, \hat{t})}{\partial \hat{t}} \right) \delta \left( \hat{L}_C \left( \frac{\partial^2 \hat{\eta}(L, \hat{t})}{\partial \hat{t} \partial \hat{x}} \right) \right) \right] d\hat{t}$$

Integrating by parts:  $\int u dv = uv - \int v du$

$$\begin{aligned} u &= \left( (\hat{M}) \right) \left( \frac{\partial \hat{\eta}(L, \hat{t})}{\partial \hat{t}} \right) & dv &= \delta \left( \hat{L}_C \left( \frac{\partial^2 \hat{\eta}(L, \hat{t})}{\partial \hat{t} \partial \hat{x}} \right) \right) & du &= \left( (\hat{M}) \right) \left( \frac{\partial^2 \hat{\eta}(L, \hat{t})}{\partial \hat{t}^2} \right) \\ v &= \hat{L}_C \left( \frac{\partial \delta \hat{\eta}(L, \hat{t})}{\partial \hat{x}} \right) \\ &= \left( (\hat{M}) \right) \left( \frac{\partial \hat{\eta}(L, \hat{t})}{\partial \hat{t}} \right) \hat{L}_C \left( \frac{\partial}{\partial \hat{x}} \right) \delta \hat{\eta}(L, \hat{t}) \Big|_{\hat{t}_1}^{\hat{t}_2} - \int_{\hat{t}_1}^{\hat{t}_2} \left( (\hat{M}) \right) \left( \frac{\partial^2 \hat{\eta}(L, \hat{t})}{\partial \hat{t}^2} \right) \hat{L}_C \left( \frac{\partial \delta \hat{\eta}(L, \hat{t})}{\partial \hat{x}} \right) d\hat{t} \\ &= - \int_{\hat{t}_1}^{\hat{t}_2} \left( (\hat{M}) \right) \left( \frac{\partial^2 \hat{\eta}(L, \hat{t})}{\partial \hat{t}^2} \right) \hat{L}_C \frac{\partial}{\partial \hat{x}} \delta \hat{\eta}(L, \hat{t}) d\hat{t} \end{aligned} \quad (F.8)$$

**Sub-term 2.3**

$$= \int_{\hat{t}_1}^{\hat{t}_2} \left[ \left( (\hat{M}) \right) \left( \hat{L}_C \frac{\partial^2 \hat{\eta}(L, \hat{t})}{\partial \hat{t} \partial \hat{x}} \right) \delta \left( \frac{\partial \hat{\eta}(L, \hat{t})}{\partial \hat{t}} \right) \right] d\hat{t}$$

Integrating by parts:  $\int u dv = uv - \int v du$

$$\begin{aligned} u &= (\hat{M}) \left( \hat{L}_C \left( \frac{\partial^2 \hat{\eta}(L, \hat{t})}{\partial \hat{t} \partial \hat{x}} \right) \right) & dv &= \frac{\partial \delta \hat{\eta}(L, \hat{t})}{\partial \hat{t}} & du &= (\hat{M}) \left( \hat{L}_C \left( \frac{\partial^3 \hat{\eta}(L, \hat{t})}{\partial \hat{t}^2 \partial \hat{x}} \right) \right) \\ v &= \delta \hat{\eta}(L, \hat{t}) \\ &= (\hat{M}) \left( \hat{L}_C \left( \frac{\partial^2 \hat{\eta}(L, \hat{t})}{\partial \hat{t} \partial \hat{x}} \right) \right) \delta \hat{\eta}(L, \hat{t}) \Big|_{\hat{t}_1}^{\hat{t}_2} - \int_{\hat{t}_1}^{\hat{t}_2} (\hat{M}) \left( \hat{L}_C \left( \frac{\partial^3 \hat{\eta}(L, \hat{t})}{\partial \hat{t}^2 \partial \hat{x}} \right) \right) \delta \hat{\eta}(L, \hat{t}) d\hat{t} \\ &= - \int_{\hat{t}_1}^{\hat{t}_2} (\hat{M}) \left( \hat{L}_C \left( \frac{\partial^3 \hat{\eta}(L, \hat{t})}{\partial \hat{t}^2 \partial \hat{x}} \right) \right) \delta \hat{\eta}(L, \hat{t}) d\hat{t} \end{aligned} \quad (F.9)$$

**Sub-term 2.4**

$$= \int_{\hat{t}_1}^{\hat{t}_2} \left[ \left( (\hat{M}) \right) \left( \hat{L}_C^2 \frac{\partial^2 \hat{\eta}(L, \hat{t})}{\partial \hat{t} \partial \hat{x}} \right) \delta \frac{\partial^2 \hat{\eta}(L, \hat{t})}{\partial \hat{t} \partial \hat{x}} \right] d\hat{t}$$

Integrating by parts:  $\int u dv = uv - \int v du$

$$\begin{aligned} u &= \left( (\hat{M}) \right) \left( \hat{L}_C^2 \frac{\partial^2 \hat{\eta}(L, \hat{t})}{\partial \hat{t} \partial \hat{x}} \right) & dv &= \delta \frac{\partial^2 \hat{\eta}(L, \hat{t})}{\partial \hat{t} \partial \hat{x}} & du &= \left( (\hat{M}) \right) \left( \hat{L}_C^2 \frac{\partial^3 \hat{\eta}(L, \hat{t})}{\partial \hat{t}^2 \partial \hat{x}} \right) \\ v &= \delta \frac{\partial \hat{\eta}(L, \hat{t})}{\partial \hat{x}} \\ &= \left( (\hat{M}) \right) \left( \hat{L}_C^2 \frac{\partial^2 \hat{\eta}(L, \hat{t})}{\partial \hat{t} \partial \hat{x}} \right) \frac{\partial}{\partial \hat{x}} \delta \hat{\eta}(L, \hat{t}) \Big|_{\hat{t}_1}^{\hat{t}_2} - \left( (\hat{M}) \right) \left( \hat{L}_C^2 \frac{\partial^3 \hat{\eta}(L, \hat{t})}{\partial \hat{t}^2 \partial \hat{x}} \right) \frac{\partial}{\partial \hat{x}} \delta \hat{\eta}(L, \hat{t}) d\hat{t} \\ &= - \left( (\hat{M}) \right) \left( \hat{L}_C^2 \frac{\partial^3 \hat{\eta}(L, \hat{t})}{\partial \hat{t}^2 \partial \hat{x}} \right) \frac{\partial}{\partial \hat{x}} \delta \hat{\eta}(L, \hat{t}) d\hat{t} \end{aligned} \quad (F.10)$$

**Similarly, Term 3**

$$= \int_{\hat{t}_1}^{\hat{t}_2} \left[ \delta \left( \frac{1}{2} J \left[ \frac{\partial^2 \hat{\eta}(L, \hat{t})}{\partial \hat{t} \partial \hat{x}} \right]^2 \right) \right] d\hat{t}$$

$$= \int_{\hat{t}_1}^{\hat{t}_2} \frac{2}{2} J \left( \frac{\partial^2 \hat{\eta}(L, \hat{t})}{\partial \hat{t} \partial \hat{x}} \right) \delta \left( \frac{\partial^2 \hat{\eta}(L, \hat{t})}{\partial \hat{t} \partial \hat{x}} \right) d\hat{t}$$

Integrating by parts:  $\int u dv = uv - \int v du$

$$\begin{aligned} u &= J \left( \frac{\partial^2 \hat{\eta}(L, \hat{t})}{\partial \hat{t} \partial \hat{x}} \right) \quad dv = \delta \frac{\partial^2 \hat{\eta}(L, \hat{t})}{\partial \hat{t} \partial \hat{x}} \quad du = J \left( \frac{\partial^3 \hat{\eta}(L, \hat{t})}{\partial \hat{t}^2 \partial \hat{x}} \right) \quad v = \delta \frac{\partial \hat{\eta}(L, \hat{t})}{\partial \hat{x}} \\ &= J \left( \frac{\partial^2 \hat{\eta}(L, \hat{t})}{\partial \hat{t} \partial \hat{x}} \right) \frac{\partial}{\partial \hat{x}} \delta \hat{\eta}(L, \hat{t}) \Big|_{\hat{t}_1}^{\hat{t}_2} - \int_{\hat{t}_1}^{\hat{t}_2} J \left( \frac{\partial^3 \hat{\eta}(L, \hat{t})}{\partial \hat{t}^2 \partial \hat{x}} \right) \frac{\partial}{\partial \hat{x}} \delta \hat{\eta}(L, \hat{t}) d\hat{t} \\ &= - \int_{\hat{t}_1}^{\hat{t}_2} J \left( \frac{\partial^3 \hat{\eta}(L, \hat{t})}{\partial \hat{t}^2 \partial \hat{x}} \right) \frac{\partial}{\partial \hat{x}} \delta \hat{\eta}(L, \hat{t}) d\hat{t} \end{aligned} \quad (F.11)$$

#### Term 4

$$\begin{aligned} &= - \int_{\hat{t}_1}^{\hat{t}_2} \delta d\hat{t} \int_0^L \frac{1}{2} EI \left[ \frac{\partial^2 \hat{\eta}(\hat{x}, \hat{t})}{\partial \hat{x}^2} \right]^2 d\hat{x} \\ &= - \int_{\hat{t}_1}^{\hat{t}_2} d\hat{t} \int_0^L \frac{1}{2} EI 2 \frac{\partial^2 \hat{\eta}(\hat{x}, \hat{t})}{\partial \hat{x}^2} \delta \frac{\partial^2 \hat{\eta}(\hat{x}, \hat{t})}{\partial \hat{x}^2} d\hat{x} \\ \therefore \delta \left[ \frac{\partial^2 \hat{\eta}(\hat{x}, \hat{t})}{\partial \hat{x}^2} \right] &= \delta \left[ \frac{\partial}{\partial \hat{x}} \left( \frac{\partial \hat{\eta}(\hat{x}, \hat{t})}{\partial \hat{x}} \right) \right] = \frac{\partial}{\partial \hat{x}} \delta \frac{\partial \hat{\eta}(\hat{x}, \hat{t})}{\partial \hat{x}} \end{aligned}$$

$$= - \int_{\hat{t}_1}^{\hat{t}_2} d\hat{t} \int_0^L EI \frac{\partial^2 \hat{\eta}(\hat{x}, \hat{t})}{\partial \hat{x}^2} \frac{\partial}{\partial \hat{x}} \delta \frac{\partial \hat{\eta}(\hat{x}, \hat{t})}{\partial \hat{x}} d\hat{x}$$

Integration by parts:  $\int u dv = uv - \int v du$

$$\begin{aligned} u &= -EI \frac{\partial^2 \hat{\eta}(\hat{x}, \hat{t})}{\partial \hat{x}^2} \quad du = -EI \frac{\partial}{\partial \hat{x}} \frac{\partial^2 \hat{\eta}(\hat{x}, \hat{t})}{\partial \hat{x}^2} \\ dv &= \frac{\partial}{\partial \hat{x}} \delta \frac{\partial \hat{\eta}(\hat{x}, \hat{t})}{\partial \hat{x}} \quad v = \delta \frac{\partial \hat{\eta}(\hat{x}, \hat{t})}{\partial \hat{x}} \\ &= \int_{\hat{t}_1}^{\hat{t}_2} d\hat{t} \left\{ -EI \frac{\partial^2 \hat{\eta}(\hat{x}, \hat{t})}{\partial \hat{x}^2} \delta \frac{\partial \hat{\eta}(\hat{x}, \hat{t})}{\partial \hat{x}} \Big|_0^L - (-) \int_0^L \frac{\partial}{\partial \hat{x}} \left[ EI \frac{\partial^2 \hat{\eta}(\hat{x}, \hat{t})}{\partial \hat{x}^2} \delta \frac{\partial \hat{\eta}(\hat{x}, \hat{t})}{\partial \hat{x}} \right] d\hat{x} \right\} \\ &= \int_{\hat{t}_1}^{\hat{t}_2} d\hat{t} \left\{ -EI \frac{\partial^2 \hat{\eta}(L, \hat{t})}{\partial \hat{x}^2} \delta \frac{\partial \hat{\eta}(L, \hat{t})}{\partial \hat{x}} - (-) EI \frac{\partial^2 \hat{\eta}(0, \hat{t})}{\partial \hat{x}^2} \delta \frac{\partial \hat{\eta}(0, \hat{t})}{\partial \hat{x}} + \right. \\ &\quad \left. \int_0^L \frac{\partial}{\partial \hat{x}} \left[ EI \frac{\partial^2 \hat{\eta}(\hat{x}, \hat{t})}{\partial \hat{x}^2} \delta \frac{\partial \hat{\eta}(\hat{x}, \hat{t})}{\partial \hat{x}} \right] d\hat{x} \right\} \end{aligned}$$

Where, by geometric boundary condition  $\frac{\partial^2 \hat{\eta}(0, \hat{t})}{\partial \hat{x}^2}$  goes to zero.

$$= \int_{\hat{t}_1}^{\hat{t}_2} d\hat{t} \left\{ -EI \frac{\partial^2 \hat{\eta}(L, \hat{t})}{\partial \hat{x}^2} \delta \frac{\partial \hat{\eta}(L, \hat{t})}{\partial \hat{x}} + \int_0^L \frac{\partial}{\partial \hat{x}} \left[ EI \frac{\partial^2 \hat{\eta}(\hat{x}, \hat{t})}{\partial \hat{x}^2} \delta \frac{\partial \hat{\eta}(\hat{x}, \hat{t})}{\partial \hat{x}} \right] d\hat{x} \right\}$$

The last term above requires further conversion:

Second integration by parts  $\int u dv = uv - \int v du$

$$\begin{aligned} u &= \frac{\partial}{\partial \hat{x}} \left[ EI \frac{\partial^2 \hat{\eta}(\hat{x}, \hat{t})}{\partial \hat{x}^2} \right] \quad du = \frac{\partial^2}{\partial \hat{x}^2} \left[ EI \frac{\partial^2 \hat{\eta}(\hat{x}, \hat{t})}{\partial \hat{x}^2} \right] \\ dv &= \frac{\partial \delta \hat{\eta}(\hat{x}, \hat{t})}{\partial \hat{x}} \quad v = \delta \hat{\eta}(\hat{x}, \hat{t}) \end{aligned}$$

$$\begin{aligned}
 &= \int_{\hat{t}_1}^{\hat{t}_2} d\hat{t} \left\{ -EI \frac{\partial^2 \hat{\eta}(L, \hat{t})}{\partial \hat{x}^2} \delta \frac{\partial \hat{\eta}(L, \hat{t})}{\partial \hat{x}} + \frac{\partial}{\partial \hat{x}} \left[ EI \frac{\partial^2 \hat{\eta}(\hat{x}, \hat{t})}{\partial \hat{x}^2} \right] \delta \hat{\eta}(\hat{x}, \hat{t}) \right|_0^L - \\
 &\int_0^L \frac{\partial^2}{\partial \hat{x}^2} \left[ EI \frac{\partial^2 \hat{\eta}(\hat{x}, \hat{t})}{\partial \hat{x}^2} \delta \hat{\eta}(\hat{x}, \hat{t}) \right] d\hat{x} \Big\} \\
 &= \int_{\hat{t}_1}^{\hat{t}_2} d\hat{t} \left\{ -EI \frac{\partial^2 \hat{\eta}(L, \hat{t})}{\partial \hat{x}^2} \delta \frac{\partial \hat{\eta}(L, \hat{t})}{\partial \hat{x}} + \frac{\partial}{\partial \hat{x}} \left[ EI \frac{\partial^2 \hat{\eta}(L, \hat{t})}{\partial \hat{x}^2} \right] \delta \hat{\eta}(L, \hat{t}) - \frac{\partial}{\partial \hat{x}} \left[ EI \frac{\partial^2 \hat{\eta}(0, \hat{t})}{\partial \hat{x}^2} \right] \delta \hat{\eta}(0, \hat{t}) - \right. \\
 &\left. \int_0^L \frac{\partial^2}{\partial \hat{x}^2} \left[ EI \frac{\partial^2 \hat{\eta}(\hat{x}, \hat{t})}{\partial \hat{x}^2} \delta \hat{\eta}(\hat{x}, \hat{t}) \right] d\hat{x} \right\}
 \end{aligned}$$

Where,  $\delta \hat{\eta}(0, \hat{t})$  goes to zero due to geometric boundary condition. Therefore, term 4 becomes

$$\begin{aligned}
 &= \int_{\hat{t}_1}^{\hat{t}_2} d\hat{t} \left\{ -EI \frac{\partial^2 \hat{\eta}(L, \hat{t})}{\partial \hat{x}^2} \delta \frac{\partial \hat{\eta}(L, \hat{t})}{\partial \hat{x}} + \frac{\partial}{\partial \hat{x}} \left[ EI \frac{\partial^2 \hat{\eta}(L, \hat{t})}{\partial \hat{x}^2} \right] \delta \hat{\eta}(L, \hat{t}) - \right. \\
 &\left. \int_0^L \frac{\partial^2}{\partial \hat{x}^2} \left[ EI \frac{\partial^2 \hat{\eta}(\hat{x}, \hat{t})}{\partial \hat{x}^2} \right] \delta \hat{\eta}(\hat{x}, \hat{t}) d\hat{x} \right\} \quad (F.12)
 \end{aligned}$$

### Term 5

$$= - \int_{\hat{t}_1}^{\hat{t}_2} \left[ \delta \left( \frac{1}{2} \varepsilon \mathcal{F} b (V_{DC} + V_{AC}(\hat{t}))^2 \left[ \frac{1}{\frac{\partial \hat{\eta}(L, \hat{t})}{\partial \hat{x}}} \left( \ln \left( \frac{d - \hat{\eta}(L, \hat{t}) - \frac{\partial \hat{\eta}(L, \hat{t})}{\partial \hat{x}} 2 \hat{L}_C}{d - \hat{\eta}(L, \hat{t})} \right) \right) \right] \right) \right] d\hat{t}$$

Evaluating term 5 with respect to space

First note:  $(X.Y)' = X'Y + Y'X$

$$[\ln(u)]' = \frac{1}{u} u'$$

Thus,

$$\begin{aligned}
 &= - \int_{\hat{t}_1}^{\hat{t}_2} \frac{1}{2} \varepsilon \mathcal{F} b (V_{DC} + V_{AC}(\hat{t}))^2 \left\{ - \frac{\frac{\partial^2 \hat{\eta}(L, \hat{t})}{\partial \hat{x}^2}}{\left[ \frac{\partial \hat{\eta}(L, \hat{t})}{\partial \hat{x}} \right]^2} \ln \left( \frac{d - \hat{\eta}(L, \hat{t}) - \frac{\partial \hat{\eta}(L, \hat{t})}{\partial \hat{x}} 2 \hat{L}_C}{d - \hat{\eta}(L, \hat{t})} \right) + \right. \\
 &\left. \frac{1}{\frac{\partial \hat{\eta}(L, \hat{t})}{\partial \hat{x}}} \left[ \frac{d - \hat{\eta}(L, \hat{t})}{d - \hat{\eta}(L, \hat{t}) - \frac{\partial \hat{\eta}(L, \hat{t})}{\partial \hat{x}} 2 \hat{L}_C} - \frac{\frac{\partial^2 \hat{\eta}(L, \hat{t})}{\partial \hat{x}^2} 2 \hat{L}_C (d - \hat{\eta}(L, \hat{t}))}{(d - \hat{\eta}(L, \hat{t}))^2} \right] \right\} d\hat{t} \\
 &= \int_{\hat{t}_1}^{\hat{t}_2} \frac{1}{2} \varepsilon \mathcal{F} b (V_{DC} + V_{AC}(\hat{t}))^2 \left\{ \frac{\frac{\partial^2 \hat{\eta}(L, \hat{t})}{\partial \hat{x}^2}}{\left[ \frac{\partial \hat{\eta}(L, \hat{t})}{\partial \hat{x}} \right]^2} \ln \left( \frac{d - \hat{\eta}(L, \hat{t}) - \frac{\partial \hat{\eta}(L, \hat{t})}{\partial \hat{x}} 2 \hat{L}_C}{d - \hat{\eta}(L, \hat{t})} \right) + \right. \\
 &\left. \frac{1}{\frac{\partial \hat{\eta}(L, \hat{t})}{\partial \hat{x}}} \frac{\frac{\partial \hat{\eta}(L, \hat{t})}{\partial \hat{x}}}{\frac{\partial \hat{\eta}(L, \hat{t})}{\partial \hat{x}}} \left[ \frac{\frac{\partial^2 \hat{\eta}(L, \hat{t})}{\partial \hat{x}^2} 2 \hat{L}_C}{d - \hat{\eta}(L, \hat{t}) - \frac{\partial \hat{\eta}(L, \hat{t})}{\partial \hat{x}} 2 \hat{L}_C} \right] \right\} d\hat{t}
 \end{aligned}$$

Taking  $\frac{\partial^2 \hat{\eta}(L, \hat{t})}{\partial \hat{x}^2} = \delta \frac{\partial \hat{\eta}(L, \hat{t})}{\partial \hat{x}}$  as a common factor. Thus,



$$= \int_{\hat{t}_1}^{\hat{t}_2} \frac{1}{2} \varepsilon \mathcal{F} b (V_{DC} + V_{AC}(\hat{t}))^2 \left\{ \frac{1}{\left[ \frac{\partial \hat{\eta}(L, \hat{t})}{\partial \hat{x}} \right]^2} \ln \left( \frac{d - \hat{\eta}(L, \hat{t}) - \frac{\partial \hat{\eta}(L, \hat{t})}{\partial \hat{x}} 2 \hat{L}_C}{d - \hat{\eta}(L, \hat{t})} \right) + \frac{\frac{\partial \hat{\eta}(L, \hat{t})}{\partial \hat{x}}}{\left[ \frac{\partial \hat{\eta}(L, \hat{t})}{\partial \hat{x}} \right]^2} \left[ \frac{2 \hat{L}_C}{d - \hat{\eta}(L, \hat{t}) - \frac{\partial \hat{\eta}(L, \hat{t})}{\partial \hat{x}} 2 \hat{L}_C} \right] \right\} \frac{\partial}{\partial \hat{x}} \delta \hat{\eta}(L, \hat{t}) d\hat{t} \quad (F.13)$$

Now, re-evaluating term 5 with respect to time

$$\begin{aligned} \text{Note: } \delta(\ln(u)) &= \frac{1}{u} \delta u = \frac{1}{u} \dot{u} \\ &= - \int_{\hat{t}_1}^{\hat{t}_2} \left[ \delta \frac{1}{2} \varepsilon \mathcal{F} b (V_{DC} + V_{AC}(\hat{t}))^2 \left\{ \frac{1}{\frac{\partial \hat{\eta}(L, \hat{t})}{\partial \hat{x}}} \left( \ln \left( d - \hat{\eta}(L, \hat{t}) - \frac{\partial \hat{\eta}(L, \hat{t})}{\partial \hat{x}} 2 \hat{L}_C \right) - \ln(d - \hat{\eta}(L, \hat{t})) \right) \right\} \right] d\hat{t} \\ &= - \int_{\hat{t}_1}^{\hat{t}_2} \left[ \frac{1}{2} \varepsilon \mathcal{F} b (V_{DC} + V_{AC}(\hat{t}))^2 \left\{ \frac{1}{\frac{\partial \hat{\eta}(L, \hat{t})}{\partial \hat{x}}} \left( \frac{-\delta \hat{\eta}(L, \hat{t})}{d - \hat{\eta}(L, \hat{t}) - \frac{\partial \hat{\eta}(L, \hat{t})}{\partial \hat{x}} 2 \hat{L}_C} \right) - \frac{-\delta \hat{\eta}(L, \hat{t})}{(d - \hat{\eta}(L, \hat{t}))} \frac{1}{\frac{\partial \hat{\eta}(L, \hat{t})}{\partial \hat{x}}} \right\} \right] d\hat{t} \\ &= \int_{\hat{t}_1}^{\hat{t}_2} \left[ \frac{1}{2} \varepsilon \mathcal{F} b (V_{DC} + V_{AC}(\hat{t}))^2 \left\{ \frac{1}{\frac{\partial \hat{\eta}(L, \hat{t})}{\partial \hat{x}}} \left( \frac{1}{d - \hat{\eta}(L, \hat{t}) - \frac{\partial \hat{\eta}(L, \hat{t})}{\partial \hat{x}} 2 \hat{L}_C} \right) - \frac{1}{(d - \hat{\eta}(L, \hat{t})) \frac{\partial \hat{\eta}(L, \hat{t})}{\partial \hat{x}}} \right\} \right] (\delta \hat{\eta}(L, \hat{t})) d\hat{t} \end{aligned} \quad (F.14)$$

### **Term 6**

$$= \int_{t_1}^{t_2} (\hat{M}) g \delta \hat{\eta}(\hat{L}_C, \hat{t}) d\hat{t} \quad (F.15)$$

### **Term 7**

$$= - \int_{t_1}^{t_2} \delta \hat{C}_{eff} \frac{\partial \hat{\eta}(\hat{x}, \hat{t})}{\partial \hat{t}} d\hat{t} = - \int_{t_1}^{t_2} \hat{C}_{eff} \frac{\partial \delta \hat{\eta}(\hat{x}, \hat{t})}{\partial \hat{t}} d\hat{t} \quad (F.16)$$

Terms 6 and 7 don't require any further evaluation. By collecting alike terms (i.e.  $\delta \hat{\eta}(\hat{x}, \hat{t})$ ,  $\delta \hat{\eta}(L, \hat{t})$ ,  $\frac{\partial}{\partial \hat{x}} \delta \hat{\eta}(L, \hat{t})$ ) from resultant equations F.6-F.16, the nonlinear governing partial differential equation of flexural motion, Eq. (F.17), and its associated natural (force-dynamic) boundary conditions, Eq. (F.18), and Eq. (F.19), are derived. Eq. (F.20) and Eq. (F.21) are geometric boundary conditions for a clamped (fixed) end that respectively resemble displacement and slope. The first term to the left of Eq. (F.19) represents shear force within the beam, while the first term to the left of Eq. (F.18) denotes the bending moment in the beam:

### The equation of motion (aggregating $\partial\hat{\eta}(\hat{x},\hat{t})$ terms)

$$\begin{aligned}
 -\rho A_{beam} \frac{\partial^2 \hat{\eta}(\hat{x},\hat{t})}{\partial \hat{t}^2} - EI \frac{\partial^4 \hat{\eta}(\hat{x},\hat{t})}{\partial \hat{x}^4} - \hat{C}_{eff} \frac{\partial \hat{\eta}(\hat{x},\hat{t})}{\partial \hat{t}} &= 0 \\
 \rho A_{beam} \frac{\partial^2 \hat{\eta}(\hat{x},\hat{t})}{\partial \hat{t}^2} + EI \frac{\partial^4 \hat{\eta}(\hat{x},\hat{t})}{\partial \hat{x}^4} + \hat{C}_{eff} \frac{\partial \hat{\eta}(\hat{x},\hat{t})}{\partial \hat{t}} &= 0
 \end{aligned} \tag{F.17}$$

The first natural boundary condition is obtained by aggregating  $\frac{\partial}{\partial \hat{x}} \delta \hat{\eta}(L, \hat{t})$  term

$$EI \left[ \frac{\partial^2 \hat{\eta}(L, \hat{t})}{\partial \hat{x}^2} \right] = -\hat{L}_C (\hat{M}) \left[ \frac{\partial^2 \hat{\eta}(L, \hat{t})}{\partial \hat{t}^2} \right] - (\hat{M} \hat{L}_C^2 + J) \left[ \frac{\partial^3 \hat{\eta}(L, \hat{t})}{\partial \hat{t}^2 \partial \hat{x}} \right] + \frac{\varepsilon b_{plate} \mathcal{F}(V_{DC} + V_{AC}(\hat{t}))^2}{2 \left( \frac{\partial \hat{\eta}(L, \hat{t})}{\partial \hat{x}} \right)^2} \left\{ \ln \left( \frac{d - \hat{\eta}(L, \hat{t}) - \frac{\partial \hat{\eta}(L, \hat{t})}{\partial \hat{x}} 2 \hat{L}_C}{d - \hat{\eta}(L, \hat{t})} \right) + \frac{\frac{\partial \hat{\eta}(L, \hat{t})}{\partial \hat{x}} 2 \hat{L}_C}{d - \hat{\eta}(L, \hat{t}) - \frac{\partial \hat{\eta}(L, \hat{t})}{\partial \hat{x}} 2 \hat{L}_C} \right\} \tag{F.18}$$

The second natural boundary condition is obtained by aggregating  $\delta \hat{\eta}(L, \hat{t})$  term

$$EI \left[ \frac{\partial^3 \hat{\eta}(L, \hat{t})}{\partial \hat{x}^3} \right] = (\hat{M}) \left[ \frac{\partial^2 \hat{\eta}(L, \hat{t})}{\partial \hat{t}^2} \right] + (\hat{L}_C (\hat{M})) \left[ \frac{\partial^3 \hat{\eta}(L, \hat{t})}{\partial \hat{t}^2 \partial \hat{x}} \right] - \frac{\varepsilon b_{plate} \mathcal{F}(V_{DC} + V_{AC}(\hat{t}))^2}{2 \frac{\partial \hat{\eta}(L, \hat{t})}{\partial \hat{x}}} \left\{ \frac{1}{d - \hat{\eta}(L, \hat{t}) - \frac{\partial \hat{\eta}(L, \hat{t})}{\partial \hat{x}} 2 \hat{L}_C} - \frac{1}{d - \hat{\eta}(L, \hat{t})} \right\} + (\hat{M})g \tag{F.19}$$

### The associated geometric boundary conditions are:

$$\hat{\eta}(0, \hat{t}) = 0 \tag{F.20}$$

$$\frac{\partial \hat{\eta}(0, \hat{t})}{\partial \hat{t}} = 0 \tag{F.21}$$

By dropping the fringing field factor, and eliminating the influence of potential energy of the gravitational force, the dynamics of the system reduces to the obtained results by Nayfeh *et al.* [198].

## F.3 Static Mode Analysis: Pull-In Phenomenon

The governing partial differential equation of motion, and its associated natural and geometric boundary conditions are normalized as in [198]. This is performed for simplicity in evaluation, and also to balance force and damping terms with nonlinear ones. Furthermore, normalization enables a better understanding of the parameters' effects on the overall biosensor dynamical system, and on each other. Therefore, by inducing the following non-dimensional variables:

$$t = \frac{\hat{t}}{T}, \quad T = \sqrt{\frac{\rho A L^4}{EI}}, \quad C_{eff} = \frac{\hat{C}_{eff}}{EI T}, \quad \eta = \frac{\hat{\eta}}{d}, \quad M = \frac{\hat{M}}{\rho A L}, \quad L_C = \frac{\hat{L}_C}{L}, \quad x = \frac{\hat{x}}{L}, \quad \text{and } x \in [0, 1].$$

Therefore, the normalized form of Eqs. (F.17-21) are:

$$\begin{aligned}
 \rho A_{beam} \frac{\partial^2 \hat{\eta}(\hat{x}, \hat{t})}{\partial \hat{t}^2} + EI \frac{\partial^4 \hat{\eta}(\hat{x}, \hat{t})}{\partial \hat{x}^4} + \hat{C}_{eff} \frac{\partial \hat{\eta}(\hat{x}, \hat{t})}{\partial \hat{t}} &= 0 \\
 \rho A_{beam} \frac{d}{dt} \frac{\partial^2 \eta(x, t)}{\partial t^2 \frac{\rho AL^4}{EI}} + EI \frac{d}{L^4} \frac{\partial^4 \eta(x, t)}{\partial x^4} + \frac{C_{eff} EI \sqrt{\frac{\rho AL^4}{EI}}}{L^4} \frac{\partial \eta(x, t)}{\partial t \sqrt{\frac{\rho AL^4}{EI}}} &= 0 \\
 \frac{\partial^2 \eta(x, t)}{\partial t^2} + \frac{\partial^4 \eta(x, t)}{\partial x^4} + C_{eff} \frac{\partial \eta(x, t)}{\partial t} &= 0
 \end{aligned} \tag{F.22}$$

Similarly for the natural and geometric boundary conditions:

$$\begin{aligned}
 EI \left[ \frac{\partial^2 \hat{\eta}(L, \hat{t})}{\partial \hat{x}^2} \right] &= -\hat{L}_C (\hat{M}) \left[ \frac{\partial^2 \hat{\eta}(L, \hat{t})}{\partial \hat{t}^2} \right] - \left( \hat{M} \hat{L}_C^2 + \frac{1}{3} \hat{M} \hat{L}_C^2 \right) \left[ \frac{\partial^3 \hat{\eta}(L, \hat{t})}{\partial \hat{t}^2 \partial \hat{x}} \right] + \\
 &\quad \frac{\varepsilon F b (V_{DC} + V_{AC}(\hat{t}))^2}{2 \left( \frac{\partial \hat{\eta}(L, \hat{t})}{\partial \hat{x}} \right)^2} \left\{ \ln \left( \frac{d - \hat{\eta}(L, \hat{t}) - \frac{\partial \hat{\eta}(L, \hat{t})}{\partial \hat{x}} 2 \hat{L}_C}{d - \hat{\eta}(L, \hat{t})} \right) + \frac{\frac{\partial \hat{\eta}(L, \hat{t})}{\partial \hat{x}} 2 \hat{L}_C}{d - \hat{\eta}(L, \hat{t}) - \frac{\partial \hat{\eta}(L, \hat{t})}{\partial \hat{x}} 2 \hat{L}_C} \right\} \\
 EI \left[ \frac{\partial^2 \eta d(1, t)}{\partial x^2 L^2} \right] &= -LL_C (M \rho AL) \left[ \frac{\partial^2 \eta d(1, t)}{\partial t^2 \frac{\rho AL^4}{EI}} \right] - \left( \frac{4}{3} M \rho AL^3 L_C^2 \right) \left[ \frac{\partial^3 \eta d(1, t)}{\partial t^2 \frac{\rho AL^4}{EI} \partial x L} \right] + \\
 &\quad \frac{\varepsilon F b (V_{DC} + V_{AC}(t))^2}{2 \left( \frac{\partial \eta d(1, t)}{\partial x L} \right)^2} \left\{ \ln \left( \frac{d - \eta d(1, t) - \frac{\partial \eta d(1, t)}{\partial x L} 2 L_C L}{d - \eta d(1, t)} \right) + \frac{\frac{\partial \eta d(1, t)}{\partial x L} 2 L_C L}{d - \eta d(1, t) - \frac{\partial \eta d(1, t)}{\partial x L} 2 L_C L} \right\} \\
 \left[ \frac{\partial^2 \eta(1, t)}{\partial x^2} \right] &= -L_C (M) \left[ \frac{\partial^2 \eta(1, t)}{\partial t^2} \right] - \left( \frac{4}{3} M L_C^2 \right) \left[ \frac{\partial^3 \eta(1, t)}{\partial t^2 \partial x} \right] + \\
 &\quad \frac{L^4 \varepsilon F b (V_{DC} + V_{AC}(t))^2}{2 EI d^3 \left( \frac{\partial \eta(1, t)}{\partial x} \right)^2} \left\{ \ln \left( \frac{1 - \eta(1, t) - \frac{\partial \eta(1, t)}{\partial x} 2 L_C}{1 - \eta(1, t)} \right) + \frac{\frac{\partial \eta(1, t)}{\partial x} 2 L_C}{1 - \eta(1, t) - \frac{\partial \eta(1, t)}{\partial x} 2 L_C} \right\}
 \end{aligned} \tag{F.23}$$

As for the normalized second natural boundary condition,

$$\begin{aligned}
 EI \left[ \frac{\partial^3 \hat{\eta}(L, \hat{t})}{\partial \hat{x}^3} \right] &= (\hat{M}) \left[ \frac{\partial^2 \hat{\eta}(L, \hat{t})}{\partial \hat{t}^2} \right] + \left( \hat{L}_C (\hat{M}) \right) \left[ \frac{\partial^3 \hat{\eta}(L, \hat{t})}{\partial \hat{t}^2 \partial \hat{x}} \right] - \\
 &\quad \frac{\varepsilon F b (V_{DC} + V_{AC}(\hat{t}))^2}{2 \frac{\partial \hat{\eta}(L, \hat{t})}{\partial \hat{x}}} \left\{ \frac{1}{d - \hat{\eta}(L, \hat{t}) - \frac{\partial \hat{\eta}(L, \hat{t})}{\partial \hat{x}} 2 \hat{L}_C} - \frac{1}{d - \hat{\eta}(L, \hat{t})} \right\} + (\hat{M}) g \\
 EI \left[ \frac{\partial^3 \eta d(1, t)}{\partial x^3 L^3} \right] &= (M \rho AL) \left[ \frac{\partial^2 \eta d(1, t)}{\partial t^2 \frac{\rho AL^4}{EI}} \right] + (LL_C (M \rho AL)) \left[ \frac{\partial^3 \eta d(1, t)}{\partial t^2 \frac{\rho AL^4}{EI} \partial x L} \right] - \\
 &\quad \frac{\varepsilon F b (V_{DC} + V_{AC}(t))^2}{2 \frac{\partial \eta d(1, t)}{\partial x L}} \left\{ \frac{1}{d - \eta d(1, t) - \frac{\partial \eta d(1, t)}{\partial x L} 2 L_C L} - \frac{1}{d - \eta d(1, t)} \right\} + (M \rho AL) g \\
 \left[ \frac{\partial^3 \eta(1, t)}{\partial x^3} \right] &= (M) \left[ \frac{\partial^2 \eta(1, t)}{\partial t^2} \right] + \left( L_C \left( M + m \frac{L_C}{L} \right) \right) \left[ \frac{\partial^3 \eta(1, t)}{\partial t^2 \partial x} \right] - \\
 &\quad \frac{L^4 \varepsilon F b (V_{DC} + V_{AC}(t))^2}{2 EI d^3 \frac{\partial \eta(1, t)}{\partial x}} \left\{ \frac{1}{1 - \eta(1, t) - \frac{\partial \eta(1, t)}{\partial x} 2 L_C} - \frac{1}{1 - \eta(1, t)} \right\} + \frac{L^3}{EI d} (M \rho AL) g
 \end{aligned} \tag{F.24}$$

Finally, the normalized geometric boundary conditions are:

$$\eta(0, t) = 0 \tag{F.25}$$

$$\frac{\partial \eta(0,t)}{\partial t} = 0 \quad (\text{F.26})$$

The steady-state mode of the system, where the beam-triangle deflection is constant in time, can be found by setting the time and AC voltage terms to zero in Eqs. (F.22-26); this leads to the static response of the system.

$$\frac{\partial^4 \eta(x)}{\partial x^4} = 0 \quad (\text{F.27})$$

$$\left[ \frac{\partial^2 \eta(1)}{\partial x^2} \right] = \frac{L^4 \epsilon F b (V_{DC})^2}{2 E I d^3 \left( \frac{\partial \eta(1)}{\partial x} \right)^2} \left\{ \ln \left( \frac{1 - \eta(1) - \frac{\partial \eta(1)}{\partial x} 2 L_C}{1 - \eta(1)} \right) + \frac{\frac{\partial \eta(1)}{\partial x} 2 L_C}{1 - \eta(1) - \frac{\partial \eta(1)}{\partial x} 2 L_C} \right\} \quad (\text{F.28})$$

$$\left[ \frac{\partial^3 \eta(1)}{\partial x^3} \right] = - \frac{L^4 \epsilon F b (V_{DC})^2}{2 E I d^3 \frac{\partial \eta(1)}{\partial x}} \left\{ \frac{1}{1 - \eta(1) - \frac{\partial \eta(1)}{\partial x} 2 L_C} - \frac{1}{1 - \eta(1)} \right\} + \frac{L^3}{E I d} (M \rho A L) g \quad (\text{F.29})$$

$$\eta_{Static}(0) = \eta'_S(0) = 0 \quad (\text{F.30})$$

Thus, the general solution of the resultant normalized static equation of motion is obtained by integrating equation (F.27) four times.

$$\eta_S(x) = A x^3 + B x^2 + C x + D$$

By evaluating the general solution by imposing the geometric boundary conditions, which yields  $C = D = 0$ . The remaining two unknown coefficients, A and B, can be evaluated by applying the natural boundary conditions, which results in two nonlinear algebraic equations, Eq. F.31, and Eq. F.32:

$$f_1(V_{DC}, A, B) = \frac{L^4 \epsilon F b}{2 E I d^3} \frac{(V_{DC})^2}{(3A+2B)^2} \left\{ \ln \left( \frac{1-A-B-(3A+2B)2L_C}{1-A-B} \right) + \frac{(3A+2B)2L_C}{1-A-B-(3A+2B)2L_C} \right\} - (6A + 2B) = 0 \quad (\text{F.31})$$

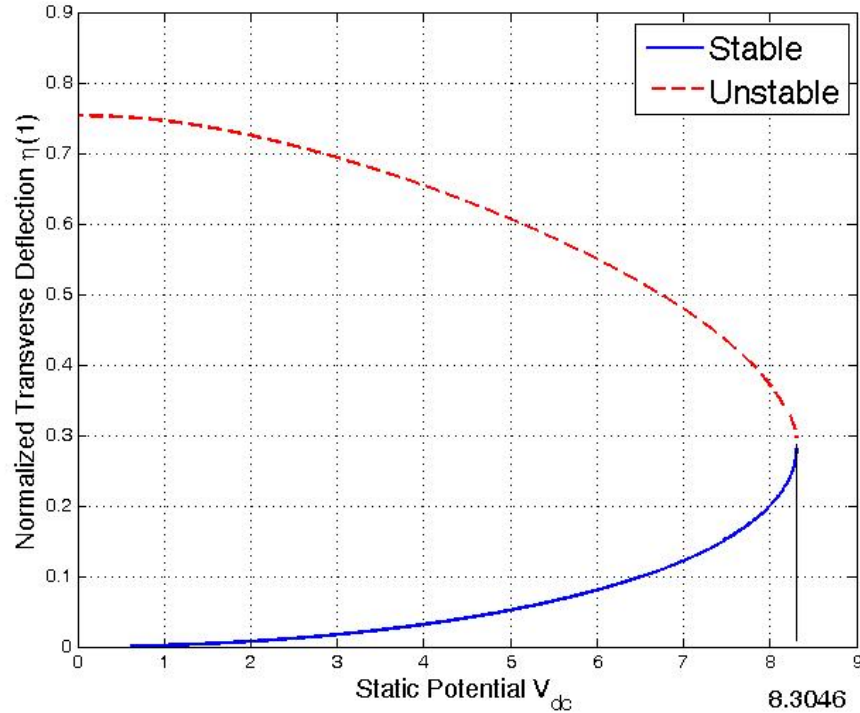
$$f_2(V_{DC}, A, B, M) = -6A - \frac{\epsilon F b L^4}{2 E I d^3} \frac{(V_{DC})^2}{3A+2B} \left\{ \frac{1}{1-A-B-(3A+2B)2L_C} - \frac{1}{1-A-B} \right\} + \frac{L^3}{E I d} (M \rho A L) g = 0 \quad (\text{F.32})$$

In static mode, two different solutions for A and B can be obtained for each applied (bias) DC potential, representing different static deflections (equilibrium configurations). The evaluation of A and B are based on the parameters of table F.1.

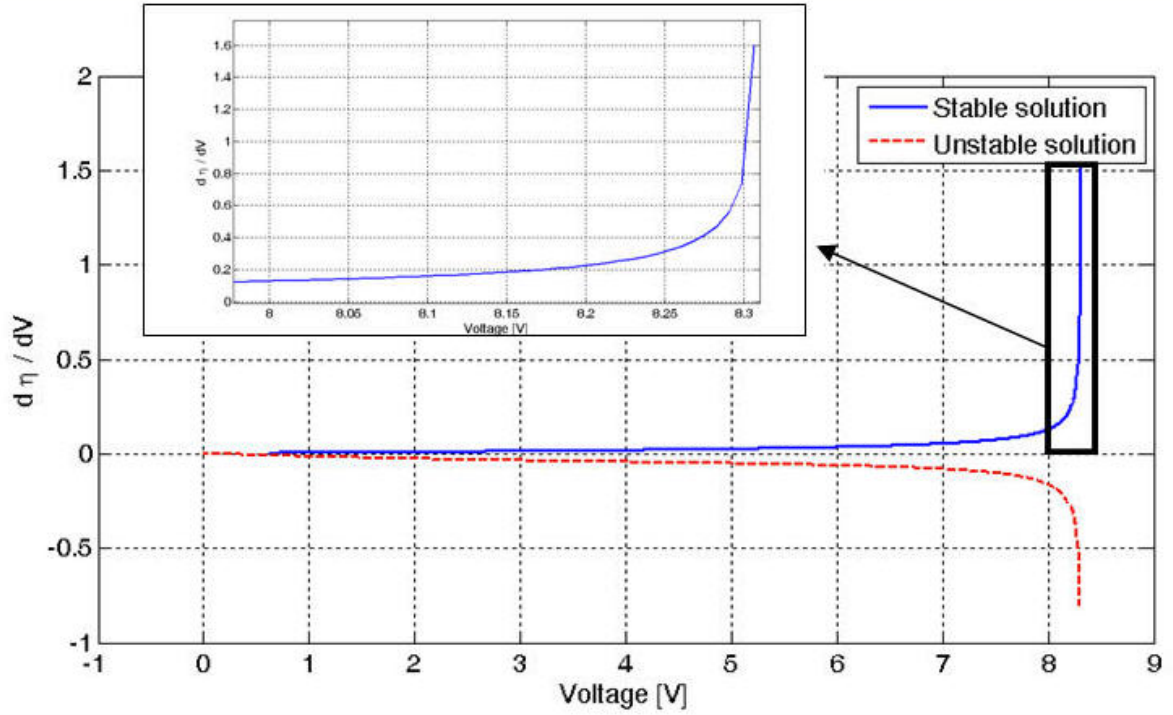
Variable	Value	Variable	Value
$b_{beam}$	5 $\mu\text{m}$	$E$	$1.6 \times 10^{11}$ Pa
$h$	1.5 $\mu\text{m}$	$\varepsilon$	$8.854 \times 10^{-12}$ F/m
$d$	4 $\mu\text{m}$	$A_{beam}$	$7.5 \times 10^{-12}$ $\text{m}^2$
$L$	250 $\mu\text{m}$	$I$	$1.40625 \times 10^{-24}$ $\text{m}^4$
$L_{paddle}$	50 $\mu\text{m}$	$\hat{L}_c$	25 $\mu\text{m}$
$b_{paddle}$	20 $\mu\text{m}$	$\hat{M}$	$3.45 \times 10^{-12}$ Kg
$\rho$	2300 $\text{kg/m}^3$	$J$	$7.1875 \times 10^{-22}$ $\text{Kg} \cdot \text{m}^2$

**Table F.1** Microcantilever design parameters.

One pair of values (low A and B), represents a stable solution, whereas the other corresponds to unstable one. This is illustrated in Figure F.4A, where the stable solid line represents the stable branch and the dotted line is the unstable one. Both branches converge into each other at a value of the voltage corresponding to the pull-in potential,  $V_p$ . For this particular cantilever-plate system, with design parameters values as exhibited in table F.1, the static pull-in voltage has a value of 8.3046V. Moreover, as manifested in Figure F.4B, the derivative of the transverse deflection with respect to induced static potential also confirms that at a very low potential, the slope of the MEMS system is zero, and as it approaches the pull-in phenomenon the slope is approaching infinity resembling instability of the system.



(A)



(B)

**Fig. F.4** (A) Normalized transverse deflection with respect to induced DC potential  $V_{DC}$  in Volt, (B) Derivative of normalized transverse deflection with respect to induced static potential in Volt.

## F.4 Sensitivity analysis

This section aims to define the sensitivity of the biosensor as the variation in transversal deflection in response to a small voltage superimposed to a given DC induced voltage – considering that the sensitivity is important to maximize the response of the cantilever-based biosensor to small variations in electrostatic force, whilst still preventing the risk of pull in.

The analytical expression for the system's sensitivity can be obtained after evaluating the partial derivatives of Equations (F.31) and (F.32) with respect to their four variables,  $A$ ,  $B$ ,  $V_{DC}$ , and  $M$ :

$$\frac{\partial f_1}{\partial V} |_{V_o, A_o, B_o, M_o} \delta V + \frac{\partial f_1}{\partial A} |_{V_o, A_o, B_o, M_o} \delta A + \frac{\partial f_1}{\partial B} |_{V_o, A_o, B_o, M_o} \delta B + \frac{\partial f_1}{\partial M} |_{V_o, A_o, B_o, M_o} \delta M = 0 \quad (\text{F.33})$$

$$\frac{\partial f_2}{\partial V} |_{V_o, A_o, B_o, M_o} \delta V + \frac{\partial f_2}{\partial A} |_{V_o, A_o, B_o, M_o} \delta A + \frac{\partial f_2}{\partial B} |_{V_o, A_o, B_o, M_o} \delta B + \frac{\partial f_2}{\partial M} |_{V_o, A_o, B_o, M_o} \delta M = 0 \quad (\text{F.34})$$

In equations (F.33) and (F.34),  $V_o$  is chosen to be the targeted DC potential within the vicinity of pull-in voltage that yields a stable solution of  $A_o$ , and  $B_o$ .  $M_o$  is a known parameter of paddle's mass. Equations (F.33) and (F.34) can be also expressed in a matrix form as:

$$\begin{bmatrix} \frac{\partial f_1}{\partial A} & \frac{\partial f_1}{\partial B} \\ \frac{\partial f_2}{\partial A} & \frac{\partial f_2}{\partial B} \end{bmatrix} \begin{bmatrix} \delta A \\ \delta B \end{bmatrix} = - \begin{bmatrix} \frac{\partial f_1}{\partial V} \\ \frac{\partial f_2}{\partial V} \end{bmatrix} \delta V - \begin{bmatrix} \frac{\partial f_1}{\partial M} \\ \frac{\partial f_2}{\partial M} \end{bmatrix} \delta M \quad (\text{F.35})$$

Where,

$$\delta A = C_{11} \delta V + C_{12} \delta M \quad (\text{F36.a})$$

$$\delta B = C_{21} \delta V + C_{22} \delta M \quad (\text{F36.b})$$

and  $C_{ij}$  ( $i=[1,2], j=[1,2]$ ) are constant terms. Also, since mass is a constant parameter, the mass terms drop in Eqs. (F36.a-b), and the transverse displacement can be defined in terms of the static potential only, resulting in:

$$\delta \eta(x) = \delta A x^3 + \delta B x^2 = \delta V (C_{11} x^3 + C_{21} x^2) \quad (\text{F.37})$$

Hence the sensitivity expression is given by:

$$\text{Sensitivity} \left( \frac{\text{meter}}{\text{volt}} \right) = \frac{\delta \hat{\eta}}{\delta V} = (C_{11} x^3 + C_{21} x^2) d \quad (\text{F.38})$$

Where, "x" represents a point along the x axis of the microcantilever-microplate structure. A representation of the sensitivity versus the induced DC voltage at the tip of the paddle for the design parameters illustrated in Table F.1, can be found in Figure F.5, and as expected maximum occurs at the tip or the paddle. In this figure, the sensitivity dramatically increases as the DC voltage approaches the pull-in potential.

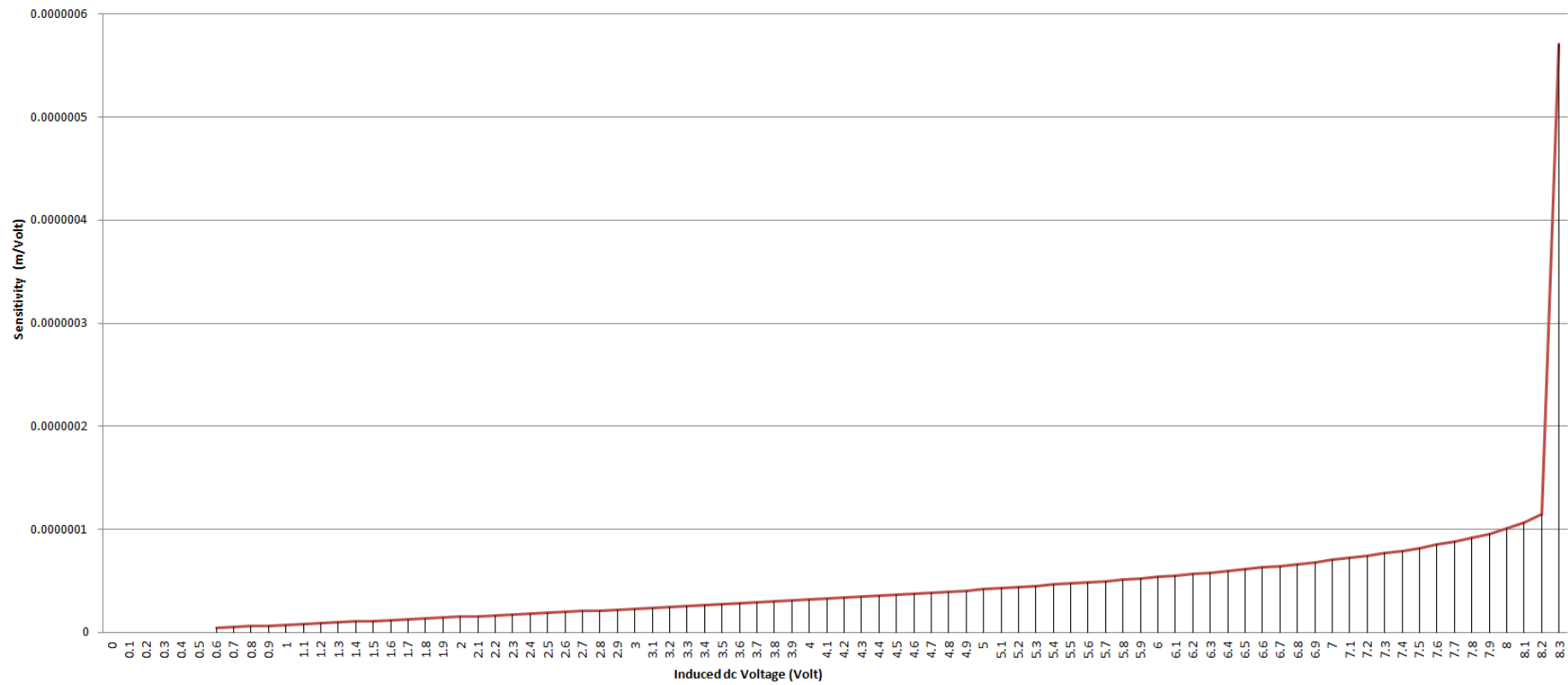


Fig. F.5 Sensitivity (m/Volt) vs. DC induced dc potential (Volt).



## F.5 Optimization of the Controlling Parameters

The proposed design optimization technique flourished in this section should assist microfabricators in producing a robust, and highly sensitive cantilever-based biosensor without enduring the hardship involved due to the iterative process during fabrication to reach a satisfactory results with optimal dimensions. In order to maintain the applicability of a slender Bernoulli-Euler beam assumption, Table F.2 defines the controlling parameters of the system in a ratio manner based on a defined length of the cantilever beam. The objective is to delay the static pull-in phenomenon, which shall avail the benefit of increasing the dynamic range of the biosensor. Also, it contributes into increasing the stability functional domain of the biosensor. Eqs. F.27-30 are evaluated numerically point-by-point based on Table F.2, where stable solutions for A-B pair are being considered.

Parameter	Definition	Defined expression	Unit
$L$	Length of the beam	$L$ (variable)	$\mu\text{m}$
$b_{beam}$	Width of the beam	$b_{beam} = 0.02 \times L$	$\mu\text{m}$
$L_{plate}$	Total length of the plate	$L_{plate} = 0.2 \times L$	$\mu\text{m}$
$b_{plate}$	Width of the plate	$b_{plate} = 0.08 \times L$	$\mu\text{m}$
$H$	Uniform thickness	$h = 0.006 \times L$	$\mu\text{m}$
$\hat{L}_c$	Half length of the plate	$\hat{L}_c = 0.1 \times L$	$\mu\text{m}$
$D$	Gap distance	$d$ (variable)	$\mu\text{m}$
$E$	Modulus of Elasticity	2.5	GPa
$\epsilon$	Permittivity of free space	$8.854 \times 10^{-12}$	F/m
$A_{beam}$	Cross sectional area of beam	$A_{beam} = b_{beam} \times h$	$\text{m}^2$
$I$	Second moment of inertia	$I = 1/12 \times b_{beam} \times h^3$	$\text{m}^4$
$\rho$	Density	1430	$\text{Kg}/\text{m}^3$
$\mathcal{F}$	Fringing Field Effect Constant	1.03	---
$\hat{M}$	Effective mass of the plate	$\hat{M} = b_{plate} \times h \times \rho \times L_{plate}$	Kg
$J$	Mass moment of inertia	$J = 1/3 \times \hat{M} \times \hat{L}_c^2$	$\text{Kg} \cdot \text{m}^2$

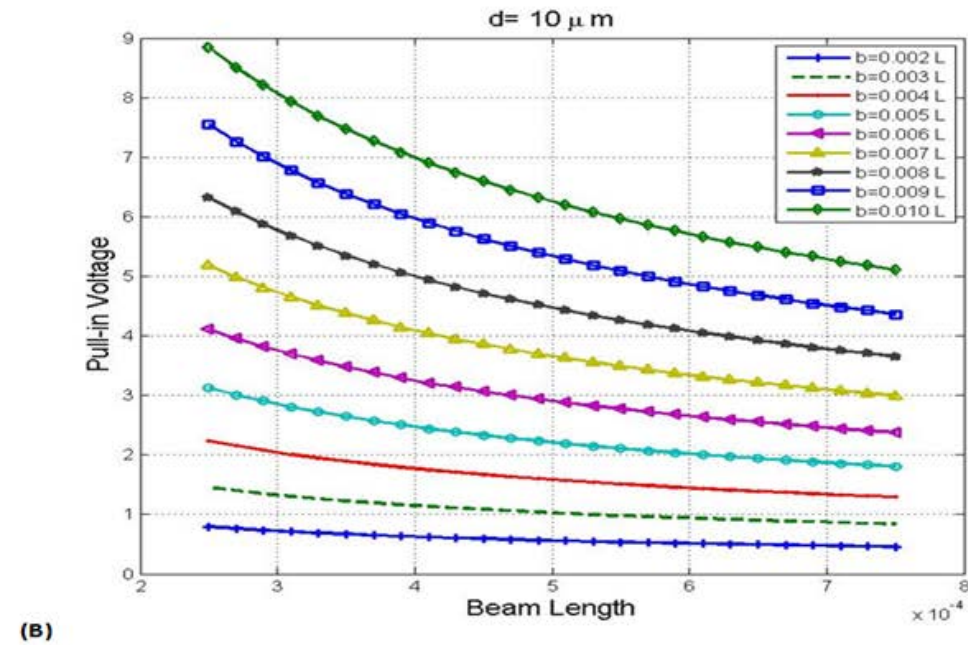
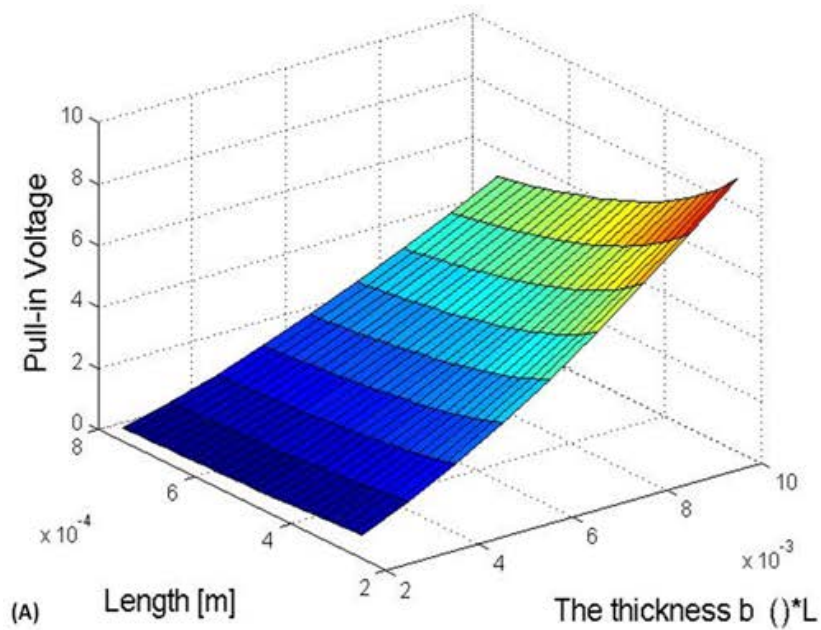
**Table F.2** Controlling parameters of the microbeam-microplate structure made of **PI-2562 Polyimide**.

The optimization process is carried out by varying beam's length, and uniform thickness of the structure with respect to static pull-in phenomenon (Fig. F.6A-B), and then varying gap distance and beam's length with respect to static pull-in phenomenon (Fig. F.7A-B). Increasing static DC potential should contribute into increasing softening spring characteristics attributable to electrostatic negative stiffness, which also resembles the quadratic nature of material nonlinearities. It is manifested in Fig. F.6, and F.7 that there is a linear relation among static pull-in potential, length of the beam, structure's uniform thickness, as well as the segregating gap distance. Thus, no optimal point is found.

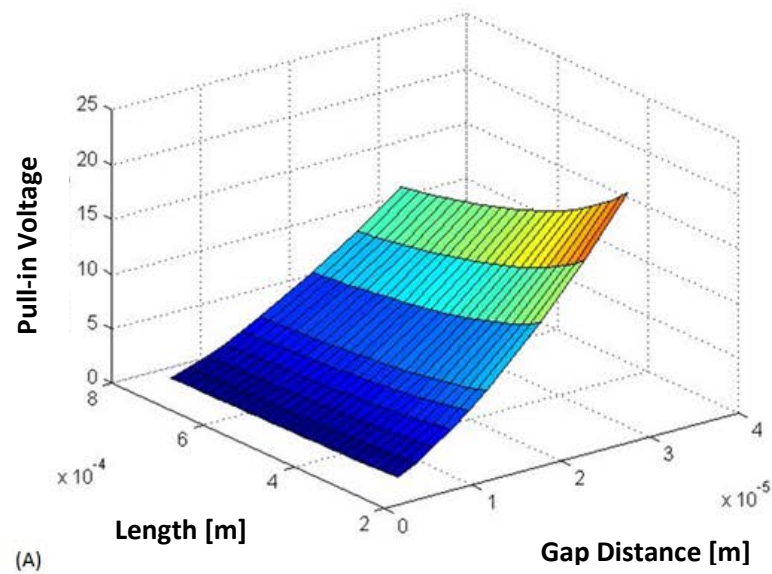
Figure F.7B can be utilized by any designers who are utilizing Polyimide 2562 conductive polymer to construct their sensor structure, regardless of their sensing applications. It should be cleared that in this 2D figure, the variations in pattern don't reflect the beam's deflection modes. This figure is read in a certain manner by first selecting a targeted pull-in potential (y-axis), which in this study is 15 Volt to be the operating dynamic range of the sensor. Second,

---

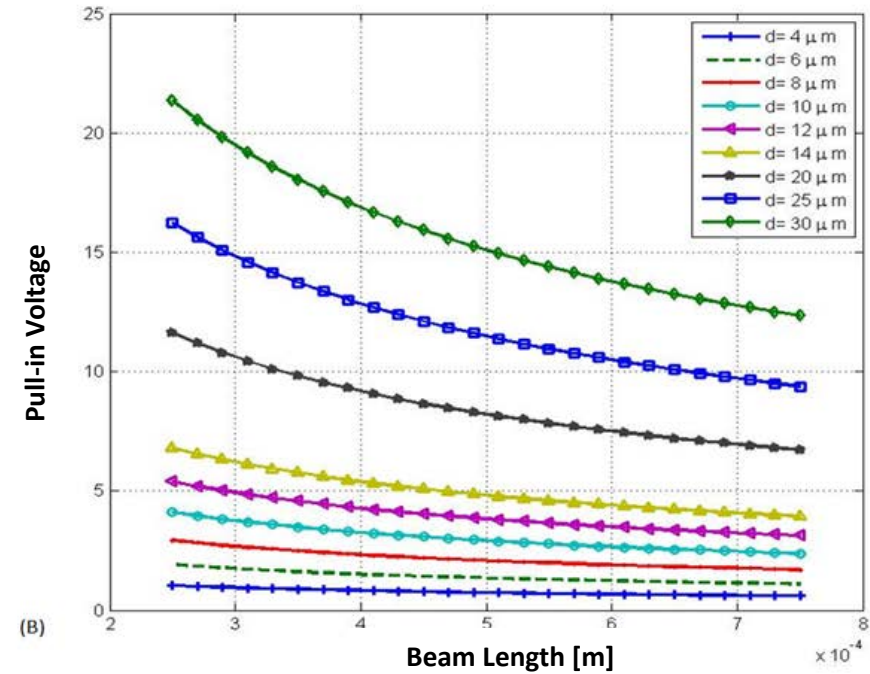
investigating the variations of beam's length (x-axis) as well as segregating gap distance that would meet the targeted pull-in value (15 Volt) – beam's length is 500  $\mu\text{m}$  with a gap distance of 30 $\mu\text{m}$ . Third, uniform thickness is achieved as per the defined expression in Table 1, being 0.006 of beam's length, and accordingly other parameters in table F.2 are followed.



**Fig. F.6** (A) 3D variations of beam length (250-750  $\mu m$ ), uniform thickness as per a defined relation of  $b = (0.002-0.010) \times L$  (where thickness is denoted as  $b$  in this figure), and static pull-in voltage (Volt). (B) 2D representations of varying beam's length, uniform thickness, and static pull-in voltage while fixing a gap distance at 10  $\mu m$ . The material is Polyimide 2562 conductive polymer.



(A)



(B)

**Fig. F.7** (A) 3D variations of beam length (250-750  $\mu\text{m}$ ), gap distance (4-30 $\mu\text{m}$ ), and static pull-in voltage (0-23 Volt). (B) 2D representations of varying beam's length, gap distance, and static pull-in voltage, whereas uniform thickness is fixed as per the defined relation in Table 1 ( $h = 0.006 \times L$ ). The material is Polyimide 2562 conductive polymer.

# **Appendix G: Reprint Permission**

Imperial College  
London

Mail > Inbox 5 results in entire mailbox

favourites

Alqabandi, Jassim

Inbox (2597)

Drafts (11)

Sent Items

Deleted Items (95)

Junk E-Mail

Notes

RSS Feeds

.....

Mail

Calendar

Contacts

Tasks

Public Folders

New ▾ Delete ▾ Move ▾ Filter ▾ View ▾

Bertil Damato

Conversations by Date ▾ Newest on Top

Older

✓

Courtesy Request of a Publ...

Alqabandi, Jassim; LOOC

20/09/2011

sign out | Alqabandi, Jassim ▾

Find Someone

Options ▾ ? ▾

Alqabandi, Jassim

20/09/2011

Cheetham Gary (RQ6) RLBUHT [Gary.Cheet...

←

←

→

Actions

To: Alqabandi, Jassim

Inbox

25 July 2011 08:10

- You forwarded this message on 20/09/2011 14:59.

Hello Jassim

Professor Damato is happy for you to use the image (see below).

Best wishes.

Gary Cheetham  
Data Manager, Liverpool Ocular Oncology Service  
0151 706 3965

Dear Gary,

Thanks. Can you say OK.

Regards,  
Bertil

394

Mail > Inbox 6 results in entire mailbox

Find Someone

Options ?

favourites

Alqabandi, Jassim

Inbox (2597)

Drafts [11]

Sent Items

Deleted Items (95)

Junk E-Mail

Notes

RSS Feeds

Mail

Calendar

Contacts

Tasks

Public Folders

New Delete Move Filter View

roger kamm

Conversations by Date Newest on Top

Older

Re:- Design and Nature 2014

Alqabandi, Jassim

21/01/2014

Reprinting Permission

Roger Kamm; Alqabandi, Jassi...

11/09/2013

Alqabandi, Jassim

Dear Prof. Kamm, Thank you so much for your email and you...

08/08/2013

Roger Kamm [rdkamm@MIT.EDU]

To: Alqabandi, Jassim

Inbox

07 August 2013 21:18

- You replied on 11/09/2013 21:24.

Dear Jassim,

Yes, you certainly have our permission to use the photograph. But I believe that Lab on Chip holds the copyrights, so you might also need to get their approval. They should have information on that on their website.

Regards,

-Roger

Alqabandi, Jassim

Sent Items

07 August 2013 21:15

Dear Prof. Roger Kamm,



**Title:**

Design, fabrication and implementation of a novel multi-parameter control microfluidic platform for three-dimensional cell culture and real-time imaging

**Author:**

Vernella Vickerman, Jennifer Blundo, Seok Chung, Roger Kamm

**Publication:** Lab on a Chip**Publisher:** Royal Society of Chemistry**Date:** Jul 18, 2008

Copyright © 2008, Royal Society of Chemistry

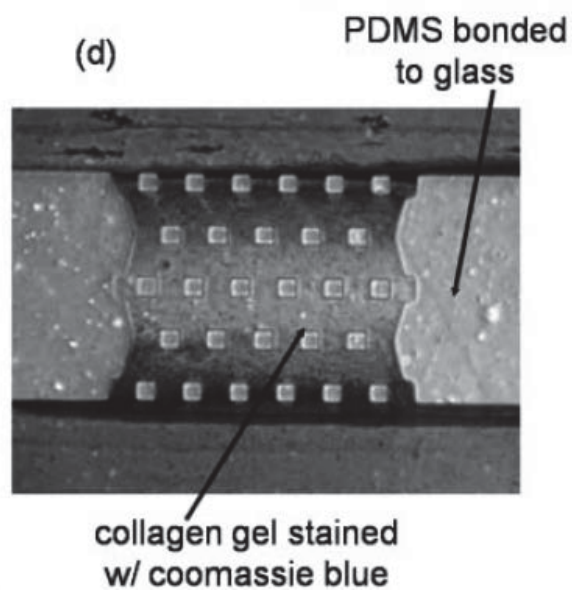
User ID	
Password	
<input type="checkbox"/> Enable Auto Login	<b>LOGIN</b>
<a href="#">Forgot Password/User ID?</a>	
<b>If you're a <a href="#">copyright.com</a> user,</b> you can login to RightsLink using your <a href="#">copyright.com</a> credentials. Already a <b>RightsLink user</b> or want to <a href="#">learn more?</a>	

This reuse request is free of charge. Please review guidelines related to author permissions here: <http://www.rsc.org/AboutUs/Copyright/Permissionrequests.asp>

**BACK****CLOSE WINDOW**

Copyright © 2013 [Copyright Clearance Center, Inc.](#) All Rights Reserved. [Privacy statement.](#) Comments? We would like to hear from you. E-mail us at [customercare@copyright.com](mailto:customercare@copyright.com)





(Reprinted with permission from Vernella, V. et al. [Ref 1])

1. V. Vernella et al., *Design, fabrication and implementation of a novel multi-parameter control microfluidic platform for three-dimensional cell culture and real-time imaging.*, *Lap Chip*, 2008, **8**, 1468-1477.

Mail > Inbox 120 results in entire mailbox

Find SomeoneOptions

favourites

Alqabandi, Jassim

Inbox (2596)

Drafts [11]

Sent Items

Deleted Items (95)

Junk E-Mail

Notes

RSS Feeds

Mail

Calendar

Contacts

Tasks

Public Folders

NewDeleteMoveFilterView

lee

Conversations by DateNewest on Top

IEEE Conference in UK.

Secoli, Riccardo

05/11/2013

Planning and Writing yo...

Bowyer, Stuart

24/10/2013

Thefts from College; ima...

Fairhurst, Guy N

10/10/2013

Postgraduate Summer Fil...

David Goldsmith - ICU Presid...

27/08/2013

Post-Grad Cinema Night:...

Cinema

19/08/2013

Reprinting Permission

Alqabandi, Jassim

07/08/2013

2nd CFP: IROS Workshop...

Rodriguez Y Baena, Ferdinan...

06/08/2013

CAREERS: Recruitment Fa...

Carpenter, Robert J

06/08/2013

Reprinting Permission

Alqabandi, Jassim

To: [ipllee@socrates.berkeley.edu](mailto:ipllee@socrates.berkeley.edu)

Cc: [ipllee@berkeley.edu](mailto:ipllee@berkeley.edu)

Attachments: [Reprinted with permission ~1.pdf \(368 KB\)](#)

Sent Items07 August 2013 20:51

Dear Prof. Lee,

I hope this finds you well!

We are doing an extensive literature review for our publication on the subject of Lab on a Chip; we will be highly appreciative if you can please give us the permission to reprint the micrograph image (attached).

Very best wishes,

Jassim



**Title:**

A novel high aspect ratio microfluidic design to provide a stable and uniform microenvironment for cell growth in a high throughput mammalian cell culture array

**Author:**

Paul J. Hung, Philip J. Lee, Poorya Sabounchi, Nima Aghdam, Robert Lin, Luke P. Lee

**Publication:** Lab on a Chip

Royal Society of Chemistry

**Date:**

Nov 2, 2004

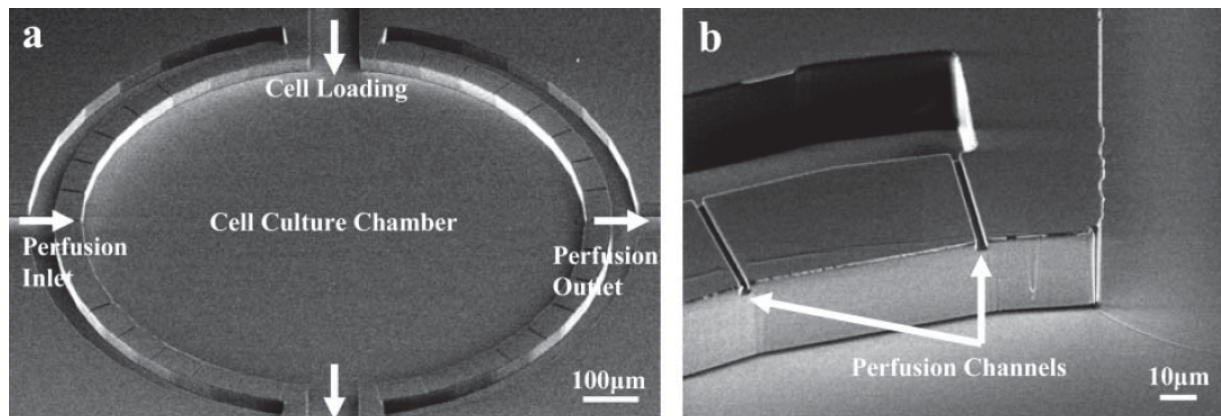
Copyright © 2004, Royal Society of Chemistry

User ID	
Password	
<input type="checkbox"/> Enable Auto Login	<b>LOGIN</b>
<a href="#">Forgot Password/User ID?</a> <b>If you're a <a href="#">copyright.com</a> user,</b> you can login to RightsLink using your <a href="#">copyright.com</a> credentials. Already a <b>RightsLink user</b> or want to <a href="#">learn more?</a>	

This reuse request is free of charge. Please review guidelines related to author permissions here: <http://www.rsc.org/AboutUs/Copyright/Permissionrequests.asp>

**BACK** **CLOSE WINDOW**

Copyright © 2013 [Copyright Clearance Center, Inc.](#) All Rights Reserved. [Privacy statement.](#) Comments? We would like to hear from you. E-mail us at [customercare@copyright.com](mailto:customercare@copyright.com)



(Reprinted with permission from Hung, P. J. et al. [Ref 1])

1. P. J. Hung, et al., *A novel high aspect ratio microfluidic design to provide a stable and uniform microenvironment for cell growth in a high throughput mammalian cell culture array.*, *Lap Chip*, 2005, **5**, 44-48.